

Robust Artificial Intelligence for Space Traffic Management

Luis Sánchez Fernández-Mellado

Submitted in fulfilment of the requirements
for the degree of Doctor of Philosophy

Aerospace Centre of Excellence
Department of Mechanical and Aerospace Engineering
University of Strathclyde, Glasgow

April 17, 2025

This thesis is the result of the author's original research. It has been composed by the author and has not been previously submitted for examination which has led to the award of a degree.

The copyright of this thesis belongs to the author under the terms of the United Kingdom Copyright Acts as qualified by University of Strathclyde Regulation 3.50. Due acknowledgement must always be made of the use of any material contained in, or derived from, this thesis.

Signed:

Date: April 17, 2025

CASANDRA. — Apolo, dios de la profecía, me encomendó el cumplimiento de este servicio.

CORIFEO. — ¿Acaso fue herido, a pesar de ser dios, por deseo amoroso?

CASANDRA. — Yo tenía antes pudor de hablar de estas cosas.

CORIFEO. — ¡Claro! Todo el mundo es más delicado, cuando es feliz.

CASANDRA. — ¡Bien que luchó para conseguirme, suspirando de amor por mí!

CORIFEO. — ¿Y llegasteis a compartir la acción de engendrar?

CASANDRA. — Luego de haber consentido, no le cumplí mi palabra a Loxias.

CORIFEO. — ¿Estabas ya entonces posesa por el arte de adivinar?

CASANDRA. — Ya venía yo vaticinando todos los sufrimientos a los ciudadanos.

CORIFEO. — ¿Cómo, entonces, quedaste indemne de la ira de Loxias?

CASANDRA. — Por haber cometido esta falta, ya no convengo a nadie de nada.

CORIFEO. — Nos parece, no obstante, que haces vaticinios dignos de creerse.

Esquilo. La Orestíada I: Agamenón [Esquilo, 1986]
(Aeschylus. Oresteia I: Agamemnon)

Acknowledgements

I would like to thank to the ESA's Space Debris Office for funding this project, and more specifically to Dr Klaus Metz and Dr Silvia Sanvido for their continuous support and advice during the PhD, and their welcoming during my stays in Germany.

During my research, I had the opportunity to collaborate with different organisations. I would like to thank CNES for hosting me in Toulouse for four great months, but especially Dr Christophe Taillan for all his dedication, both with me and the bureaucracy. I would also like to acknowledge the team at the UPM's ETSI Sistemas Informáticos for their contribution to my research in terms of Artificial Intelligence, with special emphasis on Dr Victor Rodríguez-Fernández and Emma Stevenson.

No doubt this research would not have been possible without the presence of friends all around the world, but especially those being with me in Glasgow: Alba, Ada, Qaisha, Pete and the rest of the members of the Junior Mountaineering Club of Scotland. I would like to acknowledge my colleagues at the Aerospace Centre of Excellence Simao, Paul, Marilena..., and especially Dr Yirui Wang for his infinite doses of optimism.

A mi familia, en especial a mis padres, Javier y Beba, que siempre me han apoyado, y a mis hermanos, Nacho, Arturo, Miguel y Luisa, por recordarme la importancia de diseñar lavadoras especiales.

And last but, definitely, not least, to Bea, a lifelong companion who believes in me more than myself and makes me better in every aspect. Without your constant support, this would have not been possible.

Abstract

This work proposes a new methodology to manage the increase in space traffic and ensure the safe and sustainable utilisation of space by all actors involved in the New Space context. The proposed methodology aims to improve the automation and robustness of Space Traffic Management. The resulting framework constitutes CASSANDRA, an intelligence agent to robustly support operators on complex Space Traffic Management tasks accounting for aleatory and epistemic uncertainty and implementing Artificial Intelligence techniques to address the problems.

This research presents an evidence-based framework to assist operators in the conjunction risk assessment decision-making process, using Dempster-Shafer theory of evidence to model both aleatory and epistemic uncertainty on the object's state vector. This framework assists operators in making robust decisions in space conjunction assessment based on the value of the probability of collision and its correctness from the available information. The framework is designed to cope with Conjunction Data Messages. These messages are the most common standard protocol for conjunction communication, and the proposed methodology models the epistemic uncertainty affecting them. The framework also addresses the Conjunction Avoidance Manoeuvre design by providing robust optimal strategies accounting for both aleatory and epistemic uncertainty.

The framework enhances the autonomy of Space Traffic Management using Artificial Intelligence methods. These techniques facilitate the autonomy of the decision processes through the creation of faster surrogate models, data-driven models and decision-making architectures. The use of Artificial Intelligence in this research intends to improve the automation of the Space Traffic Management system. First, a Decision Support System based on Multi-Criteria Decision-Making and Game Theory is proposed to prioritise the best avoidance strategies based on the available alternatives and the operator's criteria and constraints. Second, automation is improved by implementing Machine Learning and Deep Learning techniques, like Random Forests or Neural Networks, to speed up the conjunction assessment process accounting for

both types of uncertainty while providing reliable levels of accuracy.

Finally, this work presents some examples where the methodology is tested on a range of real and synthetic scenarios addressing the multiple-encounter events problem, presenting a pipeline integrating the different elements of the framework, and comparing the proposed framework with the current approaches followed by the European and French Space Agencies.

Contents

Acknowledgements	iii
Abstract	iv
Contents	vi
List of Figures	xii
List of Tables	xxiii
List of Algorithms	xxx
Acronyms	xxxii
1 Introduction	1
1.1 Research objectives and contributions	2
1.1.1 Publications	4
1.1.2 Thesis structure	6
1.2 Research funding	9
2 State of the Art	10
2.1 Robustness	15
2.1.1 Epistemic uncertainty	21
2.2 Automation	25
2.2.1 Artificial intelligence	27
2.2.2 Artificial intelligence for automation	38
Robust AI for STM	Luis Sánchez Fernández-Mellado
	vi

I	Methodology and algorithms	44
3	Evidence-based conjunction classification system	45
3.1	Modelling epistemic uncertainty	46
3.1.1	Dilution of the probability of collision	47
3.2	Dempster-Shafer theory of evidence	50
3.2.1	Epistemic conjunction risk assessment	53
3.2.2	Data fusion	59
3.3	Conjunction classification criteria	65
3.3.1	Probability of collision as classification criterion	65
3.3.2	Evidence-based classification criteria	66
3.3.3	Criteria comparison	67
3.3.4	Extended evidence-based classification criterion	73
3.4	Chapter summary	76
4	Modelling epistemic uncertainty in Conjunction Data Messages	77
4.1	Epistemic uncertainty in the CDMs	78
4.2	Methodology	80
4.2.1	Scaling of the CDMs	85
4.2.2	α -cuts and DSt Structures	88
4.3	Conjunction Data Message epistemic analysis	90
4.3.1	Sensitivity analysis	96
4.3.2	Robustness	104
4.4	Chapter summary	109
5	Robust collision avoidance manoeuvres	111
5.1	Linear model for impulsive manoeuvres	112
5.2	Robust optimal impulsive avoidance manoeuvre	116
5.2.1	Optimisation of impulsive manoeuvres: aleatory uncertainty . . .	116
5.2.2	Optimisation of impulsive manoeuvres: epistemic uncertainty . .	118
5.2.3	Impulse magnitude optimisation	120

5.3	Low-Thrust robust optimal avoidance manoeuvre	120
5.3.1	Magnitude and arc-length optimisation	123
5.4	Numerical scenarios	124
5.4.1	Impulsive CAM: minimisation of the PoC under aleatory uncertainty	124
5.4.2	Impulsive CAM: minimisation of the PoC under epistemic uncertainty	127
5.4.3	Low-thrust scenario	135
5.5	Chapter summary	139
6	Robust decision-making	140
6.1	Multi-criteria decision-making	141
6.1.1	Alternatives-Criteria matrix	142
6.1.2	Normalisation techniques and weights distribution	143
6.1.3	MCDM techniques	145
6.2	Game theory	147
6.2.1	Game matrix	149
6.2.2	Equilibrium points	151
6.3	Conjunction decision-making: collaborative case	152
6.3.1	Satellites information	153
6.3.2	MCDM parameters	154
6.3.3	Analysis	155
6.4	Conjunction decision-making: non-collaborative case	160
6.4.1	Satellites information	160
6.4.2	Game theory matrices	163
6.4.3	Analysis	165
6.5	Chapter summary	168
II	Applications	170
7	Robust classification system on real encounter scenarios	171

7.1	Area-based epistemic classification criterion	172
7.2	Thresholds calibration	175
7.3	Comparison against real operators approach	177
7.3.1	Space Debris Office conjunction risk assessment	178
7.3.2	CNES conjunction risk assessment	188
7.4	Statistical analysis of Swarm-A dataset	196
7.5	Chapter summary	200
8	Artificial intelligence for Space Traffic Management	202
8.1	Intelligent classification system	203
8.1.1	Synthetic dataset	204
8.1.2	Machine learning techniques and metrics	206
8.1.3	Classification results	208
8.2	Intelligent classification accounting for robust CAM	212
8.2.1	Manoeuvre-driven epistemic classification criterion	212
8.2.2	Definition of the dataset	213
8.2.3	Machine learning techniques and metrics	218
8.2.4	Prediction results	220
8.2.5	Computational time	221
8.3	Intelligent robust conjunction analysis with CDMs	222
8.3.1	Databases	223
8.3.2	Architectures	227
8.3.3	Results	233
8.4	Chapter summary	237
9	Multiple encounters	239
9.1	Multiple encounters	240
9.2	Subsequent encounters	242
9.2.1	Avoidance strategies	242
9.2.2	Risk assessment	245
9.3	Multiple encounters within a constellation	260

9.3.1	Avoiding and returning strategies	260
9.3.2	Risk assessment	262
9.4	Summary	272
10	CASSANDRA	274
10.1	CASSANDRA framework	277
10.1.1	Modules	278
10.1.2	Robust State Estimation module	280
10.1.3	Intelligent Decision Support System	284
10.1.4	Collision Avoidance Manoeuvre module	286
10.1.5	Automated Catalogue Screening module	286
10.2	Robust decision-making based on Bayesian state estimation framework .	292
10.2.1	Study case	293
10.3	Robust catalogue screening	302
10.3.1	Pipeline	303
10.3.2	Study case	308
10.4	Chapter summary	313
11	Conclusion	315
11.1	Recommendations	324
III	Appendices	329
A	Dilution-free metrics	330
A.1	Dilution of probability and epistemic uncertainty	331
A.2	Red Plausibility of Collision	332
A.3	Blue Plausibility of Collision	334
A.4	Comparison of metrics	334
A.5	Introduction to dilution-free robust conjunction assessment	337
B	Geometries for conjunction classes	340

C Algorithms for robust optimal collision avoidance manoeuvres	347
C.1 Min-max impulsive optimisation algorithm	347
C.2 Min-max impulsive magnitude optimisation algorithm	349
C.3 Low-thrust collision avoidance manoeuvre optimisation	351
C.3.1 propellant saving optimisation: acceleration reduction	352
C.3.2 propellant saving optimisation: burning-time reduction	352
D Machine learning hyperparameters	353
Bibliography	358

List of Figures

2.1	General structure of single-layer ANN model.	31
2.2	General structure of a single Decision Tree.	33
2.3	General structure of a Random Forest.	34
2.4	Example of 4-Nearest Neighbour.	35
2.5	Example of Support Vector Machine.	36
2.6	Scheme of the Light Gradient Boosting machine process.	37
3.1	Dilution of probability when increasing the standard deviation, for different values of miss distance.	48
3.2	Flattening of the Normal Distribution curve when the standard deviation increases, causing the dilution of probability.	49
3.3	Dempster-Shafer structures for μ_ξ and σ_ξ : plausibility (solid lines) and belief (dashed lines). (a) and (b): intervals equally reliable; (c) and (d): intervals non equally reliable.	55
3.4	Joint body of evidence for μ_ξ and σ_ξ with each FE's <i>bpa</i> if intervals equally and non-equally reliable, respectively.	57
3.5	<i>Bel</i> (dash line) and <i>Pl</i> (solid line) curves of the PoC. (a) Equally reliable intervals; (b) one interval being more reliable than the other.	59
3.6	Conjunction geometry on the impact plane centred on the chaser. (a) Sources equally reliable. (b) Sources non-equally reliable.	63

3.7	Dempster-Shafer structures for μ_ξ and σ_ξ , before combining sources (black and green, plausibility in solid lines, belief in dashed lines) and after combining sources with Dempster's rule (pink shaded region) and mixing rule (dashed-pointed line, blue equally reliable, red non-equally reliable): (a) and (b) sources equally reliable; (c) and (d) sources non-equally reliable.	64
3.8	Representative scenario of a single case of <i>Geo. 1</i> : (a) encounter geometry, (b) the associated <i>Bel</i> and <i>Pl</i> curves.	70
3.9	Histograms comparing criterion using (a) only the value of PoC and (b) the evidence-based <i>Criterion 1</i> . Each colour represents the fraction of samples from each bin on the histogram (a) that moves to one of the bins on the histogram (b).	71
3.10	Histograms comparing criterion using (a) only the value of PoC and (b) the evidence-based <i>Criterion 2</i> . Each colour represents the fraction of samples from each bin on the histogram (a) that moves to one of the bins on the histogram (b).	73
3.11	Histograms comparing criterion using (a) only the value of PoC and (b) the evidence-based <i>Criterion 3</i> . Each colour represents the fraction of samples from each bin on the histogram (a) that moves to one of the bins on the histogram (b).	75
4.1	Encounter geometry on the impact plane: family of ellipses from (a) a DSt analysis with one interval per source, (b) sequence of CDMs.	81
4.2	DKW region for a given set of samples. The width of the region, ε , is indicated. In solid blue the eCDF, in dashed green the DKW bands, and in dashed-pointed orange the CDF of the equally weighted sum of Gaussian distributions centred at the samples.	82
4.3	Gaussian distributions centred at the samples for building the eCDF fit. In blue the eCDF, in grey the pdf of individual Gaussian distributions, and in orange the CDF of the equally weighted sum.	83

4.4	p-box derived from a DKW region. In solid blue the eCDF, in dashed-green the DKW bands, in dashed-pointed red the p-box, and in dashed vertical black the 1% and 99% percentiles of the upper and lower p-box bounds, respectively.	85
4.5	CDMs fitting law: (a) $y' = e^{-3t'}$ (thick red line) and the dimensionless covariance determinant for some sequences of CDMs (thinner lines), (b) Fitted law (dashed-pointed red) of a single sequence of CDMs (dashed-pointed black).	87
4.6	eCDF for μ_ξ weighing the samples (blue) and with samples equally weighted (dashed red).	88
4.7	Intervals partition derived from a p-box. In solid blue the eCDF, in dashed-pointed red the p-box, in thin dotted blue and grey the alpha-cuts (1 and 7 cuts, respectively), in dashed blue the 2 intervals partition, in dashed black the 8 intervals partition.	89
4.8	Joint Body of Evidence with artificially generated FEs (top-left and bottom-right ones) not containing any sample (black dots).	90
4.9	Sequence of CDMs. (a) Evolution of the PoC in the CDMs. (b) Uncertain geometry from the series of CDMs.	91
4.10	CDMs weighting law for the whole sequence. (a) Evolution of covariance determinant (black) and fitting law (red). (b) CDM weighting versus the time to the TCA.	93
4.11	eCDF (solid blue), p-box (solid green) and Dempster-Shafer structure (pointed-dashed red) from where obtained the intervals for (a) μ_ξ and (b) σ_ξ^2	94
4.12	<i>Pl</i> and <i>Bel</i> curves for $PoC \geq PoC_0$ for 4-intervals partition.	95
4.13	<i>Pl</i> and <i>Bel</i> curves for $PoC \geq PoC_0$ with 4-intervals partition for three different values of the confident interval: $\delta=0.001$ (red), $\delta=0.5\%$ (blue), $\delta=0.999\%$ (black).	97

4.14 eCDF (solid blue) and DKW region (dashed lines) of μ_ξ for three different values of the confident interval: $\delta=0.001$ (black), $\delta=0.5\%$ (green), $\delta=0.999\%$ (red). 98

4.15 eCDF (dashed blue), p-box (dashed-pointed green) and Dempster-Shafer structure (solid lines) for μ_ξ for different α -cut partitions: black for one cut, red for three cuts, magenta five cuts, grey for seven cuts. 99

4.16 *Pl* and *Bel* curves for $PoC \geq PoC_0$ for a different number of α -cuts per variable: one (black), two (blue), three (red), four (green), five (magenta), six (yellow), seven (grey). 99

4.17 Modification on the number of CDMs: whole sequence and half of the sequence. (a) eCDF and DKW bands: solid blue and solid green for the whole sequence, dashed red and dashed black for half sequence. (b) *Pl* and *Bel* curves, black for the whole sequence, and blue for half sequence. 102

4.18 *Pl* and *Bel* curves for $PoC \geq PoC_0$ with 4-intervals partition with (black) and without (blue) removal of FEs not containing any sample. . 103

4.19 eCDF and DKW bands weighting the samples (solid blue and dashed green, respectively) and not weighting them (dashed red and dashed black, respectively). (a) μ_ξ and (b) σ_ξ^2 105

4.20 *Pl* and *Bel* curves for $PoC \geq PoC_0$ with 4-intervals partition with (black) and without (blue) weighing the CDMs. 106

4.21 Sequence of CDMs, including the poor quality ones. (a) Evolution of the PoC in the CDMs. (b) Uncertain geometry from the series of CDMs. . . 107

4.22 Dempster-Shafer structures with and without poor-quality CDMs, eCDF in solid blue and dashed red, DKW in solid green and dashed black, respectively. (a) μ_ξ , (b) σ_ξ^2 . Orange circle highlighting the region with the poor-quality CDMs. 108

4.23 *Pl* and *Bel* curves for $PoC \geq PoC_0$ for 4-intervals partition accounting for the poor quality CDMs. Black, only good quality CDMs; blue, including the poor quality CDMs. 109

5.1	General configuration of a space encounter. Two orbits in a collision path (blue and green) and the modified orbit due to a CAM (purple).	113
5.2	Impact plane of the encounter centred at the secondary object.	115
5.3	CAM strategy for the LT scenario, with burning time between θ_{m0} and θ_{mf} , thrust magnitude ϵ and direction α , and the encounter at θ_c	121
5.4	Manoeuvre geometry, with orbit in blue, manoeuvre in orange and manoeuvre angles in red.	125
5.5	Components of the unit vector $\delta\hat{\mathbf{v}}_{opt} = [\delta\hat{v}_t \ \delta\hat{v}_n \ \delta\hat{v}_h]$ parallel to the optimum impulse, $\delta\mathbf{v}_{opt}$, as a function of the angular difference between manoeuvre and encounter, $\Delta\theta = \theta_c - \theta_m$. Black, using the linear model; red, using the grid search.	126
5.6	Secondary object's position ellipsoid of uncertainty at the initial epoch. Thick green line: trajectory; orange arrow: position vector; black arrow: velocity vector; green thin line: ellipsoid.	128
5.7	Representation of the effect of the epistemic parameter λ . Purple: aleatory uncertainty ellipsoid. Pink arrows: compatible displacements due to λ_μ . Compatible ellipsoid shrink/augmentation due to λ_σ	129
5.8	Encounter geometry at the impact plane with two sources of information providing uncertain (aleatory and epistemic) information. Red triangle: nominal position. Blue and green: samples and ellipses of Source 1 and Source 2, respectively. Orange: HBR.	131
5.9	Evolution of the direction of the optimal impulse, $\delta\hat{\mathbf{v}}$, as a function of the position of the manoeuvre, $\Delta\theta$. Solid line: with optimisation of the magnitude of the impulse; points: without optimisation of the magnitude. Both cases coincide. Red: tangential component; blue: normal component; green: out-of-plane component.	132
5.10	Evolution of the impulse magnitude as a function of the position of the manoeuvre, $\Delta\theta$. Red solid line: impulsive magnitude optimised; blue dashed line: without optimising the impulse magnitude.	132

5.11 Evolution of worst-case scenario PoC with the position of the manoeuvre, $\Delta\theta$. Red, with impulse magnitude optimisation. Blue, without optimising the impulse magnitude. Solid lines: worst-case scenario. Dashed lines: the worst-case PoC among 20 ellipses per source randomly drawn from the intervals. Dashed-dotted black line, PoC threshold. 133

5.12 Worst-case scenario uncertain variables evolution with respect to the difference between encounter and manoeuvre positions, $\Delta\theta$. From left to right and top to bottom: $\mu_\xi, \mu_\zeta, \sigma_\xi^2, \sigma_\zeta^2, \sigma_{\xi\zeta}$. Red solid line: with impulse magnitude optimisation; blue solid line: without impulse magnitude optimisation. Horizontal dashed line: lower bound; horizontal dashed pointed: upper bound. Black: Source 1; green: Source 2. 133

5.13 Uncertain ellipses displaced by an impulse applied at 3.5 revolutions before the encounter. Blue and green dashed lines: uncertain ellipses according to the linear model; purple and black solid lines: uncertain ellipses according to the MC simulation. Red dashed circle centred at the origin: HBR (position highlighted with indicative arrow). Triangles (position highlighted with indicative arrows): displaced nominal position, red for linear model, black for MC simulation. Note that the good agreement of both methods makes the MC ellipses (solid) and CAM linear method ellipses (dashed) overlap. Same with the nominal miss distance positions (triangles). 134

5.14 (a) Evolution of the deflection due to the robust optimal CAM. Red lines: MC simulation, solid for ξ , dashed for ζ . Dots for the linear model: in green, ξ ; in blue, ζ . (b) Evolution of the PoC due to the manoeuvre: solid red line for MC simulation; blue dots for the linear model. 135

5.15 PoC evolution versus the difference in true anomaly between the mid-point of the Low-Thrust manoeuvre and the encounter. Blue: maximum thruster capacity and arc-length. Red: optimised acceleration magnitude. Green: optimised arc-length. Solid lines: optimal direction. Dashed line: tangential manoeuvre. 136

5.16 Acceleration magnitude evolution versus the difference in true anomaly between the mid-point of the Low-Thrust manoeuvre and the encounter. Blue: maximum thruster capacity and arc-length. Red: optimised acceleration magnitude. Green: optimised arc-length. Solid lines: optimal direction. Dashed line: tangential manoeuvre. 137

5.17 Burning time evolution versus the difference in true anomaly between the mid-point of the Low-Thrust manoeuvre and the encounter. Blue: maximum thruster capacity and arc-length. Red: optimised acceleration magnitude. Green: optimised arc-length. Solid lines: optimal direction. Dashed line: tangential manoeuvre. 137

5.18 Equivalent velocity change to the difference in true anomaly between the mid-point of the Low-Thrust manoeuvre and the encounter ($\Delta\theta = \theta_c - \theta_m$). Blue: maximum thruster capacity and arc-length. Red: optimised acceleration magnitude. Green: optimised arc-length. Solid lines: direction of the impulse according to the proposed algorithm. Dashed line: tangential manoeuvre. Black dashed line: velocity change used on the hypothetical impulsive manoeuvre. 138

6.1 TOPSIS ideal solutions given the set of alternatives $\mathcal{A} = \{A_1, \dots, A_9\}$, evaluate on criteria C_1 (Beneficial) and C_2 (Cost). 148

6.2 Criteria score versus the number of the alternative or, equivalently, the distance between manoeuvre and encounter. Blue, PoCR (beneficial criterion); green, ManC (cost criterion); ref, OpC (cost criterion). 155

7.1 Pl and Bel curves with the relevant classification parameters indicated: $PoC_0, PoC(Pl_0), Pl_0, Pl(PoC_0), DoU(PoC_0), A_{Pl,Bel}$ 175

7.2 Evolution of the normalised $A_{Pl,Bel}$ over time, for Events 1 to 4. 177

7.3 CDM information for example in Scenario #1: High-risk event. (a) Uncertain ellipses in the sequence of CDMs. Green ellipses correspond to earlier CDMs, and red ellipses to later CDMs. (b) Evolution of the PoC in the CDMs (blue solid) and PoC threshold (orange dashed) 180

7.4	Scenario #1: High-risk event. (a) Combined covariance matrix evolution (exact and fit) and (b) CDM weighting law.	182
7.5	Pl (dashed lines) and Bel (solid lines) of the PoC after having received the whole sequence of CDMs Scenario #1: High-risk event for a different number of α -cuts.	183
7.6	Collision risk assessment for Scenario #1: High-risk event.	184
7.7	CDM information for example in Scenario #2: Low-risk event. (a) Uncertain ellipses in the sequence of CDMs. Green ellipses correspond to earlier CDMs, and red ellipses to later CDMs. (b) Evolution of the PoC in the CDMs (blue solid) and PoC threshold (orange dashed).	185
7.8	Scenario #2: Low-risk event. (a) Combined covariance matrix evolution (exact and fit) and (b) CDM weighting law.	186
7.9	Pl (dashed lines) and Bel (solid lines) of the PoC after having received the whole sequence of CDMs Scenario #2: Low-risk event for a different number of α -cuts.	187
7.10	Collision risk assessment for Scenario #2: Low-risk event.	187
7.11	CDM information for example in Scenario #3: Uncertain event. (a) Uncertain ellipses in the sequence of CDMs. Green ellipses correspond to earlier CDMs, and red ellipses to later CDMs. (b) Evolution of the PoC in the CDMs (blue solid) and PoC threshold (orange dashed), TCA (vertical dashed green).	189
7.12	Scenario #3: Uncertain event. (a) Combined covariance matrix evolution (exact and fit) and (b) CDM weighting law.	190
7.13	Pl (dashed lines) and Bel (solid lines) of the PoC after having received the whole sequence of CDMs Scenario #3: Uncertain event for a different number of α -cuts.	191
7.14	Collision risk assessment for Scenario #3: Uncertain event.	191

7.15	CDM information for example in Scenario #4. (a) Uncertain ellipses in the sequence of CDMs. Green ellipses correspond to earlier CDMs, and red ellipses to later CDMs. (b) Evolution of the PoC in the CDMs (blue solid), evolution of the sPoC (dashed-pointed green) and PoC threshold (orange dashed).	194
7.16	Scenario #4. (a) Combined covariance matrix evolution (exact and fit) and (b) CDM weighting law.	195
7.17	<i>Pl</i> (dashed lines) and <i>Bel</i> (solid lines) of the PoC after having received the whole sequence of CDMs Scenario #4 for a different number of α -cuts.	196
7.18	Collision risk assessment for Scenario #4.	196
7.19	Conjunction event with conflicting CDMs: a) evolution of the relative position distribution on the impact place, b) evolution of the PoC, c) <i>Pl</i> and <i>Bel</i> curves of the whole CDMs sequence.	200
8.1	Histograms representing the distribution of the sample by Classes: (a) unbalanced dataset with criterion presented in Chapter 3, (b) unbalanced dataset with criterion in Table 8.9.	219
8.2	Multi-channel time series synthetic sample for the transformer, including padding and the padding flag.	232
8.3	Overall F2 score as a function of the lag window length for the different architectures. Solid: train in synthetic evaluated on the synthetic dataset; dashed: train in synthetic evaluated on the real dataset.	236
9.1	Alternative manoeuvres the multiple-encounter event in <i>Example 1</i> : (a) <i>Strategy A</i> and <i>Strategy B</i> ; (b) <i>Strategy C</i>	251
9.2	Alternative manoeuvres the multiple-encounter event in <i>Example 2</i> : (a) <i>Strategy A</i> and <i>Strategy B</i> ; (b) <i>Strategy C</i>	252
9.3	Effect on the risk reduction of the avoidance manoeuvres in <i>Example 1</i> : (a) <i>Strategy 0</i> and <i>Strategy 1</i> ; (b) <i>Strategy 2</i>	253
9.4	Effect on the risk reduction of the avoidance manoeuvres in <i>Example 2</i> : (a) <i>Strategy 0</i> and <i>Strategy 1</i> ; (b) <i>Strategy 2</i>	254

9.5	MCDM criteria, their classification and their quantification for the <i>One-vs-Many</i> example.	255
9.6	Difference in Earth's surface covered between the avoidance case and the nominal configuration. (a) None satellites returned to the original orbit. (b) Both satellites returned to the original orbit, only one to the original slot. (c) Both satellites return to the original slot.	268
9.7	Value of parameters used to compute the MCDM criteria as a function of the alternatives. a) PoC for the first satellite's encounter, b) PoC for the second satellite's encounter, c) Total δv of the alternative, d) total time of the operation, e) total number of manoeuvres, including CAM and returning manoeuvres, for both encounters, e) constellation metric.	275
10.1	Modules of CASSANDRA.	279
10.2	ACS <i>One-vs-All</i> mode for truncated sections of the 1-day lookback and 3-day horizon: (a) example of the input, (b) example of the output.	290
10.3	Diagram of robust Bayesian pipeline for optimal collision avoidance manoeuvre planning.	293
10.4	Impact plane 3σ ellipses for collision scenario with observations up to 48h before TCA.	297
10.5	Impact plane 3σ ellipses for collision scenario with observations up to 24h before TCA.	298
10.6	Impact plane 3σ ellipses for collision scenario after CAM.	299
10.7	Evolution of PoC bounds for collision scenario.	299
10.8	Impact plane 3σ ellipses for no-collision scenario with observations up to 48 h before TCA.	300
10.9	Impact plane 3σ ellipses for no-collision scenario with observations up to 24 h before TCA.	301
10.10	Evolution of PoC bounds for no-collision scenario.	301
10.11	Pipeline of the modules to be integrated into this work.	304

A.1	Encounter geometry and different reference frames in the impact plane used to compute the PoC and the dilution-free metrics.	332
A.2	Normalised reference frame in the impact plane used to compute the rPloC.	333
A.3	Distance distribution for different values of the miss distance. (a) pdf, (b) CDF.	335
A.4	Evolution of the conjunction assessment metrics with the covariance matrix for different values of the covariance matrix (with $\sigma'_x = \sigma'_y$). (a) Probability of collision, with dilution region, (b) Dilution-free Red Plausibility of Collision, (c) Dilution-free Blue Plausibility of Collision.	336
A.5	Comparison of the evolution with the covariance matrix for different values of the covariance matrix (with $\sigma'_x = \sigma'_y$) of the PoC (black) with the free-dilution metrics (rPloC in red and bPloC in blue).	337
A.6	Uncertain geometry of the encounter use to compute the <i>Pl</i> and <i>Bel</i> of the dilution-free metrics.	338
A.7	Plausibility and Belief curves for PoC (black), red PloC (red) and blue PloC (blue).	339
B.1	Representative scenario of a single case of <i>Geo. 2</i> : (a) encounter geometry, (b) the associated <i>Bel</i> and <i>Pl</i> curves.	341
B.2	Representative scenario of a single case of <i>Geo. 3</i> : (a) encounter geometry, (b) the associated <i>Bel</i> and <i>Pl</i> curves.	342
B.3	Representative scenario of a single case of <i>Geo. 4</i> : (a) encounter geometry, (b) the associated <i>Bel</i> and <i>Pl</i> curves.	343
B.4	Representative scenario of a single case of <i>Geo. 5</i> : (a) encounter geometry, (b) the associated <i>Bel</i> and <i>Pl</i> curves.	344

List of Tables

3.1	FE with the associated <i>bpa</i> (for intervals equally and non-equally reliable) and the minimum and maximum PoC on each FE.	58
3.2	Intervals provided by sources with their <i>bpa</i> before and after being combined with the mixing rule for the equally reliable (upper tier) and non-equally reliable (lower tier) cases.	64
3.3	Evidence-based conjunction classification <i>Criterion 1</i>	67
3.4	Bounds for upper and lower limits of the uncertain variables' intervals (μ_b and Σ_b) for each geometry set. The first row represents the bounds for Source 1 and the second row for Source 2. Units in meters.	68
3.5	Classification thresholds.	69
3.6	Evidence-based conjunction classification <i>Criterion 2</i>	72
3.7	Evidence-based conjunction classification <i>Criterion 3</i>	74
4.1	Computational time (in seconds) of the CARA analysis provided the sequence of CDMs.	95
4.2	Computational time of obtaining the <i>Pl</i> and <i>Bel</i> curves (in seconds) for different values of α -cuts and the percentage of FEs removed.	100
4.3	Computational time of obtaining the <i>Pl</i> and <i>Bel</i> curves (in seconds) when removing FEs or not, and the percentage of FEs removed for different values of α -cuts.	103
5.1	Primary and secondary objects' nominal Keplerian elements at encounter time.	124

5.2	Secondary object's covariance matrix (assumed diagonal) on the Keplerian elements at encounter time.	125
5.3	Linear model errors with respect to the grid search value for the unit vector, $\delta\hat{\mathbf{v}}_{opt}$, parallel to the direction of the optimal impulse, $\delta\mathbf{v}_{opt}$. . .	126
5.4	Initial Keplerian elements of both objects for the optimal robust CAM under aleatory and epistemic uncertainty.	127
5.5	Secondary object's position initial uncertainty. The aleatory uncertainty is modelled with a multivariate Normal distribution, while the epistemic uncertainty is modelled with the interval-valued parameter $\boldsymbol{\lambda}$	130
5.6	Bounds of the sources' intervals for the uncertain variables on the impact plane.	130
5.7	Parameters employed for the optimal LT CAM computation.	136
6.1	Top-10 alternatives in the collaborative case Scenario 1.	156
6.2	Top-10 alternatives identifier in the collaborative case Scenario 1.	157
6.3	Top-10 alternatives in the collaborative case Scenario 2.	157
6.4	Top-10 alternatives identifier in the collaborative case Scenario 2.	158
6.5	Top-10 alternatives in the collaborative case Scenario 3.	159
6.6	Top-10 alternatives identifier in the collaborative case Scenario 3.	159
6.7	Top-10 alternatives in the collaborative case Scenario 4.	160
6.8	Top-10 alternatives identifier in the collaborative case Scenario 4.	160
6.9	Objects' Keplerian elements at initial epoch t_0 . Units in km and deg. . .	161
6.10	Uncertain encounter geometry with 2 sources providing information. Upper and lower bound of the components of miss distance and covariance matrix in the impact plane.	162
6.11	PoC threshold and maximum impulse capacity of each satellite involved in the encounter for the two cases considered.	162
7.1	Evidence-based classification criterion using the area between the curves. . .	174
7.2	Threshold values.	178

7.3	Results from the statistical analysis on the SWARM-A mission, with the SDO approach and the evidence-based approach. Threshold: $PoC_0 = 10^{-4}$, $T_1 = 3$ days, $T_2 = 5$ days, $Pl_0 = 1/243$. Partition with 2 α -cuts per variable. Upper tier: $A_0^* = 0.1$ ($A_0 = 3$); middle tier: $A_0^* = 0.5$ ($A_0 = 15$); lower tier: $A_0^* = 0.8$ ($A_0 = 24$).	198
8.1	Bounds for the upper and lower values of the $[\mu_x, \mu_y]$ and $[\sigma_x, \sigma_y]$ uncertainty intervals for each of the set of geometries used for creating DB_2 . The first row represents the limits for Source 1 and the second row for Source 2.	205
8.2	Overall accuracy and precision and recall by classes. <i>System 1</i> trained with DB_{11} and tested with DB_{12} . The best technique is underlined. . .	208
8.3	Overall accuracy and precision and recall by classes. <i>System 1</i> trained with DB_{11} and tested with DB_{22} . The best technique is underlined. . .	209
8.4	Overall accuracy and precision and recall by classes. <i>System 2</i> trained with DB_{11} and tested with DB_{12} . The best technique is underlined. . .	209
8.5	Overall accuracy and precision and recall by classes. <i>System 2</i> trained with dataset DB_{11} and tested with dataset DB_{22} . The best technique is underlined.	210
8.6	Overall accuracy and precision and recall by classes. <i>System 2</i> trained with training dataset DB_{21} and tested with dataset DB_{22} . The best technique is underlined.	211
8.7	Training time (in seconds) for the best settings of each method applied to each <i>System</i>	211
8.8	Running time (in seconds) for prediction over Validation Set for the best settings of each method for each <i>System</i>	212
8.9	Manoeuvre-driven epistemic classification criterion.	214
8.10	Intervals from which the primary object's nominal initial Keplerian elements were obtained.	215
8.11	Intervals from which the nominal encounter geometry variables were obtained.	215

8.12	Intervals from which the bounds of the epistemic parameters λ_μ and λ_σ , per each geometry configuration were obtained. The upper and lower bounds of λ_μ and λ_σ are taken randomly from Λ_μ and Λ_σ , so that $\lambda_\mu \in \Lambda_\mu$ and $\lambda_\sigma \in \Lambda_\sigma$	217
8.13	Parameters employed to obtain the dataset.	217
8.14	Performance of the best models for predicting the close event <i>Class</i> . The best technique is underlined.	221
8.15	Comparison on computational time for the risk assessment: using the ICS (left) against computing the actual values of the variables involved on the criterion (right). The time is given in seconds.	222
8.16	Boundaries of the parameters used to generate the synthetic database of virtual encounters.	225
8.17	Class distribution on the three databases, in percentage.	226
8.18	Class distribution on the training and test sets, in percentage.	227
8.19	Set of hyperparameters considered to select the best model during the RF training.	229
8.20	Synthetic samples with lag step 1 used by the LGBm architectures and the RF with CDM approach. The $Class_{t-1}$ columns would be used only by the autoregressive LGBm method. Units in m , m^2 and <i>days</i>	230
8.21	Set of hyperparameters considered to select the best model during the LGBm training.	231
8.22	Set of hyperparameters considered to select the best model during the transformer training.	233
8.23	F2-score of the best model of each architecture trained on the synthetic set. Upper-tier, models evaluated on the corresponding test set (synthetic on left, real on right), lower-tier, models evaluated on the real dataset not used for training. In bold, the model with the highest overall F2-score on each database. Underlined, the best F2-score by class.	234

8.24	F2-score of the best model of each architecture trained on one of the real sets. Upper-tier, models evaluated on the corresponding test set (synthetic on left, real on right), lower-tier, models evaluated on the real dataset not used for training. In bold, the model with the highest overall F2-score on each database. Underlined, the best F2-score by class. . . .	237
8.25	Computational time (in seconds) for robust CARA with and without using AI techniques.	238
9.1	Nominal Keplerian elements at the initial time for the subsequent-encounters scenario.	245
9.2	Secondary object's initial uncertainty. Aleatory uncertainty as a 3D Gaussian distribution on the $\langle T, N, H \rangle$ reference frame. Epistemic uncertainty with the epistemic parameters, λ_1 and λ_2 , provided by two sources of information.	246
9.3	Bounds of the two sources' intervals for the uncertain variables on the impact plane of the two encounters and bounds of the intervals of the associated PoC for <i>Example 1</i>	248
9.4	Bounds of the two sources' intervals for the uncertain variables on the impact plane of the two encounters and bounds of the intervals of the associated PoC for <i>Example 2</i>	249
9.5	Weight distribution for the two analysed scenarios, for <i>Example 1</i> and <i>Example 2</i>	257
9.6	Top-10 alternatives for the two scenarios using the three MCDM methods considered for <i>Example 1</i>	257
9.7	Top-10 alternatives for the two scenarios using the three MCDM methods considered for <i>Example 2</i>	258
9.8	Number of common alternatives ranked among the top-10 between pairs of methods.	259
9.9	Uncertain encounter geometry for the first encounter: upper and lower bound of the components of miss distance and covariance matrix in the impact plane.	263

9.10 Uncertain encounter geometry for the second encounter: upper and lower bound of the components of miss distance and covariance matrix in the impact plane. 264

9.11 Alternatives as a function of the CAM execution position (θ_{mi}), measured as the angular distance to the encounter, and the returning strategy (si_j). 265

9.12 Weight distribution along the criteria for the different subscenarios. 269

9.13 Top 5 alternatives in Subscenario 0 for the 8 combinations of MCDM methods and normalisation techniques along with the combined ranking with $g_{top} = 5$ 269

9.14 Top 5 alternatives in each subscenario with $g_{top} = 5$ 270

10.1 Bounds on the initial orbital parameters of the orbits used to train the *One-vs-All* mode of the ACS. 289

10.2 Objects orbital elements from NORAD TLEs. 294

10.3 1σ position (r) and velocity (v) uncertainty of TLEs for orbits with $e < 0.1$, $i > 60$ deg, perigee altitude ≤ 800 km, in radial (U), transversal (V), and normal components (W). 295

10.4 IDSS thresholds values for the RSE-IDSS-CAM implementation. 296

10.5 Bayesian agent performance for different conjunction scenarios. 302

10.6 The 5 the potential encounters detected by the ACS: All-vs-All. 309

10.7 Initial state vector and uncertainty of objects involved in the first encounter detected by the ACS. Epoch CNESJD 25718.999594907 (31-05-2020, 23:59:25.00). 309

10.8 IDSS thresholds values for the robust screening scenario. 310

10.9 Bounds output by the RSE if no observations available. 311

10.10 Bounds output by the RSE when 10 measurements are received. The time to TCA after the last observation is 1 day. 311

10.11 List of ranked possible manoeuvres, expressed in the satellite's $\langle T, N, H \rangle$ reference frame. The last column includes the $Class_m$ of the event after the manoeuvre. 312

B.1	Classification distribution (in percentage) by sets using a criterion based only on PoC value and using E-b Criterion 1.	345
B.2	Classification distribution (in percentage) by sets using a criterion based only on PoC value and using E-b Criterion 2.	345
B.3	Classification distribution (in percentage) by sets using a criterion based only on PoC value and using E-b Criterion 3.	345
D.1	Hyperparameters of the best model of each technique on each of the four training scenarios in Section 8.1.	354
D.2	Hyperparameters of the best model of each technique on the example in Section 8.2.	355
D.3	Hyperparameters of the best model of each technique trained on the synthetic and in the real databases in Section 8.3.	356

List of Algorithms

C.1	Impulsive for robust optimal CAM with constant magnitude.	348
C.2	Impulsive robust optimal CAM with optimised magnitude.	350
C.3	LT robust optimal CAM.	351
C.4	LT robust optimal CAM. propellant saving via min. acceleration.	352
C.5	LT robust optimal CAM. propellant saving via min. burning-time.	352

Acronyms

ACE Aerospace Centre of Excellence

ACS Automated Conjunction Screening

AI Artificial Intelligence

ANN Artificial Neural Networks

ATM Air Traffic Management

Bel Belief

bpa basic probability assignment

CAM Collision Avoidance Manoeuvre

CARA Conjunction Assessment Risk Analysis

CASSANDRA *Computer Agent for Space Situational Awareness aNd Debris
Remediation Automation*

CDF Cumulative Distribution Function

CDM Conjunction Data Message

CNES Centre National D'Etudes Spatiales

CNN Convolutional Neural Networks

DKW Dvoretzky-Kiefer-Wolfowitz

DL Deep Learning

DoU Degree of Uncertainty

DSS Decision Support System

DSt	Dempster-Shafer theory of evidence
DT	Decision Tree
eCDF	empirical Cumulative Distribution Function
ECI	Earth-Centred Inertial
ESA	European Space Agency
ESOC	European Space Operations Centre
FE	Focal Element
FN	False Negative
FP	False Positive
GEO	Geostationary Orbit
HBR	Hard-Body Radius
IAA	International Academy of Astronautics
ICS	Intelligent Classification System
IDSS	Intelligent Decision Support System
JAC	<i>Java for Assessment of Conjunctions</i>
JSpOC	Joint Space Operations Center
KNN	K-Nearest Neighbours
LEO	Low Earth Orbit
LGBm	Light Gradient Boosting machine
LSTM	Long/Short Term Memory network
LT	Low-Thrust
MAE	Maximum Absolute Error
ManC	Manoeuvre Cost
ManR	Manoeuvre Risk
MC	Monte Carlo

MCDM Multi-Criteria Decision-Making
MCMDM Multi-Criteria Multi-Decision-Making
ML Machine Learning
MLP Multi-Layer Perceptron
MTM Maritime Traffic Management
NASA National Aeronautics and Space Administration
nWSM normalised Weighted Sum Method
OpC Operational Cost
pdf probability density function
Pl Plausibility
PoC Probability of Collision
PoCR Probability of Collision Reduction
RF Random Forests
RMSE Root Mean Squared Error
RPF Robust Particle Filter
RSE Robust State Estimator
SDO Space Debris Office
SEM Space Environment Management
sPoC Scaled Probability of Collision
SSA Space Situational Awareness
SST Space Surveillance and Tracking
STM Space Traffic Management
SVM Support Vector Machine
TCA Time of Closest Approach
TLE Two-Line Elements

TOPSIS *Technique for the Order of Preference by Similarity to the Ideal Solution*

TP True Positive

UAV Unmanned Aerial Vehicles

WPM Weighted Product Method

WSM Weighted Sum Method

Chapter 1

Introduction

The emergence of the New Space, with small satellites, mega-constellations and the stronger role of the private sector, has brought the necessity of new collision risk assessment approaches. The capacity of the current system to guarantee the safe use of space will soon be overwhelmed by the new context and, thus, a more robust and automated system will be required. **This research aims to propose new methodologies to deal with the increase in traffic and the characteristics of the new spacecraft and constellations to ensure and manage the sustainable use of space by the different agents involved in the space sector. This is achieved by addressing the need for robustness and automation in Space Traffic Management required to guarantee safe operations in space. In this research, a new methodology is introduced to automatise and speed up Space Traffic Management using Artificial Intelligence to support operators in the robust decision-making process.** Artificial intelligence technologies were used to enable automation and uncertainty quantification methods, modelling both aleatory and epistemic uncertainty, were developed to make possible robust space traffic management.

Automation in Space Traffic Management (STM) is a necessity due to the changes in the space environment. Machine Learning (ML) techniques have been started to be applied in the space field, and more specifically, in the space safety area to help automate and speed up some processes. Similarly, addressing uncertainty in a more complex environment is becoming paramount to ensure the safety management of the

Earth's orbital region. This work proposes improvements in both fields and combines them to create a more exhaustive framework to address STM problems, accounting for epistemic uncertainty and enhancing automation.

1.1 Research objectives and contributions

Based on the rationale presented before, the main objectives of this thesis are:

- Improve robustness of STM by accounting for epistemic uncertainty and integration its quantification in the conjunction assessment decision-making process.
- Capture the different sources of uncertainty affecting conjunction communication standards (i.e. Conjunction Data Messages (CDMs)).
- Account for aleatory and epistemic uncertainty in the design of a Collision Avoidance Manoeuvre (CAM) and the decision-making process.
- Devise a methodology to use Artificial Intelligence (AI) to automate STM.

From the list of objectives detailed above, the contributions of this thesis to achieve them are:

- Implementation of a revised collision risk model that accounts for epistemic uncertainty on the objects' position:
 - Development of an evidence-based framework to perform collision risk assessment accounting for aleatory and epistemic uncertainty using Dempster-Shafer theory of evidence (DSt).
 - Analysis of the robustness of the system accounting for several sources of uncertainty, implementing a data fusion process to fuse the risk of collision with other relevant quantities.
 - Development of an epistemic-based classification criterion for supporting operators in close encounters decision-making.

- Development of a methodology to model missing sources of epistemic uncertainty on the CDMs and its integration in the evidence-based framework.
- Development of a methodology to automatically generate optimal and robust CAMs and support the avoidance decision-making under different conjunction scenarios.
 - Development of a methodology to compute robust collision avoidance manoeuvres under aleatory and epistemic uncertainty for the impulsive and the low-thrust scenarios.
 - Implementation of an approach to support the decision-making on the execution of the robust CAMs, both in the cooperative scenario using a Multi-Criteria Decision-Making (MCDM)-based approach and in the non-cooperative case employing Game Theory.
 - Generalisation of the methodology to cope with multiple-encounter events, both for subsequent encounters of a single satellite and for simultaneous encounters within a constellation.
- Development of a methodology which uses AI to provide robust decision support to operators and enables robust automation of STM.
 - Study of different ML and Deep Learning (DL) techniques to classify close encounters events according to the confidence on their risk accounting for aleatory and epistemic uncertainty, creating faster surrogate models of the evidence-based framework.
 - Development of a prototype modular system integrating the proposed methodologies to automatise conjunction risk assessment and provide robust support to operators.
- Validation of the developed methodologies and tools to real scenarios.
 - Definition of realistic scenarios based on real encounter events.
 - Development of tuning methods for the parameters and threshold introduced in the evidence-based framework conjunction analysis.

- Comparative analysis between the proposed approach and real operators procedures on relevant real conjunction scenarios.
- Statistical comparison of approaches on databases of real satellite missions.

1.1.1 Publications

Part of the content of this thesis was published in journal articles, book chapters, and conference papers. In the following, the list of publications produced in this research period is reported.

Journal papers

1. **Sánchez, L.** and Vasile, M. (2021), “On the use of machine learning and evidence theory to improve collision risk management”, *Acta Astronautica*, Vol. 181, pp. 694-706, <https://doi.org/10.1016/j.actaastro.2020.08.004> [Sánchez and Vasile, 2021c];
2. **Sánchez, L.** and Vasile, M. (2022), “Intelligent decision support for collision avoidance manoeuvre planning under uncertainty”, *Advances in Space Research*, Special Issue: Space Environment Management and Space Sustainability, in press, <https://doi.org/10.1016/j.asr.2022.09.023> [Sánchez and Vasile, 2023];
3. **Sánchez, L.**, Vasile, M., Sanvido, S., Merz, K. and Taillan, C., “Treatment of epistemic uncertainty in conjunction analysis with Dempster-Shafer theory”, *Advances in Space Research*, submitted [Sánchez et al., 2024].

Book chapters

1. **Sánchez, L.**, Vasile, M. and Minisci, E. (2020), “AI and space safety: collision risk assessment”, In Schrogl, KU. (eds) *Handbook of Space Security*, pp. 941-959. Springer, Cham, https://doi.org/10.1007/978-3-030-23210-8_136 [Sánchez et al., 2020].

Peer-reviewed conferences papers

1. Vasile, M. and **Sánchez, L.** (2022), “Robust optimisation of coordinated collision avoidance manoeuvres in large constellations”, In 11th International Workshop on Satellites Constellations and Formation Flying (IWSCFF), Milan, Italy, 7-10 June, Paper Number: ThuSOT1.3 [Vasile and Sánchez, 2022].
2. **Sánchez, L.**, Rodríguez-Fernández, V. and Vasile, M. (2023), “Robust classification with belief functions and deep learning applied to space traffic management”, In 2024 IEEE World Congress on Computational Intelligence (WCCI), Yokohama, Japan, 30 June - 5 July. Accepted. [Sánchez et al., 2023].

Conferences papers and presentations

1. **Sánchez, L.**, Vasile, M. and Minisci, E. (2019), “AI to support decision making in collision risk assessment”, 70th International Astronautical Congress (IAC), Washington DC, US, 21-25 October. Paper number: IAC-19-A6,IP,20,x53728 [Sánchez et al., 2019];
2. **Sánchez, L.** and Vasile, M. (2020), “On the use of machine learning and evidence theory to improve collision risk assessment”, 2nd IAA Conference on Space Situational Awareness (ICSSA), Washington DC, US, 14-16 January [Sánchez and Vasile, 2020b];
3. **Sánchez, L.** and Vasile, M. (2020), “AI for autonomous CAM execution”, 71st International Astronautical Congress (IAC), The Cyber Space Edition, 12-14 October. Paper number: IAC-20-A6,2,12,x58045 [Sánchez and Vasile, 2020a];
4. Greco, C., **Sánchez, L.** and Vasile, M. (2021), “A robust Bayesian agent for optimal collision avoidance manoeuvre planning”, 8th European Conference on Space Debris, ESA/ESOC, Darmstadt, Germany, 12-14 April [Greco et al., 2021];
5. **Sánchez, L.** and Vasile, M. (2021), “CASSANDRA: Computational Agent for Space Situational Awareness and Debris Remediation Automation”, Stardust-

- R – Second Global Virtual Workshop (GVW-II), Darmstadt, Germany, 13-17 September [Sánchez and Vasile, 2021a];
6. **Sánchez, L.** and Vasile, M. (2021), “Constrained optimal collision avoidance manoeuvre allocation under uncertainty for subsequent conjunction events”, 72nd International Astronautical Congress (IAC), Dubai, EAU, 25-29 October, Paper number: IAC-21,A6,IP,9,x64861 [Sánchez and Vasile, 2021b];
 7. **Sánchez, L.**, Stevenson, E., Vasile, M., Rodríguez-Fernández, V. and Camacho, D. (2022), “An intelligent system for robust decision-making in the all-vs-all conjunction screening problem”, 3rd IAA Conference on Space Situational Awareness (ICSSA), Tres Cantos, Madrid, Spain, 4-6 April [Sánchez et al., 2022a];
 8. Hallgarten la Casta, M., **Sánchez, L.**, Amato, D. and Vasile, M. (2022), “Non-linear set propagation with generalised equinoctial orbital elements”, 5th International Workshop on Key Topics in Orbit Propagation Applied to SSA (KePASSA), Logroño, Spain, 22-24 June [Hallgarten la Casta et al., 2022];
 9. **Sánchez, L.**, Vasile, M. and Taillan, C. (2022), “Close encounter decision-making: comparing CASSANDRA and CNES operational processes”, 2nd Stardust Final Conference (STARCON-2), ESA/ESTEC, Noordwijk, The Netherlands, 7-11 November [Sánchez et al., 2022b].

1.1.2 Thesis structure

The thesis is structured in two parts and two additional chapters for the State of the Art and the Conclusions. Part I includes the theoretical and methodological developments related to the use of DSt on conjunction risk assessment, providing robust decision-making, and computing robust CAMs in single and multiple encounters. Part II contains advanced applications of those methods on STM challenges, including the use of AI techniques to the theoretical developments.

Chapter 2 presents the current State of the Art on Space Traffic Management approaches and efforts to account for uncertainty, both aleatory and epistemic. It also

shows previous works done towards the automation of STM tasks and the pioneering works on the use of AI for space safety.

In Part I, Chapter 3 presents a robust classification system to evaluate the risk of close encounters accounting for aleatory and epistemic uncertainty. While aleatory uncertainty is commonly modelled in space objects' state vectors and close encounter analysis, epistemic uncertainty is usually overlooked. An evidence-based framework using DSt is proposed to model both types of uncertainty and provide the operators robust support in the decision-making process. Chapter 4 extract the epistemic uncertainty implicit on the sequence of CDMs, capturing missing sources of uncertainty (probabilistic model, dynamic model, observations) to integrate this commonly used protocol on the DSt-based framework introduced in the previous chapter. Initially, statistical tools, like empirical Cumulative Distribution Function (eCDF), Dvoretzky-Kiefer-Wolfowitz (DKW) inequalities and p-boxes, are used to model this uncertainty in the CDMs, and later, it is inserted into the proposed decision support system. In Chapter 5, the DSt framework is extended to compute robust optimal CAMs, accounting for aleatory and epistemic uncertainty, to provide the optimal manoeuvre that reduces the risk of the worst-case scenario. If the evidence-based decision-making support system suggests to the operator an avoidance strategy should be implemented, the proposed manoeuvre should account as well for the epistemic uncertainty affecting the objects' state vector. A min-max optimisation approach methodology is presented to compute the impulsive robust optimal manoeuvre. The method is then extended to address the low-thrust scenario. Finally, in Chapter 6 the robust decision-making problem is addressed. If an avoidance strategy is required, under the evidence-based framework, a number of robust optimal solutions may be obtained, by changing some parameters such as the manoeuvre execution position or its magnitude. The task of the operator consists of selecting the most appropriate alternative according to some mission criteria, usually contradictory among them. The proposed approach uses MCDM in the collaborative scenario (when all agents are expected to follow the same outcome) and Game theory in the non-collaborative scenario (when other operators' action is not known in advance and it is not agreed) to proposed an informed ranking of the

difference avoidance strategies available.

In Part II, Chapter 7 applies the robust methodology to real conjunction scenarios. Examples in other chapters are based on simulated encounters mimicking actual scenarios. In this chapter, events provided by the European and French space agencies are analysed using the evidence-based approach, and the results are compared with the decisions made by the actual operators during the real operations of the satellites involved in the encounters. Chapter 8 proposes different intelligent models to enhance the capabilities of the robust framework introduced in Part I. These models use ML and DL techniques, like Artificial Neural Networks (ANN), Random Forests (RF), K-Nearest Neighbours (KNN), Support Vector Machine (SVM), Light Gradient Boosting machine (LGBM) or Transformers, to help the automation and speed up the conjunction risk assessment process. The objective is to quickly propose to the operators the most suitable action based on the encounter geometry by building a surrogate model of the evidence-based methodology introduced in previous chapters. In Chapter 9, the MCDM methodology introduced in Chapter 6 is applied to the multi-encounter scenario. While single encounters are currently the norm in space operations, the increase in space traffic will raise the chance of multi-event conjunctions. The chapter applies MCDM techniques to deal with two separate situations: a single satellite facing multiple encounters, and several satellites belonging to the same constellation facing an encounter with the same external object. The last chapter of this part of the thesis, Chapter 10, introduces CASSANDRA, an intelligent agent to deal with STM and Space Environment Management (SEM) problems automatically, applying AI techniques and accounting for aleatory and epistemic uncertainty. The chapter introduces some of the modules compounding the agent, which are based on the methods introduced in previous chapters, and shows two examples of their integration to solve specific space safety problems.

Finally, Chapter 11 summarises the main contributions of the thesis and presents some possible new research directions.

1.2 Research funding

This research was funded by the European Space Agency, through the Open Space Innovation Platform (OSIP): “Idea I-2019-01650: Artificial Intelligence for Space Traffic Management”.

The research focuses on leveraging AI and ML for STM, aiming to enhance decision-making processes in collision risk assessment and avoidance.

This project aligns with the Space Safety research line followed by the Aerospace Centre of Excellence (ACE) at the University of Strathclyde. The ACE carries out extensive research on planetary defence and the long-term sustainability of the space environment in combination with AI techniques to enhance automation and speed up processes. The ACE also research the development of uncertainty quantification algorithms applied to orbit propagation and control, with important studies on the quantification of epistemic uncertainty.

Chapter 2

State of the Art

The space environment around the Earth has experienced a dramatic change during the last years and is expected to keep evolving during the mid-term horizon. For decades, space traffic experienced a constant but steady increase, with space agencies, governments and communication satellites being the main actors [ESA, 2023b, NASA, 2023]. However, the New Space era [Peterson et al., 2018] is a reality bringing a plethora of changes, which range from the use of space to the available technologies, traffic density and operational practises. The space community, adapted to the slower-growing and less populated environment, will need to adapt to ensure the sustainable and safe use of space by all new and old actors.

One of the areas greatly affected by the new situation is Space Traffic Management (STM) [Muelhaupt et al., 2019]. The International Academy of Astronautics (IAA)'s *Cosmic Study on Space Traffic Management* defines STM as “the set of technical and regulatory provisions for promoting safe access into outer space, operations in outer space and returns from outer space to Earth free from physical or radio-frequency interference” [Contant-Jorgenson et al., 2006]. Currently, the STM system is tailored to the environment that arose from the Fengyun 1 antisatellite test [Pardini and Anselmo, 2009, Pardini and Anselmo, 2011] and the Iridium 33 - Cosmos 2251 [Nicholas, 2009, Pardini and Anselmo, 2011] collision in 2007 and 2009, respectively. In this scenario, the Earth's environment was dominated by space debris and with few space agents operating a reduced fleet of satellites.

In this context, STM tasks could be handled by human operators since conjunction alerts occur in a manageable number and conjunction assessment was scarce enough to be able to dedicate enough time to safely address them. The common approach by the main space agencies was similar, despite some operational differences according to their necessities [Braun et al., 2016, Merz et al., 2017, Newman et al., 2014, Newman et al., 2019, Laporte and Moury, 2013]. Events surpassing a certain risk threshold, usually measured with the Probability of Collision (PoC) metric, were short-listed to be further analysed. If the risk kept high when receiving updated information, the encounters were classified as higher-risk encounters (i.e. High-Interest Events), and further measures to mitigate the risk were studied. Finally, if an avoidance manoeuvre was required after the design stage, a go/no-go decision was made in the last days before the encounter to implement the avoidance action some revolutions before the conjunction. This process is very time-consuming, requires a lot of human workload and is based on the constant coordination among departments and operators which are based on phone calls and emails. Although it has been effective during the last few years, it has no scalability capacity [Nag et al., 2021] and relies on teams of several operators to take care of one satellite or a small fleet of satellites.

The New Space era is characterised by a shift from a governmental-led space to a commercial-focused use of space [ESA, 2023b, Peterson et al., 2018]. The first consequence is the appearance of new actors in a relatively small ecosystem, creating new relations, affecting the existing ones and competing for the limited resources. As a result, during the last years, the launching rate has accelerated dramatically, with an exponential increase in the number of satellites orbiting the Earth and the total mass they represent, in contrast with the linear increase seen before [Ailor et al., 2017, Federal Communications licensing website, 2023]. Only a proportion of those objects correspond to similar systems than already in orbit, i.e. single satellites in the Low Earth Orbit (LEO) regime. However, the more concerned contributions are represented by the small satellites and the big constellations [Bastida Virgili et al., 2016b, Lewis et al., 2017b, ESA, 2023b].

Small satellites have become very popular due to their inexpensive manufacture and

operation. New companies have specialised in them and new commercial businesses and research centres have opted to use them for providing low-cost services or research. Due to their many advantages, they present a number of challenges from the point of view of safety. Because of their small size, it is usually harder to track them or provide accurate information on their state. However, despite their size, they represent a threat to other spacecraft in case of a collision. Moreover, the smaller available space inside the platform may translate to limited capabilities and a lack of redundancy. In the case of a conjunction, the spacecraft's capabilities may be restricted, especially when the event involves a dead object. Similarly, the End-Of-Life actions may be limited, affecting the overall space safety. [Lewis et al., 2017b, Radtke et al., 2017b, Lewis et al., 2014, Bastida Virgili and Krag, 2015]

The other element impacting space safety in this new context is satellite constellations. Although there have been constellations for several decades, they were located in relatively low-density areas or involved a small number of satellites. Nevertheless, it is worth noting that the only recorded fatal collision affecting an operational satellite, the Iridium 33 - Cosmos 2251 collision, involved a spacecraft in a constellation [Nicholas, 2009]. However, modern constellations are being deployed or are projected to operate in the LEO region, already occupied by most of the operational satellites, and they include thousands of satellites, which represent the same order of magnitude as the satellites placed in orbit during the last 50 years of Space Era [Ailor et al., 2017, Federal Communications licensing website, 2023]. Such an increase in the number of objects and the fact that they need to operate in a coordinated way puts a lot of pressure on the current systems that ensure space safety. [Bastida Virgili et al., 2016a, Radtke et al., 2017a, Peterson et al., 2016, Lewis et al., 2017a, Rossi et al., 2017]

Parallel to the increase in space traffic, new technologies have impacted STM procedures. While in the past, manoeuvres involved mainly chemical propulsion, restricting the operation time to a narrow interval, modern satellites are equipped with Low-Thrust (LT) propulsion, which involves much longer operation times, potentially extending for several orbits [Hernando-Ayuso and Bombardelli, 2020, Palermo et al., 2021, De Vittori et al., 2022]. While more efficient, the orbit correction takes longer and

is more complex, which directly impacts space safety. First, being a longer operation, it is harder to compute the new orbit to predict conjunction. Second, if a conjunction is detected, the available reaction time is smaller. Third, there is a greater effect on the knowledge of the spacecraft state’s uncertainty [Bernelli-Zazzera et al., 2012, di Carlo et al., 2019].

Associated with the increase in traffic, there is a rise in the number of pieces of space debris, defined as “all non-functional, artificial objects, including fragments and elements thereof, in Earth orbit or re-entering into Earth’s atmosphere. Human-made space debris dominates over the natural meteoroid environment, except around millimetre sizes” [European Space Agency, 2021c]. Despite mitigation and remediation policies [ESA, 2023b, Frey and Lemmens, 2017], the trend of space debris fragments remains rising despite collision among background populations or not-compliant missions. Adding to that, the improvement in Space Situational Awareness (SSA) and Space Surveillance and Tracking (SST) capabilities [Haimerl and Fonder, 2015, Fonder et al., 2017] and the appearance of commercial providers (e.g. LeoLabs, ExoAnalytics, SlingShot Aerospace) have incorporated newly discovered objects, previously untracked, that now may generate collision alerts with operational spacecrafts [Peterson et al., 2018].

The combined effect of these contributions brings the current STM to the limit [Muelhaupt et al., 2019]. On the one hand, a growth in the space population will imply an increase in conjunction alerts, both from actual collisions that will require taking more avoidance or mitigation actions, and false alerts that would saturate operators’ capabilities [Peterson et al., 2018]. On the other hand, more actors are now involved in operations, SSA/SST and STM activities [Águeda Maté et al., 2021, Simarro Mecinas et al., 2022]. The current system is adapted to a low-populated environment with ad-hoc communication and leaving a great effort of the activities to the operators. The paradigm change will require a shift on the STM architecture if safety service wants to be granted for satellites. A much more robust and automated system is required [Nag et al., 2018], where operators deal with a much greater number of satellites, more similar to well-established systems like Air Traffic Management (ATM) or Maritime

Traffic Management (MTM) [Contant-Jorgenson et al., 2006].

Several steps should be taken to ensure the long-term employment of space, guaranteeing safety for users, without outstripping the STM system capabilities. They can be grouped into five different actions: policies, remediation, mitigation, robustness and automation. Policies include all protocols aiming to standardise the line of action under encounters and regulations to comply with regarding passivation, end-of-life, avoidance capabilities and responsibilities against other actors [Innocenti et al., 2013, UNOOSA, 2010, IADC, 2022, WEF, 2023, ESA, 2023a]. Mitigation measurements correspond to actions taken by manufacturers and operators to prevent the proliferation of space debris during and after the mission: end-of-life procedures and decommissioning, tracking devices, manoeuvre capabilities... [ESA, 2023a, Letizia et al., 2019, Pontijas Fuentes et al., 2019]. Remediation corresponds to those actions meant to solve the current debris situation or meant to be used if mitigation actions fail, making Active Debris Removal the best example in this group [Wormnes et al., 2013, Forshaw et al., 2018, Priyant Mark and Kamath, 2019, Weeden et al., 2019, Aglietti et al., 2019, Botta et al., 2020, McKnight et al., 2021, Briesboek et al., 2021, Wijayatunga et al., 2023]. Robustness refers to the capability to make decisions in an uncertain environment, where not all the information is available to the operators or it is partial or in conflict among sources [Newman et al., 2019, Faucher et al., 2020, Águeda Maté et al., 2021, Delmas et al., 2023]. Finally, automation of STM system is becoming essential due to the growth in the number of satellites to operate, alerts to evaluate and conflict decisions to make [Nag et al., 2018, Bastida Virgili et al., 2019, Flohrer et al., 2019]. This research focuses on the last two groups of actions, robustness and automation. While policy measurement concerns mainly the less technical aspects, mitigation measurement relates to stages previous to operations (like satellite and mission design or end-of-life) and remediation mainly affects already dead objects, automation and remediation are related to the operational stage. This step is critical for the success of the mission, and so is the importance of robust and automated STM for safe and sustainable operations. Moreover, since those two areas affect the same tasks, they can be addressed in parallel, as done in this work.

2.1 Robustness

Information in the space objects is affected by uncertainty. Their position and velocity are never perfectly known, but it is always affected by a degree of uncertainty and ignorance coming from the noise in the measurements, the precision of the dynamic models or the assumptions considered in the description of their movement. This uncertainty in the position and velocity influences the level of accuracy and confidence in the detection of high-risk events. A robust system should cope with the different sources of uncertainty affecting the conjunction events, give reliable outputs and, at the same time, provide a quantification of the confidence of those outputs.

A robust system should be able to ingest different information formats about the object's position and velocity. Conjunction Data Messaged (CDMs) [CCSDS, 2013] are the most extended way of communicating conjunction information among operators and space agents. CDMs consist of a standardised document including information about the identification of the objects involved in a given encounter, additional information about the conjunction geometry, including the risk of collision, some information regarding the observations to determine the state, and the objects' state vector and associated covariance matrix. They are not the only options, being Two-Line Elements (TLE) [Celestrack, 2022] another popular way to exchange information on the satellite position used for conjunction assessment before the appearance of CDM. Although not as popular as CDMs in the present, some operators still use them. However, these two standards provide products already pre-processed, which makes it hard to replicate or extract information on uncertainty [Carpenter, 2019]. Thus, operators' ephemeris and observations are very valuable for Conjunction Assessment Risk Analysis (CARA), usually involving smaller covariances. With more actors involved in SSA/SST activities and more telescopes and radars available to collect information, it is likely that in the near future, raw observations will be more available to operators to perform conjunction assessment. Thus, a robust STM system should be able to ingest all these types of information.

Dealing with uncertainty is one of the biggest areas of research in space operations

and conjunction risk assessment [Poore et al., 2016]. The objects' state vector is never perfectly known but is always affected by a level of uncertainty. There are several sources of uncertainty associated with different steps in the process: uncertain parameters in the models, measurements noise, orbit determination, propagation, wrong models, or lack of knowledge. [Poore et al., 2016]

There are different methods in the field of Uncertainty Quantification to deal with uncertainty and correctly model it. Uncertainty quantification deals with the identification and characterisation of the different sources to provide the right model of the uncertainty affecting a process (e.g. observation noise, propagation error, model parameters...). Some authors, especially in the field of STM tend to use the term uncertainty realism when the models characterising the uncertainty are based on probability density functions (pdfs), and covariance realism when the pdf follows a Gaussian distribution [Drummond et al., 2007, Poore et al., 2016]. In this work, this concept is not considered since, in Uncertainty Quantification, whatever the model of uncertainty, it should converge to the true uncertainty.

In CARA, PoC is used to assess the likeliness of a direct impact in an encounter. This metric computes the probability of both objects being in the same space region at a certain epoch, given their state uncertainty distributions [Foster and Estes, 1992]. Usually, it is assumed the event takes place in such a short interval of time that the fast encounter hypothesis holds [Chan, 2003b, Patera, 2003, Patera, 2006, Slater et al., 2006, Coppola, 2017, Jones and Doostan, 2016, Vittaldev and Russell, 2016, Hall et al., 2017], although there are general techniques for distributions not following this hypothesis. The main consideration when assuming the fast encounter hypothesis is that the position uncertainty follows a Gaussian distribution (the velocity is assumed to be perfectly known) and the objects follow a rectilinear movement around the point of closest approach. This allows obtaining the PoC computing a 2D integral to quantify the weight of the combined density function falling in a specified integration region, which is defined by the size of the objects, modelled as the combined radius of the objects' enclosing sphere [Alfriend et al., 1999, Chan, 1997, Chan, 2003a, Chan, 2008, Patera, 2001, Alfano, 2005a, Alfano, 2007, Serra et al., 2016].

The effects of a poorly quantified uncertainty (what some authors refer to as uncertainty or covariance irrealism) are well documented and summarised in [Poore et al., 2016, Hejduk and Johnson, 2016, Alfano and Oltrogge, 2018]. If assuming Gaussian distribution as the model of uncertainty, the size of the covariance plays an important role in the size of the PoC, which experiences a sharp increase with an increase in the covariance (unless the expected relative position falls within the integration region, in which case the PoC remains constant), until reaching a maximum, after which the PoC decreases, a phenomenon known as dilution of probability [Alfano, 2005b, Balch, 2016, Balch et al., 2019, Alfano and Oltrogge, 2018]. In the same way, the orientation of the covariance has a dramatic impact on the value of the PoC, the more notorious the more elongated the associated uncertain ellipse is. Finally, the shape of the distribution itself may be very relevant, which would correspond to a wrong model to quantify the uncertainty. While the fast encounter hypothesis assumes Gaussian distribution on the positions, it is well known that propagating an initial position Gaussian distribution through the non-linear dynamics describing the satellite movement creates a banana-shape distribution on the final position [DeMars et al., 2011, Horwood et al., 2011, Jones et al., 2013, Hallgarten la Casta et al., 2022]. Although this effect is smaller compared with the other factors [Poore et al., 2016, Ghrist and Plakalovic, 2012], it may be important for longer propagation times or when reducing the influence of the other effects.

Different efforts exist to improve uncertainty quantification. The authors in [Poore et al., 2016] include some approaches to improve the representation of the covariance size and orientation. First, they mention the Joint Space Operations Center (JSpOC)'s methods to improve the covariance matrix due to propagation errors by using scaling factors: the *Dynamic Consider Parameter* to compensate for errors in the atmospheric drag models and a scaling factor accounting for the Root Mean Squared error of the batch differential equation. As the authors mentioned, there are criticisms of the later approach, and in any case, both models try to compensate for missing or wrongly modelled terms on the dynamics just by increasing the size of the uncertainty. A similar approach to scale the secondary object's covariance matrix was developed to

assess conjunction risk on the International Space Station, assuming the errors should follow a given distribution [Foster and Frisbee Jr, 1998]. This approach also tends to compensate the limitations on the uncertainty quantification with the covariance by increasing its size and it also adds the assumption that the position errors should follow a given distribution. A related approach is followed by the Centre National D’Etudes Spatiales (CNES) [Laporte, 2014a, Laporte, 2014b]. The Mahalanobis distance between successive covariance matrices is assumed to follow a given distribution, so scaling factors are computed to modify the covariance size accordingly, computing the so-called scaled PoC, claiming to be more accurate, at earlier stages of the conjunction assessment, to estimate the value of the PoC closer to the encounter. However, this process also relies on the assumption of a specific underlying distribution for the position error and assumes the last piece of information to be more trustworthy, as it is used as the reference when computing the Mahalanobis distance. In [Alfano, 2005b], the use of the maximum PoC in relation to the covariance variability is studied, proposing the use of this maximum value instead of the computed one when falling in the dilution region. However, this approach is criticised in [Hejduk, 2016]. Moreover, this approach does not intend to avoid or minimise the dilution problem or modify the uncertainty quantification but limits itself to proposing a practical approach for operators.

Furthermore, the use of the PoC as the risk metrics presents some limitations [Carpenter, 2019]. There also exist statistical concerns on the fact that the PoC is actually a p-value and if its current utilisation is the most appropriate [Carpenter et al., 2017]. The authors of [Carpenter et al., 2017] highlight the warnings on the use of p-values in system safety and decision-making through six principles established by the American Statistical Society [Wasserstein and Lazar, 2016]. Thus, according to the first two principles, even if assuming the use of the PoC as p-value, this metric would indicate the compatibility, or lack of it, between the model and the data. Thus, a low PoC value may be due to low risk or due to poor uncertain quantification (where dilution of probability is a very well-known effect) and a high value of the metric indicates the consistency of the data, not necessarily the collision of the objects. Even a well-characterised covariance will assume some underlying error due to the wrong model

employed for the uncertainty, and the PoC behaviour will induce a reduction of the PoC (dilution) when poor quality data are available, even though a big covariance may be the right approximation of the uncertainty. The third, fifth and sixth principles focus on the inadequacy of using PoC as a stand-alone metric in relation to specific thresholds (as several operators do [Newman et al., 2014, Merz et al., 2017]) to indicate a system's risk or to set a decision-making strategy. Also, they indicate that the p-value needs extra evidence for having a meaningful value (i.e. quality of the sensors), since a specific PoC value may not necessarily indicate a high-risk (i.e. flawed tracking data). Finally, the fourth principle addresses the transparency of how the data were obtained, which directly affects how the PoC in the CDMs is computed.

Regarding the use of CDMs, they still present some limitations, despite the efforts to improve uncertainty quantification. As mentioned before, according to the fourth principle in [Carpenter et al., 2017], the data used to derive a p-value should be transparent. However, CDMs are a final product from which is hard to extract information on the quality of observations sensors or dynamic models and parameters employed for propagating the orbits [Carpenter, 2019]. Other concerns point to the lack of guarantee of generating non-positive definite covariance with the current information provided within the CDMs. [Carpenter, 2019]

There are some efforts to improve the uncertainty quantification on CDMs. In [Reihs et al., 2017], the authors study the consistency of the covariance matrices included on the CDM by comparing them with operational mission orbits. Despite the consistency, they found CDM covariances tend to be quite small, so they propose a scaling factor for the covariance. In addition to the fact that they did not find a single scaling factor due to the mission dependency, this approach may generate problems with the dilution of probability and simplifies the uncertainty modelling problem to a matter of size. Other authors proposed methods to predict the next CDMs, either using time-series ML methods [Pinto et al., 2020, Acciarini et al., 2021] or statistical learning models [Caldas et al., 2023]. Despite the very good forecasting capacities of these proposals, they still do not address the limitations on the CDMs information and uncertainty models. Finally, citing [Caldas et al., 2023]: “GMV [a space technology and services company]

is currently developing an autonomous collision avoidance system that decides if the current information is enough for the owners/operators to decide, or if they should wait for another CDM to have more information. However, the techniques used are not publicly available". This approach seems to provide operators with a further piece of information regarding the forecasting approaches, indicating whether more CDMs are required. However, due to the lack of public information, no comments on the uncertainty models can be made.

There is some research that proposes to focus not only on the risk but also on the consequences of the potential collision, in what is known as consequence metrics [McKnight et al., 2021]. This metric evaluates jointly the risk of the collision, but also the consequence it may have on the environment. These consequences are measured based on the energy of the collision, the mass involved, the location of the collision or the objects' manoeuvrability. Thus, a high-risk event with low mass and energy may be less risky than a lower-probability encounter involving two big pieces of debris in a frontal trajectory. While providing additional information from the operator point of view, these approaches do not address directly the uncertainty problem. However, uncertainty can be treated in a more complete way, modelling more elements of the problem.

However, a common aspect missed in all the works mentioned above, and partially responsible for the limitations indicated, is the lack of modelling for the epistemic uncertainty [Poore et al., 2016]. Uncertainty can be found in two basic forms: aleatory and epistemic. Aleatory uncertainty, also known as objective, stochastic or Type I uncertainty, is modelled with probabilistic theory and refers to the process's inherent uncertainty of its own randomness, and cannot be reduced, but only properly modelled; while epistemic uncertainty refers to a lack of knowledge of the system and its properties and can be reduced [Helton, 1997]. It is also known as ignorance or Type II, reducible or subjective uncertainty.

2.1.1 Epistemic uncertainty

When it comes to the computation of the probability of collision, it is generally assumed that all uncertainty affecting the objects' position is aleatory, and thus, poor quality information will be assigned a bigger covariance matrix, which leads to the phenomenon of dilution. The problem with the dilution of probability is the counterintuitive idea that having poorer-quality data translates into a safer situation. What is wrong in this reasoning is the aleatory assumption. The satellite position does not follow a random event. While some steps may introduce some random error, some of the uncertainty is associated with a lack of knowledge of the sensors or model parameters. This difference in the type of uncertainty within the conjunction assessment context is very well illustrated in the example provided in [Balch et al., 2019]:

“For example, suppose two satellites were known, with certainty, to be on a collision course, and the satellite operator could only impart an impulse of random magnitude in a random direction [...] If the mean of this distribution were the null vector, [...] then the higher the variance of the added impulse, the bigger the resulting perturbation and hence the smaller the resulting probability of collision. In this example, the mean of the resulting trajectory distribution would still have the satellites on a collision trajectory, but [...] higher variance in a satellite's trajectory really does reduce the risk of collision. However, *it is a variance in the trajectory itself that makes the satellite safer, not a variance in the estimate of that trajectory.*

It should go without saying that, given two satellites on a sure collision trajectory, simply recomputing the trajectories with lower quality data does not make them safer.”

There are proposals for using dilution-free metrics [Balch, 2016], but the source of the problem regarding dilution is a wrongly modelled uncertainty.

Enhancing robustness in decision-making requires dealing with both aleatory and epistemic uncertainty and managing different sources of information which may provide incomplete information or be in conflict with each other [Hoffman and Hammonds,

1994]. While aleatory uncertainty is well studied and implemented in CARA, epistemic uncertainty has been overlooked in space applications [Poore et al., 2016].

Opposite to aleatory information, where probabilistic theory is the established model, there is not a single theory for epistemic uncertainty [Sentz and Ferson, 2022, Ferson et al., 2003, Zervas et al., 2011, Poore et al., 2016]. When only epistemic uncertainty is involved, intervals can be used [Moore et al., 2009]. When uncertainty is compounded by both aleatory and epistemic contributions, there are different approaches, including Dempster-Shafer theory of Evidence (DSt) [Dempster, 1967, Shafer, 1976], possibility theory [Dubois and Prade, 1988, Dubois, 2006], fuzzy sets [Zadeh, 1965, Zadeh, 1984a, Walley and Cooman, 2001], or *bounds on probability* and probability boxes (p-boxes) within the probabilistic theory [Ferson et al., 2003, Destercke et al., 2008, Walley and Fine, 1982, Williamson and Downs, 1990, Berleant, 1998].

Some efforts exist to overcome the limitation of probabilistic theory for conjunction risk assessment and the exclusive use of the PoC value as the only metric to determine the risk of the encounter. The authors of [Hejduk and Johnson, 2016] criticise the use of the PoC as a point estimate and propose an approach to use a PoC density that accounts for uncertainties on the PoC inputs (covariance, positions, hard body radius...). By a resampling approach of the objects' position and covariance, they obtain a PoC distribution. Using Monte Carlo (MC) approach to account for the uncertainty on the inputs, they repeat the resampling method with both a PoC density for each input uncertainty and a total distribution accounting for all the effects. In this way, it is possible to analyse the influence of the input uncertainty on the PoC and compare the nominal value with the distribution obtained, so a more informed decision can be made.

The limitation of the CDMs to provide covariance information and the restrictions of just modifying the covariance matrix to improve the uncertainty model as the technique to improve the risk estimates is highlighted in [Carpenter, 2019], and in [Carpenter et al., 2017], the authors criticise the use of PoC as a decision-making metric. As an alternative, the authors proposed to use miss distance intervals to capture the uncertainty of the event, which also can tell about the confidence or lack of confidence

to make a decision using the value of the PoC based on the interval width.

In this line, [Hejduk and Snow, 2019] revise different methods to evaluate the conjunction risk from the perspective of the likelihood to occur and the support from the information. They use the concept of *plausibility* and *possibility* as additions to *probability*. The authors refer to *probability* as the well-defined estimation of a single value indicating the risk of an event, and *possibility* as a mere indication that a conjunction is possible. In between, they locate *plausibility*, which refers to methods that compute a probability value but include some level of uncertainty indicating the possibility of the event to occur (not confused with the *Plausibility* concept later used in this work in the context of DSt). The authors rank some of the methods mentioned before, including the PoC densities, according to their plausibility, being the standard PoC method in one end of the scale (pure *probability*) and the ellipses overlap [Balch et al., 2019], in the sense of ensuring the separation of the covariance is sufficiently high, on the other scale (pure *possibility*).

In all these examples, there is an attempt to go beyond the limitation of a single value of the PoC to compute the risk of collision and introduce some of the concepts employed in epistemic uncertainty as interval-valued variables or the concepts of *possibility* and *plausibility*. However, they do not attempt to extend the probabilistic framework and explicitly model the epistemic uncertainty affecting the problem. In fact, only a limited number of authors have directly addressed epistemic uncertainty in conjunction risk analysis [Tardioli and Vasile, 2015, Delande et al., 2018, Balch et al., 2019, Tardioli et al., 2020, Greco et al., 2021].

In this work, DSt is proposed to model both types of uncertainty in the context of conjunction assessment. Authors in [Sentz and Ferson, 2022] mention four advantages of DSt over other approaches:

- higher degree of development with respect to other theories;
- the relation between DSt and probabilistic theory. If the available evidence is coherent (i.e. there is no epistemic uncertainty), this theory simplifies into probabilistic theory, so it can be understood as the extension of the approaches already implemented [Ferson et al., 2003];

- wider literature on its application in engineering problems [Zervas et al., 2011, Liu et al., 2017b, Vasile et al., 2017a, Filippi and Vasile, 2019], and more specifically, in risk assessment problems [Helton et al., 2005, Oberkampf and Helton, 2002];
- the capacity of DSt to represent different types of uncertainty and, more interestingly, to combine sources of information [Sentz and Ferson, 2022].

On top of this, [Ferson et al., 2003] shows the equivalence between DSt and probability-bounded (p-boxes) approaches, which will be exploited later in this work.

Information in DSt is interval-valued, instead of precise quantified. The single-valued variable may not be adequate in situations driven by lack of knowledge, for example when there is little information to evaluate a probability or when information is ambiguous or in conflict [Sentz and Ferson, 2022]. The use of intervals implies that the Principle of Insufficient Reason and the axiom of additive is not imposed, which, in other words, means that there are no assumptions on the event or set of events when there is no direct evidence about them (i.e. evidence on the occurrence of an event does not imply knowledge on the non-occurrence of the event) [Sentz and Ferson, 2022]. This allows basing the decisions on a system's safety not just on a single value of the desired metrics, but providing plausible bounds on the metrics. Even more important, it allows for the quantification of the support for specific values of the safety metric and measuring the level of uncertainty (or conflict) affecting the information. Knowing the degree of uncertainty allows discerning better if high or low values of PoC correspond to risky or safety cases, or if they are related to a lack of consistency in the data. Similarly, it reduces the assumptions required, not imposing any distribution on the data other than the presence of certain intervals with a given level of support. These aspects align with the principles stated in [Carpenter et al., 2017].

Finally, DSt provides a framework to handle information originating from different sources [Koks and Challa, 2003] (e.g. a network of sensors, or information from different providers). The increase in SSA providers means that information received by operators may have different origins, which will be more or less reliable according to the sensor or information quality of the provider or on data processing (e.g. during the generation of CDM). Similarly, information may be received in different formats, from the old

TLEs to the actual CDMs, the operator's ephemeris or directly from unprocessed raw observations, which, again, will have different levels of trustworthiness. In addition, information may be in conflict, with some sensors suggesting a more likely conjunction than others. A robust STM system must be able to handle all this information reliably, ensuring operators are provided with the right information, and more importantly, with the right confidence in the different sources. Frequentist approaches already proposed some data fusion approaches based on Baye's rule [Koks and Challa, 2003]. Similarly, DSt uses combination rules [Sentz and Ferson, 2022] to bring together information and provide a measure of the level of conflict and the reliability of the desired variable of interest, with the additional advantage of fewer assumptions on the information (e.g. probability densities). However, the selection of the most adequate combination rule is a challenging process related to the degree of conflict affecting the information, the type of sources, the amount of evidence in the information or the way the operator desires to deal with it [Sentz and Ferson, 2022].

Additionally, the DSt framework allows not only to fuse information in different formats or provided by different sources but also to fuse data generated with different models. An example of this could be the propagation of orbit under atmospheric drag (or any other orbit perturbation). Density models vary considerably from source to source and from different providers. Also, the satellite state would impact the results. All of this can be combined using DSt, since differences in the atmosphere density model (or any other perturbation model) or the satellite attitude can be treated as additional uncertain parameters within the uncertainty model, in the same way as the position uncertainty.

2.2 Automation

With the increase in space traffic, space surveillance capabilities, actors involved in space operations and the emergence of new technologies automation is becoming a key element to ensure the safety of space [Nag et al., 2018, Nag et al., 2021]. Current STM protocols [Merz et al., 2017, Newman et al., 2014, Newman et al., 2019, Laporte and Moury, 2013] require intensive operator workload, constant coordination among teams

and agencies/operators, and tight decision-making windows. All the factors listed above characterising the New Space will only exacerbate the limitation of a human-based STM. For example, the conjunction alerts received by operators are dominated by low-risk encounters or false alerts, which should be analysed to make sure they do not pose an actual risk. An increase in the number of alerts may consume operators' resources making it impossible to detect actual collisions or to properly address them. Even if they are detected and addressed, the Collision Avoidance Manoeuvre (CAM) design process is complicated, involves the coordination of different mission teams and requires the nominal satellite operation to stop. Automation may help ease the operator's workload so they can focus on operational mission objectives or just on very critical conjunctions.

Different agencies and other space actors are already aware of this necessity. The National Aeronautics and Space Administration (NASA) has published plans for automating the current CARA architecture [Nag et al., 2018, Nag et al., 2021], and has proposed an automated system based on Unmanned Aerial Vehicles (UAV) Traffic Management architecture. The proposed architecture is based on Application Programming Interfaces to facilitate the interaction between STM agents, the data sharing among actors and enhance automation throughout the whole process, including risk assessment and optimal CAM search. The Application Programming Interfaces allow the building of a modular architecture to add or remove capabilities and facilitate automation through the interface among modules.

Similarly, the European Space Agency (ESA) has recognised the importance of space safety, making one of its pillars with the Space Safety Program. Among its addressed topics, it includes “an adequate pre-emptive approach concerning future activities and to enable the safe operation through an Automated Collision Avoidance System” [Bastida Virgili et al., 2019, Flohrer et al., 2019], that is, the development of an automated approach to deal with conjunction avoidance tasks. According to this program, the three topics expected to be addressed in the context of collision avoidance and STM are: reduce manpower effort, minimise the decision time, and reduce the false alerts.

Several tasks currently carried out by operators could be automatised. This includes the classification of geometries and encounters, the identification of high-risk alerts among the plethora of potential conjunctions, trends on parameters evolution or conjunction patterns, prediction of CDMs, improving uncertainty quantification or even manoeuvres design [Bastida Virgili et al., 2019]. All these tasks comprise a certain level of routine tasks and bring associated plenty of data which may be difficult to analyse by a reduced number of operators in a team.

With a more populated catalogue, the chances of finding actionable encounters or even multiple encounters for the same satellite increase, which affects the decision time reaction: if more encounters are likely to happen in a given time horizon, a faster decision time will allow addressing different events better or reducing the share of operators among events. With the increase in operational satellites, the probability of conjunction involving two of them grows, which requires even further coordination. The development of both protocols [Bast and Krag, 2019], techniques and architectures [Nag et al., 2018, Delmas et al., 2023] to support decision-making becomes paramount for the smooth operation of the STM system.

Reducing false alerts is related to the other two aspects. Being able to automatically and adequately differentiate actual high and low-risk events or to provide a confidence measurement when classifying events on either of those two categories, would reduce the decision time and the manpower efforts avoiding dealing with cases not actually possessing a high risk of collision.

In this context, Artificial Intelligence (AI) and Machine Learning (ML) can play a fundamental role due to their potential to learn from real and synthetic data, create faster dynamic-free models and provide decision support with limited computation effort. The goal is to predict events and automatise the allocation of remediation actions.

2.2.1 Artificial intelligence

Artificial Intelligence is referred to as the ability of computers to learn from data, reason, acquire knowledge, react to the environment and correct themselves to imitate

human intelligence or behaviour without being specifically programmed to do it. It is a wide knowledge area including Machine Learning, Natural Language Representation, Computer Vision, and Data Mining among many others [Russell and Norvig, 2009]. It has been studied for some decades, but only during the last years, with faster and more capable computers and the availability of big datasets, it has been possible its implementation into real applications in a broad range of disciplines, including engineering.

In this thesis, two branches of AI will be employed: ML and Decision Support System (DSS). The first one is a field of AI that learns from data to replicate behaviours. The second one, develop agents to support operators in decision making. Both may support the automation of STM via generating faster surrogate models replicating the actual models or by leveraging the decision process on complicated tasks based on conflict information.

Regarding ML algorithms, they are characterised by the ability to learn from data certain answers and replicate the answer on unseen data. There are three main branches in ML: supervised learning, unsupervised learning and reinforcement learning [Khoei et al., 2023]. Supervised learning refers to those techniques where the actual answer to the training data is known. That is, in regression problems, the value of the target variable given a set of inputs is known, and in classification problems, the label is associated with those given inputs. Thus, when training the model (fitting the parameters of the model, e.g. stochastic gradient descent [Robbins and Monro, 1951]), pairs of inputs-outputs are given sequentially and the answer of the model is used to adjust the parameters and eventually obtain a closer answer to the real target. Unsupervised algorithms, on the contrary, are not given the target output. Instead, these models are used to obtain patterns on the data or clustering the information creating their own labels. Finally, reinforcement learning techniques differ from the previous one in the sense that they learn sequentially and from the experience of interacting with the environment. In this work, only supervised learning is considered. More precisely, this study will focus on some of the most used techniques: on the one side, more traditional algorithms like Support Vector Machine (SVM) or K-Nearest Neighbours (KNN), or some of the most successful, yet simple, methods like Random Forests (RFs), gradient

boosting methods or single layers Artificial Neural Networks (ANNs).

Within ML, there is a subfield referred to as Deep Learning (DL), which has shown great results on different applications and fields (e.g. chatGPT [Brown et al., 2020]). DL, which can be supervised, unsupervised or reinforcement learning, refers to those algorithms using ANNs using several neuron layers (hence the term deep). One of the latest and most successful architectures is Transformers, which will also be considered in this work.

In supervised ML and DL, to avoid overfitting when training the algorithm, all the techniques, except KNN, are trained on a subset of the complete database. Overfitting refers to the phenomenon of adjusting the model parameters so that the model can predict very accurately within the set of data used for training but is generalised badly when predicting data not belonging to this set [Rosin and Fierens, 1995]. This can happen, for example, if the system has too many degrees of freedom (e.g. neurons in a ANN model), in the same way that a polynomial of high degree passing through every single point of a noisy linear distribution would not be a good fit.

To mitigate this risk, the available dataset is split into a Training set and a Test set, so that the models' performance is not evaluated in the Training Set, but in the Test set. The system training is then stopped when the fitting error based on the Test set starts increasing. This typically happens before the fitting error based on the Training set achieves machine zero. In this work, the split on the Training and Test sets follows an 80%-20% proportion. The score comparing the different models' performance can be obtained by predicting a third set, the Validation set, not included at any stage during the training, or using the Test Set, provided it was never used for tuning the model's hyperparameters and was just used for evaluating the performance.

Machine Learning techniques

In the following, a brief explanation of some of the most common supervised ML techniques is given. This is not an exhaustive list, but it focuses on those used in this thesis and represents common techniques used in the field (as detailed later): Artificial Neural Networks (ANN) [Kubat, 2017], Random Forests (RF) [Breiman, 2001], K-Nearest

Neighbours (KNN) [Cover and Hart, 1967], Support Vector Machine (SVM) [Cortes and Vladimir, 1995], Gradient Boosting machine [Ke et al., 2017], and Transformer architecture [Vaswani et al., 2017].

Artificial Neural Networks ANN models have experienced a relevant development during the last years thanks to the increase in computational power, currently existing a plethora of variants used for different applications like Multi-Layer Perceptron (MLP), Convolutional Neural Networks (CNN) or Long/Short Term Memory network (LSTM). Most of them fall in the field of DL. In this work, however, the focus is on the simpler, yet powerful, MLP-based ANN models.

The MLP algorithm consists of a set of connected layers of *neurons*, which can predict the quantity of a desired variable given a set of inputs after having provided a set of examples, whose actual value is known (Fig. 2.1).

The first layer, referred to as the inputs layer, consists of the components of the input variable. The last layer or output layer varies depending on the problem: for regression problems, it consists of one or more neurons (depending on the dimension of the output variable) providing the value of the corresponding variable; for classification problems, it consists of a set of neurons (as many as fields on the classification), whose value ranges in $[0, 1]$ depending on the probability of the classification value of been the correct one. In the classification case, usually, an additional layer with a single output is included with the value of the class receiving the higher probability on the previous layer. In between, there are a set of layers, called hidden layers, with a number of neurons, whose values vary, generally, between 0 and 1 (although other pairs of values are also possible).

The value of each neuron depends on the values of the previous layer's neurons and the weights that connect that node with all the neurons in the previous layer. The activation function of the neuron will dictate how it reacts to the received values. The value of the neuron is then, transmitted to the next layer. There are different activation functions in the literature [Lederer, 2021], with the sigmoid, hyperbolic tangent and

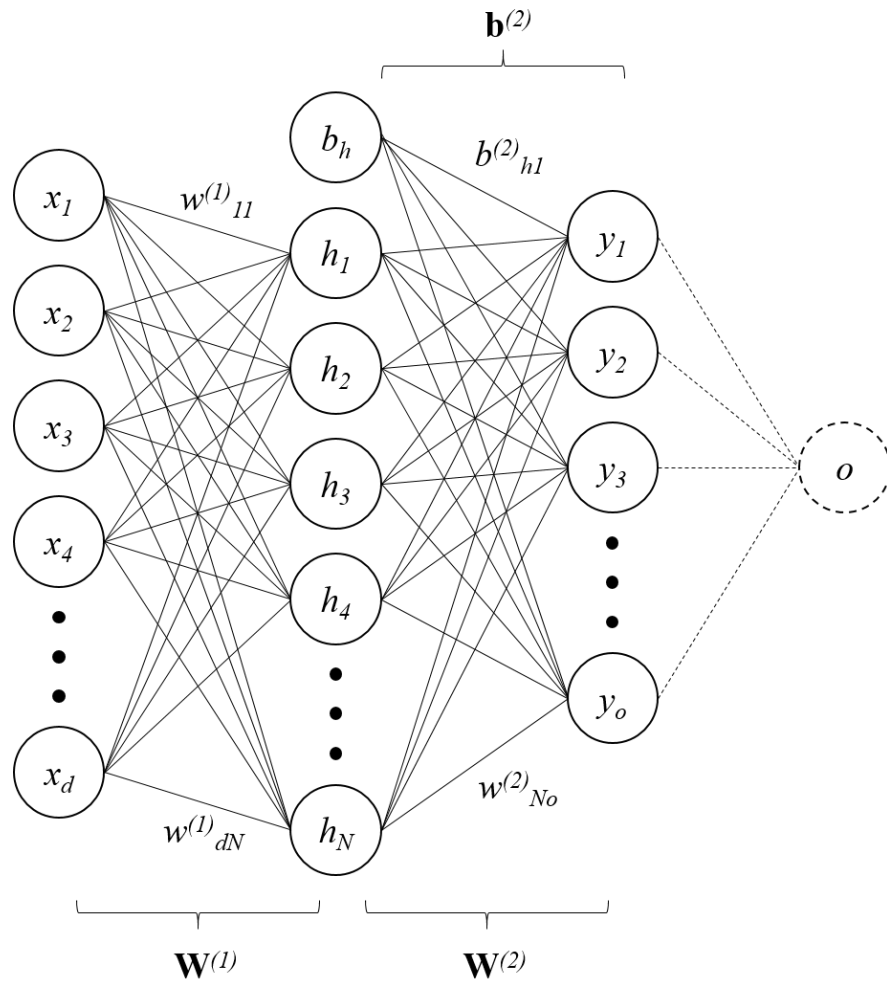


Figure 2.1: General structure of single-layer ANN model.

the Rectified Linear Unit (ReLU) functions the most popular:

$$ReLU(x) = \max(0, x) \quad (2.1a)$$

$$\sigma(x) = \frac{1}{1 + e^{-x}} \quad (2.1b)$$

$$\tanh(x) = \frac{e^x - e^{-x}}{e^x + e^{-x}} \quad (2.1c)$$

The set of neurons and layers constitute the network. The MLP may have an arbitrary number later. In this work, the analysis was limited to the single layer

case. Thus, the MLP ANN can be understood as a universal function approximator $\mathbf{f}_g(\mathbf{x}) : \mathbb{R}^{n_d} \rightarrow \mathbb{R}^{n_o}$, [Cybenko, 1989], where n_d is the size of the input vector \mathbf{x} , and n_o is the size of the output vector function \mathbf{f}_g . The outcome in the output layer is dictated by the general matrix-vector definition in Eq. (2.2) to approximate the desired function \mathbf{f}_g .

$$\mathbf{f}_g(\mathbf{x}) \approx A_2(\mathbf{b}^{(2)} + \mathbf{W}^{(2)}(A_1(\mathbf{b}^{(1)} + \mathbf{W}^{(1)}\mathbf{x}))) \quad (2.2)$$

where $\mathbf{W}^{(1)}$ is a weight matrix of size $(N \times n_d)$ and $\mathbf{W}^{(2)}$ is a weight matrix of size $(n_o \times N)$ connecting all the neurons of the input layer with the hidden layer and those in the hidden layer with the output layer, respectively, being N the number of neurons in the hidden layer; $\mathbf{b}^{(1)}$ and $\mathbf{b}^{(2)}$ are the bias (column) vectors of length N and n_o , respectively; and A_1 and A_2 are the activation functions of the hidden layer and the output layer, respectively.

The learning process consists of adjusting the values of the weights matrices and bias vectors so that, given an input vector, the network provides the actual output. This process is done by a two-step process (feed-forward and back-propagation) feeding the network with a sufficient number of cases. Each time a new example is input into the network, the predicted output is compared with the actual value. Then, a back-propagation algorithm updates every individual weight and bias on the network following a local gradient-based optimisation. Different algorithms are available for this task: Levenberg-Marquardt [Hagan and Menhaj, 1994], Adam [Kingma and Ba, 2014], RAdam [Liu et al., 2020].

Random Forest RF is an ensemble method that combines several independent Decision Tree (DT) during the training step, feeding each of them with different subsets of the training set. The predicted class is the mode of the output of every single tree in a classification problem and the mean of the trees' output in a regression problem. RF overcome the overfitting problem usually faced by DTs.

DTs are a supervised ML method that classifies the input variables hierarchically according to the value of their different features, creating subsets that end on the label class at the *leaves* level Fig. 2.2, an algorithm called *top-down induction of decision*

trees (TDIDT) [Quinlan, 1986]. The training consists of feeding the DT with several training samples (whose actual output is known) to modify the order of the features, the split value and the number of splits per node so that the correct classification rate is maximised.

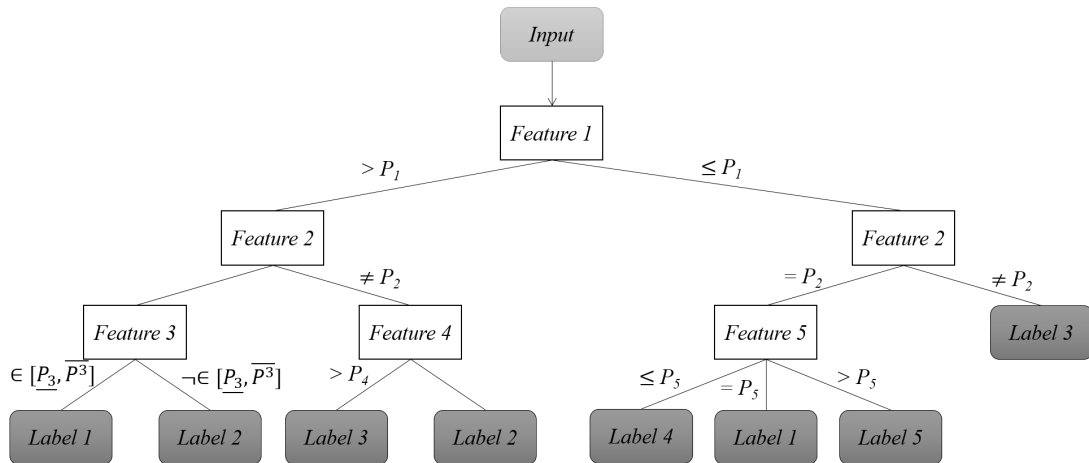


Figure 2.2: General structure of a single Decision Tree.

DTs suffer from overfitting and bias. Ensemble methods allow the combination of several classifiers introducing an amount of randomness in the process to better generalise the predictions. RFs are an ensemble of DTs, where, instead of taking all the possible configurations of features, just a selected number of them on each tree. On top of that, a bagging method [Breiman, 2001] is employed in the samples, so that, for each tree, a different subset of samples from the Training Set is drawn with replacement. The combination of both aspects (trees with different features and node distribution, and different sets of samples) provides reduced overfitting and variance in the data. The outcome of the RF will be the mode (classification problem) or the mean (regression problem) of the outcome of all the individual trees (Fig. 2.3).

K-Nearest Neighbours The KNN algorithm predicts the output of a given sample by comparing its proximity with the training samples (Fig. 2.4) under the assumption that similar points will be located close to each other [Raschka, 2018]. As opposed to the previous methods, this method lies within the *lazy learning* group of algorithms. This means that the system is not trained before making predictions, but instead, all

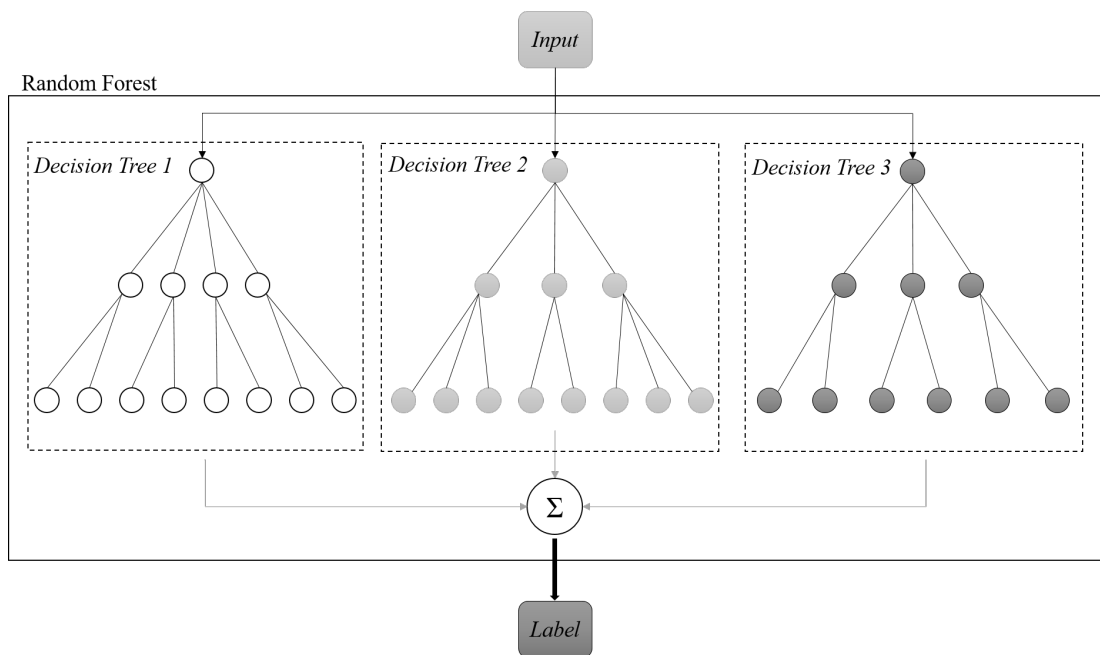


Figure 2.3: General structure of a Random Forest.

data are used every time a prediction is expected: the distance from the new point is computed each time a new sample arrives, which could be beneficial since it simplifies the algorithm and the number of parameters, but make the method suffers severely from the curse of dimensionality.

To estimate the proximity of the samples, different metrics can be employed. The easiest to visualise is the Euclidean distance ($\sqrt{\sum_i (y_i^2 - x_i^2)}$), shown in Fig. 2.4, although other metrics exist: Manhattan distance ($\sum_i |y_i - x_i|$), Minkowski distance ($([\sum_i |y_i - x_i|]^{1/p})...$). It is possible to make a variant on the algorithm so the closer the sample, the more importance it is assigned. In this way, in a 5-NN problem, if the selected sample lies very close to two samples of one class, but the next three nearest examples are from the other class, it can be still classified within the first group.

In this algorithm, the only parameter to be selected is the number of neighbours, k . However, the selected value heavily influences the final results due to overfitting or underfitting and the optimal value will depend on the specific problem.

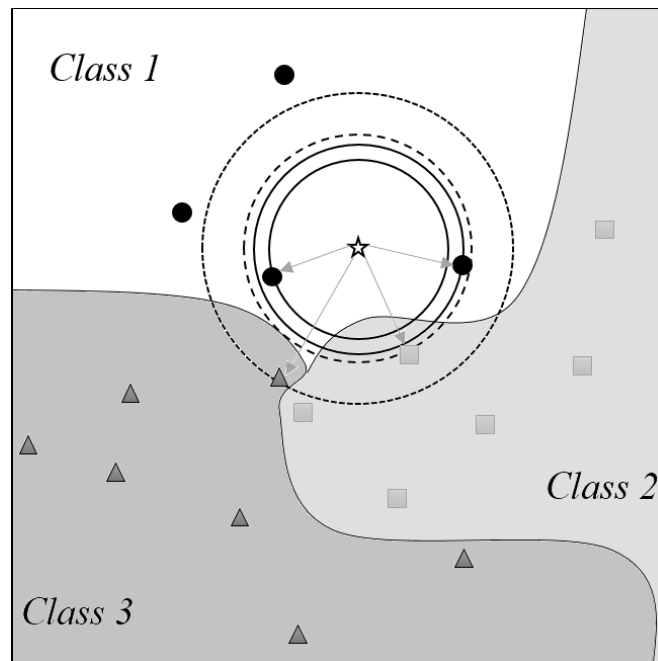


Figure 2.4: Example of 4-Nearest Neighbour.

Support Vector Machine SVM algorithms [Cortes and Vladimir, 1995] classify samples from different classes by building the hyperplane that splits the classes of the training point, maximising the distance to the nearest point on each class (Fig. 2.5).

In the linear problem, finding the hyperplane that maximises the distance to the closest points in each class and divides the space into the two classes is done by solving the Eq. (2.3).

$$\begin{cases} \min_{\mathbf{w}, b} \|\mathbf{w}\| \\ \text{s.t. } y_i(\mathbf{w}^T \cdot \mathbf{x}_i - b) \geq 1 \forall \{i, \dots, n\} \end{cases}, \quad (2.3)$$

with \mathbf{w} the vector normal to the hyperplane, b the offset of the hyperplane at the origin, $b/\|\mathbf{w}\|$ the margin between the closest point and the hyperplane, and n the number of samples in the Training Set, being the hyperplane defined as the set of points \mathbf{x} so that $\mathbf{w}^T \cdot \mathbf{x} - b = 0$. Different algorithms exist to solve the minimisation problem including sub-gradient descent or coordinate descent.

Non-linear divisions may be required for a good division among classes. Kernels can be used to define the problem in a higher dimensional space where the division may be easier (e.g. Gaussian or polynomial). An example of cases where a non-linear

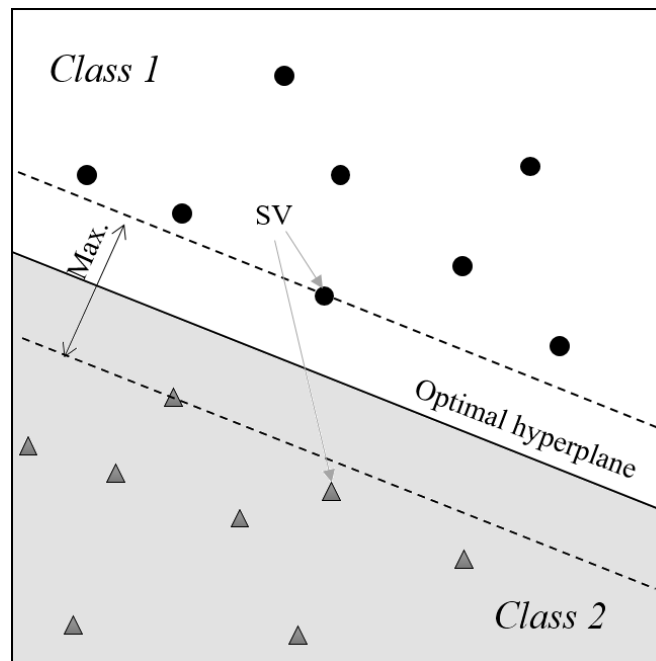


Figure 2.5: Example of Support Vector Machine.

approach will give better results may be a class defining a circumference around the other class.

Gradient Boosting machine Gradient Boosting machine is also an ensemble of DT methods, which combine different weak learners to provide an accurate prediction. A weak learner refers to a learner that makes few assumptions on the data. Iteratively, new weak learners are added to compensate for the limitations of the previous one. The algorithm adds a new weak learner (i.e. a DT) to reduce the difference between the actual value and the value provided by the ensemble model (gradient descent).

Thus, the idea is to find a learner $F(x)$ to predict the variable y , by minimising the error between the actual value, y_i and the predicted value \hat{y}_i . In different stages, a new learner F_m is added so that a new estimator, h_m is added to improve the prediction: $F_{m+1}(x_i) = F_m(x_i) + h_m(x_i) = y_i$. Thus, the algorithm aims to minimise $h_m(x_i) = y_i - F_m(x_i)$ [Li et al., 2016].

In this work, the Light Gradient Boosting machine (LGBM) algorithm [Ke et al., 2017] was implemented. This algorithm shares many of the advantages of other en-

semble and gradient boosting methods, like the simplicity and the reduced number of parameters to be defined. However, it is usually faster to train (then, the term *light*) and it is usually more precise. The main difference from other algorithms is the growth of the decision trees. Instead of growing a level at a time (level-wise growth), it grows from the node that looks more promising (leaf-wise growth) (Fig. 2.6). This approach is based on two techniques: Gradient-based one-sided sampling, which gives more importance to instances with higher gradients, dropping those with lower values, and Exclusive Feature Bundling, which reduces the dimensionality of the problem by bundling together mutually exclusive features. LGBM also presents the advantage of accepting both numerical and categorical inputs without any pre-processing of the data.

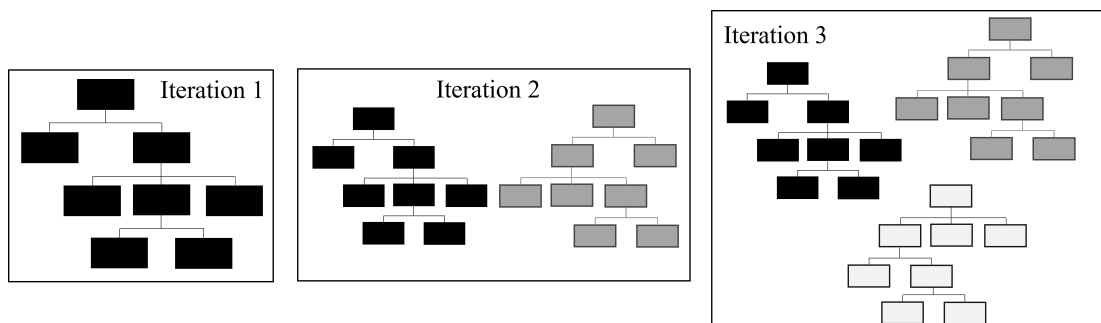


Figure 2.6: Scheme of the Light Gradient Boosting machine process.

Transformer The transformer architecture is a DL approach implementing several layers of networks based on the mechanism of attention [Vaswani et al., 2017]. It was initially developed for natural Language Processes applications, but it has been extended to other fields, like computer vision [Dosovitskiy et al., 2020] or times series [Stevenson et al., 2022a].

Transformers address the sequence of data but without the need for recurrent networks, such as LSTM, reducing the training requirements. Instead, they used the attention mechanism and an encoder-decoder structure, where the decoder is fed both by the encoder output and the previous step decoder output. The attention mechanism algorithm addresses the problem of local connectivity by comparing, in turn, every point of the sequence to all the other points to derive the most relevant part of

the sequence for each of them.

In this work, the transformer architecture is implemented based on the implementation in [Stevenson et al., 2022a], which is inspired by the computer visual application of transformers Vision Transformer [Dosovitskiy et al., 2020]. Here, each point on the time sequence is split into individual tokens, which are the input of a Convolutional Neural Network (a feature extractor) to create a new sample with a higher dimension. The re-dimensioned samples are then passed to the encoder, which consists of a series of encoder blocks, each of them conformed by a set of two neural networks: a multi-head self-attention unit and a feed-forward neural network. Finally, the output of the set of encoders is passed through a fully connected layer that provides the class probabilities.

2.2.2 Artificial intelligence for automation

AI has several qualities that make it suitable to address the challenges and the aims of automation in space, as shown below. For example, ML techniques, a field of AI, are data-driven, which means that no underlying model is required to obtain accurate predictions or reliable actions on a system. Instead, the model learns from the available information, searching for patterns and relations that explain the underlying dynamics. Thus, ML can be used to create surrogate models that reconstruct the functional relationship between a set of input and a set of output data, creating faster models that help automation. ML performs very well on repeated tasks which require pattern recognition or prediction from data relationships. With the increase in available information, precisely, this kind of task becomes more challenging for humans but makes the ML perform better. This is the case, for example, of false alert detection, where the increase in conjunction messages may overwhelm human operators but are useful for the system to learn, or anomaly detection (e.g. CAM detection), where changes in the orbit's parameters are not always obvious.

Another field of AI are DSS agents. These techniques are dedicated to supporting decision makers by gathering and analysing, diagnosing problems and providing suggestions and recommendations on the best course of action, freeing operators of this burden and enabling automation of the system. [Shim et al., 2002, Fülöp, 2005]. One of the

most common approaches is Multi-Criteria Decision-Making (MCDM) [Triantaphyllou, 2000], which evaluates alternatives (Multi-Attribute Decision Making) [Triantaphyllou and Shu, 2001] or a mathematical model (Multi-Objective Decision Making) [Rojiers and Whiteson, 2017] over a set of criteria to prioritise the best outcome according to the operator's preferences. DSS and MCDM approaches have been applied in several fields, ranging from engineering to economics and social sciences.

The use of AI can be found nowadays in every engineering field. The examples range all the AI spectrum, although image recognition and natural language processing are probably the most advanced technologies. For example, image recognition plays an important role in the automation of self-driven cars. Natural language processing is also a leading technology, with digital assistants the main example of this technology. Nevertheless, the list of cases is endless, and examples can be found in robotics, weather forecasting, medical diagnosis, and bank fraud detection, among many others.

Relevant for automation and traffic management is the application of DSS systems to assist operators. In [Ramírez-Atencia et al., 2017, Ramírez-Atencia et al., 2017], the authors employ DSS agents to automate the control of UAV swarms. In the ATM field, an Autonomous Operator Planner is employed in [Barhydt and Krishnamurthy, 2004] to provide guidance to pilots on trajectory planning, accounting for the pilots' goals, conflict detection and resolution and ATM constraints. Other space traffic management sectors have employed other AI techniques to facilitate automation. Still, on the ATM system, the authors of [Julian et al., 2016, Kochenderfer and P., 2011] use AI, DL and dynamic programming to support operators on the decision making and improve automation on collision avoidance systems. Also in the MTM system, AI methods and techniques are used to facilitate automation, as in [Statheros et al., 2008], where the authors enhance a dynamic-based method with AI for collision avoidance automation. Despite the difference, there are some similar characteristics between those systems and STM, like high-density areas in an, apparently, broad space that complicates the operations, the aim to reduce the operators' workload, the increase in traffic, and the conflict and collision avoidance management, from where the space sector can take lessons to accelerate the automation process [Nag et al., 2018, Contant-Jorgenson et al.,

2006]. Another interesting possibility would be to apply DSS model to consequence metrics [McKnight et al., 2021] and algorithms to classify events and objects based on a more comprehensive list of factors.

Artificial intelligence for space safety

In space engineering, AI has been used in a wide range of fields. Several AI-based methods can be found in different areas of space engineering, for example, image recognition algorithms are being used for autonomous navigation [Tail et al., 2020, Downes et al., 2020, Song et al., 2022, Mancini et al., 2023, Kaluthantrige et al., 2023, Pugliatti et al., 2023] and are expected to be applied for satellite inspection or swarm relative navigation [Izzo and Pettazzi, 2007, Zhu et al., 2023]; AI and reinforcement learning techniques have been applied for trajectory optimisation, guidance and control [Gaudet and Furfaro, 2014, Furfaro et al., 2020, Gaudet et al., 2020, Oestreich et al., 2021, Wilson and Riccardi, 2023, Izzo et al., 2019]; natural language processing tools have been developed to create digital assistant agents to interact with astronauts [Airbus, 2021] or to support the mission design [Berquand and Riccardi, 2020, Berquand et al., 2021, Berquand and Ladeira, 2022, Darm et al., 2022, Darm et al., 2023]; AI time-series prediction tools have been applied for space weather forecasting, especially, Sun flux and atmosphere density [Rüdisser et al., 2022, Dorelli et al., 2022, Salvatelli et al., 2022, Stevenson et al., 2022b].

More specifically, STM and SSA are two fields where the use of AI can bring great benefits to facilitate the automation of processes, speed up tasks and assistance of operators in decision-making. STM, as defined above, is compounded by those activities focused on ensuring the safe operation of satellites. SSA consist of the activities to track objects, identify them, determine their orbits and predict the future positions and threads to operators. Together, they constitute the two main pillars to ensure the safety and sustainability of the space environment and its utilisation. For this reason, agencies and other relevant actors have started different programs to incentive the use of AI for space safety [Mashiku et al., 2018, Mashiku et al., 2019, Bastida Virgili et al., 2019, Flohrer et al., 2019, Manfletti et al., 2023, Maric et al., 2023, Frontier Development

Lab Europe, 2020, Flohrer et al., 2020].

Another example illustrating the increasing trend of using AI in SSA and STM are the challenges proposed by research entities. In these challenges, a problem related to space safety is proposed to the participants along with a database containing several samples of events associated with the problem. The participants are expected to propose solutions and the best ones tend to be data-driven and ML-based, instead of models based on the dynamic laws governing the phenomenon. The ESA's Advances Concept Team has presented already several challenges through its Kelvins platform [ESA's Advanced Concepts Team, 2023]: the *Collision Avoidance Challenge* [European Space Agency, 2019, Tulczyjew et al., 2020, Tulczyjew et al., 2021, Uriot et al., 2022], where the participants are expected to predict collision risk given a set of CDMs, the *Spot the GEO* challenge [European Space Agency, 2020], whose aim was to spot the Geostationary Orbit (GEO) satellites on images of the sky, the *Pose Estimation* challenge [European Space Agency, 2021a] to determine space debris position and orientation from images, or the *Space Debris* challenge [European Space Agency, 2021b], aiming to backtrack space debris in GEO to its original parent body. The Frontier Development Lab also proposes AI inspired challenges [Frontier Development Lab Europe, 2020, Flohrer et al., 2020], like the 2020 *Constellation Challenge* where the selected team proposed an open source tool to predict CDMs [Pinto et al., 2020, Acciarini et al., 2020, Acciarini et al., 2021]. Recently, the Massachusetts Institute of Technology has proposed a similar challenge for detecting patterns of life in GEO satellites given the times series of their position for a certain period [Siew et al., 2023b, EvalAI and ARCLab - Massachusetts Institute of Technology, 2023].

During the last years, there has been a proliferation of studies on the use of AI for SSA. In [Linares and Furfaro, 2016b, Furfaro et al., 2018, Furfaro et al., 2019, Linares et al., 2020], the authors used ML and DL techniques, like Convolutional Neural Networks (CNN) to classify space objects and determine their shape and attitude based on the light curves of the objects generated with physic-based models. A similar approach of object classification with light curves was followed in [McNally et al., 2021], analysing different ML architectures. In [Vasile et al., 2023], the authors also determine the atti-

tude of the space objects and classify them using ML approaches based on hyperspectral images and the inferred surface composition. The applicability of DL models for space object characterisation from radar signals is shown in [Wu and Rosengren, 2023], while authors in [Paulete et al., 2021] propose a ML-based for object identification based on their Radar Cross Section trained on real data. Related to object observations, AI has been employed for sensor tasking to schedule observations to cope with the increase of space objects and help automation of SSA. Works range from single sensor constraint-free scheduling [Linares and Furfaro, 2016a], to multi-sensor networks [Siew et al., 2023a] via a centralised agent, using reinforcement learning approaches.

Other uses of AI for space safety fall in the intersecting area of SSA, understood as surveillance and characterisation of objects, and STM, understood as conjunction risk assessment, avoidance manoeuvres and satellite operations. This is the case of digital assistants to support operations on SSA, like VerSSA [Ludwig et al., 2019, Ludwig et al., 2021], which automates the analysis of the input data (in the background and on-demand), filters information, analysis scenarios, and provides space objects information summaries to speed the decision-making process on critical events. Other tools focus on space object behaviour analysis to support operators in the better understating of satellite operations and the prediction of future actions, facilitating the automation of tasks or the prediction of risk scenarios. The authors of [Manzi and Vasile, 2020b] used Deep Symbolic Regression to reconstruct the underlying dynamics, which allows to improve dynamics models or reconstruct orbit anomalies (e.g. manoeuvres); in [Linares and Furfaro, 2017], the authors used reinforced learning to reconstruct the optimised cost function when manoeuvring satellites, and in [Roberts and Linares, 2021], CNNs are trained to detect manoeuvres in GEO, in both cases facilitating predict future scenario for space safety; and in [Shen et al., 2019, Shen, 2020], different ML techniques were used to detect and classify satellite behaviours, which again, helps on the further prediction of operators actions.

Finally, it is possible to find examples of AI techniques applied to improve automation and increase speed on specific STM tasks. For example, the works of Peng and Bai [Peng and Bai, 2017, Peng and Bai, 2018c, Peng and Bai, 2018a, Peng and Bai,

2018b] aim to reduce the propagation error by using different ML techniques, like SVM and ANN. In their works, they show that by feeding the intelligent system with the object's orbits to predict the propagation errors and then subtracting that error from the propagation, the position accuracy can be greatly improved. There are some works on the use of DL to address the *all-vs-all* problem during catalogue screening, that is, detect all possible conjunctions among objects in a given catalogue, which is a very time-consuming task due to the necessity to compare all pairs of objects. AI can help with the prediction of these events, avoiding the propagation step and the individual comparison of pairs [Stevenson et al., 2021, Stevenson et al., 2022b]. Other works [Acciarini et al., 2021] try to predict the next CDM to improve uncertainty quantification and anticipate decision-making. Also, in the field of CAM design and allocation there are some contributions on the use of ML [Vasile et al., 2017b, Abay et al., 2017, Gonzalo et al., 2020, Stroe et al., 2021] and this is one of the main focus of ESA's CREAM program [Flohrer et al., 2019, Flohrer et al., 2020]. In [Vasile et al., 2017b], the authors presented a system for supporting the planning and implementation of CAMs using ML (Elastic Nets) and a manoeuvres dataset, with special attention to the future consequences on the global space environment. In [Abay et al., 2017], a ML-based system was presented to plan sub-optimal automatic collision avoidance manoeuvres.

As it was shown, automation in STM is a necessity due to the changes in the space environment. ML methods have started to be used in this field due to their advantages regarding their lack of physical model and their capacity to enhance automation. Following this line, this research will make use of these novel techniques to apply them to STM tasks automation. Although there are some works on object detection and classification and improving orbit propagation, conjunction detection and decision-making are areas where ML is not applied that extensively. Similarly, more effort on CAM design and allocation should be developed according to the results of previous work, extending their capabilities to the low-thrust manoeuvres, which are becoming more common in space platforms. Finally, there are other fields of AI, like DSS which have been proven to be useful in traffic management systems but are still not applied in space, which can be very useful to address complex scenarios like multi-encounter events.

Part I

Methodology and algorithms

Chapter 3

Evidence-based conjunction classification system

The content of this chapter was partially published in:

Sánchez, L. and Vasile, M. (2021), “On the use of machine learning and evidence theory to improve collision risk management”, *Acta Astronautica*. [Sánchez and Vasile, 2021c]

This chapter presents a methodology for robustly assessing space close encounters, evaluating not only the risk of the event but also the confidence in the correctness of the value. The method proposed aims to avoid the phenomenon of the dilution of PoC, which gives the counterintuitive idea that the poorer the quality of the available information for the operators, the smaller the Probability of Collision (PoC). This lack of information corresponds to an uncertainty that is epistemic in nature. Thus, Dempster-Shafer theory of Evidence (DSt) was used to address both aleatory and epistemic uncertainty. Furthermore, when different sources provide contradictory information, the level of epistemic uncertainty in the calculation of PoC can lead to false confidence in the likelihood of a collision with either an undesirable increase in the number of Collision Avoidance Manoeuvres (CAMs) or an equally undesirable number of False Negatives.

An evidence-based classification criterion, derived from the application of DSt to conjunction risk assessment, is proposed to support operators. The classification sys-

tem, as opposed to common approaches based only on the value of the PoC or derived metrics, also accounts for the confidence in the correctness of the values. Thus, a robust decision is proposed to the operator in regards to the best action to take according to the available information and the confidence according to the provided evidence. The concept of robustness is used as the capacity to provide responses accounting for both epistemic and aleatory uncertainty so that, the worst-case scenario among the possible ones is taken into account.

The rest of the chapter is structured as follows. In Section 3.1, the problem of the dilution of probability is stated and the incorrect modelling, with a lack of epistemic uncertainty in the models, is shown as the root of the problem. Section 3.2 gives an overview of the DSt for modelling both aleatory and epistemic uncertainty and introduces a collision risk assessment method based on it. Next, in Section 3.3, three different conjunction event evidence-based classification criteria are presented. Section 3.4 summarises the main contributions of this chapter.

3.1 Modelling epistemic uncertainty

Uncertainty on the objects' position involved in a close encounter is usually assumed to follow a multivariate Gaussian distribution. This assumption is limited by three main sources of uncertainty: the uncertainty in the dynamic model used to propagate the orbit from the last available observation to the time of closest approach, the uncertainty in the actual distribution at the time of closest approach, and the uncertainty in the last observed state before closest approach. It can be argued that all three forms of uncertainty are epistemic in nature since they derive from a lack of knowledge of the model, distribution and error in the observation. [Poore et al., 2016]

So far, only a limited number of authors have directly addressed epistemic uncertainty in conjunction analysis [Tardioli and Vasile, 2015, Delande et al., 2018, Balch et al., 2019, Greco et al., 2021]. Generally, the epistemic uncertainty is overlooked and efforts to manipulate the objects' position covariance (sometimes referred to as covariance realism) were made [Foster and Frisbee Jr, 1998, Alfano, 2005b, Drummond et al., 2007, Laporte, 2014a]. However, those approaches do not intend to capture the actual

nature of the source of uncertainty (the lack of knowledge) [Poore et al., 2016]. In this chapter, a robust methodology based on DSt to model epistemic and aleatory uncertainty is proposed aiming to capture the uncertainty associated with the three main sources indicated above: uncertainty model, dynamic model and observation noise.

One of the consequences of the lack of a model for epistemic uncertainty is the phenomenon of dilution of probability. Below, an introduction to the topic and the main impact on Conjunction Assessment Risk Analysis (CARA) is presented.

3.1.1 Dilution of the probability of collision

The PoC and other derived metrics (e.g. scaled PoC [Stroe et al., 2021]) have been broadly used on conjunction risk assessment to evaluate the risk of an encounter between two space objects [Merz et al., 2017, Newman et al., 2014, Laporte, 2014a]. Due to the characteristics of most of the encounters in the Low Earth Orbit (LEO) region, the computation of the PoC can be simplified under the fast encounter assumptions [Alfriend et al., 1999, Patera, 2001, Alfano, 2005a, Alfano, 2007, Serra et al., 2016]: i) the relative motion between objects is assumed to be rectilinear; ii) the uncertainty distributions of the position of the two bodies are Gaussian and uncorrelated; iii) the velocity vectors are not uncertain; iv) the objects are modelled as hard spheres. The PoC computation can be reduced to the 2D integral in Eq. (3.1). This equation integrates the Gaussian distribution defining the combined covariance ellipse projected on the impact plane, Eq. (5.9), over the Hard-Body Radius (HBR), which is the closed region $\mathcal{B}((0,0), \text{HBR})$ defined by the sphere of radius HBR enveloping the two objects involved on the conjunction [Serra et al., 2016]:

$$PoC = \frac{1}{2\pi\sqrt{\|\Sigma_b\|}} \int_{\mathcal{B}((0,0), \text{HBR})} e^{-\frac{1}{2}((\mathbf{b}-\boldsymbol{\mu}_b)^T \Sigma_b^{-1} (\mathbf{b}-\boldsymbol{\mu}_b))} d\xi d\zeta, \quad (3.1)$$

where $\mathbf{b} = [\xi, \zeta]$ is the target's two-components position relative to the chaser on the impact plane at the time of expected impact, $\boldsymbol{\mu}_b = [\mu_\xi, \mu_\zeta]$ defines the coordinates of the centre of the ellipsoid projected on the impact plane, i.e. the expected relative

position, and

$$\Sigma_b = \begin{bmatrix} \sigma_\xi^2 & \sigma_{\xi\zeta} \\ \sigma_{\xi\zeta} & \sigma_\zeta^2 \end{bmatrix} \quad (3.2)$$

is the $[2 \times 2]$ covariance matrix associated with the combined uncertainty ellipsoid projected on the impact plane, being the combined ellipsoid covariance matrix, the sum of the two objects' covariance matrices in the same reference frame: $\bar{\Sigma}_b = \bar{\Sigma}_{b,1} + \bar{\Sigma}_{b,2}$. Note that, even though the simplifications associated with this PoC computation, the following considerations are generally applicable.

Eq. (3.1) leads to the known paradoxical phenomenon of the dilution of probability [Alfano and Oltrogge, 2018]. This phenomenon is well represented in Fig. 3.1: an increase in the standard deviation yields at first an increase of the PoC, up to a maximum value, and then a progressive decrease. In the figure, PoC is computed using Eq. (3.1) with $\mu_\zeta = 6$ m, $\sigma_\zeta = 3$ m, $\sigma_{\xi\zeta} = 0$ m² and $HBR = 5$ m. Thus, if the uncertainty in the observations grows beyond the point of maximum PoC the obvious conclusion would be a lower risk of collision. In other words, Eq. (3.1) seems to suggest that the risk of a collision decreases as the amount of information on the position of the two objects decreases or, in other words, the objects seem to be safer when the quality of the information worsens.

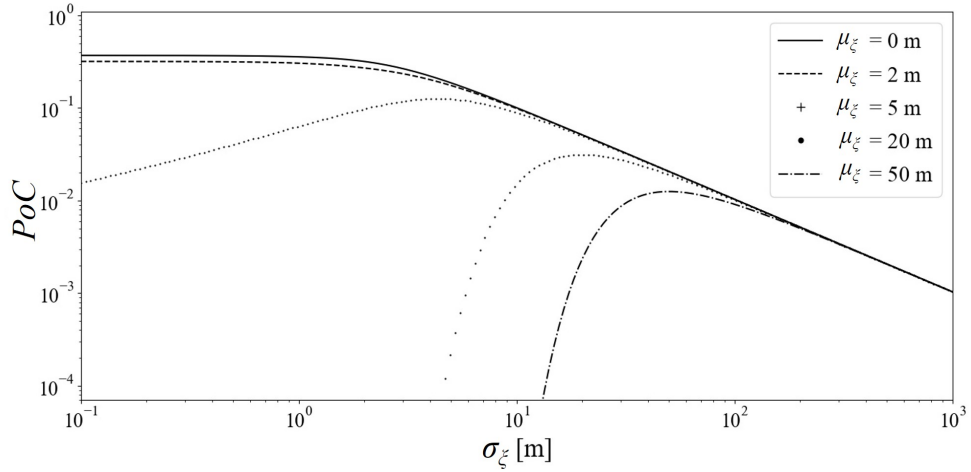


Figure 3.1: Dilution of probability when increasing the standard deviation, for different values of miss distance.

As explained also in [Balch et al., 2019], the central problem is the model of uncertainty. If the uncertainty in the position of the two objects was purely aleatory (an irreducible random process), the dilution of probability would describe an actual reduction in the risk of a collision. This can be understood from Fig. 3.2 where an increase in the standard deviation leads to a reduction of the total probability mass falling within the $HBR = 5$ m (grey region) for $\sigma_\xi > 5$ m. However, one can argue that this is true only when the uncertainty on the dynamics and sensors is perfectly known. On the contrary, when the uncertainty is epistemic, i.e. there is a lack of knowledge on the position or velocity of an object, the correct reasoning should lead to the conclusion that a higher ignorance corresponds to a higher risk of a collision, or at least, not in its reduction. Some efforts on metrics not suffering from dilution have been presented in [Balch, 2016] (see Appendix A), although lacking a model for the epistemic uncertainty.

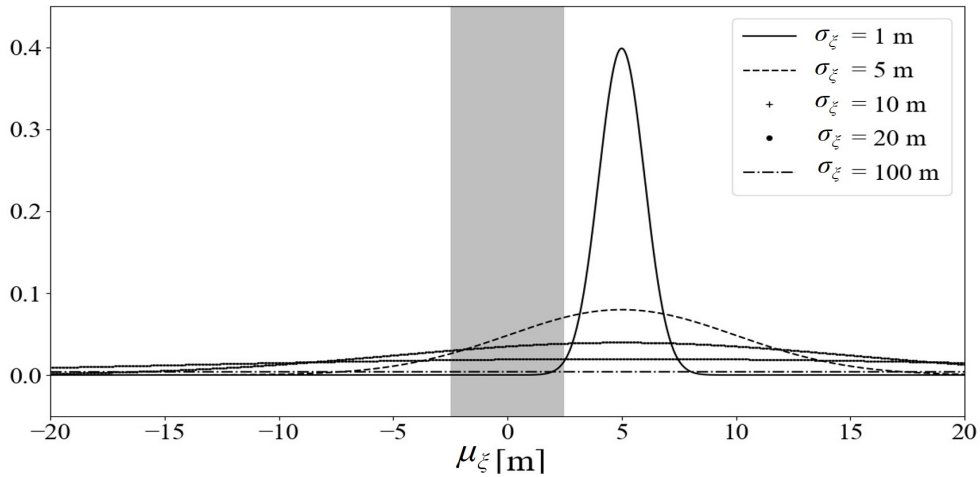


Figure 3.2: Flattening of the Normal Distribution curve when the standard deviation increases, causing the dilution of probability.

In the following, the calculation of the PoC with Eq. (3.1) is maintained, but a model for the epistemic uncertainty in the observations using DSt is proposed. In particular, the case in which the values of μ_b and Σ_b are partially known is considered and a degree of belief (or confidence) to the set to which they belong can be assigned. This situation can derive, for example, from the fusion of different conflicting observations or from a

lack of knowledge of the quality of the sensors.

3.2 Dempster-Shafer theory of evidence

In this section, an introduction to DSt is presented. This theory was proposed by Dempster [Dempster, 1967] and improved by Shafer [Shafer, 1976] to model evidence theory and address the lack of a model for epistemic uncertainty. It could be seen as a generalisation of the classical probability theory when the available information suffers from a degree of ignorance (epistemic uncertainty). In DSt, one can associate a degree of belief in the realisation of an event without exact knowledge of an associated probability distribution, based on confidence in the source of information or the lack of knowledge of some of the system's parameters.

In DSt, the evidence is not restricted to single events, but it can be associated with a set of events (represented by intervals), without the need to assume any kind of distribution or assign any degree of evidence to any specific event within the set. Moreover, DSt is not restricted to Laplace's Principle of Insufficient Reason, avoiding making assumptions about events about whom there is no knowledge: in probability theory, in a situation with three possible outcomes, if an event has a 0.3 probability to occur, it could apply 0.35 to each of the other events, even if there is no knowledge about it. DSt allows to not assign specific mass to the individual events. Not only that, if there is no information on the probability of A not occurring, this event can have a different probability than 0.7 (as it would happen in probability theory) [Sentz and Ferson, 2022].

Given an event space, the set Θ of all the mutually exclusive and collectively exhaustive elementary events (or hypotheses) is considered: $\Theta = \{\theta_1, \theta_2, \dots, \theta_{|\Theta|}\}$. The collection of all non-empty subsets of Θ , including the Empty Space and Θ itself, is the Power Set $2^\Theta = (\Theta, \cup)$. One can now assign a probability mass, called basic probability assignment (*bpa*), to the elements of 2^Θ . The *bpa* is equivalent to mapping the power set to the interval $[0, 1]$ [Sentz and Ferson, 2022]. The *bpa* assigned to the event θ can be understood as the proportion of all relevant and available evidence that supports the claim that a particular element of Θ belongs to the set θ , that is, the sum of all

the support assigned to all the single events (θ_i) and combination of events of Θ that include θ . This assignment can be derived from an expert-based decision, from the reliability of the sources of information, or from a formal method to extract the relative importance of the elements in Θ [Soundappan et al., 2004, Augustin, 2005, Jian and Deng, 2014]. The *bpa* is not exactly, but it is similar, to the generalisation to the DSt framework of the probability mass functions in probability theory [Ferson et al., 2003]. The *bpa* functions have the following properties [Sentz and Ferson, 2022]:

$$bpa(\emptyset) = 0 \quad (3.3a)$$

$$0 \leq bpa(\theta) \leq 1, \forall \theta \in 2^\Theta \quad (3.3b)$$

$$\sum bpa(\theta) = 1, \forall \theta \in 2^\Theta \quad (3.3c)$$

The *bpa* allows obtaining the Belief (*Bel*) and Plausibility (*Pl*), which are the upper and lower bounds of an interval, or the minimum and maximum support a statement receives from the available evidence. Thus, the *Bel* and *Pl* contain the precise probability of a variable in the classical (probabilistic) sense, that is if the information was precisely known, instead of interval-valued. *Bel* and *Pl* are computed according to equation Eq. (3.4). *Bel*(θ) is the sum of the *bpas* of all the elements of the Power Set containing θ , and represents the amount of complete support from the evidence. *Pl*(θ) is computed as the sum of the *bpas* of the elements of 2^Θ partially containing θ , and indicates the lack of support to the event not happening or, in other words, the amount of credibility on the event being possible to occur.

$$Bel(\theta) = \sum_{\theta_i \subset \theta, \theta_i \in 2^\Theta} bpa(\theta_i) \quad (3.4a)$$

$$Pl(\theta) = \sum_{\theta_i \cap \theta \neq \emptyset, \theta_i \in 2^\Theta} bpa(\theta_i) \quad (3.4b)$$

The *Bel* and *Pl* functions allow building the Dempster-Shafer structures (some examples in Fig. 3.3), bounding the maximum and minimum support from the evidence to a certain value of the variable of interest [Ferson et al., 2003].

DSt enables also to propagate the uncertainty throughout the system [Soundappan et al., 2004], which allows using this approach for system safety/risk assessment [Helton et al., 2005]. Having a system whose safety is defined with a variable of interest $f(\mathbf{u})$, but the information about the system is provided by a set of uncertain variables $\mathbf{u} = [u_1, u_2, \dots]$, it is possible to propagate the belief assignment from the input variables to the variable of interest. The set of intervals of uncertain variables is called the Uncertain Space, U .

First, it is necessary to build the Joint Body of Evidence, which is the mass assignment of the individual variables, but in the joint space. This is done by performing a Cartesian product of the intervals on U . The result of this operation is a set of intervals in the multi-space, whose bpa will be equal to the product of bpa associated with the intervals of the individual variables forming the interval in the joint space, as shown in Eq. (3.5), where u_i^l and u_i^u represent the lower and upper bound of the given interval for variable u_i [Soundappan et al., 2004].

$$bpa_{u_1, u_2, \dots}([u_1^l, u_1^u] \times [u_2^l, u_2^u] \times \dots) = bpa_1([u_1^l, u_1^u]) \cdot bpa_2([u_2^l, u_2^u]) \cdot \dots \quad (3.5)$$

Each element of the Joint Body of Evidence with a non-zero bpa is called a Focal Element (FE). With the set of FEs, knowing the relation between the input variables and the variable of interest, $f(\mathbf{u})$, it is possible to define the set:

$$\Upsilon = \{\mathbf{u} \in U \mid f(\mathbf{u}) \in \Phi\}, \quad (3.6)$$

where Φ is a desirable target set for f . The final step to evaluate the safety of the system is to obtain the amount of support on the variable of interest, that is, computing the Bel and Pl of Υ . Eq. (3.4) can be used, but now the sum is done on the space of the variable of interest, using the bpa of the FEs in the Joint Body of Evidence, as stated in Eq. (3.7).

$$Bel(\Upsilon) = \sum_{\gamma_i \subset \Upsilon, \gamma_i \in U} bpa(\gamma_i) \quad (3.7a)$$

$$Pl(\Upsilon) = \sum_{\gamma_i \cap \Upsilon \neq \emptyset, \gamma_i \in U} bpa(\gamma_i) \quad (3.7b)$$

The Belief and Plausibility functions have the following properties [Helton et al., 2005]:

$$Pl(\Upsilon) \geq Bel(\Upsilon) \quad (3.8a)$$

$$Bel(\Upsilon) + Pl(\neg\Upsilon) = 1 \quad (3.8b)$$

$$Bel(\Upsilon) + Bel(\neg\Upsilon) \leq 1 \quad (3.8c)$$

$$Pl(\Upsilon) + Pl(\neg\Upsilon) \geq 1 \quad (3.8d)$$

Eq. (3.7) defines the standard definition of Bel and Pl . However, in risk failure analysis (conjunction risk assessment can be understood as evaluation of the risk failure of the system, that is, the satellite), it is common to use the complimentary quantities [Helton et al., 2005] in Eq. (3.9), which, in this work, will be used to evaluate the confidence on the value of the PoC:

$$Bel(\Upsilon) = 1 - \sum_{\gamma_i \subset \Upsilon, \gamma_i \in U} bpa(\gamma_i) \quad (3.9a)$$

$$Pl(\Upsilon) = 1 - \sum_{\gamma_i \cap \Upsilon \neq \emptyset, \gamma_i \in U} bpa(\gamma_i) \quad (3.9b)$$

Finally, the Degree of Uncertainty (DoU) is the difference between Pl and Bel ,

$$DoU(\Upsilon) = Pl(\Upsilon) - Bel(\Upsilon) \quad (3.10)$$

and can be used to determine the degree of epistemic uncertainty associated with an event given the available evidence. This concept will be exploited to classify the conjunction events.

3.2.1 Epistemic conjunction risk assessment

The idea is that when μ_b and Σ_b are affected by epistemic uncertainty, their values are not precisely defined, but belong to an interval with a given belief, that is, with

a given confidence the actual value is located within the interval. A higher epistemic uncertainty will translate into a larger set or a greater number of, possibly disjoints, FEs. Then, all the pieces of evidence in support of the possible values of $\boldsymbol{\mu}_b$ and $\boldsymbol{\Sigma}_b$ are collected and the corresponding values of the PoC with Eq. (3.1) are calculated. The evidence on the values of $\boldsymbol{\mu}_b$ and $\boldsymbol{\Sigma}_b$ comes from the degree of knowledge or ignorance of the source of the observations. The *bpa* assignment can derive from a quantitative analysis (Chapter 4) or simply from a subjective opinion on the credibility of the source of information (examples appear in [Helton et al., 2005]).

This approach can be illustrated with an example. Provided a close encounter between two space objects, let a source provide uncertain information on the position and uncertainty (e.g. information extracted from a sequence of CDMs). Without loosing generality, let assume $\mu_\zeta, \sigma_\zeta^2$ and $\sigma_{\xi\xi}$ are perfectly known and equal to 6 m, 81 m², 0 m², respectively, while μ_ξ and σ_ξ^2 are affected by epistemic uncertainty. The source of information indicates that the actual value for these variables could fall in one of the two following intervals: $\mu_{\xi,1} = [4, 7]$ m, $\mu_{\xi,2} = [15, 25]$ m and $\sigma_{\xi,1} = [1, 6.25]$ m, $\sigma_{\xi,2} = [4, 36]$ m. If both intervals on each variable are equally believed to contain the true value, they will be assigned the same *bpa*, $bpa_{\mu_{\xi,1}} = bpa_{\mu_{\xi,2}} = bpa_{\sigma_{\xi,1}} = bpa_{\sigma_{\xi,2}} = 0.5$, as illustrated in Figs. 3.3a and 3.3b (blue) with the associated Dempster-Shafer structures. If, on the contrary, there is more evidence that the actual value is within one of the intervals, the value of the *bpa* would be different, for example, $bpa_{\mu_{\xi,1}} = bpa_{\sigma_{\xi,1}} = 0.9$ and $bpa_{\mu_{\xi,2}} = bpa_{\sigma_{\xi,2}} = 0.1$, as shown in Figs. 3.3c and 3.3d (red).

Due to the uncertain knowledge of the values of mean and covariance, the uncertain ellipse is not precisely defined. Instead, each set of intervals would define a family of ellipses on the impact plane.

Under the assumption of pure aleatory uncertainty, since all pieces of information (both sets of intervals) are credible and any of them cannot be discarded, the simplest approach would be to sample both families and build a joint distribution to compute the PoC. Setting aside the fitting method, not important at this stage, the key assumption is that no matter the combination rule, it would be required to build a single distribution

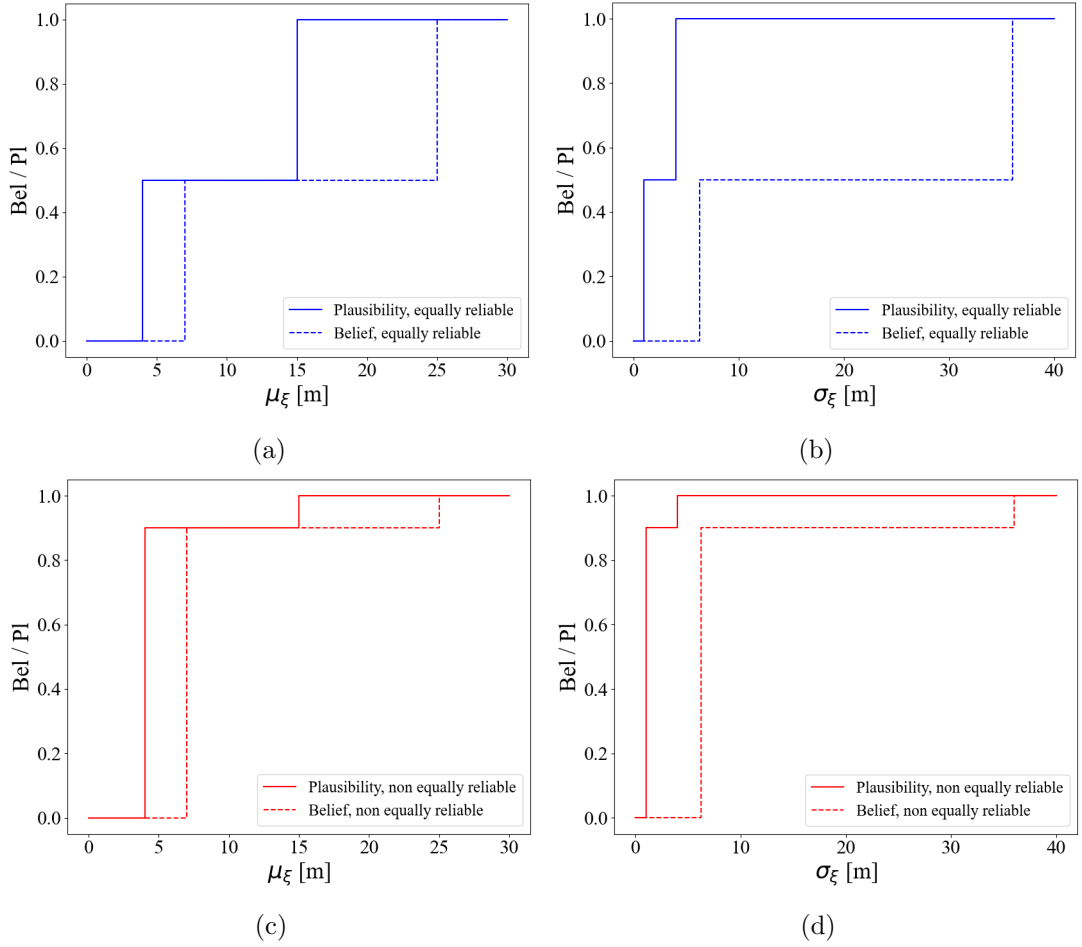


Figure 3.3: Dempster-Shafer structures for μ_ξ and σ_ξ : plausibility (solid lines) and belief (dashed lines). (a) and (b): intervals equally reliable; (c) and (d): intervals non equally reliable.

to compute the PoC. If both sets of intervals are equally reliable, the joint distribution is defined by an expected miss distance of $\boldsymbol{\mu}_b = [11.4, 6]$ m and a diagonal covariance matrix with $\sigma_\xi^2 = 1857.61$ m², $\sigma_\zeta^2 = 73.96$ m² (Fig. 3.6a). When one set is given more credibility than the other, the joint ellipse would be smaller and more similar to the set of intervals with greater weight. In this case, the joint ellipse in the non-evenly weighed case is defined by a miss distance of $\boldsymbol{\mu}_b = [6.6, 6]$ m and a diagonal covariance matrix with $\sigma_\xi^2 = 331.24$ m², $\sigma_\zeta^2 = 73.96$ m² (Fig. 3.6b). Note that more complex fitting could be implemented (e.g. Kernels, Gaussian Mixture Model), but in any case, they assume no uncertainty on the variables, and thus, no uncertainty on the computed PoC.

Independently of the weights distribution, due to the conflict among the intervals, it can be seen that the joint distribution provides a bigger uncertain ellipse than those defined by the intervals, which may make the computed PoC fall in the dilution region, giving a false sense of safety. Actually, the degree of conflict among the intervals suggests that there is a degree of epistemic uncertainty in the event that cannot be neglected when computing the risk of the event. DSt will be used to capture this uncertainty on the position and to quantify the associated uncertainty on the PoC.

Given a belief assignment to $\boldsymbol{\mu}_b$ and $\boldsymbol{\Sigma}_b$, it is possible to compute the *Joint Body of Evidence*, that is, the FEs obtained from the Cartesian product of the intervals of each uncertain variables and their associated *bpa*, obtained by multiplying the *bpa* of the intervals conforming each FE. DSt then allows to transferred the uncertainty along the system [Soundappan et al., 2004] and be used to evaluate its risk of failure [Helton et al., 2005]. If using the PoC as the metric to evaluate the risk, it is possible to compute the associated support on the PoC and use the confidence on its value to evaluate the safety of the system, i.e. the possibility of a collision. Note, that since the geometry variables are no longer single-valued, the PoC will be also interval-valued.

With reference to Eq. (3.6), $f = PoC$, computed with Eq. (3.1), and Φ would be the desired set of values for PoC. For example, one can define $\Phi = \{PoC | PoC < PoC_0\}$ with PoC_0 a given threshold on the values of PoC. Then, the joint uncertainty space U can be defined so that $\mathbf{u} = [\mu_\xi, \mu_\zeta, \sigma_\xi^2, \sigma_\zeta^2, \sigma_{\xi\zeta}]^T$ and write:

$$\Upsilon = \{\mathbf{u} \in U | PoC(\mathbf{u}) \in \Phi\} \quad (3.11)$$

With Eq. (3.11), it is possible to apply Eq. (3.9) to compute the corresponding *Bel* and *Pl* of the value of PoC. Note that using the complimentary *Bel* and *Pl* with Φ is equivalent to using the non-complimentary functions for $PoC \geq PoC_0$. These metrics would indicate the support, from the available information, that the PoC is greater than a certain value, and the degree of uncertainty affecting the correctness of the value. At this point, it is important to underline that although the theoretical development started from the simple calculation of the PoC in Eq. (3.1), this methodology is applicable to more sophisticated definitions of the PoC as long as one can identify

the source of epistemic uncertainty and translate it into a *bpa* assignment.

Coming back to the illustrative example, given the set of uncertain variables, assuming independence on the variables, and no constraints on mean and covariance, the joint body of evidence would be defined as $U = [\mu_\xi \times \sigma_\xi]$, illustrated in Fig. 3.4. Being two intervals per variable and two uncertain variables, the joint body of evidence

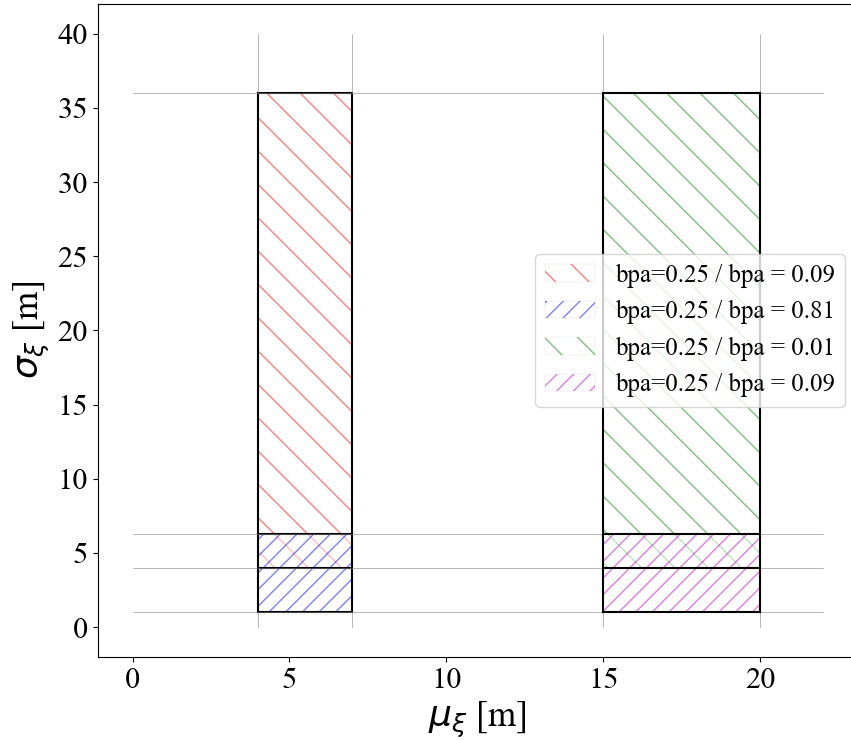


Figure 3.4: Joint body of evidence for μ_ξ and σ_ξ with each FE's *bpa* if intervals equally and non-equally reliable, respectively.

would be constituted by four FEs as detailed in Table 3.1. The first column identifies the FE bounds, the second column, the associated *bpa* if all intervals are assigned similar credibility, the third column shows the *bpa* if the first set of intervals is assigned nine more times belief than the second set, and the last two columns show the minimum and maximum PoC within each FE, which will allow building the *Bel* and *Pl* curves, respectively.

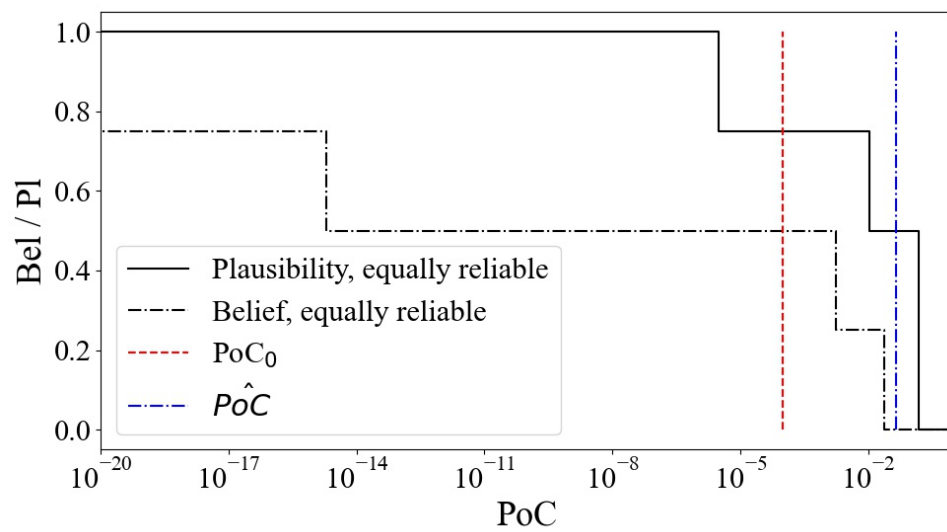
Having obtained the different FEs and the associated *bpas*, the *Pl* and *Bel* can be computed using Eq. (3.9). According to the definition of those variables, the *Bel* would

Table 3.1: FE with the associated *bpa* (for intervals equally and non-equally reliable) and the minimum and maximum PoC on each FE.

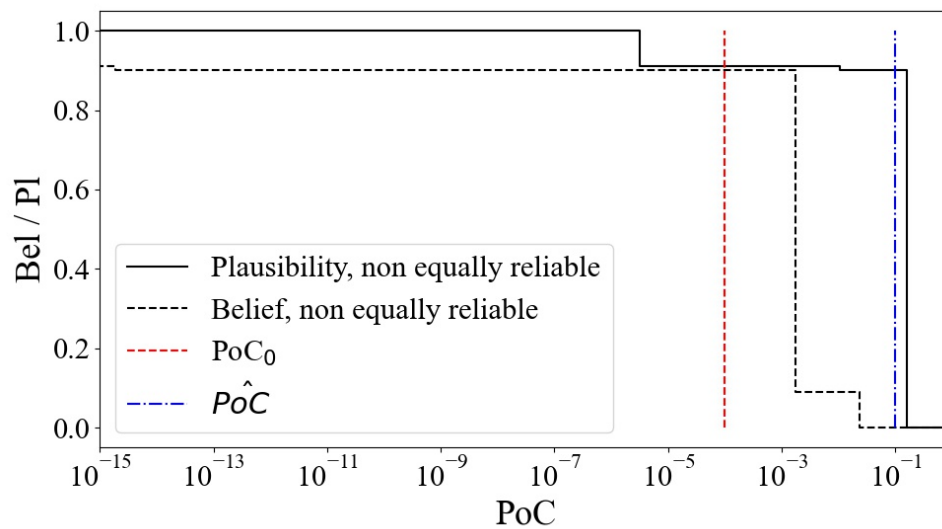
Focal Element μ_ξ, σ_ξ [m]	<i>bpa</i> (equally reliable)	<i>bpa</i> (not equally reliable)	Min PoC in FE	Max PoC in FE
[4, 7],[1, 6.25]	0.25	0.81	1.73×10^{-3}	1.58×10^{-1}
[4, 7],[4, 36]	0.25	0.09	2.37×10^{-2}	1.59×10^{-1}
[15, 20],[1, 6.25]	0.25	0.09	8.88×10^{-37}	3.12×10^{-6}
[15, 20],[4, 36]	0.25	0.01	1.91×10^{-15}	1.06×10^{-2}

take into account all FEs fully supporting Υ and the *Pl* would consider all FEs partially supporting the statement. Regarding the definition of Υ , the set of all FEs whose PoC is greater than a certain value, the computation of these variables can be performed by using the minimum and maximum values of the PoC on each FE (last two columns in Table 3.1). Thus, the *Bel* is obtained by subtracting to one the *bpa* at the associated value of the FE's minimum PoC, since it is the value of the PoC the FE stop fully supporting higher values are possible. Similarly, the *Pl* is computed by subtracting to one the value of the *bpa* of the corresponding FE at the value of its maximum PoC, when the FE stop supporting higher values of probability. The resulting curves are displayed in Fig. 3.5 for both cases: when intervals are equally credible (a) and when more belief is assigned to the first set of intervals (b).

The curves should be understood as follows. Having selected a safety threshold $PoC_0 = 10^{-4}$ (red dashed line), if both intervals are equally reliable it would indicate that values of PoC above the threshold are possible, although with limited support ($Pl = 0.75$). However, when the set of intervals $\mu_\xi = [4, 7]$ m and $\sigma_\xi = [1, 4]$ m are more reliable, it is much more likely ($Pl = 0.91$). Moreover, in this second case, the conflict between information is much smaller with a smaller gap between curves both, overall and at the PoC_0 , which makes sense if thinking that more reliability is given to the source suggesting a higher-risk encounter. In dashed-pointed blue, the joint ellipse distribution PoC, \hat{PoC} , is shown. It is worth noting the great gap between curves at that value, which indicates the uncertainty affecting this value in both cases.



(a)



(b)

Figure 3.5: *Bel* (dash line) and *Pl* (solid line) curves of the PoC. (a) Equally reliable intervals; (b) one interval being more reliable than the other.

3.2.2 Data fusion

DSt allows for the combination of different sources of information (e.g. information received from different sensors). It is common in engineering problems that information comes from different sources which may present better or worse quality and may provide coherent or conflicting information. If on top of that, information is not precisely known

(contains epistemic uncertainty), DSt's combination rules can be used to meaningfully fuse those pieces of evidence and to account for the conflict among them [Sentz and Ferson, 2022, Ferson et al., 2003].

The combination rules consist of techniques to aggregate information coming from different sources in the context of evidence theory and interval-set variables. More precisely, they combine the *bpa* assignments (or the Dempster-Shafer structures) for each variable provided by the sources to provide a single mass or *bpa* distribution.

There are many rules mainly diverging in the way they treat and quantify the conflict among rules. The main assumption common to all of them is the independence of the sources. Some rules emphasise the agreement, discarding the conflict (conjunction rules), others may prioritise one source among the others (disjunction rules), and most lie in between, giving more or less importance to the conflict among sources. It is worth noting that the selected combination rule will have a great impact on the system risk assessment, since the combined *bpa* distribution may be greatly affected [Sentz and Ferson, 2022].

The first proposed rule was Dempster's Combination rule [Dempster, 1967]. This rule completely ignores the conflict, assigning to the null set any *bpa* associated with it. Eq. (3.12) shows the formula to combine n sources of information. Thus, it may provide counterintuitive conclusions if there is very little agreement among sources (e.g. example of the doctors in [Zadeh, 1984b] p.82). Moreover, if the information from the sources is completely in conflict, this rule cannot be used.

$$\begin{cases} bpa_{1\dots n}(\gamma) = \frac{\sum_{\cap_i \gamma_i = \gamma} \prod_{i=1}^n bpa_i(\gamma_i)}{1-K} & \text{if } \gamma \neq \emptyset \\ bpa_{1\dots n}(\gamma) = 0 & \text{if } \gamma = \emptyset \end{cases} \quad (3.12)$$

$$\text{where } K = \sum_{\cap_i \gamma_i \neq \emptyset} \prod_{i=1}^n bpa_i(\gamma_i)$$

Different rules have been proposed to overcome these limitations, like Yager's rule [Yager, 1987], also known as Modified Dempster's rule, whose main difference is the assignment of conflict. Instead of ignoring conflict, it attributes the mass of the conflict to the universal set, which should be understood as the degree of ignorance: any statement supporting the whole set (that is, not prioritising any outcome) or any set

not supporting the same information should be understood as lack of knowledge on the actual system. Inagaki's rule [Inagaki, 1991] generalises Yager's rule and creates a continuous parametrised class of rules (including Dempster's and Yager's rules). Inagaki's rule works only if there is no detail on the reliability of the sources. Zhang's Center combination rule [Zhang, 1994], which allows obtaining information from one set of discernment from the information on another logically related set, modified Dempster's rule on the treatment of the intersection between sets introducing a measure of intersection. Dubois and Prade's Disjunctive rule [Dubois and Prade, 1986, Dubois and Prade, 1992], on the other hand, proposes a disjunctive rule, which may be prone to more imprecise results.

Other rules are based on the averaging process, such as a discount-combine method [Shafer, 1976], mixing rule or convolutive averaging rule [Ferson et al., 2003]. The mixing (also called averaging) rule generalises the averaging of distributions in probability theory (towards it would simplify if intervals reduce to single points), so it could be seen as the logical step coming from aleatory uncertainty [Sentz and Ferson, 2022]. The mixing rule is based on equation Eq. (3.13) [Ferson et al., 2003], where n is the number of sources, $\gamma_{1,\dots,n}$ the *bpa* of the combined sources, and γ_i the *bpa* of source "i" for the same set.

$$bpa_{1\dots n}(\gamma) = \frac{1}{n} \sum_{i=1}^n bpa_i(\gamma) \quad (3.13)$$

However, the mixing rule presents an advantage, it allows waiting for the sources of information regarding their reliability (i.e. information coming from the own sensor is usually considered more reliable than third party's sensors). In the case sources are not evenly weighted, the combined *bpa* should be computed using Eq. (3.14) [Ferson et al., 2003], where w_i is the relative weight of source "i". If the different sources provide any interval equal to another source, a final step should be added so that the *bpa* of all equal intervals is summed up.

$$bpa_{1\dots n}(\gamma) = \frac{1}{\sum_i w_i} \sum_{i=1}^n w_i bpa_i(\gamma) \quad (3.14)$$

Below, an example will show the behaviour of Dempster's rule and the Mixing

rule when two sources provide information on two variables. Note that this example resembles the previous one, however, instead of one source providing two intervals per variable, two sources provide one interval each. Both rules would operate the same if any or both of them provide more than one interval or even a different number of intervals per variable.

Two sources of information are providing information on a close encounter. μ_ζ , σ_ζ , $\sigma_{\xi\zeta}$ and the HBR are known without ambiguity, however, μ_ξ and σ_ξ are provided as intervals. Each source provides a single interval per variable, thus the *bpa* of each interval for each interval is equal to 1. Source 1 indicates that $\mu_\xi \in [4, 7]$ m and $\sigma_\xi = [1, 6.25]$ m, while Source 2 proposes that $\mu_\xi \in [15, 20]$ m and $\sigma_\xi = [4, 36]$ m. Fig. 3.6 illustrates this uncertain geometry. In the figure, the HBR centre at the chase and in the centre of the impact place reference frame appears in solid yellow. In red (dashed and pointed-dashed for the 1σ and 3σ , respectively) is the frequentist ellipse presented in some paragraphs above. It encapsulates all the information by fitting a single ellipse. Finally, the two families of 3σ ellipses provided by each source appear in blue and green, respectively. Each of those families is represented in the figure by a finite set of all possible ellipses defined by the intervals supported by the corresponding source. Thus, for Source 1, the green ellipses have sizes and positions drawn from the intervals $\sigma_\xi = [4, 36]$ m and $\mu_\xi \in [15, 20]$ m, respectively (note, the ellipses are not concentric since μ_ξ is not single-valued).

Due to the epistemic uncertainty and the interval-valued variables, the uncertain ellipses become a set of ellipses, as mentioned before. The blue ellipses are associated with Source 1, while the green ellipses are associated with Source 2. The red ellipses would correspond with the joint ellipse for the probabilistic case as explained in the previous example (Fig. 3.6a with sources equally reliable and Fig. 3.6b with sources non-equally reliable). The yellow circumference represents the HBR of the combined objects.

If combining the sources with Dempster's rule, one would obtain a combined interval for $\sigma_\xi = [4, 6.25]$ m with $bpa_{AB} = 1$. However, for μ_ξ , there would not be any value in receiving any support due to the conflict among sources

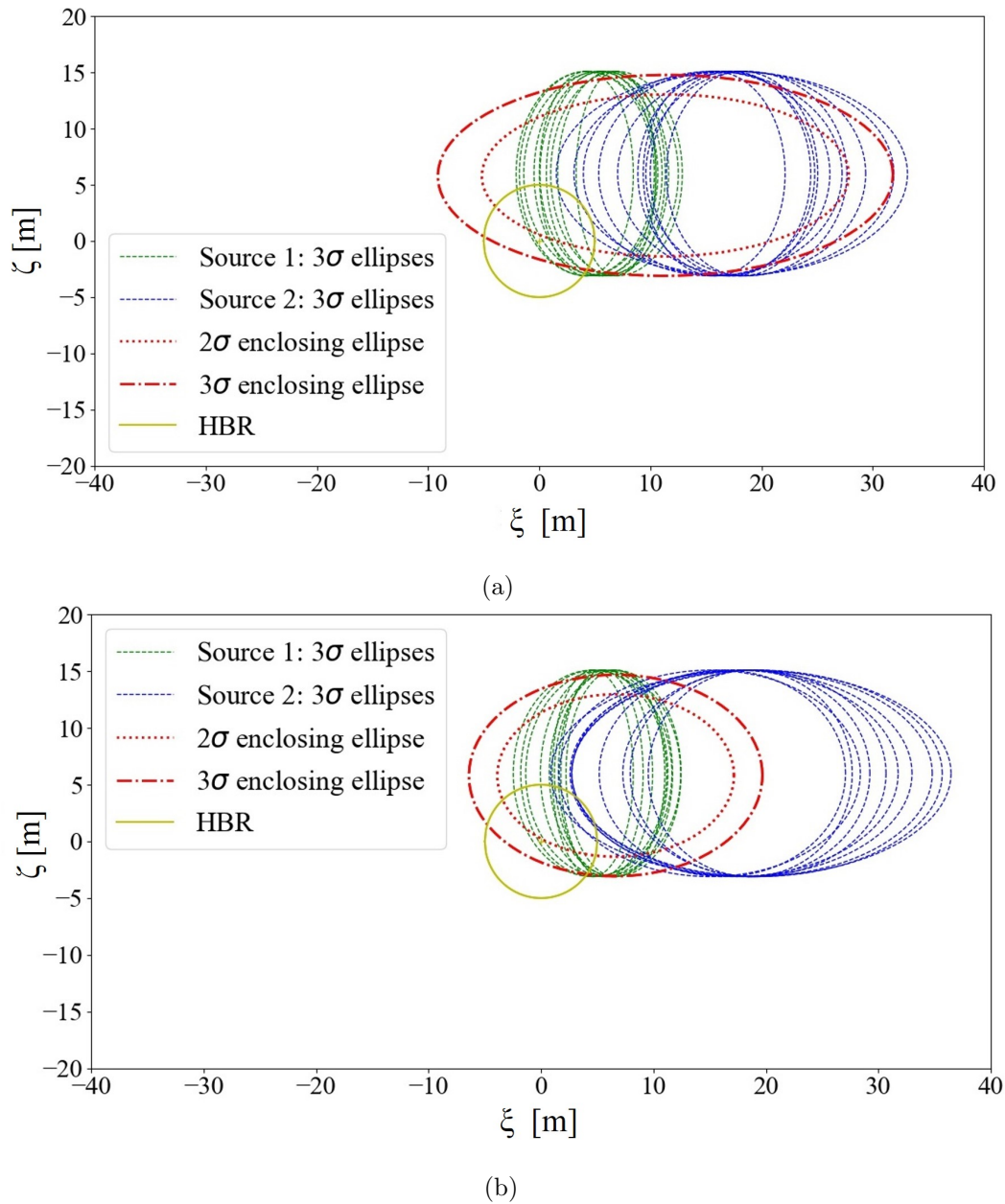


Figure 3.6: Conjunction geometry on the impact plane centred on the chaser. (a) Sources equally reliable. (b) Sources non-equally reliable.

Using the mixing rule instead, the set of intervals after combining the sources of information is included in Table 3.2, both with all sources are equally reliable ($w_A = w_B = 0.5$) and if Source 1 is more reliable ($w_A = 0.9$ and $w_B = 0.1$). Fig. 3.7 shows the combined Dempster-Shafer structures for each variable for the different situations.

Table 3.2: Intervals provided by sources with their *bpa* before and after being combined with the mixing rule for the equally reliable (upper tier) and non-equally reliable (lower tier) cases.

	Weights	Intervals μ_ξ [m]	Intervals σ_ξ [m]	bpa	Combined bpa
Source 1	0.5	[4,7]	[1,6.25]	1	0.5
Source 2	0.5	[15,20]	[4,36]	1	0.5
Source 1	0.9	[4,7]	[1,6.25]	1	0.9
Source 2	0.1	[15,20]	[4,36]	1	0.1

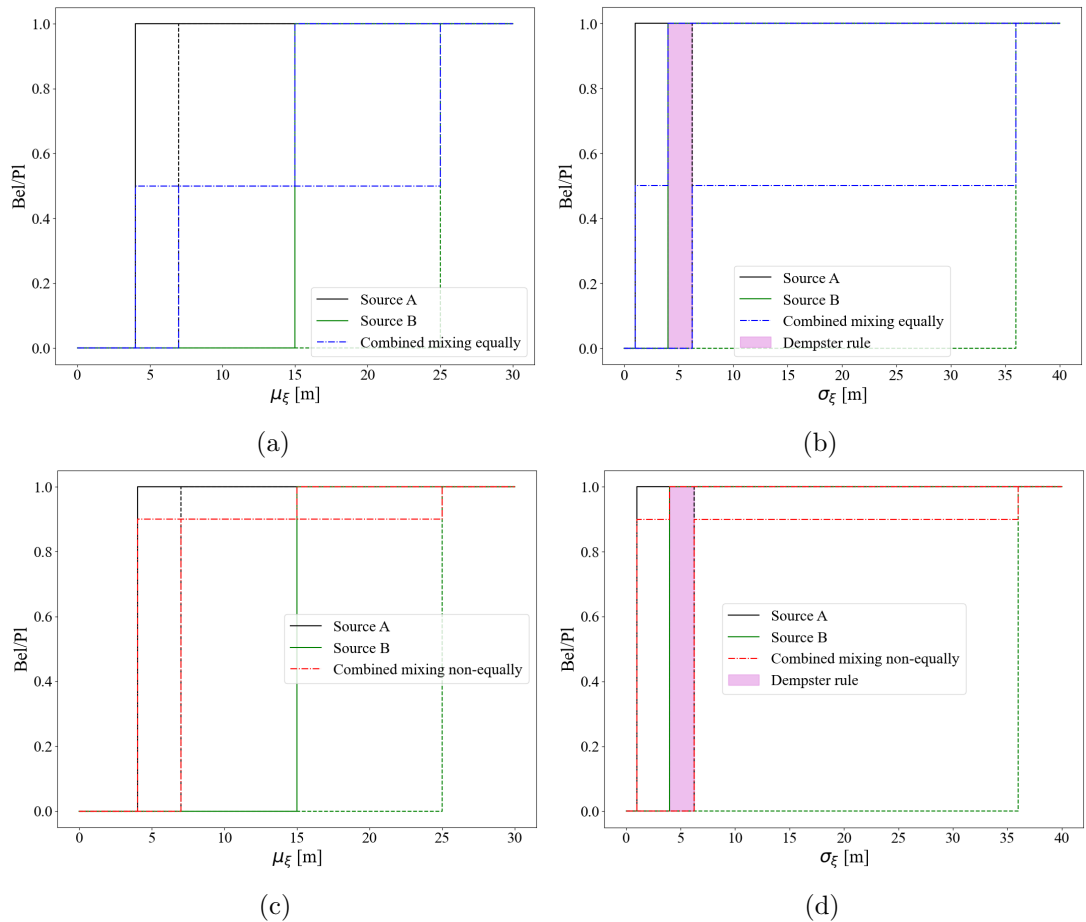


Figure 3.7: Dempster-Shafer structures for μ_ξ and σ_ξ , before combining sources (black and green, plausibility in solid lines, belief in dashed lines) and after combining sources with Dempster's rule (pink shaded region) and mixing rule (dashed-pointed line, blue equally reliable, red non-equally reliable): (a) and (b) sources equally reliable; (c) and (d) sources non-equally reliable.

Note that if there is absolute conflict among sources, as it happens for μ_ξ in the example, Dempster's rule cannot provide a combined Dempster-Shafer structure. It is worth noting that if a single source of information provides the same intervals as each of several sources of information, and assigns to them a *bpa* equal to the reliability of the sources (example in Section 3.2.1 and the example above), the final Dempster-Shafer structure is the same (compare Figs. 3.3 and 3.7). Thus, for the rest of this work, when more than one source provides information, the weighted mixing rule is applied.

3.3 Conjunction classification criteria

This section presents how to use *Bel* and *Pl* as additional criteria to classify conjunction events. A classification purely based on PoC will be compared with a classification that includes *Bel* and *Pl*. This classification criterion will form the ground for the rest of the theoretical developments and applications in the following chapters.

3.3.1 Probability of collision as classification criterion

When the PoC in Eq. (3.1) is used as the single classification criterion, it is customary [Muelhaupt et al., 2019] to define a series of thresholds on the value of PoC, each of which activates an alert or a recommended action. Different operators employ different amounts of thresholds and different values and some of them, even employ variants of the PoC to trigger the alerts, but in all the cases, the common factor is the use of the computed value of the risk metric, without taking into account the support on its correctness. More details on some of these approaches are given in Chapter 7.

Generally speaking, events presenting a value of PoC above a certain threshold start an assessment process, usually requiring additional tracking. If the risk remains at that level longer or a higher PoC is obtained, the planning of a CAM becomes necessary, and eventually, a CAM execution should be implemented. The details of the process vary from operator to operator, with variations on the specific value of the thresholds, the action to be carried out or the inclusion of other considerations, like the Time of Closest Approach (TCA), or derived metrics, as the Scaled Probability

of Collision (sPoC). For example, the CARA team of the NASA uses two thresholds (10^{-7} and 4.4×10^{-4}) [Newman et al., 2014]. Anything below the former threshold is considered to be low risk while everything above the latter threshold is considered high risk and anything in between deserves further investigations. The European Space Agency's (ESA) Space Debris Office (SDO) team also considers the time to the TCA and performs a CAM if the value of the PoC is higher than a given threshold some days before the TCA [Merz et al., 2017]. Nevertheless, no matter the specific values and metrics, all these approaches and criteria always assume that the PoC is affected exclusively by aleatory uncertainty and propose an action based on the computed value, not paying attention to the uncertainty of this value or its degree of correctness.

3.3.2 Evidence-based classification criteria

As explained in the previous section, a classification based solely on the PoC triggers actions when its value is found to be higher than the given thresholds. However, no information is given on the correctness of the PoC. Thus the operator might react to false positives or do nothing in the case of false negatives. Furthermore, unknown cases, that require further observations, are identified only by the thresholds and not by an actual quantification of the degree of ignorance of the PoC.

Consider now the case in which one can quantify the *Bel* and *Pl* that the PoC is above a given PoC_0 threshold. In this case, three additional pieces of information are available to the operator: the value of *Bel*, the value of *Pl* and the gap between the two, the DoU. A large gap between *Pl* and *Bel* implies that there is either a lack of information on the calculation of PoC or uncertainty on the available information, for example, due to conflict on the different pieces of data. If both *Bel* and *Pl* at the computed value are low, there is little evidence that the value of PoC is to be trusted, or if the *Bel* and *Pl* are low at the selected threshold, higher values are not expected. The opposite is true if those values are high: a greater value of PoC would be likely according to the available information.

Starting from these considerations one can devise a classification that allows operators to differentiate between high-risk, low-risk and uncertain events based on the

degree of uncertainty in the correctness of the $P\hat{o}C$. In Table 3.3, this possible classification criterion, *Criterion 1*, exploiting Bel and Pl is presented.

Table 3.3: Evidence-based conjunction classification *Criterion 1*.

CRITERION 1			
PoC value	DoU at $P\hat{o}C$	Bel and Pl at $P\hat{o}C$	Class
$PoC \geq PoC_0$	$DoU > \Delta$	-	NK-1
	$DoU \leq \Delta$	$Pl < Pl_0$ $Bel \geq Bel_0$	NK-2 HR
$PoC < PoC_0$	$DoU > \Delta$	-	NK-1
	$DoU \leq \Delta$	$Pl < Pl_0$ $Bel \geq Bel_0$	NK-2 LR

Criterion 1 provides three possible outputs, High-Risk (HR), Low-Risk (LR) and Not-Known (NK). The last class presents two subclasses: subclass NK-1, when PoC present a high DoU, being too much uncertainty to make a confident decision and requiring more information to be acquired; and subclass NK-2, where there is low confidence on the correctness of the PoC value, meaning a decision cannot be made based on that value of PoC.

3.3.3 Criteria comparison

In this section, a database of virtual conjunction geometries with different combinations of miss distances and standard deviations is used to compare the different classification methods: a classification method solely based on the value of PoC and the evidence-based *Criterion 1*, which uses also the Pl and Bel of the PoC.

Five different scenarios were identified, depending on the information provided by the two sources, so that relevant encounter geometries are covered. More sources could have been considered, but no new cases would appear regarding conflict among them. The definition of each type of geometry is included in Table 3.4, including the intervals of the uncertain variables characterising the encounter geometry. On each set of geometries in the table, the first row refers to the bounds for the intervals provided by Source 1 and the second row for Source 2. Geometry 1 represents cases where the fam-

ilies of ellipses provided by both sources tightly overlap each other and both intersect the HBR. In this scenario, both sources are in agreement and support the fact that a collision might occur with high probability. Geometry 2 are cases where the two sets of ellipses tightly overlap each other but do not intersect the HBR. In this scenario, both sources are in agreement and support the fact that a collision is unlikely to occur. In Geometry 3, both sources are disjoint and only one intersects the HBR. In this situation, there is a high degree of uncertainty about the correctness of the prediction. In Geometry 4, both sets are disjoint but none intersects the HBR. In this scenario, the joint distribution at 3σ is assumed not to intersect the HBR thus, although the sources are in disagreement, the conclusion is that a collision is unlikely to happen. Finally, Geometry 5 includes cases where the ellipses are disjoint not overlapping the HBR, but the joint distribution at 3σ does intersect the HBR. In this case, the sources are in disagreement but the conclusion could be that a collision is highly likely to occur because $P\hat{\delta}C$ is high. Without losing generality, the cases on the database for this analysis assume $\sigma_{\xi\zeta} = 0$.

Table 3.4: Bounds for upper and lower limits of the uncertain variables' intervals (μ_b and Σ_b) for each geometry set. The first row represents the bounds for Source 1 and the second row for Source 2. Units in meters.

Geom.	Characteristics	μ_ξ [m]	μ_ζ [m]	σ_ξ [m]	σ_ζ [m]
Geo. 1	Sets of ellipses overlapping	[0,10]	[0,7]	[0.1,4]	[0.2,2]
	Both sets overlapping HBR	[0,10]	[0,7]	[0.1,4]	[0.2,2]
Geo. 2	Sets of ellipses overlapping	[750,1000]	[-100,100]	[10,25]	[10,18]
	No set overlapping HBR	[750,1000]	[-100,100]	[10,25]	[10,18]
Geo. 3	Sets of ellipses not overlapping	[0,10]	[0,7]	[0.1,4]	[0.2,2]
	One set overlapping HBR	[750,1000]	[-100,100]	[10,25]	[10,18]
Geo. 4	Set of ellipses not overlapping	[750,1000]	[200,500]	[10,25]	[10,18]
	No set overlapping HBR	[500,800]	[-300,0]	[10,25]	[10,18]
Geo. 5	Sets of ellipses not overlapping	[30,200]	[30,200]	[3,12]	[3,12]
	No set overlapping HBR	[-200,-30]	[-200,-30]	[3,12]	[3,12]
	Combined ellipse would overlap HBR				

Geometry 1 and 2 present low conflict between the sources and can be expected to

provide high Bel at \hat{PoC} with smaller DoU. Geometry 1 will have $\hat{PoC} > PoC_0$ and Geometry 2 will have $\hat{PoC} < PoC_0$. Geometry 3 includes conflict cases, but depending on the distribution of confidence among the sources, they can present high or low values of Bel at \hat{PoC} (LR and HR, respectively) or big gaps between Pl and Bel (Not Known due to uncertainty, NK-1). The key difference between Geometry 5 and 3 is that in Geometry 5 the high value of \hat{PoC} is an artefact because both sources think that no collision is going to happen.

A total of 3,000 sample geometries were created, 600 samples for each type of geometry. Within this 600 samples per geometry, one-third (200 samples) corresponds to cases where both sources are equally reliable, another 200 samples to cases where Source 1 is nine times more reliable than Source 2 and the remaining third of the samples to cases where Source 1 is nine times less reliable than Source 2.

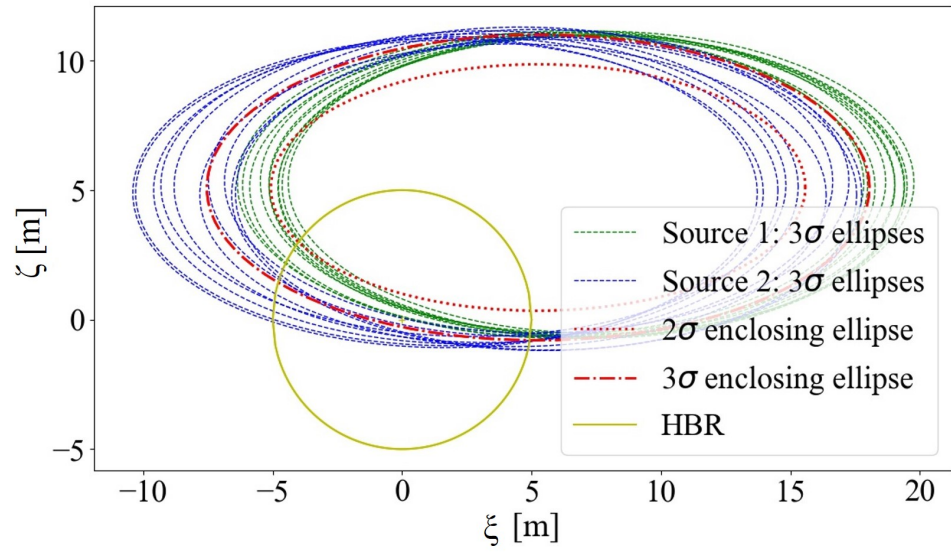
In Fig. 3.8, one can see one example of the geometry of an encounter event of the family *Geo. 1* with the associated Bel and Pl curves (black) and the key PoC values: the PoC_0 threshold, the joint ellipse \hat{PoC} value (red), and the PoC_b value at the Bel threshold (green). Examples of the other families can be found in Appendix B. It is now possible to compare the outcome of the different classification methods.

To allow for an easier classification for the purely aleatory case, only one risk threshold, PoC_0 , is considered to distinguish between Collision and No-Collision: if the computed value of the PoC is greater than the threshold, the event is classified as Collision, otherwise, it is catalogued as No-Collision. The values of this one and the other thresholds used for the classification can be found in Table 3.5.

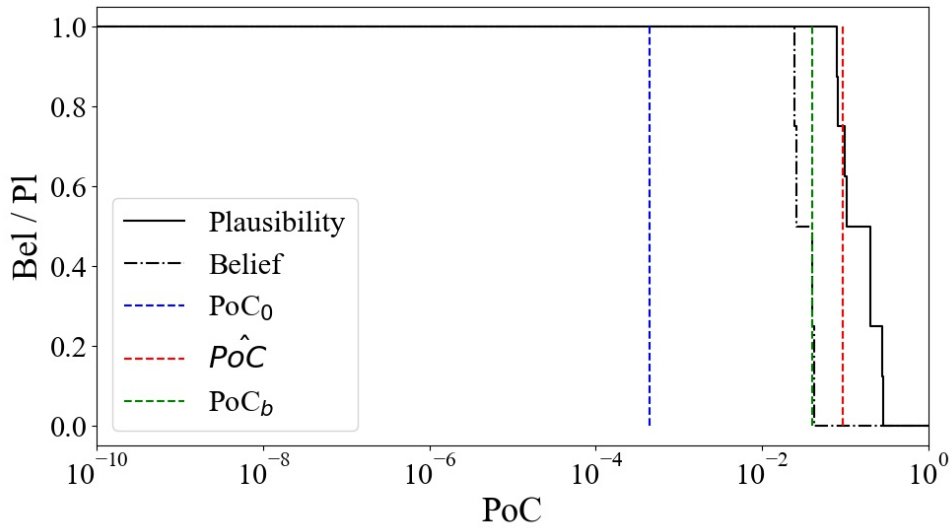
Table 3.5: Classification thresholds.

Parameter	Units	Value	Criterion
Probability of Collision (PoC_0)	[-]	$4.4 \cdot 10^{-4}$	1, 2, 3
Degree of Uncertainty (Δ)	[-]	0.3	1, 2, 3
Belief (Bel_0)	[-]	0.5	1, 2, 3
Plausibility (Pl_0)	[-]	0.5	1
Lower time threshold (T_1)	[days]	2	3
Upper time threshold (T_2)	[days]	4	3

Fig. 3.9 shows two histograms comparing a classification based only on PoC and



(a)



(b)

Figure 3.8: Representative scenario of a single case of *Geo. 1*: (a) encounter geometry, (b) the associated *Bel* and *Pl* curves.

a classification that accounts for *Bel* and *Pl* at \hat{PoC} . Blueppshaded cases correspond to events classified as collision by the PoC-based approach, while red-shaded events correspond to safe encounters according to this same criteria. Different shades corresponds to different classifications using the evidence-based criteria, with darker shades corresponding to HR, lighter shades to LR, and intermediate shades to NK-1 and NK-2

situations.

While the right histogram shows that using only the value of the PoC half of the events are safe, and only an action is required on the other half. However, when attending to the epistemic uncertainty (right histogram), it indicates that the value of the computed PoC can be trusted on a small fraction of events (a small gap between Pl and Bel), while the rest of the scenarios are affected by epistemic uncertainty. This also indicates than using a single ellipse to characterise the whole uncertainty affecting an event, no matter the type or the source, is not reliable. For the numerical values of each of the bars in Fig. 3.9, broken down by Geometry families, go to Table B.1 in Appendix B.

However, this classification, where the vast majority of events are classified as not known based on the current evidence, is not useful from the operation point of view. Thus, a new evidence-based classification criterion is proposed.

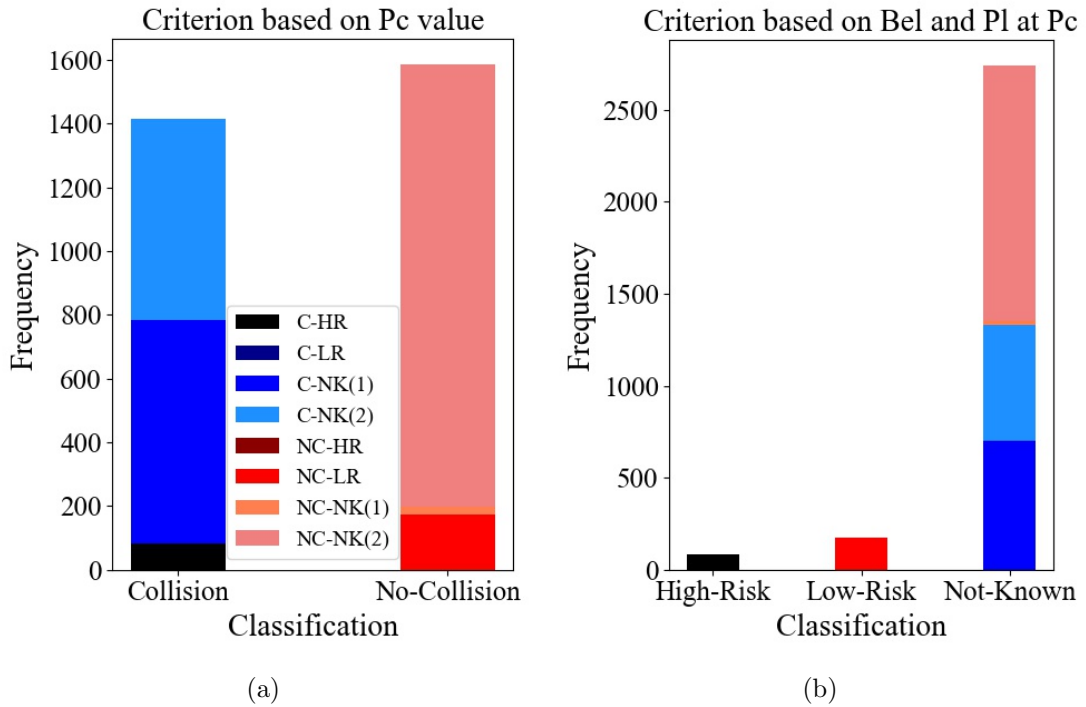


Figure 3.9: Histograms comparing criterion using (a) only the value of PoC and (b) the evidence-based *Criterion 1*. Each colour represents the fraction of samples from each bin on the histogram (a) that moves to one of the bins on the histogram (b).

Consider now the value of PoC at which Bel switches from $Bel \geq Bel_0$ to $Bel < Bel_0$, referred to as PoC_b . If $PoC_b \geq PoC_0$ the operator has enough evidence that any value of PoC between PoC_0 and PoC_b is credible and, therefore, the event has to be classified as High-Risk. If $PoC_b < PoC_0$ then one has to check the DoU gap at PoC_0 and beyond. If the gap at PoC_0 is high, then there is some evidence that supports the fact that the event might be high risk but there is not enough information to make a decision. On the contrary, if the gap is small one can consider the event low-risk. Based on this reasoning, *Criterion 2* can now be introduced as a new classification criterion as defined in Table 3.6.

Table 3.6: Evidence-based conjunction classification *Criterion 2*.

CRITERION 2		
<i>PoC</i> at Bel_0	<i>DoU</i> at PoC_0	Class
$PoC_b \geq PoC_0$	-	HR
$PoC_b < PoC_0$	$DoU \leq \Delta$	LR
	$DoU > \Delta$	NK

Using the samples of the previous example, Fig. 3.10 shows two histograms comparing the Probabilistic criteria based only on the $\hat{P}oC$ (Fig. 3.10a) and the evidence-based *Criterion 2* (Fig. 3.10b), using the thresholds indicated in Table 3.5. The left plot is the same as in Fig. 3.9, showing the encounters classified as high risk (blue-shaded) and as no collision (red-shaded). The difference is on the left side, where the newer evidence-based criterion is used. With this criterion, the classification does not rely anymore on the computed PoC, that as seen in the previous figure, is not reliable. Instead, only using the available evidence and the values of loss of support, a more informed decision can be obtained. On the one hand, the HR and LR cases are now granted to be uncertainty-free, while the cases affected by uncertainty are now a small proportion. It can be seen as well that the PoC-based criteria erroneously classify some events as high risk, where the evidence from all sources indicates it does not possess any risk (dark blue column).

For the numerical values of each of the bars in Fig. 3.10, broken down by Geometry

families, see Table B.2 in Appendix B.

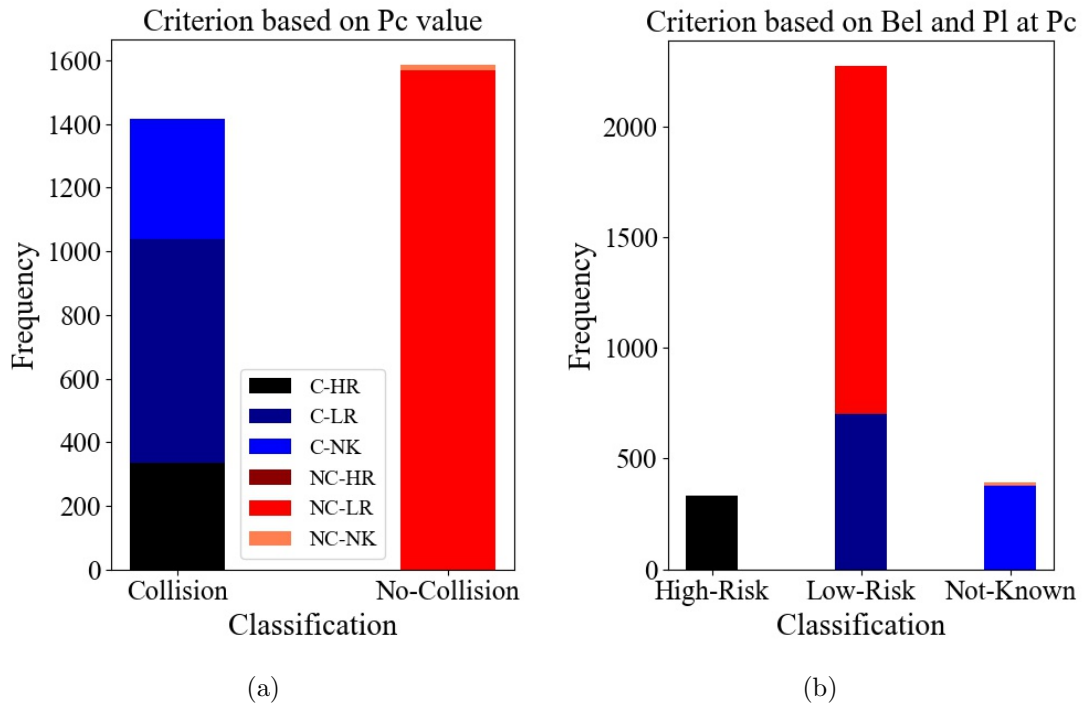


Figure 3.10: Histograms comparing criterion using (a) only the value of PoC and (b) the evidence-based *Criterion 2*. Each colour represents the fraction of samples from each bin on the histogram (a) that moves to one of the bins on the histogram (b).

All events still classified as Not-Known would suggest two actions: perform a CAM or acquire more information. The decision is often dictated by the available time and resources. If the time to impact is included, one could further refine the classification and make a decision based on the available time to obtain better-quality data.

3.3.4 Extended evidence-based classification criterion

In order to improve the decision-making process, it is desirable to include other parameters on top of *Bel* and *Pl* at a given PoC. The goal is to improve the confidence in the decisions of the operators. In particular, decision support is required in all those cases that are classified as Not-Known.

To this end, in this section, the classification process is extended by including the TCA. Two time thresholds were considered, dividing events into long-term, mid-term

and instantaneous. Table 3.7 summarises *Criterion 3* and its outcome: a 5-fold classification. Events in *Class 1* are High-Risk and require the execution of a CAM. Events in *Class 2* are High-Risk but there is time to collect better information, either to improve the manoeuvre planning or re-assess the level of risk. Events in *Class 3* are not supported by enough evidence to make a confident decision, but there is sufficient time to acquire more information and allocate new measurements. Events in *Class 4* are Low-Risk and the time to the encounter is high enough to acquire further information if desired. Events in *Class 5* are Low-Risk but there is little time to acquire further information, proposing to the operator no further actions to be taken concerning the event. Events with a high level of uncertainty but close to the TCA are classified as *Class 1*, instead of *Class 3* as the DoU would have suggested, choosing a conservative approach enhancing safety.

Further analyses can include other considerations, such as a comparison between the risk of the event and the inherent risk of executing a manoeuvre or the cost of the manoeuvre against the cost of the satellite pondered by the risk of the encounter (Chapter 8).

Table 3.7: Evidence-based conjunction classification *Criterion 3*.

CRITERION 3			
Time to TCA	PoC at Bel_0	DoU at PoC_0	Class
$t_{TCA} < T_1$	$PoC_b \geq PoC_0$	-	1
	$PoC_b < PoC_0$	$DoU \leq \Delta$	5
		$DoU > \Delta$	1
$T_1 \leq t_{TCA} < T_2$	$PoC_b \geq PoC_0$	-	2
	$PoC_b < PoC_0$	$DoU \leq \Delta$	5
		$DoU > \Delta$	3
$T_2 \leq t_{TCA}$	$PoC_b \geq PoC_0$	-	2
	$PoC_b < PoC_0$	$DoU \leq \Delta$	4
		$DoU > \Delta$	3

Fig. 3.11 shows the histograms comparing the probabilistic classification with this last Evidence-based approach using the same sample as the previous examples and the thresholds stated in Table 3.5. In order to account for the time to the TCA,

three different times to the TCA (one per each time bin: long-term, mid-term and instantaneous) were associated with each sample, creating three events per sample. For the numerical values of each of the bars in Fig. 3.11, broken down by Geometry families, see Table B.3 in Appendix B.

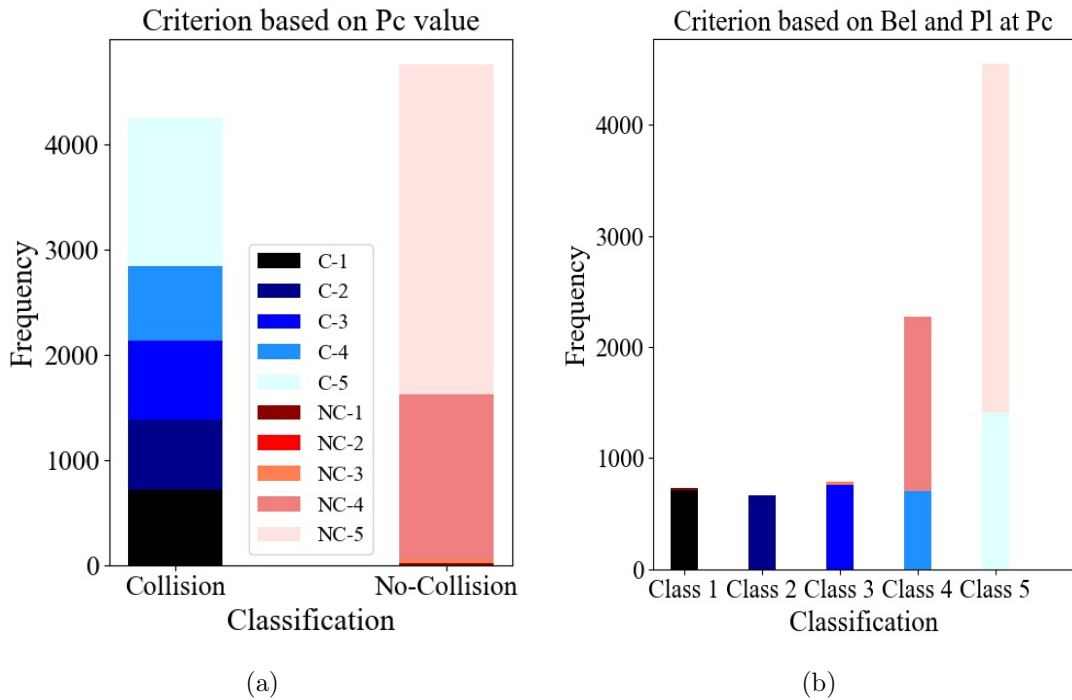


Figure 3.11: Histograms comparing criterion using (a) only the value of PoC and (b) the evidence-based *Criterion 3*. Each colour represents the fraction of samples from each bin on the histogram (a) that moves to one of the bins on the histogram (b).

The new histogram shows a more comprehensive classification, yet, clear to understand from the decision-making point of view. Most of the cases classified as No-Collision initially remain in classes associated with low risk (*Class 4* and *5*), with the exception of a very small fraction catalogued as *Class 3*, which indicates cases with a low $\hat{P}oC$ tends to be more reliable. However, cases initially classified as Collision are now spread along the different classes. Around a third are in high-risk classes (*Class 1* and *2*), associated with *Geo. 1* cases or *Geo. 3* cases with more weight in the source whose information was closer to the HBR. There are some samples where more information is required. They are related to those scenarios with sources providing conflict

information that, due to the construction of the joint distribution, were catalogued as Collision initially, although not all evidence supported that. Finally, there are Collision examples that are moved to lower-risk classes with the new classification. *Geo. 5* are the most representative cases of this situation, where the high $\hat{P}oC$ was an artificial value, and now the lower risk associated with both sources is better detected.

3.4 Chapter summary

This chapter presented a methodology to model aleatory and epistemic uncertainty on space conjunction risk assessment. Aleatory uncertainty on the position was modelled following a classical probability approach with a Gaussian distribution. Epistemic uncertainty was introduced as uncertainty on the actual value of the Gaussian distribution parameters. The method allowed evaluating the confidence in the correctness of the value of the PoC associated with the close encounter.

An evidence-based classification criterion was proposed based on the DSt method to provide operator robust decision-making support to deal with conjunction events. The criterion takes the uncertain encounter geometry, and classifies the event in one of the 5 proposed classes, depending on the level of support and the amount of uncertainty on the inputs. The methodology was compared against a classical probability approach, showing its capacity to correctly identify encounters and to detect cases where more information was required to make a confident decision.

This evidence-based framework will be the core aspect of the rest of this work, used along with the different methods and applications presented in the next chapters. The last classification criterion introduced above will be also further used in this document and extended according to the new developments introduced in the following chapters.

Chapter 4

Modelling epistemic uncertainty in Conjunction Data Messages

The content of this chapter was partially published in:
Sánchez, L., Vasile, M., Sanvido, S, Maerz, K. and Taillan, C.,
“Treatment of epistemic uncertainty in conjunction analysis with
Dempster-Shafer theory”, *Advances in Space Research*,
submitted. [Sánchez et al., 2024]

In satellite operations, it is common practice to use Conjunction Data Messages (CDMs) [CCSDS, 2013] when dealing with conjunction events. The CDMs are a communication protocol established more than a decade ago for standardising the communication shared with operators containing the information of a close encounter, its epoch, the relative state, and data of the satellites involved in the encounter, including its positions and the quantification of their uncertainty. However, the model of uncertainty is not transparent. It is customarily assumed that the distribution of possible positions of the two objects at the time of closest approach follows a multivariate Gaussian with a given mean and covariance matrix [Merz et al., 2017]. In practice, there is little transparency to retrieve the uncertainty at the observation epoch and it is virtually impossible to discern the sources of uncertainty (e.g. sensors, propagation and dynamic errors).

When receiving a series of CDMs there is no standardised protocol of how to treat

them, and more importantly, how to deal with the encoded uncertainty. In any case, it is clear that there are sources of epistemic uncertainty (lack of knowledge) on some of the steps to obtain the information on the CDM. However, most of the current applications do not take into account this type of uncertainty [Laporte and Moury, 2013, Laporte, 2014a, Newman et al., 2014, Braun et al., 2016, Merz et al., 2017, Stroe et al., 2021] in the analysis. In this chapter, a methodology to model the epistemic uncertainty implicitly contained on the CDMs sequences is proposed. This model also allows integrating this uncertainty on the Dempster-Shafer theory of Evidence (DSt) framework proposed in the previous chapter, providing a complete system to operationally assess the risk of close encounters.

The rest of the chapter is structured as follows. Section 4.1 shows the presence of epistemic uncertainty on the sequences of CDMs and the necessity to account for it. The next section, Section 4.2, introduces a methodology for accounting for the epistemic uncertainty under DSt based on the concepts of Dvoretzky-Kiefer-Wolfowitz (DKW) inequality and p-boxes. Section 4.3 shows a numerical example based on a real sequence of CDMs. A sensitivity analysis based on this example is shown along with the robustness of the methodology when dealing with poor quality CDMs. Finally, Section 4.4 indicates the main contributions of the chapter.

4.1 Epistemic uncertainty in the CDMs

The information on a given close encounter is generally available in the form of a CDM, which contains the means and covariances of the two objects at the Time of Closest Approach (TCA) [CCSDS, 2013]. As indicated, uncertainty on the objects' position involved in a close encounter is usually assumed to follow a multivariate Gaussian distribution, which is used to model the actual distribution on at the encounter, the dynamic model error and the observation noise. However, this yields some problems, like the probability of dilution, as shown in the previous chapter.

The general attempt to compensate for the uncertainty in the CDMs is to improve the covariance matrix model by improving its propagation [Aristoff et al., 2014] or by some form of updating of the dynamic model [Cano et al., 2023]. These approaches

are all very valuable but require direct access to the post-observation data. Other methods based solely on the available CDMs tried to predict the next CDMs using machine learning starting from an available time series [Pinto et al., 2020, Acciarini et al., 2021, Caldas et al., 2023] or increased the last covariance under the assumption that the series of CDMs should follow a given distribution [Laporte, 2014a, Laporte, 2014b]. This last approach does not modify the mean value or miss distance.

So far, only a limited number of authors have directly addressed epistemic uncertainty in conjunction analysis [Tardioli and Vasile, 2015, Delande et al., 2018, Balch et al., 2019, Greco et al., 2021]. In the previous chapter, a robust approach to conjunction analysis based on DSt was presented, allowing making decisions based on the degree of confidence in the correctness of a value instead of based the decision on a single value of the metric [Helton et al., 2005]. However, the available information to build the frame of discernment that is needed in DSt is often limited in a sequence of CDMs. CDMs contain little information on the three forms of uncertainty listed above and essentially only provides covariance and miss distance. Thus, one key question is how to translate the time series of CDMs into the frame of discernment used in DSt, based on interval-valued variables with the associated basic probabilistic assignment (*bpa*). The underlying assumption adopted in this work is that the CDMs are observables drawn from an unknown family of distributions defined within some bounds. Without uncertainty, one would be able to predict exactly the next CDMs as the mean and covariance would only depend on observations with known distribution and there would not be any uncertainty in the propagation model and distribution at TCA. Furthermore, the CDMs computed from observations acquired close to the TCA are assumed to be less affected by model and distribution uncertainty. This is reasonable as the propagation time is shorter and thus both nonlinearities and model errors have a lower impact on the propagation of the distribution of the possible states.

In the next section, a methodology based on the DKW inequality [Dvoretzky et al., 1956] is introduced to derive a DSt structure capturing the epistemic uncertainty in a given sequence of CDMs. From the DSt structures, one can derive the Belief (*Bel*) and Plausibility (*Pl*) that the value of the Probability of Collision (PoC) is correct and an

upper and lower bound on its value as explained in the previous chapter.

4.2 Methodology

This section presents a method to integrate sequences of CDMs within the evidence-based framework introduced in Chapter 3. The use of DSt to model epistemic uncertainty does not require any assumption on the probability of an event and also captures rare events with low probability. On the other hand with no direct information on measurements and dynamic model, one can only rely on the CDMs to define the FEs and associated probability masses.

The first step is to derive the FEs from the time series of miss distances and covariance matrices in the CDMs. In accordance with DSt, no prior assumption is made on the underlying distribution of the CDMs and, instead, it is considered that each CDM is drawn from an unknown set of probability distributions. The assumption is that the value of the uncertain vector \mathbf{u} in each CDM is a sample drawn from the set of unknown distributions. The DKW inequality [Dvoretzky et al., 1956] is used to build an upper and lower bound to the set starting from the empirical Cumulative Distribution Function (eCDF) derived from the sequence of CDMs. This confidence region resembles the Dempster-Shafer structures obtained with the intervals and *bpas* (Fig. 3.3).

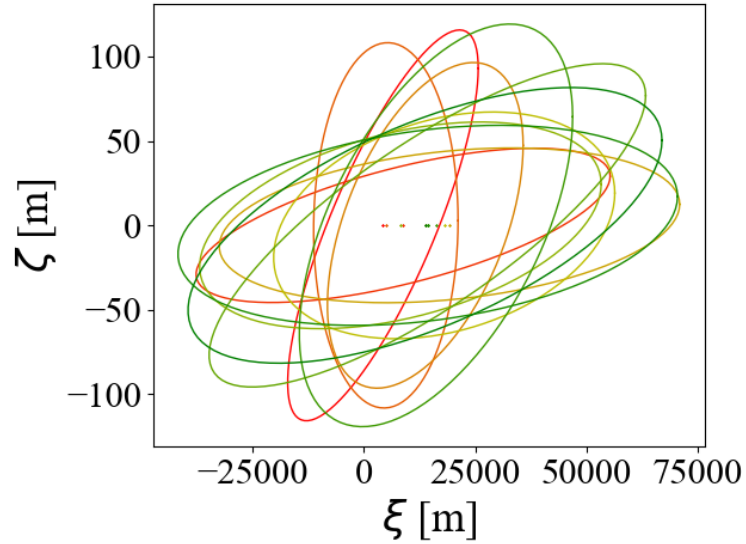
Note the similarity between the family of ellipses derived from the set of intervals in the DSt approach in Section 3.2.1 (Fig. 4.1a) and the set of ellipses from the sequence of CDMs (Fig. 4.1b). This idea lies behind the proposed method and underlines the fact that the set of CDMs presents some forms of epistemic uncertainty.

Given a sequence of CDMs, it is possible to compute the eCDF (solid blue line in Fig. 4.2) of the uncertain variables, a step-function approximating the actual unknown distributions (if any), from where the CDMs are drawn from. However, given the limited number of samples, there is a range of possible distributions compatible with the eCDF, showing the epistemic uncertainty presented in the system. The DKW inequality defines the following upper and lower bounds (dashed green lines in Fig. 4.2)

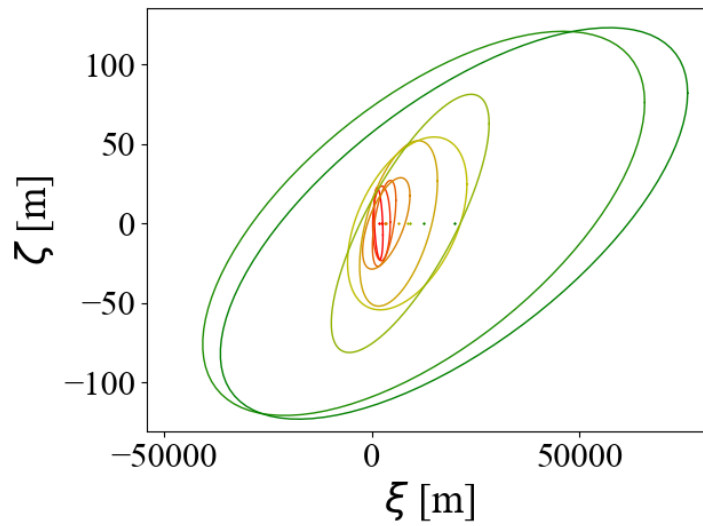
around the eCDF $F_n(x)$:

$$F_n(x) - \varepsilon \leq \mathcal{F}(x) \leq F_n(x) + \varepsilon \quad \varepsilon = \sqrt{\frac{\ln \frac{2}{\delta}}{2n}} \quad (4.1)$$

given n CDMs and the confidence level $1-\delta$ that the exact distribution $\mathcal{F}(x) \in F_n(x) \pm \varepsilon$.



(a)



(b)

Figure 4.1: Encounter geometry on the impact plane: family of ellipses from (a) a DSt analysis with one interval per source, (b) sequence of CDMs.

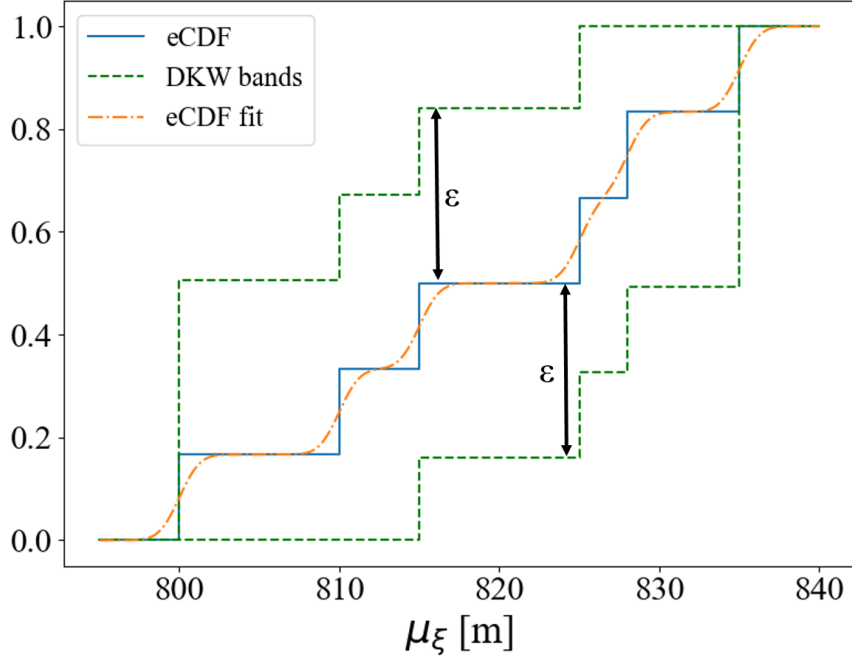


Figure 4.2: DKW region for a given set of samples. The width of the region, ε , is indicated. In solid blue the eCDF, in dashed green the DKW bands, and in dashed-pointed orange the CDF of the equally weighted sum of Gaussian distributions centred at the samples.

From the confidence region defined by the DKW bands, it is possible to derive the probability box or p-box [Ferson et al., 2003, Ferson et al., 2007, Liu et al., 2017a] of the data. A p-box is a set of all Cumulative Distribution Functions (CDFs) compatible with the data, that is, the bounded region containing all distributions from where the set of samples may have been drawn [Ferson et al., 2007]. The upper and lower bounds of the p-box should be monotonic non-decreasing curves, ranging from 0 and 1, so that $\underline{\mathcal{F}}(x) \leq \mathcal{F}(x) \leq \overline{\mathcal{F}}(x)$, with $\underline{\mathcal{F}}(x)$ and $\overline{\mathcal{F}}(x)$ the upper and lower bounds of the p-box for variable x [Ferson et al., 2003].

In this work, the p-box bounds are computed from the CDF of a weighted sum of univariate Gaussian distributions, each one centred at one of the samples. More formally, the assumption is that $\mathcal{F}(x)$ can be approximated by:

$$\mathcal{F}(x) \sim \mathcal{P}(x) = \int_{-\text{inf}}^{\text{inf}} \sum_i w_i \mathcal{N}(x_i, \sigma_i; x) dx, \quad (4.2)$$

with x_i the realisations of the uncertain variable x , w_i a weight associated with each sample, and σ_i the variance of the Gaussian distribution associated with the i^{th} sample. See Fig. 4.3 for an illustrative example. Implicitly, it implies that each sample presents some uncertainty which is modelled with a Gaussian distribution (grey lines in Fig. 4.3). This distribution represents the confidence in the sample's value.

with x_i the realisations of the uncertain variable x , w_i a weight associated with each sample, and σ_i the variance of the Gaussian distribution associated with the i^{th} sample. See Fig. 4.3 for an illustrative example. Implicitly, it implies that each sample presents some uncertainty which is modelled with a Gaussian distribution (grey lines in Fig. 4.3). This distribution represents the confidence in the sample's value. By doing so, it is admitted that when observing a sequence of CDMs it is not possible to tell from which exact distribution that sequence is drawn. This is consistent with the available sequences of real CDMs and the approach adopted by the Centre National d'Etudes Spatiales (CNES) to model the uncertainty in the covariance (see Chapter 7).

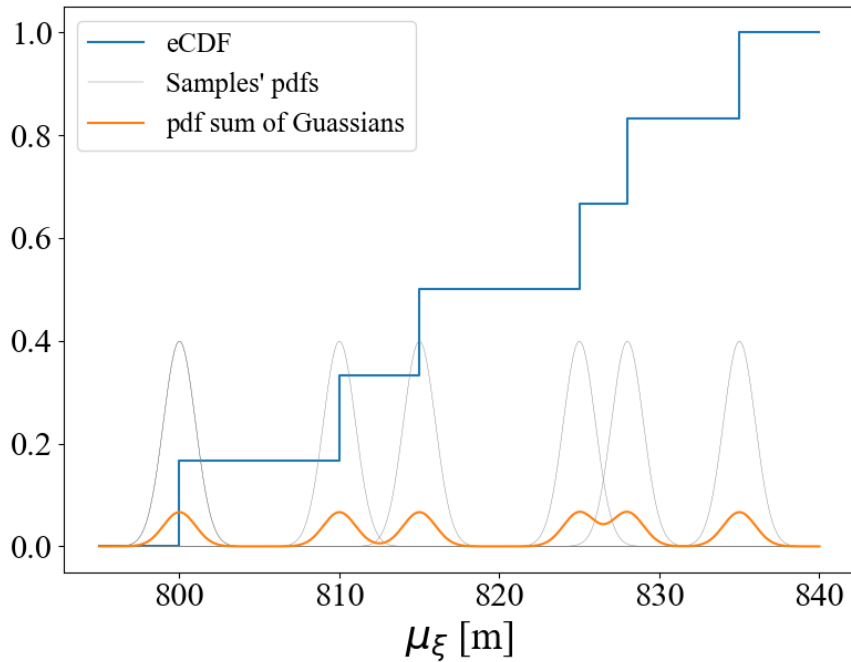


Figure 4.3: Gaussian distributions centred at the samples for building the eCDF fit. In blue the eCDF, in grey the pdf of individual Gaussian distributions, and in orange the CDF of the equally weighted sum.

In order to define the p-box's limits, the two free parameters on each Gaussian distribution on the weighted sum, w_i and σ_i , must be computed by solving these optimisation problems:

$$\begin{cases} \overline{\mathcal{P}}(x) = \max_{w_i, \sigma_i} \mathcal{P}(x; w_i, \sigma_i) \\ \underline{\mathcal{P}}(x) = \min_{w_i, \sigma_i} \mathcal{P}(x; w_i, \sigma_i) \end{cases} \text{ s.t. } \begin{cases} \overline{\mathcal{P}}(x) \leq \min(1, F_n(x) + \epsilon) \\ \underline{\mathcal{P}}(x) \geq \max(0, F_n(x) - \epsilon) \end{cases}, \quad (4.3)$$

where $\overline{\mathcal{P}}(x), \underline{\mathcal{P}}(x)$ are the upper and lower bounds of the p-box, respectively. An approximation to $\overline{\mathcal{P}}(x), \underline{\mathcal{P}}(x)$ can be computed by finding the values of w_i and σ_i in Eq. (4.2) that best fit the upper and lower DKW bands (red dashed-pointed line in Fig. 4.4):

$$\begin{cases} \overline{\mathcal{P}}(x) \approx \overline{P}(x) = \text{fit}_{w_i, \sigma_i}(F_n(x) + \epsilon) \\ \underline{\mathcal{P}}(x) \approx \underline{P}(x) = \text{fit}_{w_i, \sigma_i}(F_n(x) - \epsilon) \end{cases} \quad (4.4)$$

Eq. (4.4) gives the upper and lower bounds on the probability of realisation of a particular value of the uncertain vector \mathbf{u} , but the definition of a set of intervals for each component of \mathbf{u} requires the definition of the range of each component. Eq. (4.2) suggests that each p-box has infinite support. However, this would lead to an inconvenient infinite range for variance and miss distance. Instead, in the following a more practical interval $[\underline{x}, \overline{x}]$ is defined such that:

$$\int_{\underline{x}}^{\infty} w_1 \mathcal{N}(x_1, \sigma_1; x) dx = 0.99, \quad \int_{-\infty}^{\overline{x}} w_n \mathcal{N}(x_n, \sigma_n; x) dx = 0.99, \quad (4.5)$$

It is important to note that the assumption is that the miss distance and each component of the covariance can be treated independently. Although this is generally not the case, the independence assumption in this paper leads to a more conservative set of focal elements that cover the space of realisations of the uncertainty vector. Although this can lead to over-conservative decisions, it is deemed to be acceptable in the case of high-risk events with little available information.

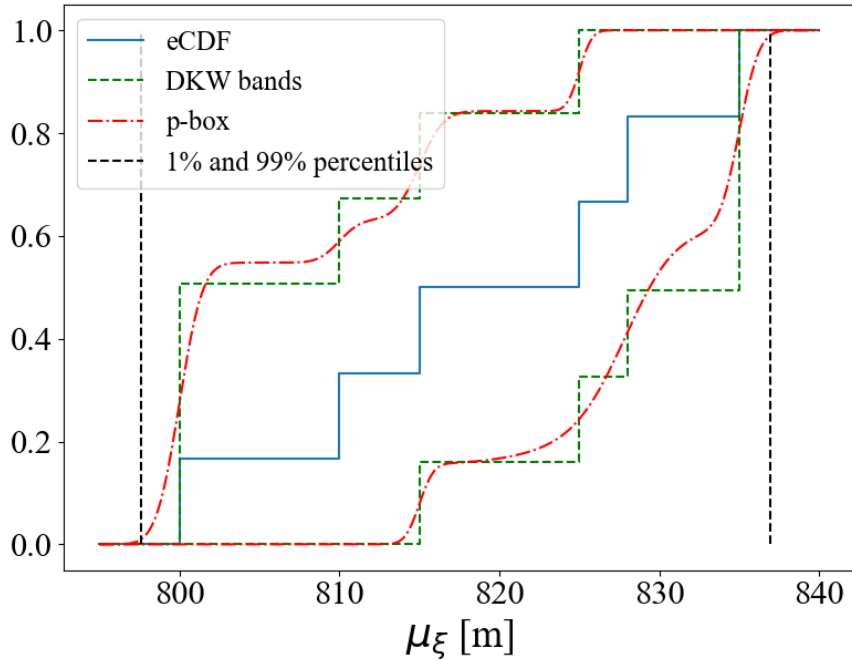


Figure 4.4: p-box derived from a DKW region. In solid blue the eCDF, in dashed-green the DKW bands, in dashed-pointed red the p-box, and in dashed vertical black the 1% and 99% percentiles of the upper and lower p-box bounds, respectively.

4.2.1 Scaling of the CDMs

The approach described in above assumes that every CDM in a sequence has the same relative importance and no additional source of information is available to qualify each individual CDM. However, as the $t2TCA$ decreases, so does the effect of the uncertainty on the true shape of the distribution on the impact plane and the effect of model uncertainty in the propagation. Fig. 4.5a shows the normalised determinant of multiple sequences of covariance matrices taken from the database of the European Space Agency’s (ESA) Collision Avoidance Kelvins Challenge [European Space Agency, 2019, Uriot et al., 2022]. The database contains 13,152 sequences of CDMs of some of the Low Earth Orbit(LEO) satellites monitored by the ESA’s Space Debris Office (SDO). The figure shows that one can fit the simple exponential law $y^* = e^{-3t^*}$ to the magnitude of the determinant (red thick line in the figure). However, one cannot simply trust later CDMs due to large uncertainty in each individual sequence. Thus,

the following fit for each individual sequence is proposed:

$$y^* = Ce^{At^*} + B \quad A, B, C \geq 0, \quad (4.6a)$$

$$y^* = \frac{\|\Sigma\|}{\max_{CDM_s}(\|\Sigma\|)} \quad (4.6b)$$

$$t^* = \frac{(1 - \max_{CDM_s}(t2TCA))}{(\min_{CDM_s}(t2TCA) - \max_{CDM_s}t2TCA)} \quad (4.6c)$$

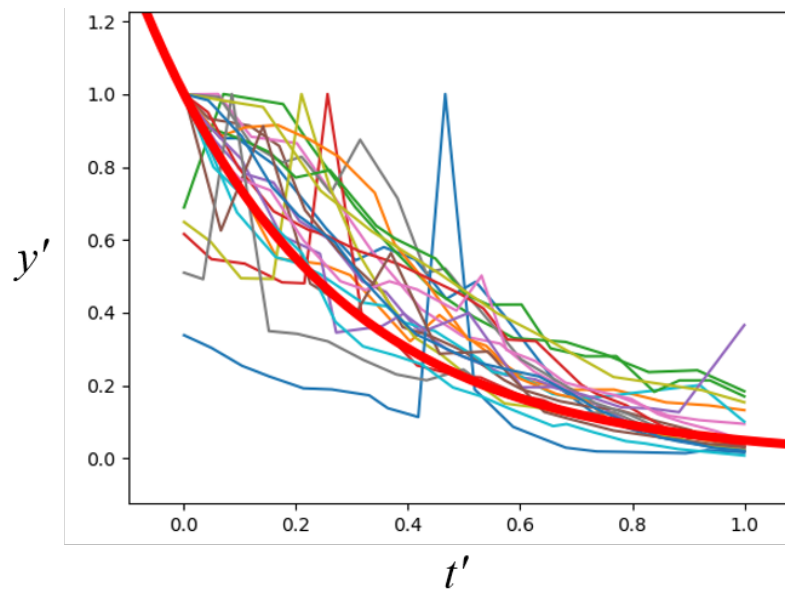
Once the parameters A, B and C are fitted to the samples from a given sequence, the following weight is associated with each CDM in that sequence. This fitting process is repeated each time a new CDM is added to the sequence.

$$w_{CDM_i} = \frac{1}{y^*(t2TCA_{CDM_i})} \quad (4.7)$$

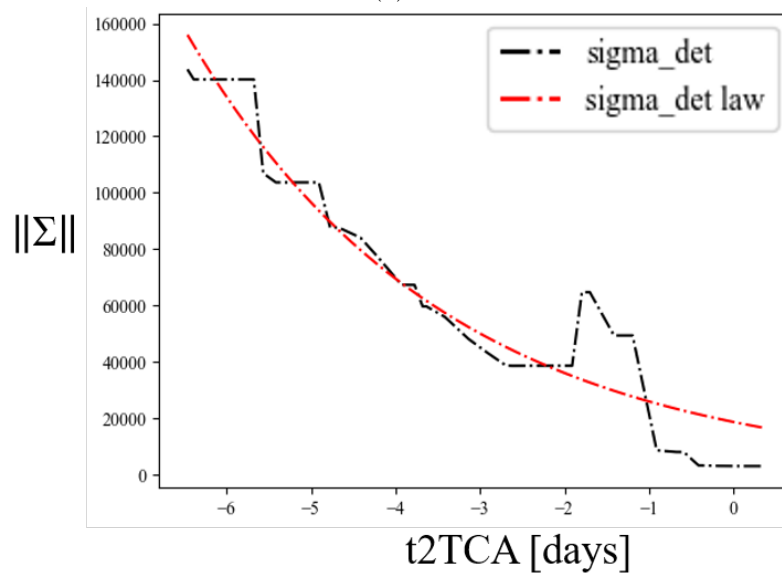
The weight is applied to each sample in the eCDF used to compute the DKW bounds: the probability mass associated with each sample is re-scaled by a factor w_{CDM_i} . See Fig. 4.6 where the eCDF of μ_ξ for an example with five observations is shown both with samples equally weighted (dashed red) or having applied the weighting law described above (blue).

This approach results in a scaling of the probability mass associated with the CDMs but still allows the quantification of highly uncertain CDMs since there is no filtering process. The reason is that, with no information on trusted sources or individual CDMs, one cannot make any assumption on which CDM is more credible.

However, the current version of this method does not account for possible correlation among CDMs in the same sequence. The correlation may be due to using the same source or the same propagation interval. Correlation may impact the way the same information is accounted for. On the other hand, the DSt includes the option of several pieces of information coming from the same source, and giving more credibility when this information is coherent. Future improvements on this method may limit the importance (weight) of future CDMs if too correlated with previous ones in the sequence and not adding additional information (i.e. new observations during the period).



(a)



(b)

Figure 4.5: CDMs fitting law: (a) $y' = e^{-3t'}$ (thick red line) and the dimensionless covariance determinant for some sequences of CDMs (thinner lines), (b) Fitted law (dashed-pointed red) of a single sequence of CDMs (dashed-pointed black).

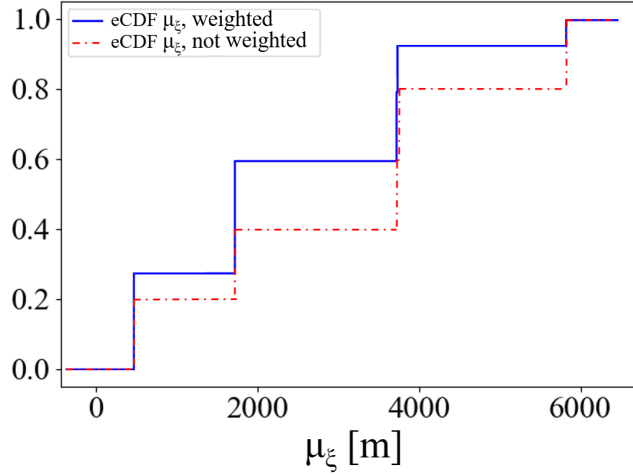


Figure 4.6: eCDF for μ_ξ weighing the samples (blue) and with samples equally weighted (dashed red).

4.2.2 α -cuts and DSt Structures

Once the p-box is defined, the intervals for each component of the uncertain vector \mathbf{u} are derived from a series of equally spaced α -cuts (light blue and grey dotted horizontal thin lines in Fig. 4.7). Each α -cut creates interval [He et al., 2015, Chojnacki et al., 2007]:

$$[x_\alpha, x^\alpha] = \{x \mid \mathcal{F}(x) \geq \alpha\}. \quad (4.8)$$

The intersection with the upper bounds in the p-box defines the lower limit of the interval, and the intersections with the lower bound define the upper limit of the interval. The number of intervals is equal to the number of cuts plus one, and the *bpa* associated with each interval, assuming the cuts are evenly spaced, is equal to the inverse of the number of cuts. The intervals and their *bpa* will define an envelope around the p-box (blue and black dashed lines in Fig. 4.7). The greater the number of α -cuts, the closer the envelope will be to the p-box, but the more computationally expensive the computation of *Bel* and *Pl* in the next step.

Once the intervals for the marginals (the uncertain variables) are obtained, the set of Focal Elements (FE) and the joint *bpas* can be computed as the Cartesian product of the intervals of the different variables, as explained in Chapter 3, and from there,

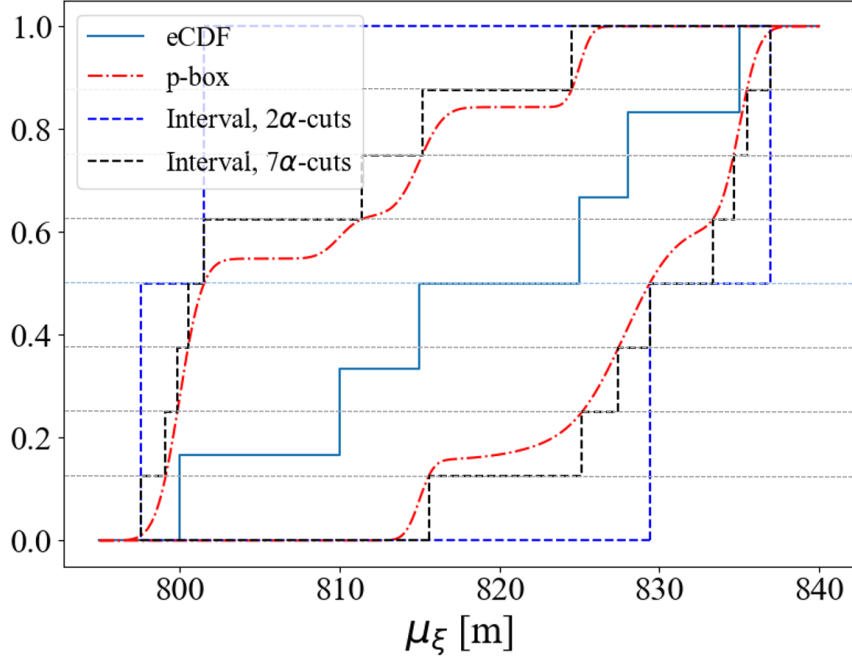


Figure 4.7: Intervals partition derived from a p-box. In solid blue the eCDF, in dashed-pointed red the p-box, in thin dotted blue and grey the alpha-cuts (1 and 7 cuts, respectively), in dashed blue the 2 intervals partition, in dashed black the 8 intervals partition.

derived the Pl and Bel of $PoC \geq PoC_0$ with Eq. (3.9), obtaining the representative curves on the confidence of the value of PoC . Finally, the event of the CDM can be classified with the criteria in Table 3.7.

Even in this case, the assumption that the variables are independent is maintained. Approaches to address dependencies already exist in the literature [Ferson et al., 2004, Hejduk, 2016], although they are not addressed in this work. The independence assumption has two implications: i) the uncertainty space U is an outer approximation of the space of all distributions of \mathbf{u} , and ii) some focal elements might not contain any sample of \mathbf{u} . The combination of the two generally leads to over-conservative results. Thus, in order to have less conservative results, yet coherent with DSt, a $bpa = 0$ is assigned to all empty FEs coming from the Cartesian product. The original bpa of those FEs is evenly distributed to the rest of FEs so that $\sum_i bpa_i = 1$.

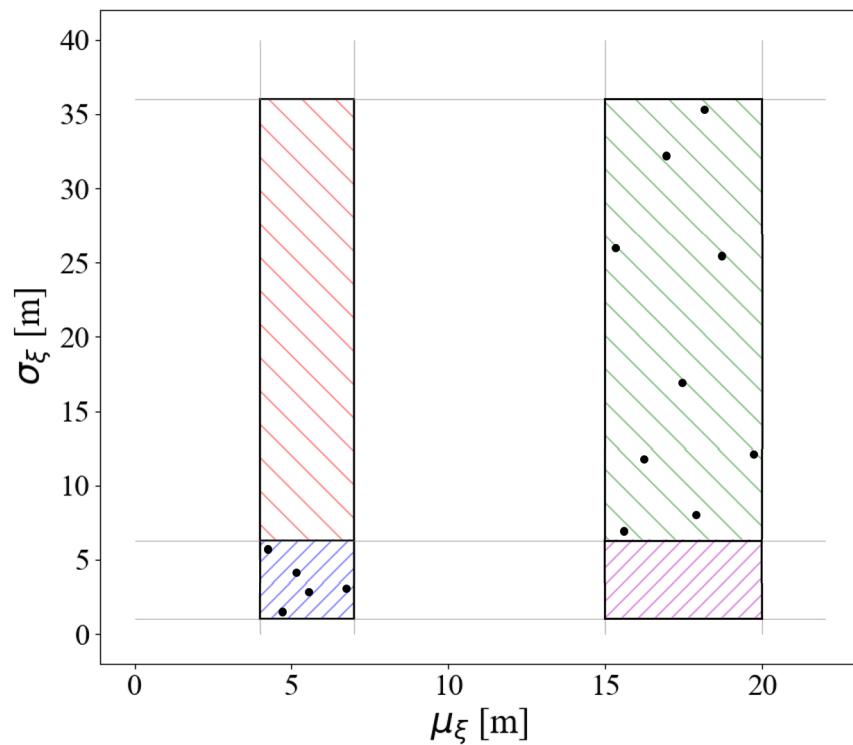


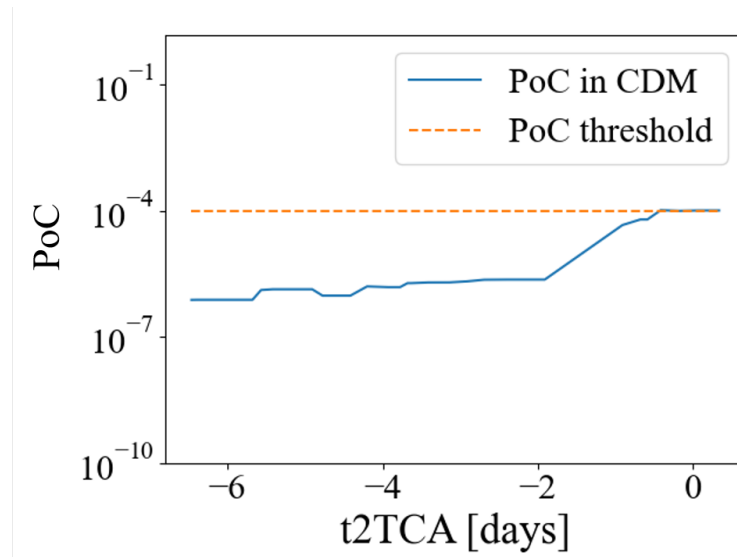
Figure 4.8: Joint Body of Evidence with artificially generated FEs (top-left and bottom-right ones) not containing any sample (black dots).

4.3 Conjunction Data Message epistemic analysis

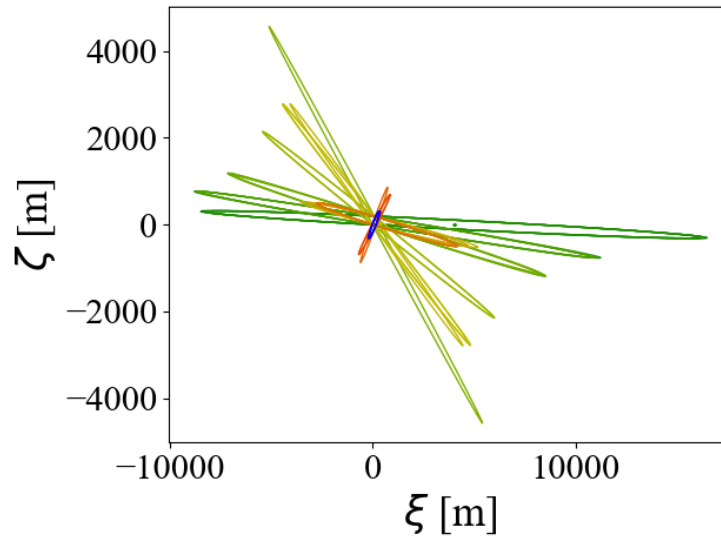
This section shows a numerical example of the proposed methodology using a real sequence of CDMs from an ESA’s operated satellite. Initially, the methodology is presented, extracting the epistemic uncertainty from the sequence and obtaining the p-boxes and the set of intervals. Then, a sensitivity analysis based on this example is carried out to show the influence of different parameters on the results. Finally, the robustness of the approach is shown by adding three poor quality CDMs discarded by ESA on the real operation during the encounter event analysis.

The sequence analysed consists of a series of 33 CDMs, whose risk increased, approximating to the PoC threshold set for this mission, although no evasive actions were finally required on the real scenario (Fig. 4.9a). When observing the geometry encounter along the whole sequence, it can be seen the great variability presented along

the series, indicating the event is probably affected by epistemic uncertainty (Fig. 4.9b).



(a)



(b)

Figure 4.9: Sequence of CDMs. (a) Evolution of the PoC in the CDMs. (b) Uncertain geometry from the series of CDMs.

In order to assess the risk of the event under the DSt approach proposed in the Chapter 3, the methodology in the previous section is applied. Initially, to obtain the eCDF of the five uncertain variables (miss distance and covariance matrix components

in the impact plane), the CDM are weighted according to the aforementioned exponential law. The best-fitted for the evolution of the covariance matrix determinant (for the whole sequence) follows the law in Eq. (4.6a) with parameters: $A = 1.113244$, $B = 2.45612646$, $C = 4.71282852 \cdot 10^{-18}$. The fitting law can be seen along with the determinant from the CDMs in Fig. 4.10a. From the fitting law, the different CDMs are weighted according to the curve in Fig. 4.10b.

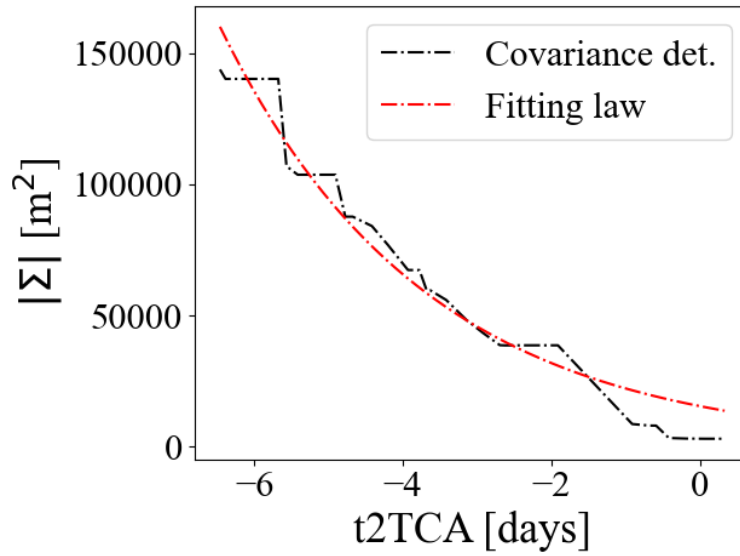
Provided the sequence and the weights of the samples it is possible to define the eCDF. Once the value of the interval of confidence is decided, it is possible to obtain the DKW region with Eq. (4.1) and the p-box with Eq. (4.3). Selecting the number of α -cuts, the Dempster-Shafer structures for each variable are derived. Fig. 4.11 includes the p-box bounding the eCDF for a value of $\delta = 0.5$ and the intervals for 3 α -cuts per variable for μ_ξ and σ_ξ^2 .

Finally, the set of intervals and the *Pl* and *Bel* curves for the PoC can be derived. Fig. 4.12 shows the resulting *Pl* and *Bel* curves for a 4-intervals partition, resulting in 1,024 FEs, from which 882 were removed for not containing any sample from the sequence.

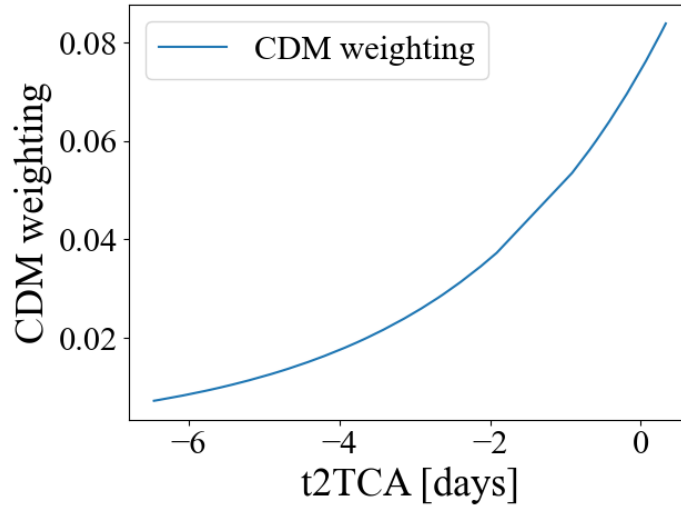
From the figure, it can be seen that values above the PoC threshold receive some support ($Pl > 0$ at $PoC = PoC_0 = 10^{-4}$). Note that in this case, the PoC threshold (purple dotted line) almost corresponds to the maximum value on the sequence and the value on the last CDM (solid and dashed green lines). However, $Bel(PoC_0) = 0$, and the separation between the curves is relatively wide, both at the threshold and overall for the range of values of PoC receiving any support. This indicates that the sequence is affected by epistemic uncertainty and should be taken into account by the operator when making a decision based on the PoC value.

Computational time

From the previous steps on the Conjunction Assessment Risk Analysis (CARA), some of them are more time-consuming than others. Also, there are some stages whose computational time would depend on the parameters chosen (as will be shown in the next section). In Table 4.1, the computation time (in seconds) of the study case, overall



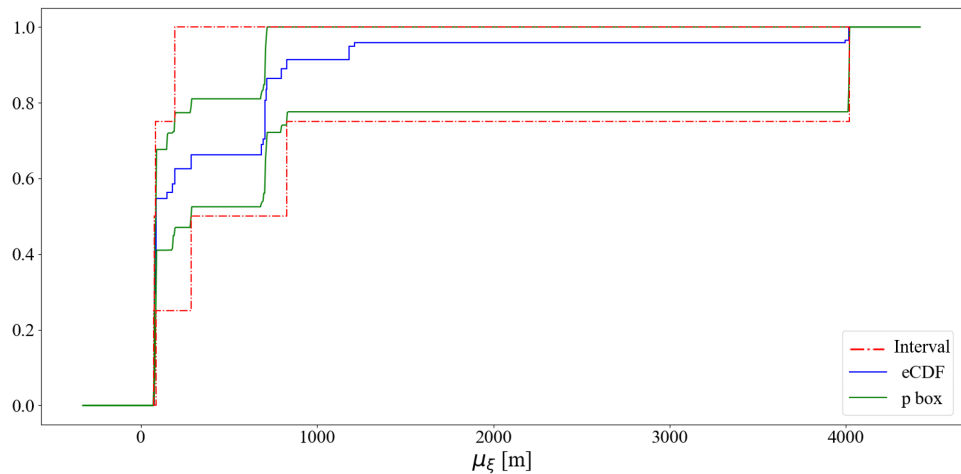
(a)



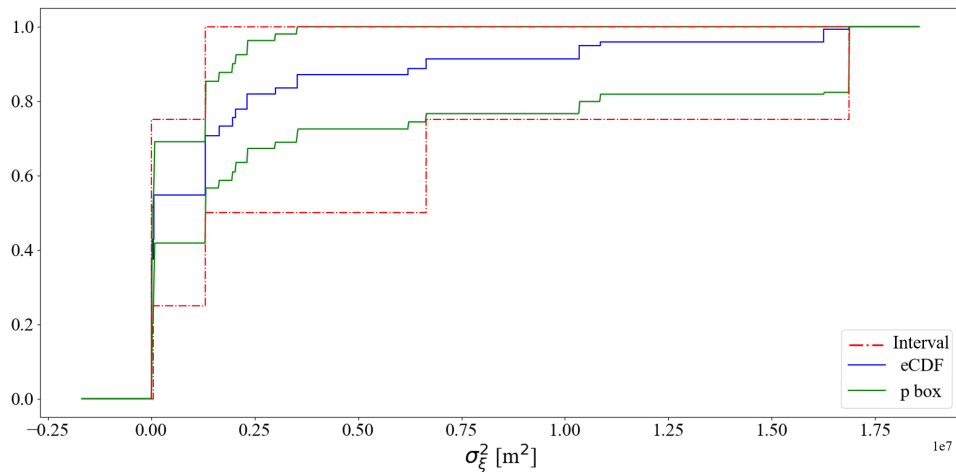
(b)

Figure 4.10: CDMs weighting law for the whole sequence. (a) Evolution of covariance determinant (black) and fitting law (red). (b) CDM weighting versus the time to the TCA.

and broken down into the different steps, is shown. The CARA analysis can be divided into three main stages: obtaining the eCDF and the DKW bands of the variables, which includes the weight of the CDMs, deriving the p-boxes for each sample, and compute the *Pl* and *Bel* curves, including the FE dropping. The time to compute the p-boxes is shown both for the optimisation in Eq. (4.3) and for the approximation using Eq. (4.4).



(a)



(b)

Figure 4.11: eCDF (solid blue), p-box (solid green) and Dempster-Shafer structure (pointed-dashed red) from where obtained the intervals for (a) μ_ξ and (b) σ_ξ^2 .

The overall time using one approach or the other is also shown in the table. However, for the rest of this chapter, only the approximated p-boxes were computed.

From the results in the table, it could be possible to identify two main bottlenecks in the process: the computation of the Pl and Bel curves and the construction of the p-boxes. When obtaining the Pl and Bel curves, several optimisation problems have to be solved: for each FE, the minimum and maximum PoC have to be obtained (which would increase with N^5 with the number of interval partitions). Besides, this

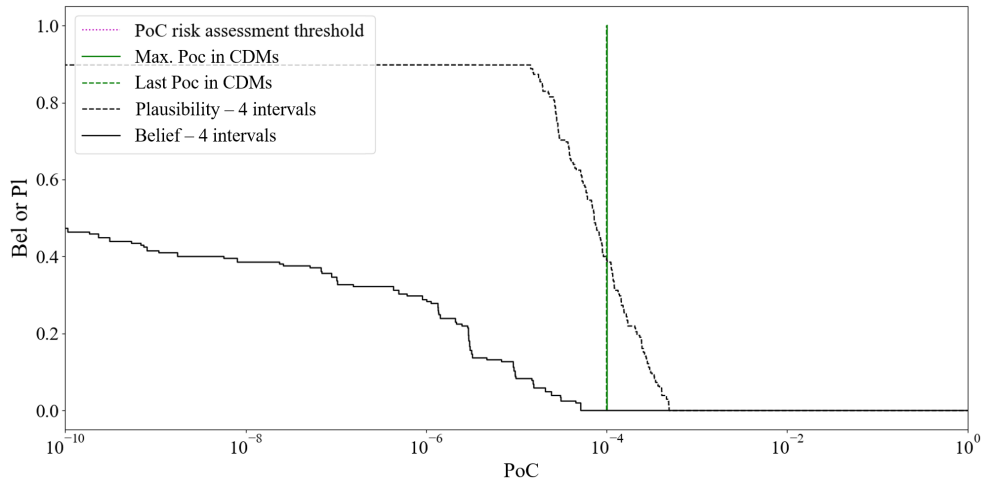


Figure 4.12: *Pl* and *Bel* curves for $PoC \geq PoC_0$ for 4-intervals partition.

Table 4.1: Computational time (in seconds) of the CARA analysis provided the sequence of CDMs.

Stage	Computational time [s]
CARA analysis (optimising/fitting)	~9635/~ 194
eCDF and DWK bands	~ 0.1
CDMs weighting	~ 0.02
p-boxes (optimising/fitting)	~9555/~ 114
<i>Pl</i> and <i>Bel</i> curves	~ 80

optimisation step considers the constraints set by the given intervals on each of the variables of interest (miss distance and covariance matrix). The author acknowledges that optimisation techniques not investigated in this work would potentially accelerate this step, however, the dependency on the number of uncertain variables and interval partitions would still influence the required computational time of this step. The other main expensive step is the computation of the p-boxes. This step has to be repeated for each of the uncertain variables and requires two optimisation steps, one per each of the bounds of the p-box. The step is highly sensitive to the number of CDMs in the sequence. Increasing the number of CDMs brings more conditions to be satisfied in the optimisation, which has to keep as close as possible to them, but ensure the p-box remains more conservative than the DKW band. Approximating the p-box with the fitting of the points considerably reduced the required time, but it is also affected by

the number of CDMs in the sequence since more points have to be fitted. As in the case of the *Pl* and *Bel*, the author recognises that other optimisation techniques to be implemented in this work may speed up the process, but the effects on the length of the sequence would remain. Comparatively, the other steps are quick and are no or less affected by the number length of the sequence or the number of intervals. In Chapter 8, some AI-based alternatives to speed up these steps are presented.

4.3.1 Sensitivity analysis

In this section, a sensitivity analysis based on the previous case is carried out. In the example, some of the parameters defining the analysis are given by the sequence itself (e.g. the number of samples), but others have to be selected by the operator (e.g. the number of cuts, the value of the confidence interval, the weighting of the samples). In the following, some of these parameters are modified to understand the impact on the construction of the Dempster-Shafer structures and the *Pl* and *Bel* curves.

Confidence interval

One of the first parameters set during the analysis was the value of the confidence interval, $1 - \delta$, containing the actual distribution from where the eCDF was drawn. A bigger value of $1 - \delta$ would better guarantee the actual CDF is captured within the DKW bands. However, it will create a wider region that, eventually, would translate into a broader p-box and bigger intervals, increasing the uncertainty associated with the event, and thus, the gap between the *Pl* and *Bel* curves.

Fig. 4.13 show the *Pl* and *Bel* curves for three situations: a 50% confidence interval ($\delta = 0.5$) in black (the above case), 0.1% confidence interval ($\delta = 0.999$) in red and 99.9% confidence interval ($\delta = 0.001$) in blue. The rest of the parameters are set as before: 3 α -cuts, removal of the FEs and weighting of the samples with the exponential law.

As expected, when increasing the confidence interval, the separation between the curves becomes bigger. Since a bigger confidence interval is associated with a widening of the region around the eCDF, which has two effects. On the one hand, it will create

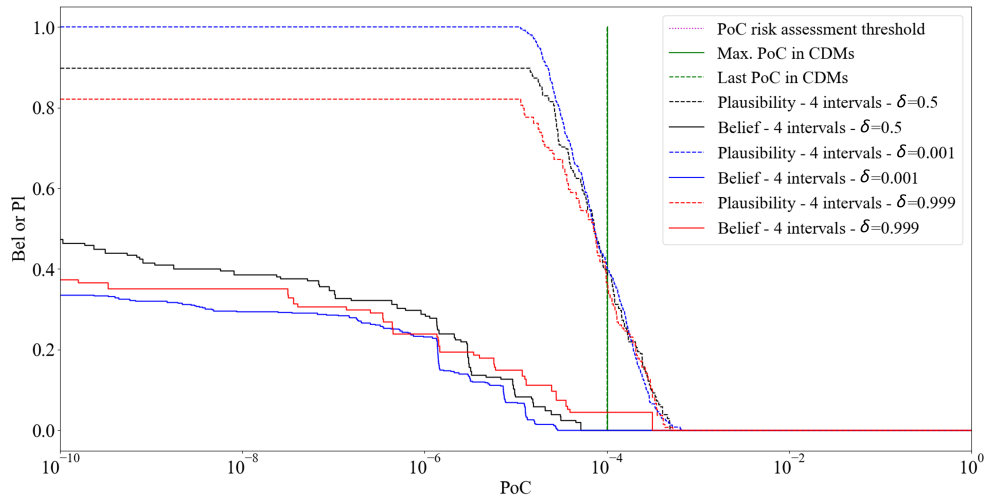


Figure 4.13: *Pl* and *Bel* curves for $PoC \geq PoC_0$ with 4-intervals partition for three different values of the confident interval: $\delta=0.001$ (red), $\delta=0.5\%$ (blue), $\delta=0.999\%$ (black).

wider p-boxes and bigger intervals (Fig. 4.14) that will include, in general, higher/upper values of PoC within the FEs. On the other hand, it will be more likely that more FEs contains samples. The combined result of these effects is a more conservative analysis (greater values of PoC received higher support) and, at the same time, more uncertainty affecting the decision (greater Degree of Uncertainty, DoU). Note that in the extreme case of 100% confidence interval ($\delta = 0$), the DKW region would look as a rectangular region ranging from 0 to 1 around the extreme values of the series, and the Dempster-Shafer structure would be that of a single interval. If reducing the confidence interval, the conclusions are the opposite, bearing in mind that, by definition, it is more likely to leave the actual CDF out of the bounded region.

Number of α -cuts

The other main parameter to be decided by the operator is the number of α -cuts. Ideally, a number of cuts high enough so that the Dempster-Shafer structure matches the p-box (or the DKW region) should be ideal since it would not add any further approximations. However, a higher number of α -cuts translates into more FEs (N^5 , with N the number of cuts, before removing those without samples) and the computational

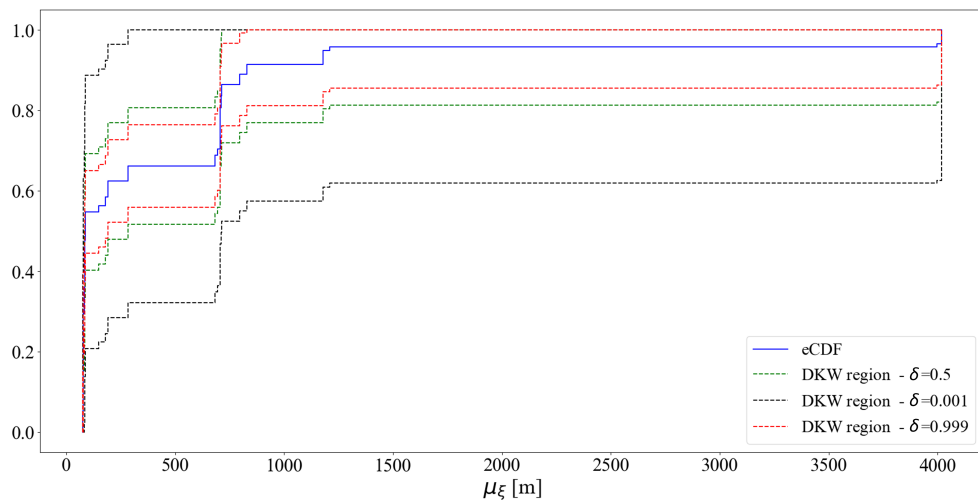


Figure 4.14: eCDF (solid blue) and DKW region (dashed lines) of μ_ξ for three different values of the confident interval: $\delta=0.001$ (black), $\delta=0.5\%$ (green), $\delta=0.999\%$ (red).

time to obtain the Pl and Bel curves grows accordingly. In the other direction, a lower number of intervals speed up the next stage but make the decision more conservative. Note that in the way the intervals are obtained, the Dempster-Shafer structure will be always more conservative than the p-box (externally bounded it). In the extreme case of not performing any cut, a single interval with $bpa = 1$ between the lower and upper values would be obtained, being extremely over-conservative.

Fig. 4.15 shows the Dempster-Shafer structures approximating the p-box of μ_ξ for different numbers of α -cuts (a similar behaviour is obtained for the other variables). As a general rule, the higher the number of cuts, the more similar both regions (p-box and Dempster-Shafer structure) are. Since the cuts are performed equally distributed along the vertical axis, there may be situations, especially for the low number of intervals, where performing one less cut provides a better approximation. This should be avoided with enough intervals.

When observing to the Pl and Bel curves (Fig. 4.16), the more the number of cuts, the less uncertainty affecting the event, both because the region is more finely approximated and because a bigger proportion of FE can be removed. Thus, while the maximum value receiving support (PoC where $Pl = 0$) is basically the same independently of the partition, the Pl curve is lower (less over-conservative approximation)

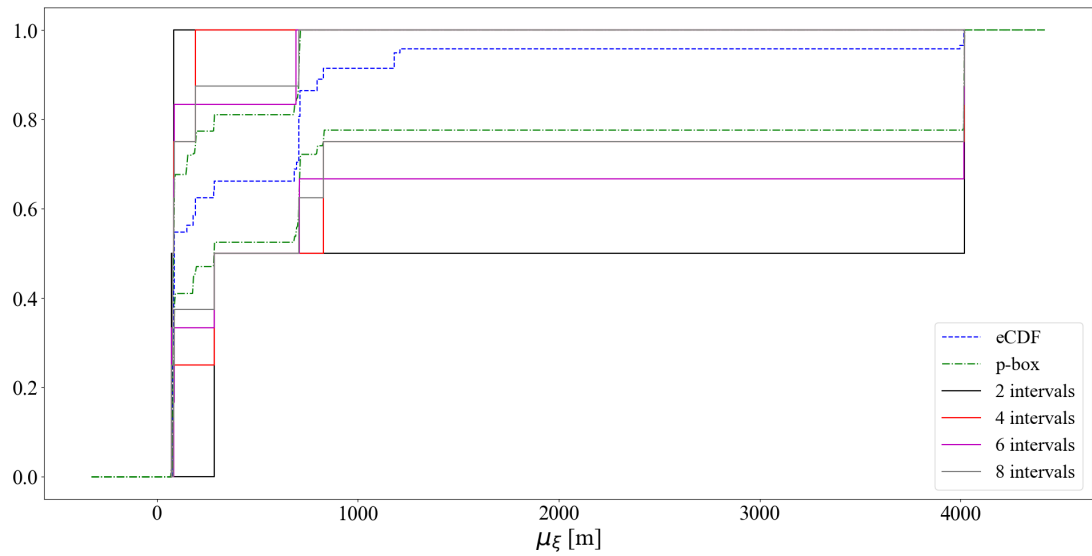


Figure 4.15: eCDF (dashed blue), p-box (dashed-pointed green) and Dempster-Shafer structure (solid lines) for μ_ξ for different α -cut partitions: black for one cut, red for three cuts, magenta five cuts, grey for seven cuts.

with more intervals. The *Bel* curves experiment a similar trend, although less accentuated. Overall, the more the number of cuts, the smaller the DoU and the less over-conservative results, but the most computationally expensive.

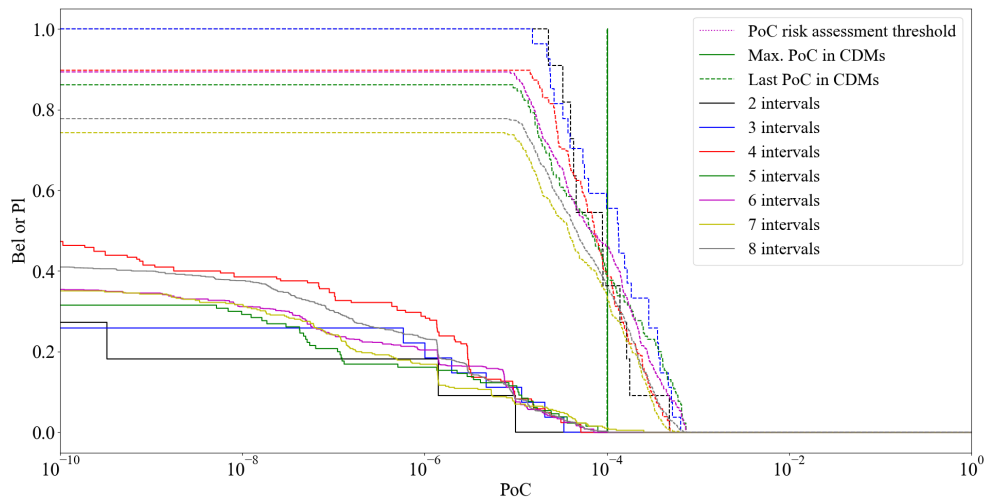


Figure 4.16: *Pl* and *Bel* curves for $PoC \geq PoC_0$ for a different number of α -cuts per variable: one (black), two (blue), three (red), four (green), five (magenta), six (yellow), seven (grey).

In Table 4.2, the comparison of the computational time to obtain the *Pl* and *Bel*

curves for different numbers of α -cuts is included. It can be seen the important impact when increasing the number of intervals. Note that the other stages take a similar

Table 4.2: Computational time of obtaining the *Pl* and *Bel* curves (in seconds) for different values of α -cuts and the percentage of FEs removed.

# α -cuts	Computational time [s]	FE removed
0	0.25	0.0% - 0 (1)
1	3.5	65.625% - 21 (32)
2	13	88.888% - 216 (243)
3	80	86.132% - 882 (1,024)
4	106	95.840% - 2,995 (3,125)
5	370	93.312% - 7,256 (7,776)
6	330	97.709% - 16,422 (1,6807)
7	860	96.201% - 31,523 (32,768)

computational time as in Table 4.1, which means that the *Pl* and *Bel* computation stage may vary from requiring a negligible computational time (with 1 or 2 α -cuts) to be as important as the p-box computation (the main contribution on the standard scenario) or even being by far the main contribution (with more than 5 α -cuts). Be aware also the fact that the higher the number of cuts, the higher the proportion of FEs removed, which can create the paradoxical situation a partition requires less computational time to compute the *Pl* and *Bel* curves than a partition with less intervals (the case of 5 and 6 α -cuts).

Number of samples

The number of samples is given by the sequence, so in general, it is not something the operator will modify. As a rule, all available CDMs should be used (see the robustness analysis in the next section). However, the number of samples is a parameter appearing in Eq. (4.1) when computing the separation of the DKW bands, ε . This section analyses the variation in the number of samples.

However, care should be taken when performing this analysis. For example, if just taking a section of the sequence (i.e. the second half), the bounds of the variables would be different, and so the FE limits. Thus, the resulting *Pl* and *Bel* analysis would correspond to a completely different case (even though it refers to the same

event), since the available information is too different. For this analysis, two different sequences were considered: one with the whole sequence, as in the standard scenario, and another with half of the CDMs, with the samples distributed throughout the whole observation period, keeping the extreme values of the variables.

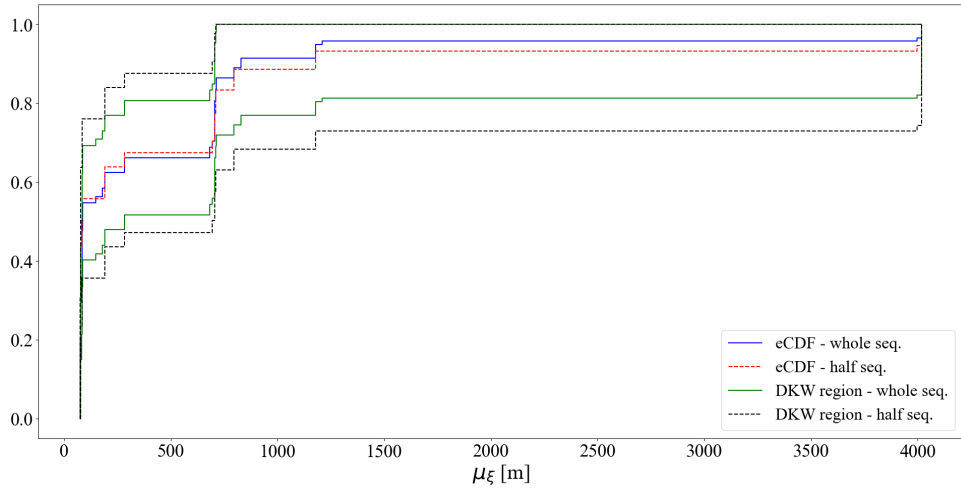
In Fig. 4.17a, it is shown how a smaller sequence creates wider bands, even though the confidence interval is set the same, which is the expected result from Eq. (4.1). Since there are fewer samples, it is more likely to find more distribution that corresponds with the eCDF, so the region should be wider to include them all. These translate into a more conservative p-box and wider intervals, which eventually, provide a more conservative risk assessment, with higher Pl and also a bigger gap between curves, as it can be seen in Fig. 4.17b.

Another impact of the number of samples is the computational time. The longer the sequence, the longer it will take to obtain the p-boxes: longer sequences imply longer sums of Gaussian distributions associated with the samples, thus the optimisation/fit of the p-box involves more parameters. Bearing in mind that it has to be done for five variables, the impact on the computational time may be important. Keeping the whole sequence, with 33 CDMs, the computational time for obtaining the p-box is about 115 seconds, while with half of the CDMs, the computational time for this stage is reduced to 15 seconds. The rest of the stages required similar computational time with both sequences.

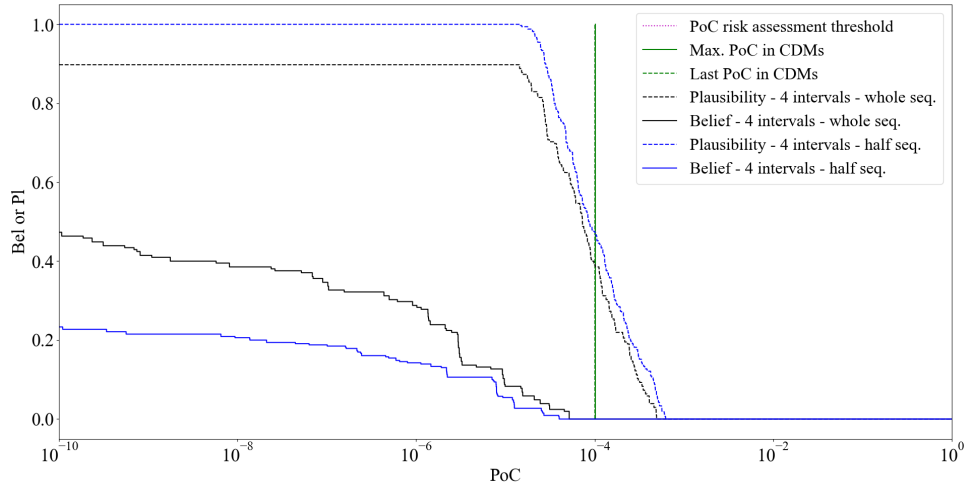
FE removal

This analysis covers the effect of taking into account the removal of those FEs not containing any samples with respect to accounting for them all. There are two main implications: first, the resulting Joint Body of Evidence, and second, the number of effective FEs, which impacts the computational time of the Pl and Bel curves.

Fig. 4.18 includes these curves for a case with $\delta = 0.5$ and 4 intervals. The black lines correspond to the case where the FEs are removed (corresponding to the standard initial case) and the blue lines if no FE is removed. Regarding the conjunction analysis, it can be seen that not removing the FEs translates into a more conservative approach.



(a)



(b)

Figure 4.17: Modification on the number of CDMs: whole sequence and half of the sequence. (a) eCDF and DKW bands: solid blue and solid green for the whole sequence, dashed red and dashed black for half sequence. (b) Pl and Bel curves, black for the whole sequence, and blue for half sequence.

Since the Joint Body of Evidence is wider, it may include (as in this encounter) a combination of miss distance and covariance matrix with a higher PoC, even though they do not appear in the sequence of CDMs. The removal of those FEs allows a better adjustment to the provided evidence without violating the theory behind the approach.

Moreover, since the number of FEs is reduced, being the main driver of the Pl and Bel computation, this step also takes less time if removing the FE (Table 4.3).

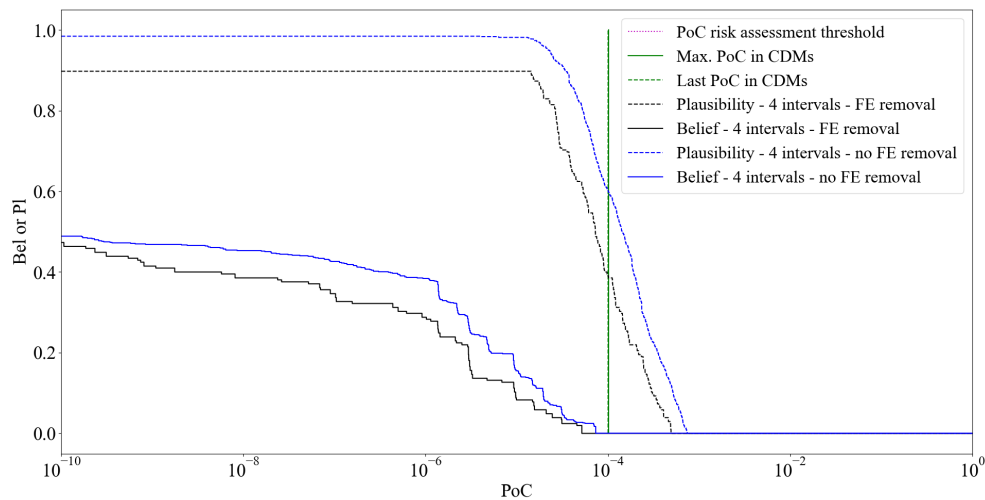


Figure 4.18: Pl and Bel curves for $PoC \geq PoC_0$ with 4-intervals partition with (black) and without (blue) removal of FEs not containing any sample.

Table 4.3: Computational time of obtaining the Pl and Bel curves (in seconds) when removing FEs or not, and the percentage of FEs removed for different values of α -cuts.

# α -cuts	FEs removed	Computational time [s]	
		No removing FEs	Removing FEs
1	65.625%	9.5	3.5
2	88.888%	96	13
3	86.132%	490	80
4	95.840%	1690	106
5	93.312%	4270	370
6	97.709%	9600	330
7	96.201%	16665	860

In summary, assigning a $bpa = 0$ to those FEs not containing samples from the sequence of CDM make the analysis less over-conservative and faster. Note, the eCDF and Dempster-Shafer structures are the same in both cases, since the removal of the FE takes place when combining the intervals, just before computing the Pl and Bel .

Weighting of samples

The last parameter to be studied in this sensitivity analysis is the weight of the samples. As in the previous case, technically, this is not a parameter to be selected by the

operator, but an approach to be applied or not, which may affect the final result.

As indicated in the previous section, the CDMs in the sequence are weighted using Eq. (4.7), which corresponds to the inverse of the best exponential fit of the covariance matrix determinant evolution. In general, although with exceptions, the determinant decreases when approaching the encounter (shorter propagation time generates smaller uncertain ellipses), thus, the later CDMs tends to be assigned more importance than earlier ones.

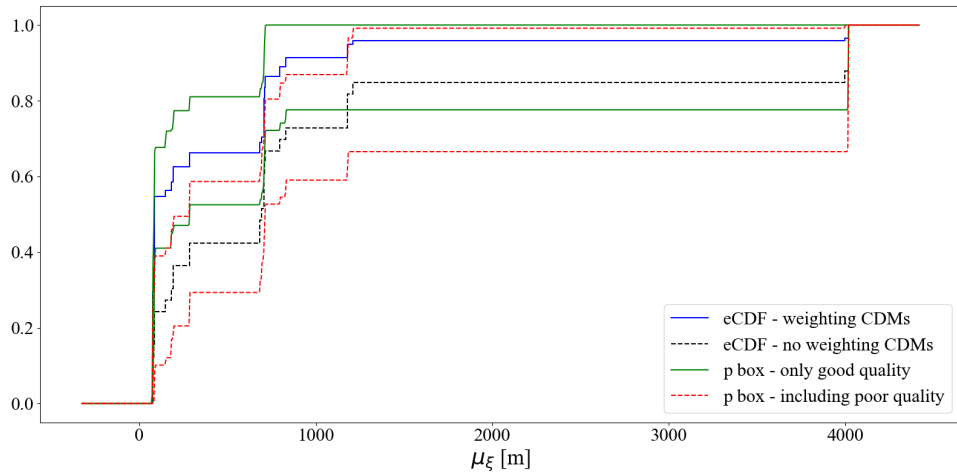
Fig. 4.19 shows the eCDF of μ_ξ and σ_ξ^2 along with the associated DKW region (with $\delta = 0.5$) both weighting the samples with the fitting law (blue for the eCDF and green for the DKW bands) or with equal weights for all samples (red and black, respectively).

For this case where the later CDMs suggest a closer encounter than at the beginning with less (aleatory) uncertainty, the figures show the eCDF for both variables grows faster for smaller values if weighing the samples. Note that for different trends, the relative position of the eCDF and the DKW bands may be different. Nevertheless, the important aspect is the potential impact of weighting the samples. In this example, the fact that the blue eCDF grows faster means that when performing the α -cuts, more relative weight will be assigned to the smaller values and the intervals will be smaller for the lower range of the variable. When computing the *Pl* and *Bel*, this means that values of PoC associated with those smaller μ_ξ and σ_ξ^2 (values of PoC on the higher range) will have greater support, as seen in Fig. 4.20, where the *Pl* and *Bel* curves when weighting the samples (black) are slightly above the curves when samples are not weighted (blue).

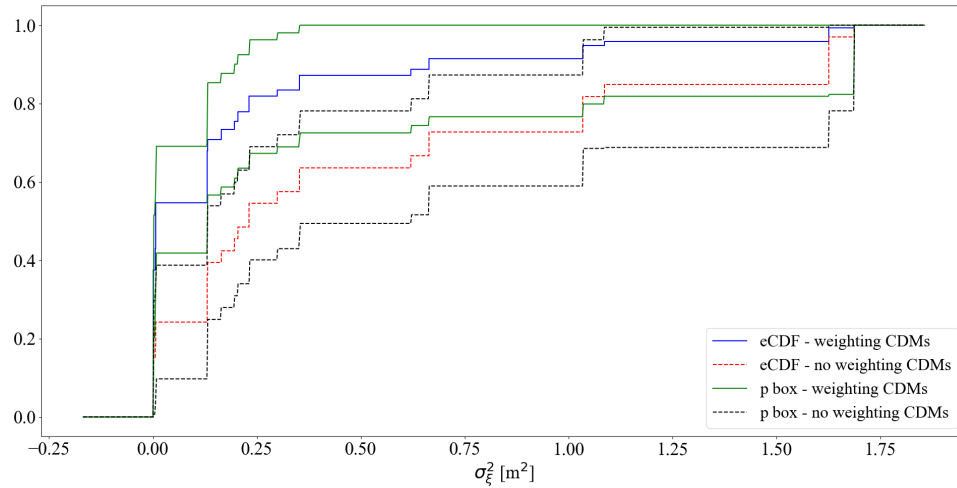
The impact on the computational time of weighing the samples is negligible, with values around a hundredth of a second.

4.3.2 Robustness

This section illustrated the robustness of the approach when poor quality CDMs is received in the middle of the sequence. In the previous examples, 3 CDMs appearing in the actual sequence were filtered out for the analysis due to the clear deviation from



(a)



(b)

Figure 4.19: eCDF and DKW bands weighting the samples (solid blue and dashed green, respectively) and not weighting them (dashed red and dashed black, respectively). (a) μ_ξ and (b) σ_ξ^2 .

the previous trend, which indicated the operators their bad quality [Sanvido, 2023]. The miss distance was clearly off compared to the previous ones, generating a null PoC for those cases. After them, the new CDMs received were in line again with the general trend in miss-distance, covariance matrix and PoC values.

However, this action, based on the knowledge and experience of the operator, does not follow a formal procedure. Moreover, if a decision on how to deal with the event had to be made when at the time of that bad quality CDMs arrived, the actual decision

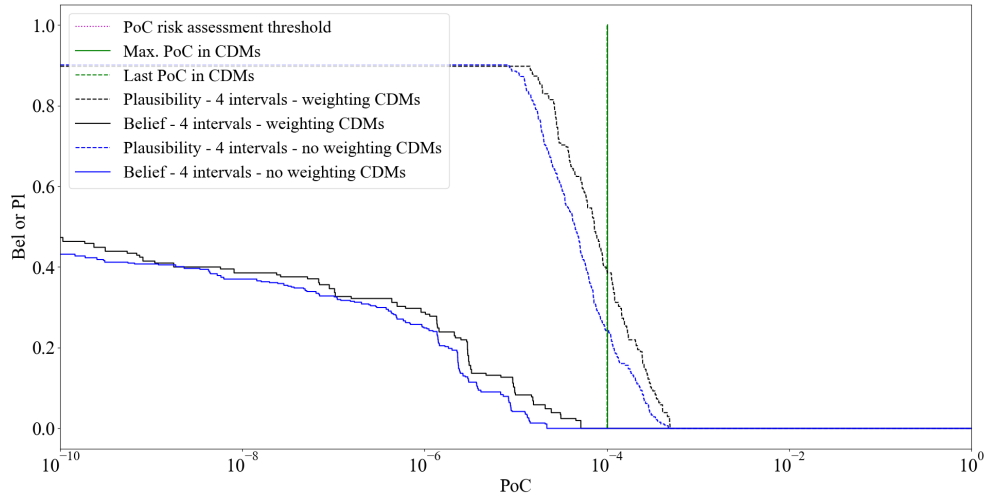


Figure 4.20: *Pl* and *Bel* curves for $PoC \geq PoC_0$ with 4-intervals partition with (black) and without (blue) weighing the CDMs.

might have been wrong or presented an important lack of knowledge.

By using the proposed epistemic approach, these offset samples are naturally integrated into the process. Thus, if they play an important role in the risk of the event, an increase in the uncertainty on the value of the PoC should be noted, otherwise, the system will be robust enough to consider these pieces of information not reliable enough. This is the reason the epistemic approach proposed here is also referred to as *robust*.

The actual sequence of CDM is presented in Fig. 4.21, where the PoC evolution and the uncertain geometry are shown. The three poor quality CDMs can be clearly identified.

In Fig. 4.22, the eCDF for μ_ξ and σ_ξ^2 of both situations (with and without the poor quality CDMs) is presented along with the associated p-box with $\delta = 0.5$. It is highlighted in the figure where the poor quality CDMs fall. While the covariance value is within the expected range (both p-boxes mainly overlap each other), the discrepancy appears in the miss distance (poorer overlapping between both p-boxes).

Performing the risk assessment analysis with 3 α -cuts per variable, after having received the whole sequence, the *Pl* and *Bel* for the PoC can be obtained, as shown in Fig. 4.23. Despite the difference in the Dempster-Shafer structures for the miss

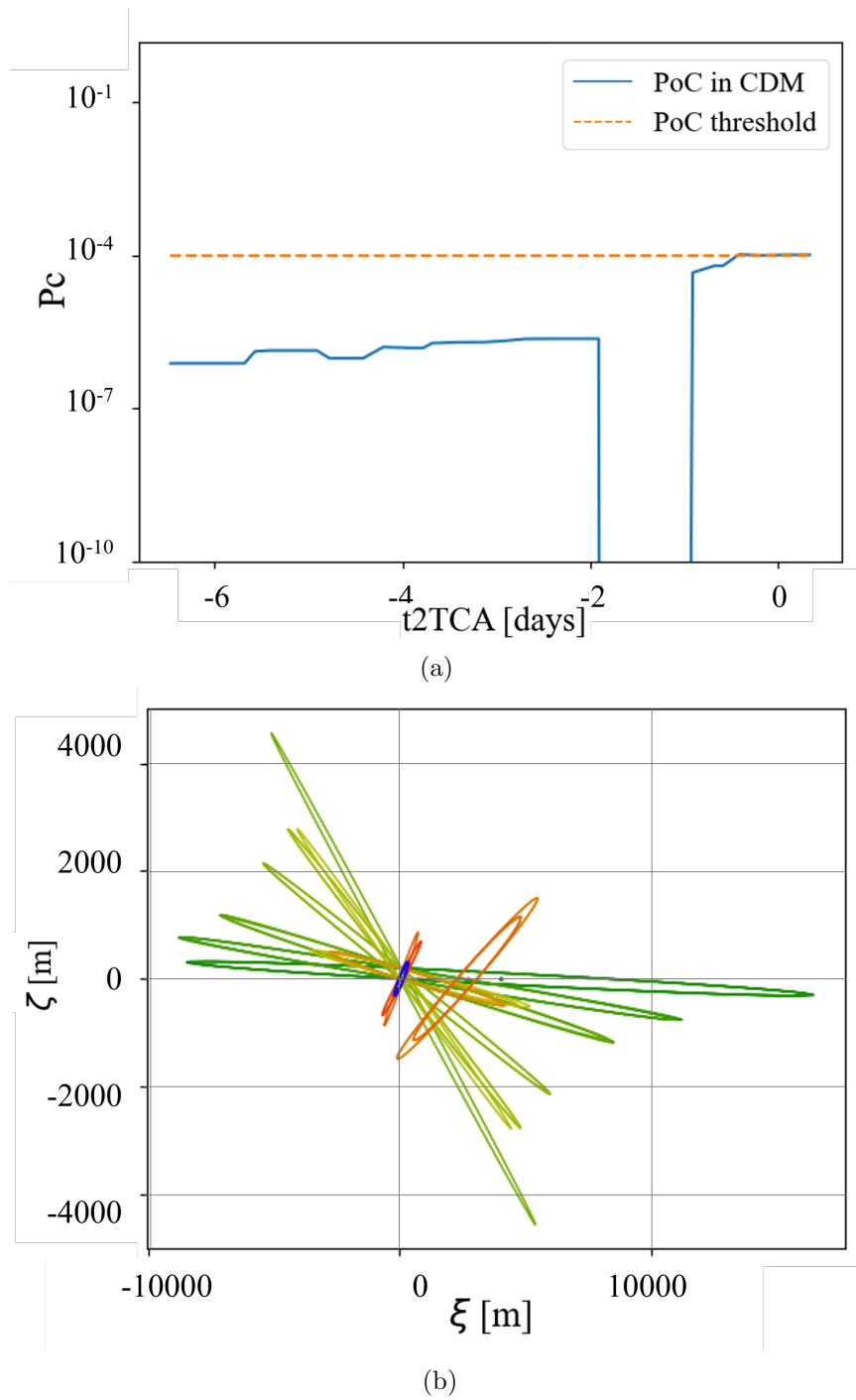
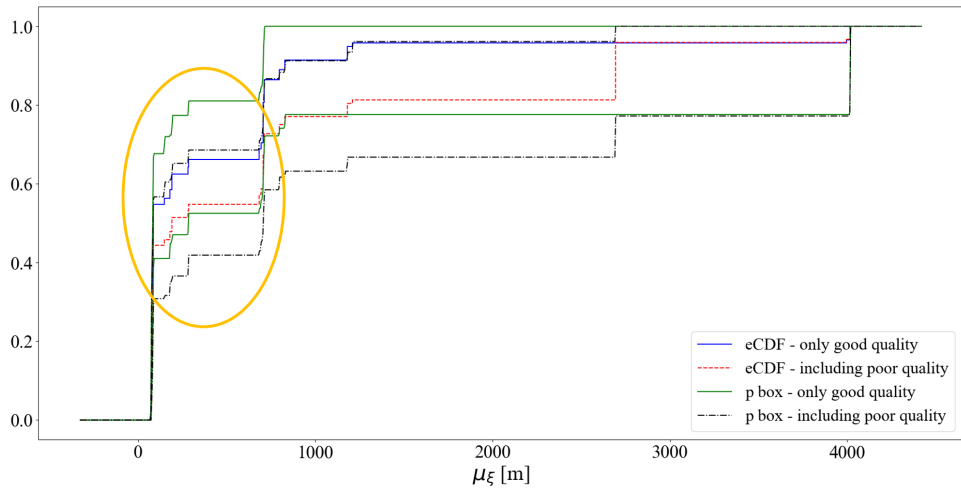
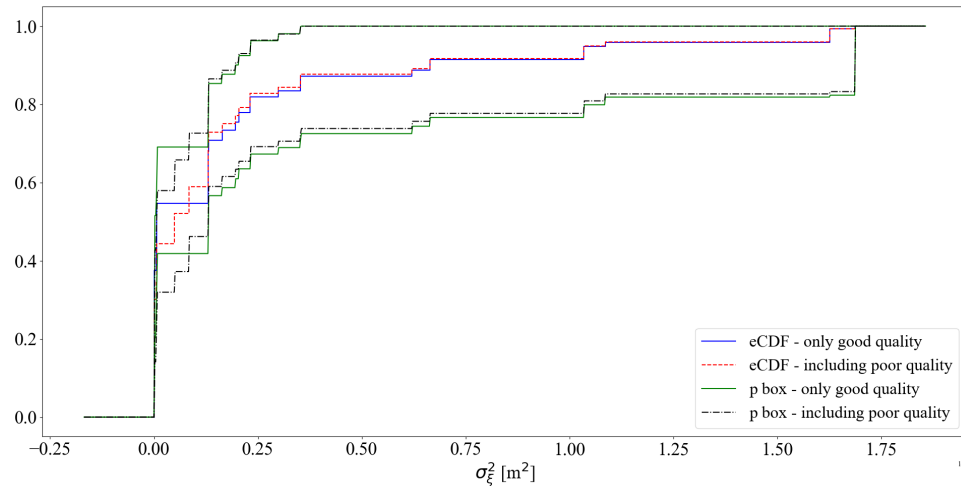


Figure 4.21: Sequence of CDMs, including the poor quality ones. (a) Evolution of the PoC in the CDMs. (b) Uncertain geometry from the series of CDMs.



(a)



(b)

Figure 4.22: Dempster-Shafer structures with and without poor-quality CDMs, eCDF in solid blue and dashed red, DKW in solid green and dashed black, respectively. (a) μ_ξ , (b) σ_ξ^2 . Orange circle highlighting the region with the poor-quality CDMs.

distance, the method is robust enough not to be biased by those values. It can be seen that the *Pl* follows a very similar trend in both cases. The *Bel* presents a slightly different trend, associated with more conflict between samples and, thus, a greater DoU. However, although for low values of PoC, the support is slightly lower, for the values of interest (around the risk threshold), both trends are similar.

These results indicate that, although there is some impact in the support for low

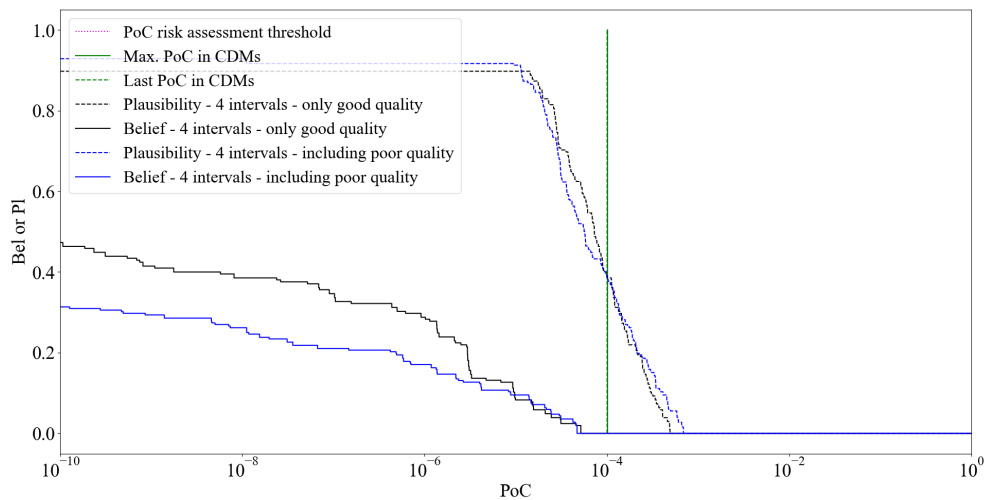


Figure 4.23: *Pl* and *Bel* curves for $PoC \geq PoC_0$ for 4-intervals partition accounting for the poor quality CDMs. Black, only good quality CDMs; blue, including the poor quality CDMs.

values of the PoC, given all the great amount of evidence from the good quality CDMs, the impact of the low-quality ones is diluted in the final results. Although, in the end, directly discarding the bad-quality CDMs provided a similar outcome, the current analysis shows that the proposed method (objective reasoning) is robust enough to reach the same conclusions without relying on the knowledge and expertise of the operator (subjective decision).

4.4 Chapter summary

This chapter proposed a methodology to model the epistemic uncertainty associated with the sequences of CDMs to integrate these pieces of information with the evidence-based conjunction risk assessment framework proposed in the previous chapter.

The key working assumption was that the value of the miss distance and covariance matrix in each CDM were drawn from a set of unknown distributions. Thus, using statistical tools such as the eCDF and the DKW inequality to derive the Dempster-Shafer structures of the uncertain variables defining the encounter geometry. From these structures, it is possible to extract the intervals and compute the *Pl* and *Bel* required to robustly assess the risk of the event.

The chapter is completed with an example based on a real sequence of CDM and a sensitivity analysis of the different parameters involved in the methodology, with special attention to the confidence interval bounding the region containing the underlying distribution and the number of evidence intervals defining the uncertain geometry. Finally, the robustness of the method was shown with the addition of three poor quality CDMs to the aforementioned sequence.

This methodology will be tested on databases of real CDMs in Chapter 7 of Part II.

Chapter 5

Robust collision avoidance manoeuvres

The content of this chapter was partially published in:

Sánchez, L. and Vasile, M. (2020), “AI for autonomous CAM execution”, 71st International Astronautical Congress, The Cyber Space Edition; [Sánchez and Vasile, 2020a]

Sánchez, L. and Vasile, M. (2022), “Intelligent agent for decision-making support and collision avoidance manoeuvre design on Space Traffic Management”, *Advances in Space Research*, in press. [Sánchez and Vasile, 2023]

This chapter introduces a methodology to compute robust Collision Avoidance Manoeuvre (CAMs), both in the impulsive and the Low-Thrust (LT) scenarios. When performing a robust conjunction risk assessment, not only aleatory uncertainty should be considered in the analysis, but also epistemic uncertainty. If the output of the evidence-based decision-making process suggests a manoeuvre should be implemented, to be coherent this manoeuvre should account for all types of uncertainty. However, computing the optimal CAM as the manoeuvre that minimises the Probability of Collision (PoC) based only on the nominal values of uncertainty leaves aside the uncertainty on the uncertainty, that is, the lack of knowledge on the position, sensors, data processing steps or dynamic models. This chapter first introduces a linear model to compute

the effect of a manoeuvre in the impact plane, and then extends the Dempster-Shafer theory of Evidence (DSt)-based framework to the computation of robust optimal CAMs.

The rest of the chapter is structured as follows. First, the linear model to obtain the effect of an impulsive manoeuvre on the relative position at the encounter is presented in Section 5.1. Then, the method to compute robust optimal manoeuvres accounting for epistemic and aleatory uncertainty is presented: in Section 5.2 for the impulsive case and in Section 5.3 for the LT scenario. Finally, Section 5.4 presents a numerical case validating the linear model and showing the behaviour of the robust optimal CAM algorithms. Section 5.5 concludes the chapter.

5.1 Linear model for impulsive manoeuvres

This section presents a model to fast compute the effect of a CAM in the relative position of two objects. The approach proposes a linear model to relate variations in velocity with modifications in position, derived from asteroid deflection works [Vasile and Colombo, 2008]. More specifically, the model computes the effect on the impact plane of an impulsive manoeuvre performed by a satellite (target or primary object) involved in a close encounter to avoid another object (chaser or secondary object), as illustrated in Fig. 5.1.

Given a manoeuvre $\delta\mathbf{v}_{tnh}$ at time t_m , the corresponding variation of position $\delta\mathbf{x}_b$ at the encounter time t_c on the impact plane (or b-plane) is:

$$\delta\mathbf{x}_b = [\delta\xi \quad \delta\eta \quad \delta\zeta]^T = \mathbf{T}\delta\mathbf{v}_{tnh} = \mathbf{B}\mathbf{A}(t_m, t_c)\mathbf{G}\delta\mathbf{v}_{tnh}. \quad (5.1)$$

The matrix \mathbf{T} , relating the impulse with the position change in the impact plane, is the product of three matrices: \mathbf{G} , $\mathbf{A}(t_m, t_c)$ and \mathbf{B} . The first of these three matrices, \mathbf{G} , relates the impulse $\delta\mathbf{v}_{tnh} = [\delta v_t, \delta v_n, \delta v_h]$ expressed in the spacecraft's centred tangential, normal, out-of-plane reference frame $\langle T, N, H \rangle$, with the instantaneous change on Keplerian elements $\delta\mathbf{k} = [\delta a, \delta e, \delta i, \delta\Omega, \delta\omega, \delta M_{t_m}]$:

$$\delta\mathbf{k}(t_m) = \mathbf{G}\delta\mathbf{v}, \quad (5.2)$$

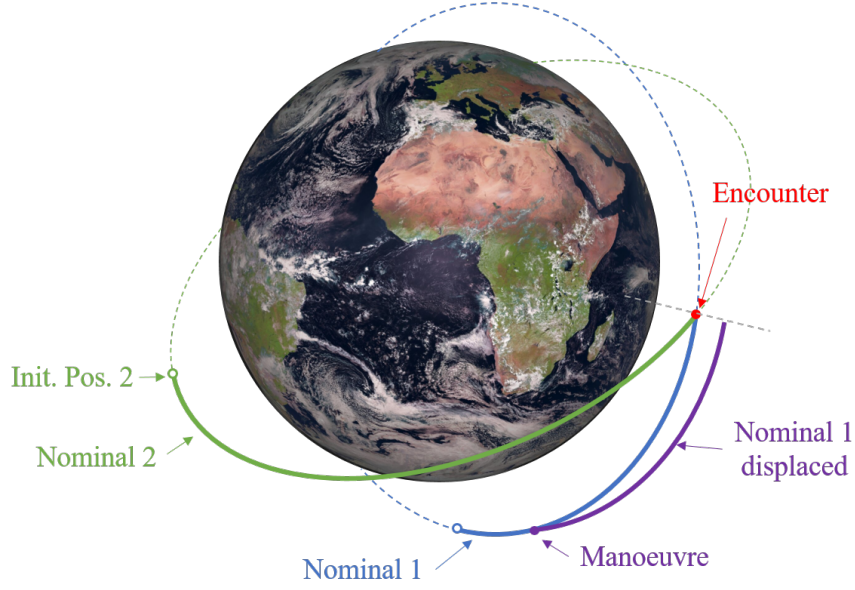


Figure 5.1: General configuration of a space encounter. Two orbits in a collision path (blue and green) and the modified orbit due to a CAM (purple).

where matrix \mathbf{G} is expressed in Eq. (5.3), with subscript “ m ” referring to the manoeuvre position/time, being $b = a\sqrt{1 - e^2}$ the semi-minor axis, $p = b^2/a$ the semi-latus rectum, $h = nab$ the specific angular momentum, $n = \sqrt{\mu/a^3}$ the mean motion, $u = \omega + \theta$ the argument of latitude, with θ the true anomaly, r_m and v_m the satellite’s unperturbed position and velocity at the manoeuvre position, and μ the Earth gravitational constant.

$$\mathbf{G} = \begin{bmatrix} \frac{2a^2 v_m}{\mu} & 0 & 0 \\ \frac{2(e + \cos \theta_m)}{v_m} & -\frac{r_m}{av_m} \sin \theta_m & 0 \\ 0 & 0 & \frac{r_m \cos u_m}{h} \\ 0 & 0 & \frac{r_m \sin u_m}{h \sin i} \\ \frac{2}{ev_m} \sin \theta_m & \frac{2e + (r_m/a)}{ev_m} \cos \theta_m & -\frac{r_m \sin u_m \cos i}{h \sin i} \\ -\frac{2b}{eav_m} \left(1 + \frac{e^2 r_m}{p}\right) \sin \theta_m & -\frac{b}{eav_m} \frac{r_m}{a} \cos \theta_m & 0 \end{bmatrix} \quad (5.3)$$

The matrix $\mathbf{A}_t(t_m, t_c)$ propagates the effect of the impulse to the encounter time, relating the change on orbital parameters at t_m with the change in position at encounter

time, $\delta \mathbf{r}_{rth}(t_c)$, expressed in the satellite's $\langle \mathbf{R}, \mathbf{T}, \mathbf{H} \rangle$ reference frame:

$$\delta \mathbf{r}_{rth}(t_c) = \mathbf{A}_t(t_m, t_c) \delta \mathbf{k}(t_m), \quad (5.4)$$

with $\mathbf{A}_t(t_m, t_c)$ expressed in Eq. (5.5), where the subscript “c” refers to the encounter time or Time of Closest Approach (TCA) and $\Delta t = t_c - t_m$ is the elapsed time between the manoeuvre execution and the encounter.

$$\mathbf{A}_t^T = \begin{bmatrix} \frac{r_c}{a} - \frac{3e \sin \theta_c}{2(1-e^2)} \frac{\sqrt{\mu}}{a^{\frac{3}{2}}} \Delta t & -\frac{3r_c}{2(\sqrt{1-e^2})^3} (1 + e \cos \theta_c)^2 \frac{\sqrt{\mu}}{a^{\frac{5}{2}}} \Delta t & 0 \\ -a \cos \theta_c & \frac{r_c \sin \theta_c}{1-e^2} (2 + e \cos \theta_c) & 0 \\ 0 & 0 & r_c \sin u_c \\ 0 & r_c \cos i & -r_c \cos u_c \sin i \\ 0 & r_c & 0 \\ \frac{ae \sin \theta_c}{\sqrt{1-e^2}} & \frac{r_c}{(\sqrt{1-e^2})^3} (1 + e \cos \theta_m)^2 & 0 \end{bmatrix} \quad (5.5)$$

Note that the variation in mean anomaly, δM , is made of two terms: δM_{t_m} and δM_n . The first term comes from the change in mean anomaly due to the manoeuvre and it is equal to:

$$\delta M_{t_m} = -\frac{b}{eav_m} \left[2 \left(1 + \frac{e^2 r_m}{p} \right) \sin \theta_m \delta v_t + \frac{r_m}{a} \cos \theta_m \delta v_n \right], \quad (5.6)$$

and is already included in \mathbf{G} . The second term refers to the delay at TCA due to the change in the semi-major axis, Eq. (5.7), and it is included in \mathbf{A}_t after approximate with Eq. (5.8).

$$\delta n = \sqrt{\frac{\mu}{a^3}} - \sqrt{\frac{\mu}{(a + \delta a)^3}} \quad (5.7)$$

$$\delta M_n = \delta n \Delta t \approx -\frac{3}{2} \frac{\sqrt{\mu}}{a^{\frac{5}{2}}} \Delta t \delta a \quad (5.8)$$

Finally, matrix \mathbf{B} is the rotation matrix between the satellite's $\langle \mathbf{R}, \mathbf{T}, \mathbf{H} \rangle$ reference frame and the impact plane reference frame, $\langle \xi, \eta, \zeta \rangle$, centred at the chaser (secondary)

object, expressed as:

$$\hat{\boldsymbol{\eta}} = \frac{\mathbf{v}_1 - \mathbf{v}_2}{\|\mathbf{v}_1 - \mathbf{v}_2\|}, \quad \hat{\boldsymbol{\xi}} = \frac{\mathbf{v}_2 \times \boldsymbol{\eta}}{\|\mathbf{v}_2 \times \boldsymbol{\eta}\|}, \quad \hat{\boldsymbol{\zeta}} = \hat{\boldsymbol{\xi}} \times \hat{\boldsymbol{\eta}}, \quad (5.9)$$

where \mathbf{v}_1 is the target's velocity vector and \mathbf{v}_2 the chaser's velocity vector. Fig. 5.2 illustrate the impact plane geometry, with the objects' orbits in blue and green, the impact plane and its reference frame in purple and the relative velocity in orange.

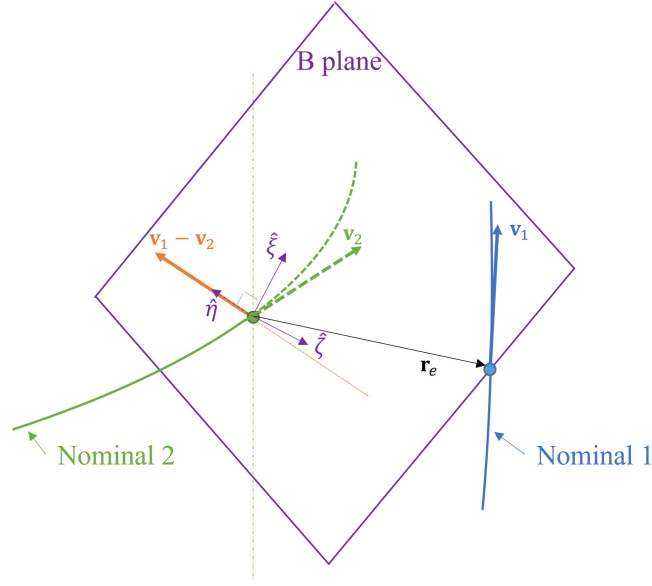


Figure 5.2: Impact plane of the encounter centred at the secondary object.

Thus, the deflection on the impact plane due to the position change originated by the impulse can be expressed as:

$$\delta \mathbf{x}_b = [\delta \xi \quad \delta \eta \quad \delta \zeta]^T = \begin{bmatrix} \hat{\boldsymbol{\xi}} & \hat{\boldsymbol{\eta}} & \hat{\boldsymbol{\zeta}} \end{bmatrix}^T \delta \mathbf{r}_{rth} = \mathbf{B} \delta \mathbf{r}_{rth}, \quad (5.10)$$

Once the model to compute the effect of a manoeuvre was introduced, an optimal CAM can be computed to avoid a close encounter. In the rest of the chapter, a method to compute the optimal CAM accounting for aleatory and epistemic uncertainty is presented.

5.2 Robust optimal impulsive avoidance manoeuvre

In this section, a method to compute robust optimal manoeuvres using the linear model introduced in the previous section is presented. While an optimal manoeuvre would minimise the PoC given by the aleatory uncertainty on the object's position, the robust optimal CAM proposed in this section will minimise the PoC of the worst-case ellipse within the families of ellipses obtained from the DSt framework introduced in previous chapters.

The assumption is that, in the limit of the linear model, the ellipsoid of uncertainty translates rigidly without deforming or rotating. This is not true in general and represents an approximation introduced by our method. This is added to the other two assumptions used along the chapter to compute optimal CAMs: the first one is the Keplerian motion, implicitly considered on the linear model, although perturbations have a minor impact on this context [Bombardelli and Hernando-Ayuso, 2015]; the second one is the fast encounter hypothesis, which include the modelling of the aleatory uncertainty as a Gaussian distribution, although as indicated in Chapter 3, the robust framework is not limited to the method to compute the PoC. Finally, for the scope of this work, the manoeuvre is assumed to introduce negligible uncertainty, although the method could cope with this source of information without requiring any modification.

5.2.1 Optimisation of impulsive manoeuvres: aleatory uncertainty

First, the method to compute the optimal CAM only under aleatory uncertainty using the linear model introduced in the previous section is presented. An optimal CAM is a manoeuvre that reduces the risk of collision in a given encounter.

Defining $\bar{\mu}_{b0} = [\mu_{\xi 0}, 0, \mu_{\zeta 0}]^T$ as the unmodified (no CAM) relative position between two objects projected in the impact plane and being $\bar{\Sigma}_b$ the combined position covariance matrix expressed in the same reference frame, the optimal CAM will be computed by minimising the PoC, which is computed using Eq. (3.1) in Chapter 3. the combined covariance matrix is the sum of both object's position covariance matrices projected on the impact plane: $\bar{\Sigma}_b = \bar{\Sigma}_{b,1} + \bar{\Sigma}_{b,2}$.

Under the assumptions that the CAM does not introduce further uncertainty and only rigidly translates the uncertainty ellipse on the impact plane, the relative position of the modified orbit will present the same covariance matrix $\bar{\Sigma}_b$, while the relative position after the manoeuvre will be equal to:

$$\bar{\boldsymbol{\mu}}_b = \bar{\boldsymbol{\mu}}_{b0} + \delta \mathbf{x}_b, \quad (5.11)$$

with $\delta \mathbf{x}_b$ the manoeuvre deflection given by Eq. (5.1).

From Eq. (3.1), the miss distance, $\boldsymbol{\mu}_b$, is the two-component vector equal to the first and third components of $\bar{\boldsymbol{\mu}}_b$, and the $[2 \times 2]$ position covariance matrix in the impact plane is equal to:

$$\Sigma_b = \bar{\Sigma}_{b,[1,3],[1,3]} = \begin{bmatrix} \sigma_\xi^2 & \sigma_{\xi\zeta} \\ \sigma_{\xi\zeta} & \sigma_\zeta^2 \end{bmatrix}. \quad (5.12)$$

Eq. (3.1) assumes that the area of the secondary object on the impact plane is the combined radial envelope of the areas of both objects (Hard Body Radius, HBR) projected on the plane, while the combined uncertainty projected on the impact plane is associated with the primary object and centred in $\boldsymbol{\mu}_b$. Under the assumption that the manoeuvre does not change the shape of the covariance, Eq. (3.1) would be equivalent to placing the HBR centred in $\bar{\boldsymbol{\mu}}_b$ and the combined ellipse of uncertainty centred at (0,0) on the impact plane.

Then, in order to minimise the PoC, one needs to solve the following maximisation problem [Bombardelli and Hernando-Ayuso, 2015]:

$$\begin{cases} \max_{\delta \mathbf{v}_{tnh}} \left(\delta \mathbf{v}_{tnh}^T \mathcal{T} \delta \mathbf{v}_{tnh} + 2 \bar{\boldsymbol{\mu}}_{b,0}^T \bar{\Sigma}_b^{-1} \mathbf{Q} \mathbf{T} \delta \mathbf{v}_{tnh} \right) \\ \text{subject to } \|\delta \mathbf{v}_{tnh}\| \leq \delta v_0 \end{cases}, \quad (5.13)$$

being δv_0 the maximum capacity of the thruster and where

$$\mathcal{T} = \mathbf{Q} \mathbf{T}^T \bar{\Sigma}_b^{-1} \mathbf{T} \mathbf{Q} \quad (5.14)$$

and

$$\mathbf{Q} = \begin{bmatrix} 1 & 0 & 0 \\ 0 & 0 & 0 \\ 0 & 0 & 1 \end{bmatrix} \quad (5.15)$$

However, if the magnitude of the manoeuvre is set constant and equal to δv_0 , the following simplified problem has to be solved instead:

$$\begin{cases} \max_{\delta \mathbf{v}_{tnh}} (\delta \mathbf{v}_{tnh}^T \mathcal{T} \delta \mathbf{v}_{tnh}) \\ \text{s.t. } \bar{\boldsymbol{\mu}}_b \cdot \mathbf{T} \delta \mathbf{v}_{tnh} > 0 \end{cases}, \quad (5.16)$$

whose solution $\delta \mathbf{v}_{opt}$ is the vector parallel to the eigenvector \mathbf{s}_1 conjugate to the maximum eigenvalue of the matrix \mathcal{T} , with magnitude δv_0 :

$$\delta \mathbf{v}_{opt} = \delta v_0 \mathbf{s}_1 \quad (5.17)$$

5.2.2 Optimisation of impulsive manoeuvres: epistemic uncertainty

When the miss distance $\boldsymbol{\mu}_b$ or the covariance matrix $\boldsymbol{\Sigma}_b$ are not precisely known, the PoC is computed accounting for a degree of uncertainty. This uncertainty is epistemic in nature and can come from a lack of knowledge of the system dynamics, the distribution of measurements, the sensor, the propagation method, and the observation data as shown in previous chapters. For the development of the robust optimal CAM methodology, all these sources of uncertainty are assumed to concur to define the epistemic uncertainty in covariance and miss distance but without entering into the detail of the origin of the lack of knowledge. In this work, as shown in Chapter 3, this epistemic uncertainty can be modelled with DSt [Shafer, 1976].

The idea is to use DSt to compute the level of confidence in the correctness of the value of the PoC, given the available evidence on the sources of information. Each component of the covariance, $[\sigma_\xi^2, \sigma_\zeta^2, \sigma_{\xi\zeta}]$, is modelled with one or more intervals and so is the mean value of the relative position $[\mu_\xi, \mu_\zeta]$. Those intervals can be derived,

for example, from a time series of CDMs (Chapter 4) or directly from the raw observations. Thus, covariance and miss distance could not be modelled with a crisp value or with a single specific distribution. Instead, the Plausibility (*Pl*) and Belief (*Bel*) on the value of PoC should be computed, as explained in Chapter 3. Based on this framework, it is possible to compute robust optimal CAMs accounting for both aleatory and epistemic uncertainty.

According to this approach, when epistemic uncertainty is considered, the relative encounter geometry is not defined by a single ellipsoid but by families of ellipsoids corresponding to the families of covariances and mean values. Thus, instead of having a single uncertain ellipse on the impact plane, one has to consider families of uncertain ellipses, each of which has to be displaced by a manoeuvre. This means that an optimal and robust manoeuvre displaces all the ellipses at once.

The presence of families of ellipses means that the optimal CAM has to be able to minimise the PoC corresponding to the worst-case ellipse, which is the uncertain ellipse leading to the highest value of the PoC. Thus, the minimisation problem presented in Eqs. (5.13) and (5.16) needs to be reformulated into the following min-max problem:

$$\begin{cases} \min_{\delta \mathbf{v}_{tnh}} \max_{\mathbf{u} \in \Upsilon} PoC \\ \text{s.t. } \bar{\boldsymbol{\mu}}_b \cdot \delta \mathbf{v}_{tnh} > 0 \end{cases}, \quad (5.18)$$

which has to be solved over the whole set of Focal Elements (FEs). Eq. (5.18) is a constrained robust optimisation problem where the optimal manoeuvre reduces the highest risk of a collision over the whole set of ellipses.

Similarly to what was proposed in [Filippi and Vasile, 2019] for the solution of general min-max optimisation problems, an iterative process is proposed. First, for each FE, the value of the uncertain vector \mathbf{u} that gives the highest PoC is computed. From there, the matrix $\mathbf{S} = \boldsymbol{\Sigma}_{fe_1}^{-1} + \boldsymbol{\Sigma}_{fe_2}^{-1} + \dots$ given by the sum of all the worst-case ellipses for all FEs is built. From \mathbf{S} it is possible to compute \mathcal{T} with Eq. (5.14) and then use Eq. (5.17) to compute the manoeuvre. Since the implementation of a manoeuvre displaces all the ellipses, the process has to be repeated until convergence of the optimised worst-case PoC value. The pseudo-code of the min-max algorithm can

be found in Algorithm C.1 in Appendix C.

5.2.3 Impulse magnitude optimisation

Up to this point, the optimisation of the manoeuvre assumed a constant magnitude, δv_0 . However, this can lead to situations where the correction of the orbit is overestimated, with a reduction of the PoC several orders of magnitude below the minimum safety threshold considered by the operator. In such situations, a smaller impulse could reduce the risk to acceptable levels without an excessive cost of the manoeuvre, as long as the thrust can be adjusted by the spacecraft.

Assuming the maximum capacity of the thruster is defined by δv_0 , the optimum value of the magnitude will be the minimum one that allows reducing the worst-case scenario PoC below the selected threshold, PoC_0 :

$$\begin{cases} \min \|\delta \mathbf{v}_{tnh}\| \\ \text{s.t. } PoC < PoC_0 \end{cases}, \quad (5.19)$$

Once the optimal direction is computed with Eq. (5.17), the minimum δv can be simply derived from the solution of Eq. (5.19). However, since the magnitude of the impulse affects the deflection of the orbit and, subsequently, the worst-case scenario, the optimal magnitude computation has to be integrated within the min-max optimisation algorithm. Algorithm C.2 in Appendix C summarises the process: an outer loop computes the manoeuvre direction at constant magnitude; after computing the optimal direction, \mathbf{d}_{opt} , with Eq. (5.17), the new worst-case ellipse is computed; if $PoC < PoC_0$ an inner loop reduces the magnitude of the impulse with a simple bisection method till $PoC = PoC_0$, recalculating the worst-case ellipse at each iteration of the inner loop until convergence.

5.3 Low-Thrust robust optimal avoidance manoeuvre

In this section, the previous method is extended to compute robust optimal manoeuvre using LT propulsion. The process is divided into two steps, illustrated in Fig. 5.3. First, a LT arc is defined (thin black) and the middle point of the arc is selected. At the

middle point of the arc, θ_m , Algorithm C.2 is used to compute an approximation of the optimal direction of the thrust along the arc (red). Then, the approximated optimal thrust direction is applied to the whole arc with constant thrust acceleration ε (green).

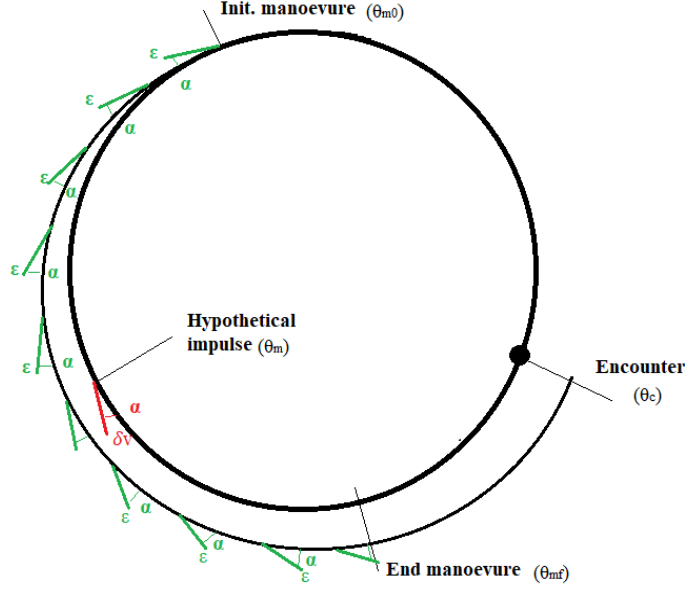


Figure 5.3: CAM strategy for the LT scenario, with burning time between θ_{m0} and θ_{mf} , thrust magnitude ε and direction α , and the encounter at θ_c .

With the arc-length, the initial arc angular position with respect to the encounter, the thrust magnitude and the direction of the manoeuvre, the analytical solution implemented in FABLE [Di Carlo et al., 2018, Zuiani and Vasile, 2014] is used to compute the effect of the manoeuvre on the impact plane. FABLE, Fast Analytical Boundary-Value Low-Thrust Estimator, is a toolbox developed at the University of Strathclyde’s Aerospace Centre of Excellence (ACE) that allows analytically propagating low thrust orbits. Given the direction and the magnitude of the thrust, FABLE computes the variation of the orbital elements along the thrust arc. The calculation is done in non-singular equinoctial elements $\mathbf{E} = [a, P_1, P_2, Q_1, Q_2, L]$ by solving Gauss’s planetary equations [Zuiani and Vasile, 2014]:

$$\frac{d\mathbf{E}}{dL} = \varepsilon F(\mathbf{E}, L, \alpha, \beta), \quad (5.20)$$

under the assumption that the thrust is small compared to the magnitude of the local gravity field. $L = \Omega + \omega + \theta$ is the true longitude, where θ is the true anomaly, ω the argument of the pericentre and Ω the right ascension of the ascending node. In Eq. (5.20), α and β are the LT direction angles in the $\langle R, T, H \rangle$ reference frame attached to the spacecraft so that the acceleration vector is defined as:

$$e_r = \varepsilon \cos \beta \cos \alpha \quad (5.21a)$$

$$e_t = \varepsilon \cos \beta \sin \alpha, \quad (5.21b)$$

$$e_h = \varepsilon \sin \beta \quad (5.21c)$$

If \mathbf{E}_0 is the set of orbital elements at the start of the thrust arc, an approximation of the value of the orbital elements at the end of the arc can be computed with the first-order expansion:

$$\mathbf{E} = \mathbf{E}_0 + \varepsilon \mathbf{E}_1 + O(\varepsilon^2) = \begin{bmatrix} a_0 + \varepsilon a_1 \\ P_{10} + \varepsilon P_{11} \\ P_{20} + \varepsilon P_{21} \\ Q_{10} + \varepsilon Q_{11} \\ Q_{20} + \varepsilon Q_{21} \end{bmatrix} + O(\varepsilon^2) \quad (5.22)$$

Substituting in Eq. (5.20) and taking only terms up to first order, it is possible to obtain:

$$\begin{cases} \frac{d\mathbf{E}_0}{dL} = 0 \\ \varepsilon \frac{d\mathbf{E}_1}{dL} = \varepsilon F(\mathbf{E}_0, L, \alpha, \beta) \end{cases} \quad (5.23)$$

Thus, the first-order term of the expansion is:

$$\mathbf{E}_1 = \int_{L_{m0}}^{L_{mf}} F(\mathbf{E}_0, \mathcal{L}, \alpha, \beta) d\mathcal{L} \quad (5.24)$$

Once the new orbital elements at the end of the thrust arc are available, FABLE is used to propagate a coast-arc ($\varepsilon = 0$) with the variated trajectory from the end of the manoeuvre to the nominal TCA (where the impact plane is defined) under the

simplifying assumption that the manoeuvre and orbit perturbations do not modify the shape of the ellipsoid of uncertainty (note that this is analogous to taking only the first two statistical moments in a full nonlinear propagation of uncertainty). Under this simplifying assumption, the LT manoeuvre, as the impulsive one, produces a translation of the uncertain ellipse on the impact plane by the quantity:

$$\delta \mathbf{x}_b = \bar{\boldsymbol{\mu}}_{b,LT} - \bar{\boldsymbol{\mu}}_{b,0}. \quad (5.25)$$

from where the PoC can be obtained. Algorithm C.3 in Appendix C summarises the LT CAM optimisation.

5.3.1 Magnitude and arc-length optimisation

The previous algorithm started from the assumption that one knows the magnitude of the thrust acceleration and the length of the thrust arc. However, the optimal value of these two parameters is not known a priori. Thus, an iterative process starting from a first guess is presented below to find the optimal values.

Once the optimal direction, \mathbf{d}_{opt} , is available for a fixed magnitude and arc-length, one can look for the optimal magnitude, the optimal arc-length or both by iterating the following process:

- Keeping the thrust-arc length constant ($\Delta L = L_{mf} - L_{m0} = L_c - L_{m0}$), the acceleration magnitude is modified so that $PoC < PoC_0$ and ε is minimal. Thus, similar to the impulsive case, the magnitude is reduced until $PoC = PoC_0$ and $\varepsilon > 0$. Algorithm C.4 in Appendix C includes the pseudo-code of this optimisation.
- Keeping the acceleration magnitude and direction constant, the arc-length is reduced. In this case, the mid-point of the arc is kept fixed, and with a bisection method, the arc size is reduced until $PoC = PoC_0$ and $\Delta\theta > 0$. Algorithm C.5 in Appendix C summarises this optimisation.

Note that in the remainder of the chapter, either the magnitude or the arc-length are optimised. The simultaneous optimisation of both is, of course, possible but in this work, the attention was limited to the effect of each individual optimisation.

5.4 Numerical scenarios

In this section, the robust CAM optimisation method is tested on different scenarios. Initially, the linear model is tested, accounting only for aleatory uncertainty. Then, epistemic uncertainty is also included in the example, to compute the robust optimal CAM in both impulsive and LT scenarios.

5.4.1 Impulsive CAM: minimisation of the PoC under aleatory uncertainty

In this example, a numerical case is presented to show the validity of the linear CAM model in Eq. (5.1). Only aleatory uncertainty is considered in this case, thus the computation of an optimal CAM reduces to problem Eq. (5.17) for a given covariance matrix. The magnitude of the impulse is kept constant and equal to $\delta v_0 = 10$ cm/s.

Table 5.1 includes the reference orbital parameters at the encounter time of both objects and Table 5.2 the diagonal Keplerian elements covariance matrix, \mathbf{D} , for the piece of debris (the secondary object), assumed diagonal. The manoeuvrable object (the primary) is assumed to be perfectly known, thus, no covariance matrix associated with it is required. The HBR of the combined objects is 10 m. The miss distance on the impact plane before the CAM is $\bar{\boldsymbol{\mu}}_{b,0} = [-0.143, 0.0, 0.494]^T$ km, and the PoC, computed with Eq. (3.1), before CAM execution is $PoC = 9.898 \cdot 10^{-6}$.

Table 5.1: Primary and secondary objects' nominal Keplerian elements at encounter time.

Variable	Units	Object 1	Object 2
Semimajor axis (a)	[km]	7,006.794	6,292.553
Eccentricity (e)	-	$5.5 \cdot 10^{-4}$	0.6684
Inclination (i)	[rad]	1.3321	2.0291
Right ascension of the ascending node (Ω)	[rad]	0.1537	6.1208
Argument of perigee (ω)	[rad]	0.0571	3.4077
True anomaly (θ)	[rad]	5.8100	2.4224

In order to validate the solution coming from the linear model in Eq. (5.16) a trivial grid search on the impulse angles ϕ, ψ in Eq. (5.26) is used to find a close to optimal pair

Table 5.2: Secondary object's covariance matrix (assumed diagonal) on the Keplerian elements at encounter time.

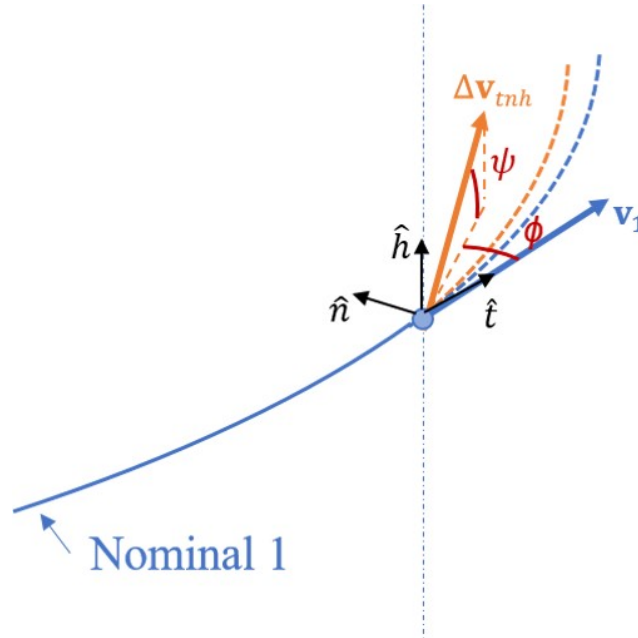
Variable	Units	Object 2
σ_a^2	[km ²]	$1.54 \cdot 10^{-3}$
σ_{ecc}^2	-	$7.24 \cdot 10^{-9}$
σ_{inc}^2	[rad ²]	$4.925 \cdot 10^{-7}$
σ_{Ω}^2	[rad ²]	0
σ_{ω}^2	[rad ²]	0
σ_{θ}^2	[rad ²]	0

of angles. The direction of the impulse can be defined by the two angles $\phi \in [-\pi, \pi]$ and $\psi \in [-\pi/2, \pi/2]$, as shown in Fig. 5.4. The relation between $[\phi, \psi]$ and the components on the $\langle T, N, H \rangle$ reference frame is:

$$\phi = \arctan \left((\mathbf{v}_1 \times \delta \mathbf{v}_{tnh}) \cdot \hat{\mathbf{h}}_1, \mathbf{v}_1 \cdot \delta \mathbf{v}_{tnh} \right) \quad (5.26a)$$

$$\psi = \arctan \left[\frac{(\delta \mathbf{v}_{tnh} \cdot \hat{\mathbf{h}}_1) \|\delta \mathbf{v}_{tnh} \times \hat{\mathbf{h}}_1\|}{\delta v^2 - (\delta \mathbf{v}_{tnh} \cdot \hat{\mathbf{h}}_1)^2} \right] \quad (5.26b)$$

For each pair of angles, the PoC at the encounter after the impulse is computed. For

**Figure 5.4:** Manoeuvre geometry, with orbit in blue, manoeuvre in orange and manoeuvre angles in red.

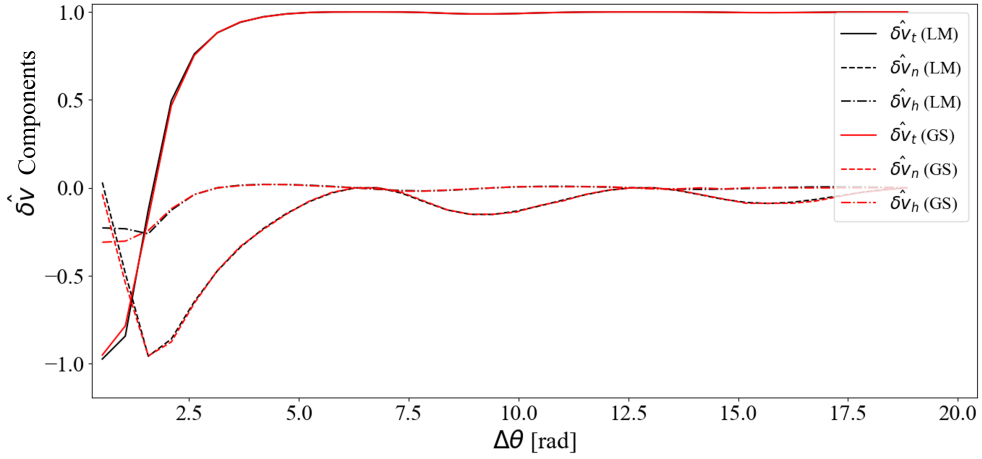


Figure 5.5: Components of the unit vector $\delta\hat{\mathbf{v}}_{opt} = [\delta\hat{v}_t \ \delta\hat{v}_n \ \delta\hat{v}_h]$ parallel to the optimum impulse, $\delta\mathbf{v}_{opt}$, as a function of the angular difference between manoeuvre and encounter, $\Delta\theta = \theta_c - \theta_m$. Black, using the linear model; red, using the grid search.

each θ_m , the optimal direction is chosen as the pair of angles providing the minimum PoC.

Fig. 5.5 shows the components of the direction of the optimal impulse vector in the primary object's <T,N,H> reference frame, $\delta\hat{\mathbf{v}}_{opt}$, applied to the primary object as a function of the angular distance between the manoeuvre and encounter positions, $\Delta\theta = \theta_c - \theta_m$. The results that optimise the PoC at each manoeuvre position θ_m obtained with the linear model appear in black, and the results from the grid search are in red. The figure shows the good agreement between both values for all the components, with only slightly greater differences for late manoeuvres (small $\Delta\theta$).

Table 5.3 includes the Root Mean Squared Error (RMSE) and the Maximum Absolute Error (MAE) of each component of $\delta\hat{\mathbf{v}}_{opt}$ computed with the linear model with respect to the grid search value.

Table 5.3: Linear model errors with respect to the grid search value for the unit vector, $\delta\hat{\mathbf{v}}_{opt}$, parallel to the direction of the optimal impulse, $\delta\mathbf{v}_{opt}$.

Variable	RMSE	MAE
$\delta\hat{v}_t$	$5.434 \cdot 10^{-2}$	$5.792 \cdot 10^{-2}$
$\delta\hat{v}_n$	$4.244 \cdot 10^{-2}$	$5.512 \cdot 10^{-2}$
$\delta\hat{v}_h$	$2.619 \cdot 10^{-3}$	$7.039 \cdot 10^{-2}$

5.4.2 Impulsive CAM: minimisation of the PoC under epistemic uncertainty

In this section, a scenario in which the miss distance and the covariance are affected by epistemic uncertainty is considered. This can be the case in which multiple Conjunction Data Messages (CDMs) are in conflict (Chapter 4) or correspond to an unknown distribution of covariance matrices (Chapter 3). In this scenario, the CAM needs to be robust enough to cope with the distribution of the covariance matrices and optimal at the same time. Two cases are analysed: one with a non-optimal impulse magnitude and one with an optimised magnitude.

In Table 5.4, the exact orbital elements at initial time t_0 of both objects are shown. The primary object, which is the manoeuvrable one, is assumed to be perfectly known. The knowledge of the orbit of the secondary object is affected by aleatory and epistemic uncertainty. The HBR of the combined objects is 10 m. Assuming Keplerian motion, the close approach occurs at the perigee of both objects ($\theta_1 = \theta_2 = 0$ rad) one and a quarter revolutions after t_0 .

Table 5.4: Initial Keplerian elements of both objects for the optimal robust CAM under aleatory and epistemic uncertainty.

Variable	Units	Object 1	Object 2
Semimajor axis (a)	[km]	7,100	7,100.5
Eccentricity (e)	-	10^{-5}	10^{-5}
Inclination (i)	[rad]	$\pi/4$	$2/3\pi$
Right ascension of the ascending node (Ω)	[rad]	0.0	0.0
Argument of perigee (ω)	[rad]	0.0	0.0
True anomaly (θ)	[rad]	4.7148	4.7148

The uncertainty is introduced on the secondary object's initial position in its $\langle T, N, H \rangle$ reference frame. The aleatory uncertainty is modelled as a 3D-Gaussian distribution, with mean $\boldsymbol{\mu}_{tnh_0}$ and covariance matrix $\boldsymbol{\Sigma}_{tnh_0}$ (see Fig. 5.6).

The epistemic uncertainty is modelled with interval-valued parameters that modify the Gaussian distribution (Fig. 5.7). Thus, the epistemic parameter $\boldsymbol{\lambda}_\mu$ defines the variability of the mean value, while the epistemic parameter $\boldsymbol{\lambda}_\sigma$, scales the covariance matrix. Note, the factor $\boldsymbol{\lambda}$ does not displace/scale the single value defined by the

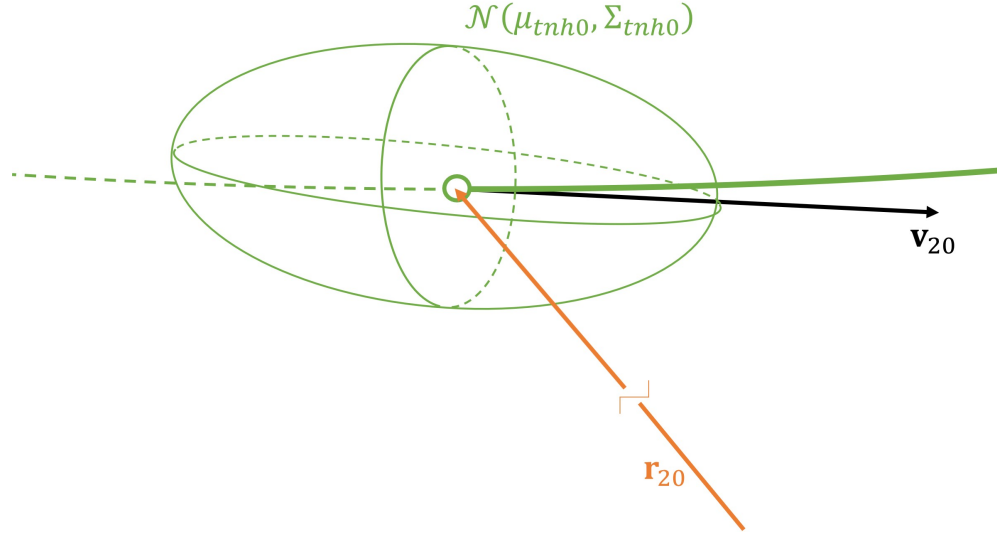


Figure 5.6: Secondary object's position ellipsoid of uncertainty at the initial epoch. Thick green line: trajectory; orange arrow: position vector; black arrow: velocity vector; green thin line: ellipsoid.

aleatory uncertainty but defines a family of ellipsoids compatible with the epistemic set. As a consequence, the single well-defined initial position uncertain ellipsoid becomes the family of ellipsoids:

$$\mathbf{x}_{tnh} = \mathcal{N}(\boldsymbol{\mu}_{tnh_0}, \boldsymbol{\Sigma}_{tnh_0}; \boldsymbol{\lambda}), \quad (5.27)$$

with $\boldsymbol{\lambda} = [\boldsymbol{\lambda}_\mu, \boldsymbol{\lambda}_\sigma]$ and

$$\begin{aligned} \boldsymbol{\mu}_{tnh} &= \boldsymbol{\mu}_{tnh_0} + \boldsymbol{\lambda}_\mu \\ \boldsymbol{\Sigma}_{tnh} &= \begin{bmatrix} \sigma_{t_0}^2 \lambda_{\sigma_t} & 0 & 0 \\ 0 & \sigma_{n_0}^2 \lambda_{\sigma_n} & 0 \\ 0 & 0 & \sigma_{h_0}^2 \lambda_{\sigma_h} \end{bmatrix}, \end{aligned} \quad (5.28)$$

It is assumed that two independent sources of information are available. Each source of information provides one interval for each of the epistemic parameters $\boldsymbol{\lambda}_\mu$ and $\boldsymbol{\lambda}_\sigma$. The intervals provided by each source are assumed to be completely disjoint and each epistemic parameter can belong to the interval provided by the corresponding source of information.

Table 5.5 includes the initial expected value, $\boldsymbol{\mu}_{tnh_0}$, and diagonal covariance matrix,

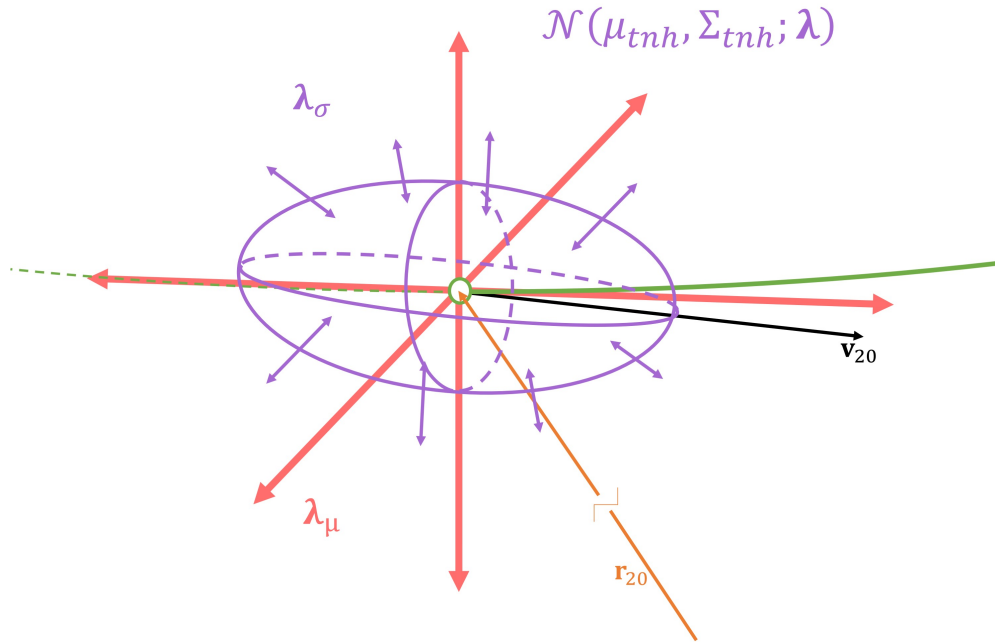


Figure 5.7: Representation of the effect of the epistemic parameter λ . Purple: aleatory uncertainty ellipsoid. Pink arrows: compatible displacements due to λ_μ . Compatible ellipsoid shrink/augmentation due to λ_σ .

Σ_{tnh_0} , for the secondary object's initial position modelling the aleatory uncertainty. It also includes the epistemic parameters that define the family of ellipsoids for each source. The first source of information supports the hypothesis that the position is closer to the nominal expected value (less than 10 m off the nominal position) and is compatible with covariance matrices scaled up to 4 times. The other source of information supports the hypothesis that the miss distance is further away (around 500 m from the nominal position) and is compatible with covariance matrices shrunk by a factor between 2 and 5.

The uncertainty is expressed in an Earth-Centred Inertial reference frame and propagated to the nominal encounter time. The propagation is carried out by sampling the initial ellipsoids defined by each source and propagating each sample to the nominal TCA. Finally, the uncertainty is projected onto the impact plane centred at the secondary object with Eq. (5.9). Since the independence of the sources is assumed, the projection on the impact plane corresponds to two families of uncertain ellipses (see Fig. 5.8), defined by the intervals in Table 5.6. The PoC accounting for epistemic un-

Table 5.5: Secondary object’s position initial uncertainty. The aleatory uncertainty is modelled with a multivariate Normal distribution, while the epistemic uncertainty is modelled with the interval-valued parameter λ .

Aleatory uncertainty			
μ_{tnh0}	[km]	[0, 0, 0]	
σ_{t0}^2	[km ²]	0.25 ²	
σ_{n0}^2	[km ²]	0.25 ²	
σ_{h0}^2	[km ²]	0.25 ²	
Epistemic uncertainty		Source 1	Source 2
$\lambda_{\mu_t} = \lambda_{\mu_n} = \lambda_{\mu_h}$	[km]	[0.00, 0.01]	[-0.53, -0.515]
$\lambda_{\sigma_t} = \lambda_{\sigma_n} = \lambda_{\sigma_h}$		[1,4]	[1/5, 1/2]

certainty varies then in the intervals $[10^{-21}, 9.1 \cdot 10^{-3}]$ and $[10^{-39}, 1.5 \cdot 10^{-8}]$ for Source 1 and Source 2, respectively, when taken independently. If one was considering one single enveloping ellipsoid, assuming both sources are equally reliable (as for the non-epistemic case in Chapter 3), the PoC would be $2.571 \cdot 10^{-5}$. When the intervals provided by the two sources are combined using the mixing rule, the epistemic uncertainty space U is composed of 32 FEs coming from the Cartesian product of two intervals for each of the 5 uncertain parameters defining the mean value and covariance matrix. The CAM has to be optimal for every value of mean and covariance in each focal element.

Table 5.6: Bounds of the sources’ intervals for the uncertain variables on the impact plane.

Variable	Units	Source 1	Source 2
μ_ξ	[km]	[0.406, 0.572,]	[0.338, 0.380]
μ_ζ	[km]	[-0.842, 0.625]	[2.708, 2.998]
σ_ξ^2	[km ²]	[0.0316, 0.312]	$[0.931, 5.611] \cdot 10^{-3}$
σ_ζ^2	[km ²]	[1.452, 20.12]	[0.3298, 0.0480]
$\sigma_{\xi\zeta}$	[km ²]	$[0.180, 2.422] \cdot 10^{-2}$	$[0.498, 3.962] \cdot 10^{-2}$

In the following figures, the optimal manoeuvre was computed at each quarter of orbit for the 12 revolutions before the TCA. Fig. 5.9 shows the evolution of the components of the unit vector parallel to the optimal impulse, $\delta\hat{\mathbf{v}}$, as a function of the angular distance from the TCA, $\Delta\theta = \theta_c - \theta_m$, for both cases: with and without optimisation of the impulse magnitude. For these examples, both strategies present the

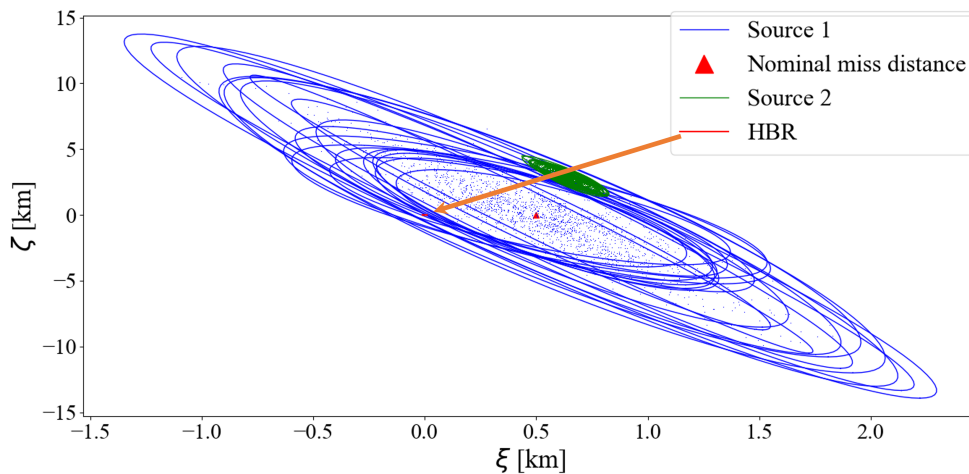


Figure 5.8: Encounter geometry at the impact plane with two sources of information providing uncertain (aleatory and epistemic) information. Red triangle: nominal position. Blue and green: samples and ellipses of Source 1 and Source 2, respectively. Orange: HBR.

same optimal direction at all manoeuvre positions, which tends to a tangential impulse. They differ, however, in the value of the magnitude for $\Delta\theta > 56.5$ rad (approximately 9 orbits before the TCA) when $PoC_{WC} < PoC_0$ (Fig. 5.10), being WC the worst-case ellipse with the highest PoC among all the FEs.

Fig. 5.11 includes the evolution of the worst-case PoC as a function of $\Delta\theta$. It can be seen how the worst-case scenario PoC remains closer to PoC_0 when optimising the magnitude of the impulse for $\Delta\theta > 56.5$ rad (red solid line). The robustly optimised PoC (solid line) is compared with the highest PoC obtained at each θ_m from a set of uncertain ellipses extracted from the intervals defined in Table 5.6.

Finally, Fig. 5.12 includes the worst-case scenario uncertain variables as a function of $\Delta\theta$ along with the sources' interval bounds. It can be appreciated how the worst-case scenario (blue and red solid lines for the non-optimal magnitude and optimal magnitude cases, respectively) is restricted to the given intervals provided by the sources of information (black and green dashed lines).

The results of the optimisation using the linear model for computing the optimal impulse are compared with a Monte Carlo (MC) simulation to prove their validity. For the MC simulation, 1,000 samples per ellipsoid and 20 ellipsoids per source are

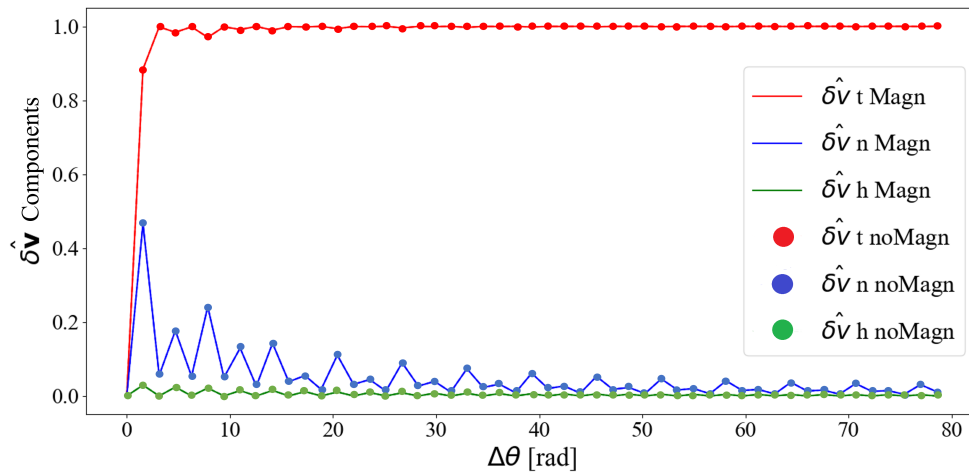


Figure 5.9: Evolution of the direction of the optimal impulse, $\delta\hat{\mathbf{v}}$, as a function of the position of the manoeuvre, $\Delta\theta$. Solid line: with optimisation of the magnitude of the impulse; points: without optimisation of the magnitude. Both cases coincide. Red: tangential component; blue: normal component; green: out-of-plane component.

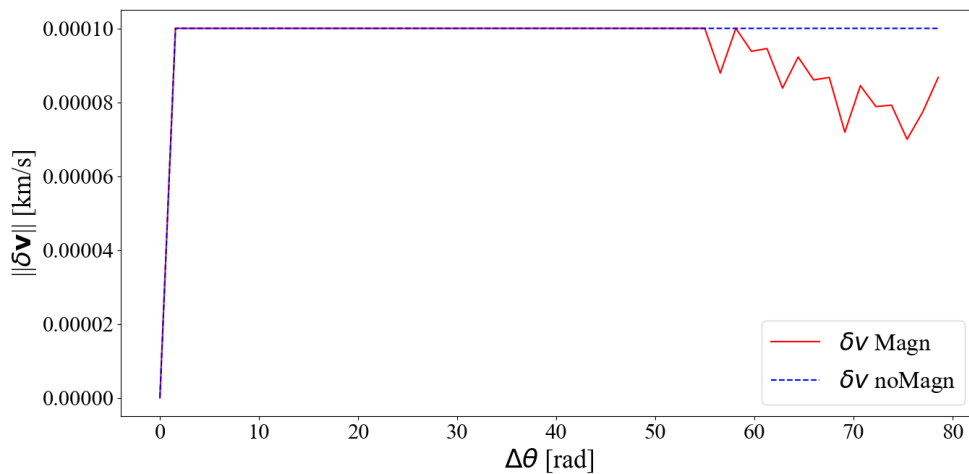


Figure 5.10: Evolution of the impulse magnitude as a function of the position of the manoeuvre, $\Delta\theta$. Red solid line: impulsive magnitude optimised; blue dashed line: without optimising the impulse magnitude.

used. The primary object's initial nominal state (not uncertain) is propagated to the manoeuvre position where the optimal impulse is added to the orbital velocity. The new modified orbit is propagated to the unperturbed nominal TCA. The secondary object is propagated as indicated before: samples from some uncertain ellipsoids on the initial position are taken and individually propagated to the nominal TCA. The

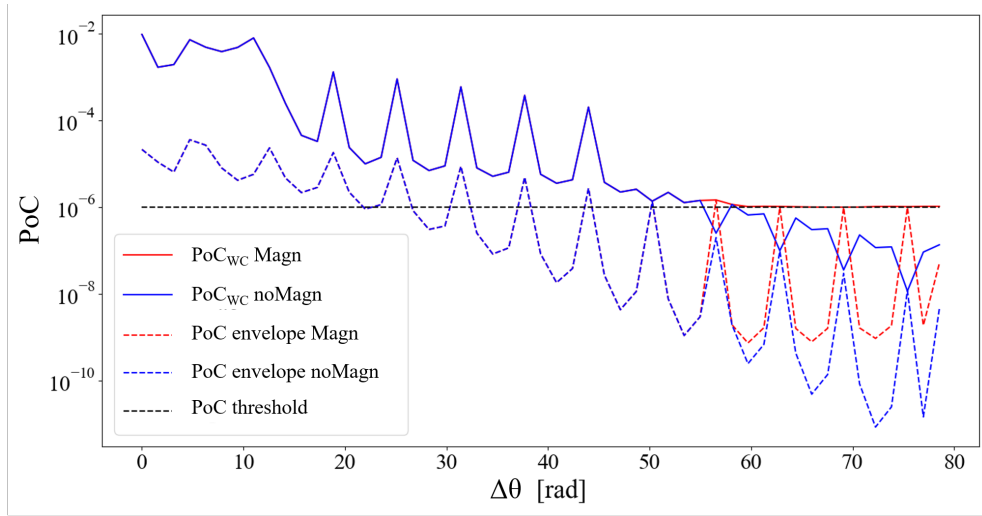


Figure 5.11: Evolution of worst-case scenario PoC with the position of the manoeuvre, $\Delta\theta$. Red, with impulse magnitude optimisation. Blue, without optimising the impulse magnitude. Solid lines: worst-case scenario. Dashed lines: the worst-case PoC among 20 ellipses per source randomly drawn from the intervals. Dashed-dotted black line, PoC threshold.

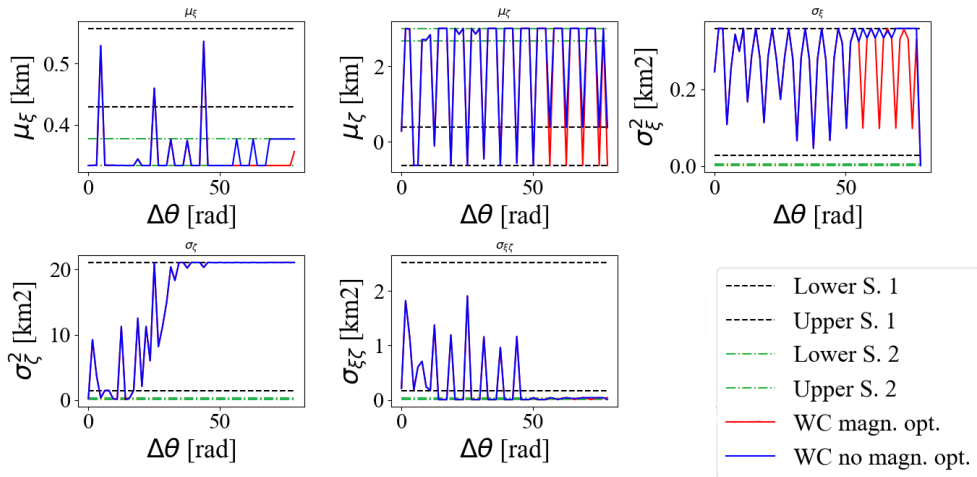


Figure 5.12: Worst-case scenario uncertain variables evolution with respect to the difference between encounter and manoeuvre positions, $\Delta\theta$. From left to right and top to bottom: μ_ξ , μ_ζ , σ_ξ^2 , σ_ζ^2 , $\sigma_{\xi\zeta}$. Red solid line: with impulse magnitude optimisation; blue solid line: without impulse magnitude optimisation. Horizontal dashed line: lower bound; horizontal dashed pointed: upper bound. Black: Source 1; green: Source 2.

relative position between the primary nominal state and the state of each sample from the secondary object is projected onto the impact plane defined at the TCA by the unperturbed nominal orbits.

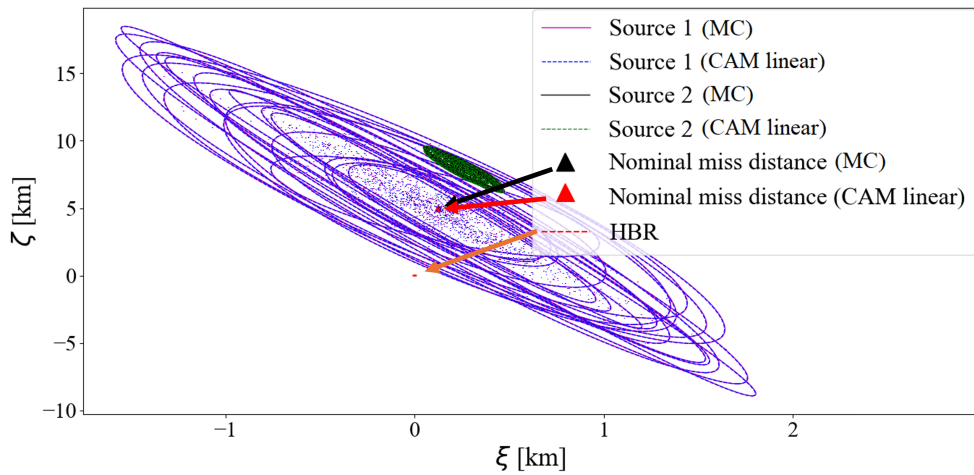


Figure 5.13: Uncertain ellipses displaced by an impulse applied at 3.5 revolutions before the encounter. Blue and green dashed lines: uncertain ellipses according to the linear model; purple and black solid lines: uncertain ellipses according to the MC simulation. Red dashed circle centred at the origin: HBR (position highlighted with indicative arrow). Triangles (position highlighted with indicative arrows): displaced nominal position, red for linear model, black for MC simulation. Note that the good agreement of both methods makes the MC ellipses (solid) and CAM linear method ellipses (dashed) overlap. Same with the nominal miss distance positions (triangles).

Fig. 5.13 shows the displacement of the set of ellipses obtained using the linear model (blue and green ellipses are associated with Source 1 and Source 2, respectively), and the uncertain ellipses families obtained with the MC simulation (black and purple ellipses are associated to Source 1 and Source 2, respectively) when applying the optimal impulse 3.5 revolutions before the encounter. The figure shows a good agreement between the two simulations to the point that the purple and black lines are nearly completely overlapped with the blue and green ones, respectively. Fig. 5.14 illustrates the evolution of the deflection due to the impulse (Fig. 5.14a) and the associated worst-case PoC (Fig. 5.14b) as a function of $\Delta\theta$. In red, the MC simulation results and with dots, the linear model. The agreement between methods for all the variables can be understood as a validation of the linear model proposed in this work also for the epistemic case.

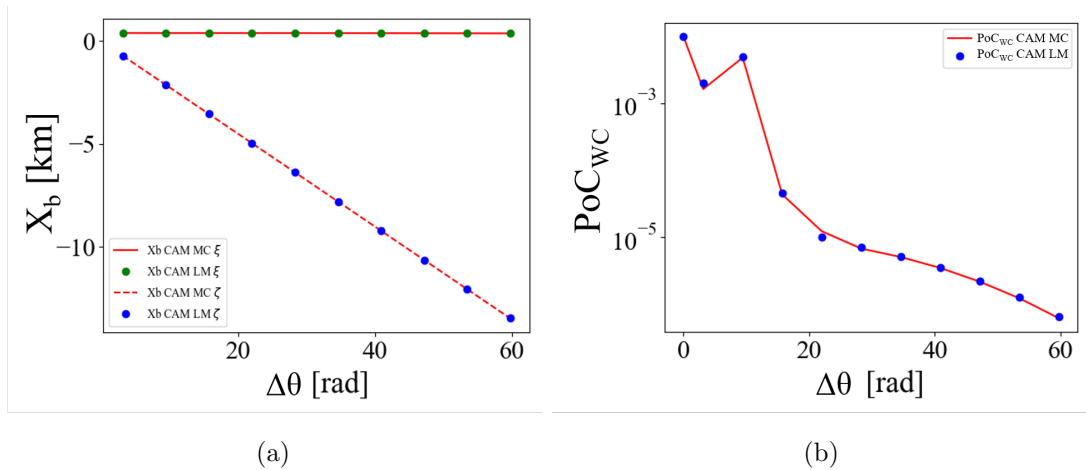


Figure 5.14: (a) Evolution of the deflection due to the robust optimal CAM. Red lines: MC simulation, solid for ξ , dashed for ζ . Dots for the linear model: in green, ξ ; in blue, ζ . (b) Evolution of the PoC due to the manoeuvre: solid red line for MC simulation; blue dots for the linear model.

5.4.3 Low-thrust scenario

In this section, an example showing the method for computing the optimal CAM for the LT case is presented. A comparison between the different algorithms presented in Section 5.3 is shown. The results of each of these algorithms are then compared against the results obtained by applying a tangential manoeuvre, as proposed by other authors [Hernando-Ayuso and Bombardelli, 2020].

The same scenario as in the previous example is investigated. The exact orbital parameters are included in Table 5.4. The primary object is assumed to be perfectly known, while the uncertainty in the initial position for the secondary object is included in Table 5.5 and the encounter uncertain variables bounds for the two sources of information are included in Table 5.6. The parameters employed for the LT scenario appear in Table 5.7. The optimal direction was computed at multiples of half orbit before the encounter for 10 revolutions.

In Figs. 5.15 to 5.18, *Strategy 0* refers to the LT manoeuvre obtained using Algorithm C.3 with $\varepsilon_{opt} = \varepsilon_{max}$ and with $\theta_{mf} = \theta_c$, thus, maximum thruster capacity and maximum arc-length. *Strategy 1* refers to the case where the acceleration magnitude is optimised, keeping the thrust until the encounter. *Strategy 2* shows the case where

Table 5.7: Parameters employed for the optimal LT CAM computation.

Variable	Units	Value
δv_{max}	[cm/s]	10
ε_{max}	[cm/s ²]	$2 \cdot 10^{-3}$
PoC_0	[-]	10^{-6}

the thrust is kept equal to the maximum capacity of the thruster and the arc-length is optimised. Those figures also show a comparison between the results obtained applying the LT in the optimal impulsive direction (solid lines) and the results obtained with a purely tangential thrust (dashed lines).

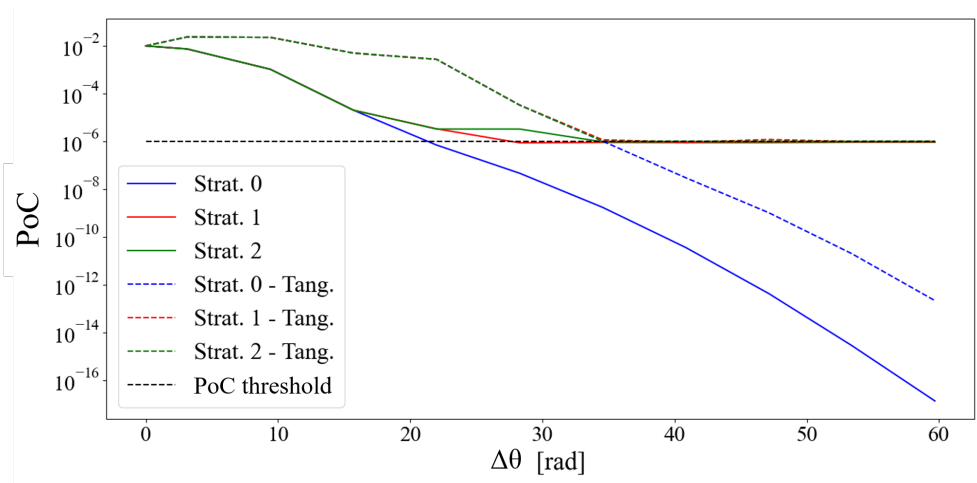


Figure 5.15: PoC evolution versus the difference in true anomaly between the mid-point of the Low-Thrust manoeuvre and the encounter. Blue: maximum thruster capacity and arc-length. Red: optimised acceleration magnitude. Green: optimised arc-length. Solid lines: optimal direction. Dashed line: tangential manoeuvre.

Fig. 5.15 includes the evolution of the PoC as a function of the difference between the true anomalies at the manoeuvre mid-point and at the encounter, $\Delta\theta$. It can be seen the difference between executing the manoeuvre with maximum capacity until the encounter (blue solid line) and optimising the acceleration magnitude (red solid line) or the burning time (green solid line). For values $\Delta\theta > 30$ rad, if using the maximum capacity and maximum burning time, the PoC drops far below the threshold, PoC_0 . However, for the other two cases, the PoC remains close, but below the threshold.

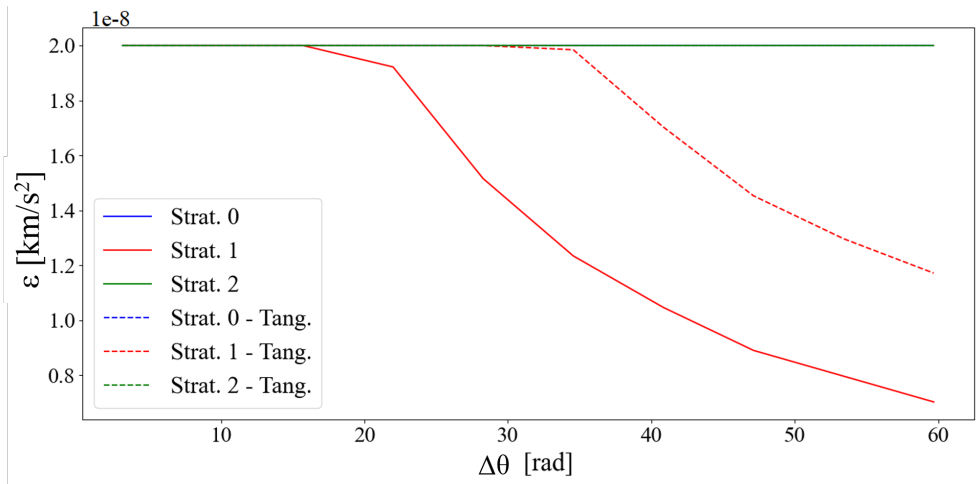


Figure 5.16: Acceleration magnitude evolution versus the difference in true anomaly between the mid-point of the Low-Thrust manoeuvre and the encounter. Blue: maximum thruster capacity and arc-length. Red: optimised acceleration magnitude. Green: optimised arc-length. Solid lines: optimal direction. Dashed line: tangential manoeuvre.

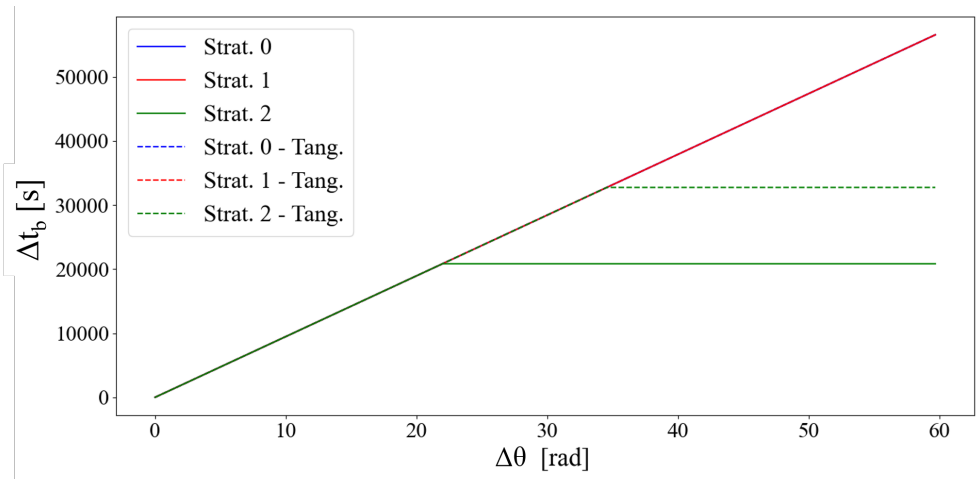


Figure 5.17: Burning time evolution versus the difference in true anomaly between the mid-point of the Low-Thrust manoeuvre and the encounter. Blue: maximum thruster capacity and arc-length. Red: optimised acceleration magnitude. Green: optimised arc-length. Solid lines: optimal direction. Dashed line: tangential manoeuvre.

In Figs. 5.16 and 5.17, it can be seen how the acceleration magnitude and the burning time are optimised, respectively. Fig. 5.16 shows that for *Strategy 0* and *Strategy 2* the acceleration magnitude is equal to the maximum capacity, $\varepsilon = \varepsilon_{max}$, but for *Strategy 1* the acceleration is optimised (red solid line). Similarly, Fig. 5.17

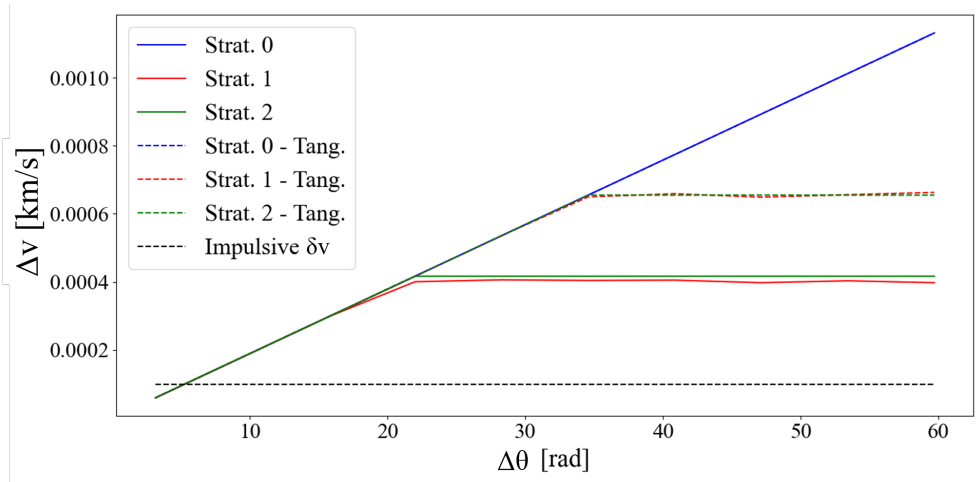


Figure 5.18: Equivalent velocity change to the difference in true anomaly between the mid-point of the Low-Thrust manoeuvre and the encounter ($\Delta\theta = \theta_c - \theta_m$). Blue: maximum thruster capacity and arc-length. Red: optimised acceleration magnitude. Green: optimised arc-length. Solid lines: direction of the impulse according to the proposed algorithm. Dashed line: tangential manoeuvre. Black dashed line: velocity change used on the hypothetical impulsive manoeuvre.

illustrates the optimisation on the burning time for *Strategy 2* (green solid line), while *Strategy 0* and *Strategy 1* present the maximum burning-time. Finally, in Fig. 5.18, the equivalent velocity change is shown for each strategy, obtained with the LT manoeuvre according to $\delta v = \varepsilon / \Delta t_b$. In general, it is different than the velocity change considered by the impulse employed to compute the optimal direction manoeuvre, which is shown as the horizontal black dashed line, being greater for most of the values of θ_m , showing the bigger efficiency of this kind of propulsion. It is also seen that the equivalent change of velocity when optimising either the thrust magnitude or the arc-length is equivalent.

When comparing with the tangential control law, it can be seen from Fig. 5.15 that, for all the approaches, the proposed method (solid line) yields a lower worst-case PoC than the tangential manoeuvre (dashed line) at any given value of $\Delta\theta$. Similarly, the optimised values of thrust magnitude, burning time and equivalent δv present worse values in the tangential case. This implies the proposed method improves over a purely tangential manoeuvre.

5.5 Chapter summary

The work in this chapter presented a method to use DSt to generate robust CAMs based on robust estimates of the correctness of the PoC. This methodology accounts for the aleatory and epistemic uncertainty that may affect a space object's position and was proven to provide accurate results with respect to a MC simulation.

The CAM methodology is based on a linear model also proposed in this chapter, inspired by asteroid deflection theories. This model was also validated and showed its accuracy in the context of close encounter avoidance.

Finally, the robust optimal CAM methodology was extended to the LT scenario, providing better results in terms of lower propellant consumption, than simple applications of a tangential thrust. This was also demonstrated in the optimisation of the burning time or the thrust magnitude.

In Part II, this method will be further used in the multiple-encounter scenario (Chapter 9), to train ML models (Chapter 8), and to be integrated along with a decision support system and other tools to solve more complex Space Traffic Management problems (Chapter 10).

Chapter 6

Robust decision-making

The content of this chapter was partially published in:

Sánchez, L. and Vasile, M. (2021), “Constrained optimal collision avoidance manoeuvre allocation under uncertainty for subsequent conjunction events”, 72nd International Astronautical Congress; [Sánchez and Vasile, 2021b]

Vasile, M. and Sánchez, L. (2022), “Robust optimisation of coordinated collision avoidance manoeuvres in large constellations”, 11th International Workshop on Satellites Constellations and Formation Flying. [Vasile and Sánchez, 2022]

When the Conjunction Assessment Risk Analysis (CARA) of a close encounter indicates a Collision Avoidance Manoeuvre (CAM) is required, it is possible to compute several robust optimal manoeuvres to avoid the event depending on several parameters: position of the manoeuvre execution, magnitude of the impulse or the thrust, the returning manoeuvre after the event or, in the case that more than one satellite or more than one encounter is involved on the event, the combination of those parameters for each satellite/encounter. Then, the operator has a set of optimal, yet non-dominant, solutions, but only one can be applied. Moreover, the selected alternative has to be chosen according to several contradictory criteria, whose importance may be modified along the mission life, making the task of choosing an optimal solution a challenging step.

This chapter proposes an approach to support operators in the decision-making process when a set of alternatives is available, allowing their evaluation under different criteria. Multi-Criteria Decision-Making (MCDM) techniques were implemented to deal with the collaborative scenario: when there is only one operator or the decided outcome will be agreed upon among different operators (if that is the case). A Game Theory-based methodology will extend this approach to the non-collaborative case when one operator does not know which will be the action finally taken by another one, being necessary to discover which is the equilibrium solution when all agents win or, at least, do not lose.

The rest of the chapter is structured as follows. In Section 6.1, MCDM theory is explained, detailing the techniques, criteria and alternatives considered to support decision-makers. Section 6.2 introduces the Game Theory and indicates how to apply it for decision-making in the event of a non-collaborative scenario (e.g. two operational satellites with no/restricted communication between operators). The next two sections, Sections 6.3 and 6.4, apply the aforementioned techniques in the context of conjunction risk assessment for a collaborative and a non-collaborative case, respectively. These sections show the application of MCDM and Game Theory to support operators in deciding the best robust optimal CAM and avoidance strategy under uncertainty. Finally, Section 6.5 concludes the chapter.

6.1 Multi-criteria decision-making

In engineering, it is common to find situations when several potential solutions are available to solve a problem, all of them being optimal under certain criteria, but sub-optimal for others. For example, adding more material to a space structure would benefit its mechanical properties, but would increase its weight and, consequently, its cost. In such situations, the decision-maker (the operator in the context of Space Traffic Management, STM) should choose in an informed way the alternative that better tackles the problem.

When different alternatives are available, each of them being optimal for some of the decision-maker criteria and there is a single agent, MCDM techniques may be used

to support the decision-maker to make informed decisions. It can be also applied when the selected alternative is known to be followed by all agents involved in the problem. These situations are known as collaborative scenarios.

MCDM is a branch of decision-making and operations research that provides a compromise solution (in the form of a sorted list) of a set of non-dominated alternatives evaluated across a set of, usually, contradictory criteria based on the decision-maker preferences [Triantaphyllou et al., 1998, Triantaphyllou, 2000].

Hence, three types of parameters should be defined to apply the different MCDM methods: the alternatives, the criteria and the weight of the criteria.

- The *alternatives* are all possible responses to a given problem built by combining the different answers of all agents. In other words, they are the options from which to select the best outcome to tackle the given problem.
- The *criteria* are quantities used to evaluate the suitability of the alternatives to optimise different aspects related to the problem: risk, cost... They can be beneficial if they want to be maximised, or non-beneficial when they want to be minimised. The criteria have to be measurable and be related to the magnitude the alternatives represent, but they may have different units among them. The most common situation is to find conflict among criteria: improving the performance in some criteria will deteriorate the score on others.
- The *weights* are associated with criteria and are used to assign more importance to certain criteria than others, enabling one to address the problem from different perspectives. They represent the decision-maker preferences. From a multi-objective point of view, weights are used to secularise the vector of decision criteria and allow a partial ranking of the alternatives.

6.1.1 Alternatives-Criteria matrix

To compare the alternatives, they have to be evaluated over different criteria. As mentioned, criteria usually conflict with each other and some alternatives perform better on some criteria than on others. The Alternatives-Criteria matrix \mathbf{A} , allows for the vi-

sualisation of the performance of each alternative on every criterion individually. Given M alternatives and N criteria, in the matrix \mathbf{A} with shape $[M \times N]$, each row represents one alternative and each column the score of the alternatives over each criterion individually. Thus, the term a_{ij} is the value of alternative i under criteria j .

$$\mathbf{A} = \begin{bmatrix} a_{11} & a_{12} & \dots & a_{1N} \\ a_{21} & a_{22} & \dots & a_{2N} \\ \dots & \dots & \dots & \dots \\ a_{M1} & a_{M2} & \dots & a_{MN} \end{bmatrix}, \quad (6.1)$$

In its plain form, the Alternatives-Criteria matrix will show just the score of the alternative with respect to the criteria. However, as mentioned before, some criteria can be *Beneficial*, meaning a higher score is desirable, while others are *Non-Beneficial* or *Cost* criteria, where lower scores indicate better performance. Thus, the values on the matrix may be misleading if not taken with care. Moreover, the function to evaluate the criteria may provide values in completely different ranges or even in different units (e.g. weight in kilograms and resistance in MPa), which makes the comparison among criteria performance meaningless.

6.1.2 Normalisation techniques and weights distribution

To be able to compare the score of the different alternatives over the different criteria, it is necessary to normalise the matrix so that the score ranges in the same interval (e.g. between 0 and 1). This enables the build of the Normalised Alternatives-Criteria matrix or Decision matrix, $\overline{\mathbf{A}}$, which contains the normalised score of the alternatives over the criteria. Although during the next step, when ranking the alternatives, some techniques are able to work with normalised alternatives differing between *Beneficial* and *Cost* alternatives, it is a good practice to use a normalisation technique that also transforms *Cost* criteria into *Beneficial* criteria, that is, eliminate the optimisation orientation [Aytekin, 2021]. Thus, no matter the criterion, an alternative with the highest score would be desirable.

There are several normalisation methods which follow different rules: distance-

based or specific value-based techniques, optimisation orientation-based methods, linear or non-linear normalisation... The method employed may influence the final ranking after applying the MCDM techniques in the next step, and the decision on which one to use may depend on the structure of the problem and the MCDM techniques employed [Vafaei et al., 2016, Aytakin, 2021]. In this work, three different methods were considered: Maximum Linear normalisation, Max-Min normalisation and Vector normalisation [Jahan and Edwards, 2015], whose expression can be seen in Eqs. (6.2) to (6.4). All of them are linear models, convert the criteria into the range [0,1] and transform the Cost criteria into Beneficial (optimisation orientation-based). The first two methods are specifically value-based, while the latter is a distance-based technique.

- *Maximum-Linear normalisation:*

$$\begin{cases} \text{if } Beneficial & \bar{a}_{ij} = a_{ij} / \max_i(a_{ij}) \\ \text{if } Cost & \bar{a}_{ij} = 1 - a_{ij} / \max_i(a_{ij}) \end{cases} \quad (6.2)$$

- *Max-Min normalisation:*

$$\begin{cases} \text{if } Beneficial & \bar{a}_{ij} = a_{ij} / \max_i(a_{ij}) \\ \text{if } Cost & \bar{a}_{ij} = \min_i(a_{ij}) / a_{ij} \end{cases} \quad (6.3)$$

- *Vector normalisation*, an Euclidean distance-based procedure:

$$\begin{cases} \text{if } Beneficial & \bar{a}_{ij} = a_{ij} / \sqrt{\sum_{i=1}^M a_{ij}^2} \\ \text{if } Cost & \bar{a}_{ij} = 1 - a_{ij} / \sqrt{\sum_{i=1}^M a_{ij}^2} \end{cases} \quad (6.4)$$

This work does not intend to make a detailed analysis of normalisation techniques, but to present a MCDM-based methodology to support operators on collision avoidance decisions. Thus, despite the great variety of methods found in the literature, this work focuses only on those three, which are widely used [Vafaei et al., 2016, Chakraborty and Yeh, 2007] and were studied for specific MCDM techniques [Vafaei et al., 2016, Vafaei et al., 2018, Vafaei et al., 2022, Chakraborty and Yeh, 2009].

Finally, it is necessary to establish the weight distribution of the criteria before

implementing any MCDM technique. As indicated above, the weights will assign more or less importance to a specific criterion according to the agent's preferences. Thus, the final ranking will be greatly impacted by this distribution. The weight assignment may respond to objective parameters (e.g. internal risk among a swarm of satellites to avoid losing the whole constellation) or to the subjective preferences of the decision-maker (e.g. prioritise cheaper manoeuvres, even though smaller risk decreases, if the satellite is at the end of life with little propellant remaining).

6.1.3 MCDM techniques

Once the Decision matrix is obtained and the criteria weight distribution defined, it is possible to rank the solutions by applying one of the several methods available in the literature [Kolios et al., 2016, Triantaphyllou, 2000, Ramírez-Atencia et al., 2020]. Similar to the normalisation methods, this work aims to present a concept to use MCDM to support operators on CARA decision-making, not to perform an exhaustive analysis of the best technique. Thus, this work limited to the following techniques: Weighted Sum Method (WSM) [Kolios et al., 2016], normalised Weighted Sum Method (nWSM) [Ramírez-Atencia et al., 2020, Mateo, 2012], Weighted Product Method (WPM) [Kolios et al., 2016, Tofallis, 2014], *Technique for the Order of Preference by Similarity to the Ideal Solution* (TOPSIS) [Kolios et al., 2016, García-Cascales and Lamata, 2012]. In the following, a brief explanation of each of them is provided. Note: in the following equations and for all the methods: $i, k = 1, \dots, N_{alt}$ and $j = 1, \dots, N_{crit}$, where N_{alt} is the number of alternatives and N_{crit} the number of criteria.

- *WSM*. Also called Simple Additive Weighting, it is one of the simplest MCDM methods. It is based on the utility add hypothesis. The weighted values of the alternatives with respect to the criteria are added. The alternative with the highest added value ranks first. If the variables present different ranges of values or different units, normalisation schemes are required. If the criteria are both *Beneficial* and *Cost*, the normalisation technique should also transform them all

into *Beneficial*.

$$A_{i,WSM} = \sum_{j=1}^{N_{crit}} w_j \cdot a_{ij}. \quad (6.5)$$

- *nWSM*. It is a variation of the previous method, which normalised the aggregated score with the maximum alternative with respect to each criterion.

$$A_{i,nWSM} = \sum_{j=1}^{N_{crit}} \frac{w_j \cdot a_{ij}}{\max(a_{:j})}. \quad (6.6)$$

where $a_{:j}$ indicates the score of all alternatives under the j^{th} criterion, and $\max(a_{:j})$ the maximum score under that criterion.

- *WPM*. This method is similar to WSM, but instead of adding the values, it compares each solution to all the others using a product of weighted ratios:

$$P_{ik,WPM} = \prod_{j=1}^{N_{crit}} \left(\frac{a_{ij}}{a_{kj}} \right)^{w_j}, \quad (6.7)$$

where $P_{ik,WPM} > 1$ indicates the i^{th} alternative is better than the k^{th} alternative. The above equation does not rank the alternatives but just provides a new matrix, \mathcal{P} , with size $[N_{alt} \times N_{alt}]$. To sort the solutions, an alternative ranks first when it has a bigger number of elements greater than one on its corresponding row:

$$A_{i,WPM} = \text{count}_k(P_{ik,WPM} \geq 1). \quad (6.8)$$

If normalisation techniques are applied to the Decision matrix, care should be taken to avoid zeros on the matrix.

- *TOPSIS*. As its name suggests, this method is based on finding the best solution according to the distance to some ideal best and worst alternatives. From the normalised and weighted Decision matrix, the ideal best and ideal worst solution (also called Positive Ideal Solution and Negative Ideal Solution, respectively) can

be obtained as:

$$\begin{aligned} A^+ &= \{\max_j(a_{ij}) \text{ if } j \in C^+, \min_j(a_{ij}) \text{ if } j \in C^-\}, \\ A^- &= \{\min_j(a_{ij}) \text{ if } j \in C^+, \max_j(a_{ij}) \text{ if } j \in C^-\}, \end{aligned} \quad (6.9)$$

whit C^+ the set of *Beneficial* criteria and C^- the set of *Non-Beneficial* criteria (this technique does not require a normalisation method that transforms all criteria into *Beneficial*, although it could be useful). That is, the best ideal solution vector would be the one compound by the elements ranking best on each criterion (maximum value if *Beneficial*, minimum if *Cost*), and the opposite for the worst ideal solution.

Then, the method ranks the solutions based on the geometrical distance between each alternative and the ideal alternatives:

$$A_{i, TOPSIS} = \frac{D_i^-}{D_i^+ + D_i^-}, \quad (6.10)$$

where

$$D_i^* = \sqrt{\sum_{j=1}^{N_{crit}} (a_{ij} - a_j^*)^2}, \text{ and } * = \{+, -\}, \quad (6.11)$$

being a_j^+ and a_j^- the elements of A^+ and A^- , respectively. The solution with higher $A_{i, TOPSIS}$ ranks first.

6.2 Game theory

When the agents are not expected to collaborate, but rather they are competitors, the outcome of the decision may not be the optimal one for every agent, in the so-called non-collaborative scenarios. This is the case, for example, when a space encounter involves two satellites operated by different operators. MCDM can address problems where there is only one decision-maker, having to evaluate the proposed solutions among its own conflict criteria, or if it is known that the several agents involved in a decision-maker problem would agree on the proposed outcome. However, the proposed problem

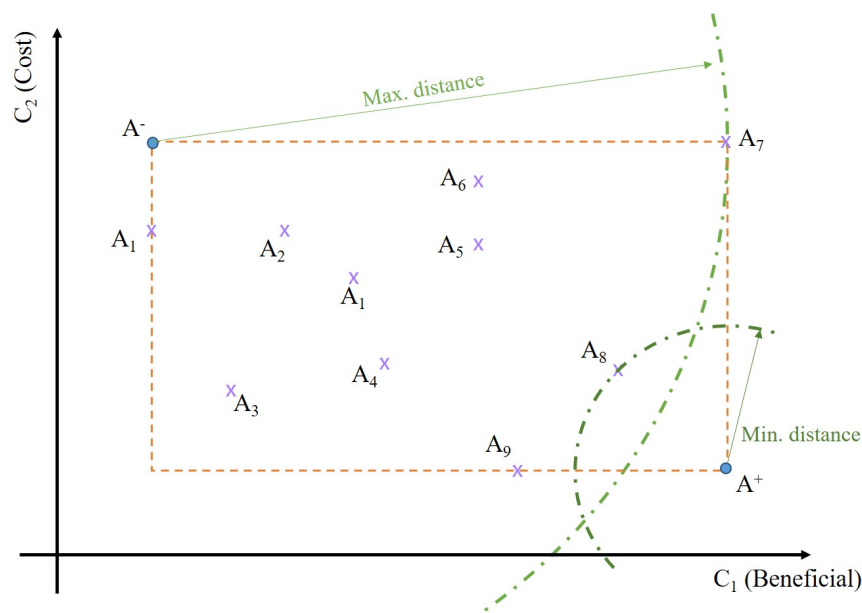


Figure 6.1: TOPSIS ideal solutions given the set of alternatives $\mathcal{A} = \{A_1, \dots, A_9\}$, evaluate on criteria C_1 (Beneficial) and C_2 (Cost).

does not fall into those categories, but in the so-called Multi-Criteria Multi-Decision-Making (MCMDM) problem [Madani and R., 2011].

A MCMDM problem presents several alternatives that have to be agreed upon by several agents, who may have different criteria or assign different importance to the same criteria. Moreover, as in the collaborative MCDM problem, criteria are usually contradictory among each other. In such situations, the MCDM approach presented before may be applied, especially in the case where each agent has only one criterion, a situation that is mathematically equivalent to a single decision-maker with several criteria [Madani and R., 2011, Hipel et al., 1993]. However, this enforces that the outcome of the analysis is restricted to those alternatives that involve collaboration among agents (non-dominant or Pareto optimal), that is, agents will follow the outcome even if it is not optimal for their interests.

However, this situation can be understood instead as a game theoretic problem with multiple players and strategies [Madani, 2010, Madani and Hipel, 2011]. Thus, Game Theory [Myerson, 1984] can be used to model and tackle this non-collaborative problem. In Game Theory, the different agents are expected to apply the solution that

better satisfies their interests, instead of agreeing on a common outcome. However, their decisions are conditional to the decision made by the other agents, which is, in principle, not known (although the possible alternative of the other agents may be known). In this context, the agents are expected to perform the action that benefits them better, assuming the other agent will do the same. Thus, Game Theory looks for the outcomes (combinations of the selected alternatives from each agent) that maximise the interest of the different decision-makers, or at least, make all of them not lose with the decision.

This section proposed a methodology that extends the MCDM method introduced above to the non-collaborative case by implementing Game Theory techniques to deal with the different agents' criteria.

6.2.1 Game matrix

While in the collaborative case, optimal decisions were derived from the Alternatives-Criteria or Decision matrix, in a game theoretic problem, decisions are derived from the Game matrix. From the Game matrix, one can assess which are the best outcomes of a given strategy. This matrix either quantifies the value of an alternative for one agent given the alternatives chosen by the others (cardinal case) or sorts the alternatives of one agent based on the other agents' decision (ordinal case). In the following, the process to obtain this matrix is explained.

The first step is to obtain the alternatives and define the criteria for each agent. Note that, contrary to the collaborative case, each agent will have its own set of alternatives, criteria and criteria weighting. Thus, each decision-maker will have its own extended Decision matrix (extended since it depends on the other agents' alternatives). For the rest of the chapter, for the sake of clarity but without losing generality, only two agents are considered. Having obtained the alternatives for each agent and having defined the criteria considered for each of them, it is possible to define the agents' extended

Alternatives-Criteria or Decision matrices:

$$\mathbf{A}^A = \left[\begin{array}{ccc|ccc|c} a_{111}^A & \dots & a_{1C1}^A & a_{112}^A & \dots & a_{1C2}^A & \dots \\ a_{211}^A & \dots & a_{2C1}^A & a_{212}^A & \dots & a_{2C2}^A & \dots \\ \dots & \dots & \dots & \dots & \dots & \dots & \dots \\ a_{A11}^A & \dots & a_{AC1}^A & a_{A12}^A & \dots & a_{AC2}^A & \dots \end{array} \right], \quad (6.12)$$

where a_{ijk}^A is the value of alternative i (can or cannot be normalised) of decision-maker A under criteria j , given that decision-maker B chooses its alternative k . A similar matrix, \mathbf{A}^B , is built for the other decision-maker. The shape of one agent's extended Alternatives-Criteria matrix is equal to $[N_{alt} \times (N_{crit,a} \cdot N_{crit,b})]$, where N_{alt} is the number of alternatives considered by the agent, $N_{crit,a}$ the number of criteria taken into account by the agent and $N_{crit,b}$ the number of criteria evaluated by the other agent.

To build the Game matrix, it is necessary to integrate the alternative scores over the different criteria given the other agent's answer into a single aggregated score [Zhang et al., 2019b]. Understanding the extended Alternatives-Criteria matrix as a set of Decision *submatrices* (one per the other agent's alternative) as the one present in the collaborative case, the objective is to integrate them into a single column. MCDM techniques (explained in the previous section) can be applied individually to each submatrix to score the alternatives (cardinal case) or rank them (ordinal case). In this work, the ordinary matrix is preferred since it is more robust to input uncertainties. The preferred order of the alternatives is less likely to change to small variations in the input values than the score of the alternatives [Madani and R., 2011]. Thus, each agent's extended Decision matrix is reduced to the integrated Alternatives-Criteria matrix, where each column represents the preferred order of the alternatives of one of the agents, given the

alternatives selected by the other:

$$\mathbf{C}^A = \begin{bmatrix} c_{11}^A & c_{12}^A & \dots & c_{1N}^A \\ c_{21}^A & c_{22}^A & \dots & c_{2N}^A \\ \dots & \dots & \dots & \dots \\ c_{M1}^A & c_{M2}^A & \dots & c_{MN}^A \end{bmatrix}, \quad (6.13)$$

where c_{ij} is the preferred order of the i^{th} alternative of agent A, having integrated all its criteria, with B choosing its alternative j . Similarly, a matrix \mathbf{C}^B can be obtained for the other decision-maker.

Combining both integrated Alternatives-Criteria matrices, \mathbf{C}^A and \mathbf{C}^B , the Game matrix can be easily obtained:

$$\mathbf{Z} = \begin{bmatrix} z_{11} & z_{12} & \dots & z_{1N} \\ z_{21} & z_{22} & \dots & z_{2N} \\ \dots & \dots & \dots & \dots \\ z_{M1} & z_{M2} & \dots & z_{MN} \end{bmatrix}, \quad (6.14)$$

where $z_{ij} = (c_{ij}^A, c_{ij}^B)$ indicates the pair of values with the ranking of decision-maker A's alternative i , given agent B has selected its alternative j , and the ranking of agent's B alternative j given decision-maker A's alternative i . Each element of the Game matrix is called an outcome of the problem, which is the same as a combination of the agents' alternatives.

6.2.2 Equilibrium points

From this matrix, it is possible to apply different stability definitions to find those outcomes that are beneficial for both agents. The stability definitions find the equilibrium outcomes (those where no player losses) by modelling the decision-makers' behaviour, risk considerations, preferences and how the game is played [Madani and Hipel, 2011]. There are different definitions: Nash Stability [Nash, 1950], General Metarationality [Howard, 1971], Symmetric Metarationality [Howard, 1971] or Sequen-

tial Stability [Fraser and Hipel, 1979], among others. In this work, the Nash Stability was implemented to show the Game Theory-based methodology. Nevertheless, other stability definitions can be applied without any major modifications to the method. According to this approach, the equilibrium points in the matrix, if any, are those where, given the other agent's alternatives, moving to another alternative implies a loss (i.e. it implies moving to alternatives with a lower ranking):

$$z_{i^*j^*} \equiv \text{equilibrium point} \iff \begin{cases} c_{i^*j^*}^A = \max_i(c_{ij}^A) \\ c_{i^*j^*}^B = \max_j(c_{ij}^B) \end{cases}. \quad (6.15)$$

Different integrated Alternatives-Criteria matrices can be obtained depending on the combination of normalisation technique (e.g. linear or vector normalisation) and the MCDM method (e.g. WSM, nWSM, WPM, TOPSIS) used to integrate the criteria. Different Game matrices and their Nash Stability points are computed for each of those combinations. The final preferred outcome will be the one being an equilibrium point more frequently. The final result is presented with the matrix **NE**:

$$\mathbf{NE} = \begin{bmatrix} n_{11} & n_{12} & \dots & n_{1N} \\ n_{21} & n_{22} & \dots & n_{2N} \\ \dots & \dots & \dots & \dots \\ n_{M1} & n_{M2} & \dots & n_{MN} \end{bmatrix}, \quad (6.16)$$

where n_{ij} indicates the total number of times the outcome formed by the i^{th} alternative of A and the j^{th} alternative of B has been identified as an equilibrium point after integrating criteria with the different combinations normalisation techniques and MCDM methods.

6.3 Conjunction decision-making: collaborative case

In the previous chapters, an approach to assess encounters under aleatory and epistemic uncertainty and a methodology to compute robust CAMs were proposed. However, depending on several factors (e.g. where to manoeuvre, magnitude of the manoeuvre),

the actual action to be taken by the operator should be selected among many possibilities. However, this decision will be subjected to the criteria the operators consider more important, which can drastically change the final option to be applied.

In this section, a methodology to apply MCDM in the context of conjunction risk assessment to select the best robust CAM is proposed. When there is only one agent involved in the problem or all the agents involved in the decision-making process are known to collaborate, that is, will agree on the decision to be taken to achieve a common goal, the problem can be addressed with MCDM methods [Madani, 2010, Madani and R., 2011, Hipel et al., 1993]. This is the case when a single operator has to select the best evasive action to avoid another object, which is going to be shown below. Other situations falling into this kind of problem would be when more than one satellite belonging to the same operator/constellation has to avoid each other or the same external object, or when a satellite has to deal with subsequent encounters, which will be treated in Chapter 9.

6.3.1 Satellites information

The proposed scenario is a continuation of the case presented in Chapter 5 to show the robust optimal CAM methodology. Two objects are involved in the encounter, one of them with manoeuvre capabilities, on which the operator will employ the MCDM methods, and another whose position is uncertainly known (e.g. a piece of space debris) The initial Keplerian elements at t_0 of both objects appear in Table 5.4. The manoeuvrable satellite is assumed to be perfectly known, while the secondary object is affected by both aleatory uncertainty, modelled with a multivariate Gaussian distribution, and epistemic uncertainty from two sources of information, modelled with the epistemic parameter λ , whose values appear in Table 5.5. The encounter takes place 7442.3 seconds after t_0 and the uncertain geometry at the Time of Closest Approach (TCA) is defined by the interval-defined miss distance and covariance matrix in the impact plane (Table 5.6). The Hard Body Radius (HBR) of the combined objects is 10m.

The manoeuvres are computed for 12.5 revolutions before the encounter, at intervals

of a quarter of orbit: $\Theta_m = k\pi/2$ with $k = \{0, 1, 2, 3, \dots, 50\}$. The maximum thruster capacity is $\delta v_{max} = 0.1$ m/s and the Probability of Collision (PoC) below which brings the risk is $PoC_{0,CAM} = 10^{-6}$. The optimised magnitude of the robust CAM and the associated worst-case PoC can be seen in Figs. 5.10 and 5.11, respectively.

6.3.2 MCDM parameters

Once the different avoidance strategies are computed, the operators need to select the best one, or to take a set of possibilities, ideally ranked in order of preference. Here is where MCDM can be applied for conjunction risk assessment and collision avoidance.

In the proposed example, there are a total of 51 alternatives (the robust optimal manoeuvres computed). Three criteria were considered by the decision-makers: two cost-wise criteria and one risk-wise:

- Collision risk. It is measured with the Probability of Collision Reduction (PoCR), which indicates how much the risk is reduced with respect to the non-avoidance situation and it is defined as:

$$\begin{cases} \text{if } PoC \geq PoC^* & PoCR = 0 \\ \text{if } PoC \leq PoC_{0,CAM} & PoCR = 1 \\ \text{else} & PoCR = \left(\frac{\log(PoC) - \log(PoC^*)}{\log(PoC_{0,CAM}) - \log(PoC^*)} \right)^{16} \end{cases}, \quad (6.17)$$

with PoC^* the PoC without manoeuvre, so that 1 indicates $PoC_{0,CAM}$ is reached and 0 means the initial risk is not reduced (this is a *Beneficial* criteria).

- Manoeuvre cost. Associating the cost of the manoeuvre to the amount of propellant, and assuming it is proportional to the magnitude of the manoeuvre, this criterion is quantified as the δv normalised with the maximum magnitude among the alternatives (this is a *Cost* criterion):

$$ManC = \frac{\delta v}{\max(\delta v)}. \quad (6.18)$$

- Operational cost. Understood as the time the satellite has to be away from its nominal orbit and thus, unable to provide services. It is measured as the angular

length of the arc between the manoeuvre and the encounter, normalised with the maximum length among the alternatives (this is a *Cost* criterion):

$$OpC = \frac{\Delta\theta_m}{\max(\Delta\theta_m)}. \quad (6.19)$$

The returning manoeuvre is not considered in this example. It would add an extra arc to be summed to the avoidance arc length. Other sources of operational cost are not taken into account in this example.

In this scenario, only the vector normalisation defined in Eq. (6.4) is considered to avoid zeros in the Normalised Alternatives-Criteria matrix (and thus, avoiding problems with some of the MCDM techniques). The normalised value of the criteria for each alternative (that is, the Decision matrix) appears in Fig. 6.2.

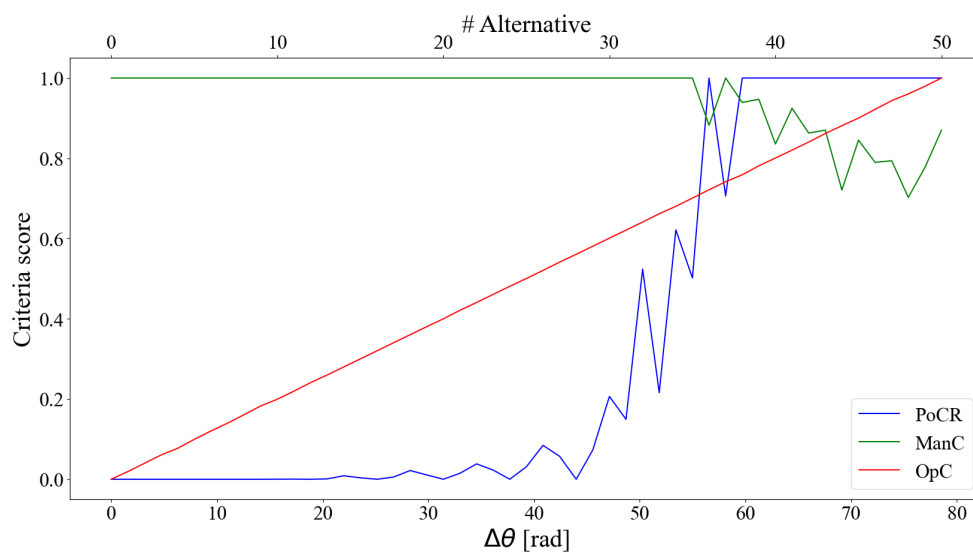


Figure 6.2: Criteria score versus the number of the alternative or, equivalently, the distance between manoeuvre and encounter. Blue, PoCR (beneficial criterion); green, ManC (cost criterion); ref, OpC (cost criterion).

6.3.3 Analysis

Given the alternatives and the criteria, it is possible to rank the alternatives to provide support to the operator once the criteria importance is defined. Four different scenarios are proposed. On the first three, only one of the criteria is prioritised: one where more

importance is given to risk reduction, a second one where more importance is given to the manoeuvre cost, and a final one where importance is given to the operational cost. The distribution is, in all cases, 80% for the more important criterion, and 10% for the other two. Finally, the last scenario shows more equally distributed weights, where contradictory criteria receive the same weight: 45% relative weight for the risk reduction and the operational cost criteria, and the remaining 10% for the manoeuvre cost criterion. In this study, the MCDM techniques used for ranking the alternatives are WSM, WPM and TOPSIS.

Scenario 1

This scenario prioritised the reduction of the PoC, so it is expected that those alternatives providing a higher PoCR rank first: manoeuvres executed half a revolution away from the position of the encounter in the orbit, and the sooner the better. Table 6.1 shows the top-10 alternatives using the different MCDM techniques.

Table 6.1: Top-10 alternatives in the collaborative case Scenario 1.

Rank.	WSM			WPM			TOPSIS		
	θ_m [rad]	PoC [-]	δv [cm/s]	θ_m [rad]	PoC [-]	δv [cm/s]	θ_m [rad]	PoC [-]	δv [cm/s]
1	56.46	10^{-6}	8.82	56.46	10^{-6}	8.82	56.46	10^{-6}	8.82
2	62.66	10^{-6}	8.35	62.66	10^{-6}	8.35	59.39	10^{-6}	9.39
3	68.95	10^{-6}	7.21	59.38	10^{-6}	9.39	61.13	10^{-6}	9.47
4	59.38	10^{-6}	9.39	68.95	10^{-6}	7.21	62.66	10^{-6}	8.35
5	61.13	10^{-6}	9.47	61.13	10^{-6}	9.47	64.19	10^{-6}	9.24
6	65.77	10^{-6}	8.62	65.77	10^{-6}	8.62	65.77	10^{-6}	8.62
7	75.16	10^{-6}	7.02	64.19	10^{-6}	9.24	67.42	10^{-6}	8.70
8	64.19	10^{-6}	9.24	67.42	10^{-6}	8.70	68.95	10^{-6}	7.20
9	67.42	10^{-6}	8.70	75.16	10^{-6}	7.02	72.14	10^{-6}	7.89

From the table, it can be seen that the preferred options are those that reduce the risk below the threshold, as could be expected when prioritising the risk reduction. Those alternatives occur when executing the CAM early and are associated with lower magnitudes of the manoeuvre. It can be seen in Table 6.2 that the different MCDM strategies agree on the ranking. The first option in all of them is the same, which

corresponds to the later manoeuvre achieving $PoC < PoC_{0,CAM}$, also with a $\delta v < \delta v_{max}$. The rest of the alternatives in the top-10 are the same, although in a slightly different order depending on the technique. In general, manoeuvres executing later, as soon as the threshold risk is reached, are preferred, although the magnitude of the CAM may modify this rule (remember that in this example, both Manoeuvre Cost (ManC) and Operational Cost (OpC) has a 10% relative weight).

Table 6.2: Top-10 alternatives identifier in the collaborative case Scenario 1.

Technique	Ranking									
WSM	36	40	44	38	39	42	48	41	43	46
WPM	36	40	38	44	39	42	41	43	48	46
TOPSIS	36	38	39	40	41	42	43	44	45	46

Scenario 2

In this case, despite seeming an opposite situation, the expected top-ranked alternatives may not differ too much, since it is the cost of the manoeuvre (which is related to the PoC reduction) which drives the decision. In this scenario, alternatives with a lower δv are expected to be preferred, which tends to occur at early manoeuvre, where the PoC can be reduced below the threshold. Table 6.3 shows the top-10 alternatives.

Table 6.3: Top-10 alternatives in the collaborative case Scenario 2.

Rank.	WSM			WPM			TOPSIS		
	θ_m [rad]	PoC [-]	δv [cm/s]	θ_m [rad]	PoC [-]	δv [cm/s]	θ_m [rad]	PoC [-]	δv [cm/s]
1	75.16	10^{-6}	7.02	68.95	10^{-6}	7.20	68.95	10^{-6}	7.20
2	68.95	10^{-6}	7.20	75.16	10^{-6}	7.02	75.16	10^{-6}	7.02
3	76.64	10^{-6}	7.76	72.14	10^{-6}	7.89	72.14	10^{-6}	7.89
4	72.14	10^{-6}	7.89	76.64	10^{-6}	7.76	76.64	10^{-6}	7.76
5	73.84	10^{-6}	7.93	73.84	10^{-6}	7.93	73.84	10^{-6}	7.93
6	62.66	10^{-6}	8.35	62.66	10^{-6}	8.35	62.66	10^{-6}	8.35
7	70.44	10^{-6}	8.45	56.46	10^{-6}	8.82	70.44	10^{-6}	8.45
8	56.46	10^{-6}	8.82	70.44	10^{-6}	8.45	65.76	10^{-6}	8.62
9	65.76	10^{-6}	8.62	65.76	10^{-6}	8.62	56.46	10^{-6}	8.82
10	67.42	10^{-6}	8.70	67.42	10^{-6}	8.70	67.42	10^{-6}	8.70

From the table, those alternatives presenting a smaller magnitude are prioritised. This classification is similar to the previous one since a reduction of the risk below $PoC_{0,CAM}$ activates the optimisation of the magnitude. It suggests that these two criteria may be combined together for a more optimised approach to this problem. Nevertheless, the classification is slightly different than in Scenario 1, ranking first earlier manoeuvres, since, they have a bigger impact reducing the cost. It also explains the better agreement (with respect to the previous scenario) between sources, as shown in Table 6.4: earlier manoeuvres benefit the magnitude criterion (with bigger relative weight), are indifferent to the reduction risk criterion (as long as the PoC threshold is achieved), and only are negative to the operational cost criterion, which has a low relative weight.

Table 6.4: Top-10 alternatives identifier in the collaborative case Scenario 2.

Technique	Ranking									
WSM	48	44	49	46	47	40	45	36	42	43
WPM	44	48	46	49	47	40	36	45	42	43
TOPSIS	44	48	46	49	47	40	45	42	36	43

Scenario 3

This example, due to the definition of the operational cost, is expected to prioritise later manoeuvres, since they require to be less time away from the operational orbit. Table 6.5 shows the top-10 alternatives.

Finally, when prioritising the operational cost the results give the expected results: the later the manoeuvre the better. For both WSM and TOPSIS, the first option is not to manoeuvre (no modification of the nominal orbit), and the following alternatives are exactly in order of the distance between the CAM execution and the encounter. The bigger weight to the only criterion prioritising later manoeuvres explains the perfect agreement between techniques shown in Table 6.6, except for WPM, whose results suggest the appearance of 0 during the normalisation process.

Table 6.5: Top-10 alternatives in the collaborative case Scenario 3.

Rank.	WSM			WPM			TOPSIS		
	θ_m [rad]	PoC [-] ($\cdot 10^{-3}$)	δv [cm/s]	θ_m [rad]	PoC [-] ($\cdot 10^{-6}$)	δv [cm/s]	θ_m [rad]	PoC [-] ($\cdot 10^{-3}$)	δv [cm/s]
1	0	9.1	10	56.46	1	8.82	0	9.1	10
2	1.49	1.77	10	59.38	1	9.39	1.49	1.77	10
3	3.11	2.09	10	61.13	1	9.47	3.11	2.09	10
4	4.73	7.3	10	62.66	1	8.35	4.73	7.3	10
5	6.04	5.24	10	64.19	1	9.24	6.04	5.24	10
6	7.79	3.95	10	65.76	1	8.62	7.79	3.95	10
7	9.40	0.5	10	67.42	1	8.70	9.40	0.5	10
8	10.93	8.02	10	68.95	1	7.20	10.93	8.02	10
9	12.59	1.61	10	53.22	1.305	10	12.59	1.61	10
10	14.30	0.207	10	58.03	1.216	10	14.30	0.207	10

Table 6.6: Top-10 alternatives identifier in the collaborative case Scenario 3.

Technique	Ranking									
WSM	0	1	2	3	4	5	6	7	8	9
WPM	36	38	39	40	41	42	43	44	34	37
TOPSIS	0	1	2	3	4	5	6	7	8	9

Scenario 4

Finally, this scenario shows a more realistic situation, where different criteria are equally important, so trade-off solutions have to be found. Table 6.7 shows the top-10 alternatives on this scenario.

The results show a trade-off between criteria. All the alternatives in the table reduce the risk below the threshold as in Scenario 1. However, the order of the alternatives follows a perfect increase in the distance to the encounter, reflecting the influence of the OpC criterion, as in Scenario 3, which prefers later manoeuvres. Earlier manoeuvres are not ranked first due to this last criterion, while earlier manoeuvres are discarded since they do not reduce the risk enough. In this case, all three techniques agree on the outcome with no difference in the top-10 (except the seventh/eighth alternative with the WSM) as can be seen in Table 6.8.

Table 6.7: Top-10 alternatives in the collaborative case Scenario 4.

Rank.	WSM			WPM			TOPSIS		
	θ_m [rad]	PoC [-]	δv [cm/s]	θ_m [rad]	PoC [-]	δv [cm/s]	θ_m [rad]	PoC [-]	δv [cm/s]
1	56.46	10^{-6}	8.82	56.46	10^{-6}	8.82	56.46	10^{-6}	8.82
2	59.38	10^{-6}	9.39	59.38	10^{-6}	9.39	59.38	10^{-6}	9.39
3	61.13	10^{-6}	9.47	61.13	10^{-6}	9.47	61.13	10^{-6}	9.47
4	62.66	10^{-6}	8.35	62.66	10^{-6}	8.35	62.66	10^{-6}	8.35
5	64.19	10^{-6}	9.24	64.19	10^{-6}	9.24	64.19	10^{-6}	9.24
6	65.76	10^{-6}	8.62	65.76	10^{-6}	8.62	65.76	10^{-6}	8.62
7	68.95	10^{-6}	7.20	67.42	10^{-6}	8.70	67.42	10^{-6}	8.70
8	67.42	10^{-6}	8.70	68.95	10^{-6}	7.20	68.95	10^{-6}	7.20
9	70.44	10^{-6}	8.45	70.44	10^{-6}	8.45	70.44	10^{-6}	8.45
10	72.14	10^{-6}	7.89	72.14	10^{-6}	7.89	72.14	10^{-6}	7.89

Table 6.8: Top-10 alternatives identifier in the collaborative case Scenario 4.

Technique	Ranking										
WSM	36	38	39	40	41	42	44	43	45	46	
WPM	36	38	39	40	41	42	43	44	45	46	
TOPSIS	36	38	39	40	41	42	43	44	45	46	

6.4 Conjunction decision-making: non-collaborative case

This section presents an example of a non-collaborative close encounter between two satellites operated by different agents.

6.4.1 Satellites information

If the two objects involved in the conjunction are active satellites operated by different agents, the optimal solution could be different for each of them, even though none of the agents desires to lose the satellite in a collision. Different perceptions of the risk, the preference of not spending propellant or not stopping the nominal activity to avoid the conjunction may lead to different optimal solutions for each decision-maker. Thus, the Game Theory approach presented in Section 6.2 should be applied.

In this example, two operational satellites in a close encounter course are proposed.

The conjunction occurs 43,200 seconds after the initial time, t_0 . The initial orbital elements at t_0 appear in Table 6.9. *Satellite A* is assumed to be perfectly known, while *Satellite B* is assumed to be affected by both aleatory and epistemic uncertainty. Note that the choice of which satellite is affected by uncertainty does not change the methodology and the outcome of the decision because both operators are assumed to be able to compute a single PoC, pre and post-manoeuvre. In the case in which the computation of the PoC of one operator is unknown to the other, the game becomes stochastic and the approach in this work has to be further extended.

Table 6.9: Objects' Keplerian elements at initial epoch t_0 . Units in km and deg.

Keplerian elements	Units	Satellite A	Satellite B
Semimajor axis (a)	[km]	7100.0	6944.26
Eccentricity (e)	[-]	0.0	0.031
Inclination (i)	[rad]	60.0	141.04
Right Ascension of the Ascending Node (Ω)	[rad]	0.0	335.26
Argument of Perigee (ω)	[rad]	0.0	116.15
True Anomaly (θ)	[rad]	252.57	47.03

The aleatory uncertainty for the *Satellite B* position is modelled by the covariance matrix at the initial position expressed in the $\langle R, T, H \rangle$,

$$\bar{\Sigma}_{2,rth}(t_0) = \begin{bmatrix} 0.104^2 & 0 & 0 \\ 0 & 0.556^2 & 0 \\ 0 & 0 & 0.139^2 \end{bmatrix} km^2, \quad (6.20)$$

while the epistemic uncertainty is modelled with the epistemic parameter $\lambda = [\lambda_\mu, \lambda_\sigma]$, one per each source of information, affecting only the size of the ellipsoid, but not its position ($\lambda_\mu = \mathbf{0}$). In this example, two sources are considered to provide information: Source a scaling up the uncertainty ellipsoids and b shrinking it, with:

$$\lambda_{\sigma,a} = [1, 4] \quad (6.21)$$

$$\lambda_{\sigma,b} = [1/5, 1/2]. \quad (6.22)$$

Thus, the encounter geometry is defined by the intervals of the uncertain variables in Table 6.10. The HBR is equal to 10m, computing the PoC with Eq. (3.1).

Table 6.10: Uncertain encounter geometry with 2 sources providing information. Upper and lower bound of the components of miss distance and covariance matrix in the impact plane.

Component	Units	Source 1	Source 2
μ_ξ	[km]	[0.02855,0.08342]	$[1.263 \cdot 10^{-3}, 0.01529]$
μ_ζ	[km]	[-0.6327,0.7230]	[-0.2317,0.2542]
σ_ξ^2	[km ²]	[0.1208,0.4353]	[0.02530,0.05332]
σ_ζ^2	[km ²]	[140.265,505.054]	[29.311,61.202]
$\sigma_{\xi\zeta}$	[km ²]	[-14.586,-4.0744]	[-1.8012,-0.8572]

As indicated in Section 6.2, the first step is to obtain the alternatives and define the criteria for each agent, in this case, the two operators of the satellites involved in the encounter. For each of the agents, the alternatives are obtained by changing the CAM execution position: $\theta_m^A \in \Theta_m^A$ and $\theta_m^B \in \Theta_m^B$, with $\Theta_m^A \neq \Theta_m^B$ in general. The robust optimal CAMs are computed at the following execution positions for each satellite: $\Theta_m^A = \{0, 9\pi, 17\pi\}$ rad, $\Theta_m^B = \{0, 7\pi, 11\pi, 15\pi\}$ rad, measured as distance to the encounter.

In this example, the two decision-makers consider the same two criteria: the risk reduction, quantified with the PoCR in Eq. (6.17), and the cost of the manoeuvre, measured as the δv required. Each agent may present different risk and cost perceptions. Two different avoidance cases were studied by changing the maximum impulse capacity of each satellite and the PoC threshold of each operator. Although in these cases both examples present the same parameters, they can be different without affecting the method. Table 6.11 includes the CAM parameters for both cases. For simplicity of the

Table 6.11: PoC threshold and maximum impulse capacity of each satellite involved in the encounter for the two cases considered.

Case	Satellite A		Satellite B	
	δv_{max}^A [km/s]	$PoC_{0,CAM}^A$	δv_{max}^B [km/s]	$PoC_{0,CAM}^B$
1	$2.5 \cdot 10^{-4}$	10^{-6}	$2.5 \cdot 10^{-4}$	10^{-6}
2	$5 \cdot 10^{-4}$	10^{-5}	$5 \cdot 10^{-4}$	10^{-5}

analysis, no returning strategy is considered. Including returning manoeuvres would only introduce new alternatives and, possibly, new criteria. Other than this, the method would remain the same.

6.4.2 Game theory matrices

This situation can be described as a MCMDM problem with 2 decision-makers with two criteria each, selecting among four alternatives the *Satellite A* and three alternatives the *Satellite B*. Eqs. (6.23) and (6.24) include the Alternatives-Criteria matrices for *Case 1*, and Eqs. (6.25) and (6.26) for *Case 2*. The even columns indicate the velocity change required for the satellite, given the other satellite's action, and the odd columns indicate the PoCR, where 0 means no improvement with respect to the pre-CAM situation, and 1 is a reduction of *PoC* below the risk threshold. Note that for *Case 1*, if only one satellite manoeuvres, the risk threshold is not reached for any of the satellites, while in *Case 2*, there are situations where if only one satellite manoeuvres, the safety threshold can be reached by the moving satellite, but also for the other one.

$$\mathbf{A}_1^A = \left[\begin{array}{cc|cc|cc|cc} 0 & 0 & 0.056 & 0 & 0.139 & 0 & 0.367 & 0 \\ 0.031 & 2.5 \cdot 10^{-4} & 1 & 1.925 \cdot 10^{-4} & 1 & 1.875 \cdot 10^{-4} & 1 & 1.75 \cdot 10^{-4} \\ 0.156 & 2.5 \cdot 10^{-4} & 1 & 1.875 \cdot 10^{-4} & 1 & 1.75 \cdot 10^{-4} & 1 & 1.675 \cdot 10^{-4} \end{array} \right] \quad (6.23)$$

$$\mathbf{A}_1^B = \left[\begin{array}{cc|cc|cc|cc} 0 & 0 & 0.031 & 0 & 0.156 & 0 & 0.367 & 0 \\ 0.056 & 2.5 \cdot 10^{-4} & 1 & 1.925 \cdot 10^{-4} & 1 & 1.875 \cdot 10^{-4} & 1 & 1.75 \cdot 10^{-4} \\ 0.139 & 2.5 \cdot 10^{-4} & 1 & 1.875 \cdot 10^{-4} & 1 & 1.75 \cdot 10^{-4} & 1 & 1.675 \cdot 10^{-4} \\ 0.367 & 2.5 \cdot 10^{-4} & 1 & 1.75 \cdot 10^{-4} & 1 & 1.675 \cdot 10^{-4} & 1 & 1.675 \cdot 10^{-4} \end{array} \right] \quad (6.24)$$

$$\mathbf{A}_2^A = \left[\begin{array}{cc|cc|cc|cc} 0 & 0 & 1 & 0 & 0.952 & 0 & 0.971 & 0 \\ 0.918 & 1.6 \cdot 10^{-4} & 1 & 9.1 \cdot 10^{-50} & 1 & 9.4 \cdot 10^{-5} & 1 & 9.6 \cdot 10^{-5} \\ 0.982 & 1.7 \cdot 10^{-4} & 1 & 8.2 \cdot 10^{-5} & 1 & 8.3 \cdot 10^{-5} & 1 & 8.5 \cdot 10^{-5} \end{array} \right] \quad (6.25)$$

$$\mathbf{A}_2^B = \begin{bmatrix} 0 & 0 & 0.918 & 0 & 0.982 & 0 \\ 1 & 1.4 \cdot 10^{-4} & 1 & 7.3 \cdot 10^{-5} & 1 & 7.6 \cdot 10^{-5} \\ 0.952 & 1.2 \cdot 10^{-4} & 1 & 6.3 \cdot 10^{-5} & 1 & 6.6 \cdot 10^{-5} \\ 0.971 & 1.0 \cdot 10^{-4} & 1 & 5.5 \cdot 10^{-5} & 1 & 5.8 \cdot 10^{-5} \end{bmatrix} \quad (6.26)$$

Five different subscenarios were analysed for each case: i) criteria in both satellites equally weighted, ii) both satellites giving more importance to PoCR, iii) both satellites giving more importance to ManC, iv) *Satellite A* giving more importance to PoCR and *Satellite B* to the ManC, v) *Satellite A* giving more importance to ManC and *Satellite B* to PoCR.

For all the subscenarios, the criteria are integrated considering two normalisation approaches: maximum-linear and vector; and four MCDM methods: WSM, nWSM, WPM, TOPSIS. An example of the ordinal integrated Alternatives-Criteria matrices, \mathbf{C}^A and \mathbf{C}^B , for *Case 1 - Subscenario i* using Maximum-Linear normalisation and WPM method to integrate the criteria are presented in Eq. (6.27), and for *Case 2 - Subscenario i* using Maximum-Linear normalisation and WPM method in Eq. (6.28).

$$\mathbf{C}_{1,\text{lin},\text{WPM}}^A = \begin{bmatrix} 1 & 2 & 2 & 2 \\ 2 & 1 & 1 & 1 \\ 1 & 0 & 0 & 0 \end{bmatrix}, \quad \mathbf{C}_{1,\text{lin},\text{WPM}}^B = \begin{bmatrix} 1 & 2 & 1 \\ 1 & 0 & 0 \\ 2 & 1 & 2 \\ 3 & 3 & 3 \end{bmatrix}, \quad (6.27)$$

$$\mathbf{C}_{2,\text{lin},\text{WPM}}^A = \begin{bmatrix} 1 & 2 & 2 & 2 \\ 2 & 1 & 1 & 1 \\ 1 & 0 & 0 & 0 \end{bmatrix}, \quad \mathbf{C}_{2,\text{lin},\text{WPM}}^B = \begin{bmatrix} 1 & 3 & 3 \\ 1 & 0 & 0 \\ 2 & 1 & 1 \\ 3 & 2 & 2 \end{bmatrix}, \quad (6.28)$$

where the element c_{ij}^A indicates the order preference of the i^{th} alternative of *Satellite A*, given *Satellite B* chooses alternative j , with the highest values for the most preferred alternatives in each column; and the element c_{kp}^B the preference of the k^{th} alternative of *Satellite B*, given the *Satellite A* chooses alternative p . A lower number indicated a prioritised option.

6.4.3 Analysis

In the following, each subscenario for both cases is analysed. The Game matrices are shown, with the best outcome in bold as the solution appearing as a Nash equilibrium point for most of the normalisation and MCDM techniques combinations.

Case 1

In this scenario, is only one satellites manoeuvre, the risk reduction is not reached by any, making more likely to find an agreed solution.

- *Subscenario i.*

$$\mathbf{NE}_i = \begin{bmatrix} 0 & 0 & 0 & 2 \\ 0 & 0 & 0 & 0 \\ 2 & 0 & 0 & \mathbf{4} \end{bmatrix}. \quad (6.29)$$

This subscenario tries to optimise both cost and risk for both satellites. The preferred outcome is both satellites manoeuvring the earlier, so both reduce the risk below the threshold ($PoCR^A = PoCR^B = 1$) and both have to expend less propellant, assuming the other will do the same. However, not all the combinations of normalisation and MCDM techniques agree on this outcome.

- *Subscenario ii.*

$$\mathbf{NE}_{ii} = \begin{bmatrix} 0 & 0 & 0 & 0 \\ 0 & 0 & 0 & 0 \\ 0 & 0 & 0 & \mathbf{8} \end{bmatrix}. \quad (6.30)$$

If the PoC is to be minimised, the preferred option, independently of the method, is an outcome where both satellites manoeuvres, reducing the risk below the threshold ($PoCR^A = PoCR^B = 1$).

- *Subscenario iii.*

$$\mathbf{NE}_{iii} = \begin{bmatrix} \mathbf{7} & 0 & 0 & 2 \\ 1 & 0 & 0 & 0 \\ 0 & 0 & 0 & 0 \end{bmatrix}. \quad (6.31)$$

If the cost is prioritised, the preferred option is, obviously, where no satellites manoeuvre ($\delta v^A = \delta v^B = 0$), even if there is no reduction of risk ($PoCR^A = PoCR^B = 0$).

- *Subscenario iv.*

$$\mathbf{NE}_{iv} = \begin{bmatrix} \mathbf{4} & 0 & 0 & 0 \\ \mathbf{3} & 0 & 0 & 1 \\ 0 & 0 & 0 & 0 \end{bmatrix}. \quad (6.32)$$

When *Satellite A* prioritises the risk and *Satellite B* the reduction of the cost, a curious situation is obtained: the most common equilibrium points appear for the outcome where no manoeuvre is executed. The explanation can be that due to the prioritisation of cost reduction for *Satellite B*, it will prefer alternatives where it does not manoeuvre. Given this outcome, the reduction of PoC for *Satellite A* is very small no matter the manoeuvre, so the small contribution of the ManC criterion on this satellite may prioritise the lack of manoeuvre. Other than this, the second alternative is a more expected outcome where only *Satellite A* manoeuvres.

- *Subscenario v.*

$$\mathbf{NE}_v = \begin{bmatrix} 0 & 0 & 0 & \mathbf{8} \\ 0 & 0 & 0 & 0 \\ 0 & 0 & 0 & 0 \end{bmatrix}. \quad (6.33)$$

This scenario is the opposite of the previous one: *Satellite A* search to minimise the cost, while *Satellite B* to minimise the risk. The preferred option, independently of the method, is the one where *Satellite A* does not manoeuvre (minimising the cost) and *Satellite B* manoeuvres the earliest: reducing the risk to the threshold ($PoCR^B = 0.367$). In this case, the manoeuvre of *Satellite B* has a bigger impact on the PoC reduction, so the no manoeuvring option is discarded.

Case 2

In this case, if only one satellite manoeuvres, the risk threshold is reached for both satellites, making finding a trade-off solution more challenging.

- *Subscenario i.*

$$\mathbf{NE}_i = \begin{bmatrix} 0 & 0 & 0 & \mathbf{8} \\ 0 & 0 & 0 & 0 \\ 0 & 0 & 0 & 0 \end{bmatrix}. \quad (6.34)$$

The preferred option, in this case, is where only one satellite manoeuvres, executing the CAM at the cheapest position, since in this way, the threshold is reached, and the cost is minimised. One satellite does not spend anything and the other spends the minimum possible: for the outcome (1,4), being an equilibrium point eight times, $\delta v^A = 0$ cm/s and $\delta v^B = 10$ cm/s, while $PoCR^A = PoCR^B = 0.971$.

- *Subscenario ii.*

$$\mathbf{NE}_{ii} = \begin{bmatrix} 0 & 0 & 0 & \mathbf{7} \\ 0 & 0 & 0 & 0 \\ \mathbf{7} & 0 & 0 & 0 \end{bmatrix}. \quad (6.35)$$

Similarly, the preferred outcomes are those where only one satellite manoeuvres. Since the threshold is reached (or almost) when a single satellite manoeuvres, these options are preferred over those with the two satellites manoeuvring. The alternative is always the manoeuvre which reduces the risk the most, implementing the action the earliest. The complication of this situation is that both satellites would choose the outcome where the other one manoeuvres, potentially jeopardising the safety of the encounter.

- *Subscenario iii.*

$$\mathbf{NE}_{iii} = \begin{bmatrix} \mathbf{6} & 0 & 0 & 2 \\ 2 & 0 & 0 & 0 \\ 0 & 0 & 0 & 0 \end{bmatrix}. \quad (6.36)$$

As in the previous case, if the cost is to be optimised by both satellites, the preferred option is no manoeuvring, so no propellant is expended and the manoeuvre

has no cost.

- *Subscenario iv.*

$$\mathbf{NE}_{iv} = \begin{bmatrix} 0 & 0 & 0 & 2 \\ 1 & 0 & 0 & 0 \\ \mathbf{7} & 0 & 0 & 0 \end{bmatrix}. \quad (6.37)$$

If *Satellite A* prioritised the risk and *Satellite B* the cost, the preferred option where *Satellite B* does not manoeuvre and *Satellite A* does it at the option where the maximum risk reduction is achieved: $PoCR^A = 0.982$.

- *Subscenario v.*

$$\mathbf{NE}_v = \begin{bmatrix} 0 & \mathbf{7} & 0 & 1 \\ 0 & 0 & 0 & 0 \\ 0 & 0 & 0 & 0 \end{bmatrix}. \quad (6.38)$$

If *Satellite A* prioritised the cost and *Satellite A* the risk, the situation is the opposite than in the previous scenario and the same for the preferred option: *Satellite A* does not manoeuvre and *Satellite B* does it at the position where a maximum risk reduction is achieved: $PoCR^B = 1$.

6.5 Chapter summary

This chapter presented a decision-making system to support operators with the robust optimal CAM allocation tasks under different criteria. If the CARA analysis of a close encounter requires a CAM, several manoeuvres may be possible (e.g. changing the execution position, the magnitude). This chapter introduced two methodologies to deal with this situation.

A MCDM-based method was presented to rank a set of alternatives in the collaborative scenario. This case includes situations involving a single operator (both operating one or more satellites) or a number of operators agreeing on the outcome. The method was illustrated with an example when the set of robust optimal manoeuvres executed at different distances to the encounter had to be ranked according to contradictory criteria. A comparison of the use of different techniques and different criteria importance

was performed.

This decision-making support method based on MCDM will be applied in Chapter 9 to more challenging situations involving multiple encounters.

The chapter also introduced a methodology to deal with non-collaborative scenarios, where the outcome of the decision-makers may not reach a consensus outcome. Game Theory in combination with MCDM was implemented to obtain the best equilibrium solution for the agents involved in the problem, that is, to find the solution where no agent loses, thus, being the most likely solution to be implemented by all of them. More specifically, the methodology was applied to a close encounter involving two different operators, with no communication between them, and where none of them is certain about the other's action. Different scenarios were used to illustrate the methodology and highlight the differences in the reached equilibrium points according to the hypothesis used, that is, the criteria and their importance for each decision-maker.

Part II

Applications

Chapter 7

Robust classification system on real encounter scenarios

The content of this chapter was partially published in:
Sánchez, L., Vasile, M., Sanvido, S, Maerz, K. and Taillan, C.,
“Treatment of epistemic uncertainty in conjunction analysis with
Dempster-Shafer theory”, *Advances in Space Research*,
submitted. [Sánchez et al., 2024]

The first Part I of this work focused on the development of new methods to address the problem of epistemic uncertainty in the conjunction risk assessment, developing a framework to provide support to operators on robust conjunction risk assessment. However, the proposed methodologies were tested on synthetic data. This chapter verifies the proposed approaches by running the risk assessment on a number of real encounters and comparing the analysis with the real decision process carried out by the operators. This step is essential to prove the right operation of the system if it aims to be implemented as an operational tool.

The rest of the chapter is structured as follows. Initially, in Section 7.1, the epistemic classification criterion introduced in Chapter 3 is revised to use the area between the curves as the uncertainty metric. Section 7.2 proposes a methodology to obtain adequate values for the epistemic threshold used by the classification criterion. In Section 7.3, real encounters examples provided by Centre National d’Etudes Spatiales

(CNES) and the European Space Agency's (ESA) European Space Operations Centre (ESOC) are analysed using the epistemic classification criterion and the methodology introduced in Chapter 4. Section 7.4 extends the approach in the previous section to perform a statistical comparison between ESOC approach and the proposed methodology in a database of thousands of real Conjunction Data Messages (CDMs). Finally, Section 7.5 concludes the chapter.

7.1 Area-based epistemic classification criterion

When using the classification criterion proposed in Chapter 3 on real conjunctions, there is the necessity to incorporate an additional class to the existing ones. For detected encounters whose time to the conjunction is close ($t2TCA < T_1$), the criterion classified events within two possible categories: *Class 5* if no further action is required due to low-risk, and *Class 1* if a manoeuvre is proposed to the operator. However, the latter category can be achieved either when there is high evidence of the high risk of the event or due to uncertainty in making a confident decision on the level of risk. For *Class 1* events, although the final outcome is the same from the methodological point of view, from the operational point of view, it is relevant to distinguish between these two categories, so the operator can have an extra piece of information regarding the uncertainty of the event when designing the Collision Avoidance Manoeuvre (CAM) or deciding on its final execution. *Class 0* is thus proposed for those highly uncertain events whose last observation update is close to the conjunction time.

Moreover, certain situations can lead to contradictory results when using the vertical gap (Degree of Uncertainty, DoU) to determine the level of uncertainty on the sequence of CDMs. In general, a big gap between the Plausibility (Pl) and the Belief (Bel) at a given value of Probability of Collision (PoC) indicates a lack of confidence in that value due to epistemic uncertainty, but limiting the evaluation of the gap to a single value restrict the analysis capacity. One example is when $Bel(PoC_0) = 0$ and $Pl(PoC_0) < 1$. It may happen that for $PoC < PoC_0$, the gap is greater than the threshold. However, due to a lack of support on bigger values of PoC , the value of Pl decreases and combined

with the null value of the Bel , limits the maximum value $DoU(PoC_0) < \Delta$ may achieve. This lower value on DoU would not happen due to the lack of uncertainty, but because of the minimum and maximum values that Pl and Bel may take, as occur in Fig. 7.13. A different example can be found in Section 7.3.1, where a clear high-risk event may be misclassified as *Uncertain* if only considering the vertical gap: while DoU is zero or close to zero for most of the PoC values, around the PoC threshold, the values is close to one. Since the values of PoC in the sequence of CDMs are concentrated in a narrow range close to the risk threshold, the Bel sharply jump from one to zero, while the value of Pl remains high, before drastically jumping as well to values close to zero, as seen in Fig. 7.5. This implies that $DoU(PoC_0) \sim 1$, while the actual epistemic uncertainty affecting the event is low. In this case, adding information on the horizontal gap would provide a more precise classification.

To overcome the limitations of the use of the vertical gap, a modification of the evidence-based classification criterion in Table 3.7 is proposed here based on the total area between the Pl and Bel curves. This new criterion appears in Table 7.1. This change is reflected in the third column (the confidence filter), where the value of the DoU at the risk threshold is changed by the area between the curves, $A_{Pl,Bel}$, and the Δ threshold is replaced by an area threshold, A_0 . The addition of the sixth class can be seen in the fourth column, with the inclusion of the *Class 0*. Two additional minor changes are included in this new criterion. First, the support filter (the second column of the table) is based now on the value of the Pl at the risk threshold, instead of the value of the Bel . The reason for the change is that after evaluating the criterion on real data, it was detected that Bel tends to drop quicker than in virtual data, leading to overestimated risk of safe encounters. The other modification on the criterion affects encounters with $t2TCA \geq T_2$ (last row of the table). Due to the relatively long distance to the encounters and, generally, the scarcer data up to this point, it is common not to completely discard events at this stage since confidence decisions are, in general, hard to make. Thus, events detected well in advance are classified as *Class 3*.

When computing the area between the curves, one consideration should be taken. Although the horizontal axis is represented by the PoC, using directly this value may

Table 7.1: Evidence-based classification criterion using the area between the curves.

Time to TCA	Pl at PoC_0	Area	Class
$t_{TCA} < T_1$	$Pl(PoC_0) < PoC_0$	-	5
	$Pl(PoC_0) \geq Pl_0$	$A_{Pl,Bel} \leq A_0$	1
		$A_{Pl,Bel} > A_0$	0
$T_1 \leq t_{TCA} < T_2$	$Pl(PoC_0) < Pl_0$	-	4
	$Pl(PoC_0) \geq Pl_0$	$A_{Pl,Bel} \leq A_0$	2
		$A_{Pl,Bel} > A_0$	3
$T_2 \leq t_{TCA}$	-	-	3

lead to wrong classifications: for example, assuming a jump from one to zero in *Bel* at a certain value of PoC and the same jump for *Pl* at a higher value of risk, the value of the area if using the PoC in the horizontal axis would be much greater when the jump occurs at higher values of PoC. For example, if the jump in *Bel* takes place at 10^{-5} and the jump in *Pl* at 10^{-4} , the area between curves would be equal to $9 \cdot 10^{-5}$. However, if the lost of confidence takes place at 10^{-2} and 10^{-1} , respectively, the value of the are is 0.09. It seems that the second case is much more affected by uncertainty, while in reality, the level of uncertainty is the same in both cases.

If in the figures presented in the previous chapters showing the evolution of *Pl* and *Bel* curves, the horizontal axis was presented using the logarithmic scale for the horizontal axis, $\log PoC$ (see Fig. 7.1). Thus, the area between curves should be computed as:

$$A_{Pl,Bel} = \int_{\log(\underline{PoC})}^0 Pl(\Omega) d(\log(PoC)) - \int_{\log(\underline{PoC})}^0 Bel(\Omega) d(\log(PoC)) \quad (7.1)$$

where $\underline{PoC} > 0$ is a minimum value for the PoC to avoid error in the logarithm, since $PoC \in [0, 1]$. Thus, the area may vary in $A_{Pl,Bel} \in [0, A_{max}]$ with $A_{max} = -\log_{10}(\underline{PoC})$. The case where $A_{Pl,Bel} = 0$ indicates a case where $Pl = Bel$ for all values of $PoC \in [\underline{PoC}, 1]$ (no epistemic uncertainty), while the case of $A_{Pl,Bel} = A_{max}$ represents a case dominated by epistemic uncertainty when every value is possible, $Pl = 1$, but no value receives full support, $Bel = 0$, for all values of $PoC \in [\underline{PoC}, 1]$.

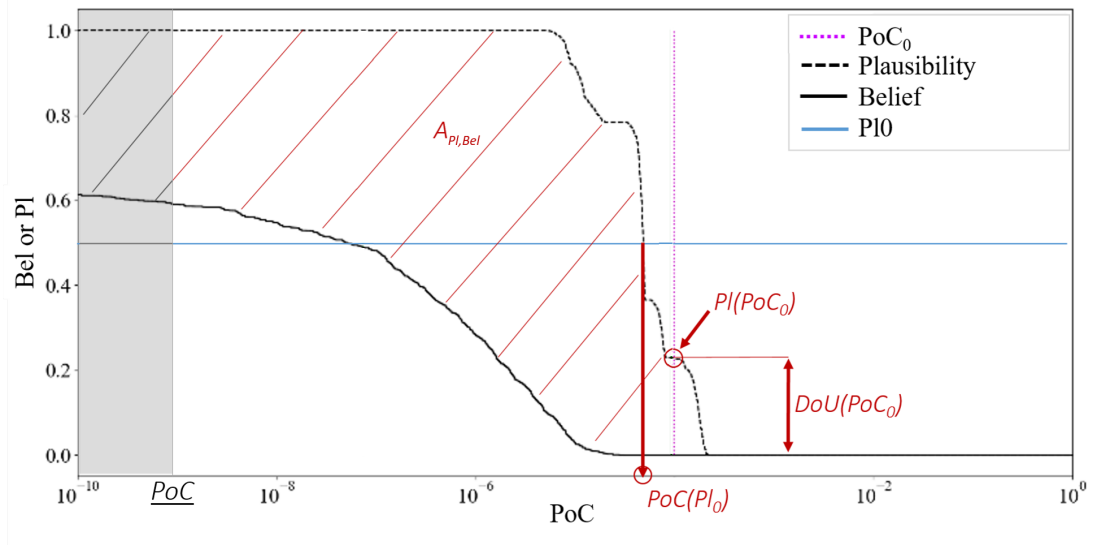


Figure 7.1: Pl and Bel curves with the relevant classification parameters indicated: PoC_0 , $PoC(Pl_0)$, Pl_0 , $Pl(PoC_0)$, $DoU(PoC_0)$, $A_{Pl,Bel}$.

7.2 Thresholds calibration

When performing robust Conjunction Assessment Risk Analysis (CARA) using the proposed approach in Part I, the evidence-based classification criterion contains some thresholds whose value has to be selected by the operator. Some thresholds, such as the risk threshold, PoC_0 , and the time thresholds, T_1, T_2 , can be selected following the current practice employed by operators since they are defined in the same way as in current approaches. However, the epistemic-based thresholds, like Pl_0 and A_0 , which are required to make a decision on the uncertainty in the PoC, need to be tuned on known conjunction scenarios. Thus, the test in this section is used to tune Pl_0 and A_0 on a database of synthetic cases with known outcomes.

The methodology proposed requires the prior definition of the values of two thresholds: Pl_0 and A_0 . These two thresholds should be tuned by analysing a large dataset of conjunction events with known outcomes. However, in every database of CDMs available, the number of provable *Class 1* and *2* conjunctions is very small or zero.

Since A_0 does not affect *Class 4* and *5*, which depend only on Pl_0 , but influences the number of True Positives (TPs) (actual collisions) and False Positives (FPs) (no-collisions believed to be collisions), one can define Pl_0 first and then use A_0 to quantify

the degree of uncertainty in the class associated to an event.

According to the classification in Table 7.1, the expected outcome is that low values of Pl_0 would increase the number of events classified as *Class 1* or *2*, reducing, at the same time, the number of False Negatives (FNs) (collisions believed to be no-collisions) and increasing the amount of TPs. If this is combined with high values of A_0 , the chances of detecting all high-risk events are high, but at the cost of increasing the number of FPs. If instead, A_0 is low, more events will be classified as uncertain (*Class 0* and *3*). On the contrary, a higher value of Pl_0 would reduce the false alerts, FPs, but at the risk of increasing the number of FN's.

The value for Pl_0 is set by using the Dempster-Shafer theory of Evidence (DSt) structure. If there is at least one Focal Element (FE) supporting $PoC > PoC_0$, it means that there exists at least one piece of evidence suggesting that the PoC can be correct. This piece of evidence may correspond to an extreme event with low probability. Following this idea, it is proposed the value $Pl_0 = \min_i(bpa(\gamma_i))$. This implies that even a PoC that corresponds to a rare event in the generation of a CDM is considered to be plausible.

The value of A_0 is selected by balancing the number of TPs and FPs. The idea is to try to reduce the number of FPs by reclassifying them as uncertain cases and presenting the level of such uncertainty to the operator. A low value of A_0 implies that the operator accepts very little uncertainty in the sequence of CDM, which reduces the number of FPs but potentially classifies some TPs as uncertain. On the other hand, a greater value of A_0 implies that the operator is very conservative and accepts to treat a number of FPs as TPs. Thus, the decision to execute a CAM is related to the confidence of the operator in the quality of the CDMs. For highly uncertain sequences of CDMs, a low A_0 is recommended, but if the quality of the CDMs is high, a higher A_0 should be used.

In the following, rather than selecting the value of the area threshold A_0 , it is the value of the normalised area $A_0^* = \{0, 0.05, 0.1, 0.15, \dots, 0.95, 1\}$, where A_0^* is the fraction of the maximum possible area between the *Bel* and *Pl* curves, that is, when *Bel* drops to zero at the minimum value of PoC, \underline{PoC} , and *Pl* remains equal to one until $PoC = 1$.

In this tuning exercise the area is computed by taking the lower limit $\underline{PoC} = 10^{-30}$ for the PoC as this is the lowest value computed from all the sequences of CDMs in the databases. For all the first four tests in this chapter, a value of $A_0^* = 0.1$ is used, which allows one to clearly differentiate Event 1 from Events 3 and 4 in the following section. In the last test, the sensitivity of the number of recommended CAMs to the value of A_0^* is presented.

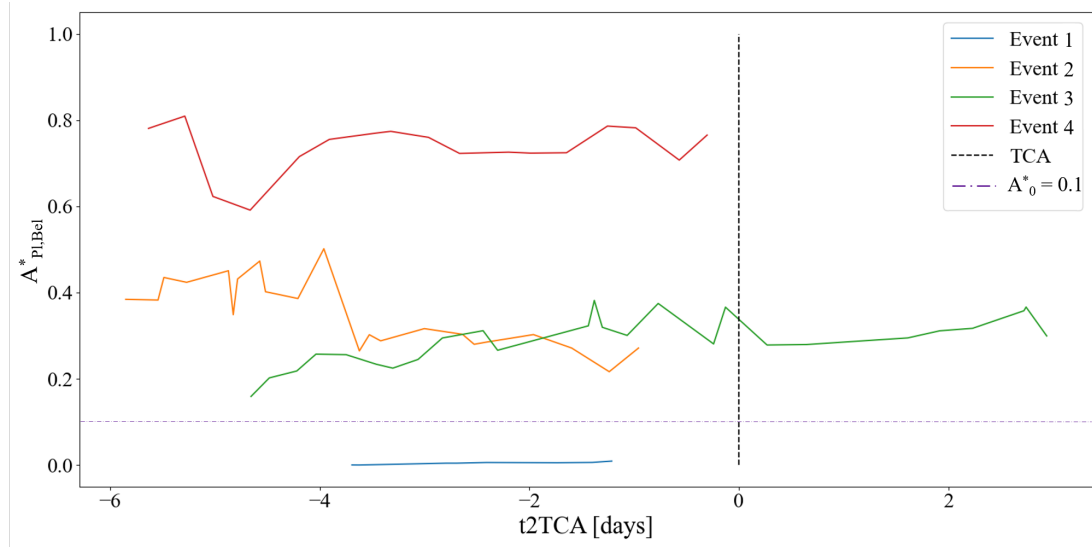


Figure 7.2: Evolution of the normalised $A_{Pl,Bel}$ over time, for Events 1 to 4.

7.3 Comparison against real operators approach

This section presents the conjunction risk assessment on a selected number of representative real CDM sequences, comparing the approach the evidence-based method would suggest against the actual decision-making process carried out by real operators, both at the European and the French space agencies, ESA's Space Debris Office (SDO) at ESOC and CNES, respectively.

For all examples the values of the thresholds are reported in in Table 7.2. The evolution of the normalised area gap between the Pl and Bel curves, or $A_{Pl,Bel}$, over time, for all four cases can be found in Fig. 7.2, where $A_{Pl,Bel}^* = A_{Pl,Bel}/\max(A_{Pl,Bel})$ is the normalised area between curves, $A_{Pl,Bel}$, defined in Eq. (7.1). The Figure confirms

Table 7.2: Threshold values.

Threshold	Units	Value
T_1	days	3
T_2	days	5
PoC_0	-	10^{-4}
Pl_0	-	$1/\#FE$
A_0^*	-	0.1
\underline{PoC}	-	10^{-30}

that an $A_0^* = 0.1$ is appropriate to differentiate between cases like Event 1 from cases like Event 3 and 4. All four cases are presented in more detail in the following subsections.

7.3.1 Space Debris Office conjunction risk assessment

The approach followed by the ESA’s SDO is probability-based, relying mainly on the value of the PoC computed with the information from the CDMs, if not the PoC include on the CDM. The following quote may summarise the generic SDO’s conjunction risk assessment process: “For a given close approach the last obtained CDM, including the computed risk, can be assumed to be the best knowledge we have about the potential collision and the state of the two objects in question. In most cases, the Space Debris Office will alarm control teams and start thinking about a potential avoidance manoeuvre 2 days prior to the close approach in order to avoid the risk of collision, to then make a final decision 1 day prior” [European Space Agency, 2019]. Nevertheless, each mission monitored by the SDO will have a specific procedure based on this general approach according to its characteristics and constraints [Merz et al., 2017].

Under this generic approach, each mission will introduce its own operational constraints (e.g. the time needed to prepare, execute the manoeuvre) and will have its own risk and time threshold. While the time threshold will be highly related to the mission constraints, generally 2 or 3 days to the encounter, the mission team is informed about the possible collision, with a final decision usually made (when possible), 1 day to the conjunction [European Space Agency, 2019]. The risk threshold is determined statistically based on the overall collision risk and the annual frequency of close approaches,

trading off the ignored risk and the avoided risk by selecting the risk threshold at the cost of an expected number of annual manoeuvres [Merz et al., 2017]. Generally, for missions in the Low Earth Orbit (LEO) regime, a threshold of $PoC_0 = 10^{-4}$ leads to a risk reduction of around 90% at the expense of 1 to 3 manoeuvres per year. However, a lower threshold, around 10^{-5} , may be selected to ensure potential escalating events are detected with sufficient time to prepare an avoidance strategy [Merz et al., 2017].

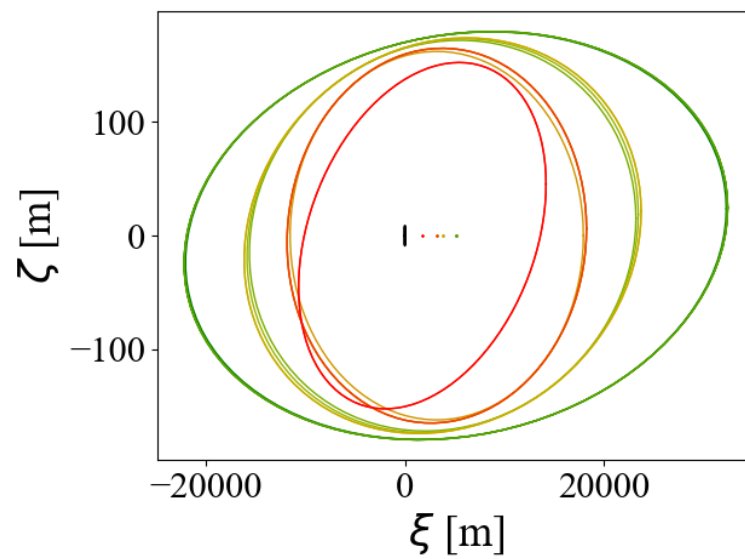
Thus, when the last CDM's PoC is bigger than the threshold, the event is escalated for further and more detailed analysis. If the risk is still above the threshold at the decision time, a CAM is designed in cooperation with the mission team, whose final decision will be made based on the value of PoC included in the last CDM received before the go/no-go decision time. More detailed information on the SDO's CARA process can be found in [Merz et al., 2017].

In the following, a number of real conjunction events, representative of the different evidence-based criterion cases (high-risk, low-risk and uncertain scenario), are presented. A comparison of the different operational approaches is made. For the next three examples, a simplified scenario only with CDMs generated from the *MiniCat* database was considered.

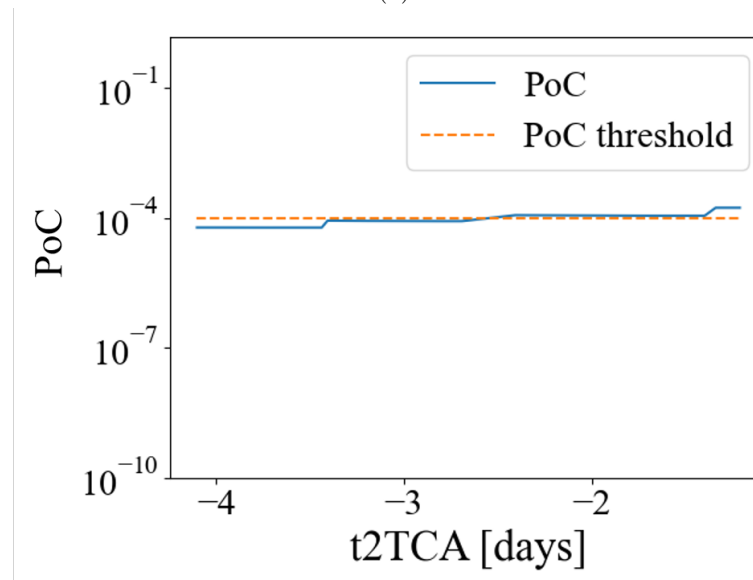
Event #1

This event represents a high-risk scenario provided by the ESA's SDO. The uncertain geometry in the impact plane, with the whole sequence of CDMs and the PoC evolution appear in Fig. 7.3. Events with PoC above the threshold for times to the Time of Closest Approach (TCA) greater than T_1 make the event escalate, that is, they are further analysed and possible alerts to the mission's team can be triggered, while high-risk CDMs received in the last 72 hours start a CAM procedure.

From Fig. 7.3b, it can be seen that the PoC remains high along the whole sequence. Even if at the beginning it is below the threshold, its proximity to PoC_0 along with the increasing trend made the operator escalate the event. Finally, the PoC threshold was violated within the last days before the encounter, which led to a CAM execution



(a)



(b)

Figure 7.3: CDM information for example in Scenario #1: High-risk event. (a) Uncertain ellipses in the sequence of CDMs. Green ellipses correspond to earlier CDMs, and red ellipses to later CDMs. (b) Evolution of the PoC in the CDMs (blue solid) and PoC threshold (orange dashed)

to reduce the risk of the event.

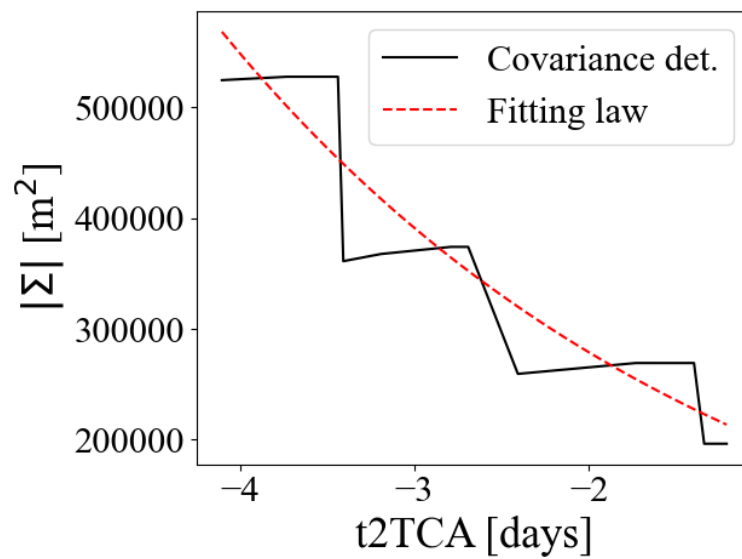
The robust conjunction analysis is made following the method presented in Chapter 4. To obtain the Dvoretzky-Kiefer-Wolfowitz (DKW) bands, a confidence interval

parameter of $\delta = 0.5$ is selected. The CDMs are weighted according to the exponential law in Eq. (4.6). Fig. 7.4a shows the fitting law after having received all the CDMs (red) along with the value of the combined covariance matrix determinant for the sequence (black). For the fitting law in Fig. 7.4b, the value of the dimensionless parameters in Eq. (4.6a) after having received the whole sequence are: $A = 1.0752, B = 0.9811, C = 0.001716$. Note that the value of the parameters varies with the number of CDMs received to better fit the covariance determinant evolution up to that time.

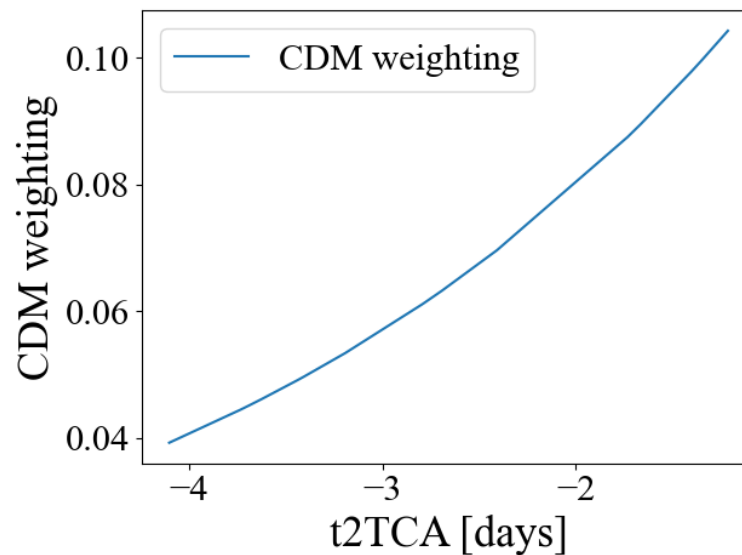
The robust analysis is performed for a different number of α -cuts per uncertain variable: $\#\alpha\text{-cuts} = \{1, 2, 3, 4, 5, 7\}$. These cuts lead to a number of intervals per variable equal to $\#\text{intervals} = \{2, 3, 4, 5, 6, 8\}$, which translates into a number of FEs (before removing those without samples from the CDMs) equal to $\#\text{FE} = \{32, 243, 1024, 3125, 7776, 16807\}$, respectively. The *Pl* and *Bel* curves for the PoC, for each number of cuts, are presented in Fig. 7.5, after having received the whole sequence of CDMs. The *Bel* is represented by the solid line, and the *Pl* by the dashed lines, where each colour represents a different number of α -cuts. The vertical solid line indicates the PoC on the last CDM, the vertical dashed vertical line represents line the maximum PoC on the sequence and the purple pointed vertical line shows the PoC threshold.

Fig. 7.5 shows that, although the increasing number of α -cuts provides a more refined set of curves, their shape and values almost do not differ as function of the number of intervals. In this case, the *Bel* and *Pl* curves overlap for most values of PoC except for a small interval around the PoC_0 , as it could be expected both from the uncertainty geometry in Fig. 7.3a and the values of the PoC in Fig. 7.3b. Since the information in the CDM is coherent across the whole sequence, the gap between *Pl* and *Bel* curves is small, indicating a small epistemic uncertainty affecting this sequence.

Fig. 7.6 shows the classification, purple solid line, as a function of the time to the TCA from the last received CDM. The vertical line indicates the time threshold, the horizontal dashed black line the PoC threshold and the horizontal solid lines represent the different levels of risk: green, low risk-uncertain boundary; yellow, uncertain-high risk boundary; red, mid-term high risk-long term high-risk boundary. The crossed



(a)



(b)

Figure 7.4: Scenario #1: High-risk event. (a) Combined covariance matrix evolution (exact and fit) and (b) CDM weighting law.

orange line shows the computed PoC in the CDM. Note that the classification is the same, no matter the number of α -cuts, so in the figure, the solid lines corresponding to classification with different interval partitions overlap each other.

Initially, the event is classified as *Class 4* and rapidly falls to *Class 5*, since there is

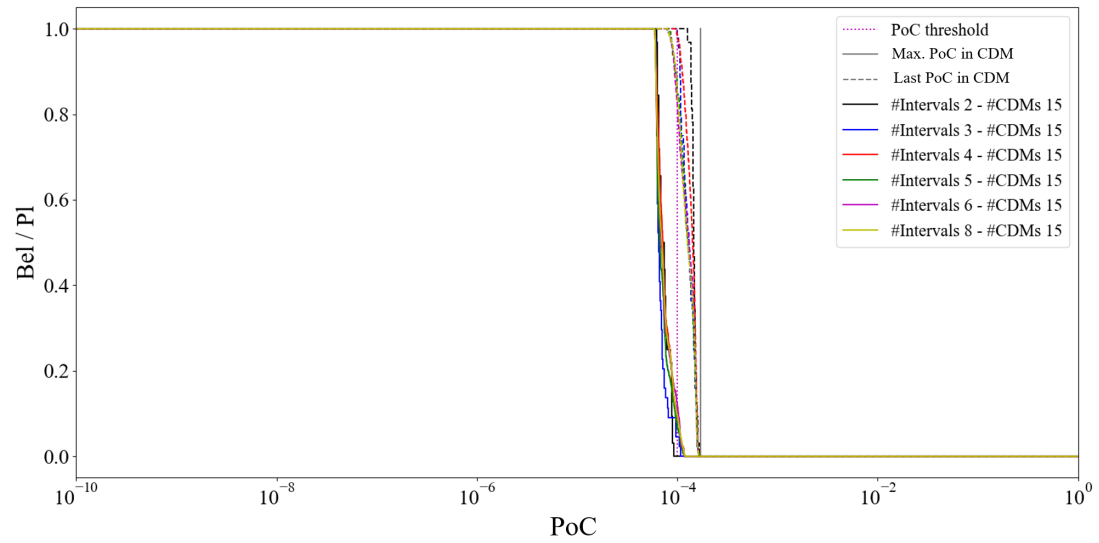


Figure 7.5: Pl (dashed lines) and Bel (solid lines) of the PoC after having received the whole sequence of CDMs Scenario #1: High-risk event for a different number of α -cuts.

little evidence supporting a higher PoC ($Pl(PoC_0) < Pl_0$). However, at 2.5 days from TCA the PoC consistently grows above the threshold. Given the little uncertainty in the sequence of CDMs event is reclassified as *Class 1* and a CAM is recommended. This is the same decision finally taken by the SDO. As seen in Fig. 7.5, the support for a high value of PoC is high and the gap between the curves (level of uncertainty) is very small. Thus, the outcome for the operator for any decision made in the last days prior to the encounter would be that a manoeuvre should be implemented to reduce the risk of a collision.

Event #2

A similar analysis is done for the Low-risk conjunction event illustrated in Fig. 7.7, also provided by the ESA's SDO. Opposite to the previous scenario, in this case, the PoC remains well below the threshold, so no alert was required to be triggered and no CAM was required to be designed or executed in the real scenario.

The robust analysis is performed using the same parameters as before: $\delta = 0.5$ for the DKW bands, with a different number of cuts: $\#\alpha\text{-cuts} = \{1, 2, 3, 4, 5, 7\}$ per

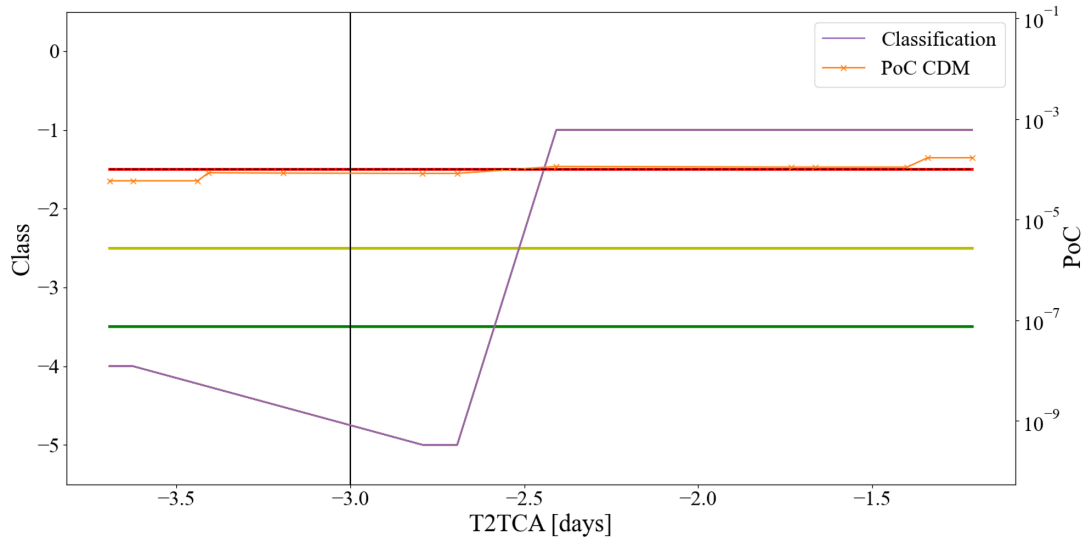
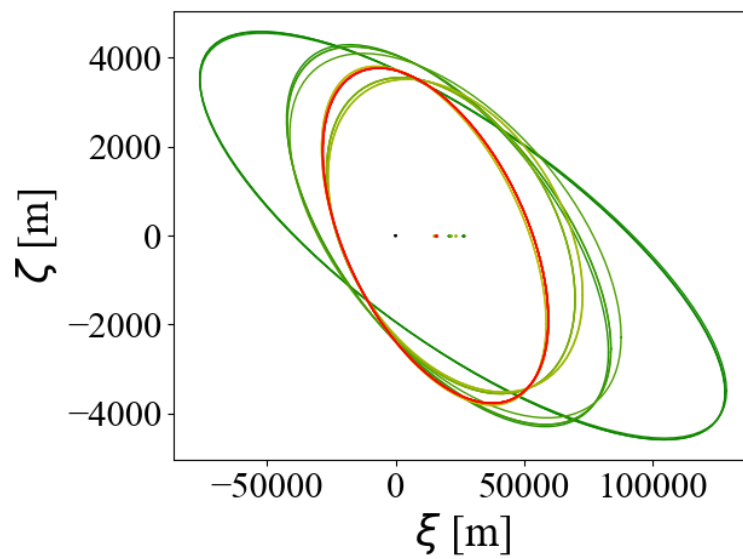


Figure 7.6: Collision risk assessment for Scenario #1: High-risk event.

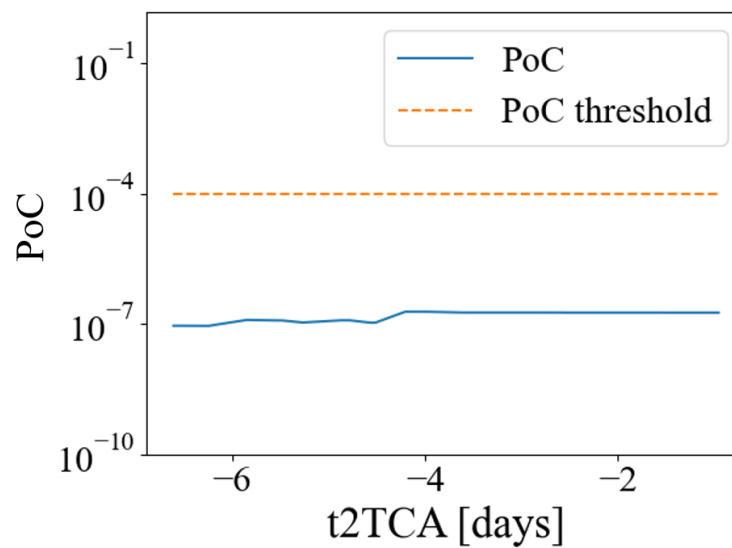
variable. The CDMs after having received the whole sequence were weighted with the exponential fitting law Eq. (4.6a) using the following parameters: $A = 0.6049$, $B = 5.0896$, $C = 0.4518$. The fitting law (red) and the combined covariance matrix determinant in the CDMs (black) appear in Fig. 7.8. Note the convergence in the second half of the sequence.

In Fig. 7.9, the corresponding Pl and Bel curves on the value of PoC after having received all the CDMs of the event are shown. Again, increasing the number of α -cuts makes the curves smoother, but does not change the overall confidence in the value PoC. The maximum value of PoC with some supporting evidence is well below the threshold, indicating that the event can be deemed to be safe. However, the left-most part of the Bel and Pl curves shows a significant gap. This can be explained by the fact that the ellipses are not too different from each other (Fig. 7.7a) and they tend to converge to a single ellipse for the later CDMs, as shown in Fig. 7.7b. Thus, the initial information content in each CDM tends to support lower values of PoC, which explains the lower value of Bel on the left of the graph. However, due to the concentration of information around the later CDMs, the big drop both in Pl and Bel occurs at $PoC \sim 10^{-7}$.

Finally, the conjunction assessment for the whole sequence is shown in Fig. 7.10.



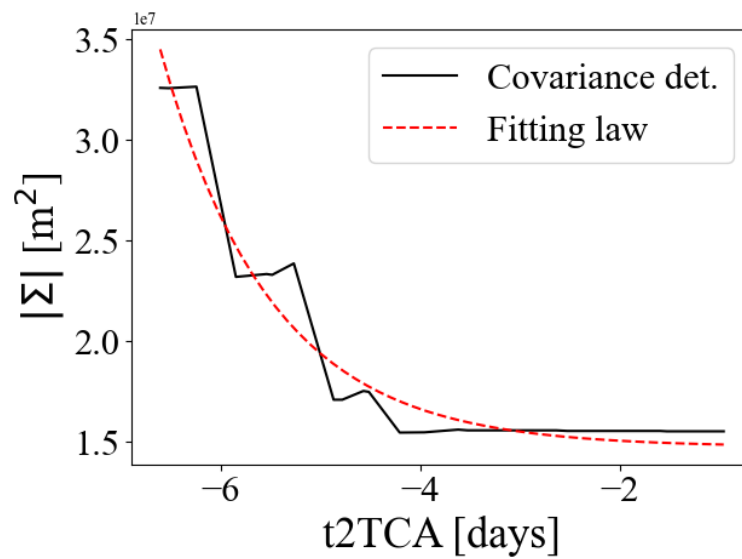
(a)



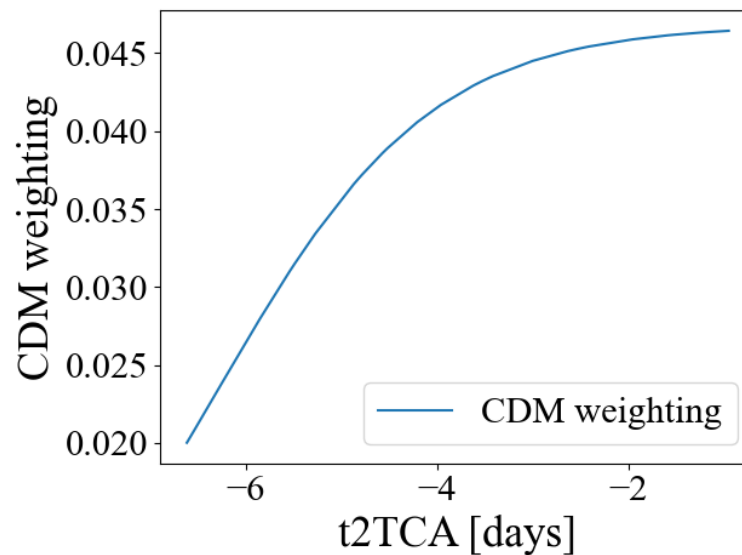
(b)

Figure 7.7: CDM information for example in Scenario #2: Low-risk event. (a) Uncertain ellipses in the sequence of CDMs. Green ellipses correspond to earlier CDMs, and red ellipses to later CDMs. (b) Evolution of the PoC in the CDMs (blue solid) and PoC threshold (orange dashed).

Despite the greater uncertainty with respect to the previous scenario, it affects only very small values of the PoC. For values of the PoC greater than 10^{-7} , there is no uncertainty: those higher values do not receive any support ($Pl = Bel = 0$), meaning



(a)



(b)

Figure 7.8: Scenario #2: Low-risk event. (a) Combined covariance matrix evolution (exact and fit) and (b) CDM weighting law.

higher values of PoC are not likely to happen according to the available evidence. Thus, the event is initially classified as *Class 4* ($t2TCA > T_1$) and then dropped to *Class 5* ($t2TCA \leq T_1$) for the whole sequence, meaning that no further action should be taken by the operator. Note that the same conclusions are reached no matter the number of

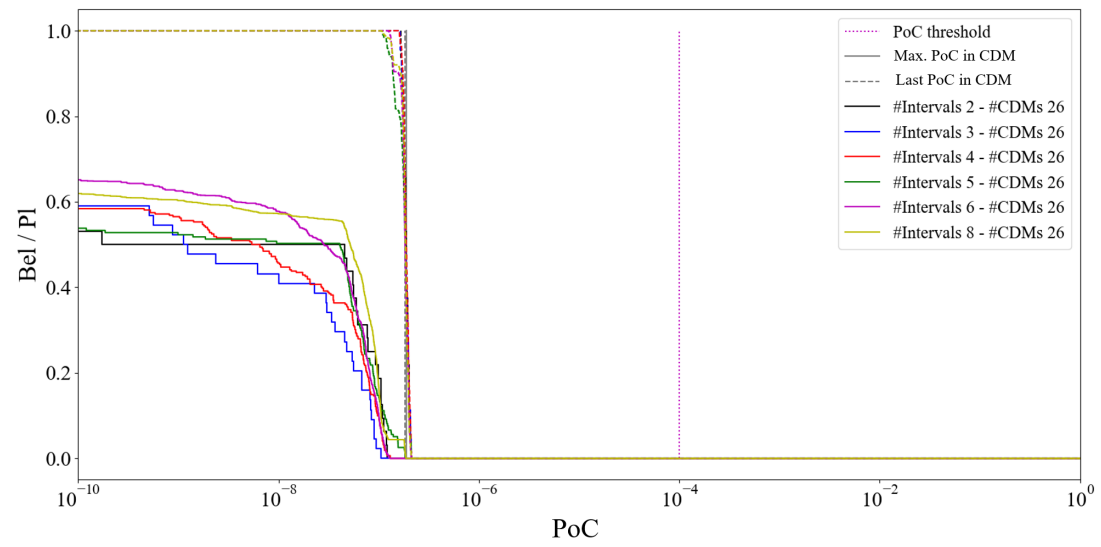


Figure 7.9: Pl (dashed lines) and Bel (solid lines) of the PoC after having received the whole sequence of CDMs Scenario #2: Low-risk event for a different number of α -cuts.

α -cuts. This is the same decision made by the SDO.

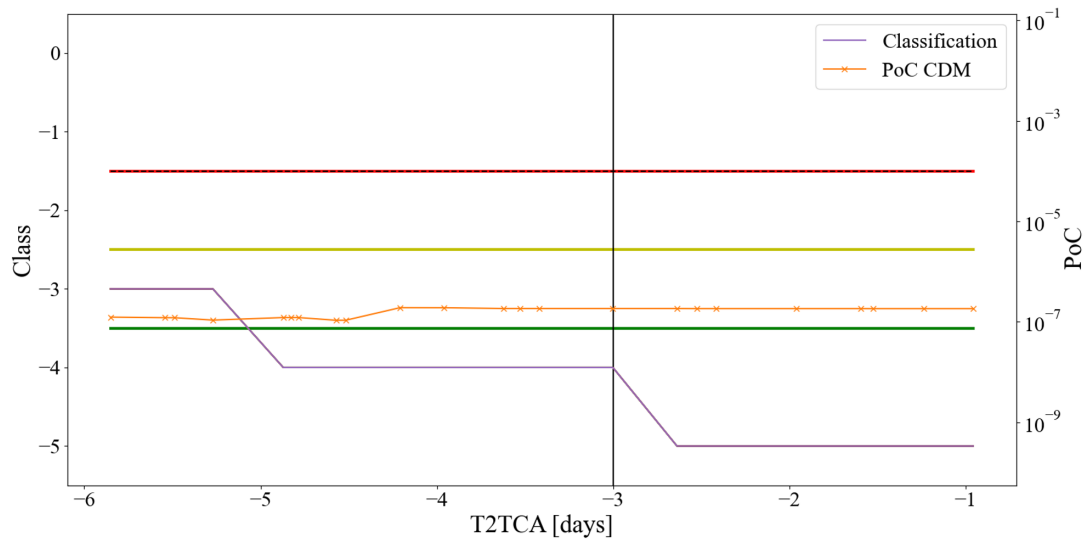


Figure 7.10: Collision risk assessment for Scenario #2: Low-risk event.

Event #3

This last event is affected by a significant level of uncertainty. The encounter

geometry and the evolution of the PoC in the CDMs are shown in Fig. 7.11. Despite the initial higher risk, with values of PoC close to the threshold, the final decision of the SDO was not to take any further action. This decision was driven by the latest values of PoC, notably lower than the initial ones, and considerably below PoC_0 .

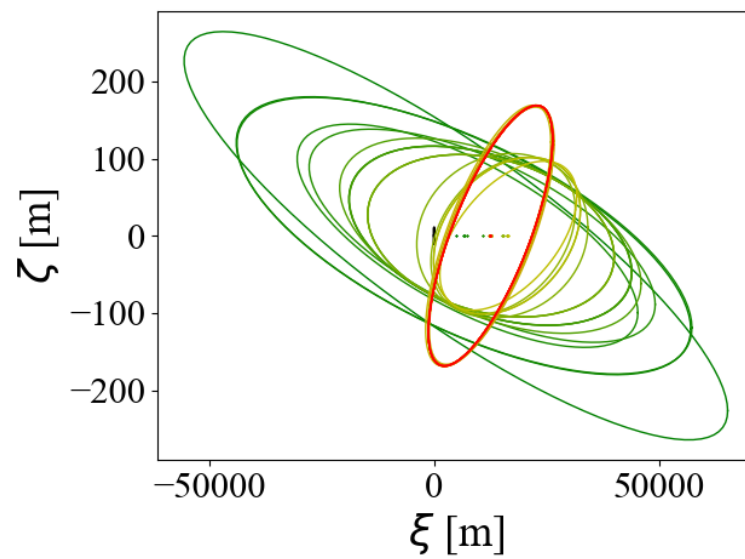
The robust analysis is performed with the same parameters as before: $\delta = 0.5$ for the DKW bands. The exponential fitting law Eq. (4.6a) to weight the CDMs, after having received the whole sequence, uses the following parameters $A = 0.7917, B = 7.1471, C = 0.1858$ and is shown in Fig. 7.12 (red) along with the covariance matrix determinant from the CDMs (black).

The Pl and Bel curves for the PoC are for different α -cuts: $\#\alpha\text{-cuts} = \{1, 2, 3, 4, 5, 7\}$. The curves are shown in Fig. 7.13. In this case, there is a significant gap between Pl and Bel for all the values of PoC for which $Pl > 0$. This uncertainty (or level of disagreement between CDMs) can be seen in Fig. 7.11a, which shows the variety of the uncertainty ellipses from the beginning of the sequence to the last CDMs. In this case the supporting evidence that a value of $PoC > PoC_0$ is plausible does not go to zero but the gap between the Pl and Bel curves suggests that a further analysis is required although the value of Pl is low and Bel is zero.

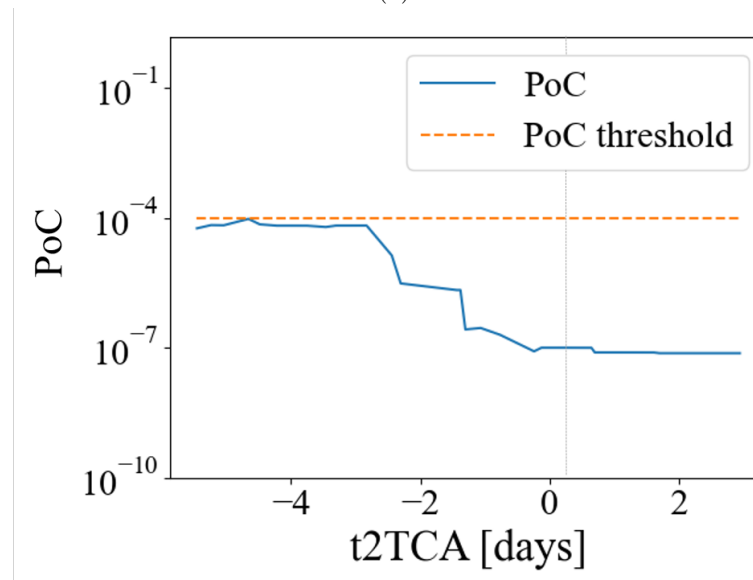
Fig. 7.14 shows the result of the classification: the event starts at *Class 2*, given the potential high risk suggested by the initial CDMs but quickly drops to *Class 3* ($t2TCA > T_1$) because of the level of uncertainty and is finally classified as *Class 0* (for $t2TCA \leq T_1$). In this case, the proposed approach would suggest a further analysis due to the non-zero plausibility of a high PoC and a high difference between Pl and Bel , while the decision made by the SDO was to take no further action. The more prudent recommendation coming from the robust classification system would lead to a further inspection of the Pl curve with the realisation that the supporting evidence is small, albeit not zero.

7.3.2 CNES conjunction risk assessment

As shown in Eq. (3.1), the value of the PoC is very sensitive to the position covariance matrix of the objects involved in the encounter, whose value from CDM can be underes-



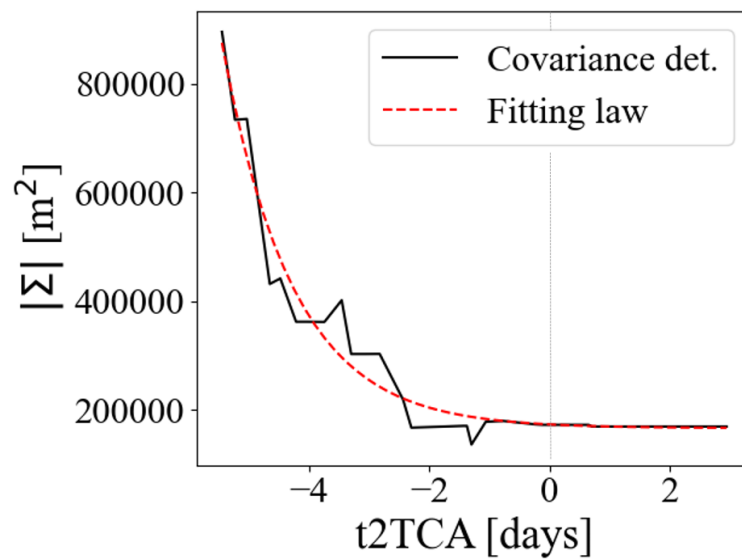
(a)



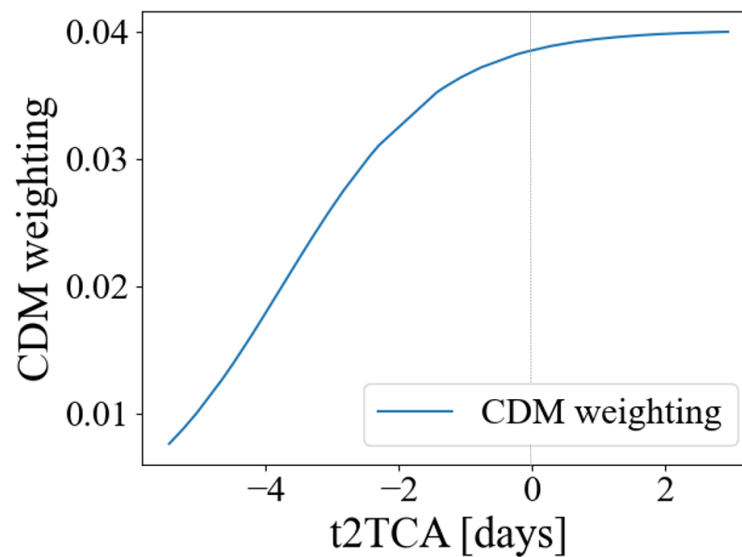
(b)

Figure 7.11: CDM information for example in Scenario #3: Uncertain event. (a) Uncertain ellipses in the sequence of CDMs. Green ellipses correspond to earlier CDMs, and red ellipses to later CDMs. (b) Evolution of the PoC in the CDMs (blue solid) and PoC threshold (orange dashed), TCA (vertical dashed green).

timated or overestimated. In order to have a value that accounts for this miss-estimation on the CDMs covariance matrices, CNES operators use *Java for Assessment of Conjunctions* (JAC) for conjunction risk assessment [Laporte, 2014a, Laporte, 2014b]. JAC



(a)



(b)

Figure 7.12: Scenario #3: Uncertain event. (a) Combined covariance matrix evolution (exact and fit) and (b) CDM weighting law.

employs the so-called scaled PoC (sPoC), instead of the PoC, as the metric to make decisions [Stroe et al., 2021]. To compensate for the possible poor model of the covariance matrices, the scaling factor $k_p \in K_P$ and $k_s \in K_S$ are employed to scale it up and down. The sPoC is obtained by solving Eq. (7.2) as the maximum value of the

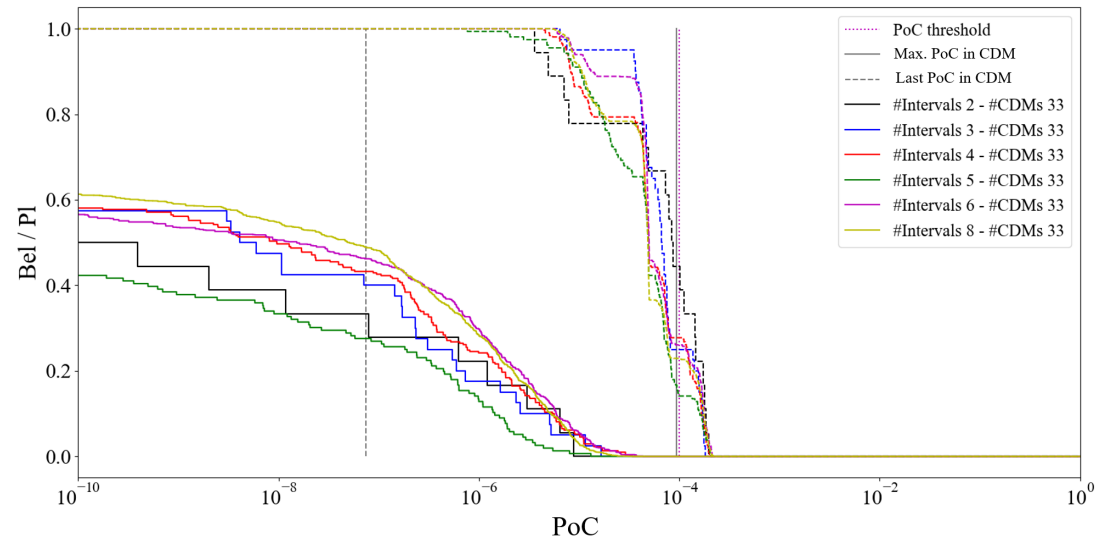


Figure 7.13: Pl (dashed lines) and Bel (solid lines) of the PoC after having received the whole sequence of CDMs Scenario #3: Uncertain event for a different number of α -cuts.

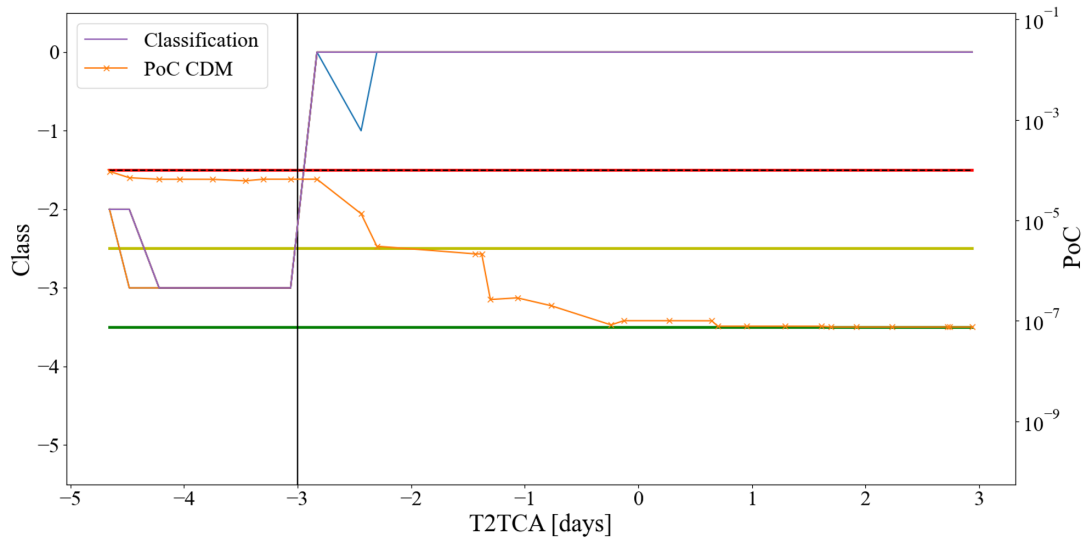


Figure 7.14: Collision risk assessment for Scenario #3: Uncertain event.

PoC among the different combinations of scaling factors for the primary and secondary objects.

$$\begin{cases} sPoC = \max_{K_P, K_S}(PoC) \\ \text{with } \Sigma = k_p^2 \Sigma_p + k_s^2 \Sigma_s \end{cases}, \quad (7.2)$$

where Σ_p and Σ_s are, respectively, the primary and secondary covariance matrices in the last CDM associated with the conjunction event.

The default bounds of K_P and K_S in JAC software are $[0.25, 4]$, although more realistic boundaries can be obtained based on the sequence of CDMs. However, it goes at the expense of making two assumptions: the sequence of CDMs represents a set of samples from an underlying distribution, and the last CDM is given more relevance. Thus, using the last CDMs as the reference, it is possible to compute the Mahalanobis distance of previous CDMs uncertainty ellipses, and assuming the uncertainty in position follows a Gaussian distribution. The Mahalanobis distance must follow a X^2 distribution with 3 degrees of freedom. Performing a Kolmogorov-Smirnov test between the actual distribution and the theoretical one, and setting a desired level of realism, it is possible to find more realistic boundaries for K_P and K_S . More details can be found in [Stroe et al., 2021].

CNES decision-making is then based on both geometric criteria and sPoC-based criteria. Events with values of $sPoC > 5 \cdot 10^{-4}$ are treated as High-Interest Events, the more risky classification level (red level). For values of $10^{-4} < sPoC < 5 \cdot 10^{-4}$, the events are classified as an Interest Events, the second level of risk (orange level). If the value of the $sPoC$ is below those thresholds, caution geometric criteria are applied: miss distance below 1 km or radial distance below 200 m. Note that these threshold values are the default ones and may change from mission to mission. If the CDMs are received early in time (generally, around 4-5 days before the encounter), no alerts are raised independently of the level of risk of the conjunction, although the event is decided to be under study if some of the criteria are violated. For later CDMs, alerts may be raised according to the level of risk of the event (orange or red). Finally, if the high risk continues after the decision time (usually 2 days before the encounter), a final decision is made before the TCA. [Taillan and Laporte, 2022]

Event #4: CNES approach

This scenario presents a high-risk collision case for a real close encounter where CNES had to implement a manoeuvre to reduce the risk. This scenario is interesting since it allows comparing the CNES approach, based on the sPoC, with both the robust

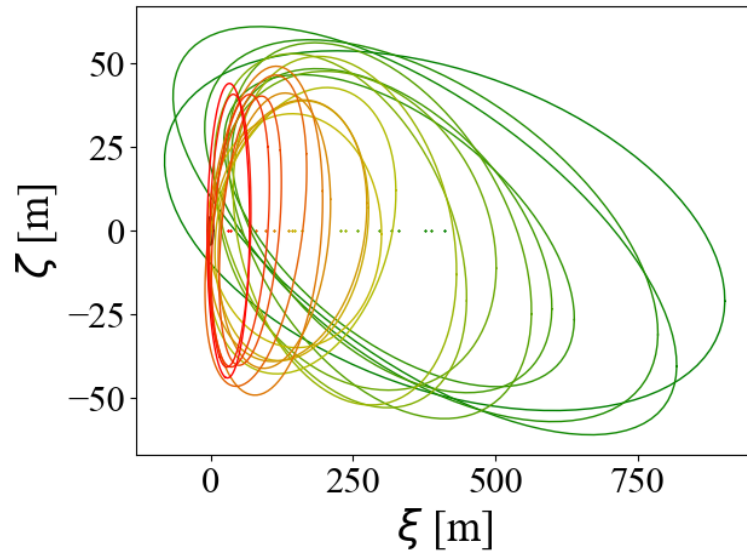
approach proposed in this paper and the approach based exclusively on the value of the PoC.

Fig. 7.15a shows the geometry of the event, where initial CDMs (greener colours) suggested a lower PoC, while later ellipses (yellow and red) approach to the Hard Body Radius (HBR). This is reflected in the value of the PoC in Fig. 7.15b, where the value of the PoC increases when approximating to the encounter. This figure also shows the sPoC which already suggests from the beginning value above the risk threshold and a higher risk than the value of PoC in the CDM. It can also be seen how the sPoC already predicted a value of risk above 10^{-4} , close to the PoC value of the last CDM, while the PoC in the sequence of CDMs required to be much closer to the encounter to proposed such values, and even then, with a less stable behaviour. This is reflected in the decision-making process followed by CNES's operators on this event: the event is catalogued as *High-Interest Event*, meaning careful monitoring should be taken, from the 12th CDM (2.96 days before the TCA), and a final decision for performing a manoeuvre is taken 30 hours before the encounter. Note that the last CDM received by the decisions time indicates a $PoC < 10^{-5}$, well below the risk threshold, while the sPoC indicates a risk above 10^{-3} , which aligns better with the last three CDMs received between the decision time and the CAM execution time.

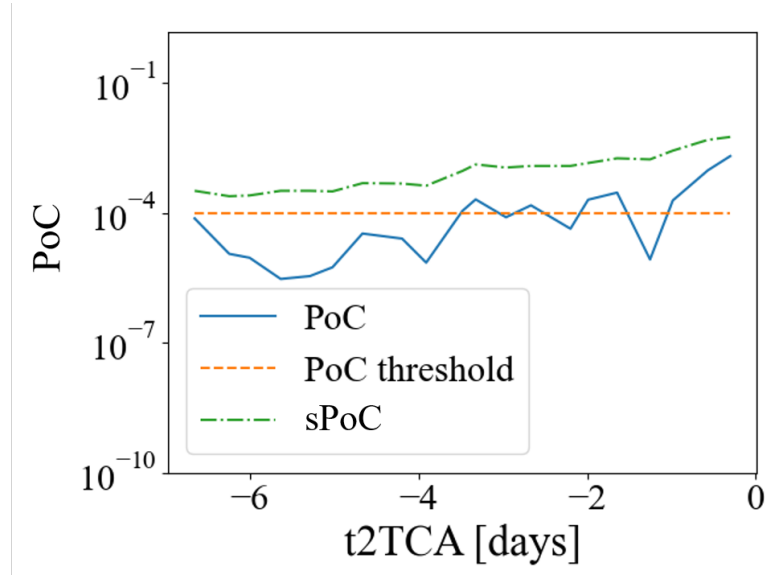
The evidence-based analysis is performed following the same approach as for the SDO cases and with the same thresholds: $PoC = 10^{-4}$, $T_1 = 3$ days, $T_2 = 5$ days, $Pl_0 = 1/243$, $A_0^* = 0.1$, and with $\#intervals = \{2, 3, 4, 5, 6, 8\}$ intervals per variable and CDM weighed according to the exponential law in Fig. 7.16.

The Pl and Bel corresponding to the whole sequence of CDM are shown in Fig. 7.17, and the classification sequence for different numbers of intervals is shown in Fig. 7.18. In Fig. 7.17 one can see that $Pl(PoC_0)$ is nearly 1, and $Pl(sPoC) > 0$ along the whole time series. In fact, $Pl = 0$ at $PoC \sim 10^{-2}$, while $\max(sPoC) = 5 \cdot 10^{-3}$. However, the gap between the Pl and Bel curves is very high, indicating a degree of uncertainty in the sequence of CDMs. This is due to the variability in the CDMs. Thus the event is classified as *Class 0*.

Although this event is placed in the same class as Event 3, the supporting evidence



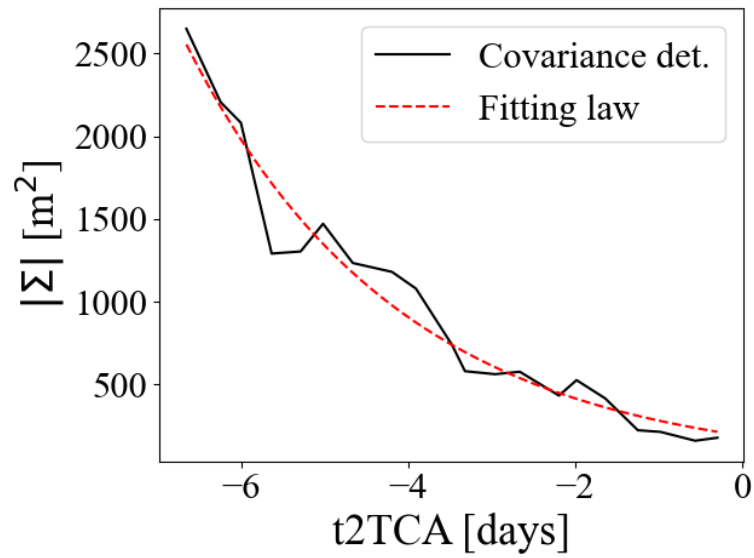
(a)



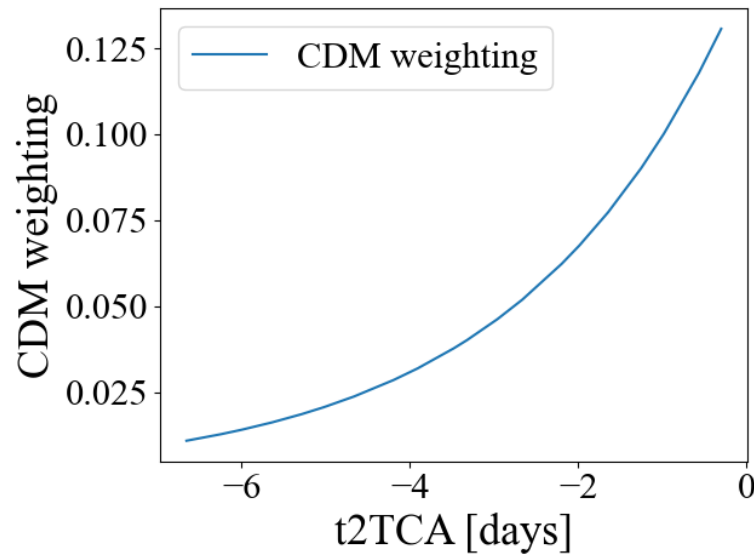
(b)

Figure 7.15: CDM information for example in Scenario #4. (a) Uncertain ellipses in the sequence of CDMs. Green ellipses correspond to earlier CDMs, and red ellipses to later CDMs. (b) Evolution of the PoC in the CDMs (blue solid), evolution of the sPoC (dashed-pointed green) and PoC threshold (orange dashed).

is quite different. Event 4 has a $Pl \approx 1$ and Bel different from zero at PoC_0 while Event 3 has $Bel = 0$ and $Pl < 0.2$ at PoC_0 . This means that, although in this paper we opted for a very conservative classification of the events such that both Events 3 and



(a)



(b)

Figure 7.16: Scenario #4. (a) Combined covariance matrix evolution (exact and fit) and (b) CDM weighting law.

4 fall in the same uncertainty class, a simple analysis of the *Bel* and *Pl* curves would suggest that the available evidence for Event 4 supports a high probability of collision, up to 10^{-2} in fact, while for Event 3 the supporting evidence at PoC_0 is quite low.

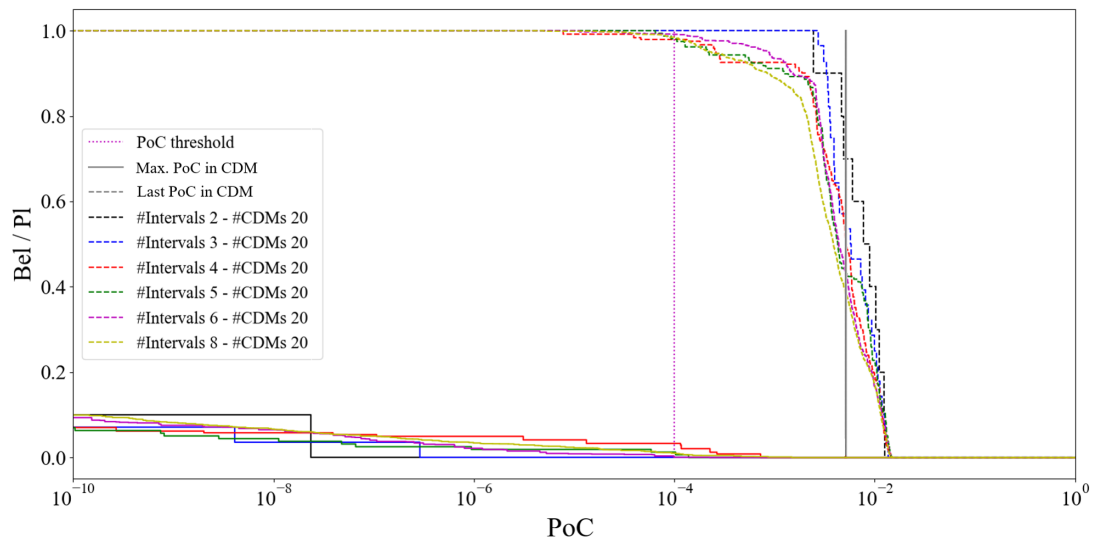


Figure 7.17: Pl (dashed lines) and Bel (solid lines) of the PoC after having received the whole sequence of CDMs Scenario #4 for a different number of α -cuts.

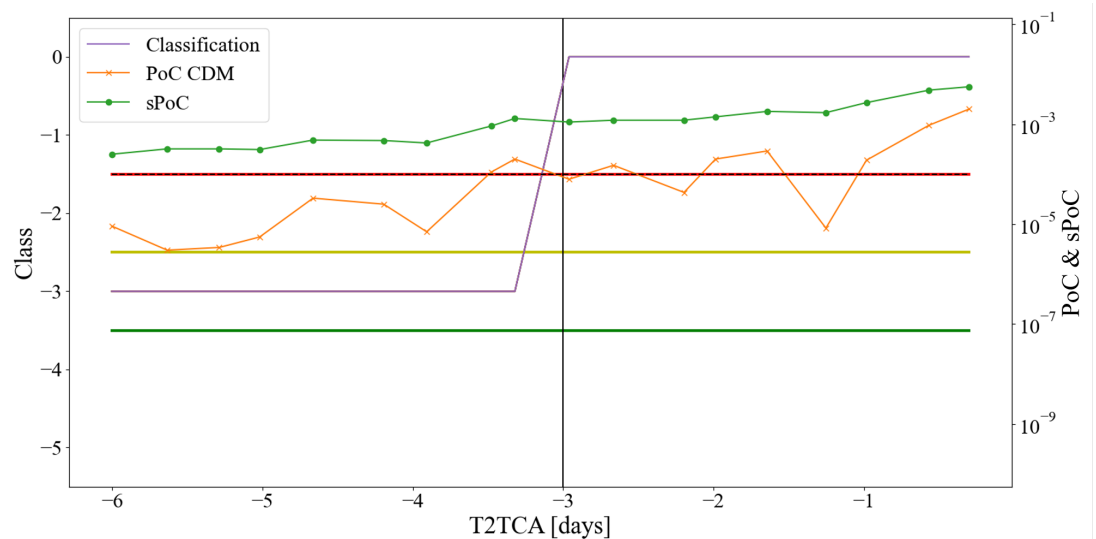


Figure 7.18: Collision risk assessment for Scenario #4.

7.4 Statistical analysis of Swarm-A dataset

After having compared the proposed evidence-based conjunction assessment approach against real operations on specific cases, in this section a comparison is made on how many CAMs are executed or recommended in a large number of real conjunctions.

The selected mission is the ESA’s SWARM-A satellite, orbiting in the LEO regime (circular polar orbit of 87.7 deg at 511 km of altitude), dedicated to studying the Earth’s magnetic field as part of a constellation of three satellites [ESA, 2020]. The mission thresholds to trigger conjunction alerts are $PoC_0 = 10^{-4}$ and $T_1 = 72$ hours. Thus, any satellite with a PoC above the threshold in the last 3 days would escalate and would require further analysis, and eventually, a possible CAM design or execution. Nevertheless, encounters presenting a higher risk or an increasing trend before T_1 may be escalated if the operator considers that there is a potential risk for the mission. Finally, the go/no-go decision is subject to operational constraints: the time required to design a CAM after receiving the triggering manoeuvre, the possibility to upload and check the design manoeuvre and the ground station availability.

The database of CDMs includes alerts from 2015 to 2022, with a total of 36,072 events. Overall, most of the events in the database did not represent a threat to the satellite, with only 20 samples representing escalated events. As explained before, an escalated event is an encounter where the PoC, or the PoC trend, suggests that the conjunction may be high risk. From those escalated events, only 2 cases required a CAM to be executed.

The evidence-based analysis was performed with the same thresholds as the previous study cases (Table 7.2): $PoC_0 = 10^{-4}$, $T_1 = 3$ days, $T_2 = 5$ days, $Pl_0 = 1/243$, $A_0^* = 0.1$, with $\underline{PoC} = 10^{-30}$, and $A_0 = 3$. The DKW bands were obtained assuming a confidence interval of $\delta = 0.5$. As shown before, a higher number of α -cuts would refine the Pl and Bel curves, providing closer curves that better represent the actual epistemic uncertainty. However, this is at the expense of increasing the computational cost and with limited impact on the final classification. Thus 2 α -cuts (3 intervals) per variable, with a total of 243 FEs per analysis were used.

Since the evidence-based analysis lacks the real information available in the actual operation of the satellite that may have affected the operator decision (for example, the ground station availability or the mission constraints), the statistics were computed at four decision times: $T_d = 3$ days to the TCA, corresponding with the mission time threshold, T_1 ; $T_d = 2$ days to the TCA, allowing for more data to arrive; $T_d = 1$ day to

the encounter, the usual go-no go decision time in ESA’s missions, [Merz et al., 2017]; and the epoch of the last CDM in the sequence, $T_d = 0$. For simplicity, it is assumed that there is no operational constraint that prevents or modifies the final decision and all information is, thus, available.

Table 7.3 includes the results from the analysis, compared with the actual statistics provided by the SDO. It is important to bear in mind the differences between the approaches. An event classified as *Class 3* or *Class 0* (labelled as *Uncertain*), with the evidence-based approach, would not correspond, necessarily, to an escalated event, since the meaning is different: while an escalated event assumes a certain level of risk, a *Class 0* or *3*, suggests a degree of uncertainty that requires further investigation before making a final decision. This further investigation might be simply limited to an inspection of the *Bel* and *Pl* curves as in Events 3 and 4 above or might require additional observations. On the other hand, for all *Class 1* events, the recommendation is to perform a CAM.

Table 7.3: Results from the statistical analysis on the SWARM-A mission, with the SDO approach and the evidence-based approach. Threshold: $PoC_0 = 10^{-4}$, $T_1 = 3$ days, $T_2 = 5$ days, $Pl_0 = 1/243$. Partition with 2 α -cuts per variable. Upper tier: $A_0^* = 0.1$ ($A_0 = 3$); middle tier: $A_0^* = 0.5$ ($A_0 = 15$); lower tier: $A_0^* = 0.8$ ($A_0 = 24$).

SDO		Evidence-based					
# events	A_0^*	# events	$T_d = 3$	$T_d = 2$	$T_d = 1$	$T_d = 0$	
Total	36,072	Total	24,296	27,918	32,108	36,072	
Escalated	20	0.1	Unc.	120	130	172	293
CAM	2		CAM	1	2	3	2
	0.5	Unc.	102	98	107	154	
		CAM	19	34	68	141	
	0.8	Unc.	95	83	77	75	
		CAM	26	49	98	220	

From the upper tier in Table 7.3 (with $A_0^* = 0.1$), one can observe that: i) the total number of events increases with the delay in the decision time because more CDMs are available for a decision; ii) the number of manoeuvres proposed by the evidence-based

approach is similar to the number of CAMs proposed by the SDO operators; iii) the evidence-based classification system found many more uncertain cases than the SDO. The Table shows also the number of CAMs and uncertain events for A_0^* equal to 0.5 and 0.8. As expected, an increase in the values of A_0^* increases the number of CAMs and reduces the number of uncertain cases.

Even if the Pl_0 threshold is quite low, the number of events escalating to *Class 1* remains small. Thus, in this test case, the system is robust enough to remove false negatives without introducing false alerts. Also, the number of CAMs remains roughly constant independently of the decision time (especially, for the selected default value of $A_0^* = 0.1$). The number of uncertain cases increases when approaching the TCA, despite the more information available, especially for lower area thresholds. This is partially due to the higher increase in the total number of events and partially due to the likely discrepancy between initial and final CDMs, as can be deduced from the decrease when the areas threshold is bigger. More relevant is that the number of *Class 0* events is between 6 and 15 times higher than the number of escalated events proposed by ESOC. It is here where the evidence-based system differentiates from the probabilistic approach used by ESOC. *Class 0* events are those with $Pl(PoC_0) > Pl_0$, but are still deemed uncertain because $A_{Pl,Bel} > A_0$. Pl captures all realisations, within each FE, that correspond to extreme cases, extreme low or extreme high PoC, compatible with the observed sequence of CDMs. Hence, a large $A_{Pl,Bel}$ with high Pl signifies that there is evidence that a high PoC event can occur but is uncertain. As in the case of Event 3, many of these cases display a low Pl and zero Bel . Others present conflicting CDM, that cannot be resolved without further observations, or a high Pl for high PoC values, as in Event 4 but with a low Bel . An example can be seen in Figure 7.19. The evolution of the combined covariance shows a radical rotation of nearly 90 degrees at 4 days to the TCA. The evolution of the PoC does not provide any evidence that the covariance had a step change but remains close to the threshold limit. The evidence-based approach, instead, shows quite some uncertainty and maintains a high Pl till the end of the sequence, suggesting that the event cannot be discarded and requires further analysis.

Note that the percentage of events in this category increases when delaying the decision. This indicates a growing disagreement among CDMs in the sequence as the time approaches TCA, an aspect usually overlooked by probabilistic-based approaches.

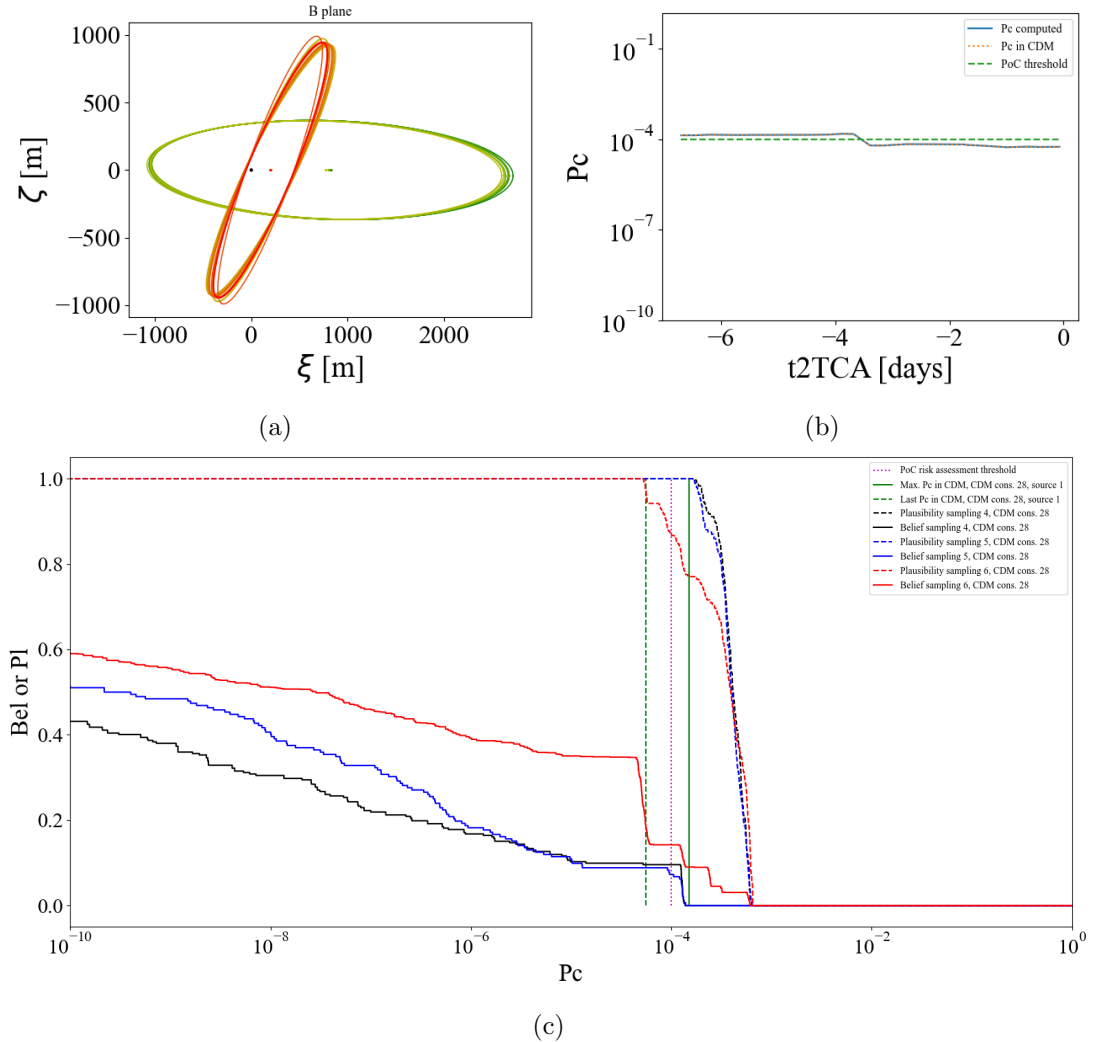


Figure 7.19: Conjunction event with conflicting CDMs: a) evolution of the relative position distribution on the impact plane, b) evolution of the PoC, c) Pl and Bel curves of the whole CDMs sequence.

7.5 Chapter summary

This chapter tested against real operations the methodology proposed to quantify uncertainty in sequences of CDMs and to provide robust conjunction risk assessment

accounting for aleatory and epistemic uncertainty on a number of real scenarios.

A modification of the evidence-based classification criteria presented in previous chapters was introduced, so the uncertainty on the event is now based on the area between the Pl and Bel curves, $A_{Pl,Bel}$, instead of only on the vertical gap at a certain PoC value. This facilitates capturing better the whole uncertainty of the event and is less sensitive to narrow gaps on the curve that do not represent the actual epistemic uncertainty of well-known events. The values of the two epistemic thresholds (Pl_0 and A_0) are selected with a proposed methodology so that Pl_0 reduces the number of missing events detected (FN) and A_0 minimises the false alerts (FP).

The method is compared with real operators' responses to actual events. Three of the scenarios were provided by ESA and represent the main three possible outcomes of the analysis. If the information was coherent along the sequence (high-risk or low-risk) both answers were similar, while when the sequence presented a higher degree of variability or a degree of inconsistency, the proposed evidence-based approach provided a quantification of the related uncertainty and classifies the events accordingly. When comparing with the CNES and the concept of sPoC, the proposed evidence-based approach provided consistent decisions but with a higher level of information on the uncertainty in the decision.

Finally, the method was applied to a whole set of sequences for a statistical analysis of the proposed CAM and uncertain events on a real mission operated by ESA. The main difference was not in the number of CAM, but in the number of uncertain cases and escalated events, which has to be further investigated.

Chapter 8

Artificial intelligence for Space Traffic Management

The content of this chapter was partially published in:

Sánchez, L. and Vasile, M. (2021), “On the use of machine learning and evidence theory to improve collision risk management”, *Acta Astronautica*; [Sánchez and Vasile, 2021c]

Sánchez, L. and Vasile, M. (2022), “Intelligent agent for decision-making support and collision avoidance manoeuvre design on Space Traffic Management”, *Advances in Space Research*, in press [Sánchez and Vasile, 2023];

Sánchez, L., Rodríguez-Fernández, V. and Vasile, M. (2024), “Robust Classification with Belief Functions and Deep Learning Applied to Space Traffic Management”, 2024 IEEE World Congress on Computational Intelligence (WCCI), submitted. [Sánchez et al., 2023]

This chapter addresses the use of Machine Learning (ML) to assist operators in the conjunction of risk assessment and decision-making processes. Different ML techniques and architectures are assessed on their ability to predict the risk of the conjunction events. The objective is to build surrogate models of the methods developed in Part I, allowing a faster, yet accurate, evaluation of the risk, to help with the automation of the decision-making process.

The rest of the chapter presents a set of applications of different ML techniques to encounter scenarios based on the methods presented in Part I. In Section 8.1, an analysis of the use of ML for the classification criterion presented in Chapter 3 is shown, and in Section 8.2, these ML techniques are applied to the classification criterion which takes into account the robust Collision Avoidance Manoeuvre (CAM) approach introduced in Chapter 5. Section 8.3 applies that ML techniques to predict the conjunction class using the Conjunction Data Messages (CDMs) analysis presented in Chapter 4. Section 8.4 concludes the chapter.

8.1 Intelligent classification system

This section introduces an Intelligent Classification System (ICS) that exploits the evidence-based classification criterion presented in previous chapters to provide decision-making support to operators. The Intelligent Classification System (ICS) uses ML techniques to predict the classes of risk of the events given the uncertain close encounter geometry. The main advantage of such a system is that it can provide a fast, automatic and robust classification of conjunction events from the objects' information.

Two intelligent event classification systems are proposed based on the classification criterion in Table 3.7 to provide the risk level of the event, that is, its *Class*. The objective is to build a surrogate model of the classification criterion. The first one, *System 1*, takes the three classification parameters of the criterion. Thus, the inputs are the time to the encounter from the last position update, $t2TCA$, the Degree of Uncertainty (DoU) at the risk threshold $DoU(PoC_0)$, and the value of the Probability of Collision (PoC) at the Belief (*Bel*) threshold PoC_b . The single output is the *Class* of the event.

The second proposal, *System 2*, goes one step backwards in the classification algorithm. Instead of taking the classification parameters, it takes the variables that allow to obtain them: the time to the encounter ($t2TCA$) and the bounds of the uncertain geometry at the impact plane (miss distance and combined covariance matrix, $\mathbf{u} = [\mu_\xi, \mu_\zeta, \sigma_\xi, \sigma_\zeta, \sigma_{\xi,\zeta}]$). If more than one interval is provided or more than one source provides information, the intervals' basic probability assumptions (*bpa*) are also pro-

vided as inputs. Then, the number of inputs is equal to three times the number of sources (the upper and lower bounds and the bpa) times the number of uncertain variables (5) plus one more input (the time to the Time of Closes Approach, TCA). For example, if three intervals per variable are available, the number of inputs would be equal to $3 * 3 * 5 + 1 = 46$. In the case of a single interval per variable, the number of inputs is equal to $2 * 5 + 1 = 11$ corresponding to the two bounds of the five uncertain variables and the time to the encounter. Without losing generality and in agreement with the examples shown in Chapter 3, the cases shown in this section assumed $\sigma_{\xi\zeta} = 0$, reducing the number of uncertain variables to 4, $\mathbf{u} = [\mu_{\xi}, \mu_{\zeta}, \sigma_{\xi}, \sigma_{\zeta}]$, and consequently, the number of inputs. The single output of the system is the *Class* of the event.

8.1.1 Synthetic dataset

To test the two classification systems, two datasets of synthetic encounters are generated representing a variety of conjunction scenarios: dataset DB_1 and dataset DB_2 . DB_1 contains 9,000 different conjunction scenarios built using the intervals in Table 3.4, assuming two sources of information providing a single interval each and combined with the mixing rule. Each set of geometries contributes with 1,800 samples where the encounter geometry is provided by two sources of information in the form of intervals for each of the uncertain variables and associated $bpas$. These 1,800 samples are distributed in groups of 600 samples into each of the three times bins indicated in the robust classification criterion: immediate encounters ($t2TCA < T_1$), medium-term encounters ($T_1 \leq t2TCA < T_2$) and long-term encounters ($t2TCA \geq T_2$), where $t2TCA$ is the time to the TCA. Each of these groups is composed of three subgroups of 200 samples: in one subgroup the sources are equally reliable ($bpa_1 = bpa_2 = 0.5$), in a second subgroup Source 1 has an associated $bpa_1 = 0.9$ and Source 2 an associated $bpa_2 = 0.1$, and in the third sub-group, Source 1 has an associated $bpa_1 = 0.1$, and Source 2 and associated $bpa_2 = 0.9$.

The dataset DB_2 includes other 19,800 samples, out of which 9,000 are obtained in a similar way to the samples in DB_1 and the other 10,800 samples feature an extended set of geometries divided into 9 sub-sets characterised by the intervals in Table 8.1.

For each of the 9 sub-sets half of the samples have both sources equally reliable (see the *bpas* defined for DB_1), and in the other half, Source 1 is more reliable than Source 2. Within each half of the data, three different encounters are generated by changing the time to the TCA, one geometry per each of the three time bins of the classification criterion. In addition to those samples, DB_2 includes the 9,000 examples of DB_1 . In total, this second dataset is made of 28,800 samples.

For each dataset, 80% of the samples are used for training and 20% for evaluating the performance (Validation Set), so DB_{11} and DB_{12} are the training and valida-

Table 8.1: Bounds for the upper and lower values of the $[\mu_x, \mu_y]$ and $[\sigma_x, \sigma_y]$ uncertainty intervals for each of the set of geometries used for creating DB_2 . The first row represents the limits for Source 1 and the second row for Source 2.

Geom.	Characteristics	μ_ξ [m]	μ_ζ [m]	σ_ξ [m]	σ_ζ [m]
Geo. 1	Low μ	[0,4]	[0,4]	[0.1,5]	[0.1,5]
	Low σ	[2,20]	[2,20]	[0.1,5]	[0.1,5]
Geo. 2	Low μ	[0,4]	[0,4]	[10,20]	[10,20]
	High σ	[2,20]	[2,20]	[10,20]	[10,20]
Geo. 3	Low μ	[0,4]	[0,4]	[0.1,20]	[0.1,20]
	Wide σ	[2,20]	[2,20]	[0.1,20]	[0.1,20]
Geo. 4	High μ	[100,2000]	[100,2000]	[10,100]	[10,100]
	Low σ	[100,2000]	[100,2000]	[10,100]	[10,100]
Geo. 5	High μ	[100,2000]	[100,2000]	[500,5000]	[500,5000]
	High σ	[100,2000]	[100,2000]	[500,5000]	[500,5000]
Geo. 6	High μ	[100,2000]	[100,2000]	[10,5000]	[10,5000]
	Wide σ	[100,2000]	[100,2000]	[10,5000]	[10,5000]
Geo. 7	Low μ Low σ	[0,5]	[0,5]	[0.1,5]	[0.1,5]
	High μ Low σ	[100,500]	[100,500]	[10,100]	[10,100]
Geo. 8	Low μ High σ	[0,5]	[0,5]	[10,20]	[10,20]
	High μ Low σ	[100,500]	[100,500]	[10,100]	[10,100]
Geo. 9	Low μ Low σ	[0,5]	[0,5]	[0.1,5]	[0.1,5]
	High μ High σ	[100,500]	[100,500]	[500,2000]	[500,2000]

tion datasets from DB_1 , respectively, and DB_{21} and DB_{22} the training and validation datasets from DB_2 , respectively. The training sub-sets (DB_{11} and DB_{21}) are further divided into 80% for samples used to tune the model parameters (Training Set) and 20% for the test samples (Test Set) used during the training process to avoid overfitting the system.

8.1.2 Machine learning techniques and metrics

Different ML techniques are studied, each one with different combinations of hyper-parameters. To select the best model for each technique and compare the different techniques, the systems' performance is measured using the following metrics on the Validation Set:

- *Accuracy*, the percentage of samples correctly predicted over all the samples,

$$Accuracy = \frac{\# \text{ Correct predict classes}}{\# \text{ Total number of samples}} \quad (8.1)$$

- *Precision*, the percentage of the samples correctly predicted from a certain class over the total number of samples predicted in this class.

$$Precision = \frac{\text{True positives}}{\text{True positives} + \text{False positives}} \quad (8.2)$$

- *Recall*, the percentage of samples correctly predicted on a certain class over the total number of samples in that class,

$$Recall = \frac{\text{True negatives}}{\text{True negatives} + \text{False positives}} \quad (8.3)$$

The Artificial Neural Network(ANN) trained in this work contains only one hidden layer. Since it is a classification problem, the output layer contains five nodes, one per *Class*, indicating the probability of the output being one of them. The final output corresponds to the *Class* presenting a higher probability. Ideally, when inputs of a *Class* k are provided, all nodes in the output layer should score 0 but node k , which should

score 1. The only hyperparameter modified in this study is the number of neurons in the hidden layer: 10, 20, 50, and 100. Each neuron possesses a hyperbolic tangent activation function. The optimiser is based on the Levenberg-Marquardt algorithm [Hagan and Menhaj, 1994] and the loss function is the Multi-Class Cross-Entropy [Bishop, 2006]. Each configuration is trained iteratively 10 times with different initialisation of the parameters (weights and bias of the neurons). The ANN providing the lowest value of the loss function on the Test Set is selected as the best model. The ANN is implemented using MATLAB's *Deep Learning* Toolbox [Matlab, 2021].

Several Random Forests (RF) configurations are trained, by modifying the number of trees in the forest, `n_estimators = {50, 100, 200, 400}`, the maximum depth of the tree, `max_depth = {'None', 50, 100}`, the minimum number of samples required to be at a leaf node, `min_samples_leaf = {1, 10-4, 10-7}`, the minimum number of samples to split a node, `min_samples_split = {2, 20}`, and the number of features to consider when looking for the best split, `max_features = {'auto', 0.5, 'log2'}`. All the other parameters are kept equal to the default values in Python's Scikit library [Scikit-learn, 2021b]. The model with the combination of hyperparameters that provides the best results over the Test Set is saved as the best model.

Different K-Nearest Neighbours (KNN) models are trained, each one with a different number of neighbours, `n_neighbors = {1, 3, 5}`, weight function, `weights = {'uniform', 'distance'}` and leaf size, `leaf_size = {30, 60}`. All the other hyperparameters are kept equal to the default values in Python's Scikit library [Scikit-learn, 2021a]. The model with the combination of hyperparameters that provides the highest accuracy over the Test Set is saved as the best model.

For Support Vector Machine (SVM) techniques, the models only modified the hyperparameter indicating the decision function of shape, `decision_function_shape = {'ovo', 'ovr'}` are considered, leaving as default the rest of parameters in Python's Scikit library on SVM [Scikit-learn, 2021c]. The best model is the one with the highest accuracy over the Test Set.

8.1.3 Classification results

Table 8.2 shows the results using the best settings of each ML technique for *System 1*, trained in DB_1 and validated in DB_2 . It can be seen that all ML methods provide good results and accurate classification. RF and ANN show slightly better results, with overall accuracy and class precision/recall very close to 100%. The hyperparameters selected for the best model of each technique can be found in Table D.1 in Appendix D.

Note, however, that the Validation Set contains only 5 representative geometries because it is taken from DB_1 . Thus, the same ML models are put to the test by taking DB_2 as the Validation Set. The result can be found in Table 8.3. It can be seen that the performances of all the techniques, if slightly worse, are in general above 90% accuracy, even close to 100% for RF. Apart from the levels of accuracy, it also demonstrates that different geometries correspond to similar classifications using the *Bel* and Plausibility (*Pl*) curves.

Table 8.4 presents the performance of all ML techniques on classification System 2, trained with the training set DB_{11} and validated on dataset DB_{12} . When using classification System 2 the performance of all ML methods degrades due to the wider set of input parameters and the more complex relationship between input parameters

Table 8.2: Overall accuracy and precision and recall by classes. *System 1* trained with DB_{11} and tested with DB_{12} . The best technique is underlined.

Method	Total Acc.		Class 1	Class 2	Class 3	Class 4	Class 5
ANN	0.999	Prec.	0.988	0.998	1.00	1.00	0.999
		Rec.	1.00	0.996	0.994	0.998	1.00
<u>RF</u>	<u>0.999</u>	Prec.	<u>1.00</u>	<u>1.00</u>	<u>0.994</u>	<u>1.00</u>	<u>1.00</u>
		Rec.	<u>0.988</u>	<u>1.00</u>	<u>1.00</u>	<u>1.00</u>	<u>1.00</u>
KNN	0.970	Prec.	0.889	0.934	1.00	0.998	0.998
		Rec.	0.988	0.996	0.938	0.963	0.977
SVM	0.992	Prec.	0.987	1.00	1.00	0.992	0.990
		Rec.	0.963	0.991	0.938	0.996	1.00

Table 8.3: Overall accuracy and precision and recall by classes. *System 1* trained with DB_{11} and tested with DB_{22} . The best technique is underlined.

Method	Total Acc.		Class 1	Class 2	Class 3	Class 4	Class 5
ANN	0.956	Prec.	0.913	0.844	1.00	0.997	0.998
		Rec.	0.734	0.950	0.991	0.998	1.00
<u>RF</u>	<u>0.999</u>	Prec.	<u>0.996</u>	<u>1.00</u>	<u>1.00</u>	<u>1.00</u>	<u>1.00</u>
		Rec.	<u>1.00</u>	<u>0.998</u>	<u>0.997</u>	<u>1.00</u>	<u>1.00</u>
KNN	0.936	Prec.	0.907	0.903	0.960	0.967	0.955
		Rec.	0.916	0.859	0.926	0.960	0.966
SVM	0.852	Prec.	0.966	0.996	0.922	0.818	0.817
		Rec.	0.633	0.500	0.913	0.994	1.00

and risk classes. This drop is especially remarkable for KNN and SVM techniques. In any case, the accuracy of both ANN and RF remains relatively high, with values above 80%.

Table 8.4: Overall accuracy and precision and recall by classes. *System 2* trained with DB_{11} and tested with DB_{12} . The best technique is underlined.

Method	Total Acc.		Class 1	Class 2	Class 3	Class 4	Class 5
<u>ANN</u>	<u>0.846</u>	Prec.	<u>0.487</u>	<u>0.752</u>	<u>0.904</u>	<u>0.993</u>	<u>0.995</u>
		Rec.	<u>97.5</u>	<u>98.6</u>	<u>0.815</u>	<u>0.844</u>	<u>0.842</u>
RF	0.844	Prec.	0.487	0.737	0.894	0.995	0.995
		Rec.	0.975	0.986	0.784	0.844	0.844
KNN	0.583	Prec.	0.441	0.680	0.734	1.00	0.65
		Rec.	0.790	0.848	0.512	0.771	0.865
SVM	0.513	Prec.	0.0	0.434	0.0	0.0	0.641
		Rec.	0.0	0.844	0.0	0.0	0.890

Table 8.5 shows the prediction accuracy of the ML algorithms using classification System 2, DB_{11} for training and DB_{22} for validation. It can be seen, that opposite to what happened in Table 8.3 where accuracy levels remained high, here they fall for

Table 8.5: Overall accuracy and precision and recall by classes. *System 2* trained with dataset DB_{11} and tested with dataset DB_{22} . The best technique is underlined.

Method	Total Acc.		Class 1	Class 2	Class 3	Class 4	Class 5
ANN	0.636	Prec.	0.774	0.599	0.159	0.774	0.864
		Rec.	0.517	0.564	0.604	0.676	0.689
<u>RF</u>	<u>0.778</u>	Prec.	<u>0.835</u>	<u>0.705</u>	<u>0.577</u>	<u>0.789</u>	<u>0.801</u>
		Rec.	<u>0.628</u>	<u>0.473</u>	<u>0.479</u>	<u>0.930</u>	<u>0.929</u>
KNN	0.589	Prec.	0.732	0.586	0.304	0.500	0.606
		Rec.	0.628	0.479	0.479	0.930	0.929
SVM	0.533	Prec.	0.0	0.419	0.0	0.0	0.607
		Rec.	0.0	0.871	0.0	0.0	0.878

all ML algorithms. The main reason is the extended range of the input parameters combined with the more nonlinear link between input and output underneath System 2. In this case, a broad range of geometries actually translates into a broad range of inputs that complicates the prediction.

More complex ML models, for example, deeper RF or ANN with more hidden layers, might improve the results. However, the limitation here is probably the restricted range of the training set rather than the ML algorithms. A more sensible approach would be using a bigger and, especially, wider training set. Table 8.6 shows the results of the best model of all ML algorithms using classification System 2, training dataset DB_{21} and validation dataset DB_{22} . It can be seen that results improve due to the extended training dataset, obtaining results even better than those achieved in Table 8.4, where both Training and Validation Sets were restricted to the 5 geometries. Thus, while different geometries led to similar *Bel* and *Pl* structures as shown with *System 1*, when feeding with the geometry (*System 2*), the richer the dataset, the better.

Table 8.7 shows the training time for the best settings of each ML method. The running time during the testing phase is included in Table 8.8, for each of the cases studied in this example. The machine used for the training and prediction of all the models was an Intel Core i7-3520M CPU @ 2.90GHz.

Table 8.6: Overall accuracy and precision and recall by classes. *System 2* trained with training dataset DB_{21} and tested with dataset DB_{22} . The best technique is underlined.

Method	Total Acc.		Class 1	Class 2	Class 3	Class 4	Class 5
ANN	0.924	Prec.	0.880	0.821	0.750	0.991	0.991
		Rec.	0.987	0.963	0.714	0.918	0.919
<u>RF</u>	<u>0.933</u>	Prec.	<u>0.884</u>	<u>0.835</u>	<u>0.829</u>	<u>0.992</u>	<u>0.992</u>
		Rec.	<u>0.987</u>	<u>0.974</u>	<u>0.777</u>	<u>0.924</u>	<u>0.924</u>
KNN	0.619	Prec.	0.737	0.621	0.615	0.667	0.600
		Rec.	0.594	0.782	0.438	0.0	0.885
SVM	0.538	Prec.	0.0	0.460	0.0	0.0	0.576
		Rec.	0.0	0.460	0.0	0.0	0.576

From the comparison between Table 8.7 and Table 8.8 one can see that training is the most expensive step. The training time grows with the size of the dataset, as the difference in training time between DB_{11} and DB_{21} demonstrates. Among the different methods, the ANN requires the longest training time, which is due to the more complex structure and the greater number of parameters. The complexity of ANN also explains the longer training time in the case of System 2. Nevertheless, from the point of view of the automation of operations, training times are not as relevant as prediction times. Furthermore, the initial training is expected to be the most time demanding while all following updates to improve predictions with new verified data are expected to be faster.

Table 8.7: Training time (in seconds) for the best settings of each method applied to each *System*.

	System 1		System 2	
	DB_{11}	DB_{21}	DB_{11}	DB_{21}
ANN	54.378	1151.576	429.119	9899.855
RF	0.481	0.494	0.577	7.543
KNN	0.997	0.256	0.146	0.795
SVM	0.809	7.987	1.668	19.730

From the operational point of view, the prediction time is what actually counts for automating the evaluating process (training can be made offline). Table 8.8 shows that prediction times range from tens of seconds to a few seconds to generate predictions over the whole Validation Set.

Table 8.8: Running time (in seconds) for prediction over Validation Set for the best settings of each method for each *System*.

	System 1		System 2		
Trained in:	DB_{11}		DB_{11}	DB_{21}	
Validated in:	DB_{12}	DB_{22}	DB_{12}	DB_{22}	DB_{22}
ANN	1.275	1.296	1.221	1.554	1.523
RF	0.045	0.084	0.318	0.220	0.555
KNN	0.122	0.282	0.227	0.615	0.905
SVM	0.144	0.321	0.401	1.032	3.702

8.2 Intelligent classification accounting for robust CAM

The system presented in this section extends the ICS approach. When a manoeuvre is suggested by the decision-making system, different alternatives can be proposed, as shown in Chapter 6. The system below proposes the use of ML techniques to predict the class, as before, but based on a different classification criterion that takes into account the CAM alternatives on the reduction of the risk.

8.2.1 Manoeuvre-driven epistemic classification criterion

The classification criterion introduced in Section 3.3.3 classifies events based on the proximity of the event to the encounter and the support and confidence on the value of the PoC based on the available information. Using the classification criterion described there, events can be categorised into 5 classes, where two of them (*Class 1* and *2*) propose a CAM, another two are associated with low-risk events (*Class 4* and *5*), and the remaining one informs about uncertainty on the information (*Class 3*). When a manoeuvre is required, the method proposed in Chapter 5 can provide a set of robust alternatives.

When the magnitude and effect of a CAM are available, the classification can be modified to consider if and when a manoeuvre should be executed Table 8.9. *Class 4* and *5*, which do not consider the possible execution of a manoeuvre, thus they are not affected by the information on the CAM. *Class 1* recommends a CAM execution independently of the magnitude or position, and it is not affected either since it already represents the highest degree of risk.

Once the CAM is computed, *Class 2* is reclassified to *Class 1* if a CAM is below a given threshold at any orbital position prior to TCA, i.e. $\delta v < \delta v_0 \forall \theta_m \in \Theta_m$, where Θ_m is the set of angular positions where the robust optimal CAMs are computed. Since the cost of the manoeuvre is already low, the reclassification would allow anticipating the execution if desired, knowing the event poses a high risk even if it happens further in time. On the contrary, if the cost of the CAM is higher than the threshold δv_0 , *Class 2* will remain unchanged but new measurements are recommended before recomputing the CAM, having the possibility to refine the CAM with the new information, obtaining a cheaper manoeuvre.

Class 3 is reclassified as *Class 1* or *2* depending on the magnitude of the CAM. When the CAM cost is above the threshold for any orbital position the event remains as *Class 3*, indicating more measurements are required to make a confident decision, since manoeuvring would not bring any benefit from the point of view of the cost. However, if an earlier CAM is smaller than a later one, the event is reclassified as *Class 1* and the optimal CAM and position are provided, seeking for the saving in propellant. If the CAM is below the threshold for every orbital position, i.e. $\delta v < \delta v_0 \forall \theta_m \in \Theta_m$, the event is reclassified as *Class 2*: the low cost of the manoeuvre may justify its execution, but the higher degree of uncertainty and the fact that a later manoeuvre does not increase the cost supports the fact that acquiring more measurements can lead to a better decision.

8.2.2 Definition of the dataset

As shown in the previous case, the manoeuvre-driven ICS needs to be trained on a carefully constructed dataset with a variety of encounter geometries and an inclusive

Table 8.9: Manoeuvre-driven epistemic classification criterion.

Class in Table 3.7	δv criterion	New Class
<i>Class 1</i>	-	1
<i>Class 2</i>	$\delta v < \delta v_0 \forall \theta_m$ else	1 2
<i>Class 3</i>	$\begin{cases} \delta v < \delta v_0 \text{ for } \theta_m > \theta_{m0} \\ \delta v \geq \delta v_0 \text{ for } \theta_m < \theta_{m0} \end{cases}$ $\delta v < \delta v_0 \forall \theta_m$ else	1 2 3
<i>Class 4</i>	-	4
<i>Class 5</i>	-	5

uncertainty set. To test the performance of ML techniques applied to the manoeuvre-driven classification criterion, a new synthetic dataset is created with close encounters between simulated space objects in Low Earth Orbit (LEO) whose orbit and associated covariances (or set of CDMs) are assumed to be provided by two sources. The dataset contains the following features: the time to the TCA, the upper and lower bounds of the five uncertain variables, $\mathbf{u} = [\mu_\xi, \mu_\zeta, \sigma_\xi^2, \sigma_\zeta^2, \sigma_{\xi\zeta}]$, provided by each of the two sources of information, the *bpa* of the source, and the set of positions (measured as the difference in true anomaly between execution and encounter positions) where the optimal CAM is computed along with the value of the manoeuvre at those positions, expressed in <T,N,H> reference frame. Finally, the *Class* of the event according to the new classification criterion in Table 8.9 is also included as the label to be predicted.

The close encounters are obtained by propagating the uncertain initial state from an initial position (i.e. the position at the last observation) to the nominal TCA, assuming Keplerian motion. One of the objects is assumed to be perfectly known and manoeuvrable (e.g. an operational satellite), while the other is affected by uncertainty on the position and has no manoeuvre capabilities (e.g. a piece of space debris). The close encounters are defined using the exact nominal orbital parameters. The values of the nominal initial Keplerian parameters of the primary object are sampled from the intervals defined in Table 8.10. The nominal initial state of the secondary object

is obtained by propagating backwards the nominal state from the encounter. The secondary object's nominal state at the encounter is obtained from the nominal encounter geometry, adding to the primary object's state vector, the relative position and velocity, defined by taking values from the intervals defined in Table 8.11. In the table, \mathbf{r}_e is the miss distance in the impact plane, χ the ratio between secondary and primary objects' speed, ϕ the angle between both velocities within the primary's orbital plane and ψ the out-of-plane angle [Bombardelli and Hernando-Ayuso, 2015].

Table 8.10: Intervals from which the primary object's nominal initial Keplerian elements were obtained.

Parameter	Units	Interval
Semimajor axis (a)	[km]	[7000, 7100]
Eccentricity (e)	-	$[10^{-5}, 10^{-4}]$
Inclination (i)	[deg]	[70, 90]
Right ascension of the ascending node (Ω)	[deg]	[0, 20]
Argument of perigee (ω)	[deg]	[0, 20]
True anomaly (θ)	[deg]	[0, 360]

Table 8.11: Intervals from which the nominal encounter geometry variables were obtained.

Parameters		Units	Interval
Relative position	$r_{e\xi}$	[m]	[-5, 5]
	$r_{e\eta}$	[m]	[-5, 5]
	$r_{e\zeta}$	[m]	[-5, 5]
Speed ratio	χ	-	[0.9, 1.1]
Relative velocity angles	ψ	[deg]	[-90, 90]
	ϕ	[deg]	[0, 90]

The uncertainty, assumed to follow a multivariate Gaussian distribution, is included in the secondary object's initial position as explained in Section 5.4.2 (Figs. 5.2 and 5.4). Then, the initial uncertainty position can be defined as:

$$\mathbf{x}_{tnh}^{(2)} = \mathcal{N}(0, \Sigma_{tnh_0}; \boldsymbol{\lambda}). \quad (8.4)$$

The uncertainty is then propagated to the nominal TCA and projected on the nominal impact plane. The intervals for the encounter of uncertain variables (miss distance and

combined covariance matrix in the impact plane) can be then obtained. Note that the simplifying and conservative assumption that the intervals for the miss distance and covariance associated with the propagated ellipsoids can be computed independently is used.

The dataset is generated considering two sources of information and the associated epistemic uncertainty intervals on the miss distance and the covariance matrix, chosen so that the events could be grouped according to five families of encounter geometries. These geometry configurations indicate the different degrees of uncertainty, represented by the combination of the relative position of the sources' sets of ellipses and the Hard Body Radius (HBR), according to Table 3.4. The information from the two sources is fused using the mixing rule.

The samples for each geometry are obtained as follows. The aleatory component of the uncertainty is modelled in the same fashion for all the sets of geometries. The mean of the initial position of the secondary object is set to zero for all the samples, $\boldsymbol{\mu}_{tnh_0} = [0, 0, 0]$ km. The three diagonal terms, $\sigma_{t_0}^2, \sigma_{n_0}^2, \sigma_{h_0}^2$, of the aleatory component of the covariance matrix, $\boldsymbol{\Sigma}_{tnh_0}$, are drawn from the intervals $[0.05, 0.1]$, $[0.01, 0.1]$, $[0.01, 0.1]$ km², respectively. The epistemic component is obtained, for each geometry family, by sampling from the intervals included in Table 8.12. Each ellipsoid within each family of ellipsoids is sampled and the samples are then propagated to the encounter epoch. For each of the ellipsoids before the propagation, an uncertain ellipsoid is fit from the samples, which is then projected on the impact plane.

Finally, the optimal CAM (assumed impulsive) is computed. These five angular positions are used to classify the events according to the new classification criterion introduced in Table 8.9. Table 8.13 includes the rest of the parameters employed to create the dataset. The HBR is kept constant for all the virtual encounters. Likewise, the threshold in PoC, Bel and DoU (PoC_0 , Bel_0 and Δ , respectively) are kept constant for all the encounters. Two time thresholds are considered, $T_2 > T_1$. The robust optimal CAM for each encounter is computed at the five positions, Θ_m , measured as the True Anomaly arc-length to the TCA. The CAM magnitude is optimised so that the risk of the worst-case scenario remained just below the PoC threshold, $PoC^* = PoC_0$, with a

Table 8.12: Intervals from which the bounds of the epistemic parameters λ_μ and λ_σ , per each geometry configuration were obtained. The upper and lower bounds of λ_μ and λ_σ are taken randomly from Λ_μ and Λ_σ , so that $\lambda_\mu \in \Lambda_\mu$ and $\lambda_\sigma \in \Lambda_\sigma$.

Geometry	Parameter	Units	Source 1	Source 2
Geometry 1	Λ_μ	[km]	[-0.01, 0.01]	[-0.01, 0.01]
	Λ_σ	[-]	[0.1, 0.4]	[0.1, 0.4]
Geometry 2	Λ_μ	[km]	[0.35, 0.45]	[0.35, 0.45]
	Λ_σ	[-]	[0.5, 2]	[0.5, 2]
Geometry 3	Λ_μ	[km]	[-0.01, 0.01]	[0.35, 0.45]
	Λ_σ	[-]	[0.1, 0.4]	[0.5, 2]
Geometry 4	Λ_μ	[km]	[-0.1, -0.05]	[0.18, 0.23]
	Λ_σ	[-]	[0.1, 0.4]	[0.1, 0.4]
Geometry 5	Λ_μ	[km]	[-0.15, -0.1]	[0.1, 0.15]
	Λ_σ	[-]	[0.1, 0.4]	[0.1, 0.4]

maximum capacity of the thruster of δv_{max} .

Table 8.13: Parameters employed to obtain the dataset.

Parameter	Units	Value
HBR	[m]	10
PoC_0	[-]	10^{-6}
Bel_0	[-]	0.5
Δ	[-]	0.3
T_1	[days]	2
T_2	[days]	4
δv_{max}	[cm/s]	10
Θ_m	[rad]	$[\pi, 3\pi, 5\pi, 11\pi, 19\pi]$

A total of 18,000 simulated encounters are considered. From them, 3,600 come for each of the five sets of geometries. Each group of 3,600 encounters are evenly distributed over the three time bins used in the classification: short-term, mid-term and long-term. For each time bin and each encounter configuration, in one third, the PoCs is computed using two equally reliable sources of information, on another third, using two sources where one is nine times more reliable than the other, and in the remaining third, the other source is nine times less reliable than the first one. The manoeuvre-driven criterion is then applied, with the resulting classification in Fig. 8.1. There, the dataset classified without accounting for the execution of the manoeuvre,

Fig. 8.1a, is compared to the same dataset classified including the CAM, Fig. 8.1b.

From the figure, it can be seen that *Class 2* and *3* are underrepresented. This is mainly because the magnitude of the manoeuvre tends to classify *Class 2* and *3* geometries as *Class 1*. Due to this unbalanced distribution, the average performance of the ICS system is negatively affected, with a limited ability to correctly predict *Class 2* and *3* scenarios, as shown later. Performing the undersampling technique, a less populated but more balanced dataset can be obtained, providing better prediction capabilities. Thus a new dataset which contains 174 samples per *Class* (from the least populated class), making a total of 870, is created for the training of the ICS.

The features of the datasets are the time to TCA, the sources' *bpa*, and the upper and lower bounds of the uncertain variables, constituting $1 + 2 * 3 * 5 = 31$ inputs. The label of the datasets is the *Class* of the events. The datasets are split into two sets: 80% of the data points forming the Training Set and 20% of data points used as the Test set. The Training Set is used to train the models. The Test Set is used to evaluate the performance of the trained models during the hyperparameter tuning (see next section). Note that the data in the Test Set are not seen by the models during the training process but are used only to assess the performance of each model for a given combination of the hyperparameters. For this reason, the final model performance and comparison are provided on the Test Set acting as the Validation Set.

8.2.3 Machine learning techniques and metrics

The performance of each ML technique is obtained by predicting the results of the samples in the Test Set. The metrics employed to assess the models are the same as in the previous case: the overall accuracy (the percentage of samples correctly predicted over all the samples), the precision by class (the fraction of samples correctly predicted among the total number of samples predicted in that class), the recall by class (the fraction of samples correctly predicted in one class over the total number of samples actually belonging to that class); however, a fourth additional metric is included: the F2-score, both by class and the mean of across categories. The F2-score combines both recall and precision, giving more importance to recall, that is, penalising more False

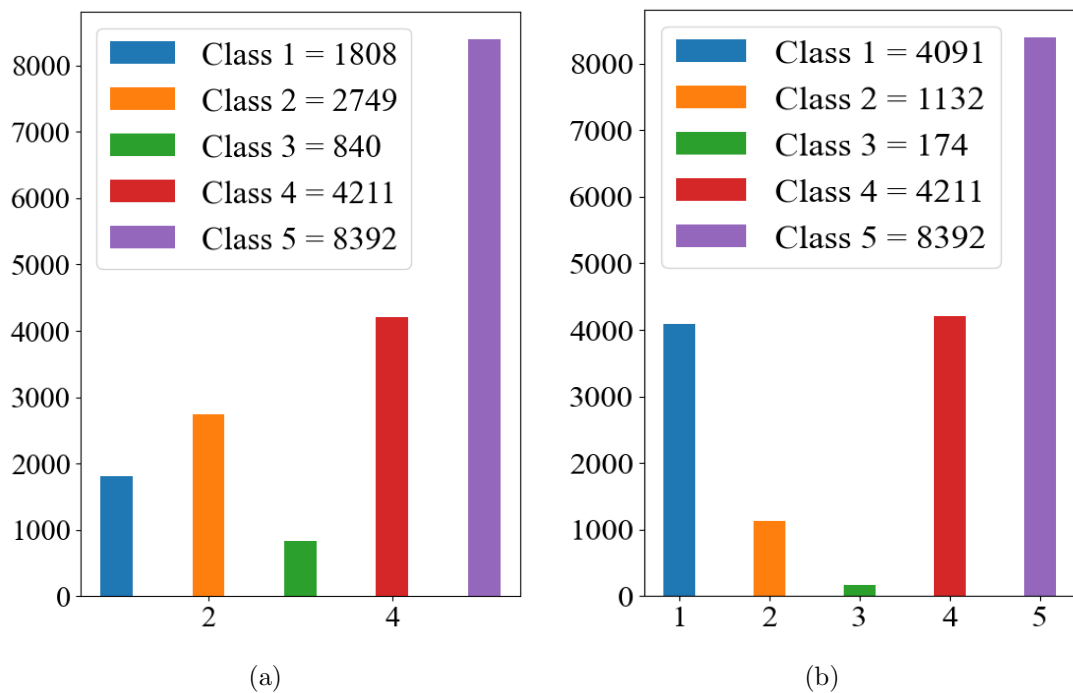


Figure 8.1: Histograms representing the distribution of the sample by Classes: (a) unbalanced dataset with criterion presented in Chapter 3, (b) unbalanced dataset with criterion in Table 8.9.

Negatives (FN) or missed conjunctions than False Positives (FP) or false alerts.

$$F_2 = 5 \frac{\text{recall} * \text{precision}}{4 * \text{recall} + \text{precision}} \quad (8.5)$$

From the previous section, it was clear that RF and ANN techniques performed much better on this classification problem than the other techniques analysed. Thus, for this system, whose basic structure is similar, only those two techniques are implemented.

The hyperparameters of both techniques are the same as in the previous study case. For the ANN models, the only modified parameter is the number of neurons in the single hidden layer considered: 10, 20, 50, and 100 neurons. The rest of the parameters are kept fixed during the analysis. Similarly, for the RF models, the only four parameters modified during the analysis were: the number of trees in the forest, `n_estimators` = {50, 100, 200, 400}, the maximum depth of the tree, `max_depth` =

`{'None', 50, 100}`, the minimum number of samples required to be at a leaf node, `min_samples_leaf = {1, 10-4, 10-7}`, the minimum number of samples to split a node, `min_samples_split = {2, 20}`, and the number of features to consider when looking for the best split, `max_features = {'auto', 0.5, 'log2'}`. In both cases, each combination of hyperparameters was trained on the Training Set using a 4-fold cross-validation approach [Hastie et al., 2009]. The model giving the best F2-score value is saved as the best model of each technique.

8.2.4 Prediction results

Table 8.14 shows the performance of the system using the best RF and ANN models over the Test Set of the balanced dataset. The best ANN model contains 100 neurons on the hidden layer. The best performing RF model's hyperparameters are: 100 trees, automatically determined depth of the trees (`max_depth = 'None'`), the minimum samples at a leaf note equal to 1, the minimum number of samples to split a node equal to 2 and the `'auto'` the value of the variable indicating the number of features to consider then looking for the best split (`max_features = 'auto'`).

It can be seen from the table that RF outperforms ANN, both in mean F2-score and on almost all individual *Class* F2-score. Overall, the performance of the system is good, with a mean F2-score near 90%. Breaking down by *Class*, it is worth noting how *Class 4* and *5* are almost perfectly predicted, while *Class 3* presents the worst prediction score. The reason for a lower score, in this *Class*, is the lack of direct information on the magnitude of the manoeuvre. In fact, the CAM itself is not an input and the ICS has to assume the presence of the CAM from the allocated *Class*. Since *Class 3* is the more ambiguous one, events are miss-classified as *Class 1* or *2*. Note also the low recall of *Class 1*, and the corresponding low precision of *Class 2*. This suggests that the ICS tends to generate a number of false *Class 1* that would induce the operator to acquire additional information before executing a CAM. Although the situation might improve with an extended dataset, this result is still positive, as it is, because it leads to the acquisition of more information. Indeed since *Class 1* usually corresponds to short TCAs, the operator can anyway decide to implement a manoeuvre if there is no

Table 8.14: Performance of the best models for predicting the close event *Class*. The best technique is underlined.

Technique	Class	Accuracy	Precision	Recall	F2
<u>RF</u>	Overall	<u>0.9033</u>	-	-	<u>0.8724</u>
	1	-	<u>0.9234</u>	<u>0.7647</u>	<u>0.7919</u>
	2	-	<u>0.7754</u>	<u>0.9404</u>	<u>0.9020</u>
	3	-	<u>0.8387</u>	<u>0.7027</u>	<u>0.7262</u>
	4	-	<u>0.9867</u>	<u>0.9823</u>	<u>0.9831</u>
	5	-	<u>0.9769</u>	<u>0.9546</u>	<u>0.9589</u>
ANN	Overall	0.8767	-	-	0.8145
	1	-	0.8894	0.8009	0.8171
	2	-	0.7556	0.8681	0.8430
	3	-	0.6000	0.4865	0.5056
	4	-	0.9601	0.9602	0.9602
	5	-	0.9676	0.9414	0.9465

time to allocate a new observation.

From these results, it can be concluded that the system can predict, with a reasonable level of accuracy, the correct *Class* of a close encounter event, except *Class 3*. However, *Class 3* is characterised by a medium-to-long-term event and further decisions can be made. Furthermore, an *Class 3* event, with the added δv criterion, is miss-classified as more stringent *Class 1* and *2*. It can also be concluded that out of the two tested ML algorithms, RFs worked better for this problem.

As shown below, the classification errors have a significantly lower computational time compared to the exact calculation of *Bel* and *Pl*. When the number of uncertain intervals and dimensions increases, the direct computation of *Bel* and *Pl* would make the screening of the whole catalogue of resident objects quite time-consuming. Furthermore, all incorrect classifications would lead the operators to take the robust decision to prepare a CAM and acquire more information unless the available time is too short.

8.2.5 Computational time

In this section, the computational time required to the ICS to indicate the *Class* of an event and suggest action is compared against the computational time required to generate the same output but without ML. The numerical case used in Section 5.4.2

was used as a reference. The bounds of the uncertain variables on the impact plane are included in Table 5.6, both sources are assumed to be equally reliable ($bpa_1 = bpa_2 = 0.5$) and the time to the nominal TCA is 2.0673 hours. This information represents the input to the ICS. With these values, the ICS indicates that the event has to be classified as *Class 1*: a CAM should be implemented.

Table 8.15 shows the computation time required to evaluate the risk and classify the event. It can be seen that the use of the ML model in the ICS leads to a reduction of the computation time by three orders of magnitude. Note that these times refer to a case with 2 sources of information. If more sources of information were available the *Time Pl/Bel* would have increased, or if more positions had been included in Θ_m , *Time CAM*, the calculation of CAM, would have also been greater. This demonstrates the utility of the ICS at processing a potentially large number of events.

Table 8.15: Comparison on computational time for the risk assessment: using the ICS (left) against computing the actual values of the variables involved on the criterion (right). The time is given in seconds.

Prediction with ML		Computing actual values	
Time ML [s]	0.1875	Time Pl/Bel [s]	29.7916
		Time CAM at Θ_m [s]	93.7321
		Time criterion [s]	1.5798
Total time [s]	0.1875	Total time [s]	125.1035

8.3 Intelligent robust conjunction analysis with CDMs

This section proposed the application of ML and Deep Learning (DL) techniques to improve the automation of the robust prediction using the sequence of CDMs. Based on the methodology presented in Chapter 4, RF, Light Gradient Boosting machine (LGBm) and Transformers are employed to skip the most computationally expensive steps of the method: the optimisation of the p-boxes and the computation of the *Pl* and *Bel* curves.

8.3.1 Databases

The architectures proposed in the next section are tested on three different databases of close encounters, sharing the same structure. One of the databases is composed exclusively of virtual encounters, while the other two correspond to encounters faced by two real missions operated by the European Space Agency ESA. The datasets include information about the uncertain variables derived from the CDM sequences of a number of encounters and include the object ID (if any), the encounter identification, the number of the CDM on the list, the time to the encounter from the CDM creation and the miss distance and combined covariance matrix at the impact plane corresponding to each CDM. For each new sample, that is, for each CDM in the sequence, the database associates a label indicating the class according to the methodology exposed Chapter 4, accounting for all the CDMs of the event received up to that stage.

$$s_{gen} = \left[\text{EvID} - \text{ObjID1} - \text{ObjID2} - \#\text{CDM} - t2TCA - \mu_{\xi} - \mu_{\zeta} - \sigma_{\xi}^2 - \sigma_{\zeta}^2 - \sigma_{\xi\zeta} - \text{Class} \right] \quad (8.6)$$

For the rest of this section, the class in the databases is computed using the criterion in Section 7.1 and the following parameters and thresholds: $\delta = 0.5$, $T_1 = 3$ days, $T_2 = 5$ days, $PoC_0 = 10^{-4}$, $Pl_0 = 1/243$, $A_0^* = 0.1$, $\underline{PoC} = 10^{-30}$ and $N = 3$. For more information, refer to Chapter 7.

Synthetic database

A synthetic database composed of virtual encounters is generated. The reason for using a synthetic database is double. First, the real orbit of the satellites (nominal orbit on the next) allows having an actual grown truth for the events, that is, it is possible to know whether the satellites are in an actual collision track. Second, if the ML models trained exclusively on the synthetic database perform well in the real ones, it will make it possible not to get limited to the unbalanced real databases and create databases tailored to the operators' necessities.

This database comprises 1,000 encounters, 50% of whom are collision scenarios. Each event is created as follows: the primary object's Keplerian elements at the nominal

TCA are randomly drawn from the bounds in Table 8.16. The HBR of both objects and the nominal miss distance, $x_b = \sqrt{\mu_\xi^2 + \mu_\zeta^2}$, are drawn from the respective sets making sure the proportion of collision/no-collision events remained balanced. The secondary object's position is then derived from the miss distance and its velocity is randomly selected so that its Keplerian elements at the encounter fall within the same boundaries used for the primary object. Both objects are back-propagated to the first observation epoch, whose difference to the encounter epoch is randomly drawn from [1.5, 7] days, assuming Keplerian motion.

Once the nominal orbit is defined, a preliminary error is added to both objects' states assuming a Gaussian distribution, $\mathcal{N}(\boldsymbol{\mu}_0, \boldsymbol{\Sigma}_0)$ (i.e. simulating the filtering process outcome from a set of observed positions). The expected value of the distribution is drawn from $x_0 \in [0.02, 5]$ m for the collision cases and $x_0 \in [0.02, 200]$ m for the no-collision events, with $x_0 = \|\boldsymbol{\mu}_0 - \mathbf{x}\|$, being $\boldsymbol{\mu}_0$ the expected position and \mathbf{x} the nominal position. There is no offset in the velocity vector. The covariance matrix in the object's $\langle R, T, H \rangle$ frame at the first observations epoch is assumed to be diagonal and the values are from the values in Table 8.16. For each object, random observation epochs are determined, so that the total number of observations (and thus, the final length of the CDM sequence) falls within [15, 30].

At each observation epoch, an observation error based on the preliminary Gaussian distribution defined above, assuming Gaussian distribution $\mathcal{N}(\boldsymbol{\mu}_i, \boldsymbol{\Sigma}_i)$, is added to the nominal state in one of the following three alternatives:

- i) no position offset is assumed in any observation (including the first one), $\boldsymbol{\mu}_i = \mathbf{0}$, and the same covariance error as in the first observations is assigned at every observation, $\boldsymbol{\Sigma}_i = \boldsymbol{\Sigma}_0$;
- ii) the same observation offset of the first observations is assumed for the rest of the observations, $\boldsymbol{\mu}_i = \boldsymbol{\mu}_0$, while the same covariance matrix is assumed for each observation ($\boldsymbol{\Sigma}_i = \boldsymbol{\Sigma}_j$), derived from a rotated and resized version of $\boldsymbol{\Sigma}_0$;
- iii) at each observation, a different offset and covariance matrix are assigned ($\boldsymbol{\mu}_i \neq \boldsymbol{\mu}_j$, $\boldsymbol{\Sigma}_i \neq \boldsymbol{\Sigma}_j$), with $\boldsymbol{\mu}_i$ obtained in the same way as $\boldsymbol{\mu}_0$, and $\boldsymbol{\Sigma}_i$ being a rotated and

Table 8.16: Boundaries of the parameters used to generate the synthetic database of virtual encounters.

Parameters	Units	Range of values
Semimajor axis (a)	[km]	[6850, 7200]
Eccentricity (e)	[-]	[0, 10^{-4}]
Inclination (i)	[rad]	[0, π]
Right Ascension of the Ascending Node (Ω)	[rad]	[0, 2π]
Argument of Perigee (ω)	[rad]	[0, 2π]
True Anomaly	[rad]	[0, 2π]
Time to encounter ($t2TCA_0$)	[days]	[1.5, 7]
Hard Body Radius (HBR)	[m]	[1,12]
Miss distance - Col. (x_0)	[m]	[0.02, 5]
Miss distance - No Col. (x_0)	[m]	[0,02, 200]
Covariance $\sigma_{rr,0}$	[km]	[0.1, 0.15]· 10^{-4}
Covariance $\sigma_{tt,0}$	[km]	[0.5, 0.6]· 10^{-4}
Covariance $\sigma_{hh,0}$	[km]	[0.1, 0.15]· 10^{-4}
Covariance $\sigma_{vrvr,0}$	[km/s]	[5, 6]· 10^{-8}
Covariance $\sigma_{vtvt,0}$	[km/s]	[1, 1.5]· 10^{-8}
Covariance $\sigma_{vhvh,0}$	[km/s]	[1, 1.5]· 10^{-8}
CDM sequence length	[-]	[15,30]

resized version of Σ_0 .

From each observation epoch, each uncertainty ellipsoid is propagated to the nominal TCA using a Monte Carlo run. Following the CDM assumption, the distribution at the encounter epoch is assumed to remain Gaussian. Thus, the propagated samples of both objects are fitted to a Gaussian distribution, $\mathcal{N}(\mu_{TCA}, \Sigma_{TCA})$, to obtain the associated CDM, from where the relative position and the combined covariance matrix in the impact plane, that is, the uncertain variables, are derived.

A total of 17,051 are generated, from which 52.6% corresponds to collision scenarios and the other 47.4% to no-collision cases. After classifying them with the evidence-based approach, the distribution in Table 8.17 is obtained.

The database is relatively well distributed, although some classes (especially, *Class 3*, *4* and *5*) present a lower percentage of samples. This effect is due to the epistemic threshold selection (Chapter 7), which moves some low-risk cases to the uncertainty classes. Nevertheless, the threshold tuning falls out of the scope of this section.

Real databases

Two real databases are used in this work. They correspond to two different missions operated by ESA in the same LEO region (within the boundaries of the synthetic database for the Keplerian elements and other parameters). The databases are compounded by the CDMs received and analysed by the ESA's Space Debris Office (SDO) during the period 2015-2022. The objective of the real databases is also double: first, to analyse the performance of the ML models trained on the synthetic database; second, to study the capacity to extrapolate prediction results from one mission to another, by training the models in one of the two real databases and making predictions on the other.

The first real database contains 36,071 encounters and a total of 239,521 CDMs. The second real database contains 36,160 events and a total of 249,943 CDMs. The class distribution for both databases after the robust conjunction analysis appears in Table 8.17.

The main characteristic of the real databases is the marked unbalanced structure, where the immense majority of cases correspond to low-risk scenarios, with only a handful of events falling in classes associated with high-risk or CAM execution.

Table 8.17: Class distribution on the three databases, in percentage.

	Cl. 0	Cl. 1	Cl. 2	Cl. 3	Cl. 4	Cl. 5
Synth.	25.3	46.6	10.0	6.03	5.07	7.00
Real 1	0.46	0.03	0.01	10.7	30.9	57.9
Real 2	0.48	0.01	0.01	10.5	31.3	57.7

Database split

To avoid overfitting during the training stage, The databases are split into a training set (80%) and a test set (20%). The test set remained unseen for the models during the training phase and is only used to make predictions and compare the models' performance (acting also as the validation set). Thus, the same test split is shared by all the models.

Since from each event, several samples are obtained (one sample per each new CDM

on the sequence), to avoid data leaking, having two very similar samples coming from the same event in the training and the test set, the division is made at an encounter level, splitting the database using the *Event ID*. That is, the training set is compounded by the 80% of the events, which is close, but not necessarily equal, to the 80% of the samples due to the difference in the length of the CDM sequences.

Table 8.18 shows the distribution of classes in the two sets, both for the synthetic database and one of the real databases. The remaining real database is not used for training, but only for testing the extrapolation capabilities of the models, and thus, is not split.

Table 8.18: Class distribution on the training and test sets, in percentage.

	Cl. 0	Cl. 1	Cl. 2	Cl. 3	Cl. 4	Cl. 5
Synth Train.	25.9	45.6	10.3	6.13	4.98	7.09
Synth Test	23.2	50.4	8.64	5.66	5.09	7.01
Real Train.	0.46	0.02	0.02	10.7	30.8	58.0
Real Test	0.54	0.05	0.01	10.7	31.1	57.6

8.3.2 Architectures

This section presents the different architectures analysed in this work to predict the class obtained with the evidence-based classification criterion presented in Chapter 4 given a sequence of CDMs. These models aim to skip all or some of the computationally expensive steps by building a faster mapping between uncertain geometry and the robust class. Five different architectures are proposed, two of them using RF, another two using LGBm and the last one employing Transformers.

RF [Breiman, 2001] is an ensemble method that combines several independent Decision Trees during the training step, feeding each of them with different subsets of the training set. The predicted class is the mode of the output of every single tree. RFs allow for overcoming the overfitting and bias problem presented by Decision Trees while maintaining the simple architecture.

LGBm [Ke et al., 2017] is a variant of the Gradient Boosting methods, also based on the ensemble of Decision Trees (*Boosting*). LGBm present the advantages of other Gra-

Gradient Boosting models, like the simplicity of implementation, and the reduced number of parameters required to be tuned, but it allows for faster training and higher accuracy. The main difference to other Decision Trees-based algorithms is that it does not present a level-wise growth (growing a new row from the previous nodes at a time), but a more efficient leaf-wise growth, where only the most promising node generates a new row. One important advantage to other architectures is that it accepts, simultaneously, continuous and categorical variables without any pre-processing.

The Transformer architectures [Vaswani et al., 2017], originally proposed for the task of machine translation in the field of Natural Language Processing (NLP) and now applied to a wider range of tasks, leverages the ideas from attention-based models and proposes to construct a model to process sets and sequences by using only an attention mechanism between a data encoder and a decoder. The term “attention mechanism” in neural networks is used to represent a specific class of algorithms, in which the model looks at each element of the sequence in turn, and compares it to every other point, attempting to determine the most relevant part of the sequence for each point. This overcomes the limitation of local connectivity, at the cost of the quadratic complexity that the attention matrix has in terms of memory usage. The network implemented here follows the structure used in [Stevenson et al., 2022a].

Random forest with intervals

This architecture uses RF to classify the events taking the interval bounds of the uncertain variables instead of the CDM samples. That is, this approach skips the second optimisation step (the computation of the Pl and Bel) in Chapter 4, but it still requires to derive the set of intervals using the Dvoretzky-Kiefer-Wolfowitz (DKW)-based approach.

RF requires the tabular inputs, thus, the length of every sample should be the same. Since sequences of CDM have different lengths, this approach takes advantage of the tabular format of the Dempster-Shafer theory of Evidence (DSt) structures after performing the α -cuts. However, the number of inputs grows with the number of cuts, thus a trade-off between accuracy (of the DSt structure) and complexity (of the input

Table 8.19: Set of hyperparameters considered to select the best model during the RF training.

Hyperparam.	Values
n_estimators	{50, 100, 200, 400}
max_depth	{None, 50, 100}
min_samples_split	{2, 20}
min_samples_leaf	{ 10^{-7} , 10^{-4} , 1}
max_features	{‘auto’, ‘log2’, 0.5}

data) should be achieved. As indicated before, in this work, two α -cuts per variable are performed, thus $N = 3$ for each variable.

The features are structures for this architecture so they take the lower and upper bound of each interval and its associated bpa , for each of the uncertain variables, and the time to the encounter. Thus, the number of features is equal to: $\#feat_{RF,int} = 3 * N * m + 1 = 3 * 3 * 5 + 1 = 46$, with N the number of intervals and m the number of uncertain variables:

$$s_{RF,int} = [\underline{\mu}_{\xi,1}, \overline{\mu}_{\xi,1}, bpa_{\mu_{\xi,1}}, \underline{\mu}_{\xi,2}, \overline{\mu}_{\xi,2}, bpa_{\mu_{\xi,2}}, \dots, \underline{\sigma}_{\xi,1}^2, \overline{\sigma}_{\xi,1}^2, bpa_{\sigma_{\xi,1}^2}, \dots] \quad (8.7)$$

The method was implemented using Python’s “scikit-learn” library [Scikit-learn, 2021b]. A hyperparameters search was carried out among the values included in Table 8.19. The rest of the arguments took the default values in the library, including the loss function (cross-entropy).

Random forest with CDMs

This architecture also uses RF, but it takes directly the information from the CDMs instead of the intervals. Thus, it skips the two computationally expensive optimisation steps. To avoid the different lengths of the sequences, this approach uses a lag window, so it takes a certain number of CDMs previous to the latest one in the sequence. While this solves the problem of the tabular inputs, it is at the cost of losing some information on the sequence. Note that the class of the event takes into account the whole sequence of CDM (Chapter 4). This allows training the model on a database with more accurate

Table 8.20: Synthetic samples with lag step 1 used by the LGBm architectures and the RF with CDM approach. The $Class_{t-1}$ columns would be used only by the autoregressive LGBm method. Units in m , m^2 and $days$.

#Sample	$\mu_{\xi,t}$	$\mu_{\zeta,t}$	$\sigma_{\xi,t}^2$	$\sigma_{\zeta,t}^2$	$\sigma_{\xi\zeta,t}$	$t2TCA_t$...
0	37.51	$7 \cdot 10^{-11}$	$9.4 \cdot 10^5$	$5.1 \cdot 10^5$	$-6.9 \cdot 10^5$	2.79	...
1	25.37	$4 \cdot 10^{-10}$	$3.4 \cdot 10^5$	$1.6 \cdot 10^6$	$6.3 \cdot 10^5$	2.64	...
2	22.59	$-7 \cdot 10^{-11}$	$1.7 \cdot 10^{-5}$	$8.5 \cdot 10^5$	$-3.8 \cdot 10^5$	2.36	...
3	32.99	$4 \cdot 10^{-10}$	$5.9 \cdot 10^5$	$4.7 \cdot 10^5$	$5.3 \cdot 10^{-10}$	2.23	...
...
(#Sample)	$\mu_{\xi,t-1}$	$\mu_{\zeta,t-1}$	$\sigma_{\xi,t-1}^2$	$\sigma_{\zeta,t-1}^2$	$\sigma_{\xi\zeta,t-1}$	$t2TCA_{t-1}$	$Class_{t-1}$
(0)	177.1	$-5 \cdot 10^{-10}$	$1.8 \cdot 10^6$	$2.6 \cdot 10^4$	$2.1 \cdot 10^5$	2.86	-
(1)	37.51	$7 \cdot 10^{-11}$	$9.4 \cdot 10^5$	$5.1 \cdot 10^5$	$-6.9 \cdot 10^5$	2.79	1
(3)	25.37	$4 \cdot 10^{-10}$	$3.4 \cdot 10^5$	$1.6 \cdot 10^6$	$6.3 \cdot 10^5$	2.64	1
(3)	22.59	$-7 \cdot 10^{-11}$	$1.7 \cdot 10^{-5}$	$8.5 \cdot 10^5$	$-3.8 \cdot 10^5$	2.36	1
...

classes obtained from a finer p-box partition without increasing the number of inputs. However, to compare the models' predictions across the different alternatives, the same 3 intervals partition is used for to train this model.

The structure of the features takes the last CDM uncertain variables and the time to the encounter plus the same variables of the previous CDMs included on the lag window: $\#feat_{RF,lag} = (m + 1) * (l + 1)$, where l is the lag window and $l = 0$ means that only the last CDM is considered. In Table 8.20, an example of the samples with $l = 1$ can be seen (note the last column is not used in this case architecture).

The same implementation, hyperparameters and loss function as in the previous model are employed here.

LGBm with CDMs

The same approach as before is followed here, but using LGBm architecture instead. The inputs (Table 8.20 without the last column) and output are the same. Thus, the influence of the model can be also analysed, as a mid-step between the previous and the next approaches.

The method was implemented using Python's "LightGBM" library [Python, 2023],

Table 8.21: Set of hyperparameters considered to select the best model during the LGBm training.

Hyperparam.	Values
n_estimators	{1, 2, 5, 10}
max_depth	{2, 7, 10, 15}
subsample	{0.7, 0.8, 0.9}
colsample_bytree	{0.7, 0.8, 0.9}
boosting_type	{'gbdt', 'rf'}

following the same approximation as in the previous scenarios. The set of hyperparameters considered in the search appears in the Table 8.21, with the rest of the argument's values set as default, with cross-entropy as loss function.

Autoregressive LGBm with CDMs

This approach follows a similar approach to the previous one, but instead, it uses the previous class as a feature (all columns in Table 8.20). Due to the possibility of combining numerical and categorical features in the input data, this alternative applies a sort of autoregressive implementation, including the class to be predicted in the previous time series instance as a feature (last column in Table 8.20).

To have a tabular structure on the input data, a lag window is also employed to take the information from the last and the previous l CDMs, and additionally, the class associated with those previous cases. Thus, the number of features is equal to $\#feat_{LGBm} = m + (m + 1) * l$.

The aim of this *autoregressive* technique is to include the sequential character of the inputs, expecting that the classification is influenced by the incremental amount of information received with the new CDMs. With this approach, it is expected to recover some of the information from previous CDM lost with the lag window, since the previous class implicitly contains information from the whole sequence.

The same implementation as the previous case is followed, using Python's "LightGBM" library [Python, 2023] and the hyperparameters in Table 8.21.

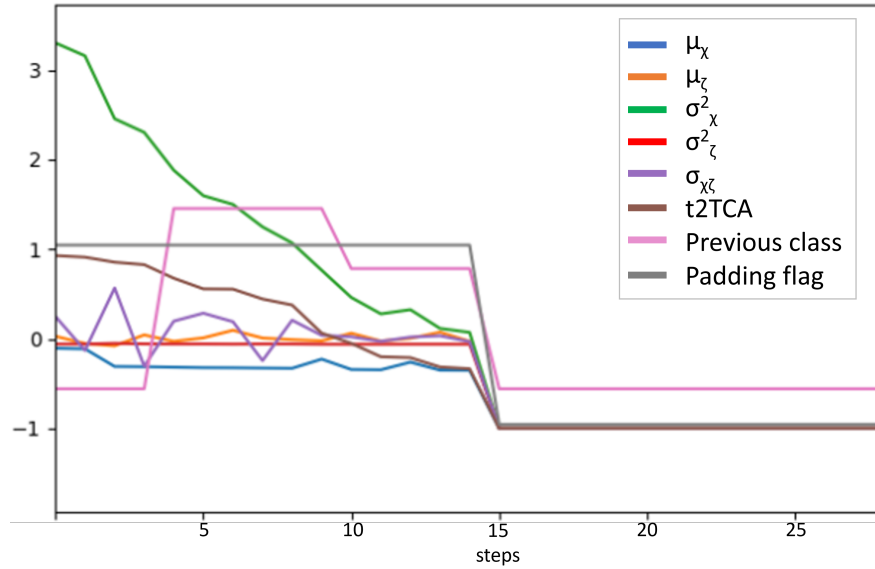


Figure 8.2: Multi-channel time series synthetic sample for the transformer, including padding and the padding flag.

Transformers with CDMs time series

Finally, this last proposal implements the Transformer architecture. to classify the time series of CDMs. As in the two previous implementations, from an event with N CDMs, $N - 1$ samples are extracted (at least two samples are required to perform the proposed methodology). However, in this case, each sample is compounded by a set of eight time series corresponding to the five uncertain variables, the time to the encounter, the previous class (categorical) and a padding flag. To have regularly spaced time series of equal length, the samples in the time series are sorted according to their index on the series, including the time as a feature (time to the encounter), and the length of the time series is set equal to the maximum length, filling shorter times series with a padding value. The padding flag indicates if the value comes from the CDM or is a filling value. The variables are normalised before being fed to the network. Fig. 8.2 includes an example of a normalised sample.

The model is implemented using Python’s “tsai” library [tsai, 2023]. The models are compared using the F2-score metric. For the optimiser, Ranger is used, an extension of the Adam optimiser [Stevenson et al., 2022a]. Weights and momentum are instanti-

Table 8.22: Set of hyperparameters considered to select the best model during the transformer training.

Hyperparameters	Values
depth	{1, 2, 3, 4, 5}
attn_dropout	{0, 0.1, 0.2, 0.3, 0.5 }
res_dropout	{0, 0.1, 0.2, 0.3, 0.5 }
wd	{0, 0.1, 0.3}
n_epochs	{10, 25, 50}

ated as default, the loss function used is also cross-entropy and a variable “one-cycle” learning rate is applied. The hyperparameters modified appear in Table 8.22.

Training and hyperparameter search

The same hyperparameters search process is performed on each architecture while training. The process performs a random search on the space defined in Tables 8.19, 8.21 and 8.22 for each architecture. The model defined by the selection of hyperparameters is trained on the training set and evaluated on the test set. The process is repeated for several combinations of hyperparameters, and the best model is selected as the one performing better on the test set. Due to the class imbalance and the higher importance of avoiding miss encounters than the false alert, the performing metric used is the average F2 score, $\overline{F_2}$,

$$\overline{F_2} = \frac{\sum_i^N F_{2,i}}{N}, \quad F_{2,i} = \frac{5 \cdot precision_i \cdot recall_i}{4 \cdot precision_i + recall_i}, \quad (8.8)$$

being N the number of labels. For the architectures using a lag window, the best model for a different window length is saved for further analysis in the next section.

8.3.3 Results

This section compares the different models’ performance across the different databases, after having been trained on the synthetic database and in one real database. Table D.3 in Appendix D shows the hyperparameters of the best model for each technique in both cases.

Table 8.23: F2-score of the best model of each architecture trained on the synthetic set. Upper-tier, models evaluated on the corresponding test set (synthetic on left, real on right), lower-tier, models evaluated on the real dataset not used for training. In bold, the model with the highest overall F2-score on each database. Underlined, the best F2-score by class.

	Overall	Cl. 0	Cl. 1	Cl. 2	Cl. 3	Cl. 4	Cl. 5
RF interv. (test set)	.854	.902	.947	.868	.841	.805	<u>.873</u>
RF CDMs (test set)	.748	.780	.933	.820	.798	.803	.581
LGBm CDMs (test set)	.759	.788	.930	.766	.798	.774	.449
LGBm (test set)	.879	<u>.916</u>	.948	.883	.859	<u>.838</u>	.847
Transformer (test set)	.881	.873	.970	.909	.894	.830	.824
RF interv. (real)	.523	.079	.024	.009	.823	<u>.975</u>	<u>.958</u>
RF CDMs (real)	.270	.015	<.001	.043	.459	.766	.599
LGBm CDMs (real)	.403	.020	.003	.008	.830	.915	.806
LGBm (real)	.601	.672	.026	.016	.907	.903	.950
Transformer (real)	.302	.240	.005	<u>.101</u>	.581	.445	.536

Training on synthetic database

Table 8.23 shows the performance of the different approaches trained on the synthetic set both evaluated on the synthetic test set (upper tier) and the real database (lower tier). The prediction on the synthetic test set, with similar characteristics to the training set, presents a generally good F2 score, both overall and by classes. RF with intervals has good prediction capabilities since the inputs are some steps closer to the output in the underlying model. However, the autoregressive LGBm and the Transformer architectures (which also include the previous class among the inputs) match or improve those results, even though they are fed directly with the uncertain geometry. Regarding the score by class, there is a slightly better score in the more populated categories, although good prediction capabilities are obtained across the classes. In any case, the synthetic database does not present a sharp imbalance trend. Nevertheless, it seems that an equally distributed and enough populated database could level those scores.

However, the extrapolation capabilities to a real database do not provide good results. The autoregressive LGBm still provides the best results, with better extrapolation capabilities, although with a score some points below the previous case. While

the populated classes still score well, the scarcely populated categories are not well predicted. This pattern is repeated across all the methods, including also the RF with intervals, despite the less complex model tried to be replicated. This method scores especially well on labels 4 and 5, but very poorly on the others. Surprisingly, the transformer does not extrapolate well the predictions from the virtual database to the real one. Such an imbalanced database, with very few high-risk cases and so differently distributed from the training set is, at least partially, behind those poorer results. It is possible, given the score in the synthetic database, that a more equally distributed database should provide better scores in the lower database. Regarding the scarcity of real high-risk data, a potential approach is to evaluate the model during training in a validation set simulating the distribution on the real set, so it prioritises models scoring highs on such databases.

From this analysis, it was observed that the length of the lag window has little influence on the performance, even though it adds more information to the model. In Fig. 8.3, it can be seen that the score is almost indifferent to the lag step. For the RF and LGBm using the CDMs (green and red, respectively), the score both in the synthetic validation set and in the real set is almost constant. The LGBm has slightly better performance and better extrapolation capabilities, but they provide very similar results. However, when observing the autoregressive LGBm score, it can be seen that adding a 1-step lag window significantly increases the performance, but longer windows have no effect. This allows the conclusion that including the previous class is what improves the model prediction capabilities.

Training on real database

This section presents the same analysis, but having trained the model on one of the real databases. On Table 8.24, the performance of the models on the validation set of the real database (upper tier) and in the whole dataset of the other real mission (lower tier) are shown.

The performance of the validation is greatly affected by the imbalance in the dataset. The overall F2 score is lower than when trained on the synthetic database, affected by

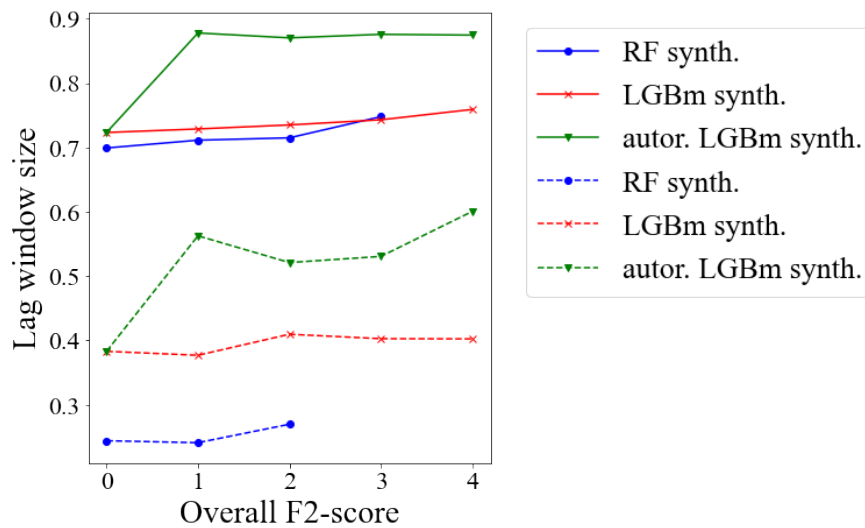


Figure 8.3: Overall F2 score as a function of the lag window length for the different architectures. Solid: train in synthetic evaluated on the synthetic dataset; dashed: train in synthetic evaluated on the real dataset.

the poor performance in the less populated categories, especially Class 1 and Class 2, where some methods are not able to predict any sample. Nevertheless, the autoregressive LGBm and the transformer are the better models, performing well along all the classes (including Class 0), except the least populated. More interestingly, when comparing the performance of the models trained on the synthetic dataset and validated in the real set, the performance is, in general, better for these two techniques, especially the transformer.

When extrapolating the results to the other real dataset, the autoregressive LGBm and the transformer perform also better than the other models. Although not achieving the same scores as when validating in the synthetic dataset due to the imbalance character of the real set, they achieve almost similar results as when predicting on the real test set. Moreover, the extrapolation capabilities of the transformer improve when compared when training on the synthetic set, achieving good scores except for Class 2 (where is not able to predict any sample as the rest of the architectures). Again, a better-distributed database for training is likely to improve scores on the less populated categories.

Table 8.24: F2-score of the best model of each architecture trained on one of the real sets. Upper-tier, models evaluated on the corresponding test set (synthetic on left, real on right), lower-tier, models evaluated on the real dataset not used for training. In bold, the model with the highest overall F2-score on each database. Underlined, the best F2-score by class..

	Overall	Cl. 0	Cl. 1	Cl. 2	Cl. 3	Cl. 4	Cl. 5
RF interv. (test set)	.663	.637	.000	<u>.731</u>	<u>.999</u>	<u>.998</u>	<u>.997</u>
RF CDMs (test set)	.509	.436	.000	.000	.954	.936	.924
LGBm CDMs (test set)	.580	.000	.000	.000	.950	.935	.922
LGBm (test set)	.640	<u>.835</u>	<u>.434</u>	.000	.949	.926	.924
Transformer (test set)	.732	.807	.294	.000	.961	.935	.981
RF interv. (real)	.566	.578	.000	.000	<u>.998</u>	<u>.999</u>	<u>.995</u>
RF CDMs (real)	.489	.250	.000	<u>.322</u>	.944	.930	.908
LGBm CDMs (real)	.441	.000	.000	.000	.944	.931	.907
LGBm (real)	.579	<u>.824</u>	.098	.000	.944	.923	.910
Transformer (real)	.618	.549	.898	.000	.914	.949	.963

Training on real database

Table 8.25 shows a comparative of the computational time saved by the different AI approaches with respect to using the model-based approach for a case with 15 CDMs and 3 α -cuts. It can be seen that proposed approaches save time by skipping specific steps: the derivation of the p-boxes (except for the RF with intervals) and the computation of the *Pl* and *Bel* curves. The required time is one or two orders of magnitude smaller when using the ML approaches directly with the sequences. Note that, if increasing the number of α -cuts, the time required for the computation of *Pl* and *Bel* increases significantly (in the table, indicated in parenthesis), while the classification with AI-based approached remains indifferent.

8.4 Chapter summary

This chapter introduced the use of ML methods to enhance the capabilities of the robust decision-making system proposed in previous sections of this work. The objective of those ML models is to make the automation of the STM system more likely thanks to their capacity to learn from data, improving capabilities when more available information, and speeding up the tasks by providing faster surrogate models.

Table 8.25: Computational time (in seconds) for robust CARA with and without using AI techniques.

	p-box	P1/Bel	Class.	Total
No AI	75.4	2.37 (~150)	0.02	78.1 (~225)
RF inter.	75.4	-	0.06	75.8
RF CDMs	-	-	0.15	0.16
LGBm CDMs	-	-	0.03	0.03
LGBm	-	-	0.03	0.03
Transf.	-	-	0.07	0.08

Several ML systems were proposed to predict the classification risk of the conjunction events affected by epistemic uncertainty, applying different ML techniques, being RF and ANN the most successful. Good accuracy was obtained when trained and validated on synthetic datasets. The proposed system was extended to cope with the information provided as CDMs, a common practice with real operators. This allows as well to try the models on datasets of real conjunctions. Although the performance was reduced in this case, the results still suggest ML can be a useful tool for STM.

One important aspect of the training and validation process is the impact of the datasets. Having varied examples within the datasets seems to improve notably the results without the need to add complexity to the ML models. Balanced datasets proved to be necessary for achieving good-quality predictions, although this is not always the case on datasets of real scenarios. Related to this, the build of realistic datasets representative of the real scenarios is a challenging process. However, the potential benefits (more populated and balanced datasets with a wider range of inputs) compensate for the difficulties.

Chapter 9

Multiple encounters

The content of this chapter was partially published in:

Sánchez, L. and Vasile, M. (2021), “Constrained optimal collision avoidance manoeuvre allocation under uncertainty for subsequent conjunction events”, 72nd International Astronautical Congress; [Sánchez and Vasile, 2021b]

Vasile, M. and Sánchez, L. (2022), “Robust optimisation of coordinated collision avoidance manoeuvres in large constellations”, 11th International Workshop on Satellites Constellations and Formation Flying. [Vasile and Sánchez, 2022]

This chapter addresses the multiple-encounter decision-making issue by extending the method proposed in Chapter 6. If avoiding a single encounter already requires some decision-making that may be problematic, the challenge increases when the avoidance strategy involves more than one satellite, more than one encounter or both situations simultaneously. The number of alternatives and the criteria to be taken into account will increase in such situations. Thus, the Multi-Criteria Decision-Making (MCDM)-based approach proposed then can support operators in taking the best alternative in the multiple-encounter event.

The rest of the chapter is structured as follows. In Section 9.1, a definition of a multiple-encounter event and an explanation of why this should be a concern in the near future is presented. Section 9.2 proposes the use of the MCDM approach to deal

with subsequent encounters faced by a single satellite (One-vs-Many), that is, when an operational satellite has to avoid more than one encounter, either with the same or different objects. A numerical example is presented, showing different scenarios that will affect the best approach. In Section 9.3, the MCDM is adapted to cope with encounters affecting constellations. More specifically, a situation where more than one satellite need to manoeuvre (Many-vs-One or Many-vs-Many, depending on the number of secondary objects) and the constellation configuration may be compromised. Finally, the chapter finishes with the main remarks in Section 9.4.

9.1 Multiple encounters

Space is getting more crowded in recent years with the exponential growth of the commercial market, the appearance of very small and accessible satellites and the emergence of mega-constellation [ESA, 2023b]. The so-called New Space is a reality and, together with new opportunities, it will bring new challenges [Muelhaupt et al., 2019]. One of those new problems to be faced by future operators is the occurrence of multiple encounter events [Masson et al., 2022, Kim et al., 2012]. These events involve one or more satellites that need to avoid several encounters. Although they do not present a current issue, which is reflected in the few studies on this topic [Duncan et al., 2011, Kim et al., 2012, Masson et al., 2022, Arias et al., 2023], a more populated space will increase the number of conjunction alerts [Muelhaupt et al., 2019], which will necessarily increase the chances of having more than one encounter within the operator time horizon.

A multiple-encounter can be defined as a series of successive close conjunctions between one satellite and one or more space objects, either operational satellites or pieces of space debris, within a given time horizon. In this context, the individual encounters involved in the multiple event may be classified as:

- Primary encounter, the first conjunction between Object A (e.g. operational satellite) and Object B (e.g. another satellite or a piece of space debris).
- Secondary encounters, the subsequent conjunctions between Object A and Object B.

- Tertiary encounter, an encounter between Object A and Object C (e.g. another satellite or piece of space debris) taking place after the primary encounter.

For the sake of clarity on the methodology and without losing generality, in the rest of the analysis, only secondary encounters were considered, and more precisely, two-encounters events (that is, one secondary event). Nevertheless, the method can be applied without any modification for more than one secondary event and is easily extended to cope with tertiary encounters.

From a different perspective, also affecting the New Space context, a constellation operator may face situations where more than one of its satellites is involved in an encounter. This multiple-encounter event affecting the constellation creates a more complex scenario than the single satellite one due to the effect on the constellation geometry, and thus, the provision of services [Petit et al., 2021]. In this case, a multiple-encounter is defined as an event, given a time horizon, where more than one encounter has to be avoided by the constellation, either by a single satellite or more than one satellite, affecting its overall configuration [Ayala Fernández et al., 2021]. The encounters may be caused by a single external object (operational satellite or piece of space debris) or by several objects.

Under this definition, situations when several satellites have to manoeuvre almost at the same time are now contemplated as well. Considering that the constellation service is optimally delivered when the satellites keep the nominal configuration of the constellation [Stoll et al., 2011, Ayala Fernández et al., 2021], this situation introduces a greater disruption in the relative position among satellites than the single satellite scenario, especially if taking into account the returning strategies to recover the adequate configuration.

In any case, both scenarios, the One-vs-Many and Many-vs-One, fall within the collaborative problems defined in Chapter 6. In the case of a single satellite with a single decision-maker, by definition, it is a collaborative scenario. In the case of the constellation, despite involving several satellites, there is only one supra-agent looking for the most common beneficial outcome, which represents a collaborative case as well. Only, if the external object was an operational satellite, this scenario could be classified

as a non-collaborative one, a situation not considered in this work. Thus, MCDM techniques can be used to support decision-makers in the multiple encounters events treated in this work.

In the next lines, the MCDM-based system presented in Part I is extended to deal with these more complex scenarios. Note that only impulsive manoeuvres are considered. Although the application of the MCDM methodology on the Low-Thrust (LT) case would not be altered, the computation of the alternatives (avoidance and returning strategy) would require some modification with respect to the approach presented in the next sections, especially in the referring to the returning strategy or strategies avoiding more than one encounter simultaneously.

9.2 Subsequent encounters

This section applies the MCDM-based method to provide robust decision-making in Conjunction Assessment Risk Analysis (CARA) to deal with subsequent encounters faced by a single satellite.

9.2.1 Avoidance strategies

Several different strategies can be carried out to avoid the encounters:

- *Single manoeuvre - single encounter avoidance (Strategy A)*. This approach only addresses one of the encounters (e.g. the closest in time, the one involving a higher risk), and computes the robust optimal manoeuvre to avoid it, leaving the reduction of risk on the other encounters as the secondary result of the manoeuvre. It presents the advantage of simplifying the computation and requiring fewer manoeuvres to be implemented (saving the associated risk of the execution of the manoeuvres), although it has the risk of not reducing enough, or even increasing, the risk associated with the not avoided event. The optimal impulse would be computed by solving Eq. (5.18), where Υ is composed only for the family of ellipses of the conjunction considered.
- *Single manoeuvre - multiple encounters avoidance (Strategy B)*. This strategy

takes advantage of the reduction of cost and risk associated with the Collision Avoidance Manoeuvre (CAM) due to the lower number of manoeuvres (only one) while minimising the risk of all the encounters simultaneously. Assuming all the encounters involved the same pair of objects, their uncertainties are correlated and they can be added together. Thus, the set Υ is now constituted by the set of families of all the encounters, increasing in size accordingly. The solution of the process is a manoeuvre that optimises the worst-case scenario of the combined event, presenting the additional advantage of being robust. However, the impulse may not be optimal from the point of view of each encounter: the worst-case scenario of each encounter after executing this proposed manoeuvre may present a higher Probability of Collision (PoC) compared to the separate optimisation of the individual conjunctions (next strategy).

- *Multiple manoeuvres - multiple encounters avoidance (Strategy C)*. This strategy consists of implementing an individual manoeuvre for each of the encounters. The main advantage is that each encounter is optimised individually, overcoming the disadvantages of the previous approaches. However, it introduces some challenges: more than one manoeuvre is required (with the associated execution risk), additional cost (both for the CAM and for the time out of normal operation), more optimisation runs required... To obtain the optimal impulse, the process is different for the primary encounter than for the subsequent encounters. The impulse for the first encounter is obtained by solving Eq. (5.18). For the next conjunction, the new relative position after executing the previous manoeuvre has to be obtained, which will modify the encounter geometry and the PoC with respect to the unperturbed scenario. Once the new geometry is obtained, the optimal CAM is obtained by solving again Eq. (5.18). Note that in this work, if choosing this strategy, the satellite is assumed not to return to the original orbit after all the close encounters were avoided.

In case more than two encounters are involved in the event, a combination of the previous strategies can be also possible (for example: avoiding two encounters with a single manoeuvre and the third one with a dedicated one). This situation will be

necessary if one or more of those encounters involves a third object.

In addition to the avoidance strategies, one could consider the returning strategy. Assuming the satellite is not returning to the original orbital after all events have passed, the returning strategy to the nominal orbit should present small differences among alternatives compared to the other variables (both in terms of cost and risk). Thus, no returning strategy is considered in this case. However, it will be of major importance in the following scenario (Section 9.3).

The combination of avoidance strategies with the manoeuvre execution position will generate a set of alternatives from which the operator will have to select the most appropriate one according to the mission's needs. For example, the operator may need to discern between a late single strategy manoeuvre avoiding the riskiest encounter, an early manoeuvre optimising both encounters simultaneously, an early first manoeuvre to avoid the first encounter with a late manoeuvre to avoid the second one, or two late manoeuvres to avoid each of the encounters separately, among many others possibilities. The right alternative may depend on the risk the operator is willing to assume (both on the encounter and in the CAM execution), the mission's lifespan moment, the remaining propellant, the cost associated with implementing manoeuvres... Thus, MCDM techniques can be used to rank the alternatives, provided the criteria and weights are defined.

Certain strategies may create incompatibilities between the manoeuvres to avoid each encounter. For example: avoiding a second encounter by manoeuvring earlier than the previous one takes place may lead to an increase in the risk of that first conjunction or conflict with the strategy to avoid it. Thus, the system has to take into account certain constraints related to the geometry of the problem. Associated with this, other operational constraints may be desired by the operators (operational constraints), which will be similarly treated by the system. For example, not executing manoeuvres in the last orbits (to have time to check the right upload of the commands or having an extra opportunity with an additional pass), avoiding certain regions of the orbit (eclipse areas) or certain times (avoid not-working hours), or exclude certain directions (protection of certain sensor, only tangential manoeuvres), among other considerations.

9.2.2 Risk assessment

In the following, an example of how to use MCDM to support operators in the decision-making to deal with subsequent encounters is presented. Two scenarios are proposed in this example. In both cases, two objects are facing two subsequent encounters between each other. One of the objects is an operational manoeuvrable satellite, while the other has no manoeuvre capabilities (e.g. a piece of space debris or a small satellite). The difference between the two scenarios is that in the first one (*Example 1*), the two conjunctions take place in the same orbit region, while in the second case (*Example 2*), they occur on opposite sides of the orbit. In this example, Keplerian motion is assumed on the propagation of the objects and their uncertainty, and the Normality of the distribution is also assumed before and after the propagation.

Initial and encounter information

Having two space objects with the orbital elements at a specific epoch, state as initial time, specified in Table 9.1, two scenarios are presented. Note: the secondary object in *Example 1* has a period five times greater than the manoeuvrable satellite.

Table 9.1: Nominal Keplerian elements at the initial time for the subsequent-encounters scenario.

Variable	Units	Object 1	Object 2 (Example 1)	Object 2 (Example 2)
Semi-major axis (a)	[km]	7,100.0	20,760.53	7,100.05
Eccentricity (e)	-	10^{-5}	0.658	10^{-5}
Inclination (i)	[rad]	$\pi/4$	$2/3\pi$	$\pi/3$
Right ascension asc. node (Ω)	[rad]	0.0	0.0	π
Argument of perigee (ω)	[rad]	0.0	0.0	π
True anomaly (θ)	[rad]	$\pi/2$	3.9723	$\pi/2$

The primary object is assumed to be perfectly known. The uncertainty on the secondary's initial position has two components: aleatory and epistemic. The aleatory term is modelled with a 3D Gaussian distribution, expressed on the object's <T,N,H> reference frame: $\mathcal{N}(\boldsymbol{\mu}_{tnh_0}, \boldsymbol{\Sigma}_{tnh_0})$. The epistemic uncertainty is modelled using the Dempster-Shafer theory of Evidence (DSt). Thus, the epistemic component is expressed

with two interval-valued epistemic parameters: $\boldsymbol{\lambda} = [\boldsymbol{\lambda}_\mu, \boldsymbol{\lambda}_\sigma] = [[\underline{\lambda}_\mu, \overline{\lambda}_\mu], [\underline{\lambda}_\sigma, \overline{\lambda}_\sigma]]$, such that:

$$\boldsymbol{\mu}_{tnh} = \boldsymbol{\mu}_{tnh_0} + \boldsymbol{\lambda}_\mu \quad (9.1a)$$

$$\boldsymbol{\Sigma}_{tnh} = \begin{bmatrix} \sigma_{t_0}^2 \lambda_{\sigma_t} & 0 & 0 \\ 0 & \sigma_{n_0}^2 \lambda_{\sigma_n} & 0 \\ 0 & 0 & \sigma_{h_0}^2 \lambda_{\sigma_h} \end{bmatrix}. \quad (9.1b)$$

The uncertain initial position of the secondary object can be defined as:

$$\mathbf{x}_{tnh_0} = \mathcal{N}(\boldsymbol{\mu}_{tnh_0}, \boldsymbol{\Sigma}_{tnh_0}; \boldsymbol{\lambda}). \quad (9.2)$$

Since DSt allows the inclusion of more than one source of information, in this example, two equally reliable sources are assumed to provide conflict information. Thus, two sets of epistemic parameters are provided. The values of the initial uncertainty for the secondary object are shown in Table 9.2.

Table 9.2: Secondary object's initial uncertainty. Aleatory uncertainty as a 3D Gaussian distribution on the <T,N,H> reference frame. Epistemic uncertainty with the epistemic parameters, $\boldsymbol{\lambda}_1$ and $\boldsymbol{\lambda}_2$, provided by two sources of information.

Aleatory	Units	Example 1	Example 2
$\boldsymbol{\mu}_{tnh_0}$	[km]	[0, 0, 0]	[0, 0, 0]
$\sigma_{t_0}^2$	[km ²]	0.1 ²	0.05 ²
$\sigma_{n_0}^2$	[km ²]	0.1 ²	0.05 ²
$\sigma_{h_0}^2$	[km ²]	0.1 ²	0.05 ²
Epistemic (Examples 1 & 2)		Source 1	Source 2
λ_{μ_i}	[km]	[0.00, 0.01]	[-0.53, -0.515]
λ_{σ_i}		[1,4]	[1/5, 1/2]

The nominal position is propagated for $T_{inter} = 1$ days, appearing some close encounters. For the scope of these scenarios, a close encounter is defined when the nominal relative distance between both objects is smaller than a selected threshold: $D \leq D_0 = 10$ km. Since there are only two bodies involved, only primary and secondary encounters may occur. Thus, two encounters are detected in each scenario. In

Example 1, the primary encounter is located at $t_1 = 34,235$ s from the initial time (5.75 revolutions for the primary satellite after the initial time) and the secondary encounter at $t_2 = 64,004$ s (5 revolutions after the primary encounter for the operational satellite, $\Delta\theta_{1,2} = 10\pi$ rad), with a nominal miss distance of $D_1 = 2.69$ km and $D_2 = 1.33$ km, respectively. Both encounters take place at the perigee of the orbits. In *Example 2*, the primary encounter occurs at 34,235 s from the initial time (5 revolutions for the manoeuvrable object) with a relative distance of 3.73 km, and the secondary encounter takes place at 66,981 s from the initial time with a relative distance of 1.84 km (5.5 revolutions after the first encounter for the primary object, $\Delta\theta_{1,2} = 11\pi$ rad). In this case, the primary encounter takes place at the perigee and the secondary encounter at the apogee of the operational satellite's orbit.

The initial uncertainty is propagated to the encounters using a Monte Carlo (MC) run. From each set of distributions defined by each of the two sources of information, a number of ellipsoids are drawn within the interval limits. Those ellipsoids are sampled and each sample is propagated to the encounter times and projected on the respective impact planes. In this work, the Normality of the distributions remains after the propagation is assumed, so from each initial ellipsoid, an uncertain ellipse in the impact plane is obtained. Since the primary object is assumed to be perfectly known, the combined covariance matrix at the encounter is equal to the secondary object covariance matrix. At each encounter's impact plane, two sets of uncertain ellipses, associated with each source of information, are obtained. These sets are modelled, according to DSt, with intervals defined by the minimum and maximum values of each of the uncertain variables within the set, which are fused using the Mixing rule [Ferson et al., 2003] explained in Chapter 3. The uncertain variables are the miss distance and covariance matrix elements, whose bounds are shown in Tables 9.3 and 9.4. From the intervals, it is possible to obtain the Plausibility (*Pl*) and Belief (*Bel*) curves required for the robust CARA analysis of the encounters.

Table 9.3: Bounds of the two sources' intervals for the uncertain variables on the impact plane of the two encounters and bounds of the intervals of the associated PoC for *Example 1*.

Variable	Units	Source 1	Source 2
Primary encounter			
μ_ξ	[km]	[-0.02948, 0.03158]	[-0.01485, -0.09976]
μ_ζ	[km]	[2.4001, -0.3924]	[12.298, 13.497]
σ_ξ^2	[km ²]	[0.01435, 0.04358]	[2.045, 4.893]·10 ⁻³
σ_ζ^2	[km ²]	[9.258, 39.255]	[1.858, 5.009]
$\sigma_{\xi\zeta}$	[km ²]	[-1.024, -0.1559]	[-0.1247, 2.983]
P_C	-	[0.523, 1.382]·10 ⁻⁴	[0.0, 10 ⁻¹³]
Secondary encounter			
μ_ξ	[km]	[-0.01978, 0.03996]	[-0.09024, -0.06255]
μ_ζ	[km]	[-4.282, -0.307]	[24.537, 26.855]
σ_ξ^2	[km ²]	[0.01301, 0.04937]	[1.470, 3.907]·10 ⁻³
σ_ζ^2	[km ²]	[34.391, 152.602]	[6.898, 18.498]
$\sigma_{\xi\zeta}$	[km ²]	[-2.103, -0.279]	[-0.172, -2.103]
P_C	-	[2.523, 9.152]·10 ⁻⁵	[0.0, 10 ⁻¹²]

Events classification

Once the uncertain relative geometry at each of the encounters is obtained, the decision-making system introduced above (Chapter 3). Anything that categorised at least one of the two encounters as *Class* < 3 would require the design of a CAM.

Assuming both sources are equally reliable, $bpa_1 = bpa_2 = bpa = 0.5$, and knowing the time to the Time of Closest Approach (TCA) for both encounters, it is possible to classify the event. Using the following values for the mission thresholds: $PoC_0 = 10^{-4}$, $T_1 = 2$ days, $T_2 = 4$ days and the values derived from Chapter 7 for the epistemic thresholds in both scenarios and in both the primary and secondary encounters, all of the events are classified as *Class 1*. This means a CAM should be implemented to avoid both conjunctions in both scenarios.

Table 9.4: Bounds of the two sources' intervals for the uncertain variables on the impact plane of the two encounters and bounds of the intervals of the associated PoC for *Example 2*.

Variable	Units	Source 1	Source 2
Primary encounter			
μ_ξ	[km]	[-0.02948, 0.03158]	[-0.2405, -0.1936]
μ_ζ	[km]	[-1.4605, 1.335]	[12.457, 14.163]
σ_ξ^2	[km ²]	[0.01311, 0.06118]	[2.1843, 6.008]·10 ⁻³
σ_ζ^2	[km ²]	[12.045, 53.657]	[2.4137, 6.5185]
$\sigma_{\xi\zeta}$	[km ²]	[0.3298, 1.6396]	[0.0592, 0.1761]
P_C	-	[0.574, 1.311]·10 ⁻⁴	[0.0, 0.0]
Secondary encounter			
μ_ξ	[km]	[0.0351, 0.1214]	[-0.7497, -0.7172]
μ_ζ	[km]	[-4.355, 0.9630]	[21.840, 25.081]
σ_ξ^2	[km ²]	[0.01559, 0.06119]	[0.8778, 2.3635]·10 ⁻³
σ_ζ^2	[km ²]	[4.360, 19.430]	[8.735, 23.598]
$\sigma_{\xi\zeta}$	[km ²]	[-3.288, -0.6823]	[-0.1567, -0.0251]
P_C	-	[2.453, 9.533]·10 ⁻⁵	[0.0, 0.0]

Alternatives

The alternatives are defined by the selected strategy and by the position of the manoeuvres. Thus, each alternative on \mathcal{A} is defined as:

$$\mathcal{A} = [\Delta\theta_{m,n}, \delta\hat{v}_n, \delta v_n] \mid n = 1, \dots, N_{man}, \quad (9.3)$$

where $\Delta\theta_{m,n} = \theta_{m,n} - \theta_c$ is the execution positions measured as the angular distance in true anomaly with respect to the encounter they are avoiding (if only one manoeuvre, it refers to the primary encounter); $\delta\hat{v}$ is the direction of the manoeuvre expressed in the satellite's <T,N,H> reference frame; and δv_n is the magnitude of the impulse, for each of the required manoeuvres.

The optimal manoeuvres are obtained for the 9 revolutions before the encounter, executed half an orbit before the encounter position in the orbit: $\Theta_m = \{\pi, 3\pi, \dots, 17\pi\}$ rad. The operator sets two constraints: if a single manoeuvre per encounter is executed, the manoeuvre for the second conjunction cannot be executed after the first one is

avoided (thus, $\theta_{m,2} < \theta_{1,2}$), and the manoeuvre cannot be executed during the last two orbits so that the operator keeps some time to confirm the correct preparation of the CAM: $\theta_{m,n} > 6\pi$ rad.

A total of $N_{alt} = 35$ alternatives for *Example 1* are obtained: seven from *Strategy A* (one manoeuvre optimising the first encounter), 7 from *Strategy B* (one manoeuvre optimising the two encounters simultaneously), and 21 from the multi-manoeuve strategy or *Strategy C*. Alternatives are numbered so the first 7 alternatives correspond to *Strategy A*, starting from the manoeuvre executed closer to the encounter, the next 7 correspond to the *Strategy B* also starting from the manoeuvre position closer to the encounter, and the rest of the alternatives (*Strategy C*) are numbered according to the proximity of the first manoeuvre to the primary encounter and, when equal, according to the proximity of the second manoeuvre to the secondary encounter. For the *Example 2*, with the encounters taking place at the opposite sides of the orbit, $N_{alt} = 42$ alternatives are obtained (Fig. 9.2): 7 from *Strategy A*, 7 from *Strategy B* and 28 for *Strategy C*, numbered in the same fashion as in *Example 1*.

Figs. 9.1 and 9.2 shows the robust optimal CAM in the object's $\langle T, N, H \rangle$ reference frame, for *Example 1* and *Example 2*, respectively. Subfigure (a) includes *Strategy A* and *Strategy B*, and (b) shows *Strategy C*. The shaded areas correspond to the excluded constrained regions.

Strategy A is represented in Figs. 9.1a and 9.2a with the solid lines: red, blue and green for the tangential, normal and out-of-plane components, respectively. In both examples, a tangential manoeuvre to avoid the first encounters seems to be the optimal solution. For *Example 1*, the impulse in the direction of the velocity (in most of the cases), in *Example 2*, opposite to the velocity vector. Those two figures also include *Strategy B* with dots. A very similar result is proposed when optimising both encounters simultaneously, with an optimal CAM very close to the tangential direction.

Figs. 9.1b and 9.2b shows the manoeuvre proposed for the second encounter using *Strategy C*. Each colour represents a manoeuvre position to avoid the first encounter (the solid lines corresponding to *Example 1* in Figs. 9.1a and 9.2a). The solid lines correspond to the tangential component for the secondary encounter manoeuvre (the

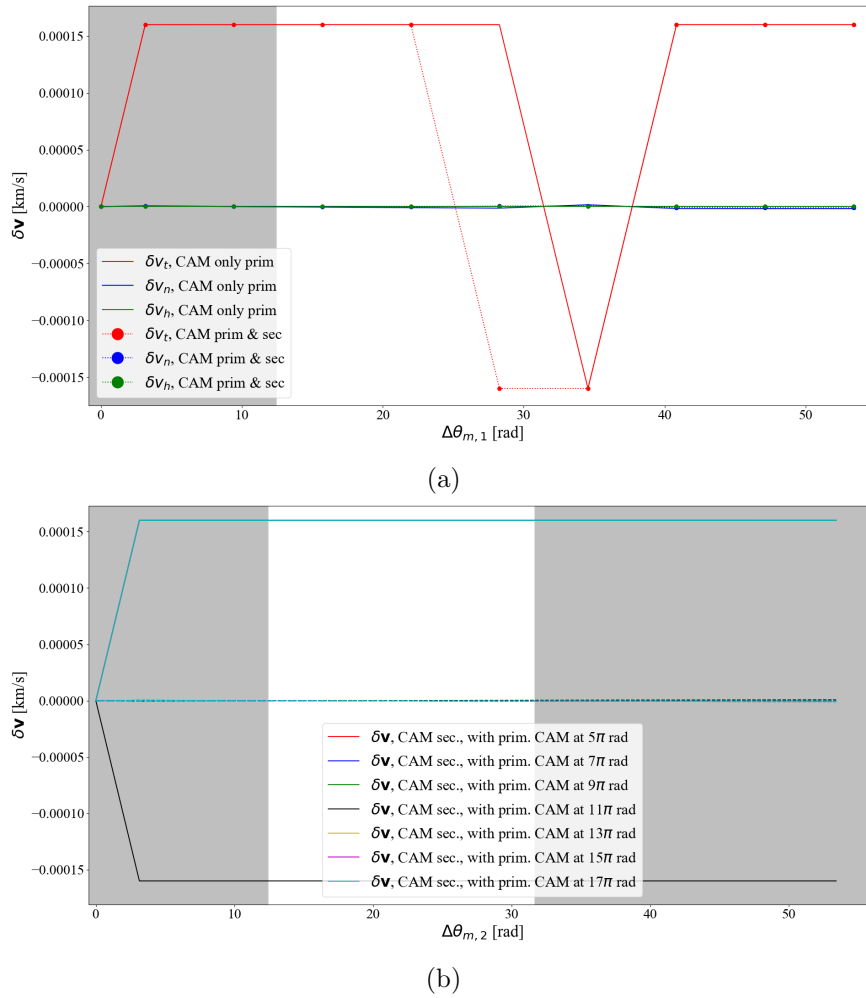


Figure 9.1: Alternative manoeuvres the multiple-encounter event in *Example 1*: (a) *Strategy A* and *Strategy B*; (b) *Strategy C*.

other two components, in dashed and pointed-dashed lines, overlap at ~ 0.0 m/s). For the second encounter, the optimal manoeuvre seems to be also a tangential one, in the same or opposite direction as the velocity vector depending on the case.

Figs. 9.3a and 9.4a show the evolution of the worst-PoC for single-manoevres strategies. The solid red line shows the evolution for the primary encounter and the blue solid line, the evolution for the secondary encounter worst-PoC when only optimising the first conjunction (*Strategy A*). The black solid line shows the worst-PoC of the combined encounter (*Strategy B*), while the red-pointed and blue-pointed line shows the evolution of the worst-PoC for the first and second encounter, respectively, when

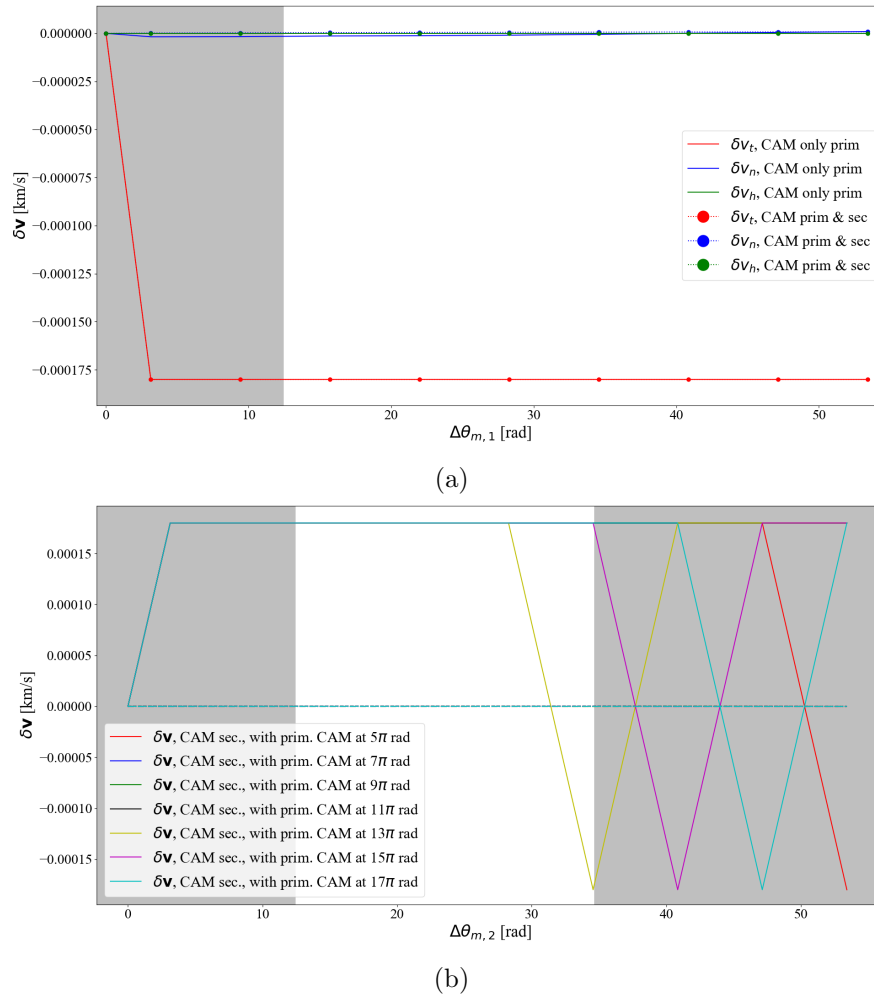


Figure 9.2: Alternative manoeuvres the multiple-encounter event in *Example 2*: (a) *Strategy A* and *Strategy B*; (b) *Strategy C*.

optimising the combined encounter. It can be seen that the combined encounter PoC represent a sort of envelope for the individual encounters. Also, it shows that both first and second avoidance strategies do not differ too much. More importantly, there are differences between both examples: while in *Example 1*, where both encounters take place in the same orbit region, a single manoeuvre seems to reduce the risk of both of them, in *Example 2*, where encounters take place at opposite sides of the orbit, optimising the first encounter has little effect on the second one.

Finally, Figs. 9.3b and 9.4b show the PoC of the secondary encounter for *Strategy C*. Each colour on the solid line represents a different execution position for the first

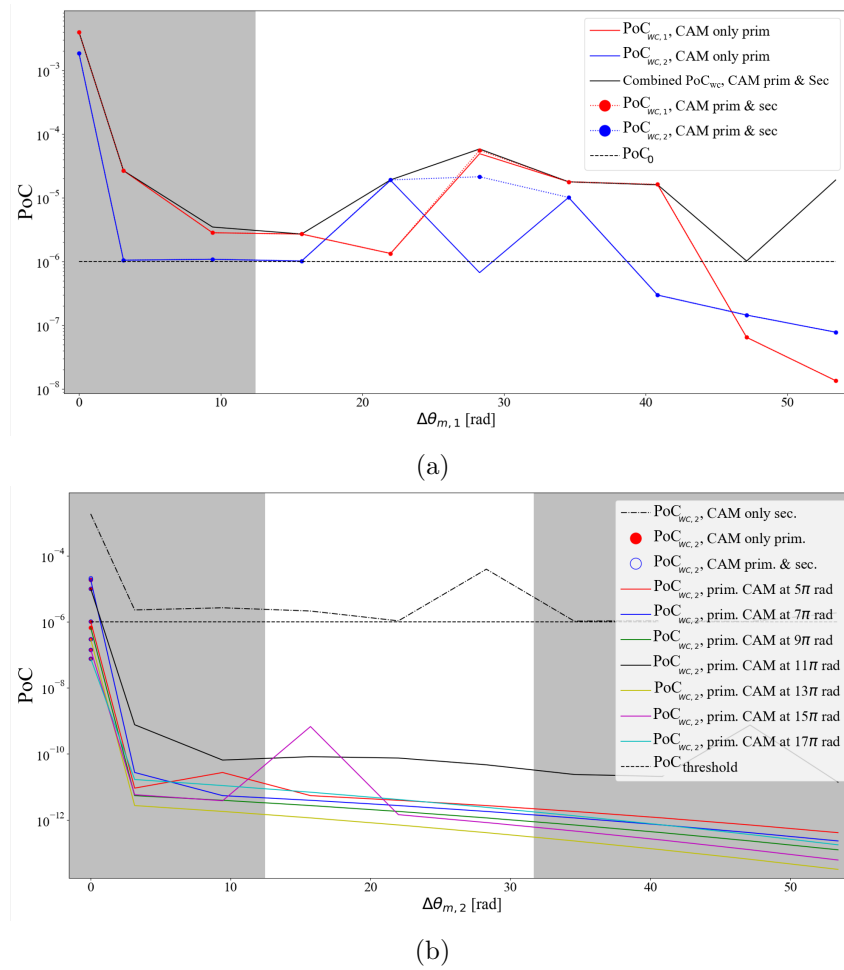


Figure 9.3: Effect on the risk reduction of the avoidance manoeuvres in *Example 1*: (a) *Strategy 0* and *Strategy 1*; (b) *Strategy 2*.

encounter (*Strategy A*). The black dashed-solid line indicates the worst-PoC if only the second event is avoided (no manoeuvre to avoid the primary encounter). The dots indicate the PoC on the secondary when only one manoeuvre is executed: red dot for *Strategy A*, blue empty dot for *Strategy B*. Again, it is possible to spot the difference between the two examples, and how important is the position on the orbits of the different conjunctions compounding the multiple-encounters event.

Criteria

The criteria used for this example are indicated in Fig. 9.5, classified as risk or cost. More details on each criterion are given in the below:

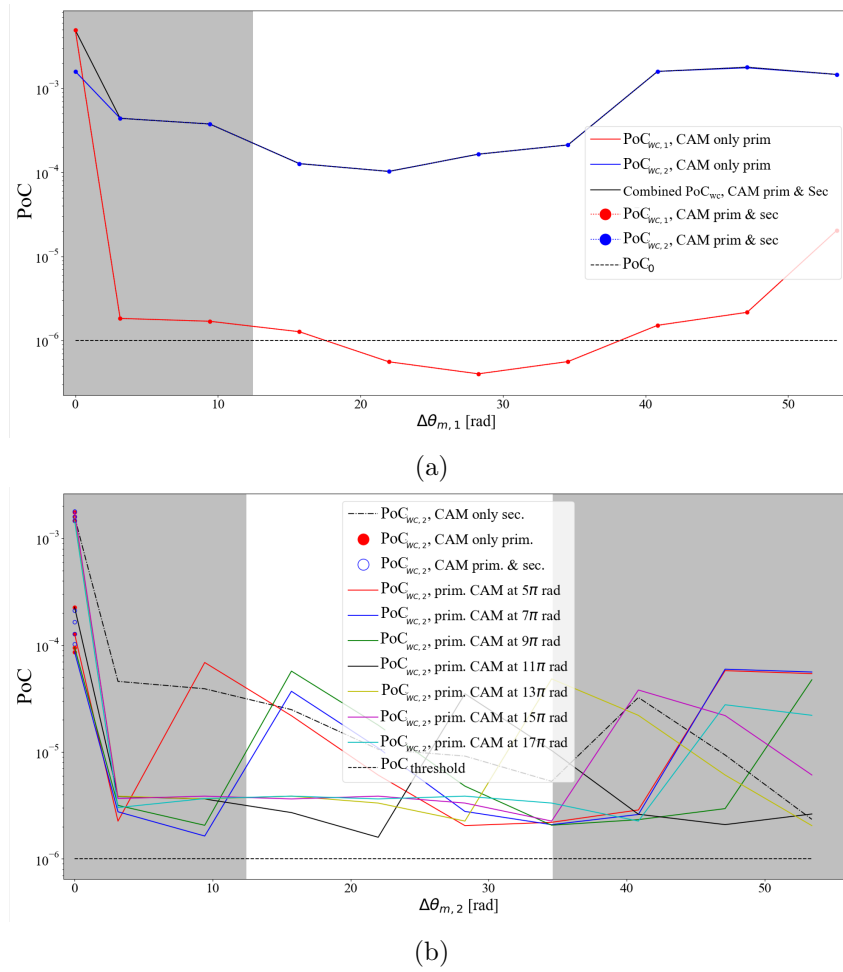


Figure 9.4: Effect on the risk reduction of the avoidance manoeuvres in Example 2: (a) Strategy 0 and Strategy 1; (b) Strategy 2.

- *Probability of Collision Reduction (PoCR)*, introduced in Eq. (6.17), indicates how much the worst-PoC was reduced with respect to the non-manoevre risk ($PoCR = 0$) and the risk threshold ($PoCR = 1$). This *Beneficial* criterion appears as many times as encounters occur in the event.
- *Manoeuvre Risk (ManR)*. Since the manoeuvre execution poses an inherent risk, this criterion prioritises those strategies that involve fewer manoeuvres. Since the risk of the manoeuvre will increase each time one has to be executed, this criterion was modelled as:

$$ManR = N_{man}/N_{enc}, \quad (9.4)$$

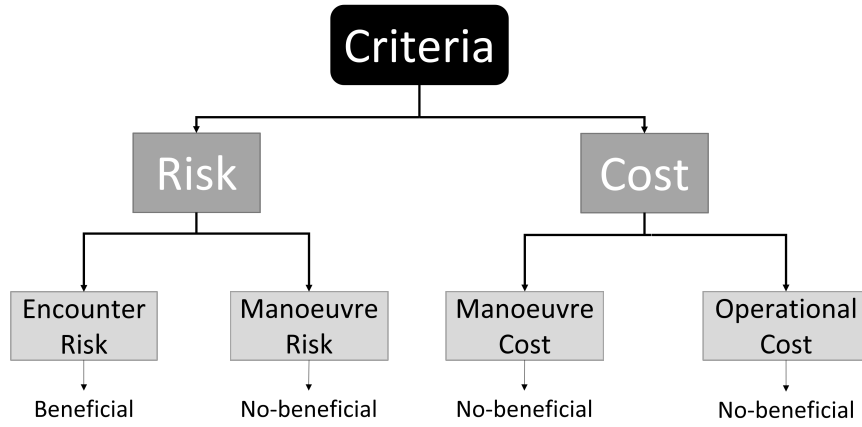


Figure 9.5: MCDM criteria, their classification and their quantification for the *One-vs-Many* example.

where N_{man} is the number of manoeuvres required and N_{enc} is the number of encounters on the event. While more manoeuvres than encounters are possible, in this work, the manoeuvres are limited to a maximum of one per encounter: $ManR \in [0, 1]$. It is a *Non-Beneficial* criterion.

- *Manoeuvre Cost (ManC)*. The cost of the manoeuvre refers to the amount of propellant required, which is directly proportional to the magnitude of the impulse. It is a *Non-Beneficial* criterion that follows the same definition as in Eq. (6.18). However, due to the higher number of encounters per event, the definition is modified so it follows Eq. (9.5), that is, the sum of the impulses of the strategy is normalised with the maximum capacity of the thrust at each manoeuvre:

$$ManC = \sum_{n=0}^{N_{man}} \frac{\delta v_n}{\delta v_{n,max}}. \quad (9.5)$$

- *Operational Cost (OpC)*. This criterion refers to the cost associated with placing the satellite out of the nominal orbit, as modelled in Eq. (6.19). In this case, since there is more than one encounter, it is assumed that the nominal operation is not recovered until the last encounter is avoided. Thus, this *Non-Beneficial* criterion is modelled as the arc-length the satellite is away from the nominal position due to the manoeuvre, starting at the first manoeuvre, and normalised

with the maximum arc-length among all the alternatives:

$$OpC = \frac{\Delta\theta_{m,1}}{\max_i(\Delta\theta_{m,i})}, \quad i = 1, \dots, N_{alt}, \quad (9.6)$$

with N_{alt} the number of alternatives.

The Decision matrix is normalised using the maximum-linear model in Eq. (6.2) to make all criteria *Beneficial* and ranging between zero and one.

In this example, the risk threshold for the CAM is $PoC^* = 10^{-6}$ for all the encounters. The magnitude of the manoeuvres is not optimised in *Example 1*, with a thruster capacity of $\delta v_0 = 18$ cm/s. In *Example 2*, the magnitude is optimised in case the PoC threshold is reached with the maximum thruster capacity, being $\delta v_{max} = 18$ cm/s.

Results analysis

For each multi-encounter event example, two scenarios are proposed depending on the operator's priorities. In the first scenario, the operators give more importance to the reduction of the risk of collision. This could be understood as the *standard* approach, being the collision avoidance the priority. The second scenario prioritises the cost associated with the action, both the manoeuvre and the operational cost. This may represent a more critical situation where, for example, the spacecraft is running out of propellant, or a critical operation is already planned (e.g. data downloading).

The different scenarios are defined by the weights assigned to the criteria, which are detailed in Table 9.5. Since there are two encounters, the risk of each of them is included as a different criterion. In *Example 1*, since the magnitude of each manoeuvre is the same, the total cost of an alternative will be proportional to the number of manoeuvres, as it does the manoeuvre risk. This means the two criteria are correlated and one can be eliminated. In this case, Manoeuvre Risk (ManR) was excluded from the analysis. Thus, the total number of criteria is $N_{crit,1} = 4$ for *Example 1* and $N_{crit,2} = 5$ for *Example 2*.

Having set the weights for the different scenarios, it is possible to obtain the Decision matrix from where to rank the alternatives for the different scenarios. To sort

Table 9.5: Weight distribution for the two analysed scenarios, for *Example 1* and *Example 2*.

Scenario	PoCR1	PoCR2	ManR	ManC	OpC
Example 1					
Risk priority	0.45	0.45	-	0.05	0.05
Cost priority	0.05	0.05	-	0.45	0.45
Example 2					
Risk priority	0.4	0.4	0.1	0.05	0.05
Cost priority	0.05	0.05	0.1	0.4	0.4

the alternatives, some of the MCDM techniques and the methodology explained in Section 6.1 are employed, in this example: Weighted Sum Method (WSM) [Kolios et al., 2016], Weighted Product Method (WPM) [Kolios et al., 2016, Tofallis, 2014] and TOPSIS [Kolios et al., 2016, García-Cascales and Lamata, 2012]. The ranking lists for each scenario, using the different techniques, showing the top-10 alternatives, are presented in Tables 9.6 and 9.7, for *Example 1* and *Example 2*, respectively.

Table 9.6: Top-10 alternatives for the two scenarios using the three MCDM methods considered for *Example 1*.

Scenario 1			Scenario 2		
WSM	WPM	TOPSIS	WSM	WPM	TOPSIS
6	6	6	8	8	8
13	13	13	1	1	1
7	7	7	9	15	9
14	14	14	2	16	2
32	32	32	3	17	15
31	31	31	17	20	16
30	30	30	15	19	17
35	35	35	16	18	3
33	33	33	10	13	10
34	34	34	6	6	11

Regarding the results from these tables, before comparing both examples, some aspects should be noted. It can be seen from the tables that in all the scenarios but one, the three methods agree on the best solution. If observing the top-10 results, although the order may vary from one method to another, in general, the proposed

Table 9.7: Top-10 alternatives for the two scenarios using the three MCDM methods considered for *Example 2*.

Scenario 1			Scenario 2		
WSM	WPM	TOPSIS	WSM	WPM	TOPSIS
28	28	28	8	17	8
9	33	22	1	18	1
10	17	33	2	22	2
11	22	27	9	21	9
22	18	9	3	28	3
2	27	10	10	26	17
4	38	11	4	16	18
33	26	21	11	27	16
27	32	17	17	2	15
17	31	2	18	33	10

alternatives in each scenario are the same for WSM and TOPSIS. This is especially true for *Example 1*. However, the WPM seems to provide slightly different alternatives, other than the best alternative. Most likely, the discrepancy of this method is associated with the appearance of zeros in the Decision matrix.

The proximity of the rankings can be compared using the number of common alternatives ranked among the top-10 solutions. In Table 9.8, it can be seen how, in fact, WSM and TOPSIS agree better (8, 9 and 10 common alternatives out of 10 possibilities depending on the scenario). Also, it shows that *Example 1* presents a better agreement among the top-10 proposed alternatives than *Example 2*. This suggests, as expected, that *Example 1* is easier to decide on since the manoeuvre executed for the first encounter also helps the second one.

When comparing both examples, more differences can be found. When observing Scenario 1 (more weight to the PoC reduction), the top-4 alternatives in *Example 1* correspond to single-manoevres strategies, which proved to be beneficial for both encounters. More specifically, they are proposed at the earliest positions where the $PoC_{WC} < PoC^*$ in both encounters: $\Delta\theta_{m,1} = 15\pi$ rad and $\Delta\theta_{m,1} = 17\pi$ rad (see Fig. 9.3a), which is also beneficial for the risk reduction and the operational cost. Only later, alternatives with two manoeuvres appear on the list (and in any case, involving an early first manoeuvre, $\Delta\theta_{m,1} > 15\pi$, which ensures a greater reduction of $PoC_{WC,1}$).

Table 9.8: Number of common alternatives ranked among the top-10 between pairs of methods.

Example 1		
	Scenario 1	Scenario 2
WSM-WPM	10	6
WSM-TOPSIS	10	9
WPM-TOPSIS	10	5
Example 2		
	Scenario 1	Scenario 2
WSM-WPM	5	3
WSM-TOPSIS	9	8
WPM-TOPSIS	5	4

However, in *Example 2*, the situation is not so simple. The best alternative is always a two-manoeuvre strategy, but the rest of the top-10 alternatives are, more or less, evenly distributed between single or multiple manoeuvres strategies (excluding WPM ranking). This is related to, firstly, the fact that none of the proposed alternatives achieved $PoC_{WC,2} < PoC^*$ and, secondly, that a single manoeuvre does not reduce significantly the risk of the second encounter (Figs. 9.4a and 9.4b).

When prioritising the cost of the manoeuvre (Scenario 2), both examples behave similarly. In fact, the 4 or 5 best alternatives in both scenarios with WSM and TOPSIS are the same: a single manoeuvre executed close to the event. The first alternative is a manoeuvre optimising the combined encounter executed at $\Delta\theta_{m,1} = 5\pi$, which makes sense: a single manoeuvre has a lower ManC associated, and late manoeuvres have a smaller impact on the OpC. It is worth noting how the best alternatives differ with respect to Scenario 1 and, in fact, do not accomplish $PoC_{WC,1} < PoC^*$ and $PoC_{WC,2} < PoC^*$. This highlights the challenging environment operators face when selecting the best strategy to deal with a multi-encounter event if conflict criteria are considered.

Finally, it is interesting to note the similarity between the top-ranked alternatives. For instance, in Scenario 2 of both examples, the top-ranked solutions are 8, 1, 9, and 2. However, solutions 8 and 1 are single-manoeuvre approaches executed 2.5 revolutions

before the encounter. The only difference is that Alternative 1 is computed optimising only the first encounter and Alternative 8 optimising both encounters simultaneously (and similar for alternative 2 and 9, but executing the manoeuvre 3.5 revolution before the encounter): both alternatives propose a similar CAM, almost a tangential impulse in the same direction, and the reduction of the probability of collision is also very similar. The same conclusion can be reached with the top alternatives in Scenario 1 of *Example 1*. Thus, it would be interesting to include a final step in the decision-making system that filters the ranked alternatives according to the similarity to the solutions listed immediately above regarding their proximity as proposed in Ramirez-Atencia et al. [Ramírez-Atencia et al., 2020].

9.3 Multiple encounters within a constellation

This section addresses the other multiple-encounter situation analysed in this chapter: several satellites belonging to the same constellation having to avoid some encounters within a given time horizon, aiming to reduce the impact on the constellation configuration.

9.3.1 Avoiding and returning strategies

In this case, the avoiding strategies are simpler, since each satellite is facing a single encounter. Thus, the avoidance strategy consists only of performing a CAM at a certain arc-length before the encounter, robustly optimised independently for each encounter using Eq. (5.18).

However, in this scenario, the returning strategy of the satellites to the nominal constellation configuration is more relevant. The returning strategy defines how the satellites return to the original orbital plane, original orbit within the plane and original slot within the orbit to keep the operational configuration. In this sense, the final constellation strategy to avoid multiple encounters would be determined by the individual satellite's avoidance and, especially, the returning strategies.

Three different actions can be followed by the satellites after the conjunction. The

first approach consists of not executing any further action after the encounter, which means not recovering, in general, the nominal constellation configuration. However, this strategy is simpler, faster and requires fewer manoeuvres. The other two options involve executing one or more manoeuvres after the encounter to recover the constellation configuration. The first of those two approaches proposes to execute a single manoeuvre a certain distance after the encounter, so that the satellite returns to the original orbit within the constellation, although not in the same slot as before the avoidance manoeuvre. This is a compromise between the other two strategies in terms of constellation configuration, number of manoeuvres and operational time. The final alternative requires two manoeuvres, one to enter into a phasing orbit, and another manoeuvre to recover the original slot in the constellation. This approach requires more time and more manoeuvres (with the associated cost and risk), with the benefit of not disturbing the constellation after the event.

Note that it could be possible to extend the last two alternatives by delaying the recovering manoeuvres. For example, allowing for a natural delay in the avoidance orbit so that a single manoeuvre would restore the satellite to the original slot, or allowing more time between manoeuvres to ensure their correct execution, or coordinating both satellites to recover simultaneously. Similarly, if the constellation is constituted by a sufficiently small number of satellites (or the number of satellites involved in an encounter for a given time horizon is high enough), another strategy to recover the original configuration could be to move the objects not affected by any encounter. Nevertheless, for the scope of this work, and without losing generality, these last alternatives are not considered, since the goal of the chapter is to show the methodology under this kind of event.

To simplify the problem, in this section, in the second strategy, the recovery manoeuvre is executed half a revolution after the conjunction, and in the third strategy, the satellite enters the phasing orbit half a revolution after the encounter, and the last manoeuvre is executed after one revolution in this transition orbit.

9.3.2 Risk assessment

In the rest of the chapter, an example of a multiple-encounter event within a constellation is presented. In the example, two manoeuvrable satellites belonging to the same constellation experience a close encounter with a non-manoevrable external object (e.g. a piece of space debris). Opposite as in the previous section, each encounter is now addressed independently, since each of the operational satellites only faces a single encounter. Different scenarios are presented depending on the criteria the operator wants to prioritise. Keplerian motion is assumed in the example, as well as the Normality of the uncertainty.

Constellation

The proposed constellation is comprised of 60 satellites in a Walker constellation [Walker, 1977], 60:18/3/1, distributed along three different orbital planes, following a circular orbit of 7,100 km in radius. Each satellite is equipped with a 60-degree aperture Nadir-pointing antenna. The objective of the constellation is to cover as much area of the Earth's surface as possible. Thus, the quality of the constellation configuration can be measured as the total area covered by the satellites' antenna (removing overlapping of different satellites' coverage). Two of the 60 satellites are involved in the encounter, each belonging to a different plane. In the case where they belong to the same orbital plane, the returning strategies may be slightly different.

Initial and encounters information

The external object is defined by the following orbital parameters at time t_0 :

$$\mathbf{q}_2(t_0) = [6944.26, 0.031016, 141.04, 335.27, 116.15, 47.03], \quad (9.7)$$

in km and deg. The time interval of analysis is one day ($T_{inter} = 86,400$ s). The first encounter takes place at $t_1 = 43,200$ s from the initial time, and the second encounter at $t_2 = 64,800$ s after t_0 .

The satellites of the constellation are assumed to be perfectly known. The state

vector of the external object is affected by aleatory uncertainty, expressed in the object's $\langle R, T, H \rangle$ reference frame at t_0 :

$$\Sigma_{2,rth}(t_0) = \begin{bmatrix} 0.104^2 & 0 & 0 \\ 0 & 0.556^2 & 0 \\ 0 & 0 & 0.139^2 \end{bmatrix} km^2.$$

Assuming two sources (*Source A* and *Source B*) provide information about the object, there are two components of epistemic uncertainty. It is quantified through an epistemic parameter, that displaces the nominal miss distance or scales up and down the covariance matrix providing a range of possible values (Section 9.2). This implies that the uncertainty ellipse in the impact plane becomes a family of ellipses per source of information. In this example, only the position covariance is assumed to be affected by epistemic uncertainty:

$$\lambda_{\sigma,A} = [1, 4]$$

$$\lambda_{\sigma,B} = [1/5, 1/2]$$

Thus, the uncertain geometries of the encounters are defined by the intervals in Tables 9.9 and 9.10, and the PoC is computed assuming the fast encounter hypothesis using Eq. (3.1), with a Hard Body Radius (HBR) of 10 m. The information from both sources is combined using the mixing rule introduced.

Table 9.9: Uncertain encounter geometry for the first encounter: upper and lower bound of the components of miss distance and covariance matrix in the impact plane.

Component	Units	Source A	Source B
μ_ξ	[km]	[0.02855,0.08342]	[1.263·10 ⁻³ ,0.01529]
μ_ζ	[km]	[-0.6327,0.7230]	[-0.2317,0.2542]
σ_ξ^2	[km ²]	[0.1208,0.4353]	[0.02530,0.05332]
σ_ζ^2	[km ²]	[140.265,505.054]	[29.311,61.202]
$\sigma_{\xi\zeta}$	[km ²]	[-14.586,-4.0744]	[-1.8012,-0.8572]

If both encounters are classified as $Class < 3$, the MCDM starts to rank the possible avoidance and return strategies. If only one encounter is classified within those classes,

Table 9.10: Uncertain encounter geometry for the second encounter: upper and lower bound of the components of miss distance and covariance matrix in the impact plane.

Component	Units	Source A	Source B
μ_ξ	[km]	$[-0.1065, 5.970 \cdot 10^{-3}]$	$[-7.415 \cdot 10^{-3}, 8.664 \cdot 10^{-3}]$
μ_ζ	[km]	$[-0.7490, 0.6741]$	$[-0.2729, 0.2292]$
σ_ξ^2	[km ²]	$[0.4547, 1.2045]$	$[0.07724, 0.1487]$
σ_ζ^2	[km ²]	$[154.274, 560.924]$	$[32.537, 68.346]$
$\sigma_{\xi\zeta}$	[km ²]	$[3.0797, 10.613]$	$[0.6213, 1.3313]$

the analysis would be similar, but with a much-reduced number of alternatives, since only one satellite will be involved in the problem. The scenario would reduce to the collaborative case in Section 6.3, adding the returning strategies to the alternatives. Using the same basic probabilistic assumptions (*bpa*) and threshold values as in the previous study case in this chapter (Section 9.2), both events are classified within the high-risk categories, initiating the next analysis step.

Alternatives

The different alternatives are defined by the following parameters: the CAM execution position for each satellite, θ_{mi} , and the strategy followed after the encounter, s_i : not performing any further action and remaining in the new orbit (*Strategy 0* or s_0), execute one manoeuvre to return to the original orbit (*Strategy 1* or s_1), or execute two manoeuvres to return to the original position within the original orbit (*Strategy 2* or s_2).

For each of the satellites involved in a close encounter, the robust optimal CAM is computed at 6 different positions. Including the alternative of not executing a CAM by one of the satellites, the space of CAM execution position (measured as distance to the encounter) for both objects is $\Theta_{m,i} = \{0, p\pi\}$ rads, with $p = 1, 3, \dots, 11$. The magnitude of the impulse was set fixed and equal to $\delta v_0 = 10$ cm/s and the constellation threshold is $PoC^* = 10^{-6}$.

In order to establish the alternatives, for each manoeuvre position there are three possible returning strategies, except for $\theta_m = 0$ which accepts only one strategy (s_0).

This makes 22 options per satellite. Thus, for each first encounter alternative, there are 22 options for the second encounter, making a total of 484 alternatives. Each alternative can be identified according to the indexes in Table 9.11, which follows the rule in Eq. (9.8),

$$N = N_1(M_2 \cdot S_2 + 1) + N_2$$

$$N_i = \begin{cases} \text{if } n_i = 0 \rightarrow N_i = 0 \\ \text{else } N_i = (n_i - 1)S_i + si_j + 1 \end{cases} \quad (9.8)$$

where N is the number of the alternative, N_i is the number of the alternative for the i^{th} encounter, n_i is the argument of θ_{mi} in Θ_{mi} for the i^{th} encounter, si_j is the j^{th} returning strategy for the i^{th} encounter, S_i is the total number of returning strategies considered for the i^{th} encounter, and M_i is the size of Θ_{mi} .

Table 9.11: Alternatives as a function of the CAM execution position (θ_{mi}), measured as the angular distance to the encounter, and the returning strategy (si_j).

N	N ₁	θ_{m1} [rad]	Strat. 1	N ₂	θ_{m2} [rad]	Strat. 2
0	0	0	s1 ₀	0	0	s2 ₀
1	0	0	s1 ₀	1	0.5	s2 ₀
2	0	0	s1 ₀	2	0.5	s2 ₁
3	0	0	s1 ₀	3	0.5	s2 ₂
...
21	0	0	s1 ₀	21	6.5	s2 ₂
22	1	0.5	s1 ₀	0	0	s2 ₀
23	1	0.5	s1 ₀	1	0.5	s2 ₀
24	1	0.5	s1 ₀	2	0.5	s2 ₁
25	1	0.5	s1 ₀	3	0.5	s2 ₂
...
43	1	0.5	s1 ₀	21	6.5	s2 ₂
44	2	0.5	s1 ₁	0	0	s2 ₀
45	2	0.5	s1 ₁	1	0.5	s2 ₀
46	2	0.5	s1 ₁	2	0.5	s2 ₁
47	2	0.5	s1 ₁	3	0.5	s2 ₂
...
65	2	0.5	s1 ₁	21	6.5	s2 ₂
...
483	21	6.5	s1 ₂	21	6.5	s2 ₂

Criteria

Once the alternatives are defined, the next step is to define the criteria to evaluate the alternatives. Four criteria are proposed with information on all satellites involved in the event and other two criteria per each encounter. Thus, in a multiple encounter event involving two satellites of the constellation, a total of eight criteria will be considered:

- *ManR*, accounting for the total number of manoeuvres of all the satellites. This quantifies the inherent risk of executing manoeuvres, assuming that the higher the number of manoeuvres, the higher the risk, Eq. (9.4).
- *ManC*, the total cost of the avoidance action, measured as the sum of all δv , both in the CAM and in the returning strategy, of all satellites:

$$\delta v_q = \sum_i (\delta v_i + \sum_k \delta v_{ik}^{-1}), \quad (9.9)$$

where k the returning strategy, i the encounter, and q the alternative.

- *ManC per satellite*. This criterion appears as many times as satellites of the constellation require a manoeuvre.

$$\delta v_{qi} = \delta v_i + \sum_k \delta v_{ik}^{-1}. \quad (9.10)$$

This criterion is included to quantify possible operational constraints as it can be the limitation of manoeuvres in a single satellite due to propellant shortage (e.g. at the end of life). It can be tuned according to the necessities with the appropriate weight.

- *OpC*, measured as the total time of the operation, from the time the first manoeuvre is executed by any satellite to the moment the last manoeuvre is executed by any satellite, Eq. (6.19). This criterion associated with the cost of the operation is related to the time the satellites are out of the nominal orbit or unable to perform routine activities.

- *PoCR* for each encounter, quantified with Eq. (6.17), indicating the effectiveness of the manoeuvre regarding the reduction of the risk.
- *Constellation's figure of merit*. In this example, this quantity is modelled based on the total area covered by the constellation assuming sensors mounted on each satellite and pointing to Nadir. The figure of merit is defined as the integral, over the considered interval of time, T_{inter} , of the difference in the Earth's surface covered by the constellation with respect to the nominal configuration:

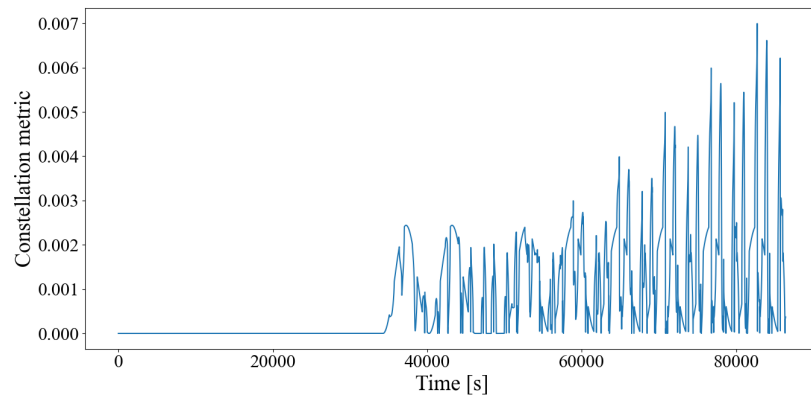
$$CFM_q = \int_{t_0}^{t_f=t_0+T_{inter}} \frac{\|A_q(t) - A_0(t)\|}{A_{Earth}} dt, \quad (9.11)$$

where $A_q(t)$ is the area covered at instant t by the constellation in alternative q , and $A_0(t)$ is the area the constellation would cover in the nominal configuration at the same epoch. Note that the area is made dimensionless by normalising with the Earth's surface, A_{Earth} . Fig. 9.6 includes the difference in covered area as a function of time for three cases: none of the satellites returning to the original orbit (Fig. 9.6a), both satellites returning to the original orbit, but only one to the original slot (Fig. 9.6b), and both satellites returning to the original slot (Fig. 9.6c).

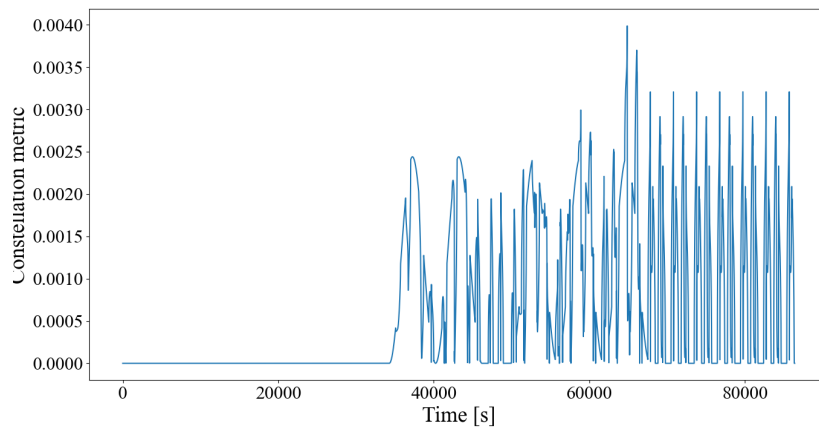
Fig. 9.7, at the end of the chapter, shows the behaviour of the parameters defining the criteria as a function of the alternatives. This work uses two normalisation techniques: the maximum-linear Eq. (6.2) and the vectorEq. (6.4) normalisation approaches (Chapter 6).

Results analysis

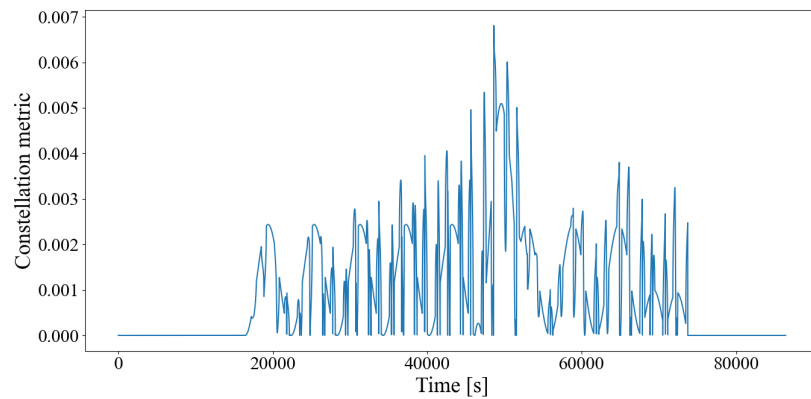
Seven different subscenarios are studied in this example. Each of those scenarios gives more importance to one or more criteria by assigning different relative weights distribution (Table 9.12). *Subscenario 0* weights all criteria equally, *Subscenario 1* gives more importance to the safety of the satellites ($PoCR_1$ and $PoCR_2$), *Subscenario 2* prioritises the manoeuvre cost reduction (ManC), *Subscenario 3* focuses on keep the constellation configuration and *Subscenario 4* gives more importance to OpC. The other two



(a)



(b)



(c)

Figure 9.6: Difference in Earth's surface covered between the avoidance case and the nominal configuration. (a) None satellites returned to the original orbit. (b) Both satellites returned to the original orbit, only one to the original slot. (c) Both satellites return to the original slot.

subscenarios are combinations of some of the previous ones: *Subscenario 5* prioritises the service disruption, that is, the configuration of the constellation and the operation cost, and *Subscenario 6* the sustainability of the service: the safety of the satellites (PoCR₁ and PoCR₂) combined with the configuration of the constellation.

Table 9.12: Weight distribution along the criteria for the different subscenarios.

Subsc.	ManR	ManC	ManC ₁	ManC ₂	OpC	PoCR ₁	PoCR ₂	Const.
0	1/8	1/8	1/8	1/8	1/8	1/8	1/8	1/8
1	0.1/6	0.1/6	0.1/6	0.1/6	0.1/6	0.45	0.45	0.1/6
2	0.1/7	0.9	0.1/7	0.1/7	0.1/7	0.1/7	0.1/7	0.1/7
3	0.1/7	0.1/7	0.1/7	0.1/7	0.1/7	0.1/7	0.1/7	0.9
4	0.1/7	0.1/7	0.1/7	0.1/7	0.9	0.1/7	0.1/7	0.1/7
5	0.1/6	0.1/6	0.1/6	0.1/6	0.45	0.1/6	0.1/6	0.45
6	0.1/5	0.1/5	0.1/5	0.1/5	0.1/5	0.3	0.3	0.3

The normalised alternatives evaluated on the criteria are sorted using WSM, nWSM, WPM, TOPSIS (Chapter 6). Each combination of MCDM method with normalisation technique (eight in total) provides a different ranking for the subscenarios. Table 9.13 provides the top 5 alternatives for each of the eight rankings for *Subscenario 0*.

Table 9.13: Top 5 alternatives in Subscenario 0 for the 8 combinations of MCDM methods and normalisation techniques along with the combined ranking with $g_{top} = 5$.

	WSM		nWSM		WPM		TOPSIS		Combined
	Linear	Vector	Linear	Vector	Linear	Vector	Linear	Vector	
0	22	22	41	41	41	41	414	65	41
22	41	41	42	42	42	42	417	87	42
44	42	42	63	63	63	63	477	351	63
88	63	44	64	64	64	64	480	417	64
110	64	63	85	85	85	85	483	483	22

Since each combination of normalisation and MCDM techniques may lead to a different ranking of the alternatives, it is possible to end up with 8 different *best* alternatives. Those sorted lists can be combined using the following approach. Alternatives appearing among the top of the ranking for several combinations of MCDM and normalisation techniques seem to generate more consensus than an alternative appearing

as the best alternative, but also in one ranking (and not showing in the top position for other combinations). Thus, the combination method counts how many times each alternative appears in the g_{top} -top values of all the rankings, and sorts those alternatives according to the number of appearances. Note that the value of g_{top} may influence the final combined ranking. The last column of Table 9.13 includes the combined ranking for *Subscenario 0* with $g_{top} = 5$. The combined rankings, with $g_{top} = 5$, for all the subscenarios appears in Table 9.14.

Table 9.14 includes the top-5 alternatives for the seven subscenarios already having combined the eight rankings with $g_{top} = 5$.

Table 9.14: Top 5 alternatives in each subscenario with $g_{top} = 5$.

Subsc. 0	Subsc. 1	Subsc. 2	Subsc. 3	Subsc. 4	Subsc. 5	Subsc. 6
41	85	0	44	0	22	63
42	41	1	66	22	44	64
63	42	41	0	44	66	85
64	63	42	2	88	0	86
22	64	64	3	66	110	65

In the rest of the section, an analysis of the results is provided.

- *Subscenario 0: Criteria equally weighted.* Basically, it is an equilibrium of criteria, not giving as much information as the rest of the subscenarios. The preferred alternatives correspond to situations where the first satellite manoeuvres 0.5 revolutions before the encounter ($\theta_{m1} = 0.5$ rad) without returning, $s1 = 0$, and the second satellite moves at $\theta_{m2} = 6.5$ rad, with no returning manoeuvre, $s2 = 0$ (alternative 42), or returning also to the original orbit, $s2 = 1$ (alternative 43). The equivalent alternatives, but with the first satellite returning to the original orbit are also well-ranked (alternatives 63 and 64).
- *Subscenario 1: Importance given to PoC.* The preferred options are a combination of late manoeuvres in the first encounter and early manoeuvres in the second one: second satellite performing the manoeuvre at $\theta_{m2} = 6.5$ rad, without returning manoeuvre, $s_2 = 0$, or returning to the original orbit, $s_2 = 1$, with *Satellite A* manoeuvring late, $\theta_{m1} = 0.5$ rad, without difference among the returning criteria:

$s_1 = 0$ first (alternatives 41 and 42), $s_1 = 1$ later (alternatives 63 and 64) and $s_2 = 2$ afterwards (alternatives 85). This combination of CAM execution position provides the smallest PoC for both encounters, minimising other criteria such as time of operation, the number of manoeuvres or the total δv required.

- *Subscenario 2: Importance given to manoeuvre cost.* This is the only subscenario presenting results more challenging to interpret. For the first encounter, in general, the CAM of the top alternatives presents a lower δv , which is not the case for the second encounter. Overall, the alternatives are within the lower range of total δv , but they are not the lowest. This could be due to the (small) influence of other criteria: if some of the other criteria, although with a small weight, commonly preferred an alternative with a slightly higher δv , it can explain why not just the alternatives with the lowest total impulse magnitude are selected. In any case, the preferred alternative is no satellite manoeuvring (alternative 0) or only the second one doing so the closest to the TCA, $\theta_{m1} = 0.5$ rad, without returning strategy, $s_1 = 0$ (alternative 1). The other strategies (41, 42, 64) are associated with alternatives with the first satellite manoeuvring late ($\theta_{m1} = 0.5$ rad) and the other performing the CAM early ($\theta_{m2} = 6.5$ rad).
- *Subscenario 3: Importance given to constellation configuration.* The preferred alternatives are those with either no manoeuvre by any satellite: alternative 0 (obviously, since there is no disruption of the constellation), or where there is only a CAM in one encounter, with the CAM executed close to the encounter (less disruption of the constellation configuration), with both situations: returning to the original position (no further disruption of the constellation) or not returning to the original orbit (but, due to the late CAM, the disruption after the encounter is small): alternatives 2 and 3 when manoeuvres the satellite in the second encounter and alternatives 44 and 66 when the CAM is only performed in the second encounter.
- *Subscenario 4: Importance given to the time of operation.* The preferred alternative is not manoeuvring (alternative 0) and, otherwise, only manoeuvring for

one encounter (the first one), as close to the TCA as possible. For the top alternatives, the time of the operation is restricted from half a period (alternatives 22, 44, 66) to a period and a half (alternative 88), essentially. The alternatives where only the other satellite manoeuvres do not rank as high, probably due to the smaller reduction of probability.

- *Subscenario 5: Importance given to constellation configuration and time of operation.* The preferred options are those shared by subscenario 3 and 4. The manoeuvre is executed only for one encounter (again, the first one), or even for none of the encounters (alternative 0). The CAM is executed close to the encounter ($\theta_{m1} = 0.5$ rad for alternatives 22, 44, 66 and $\theta_{m1} = 1.5$ rad for alternative 110). These alternatives require less operation time and less disruption of the constellation configuration, and in all of them, the satellites follow a returning strategy to the original position.
- *Subscenario 6: Importance given to constellation configuration and PoC.* It is similar to the subscenario 2, where PoC was prioritised. The preferred alternatives are situations with the CAM is executed late for the first encounter and early for the second one, where the minimum values of PoC are found (alternatives 63, 64, 85). However, there is a preference to execute a returning manoeuvre to the original orbit (alternative 86) or to the original position (alternative 65), due to the higher weight on the constellation criteria than in subscenario 2.

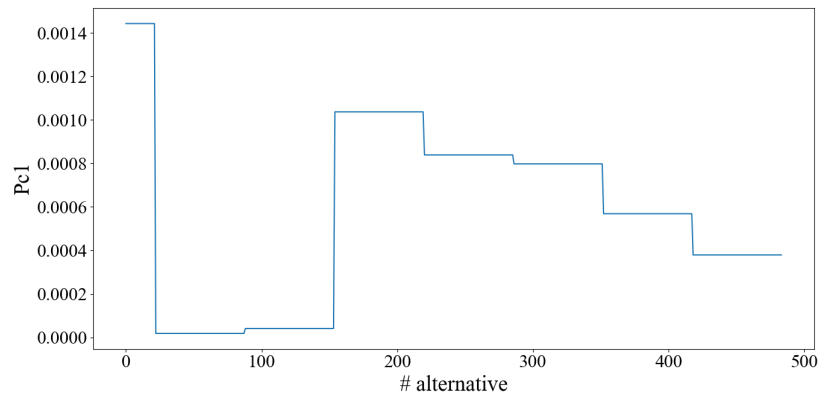
9.4 Summary

In this chapter, the multiple-encounter problem was addressed, proposing a MCDM-based method to support operators in the decision on the best avoidance and returning strategy.

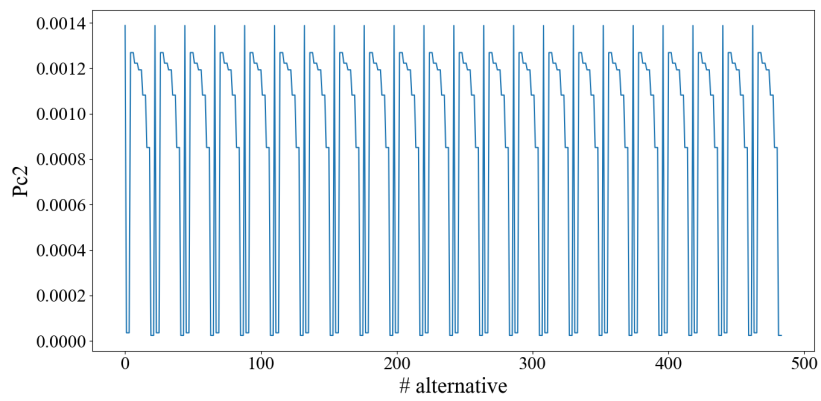
Initially, a single-agent (single-satellite) scenario was analysed. When a single satellite faces subsequent encounters, different avoidance strategies are possible (single or multiple manoeuvres) and operational constraints may restrict the available possibilities. The proposed MCDM method ranked the alternatives under different criteria

importance. It showed the influence of the relative location in the orbit of the encounters on the best decision to be adopted.

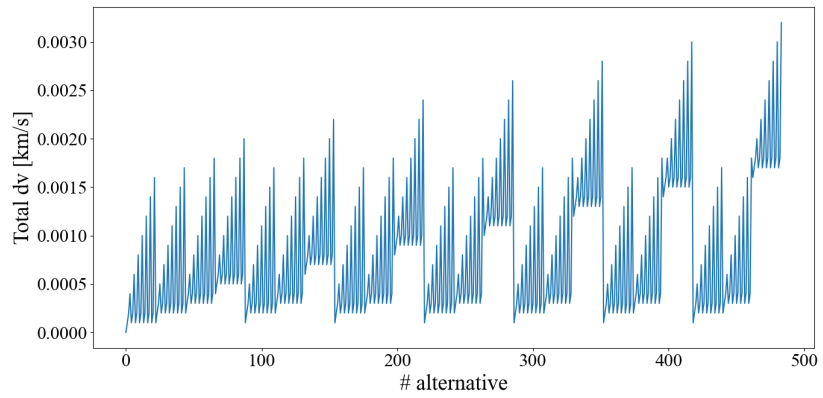
Then, a supra-agent scenario (multiple encounters within a constellation) was addressed. In this situation, each satellite only faces a single encounter, but the constellation operator treats the encounter as a multiple encounter. In this case, the returning strategy becomes as important as the avoidance one. Also, the coordination between the satellites may be crucial in the best way to act, depending on the importance of some criteria, such as the constellation configuration.



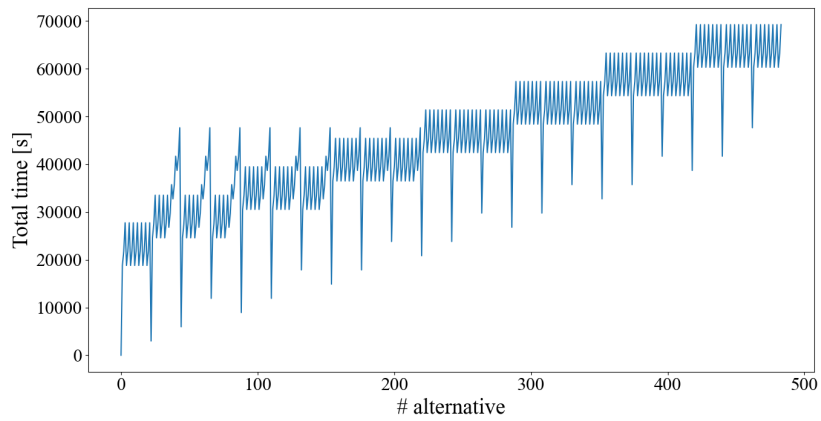
(a)



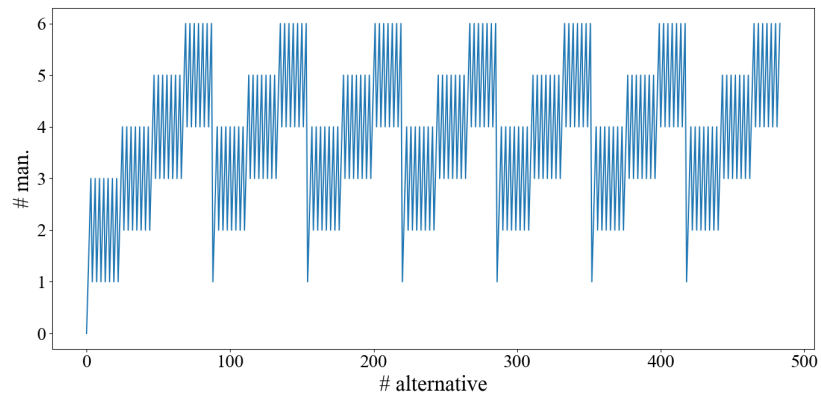
(b)



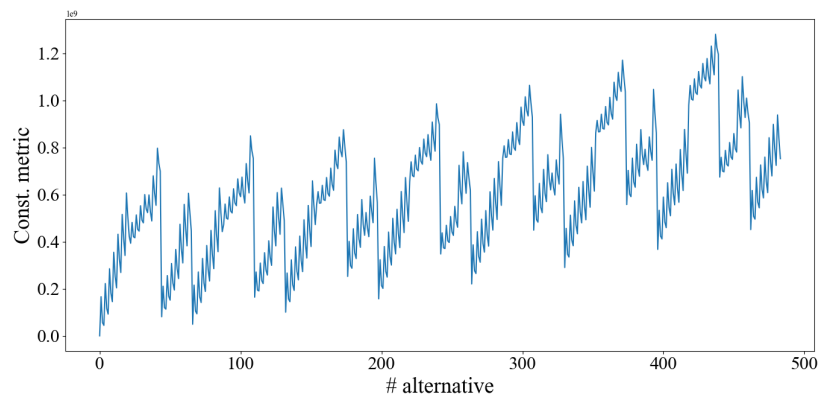
(c)



(d)



(e)



(f)

Figure 9.7: Value of parameters used to compute the MCDM criteria as a function of the alternatives. a) PoC for the first satellite's encounter, b) PoC for the second satellite's encounter, c) Total δv of the alternative, d) total time of the operation, e) total number of manoeuvres, including CAM and returning manoeuvres, for both encounters, e) constellation metric.

Chapter 10

CASSANDRA

The content of this chapter was partially published in:

Greco, C., Sánchez, L. and Vasile, M. (2021), “A robust Bayesian agent for optimal collision avoidance manoeuvre planning”, 8th European Conference on Space Debris; [Greco et al., 2021]

Sánchez, L. and Vasile, M. (2021), “CASSANDRA: Computational Agent for Space Situational Awareness aNd Debris Remediation Automation”, Stardust-R – Second Global Virtual Workshop (GVW-II); [Sánchez and Vasile, 2021a]

Sánchez, L., Stevenson, E., Vasile, M., Rodríguez-Fernández, V. and Camacho, D. (2022), “An intelligent system for robust decision-making in the all-vs-all conjunction screening problem”, 3rd IAA Conference on Space Situational Awareness (ICSSA). [Sánchez et al., 2022a]

In the New Space context, Space Environment Management (SEM) should tend towards automation [Muelhaupt et al., 2019]. The continuous growth of space objects, with the associated rise in close encounters and fragmentation events, tracking campaigns, or re-entry episodes, implies that the required workload may threaten the capacity of current human-based systems. New technologies should be implemented, with Artificial Intelligence (AI) and Machine Learning (ML) being strong candidates [Bastida Virgili et al., 2019, Mashiku et al., 2019].

Along this work, some theoretical developments towards automation were introduced along with some applications to deal with Space Traffic Management (STM)

problems. This chapter presents the integration of some of them to address more complex scenarios compounding the foundations of the *Computer Agent for Space Situational Awareness aNd Debris Remediation Automation* (CASSANDRA).

In this chapter, the integration of those modules along with other modules previously developed to address specific STM tasks is presented. Thus, in Section 10.1, the main concept of the system and its modules are introduced. Further details on the modules used in the next sections are also included. Section 10.2 and Section 10.3 present two examples of the integration to address specific STM problems. Section 10.4 concludes the chapter with the final remarks.

10.1 CASSANDRA framework

CASSANDRA is an intelligent agent to support operators on SEM. The intelligent agent is constituted by separate modules which carry out specific tasks. CASSANDRA is responsible for automatically managing the relationships among blocks (input/output interfaces, activate appropriate modules, data management) to ensure the complete analysis of complex SEM events.

Two main drivers on the development of CASSANDRA are the use of AI and the treatment of uncertainty. AI techniques are employed to extract information from available data to make predictions in satellites' states or space weather, but also for supporting operators with decision-making aid tools or for modelling the long-term evolution of the space environment. Regarding uncertainty, the aim is to widen the perspective on its modelling by incorporating not only aleatory but also epistemic uncertainty. While the former is inherent to the process and cannot be reduced, the latter refers to the lack of knowledge of the process or the limitations on the modelling of the phenomenon. It could be reduced if more information about the system was available.

10.1.1 Modules

A number of modules assist CASSANDRA in managing SEM events. All these blocks can work as stand-alone tools without interacting with the other modules and providing the corresponding information: observations, conjunction alerts, object's state estimation, the outcome of a decision-making process... The aggregate value of CASSANDRA is that it can coordinate the different modules to address more complex problems. Fig. 10.1 shows the modular architecture of CASSANDRA. A brief description of each of the packages is provided below:

- **Radar:** Responsible for acquiring radar measurements of space objects and their associated position uncertainty [Díaz Riofrío et al., 2021].
- **Automated Conjunction Screening** or ACS: AI-based module for predicting close encounters and generating conjunction alerts, both on the *All-vs-All* and in the *One-vs-All* scenarios [Stevenson et al., 2021, Sánchez et al., 2019]. More information can be found in the following sections.
- **InteLLIgent Atmospheric Density modelling for space operations** or IL-IAD: AI-based system for space weather forecasting [Stevenson et al., 2022b] and atmospheric density modelling [Manzi and Vasile, 2021].
- **Anomaly detection:** AI-based module for predicting unmodelled terms on the dynamics [Manzi and Vasile, 2020a]. Potential uses can be the detection of manoeuvres [da Graça Marto et al., 2023] or alterations on perturbing forces.
- **Intelligent Decision Support System** or IDSS: AI-based decision-making system for supporting operators in the event of a close approach [Sánchez and Vasile, 2021c, Sánchez et al., 2024]. Its output may suggest the execution of an avoidance manoeuvre or the acquisition of more observations. More information in Chapters 3, 4 and 8.
- **Robust State Estimation:** Module for robust estimation and propagation of state vector and uncertainty (aleatory and epistemic). It also includes func-

tionalties for updating the state when receiving new observations [Greco et al., 2021, Greco and Vasile, 2021]. More information can be found below.

- **Collision Avoidance Manoeuvre** or CAM: Module for computing the optimal CAM accounting for aleatory and epistemic uncertainty [Sánchez and Vasile, 2023, Greco et al., 2021]. More information in Chapter 5.
- **TITAN**: Module responsible for the analysis of re-entry events, including the estimation of re-entry time and on-ground risk [Falchi et al., 2017, Peddakotla et al., 2022].
- **Fragmentation**: Module taking care of the fragmentation events of space objects [Celletti et al., 2021].

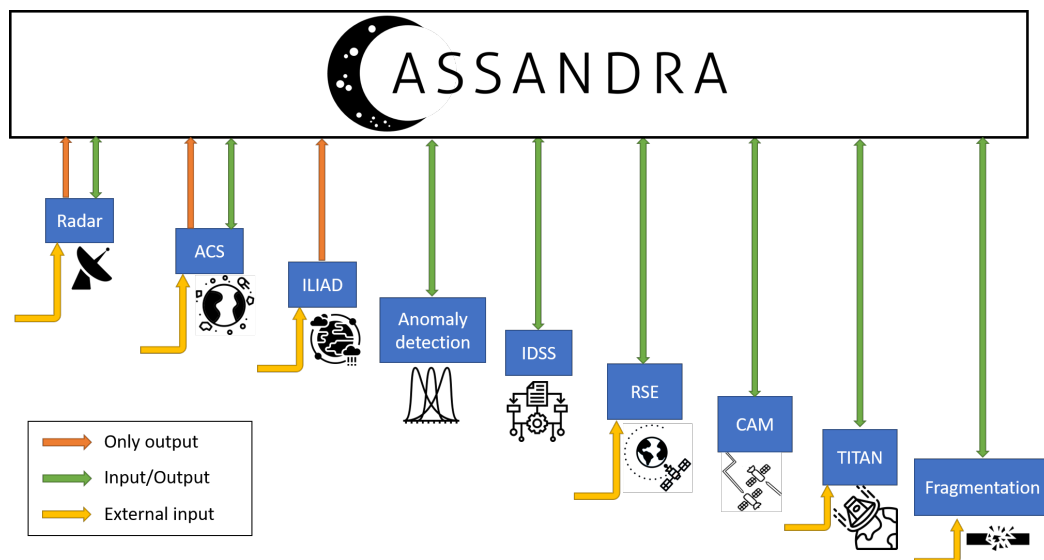


Figure 10.1: Modules of CASSANDRA.

An important role of CASSANDRA is the management of the relations between different modules. Even if each of them is a complex tool, real scenarios will likely involve the combination of more than one. For the automatic operation of CASSANDRA, it is essential to set the allowed interaction between modules and specify the format of the module's inputs and outputs. It is important to note that, due to the modular architecture of CASSANDRA, these relationship pathways may be altered due to the

inclusion of new modules or new problems to be addressed.

In the next sections, two module integration proposals are presented to address some STM problems combining some of the modules listed above. More specifically, in Section 10.2, the Robust State Estimator (RSE), Intelligent Decision Support System (IDSS), Collision Avoidance Manoeuvre (CAM) are integrated to address a single conjunction among two satellites whose position is known with uncertainty. Section 10.3 presents an extension of the previous example by adding the Automated Conjunction Screening (ACS) module and the multi-encounter analysis capabilities of the system, addressing the catalogue screening and the possibility of multiple conjunction events within the catalogue. Before, a more detailed explanation of them is provided below.

10.1.2 Robust State Estimation module

The RSE is the module in charge of the precise state propagation, but more importantly, of the uncertainty propagation and the state updating when observations are received. This module is able to account both for aleatory and epistemic uncertainty. The RSE provides, in addition to the propagated state, an estimation of the confidence interval of the expected value of any parameters related to the encounter, like the uncertain geometry or the probability of collision. These intervals can be used later by the IDSS to make the decision or the CAM to compute robust manoeuvres. A comprehensive explanation of the RSE can be found in [Greco and Vasile, 2021], where Dr. C. Greco first introduced this work.

Robust formulation

To provide robust decision-making, the system should account for epistemic uncertainty. In the next lines, a brief explanation is included of how the filtering problem of propagation and observation update is reformulated to account for this type of uncertainty.

The problem can be formulated as:

$$\dot{\mathbf{x}} = f(t, \mathbf{x}, \mathbf{d}), \tag{10.1}$$

$$\mathbf{y}_k = h(t_k, \mathbf{x}_k, \boldsymbol{\varepsilon}_k), \quad (10.2)$$

where Eq. (10.1) is the equation of motion, with t the time, \mathbf{x} the state vector and $\mathbf{d} \in \mathbb{R}$ the model parameters, with initial conditions $\mathbf{x}_0 = \mathbf{x}(t_0)$. Eq. (10.2) represents the noisy observations of the state vector at certain times $t_k, k = 1, \dots, M$, where $t_k < t_{k+1}$ and $\boldsymbol{\varepsilon}_k$ the measurement noise. The initial condition, the model parameters and the observations are modelled as random variables: $\mathbf{X}_0, \mathbf{D}, \mathbf{E}_k$, being \mathbf{x}_0, \mathbf{d} and $\boldsymbol{\varepsilon}_k$ specific realisation within their respective sample spaces: $\Upsilon_{\mathbf{x}_0}, \Upsilon_{\mathbf{d}}$ and $\Upsilon_{\boldsymbol{\varepsilon}}$. The probability density function (pdf) of the initial state and the dynamic model parameters are represented by $p(\mathbf{x}_0)$ and $p(\mathbf{d})$, and the likelihood of the observations is expressed as $p(\mathbf{y}_k | \mathbf{x}_k)$. The transition distribution $p(\mathbf{x}_k | \mathbf{x}_{k-1})$ induced by the uncertainty in the model parameters indicates how likely a realisation \mathbf{x}_k at t_k is given the previous state at t_{k-1} . The pdf of the state at time t_k given the observations acquired up to this time is $p(\mathbf{x}_k | \mathbf{y}_{1:k})$, with $k > 0$, also known as posterior distribution.

If epistemic uncertainty is introduced, the pdfs are no longer precisely known, but defined within imprecise sets, which can be expressed as:

$$\begin{aligned} \mathcal{P}_{x_0} &= \{p(\mathbf{x}_0; \boldsymbol{\lambda}_0) \mid \boldsymbol{\lambda}_0 \in \Upsilon_{\boldsymbol{\lambda}_0}\}, \\ \mathcal{P}_{x_k | x_{k-1}} &= \{p(\mathbf{x}_k | \mathbf{x}_{k-1}; \boldsymbol{\lambda}_{x_k}) \mid \boldsymbol{\lambda}_{x_k} \in \Upsilon_{\boldsymbol{\lambda}_{x_k}}\}, \\ \mathcal{P}_{y_k | x_k} &= \{p(\mathbf{y}_k | \mathbf{x}_k; \boldsymbol{\lambda}_{y_k}) \mid \boldsymbol{\lambda}_{y_k} \in \Upsilon_{\boldsymbol{\lambda}_{y_k}}\}, \end{aligned} \quad (10.3)$$

so that:

$$\begin{aligned} \mathbf{X}_0 &\sim p(\mathbf{x}_0; \boldsymbol{\lambda}_0) && \in \mathcal{P}_{x_0} \\ \mathbf{X}_k &\sim p(\mathbf{x}_k | \mathbf{x}_{k-1}; \boldsymbol{\lambda}_{x_k}) && \in \mathcal{P}_{x_k | x_{k-1}} \\ \mathbf{Y}_k &\sim p(\mathbf{y}_k | \mathbf{x}_k; \boldsymbol{\lambda}_{y_k}) && \in \mathcal{P}_{y_k | x_k}, \end{aligned} \quad (10.4)$$

for $k = 1, \dots, M$, where $\boldsymbol{\lambda}_k = [\boldsymbol{\lambda}_0, \boldsymbol{\lambda}_{x_{0:k}}, \boldsymbol{\lambda}_{y_{0:k}}] \in \Upsilon_{\boldsymbol{\lambda}_k}$ are the epistemic parameters for the initial position, model parameters and observations, respectively. Similarly, the epistemic distribution of the state at time t_k given the observation up to that time (the

posterior distribution) can be expressed as an imprecise set as well, as in Eq. (10.5).

$$\mathcal{P}_{x_k} = \{p(\mathbf{x}_k | \mathbf{y}_{1:k}; \boldsymbol{\lambda}_k) | \boldsymbol{\lambda}_k \in \Upsilon_{\lambda_k}\}. \quad (10.5)$$

Robust Particle Filter

To compute the generic posterior Eq. (10.5), a two-steps Robust Particle Filter (RPF) is executed iteratively from t_0 to t_k :

- *uncertainty propagation*: the posterior distribution at time t_{k-1} is propagated to time t_k through mapping

$$p(\mathbf{x}_{k-1} | \mathbf{y}_{1:k-1}) \rightarrow p(\mathbf{x}_k | \mathbf{y}_{1:k-1}) . \quad (10.6)$$

The resulting distribution is called prior at time t_k . This propagation is performed in two steps: the propagation of the polynomial representation of all possible states at time t_k as a function of the states at time t_{k-1} , followed by the propagation of particles by inexpensive polynomial evaluations. In this way, the cost of the particle propagation, which is the most expensive step, is reduced [Greco and Vasile, 2021, Greco et al., 2022];

- *observation update*: at discrete instances, the prior distribution is updated to incorporate the last observation according to the unnormalised sequential Bayes' rule

$$p(\mathbf{x}_k | \mathbf{y}_{1:k}) \propto p(\mathbf{y}_k | \mathbf{x}_k) p(\mathbf{x}_k | \mathbf{y}_{1:k-1}) . \quad (10.7)$$

The equation is evaluated for each particle to compute the corresponding weight.

In addition to uncertainty propagation, the RSE can provide the expectation on any variable of interest, $\phi(\mathbf{x}_{0:k})$, function of the propagated state (e.g. geometry variables on the impact plane or probability of collision) with Eq. (10.8).

$$\mathbb{E} [\phi(\mathbf{X}_{0:k}) | \mathbf{y}_{1:k}; \boldsymbol{\lambda}] = \int_{\mathbf{r}_{x_k}} \phi(\mathbf{x}_{0:k}) p(\mathbf{x}_{0:k} | \mathbf{y}_{1:k}; \boldsymbol{\lambda}) d\mathbf{x}_{0:k} \quad (10.8)$$

This expectation depends on the posterior distribution. Due to the epistemic uncertainty, the expectation is not single-valued but interval-valued. The RSE is then able to provide the upper and lower bound of the expectation as a function of the epistemic parameters solving the optimisation problem in Eq. (10.9). This interval-valued expectation of the desired variables resembles the interval bounds of the epistemic framework introduced in Chapter 2.

$$\underline{\mathbb{E}} = \min_{\lambda \in \Upsilon_\lambda} (\mathbb{E} [\phi(\mathbf{x}_k)]) \quad (10.9a)$$

$$\overline{\mathbb{E}} = \max_{\lambda \in \Upsilon_\lambda} (\mathbb{E} [\phi(\mathbf{x}_k)]) \quad (10.9b)$$

The integral involving the expectation computation has no closed-form solution due to the non-parametric nature of the posterior pdf for generic distributions. In addition, it is not practical to draw samples from non-parametric distributions to obtain a numerical approximation of the integral. The chosen alternative is to use importance sampling [Greco and Vasile, 2021] to construct an estimator of the expectation:

$$\mathbb{E} [\phi(\mathbf{X}_{0:k}) | \mathbf{y}_{1:k}; \boldsymbol{\lambda}] \approx \hat{\theta}(\boldsymbol{\chi}_{0:k}; \boldsymbol{\lambda}_k) = \sum_{i=1}^N \hat{w}_k^{(i)}(\boldsymbol{\lambda}_k) \phi(\mathbf{x}^{(i)}), \quad (10.10)$$

This estimator, which exploits the sequential nature of the problem, is a weighted sum of $\phi(\mathbf{x}^{(i)})$ evaluated on fixed samples and importance weights that depend on the epistemic parameters. The symbol $\boldsymbol{\chi}_{0:k} = \{\mathbf{x}_{0:k}^{(1)}, \dots, \mathbf{x}_{0:k}^{(N)}\}$ indicates the collection of N trajectories represented by samples at $k + 1$ discretised time. Thus, the function of interest can be pre-computed with a fixed number of samples, $\mathbf{x}_k^{(i)}$, drawn for a proposal posterior distribution, $\pi(\mathbf{x}_k | \mathbf{x}_{0:k-1}, \mathbf{y}_{1:k})$, which does not depend on the epistemic parameters. Only the weights depend on the epistemic parameter:

$$\begin{aligned} w_k^{(i)}(\boldsymbol{\lambda}) &= \frac{p(\mathbf{y}_k | \mathbf{x}_k^{(i)}; \boldsymbol{\lambda}_{y_k}) p(\mathbf{x}_k^{(i)} | \mathbf{x}_{k-1}^{(i)}; \boldsymbol{\lambda}_x)}{\pi(\mathbf{x}_k^{(i)} | \mathbf{x}_{0:k-1}^{(i)}, \mathbf{y}_{1:k})} \hat{w}_{k-1}^{(i)}(\boldsymbol{\lambda}) \\ \hat{w}_k^{(i)}(\boldsymbol{\lambda}) &= \frac{w_k^{(i)}(\boldsymbol{\lambda})}{\sum_{j=1}^N w_k^{(j)}(\boldsymbol{\lambda})}, \end{aligned} \quad (10.11)$$

In this way, it is possible to split the problem. The particles can be drawn and propagated once, while the optimisation over the epistemic parameters is executed only on the weights of the pre-computed distribution. Thus, the upper and lower bound of the expectation estimator can be computed by solving Eq. (10.12).

$$\begin{aligned}\underline{\hat{\theta}}(\boldsymbol{\chi}_{0:k}) &= \min_{\boldsymbol{\lambda}_k} \hat{\theta}(\boldsymbol{\chi}_{0:k}; \boldsymbol{\lambda}_k) \\ \overline{\hat{\theta}}(\boldsymbol{\chi}_{0:k}) &= \max_{\boldsymbol{\lambda}_k} \hat{\theta}(\boldsymbol{\chi}_{0:k}; \boldsymbol{\lambda}_k).\end{aligned}\tag{10.12}$$

These optimisation problems are generally nonlinear and multimodal. Therefore, a Branch and Bound approach over simplicial subdomains exploiting the estimator Lipschitz continuity is developed in [Greco and Vasile, 2021]. This algorithm ensures asymptotic convergence to the global bound and a measure of the distance from it at each iteration.

In the context of the robust conjunction risk assessment addressed in this framework, the desired quantities to be bounded are the uncertain variables defining the encounter geometry used by the IDSS to robustly classify the risk of the event: the component of the miss distance and the components of the combined covariance matrix in the impact plane, $\mathbf{u} = [\mu_\xi, \mu_\zeta, \sigma_\xi^2, \sigma_\zeta^2, \sigma_{\xi\zeta}]$.

10.1.3 Intelligent Decision Support System

This section describes the *Intelligent Decision Support System* module of Fig. 10.3. In particular, the IDSS automatically allocates the most appropriate action to be taken by an operator in the event of a close encounter. This system is the application of the methodology introduced in Chapter 3 to account for epistemic uncertainty in conjunction risk assessment using Dempster-Shafer theory of Evidence (DSt) and the implementation of ML tools, more specifically Random Forest (RF) models, to predict the risk of the encounter, as shown in Chapter 8.

This example shows the robustness and flexibility of the IDSS and the evidence framework behind it. While in Chapter 4 the input intervals of the evidence framework were derived from a sequence of CDM, in this case, the IDSS receives the inputs

directly from the synthetic measurements. Thus, the upper and lower estimation from Eq. (10.12) of the miss distance and the covariance matrix in the impact plane are ingested in the IDSS, which will provide the operator with the best action to avoid the encounter.

The IDSS implements RF multi-label classification models to skip the computationally expensive step of computing Plausibility (Pl) and Belief (Bel) of the Probability of Collision (PoC), defined in Eq. (3.9), from the set of intervals of the uncertain encounter geometry. The ML model receives as input the intervals and associated $bpas$ and the time to the encounter from the last observation. The model employed in the IDSS was trained on 28,800 synthetic conjunction events with different geometries and different values of the uncertain variables, \mathbf{u} , as explained in Chapters 3 and 8.

The outcome of the system is one of the classes established in Table 7.1 in Chapter 7, whose meaning is refreshed here:

- *Class 0.* Manoeuvre due to the proximity of the event and the possibility of high risk.
- *Class 1.* Perform a CAM due to the support of immediate high risk.
- *Class 2.* Design a CAM due to a possible high-risk event in the mid-term
- *Class 3.* Collect more measurements due to the impossibility of making a confident decision.
- *Class 4.* Potential low-risk scenario. Keep monitoring although no further action is initially required.
- *Class 5.* No further action due to the low risk of the event.

Classes 4 and 5 are associated with safer events, thus, the *Low risk* and *No action* path in Fig. 10.3 would be followed. Since *Class 3* is associated with uncertain events and the lack of possibility to make confident decisions, further measurements are required (*Uncertain* and *Collect new measurements* in Fig. 10.3). Finally, the rest of the classes would require the design and/or implementation of a CAM, following *High risk* path in Fig. 10.3 and activating the CAM module, explained next.

10.1.4 Collision Avoidance Manoeuvre module

The robust optimal avoidance strategy is computed by the CAM module of CASSANDRA, activated when the event is categorised with $Class < 3$. This module provides the best avoidance strategy to avoid a potential collision, accounting for aleatory and epistemic uncertainty. It uses the approach presented in Chapter 5, based on the linear model in Eq. (5.1) and the optimisation problem in Eq. (5.18). Thus, given the uncertain encounter geometry, defined by the intervals of the miss distance and the covariance matrix, the system computes the best manoeuvre to reduce the risk of the worst-case ellipse, that is, the case, among the sets of ellipses, with a higher PoC. The magnitude of the event may be also optimised, so that the propellant consumption is minimised, as long as a safety risk threshold PoC_{CAM} is achieved, as in Eq. (5.19).

The module's inputs are, other than the uncertain geometry, the thruster capacity (either chemical or low-thrust) and the set of positions where compute the optimal manoeuvres, Θ_m . It provides the direction and magnitude of the robust optimal manoeuvres executed at the desired positions, along with the worst-case PoC after the CAM and its associated set of uncertain parameters.

Note that an extra layer could be included in this module by applying the Multi-Criteria Decision-Making (MCDM) techniques presented in Chapter 6 to rank the computes manoeuvres. The first integration example does not make use of it, for better clarity on the closing loop process. The second integration example does include this layer if a manoeuvre is required to reduce the conjunction risk.

10.1.5 Automated Catalogue Screening module

This section details the ACS module, which is designed to predict close encounters between catalogued objects. This is typically the first stage of the conjunction assessment procedure and is responsible for determining which (and when) object pairs fall within a given screening volume over a given screening period. These pairs are then subjected to a more detailed risk assessment to establish if mitigation actions are required to avoid a possible collision, i.e. using the RSE and IDSS modules within CASSANDRA, as discussed before and illustrated in Section 10.3.

The ACS module has two actionable modes: *All-vs-All* and *One-vs-All*, which are described in more detail below.

All-vs-All

The *All-vs-All* mode was designed for fast inference in large-scale conjunction screening, specifically in the context of the *All-vs-All* problem, where conjunctions between all possible sets of catalogued objects, both active and debris, are considered. This work was first introduced by Dr. E. Stevenson in [Stevenson et al., 2021]. This scenario is computationally challenging, scales quadratically with the growing number of catalogued space objects, and must cope with hundreds of millions of object pairs. To handle these scales efficiently, the ACS was developed using ML and DL AI techniques, which are promising in this context owing to their ability to process and exploit large datasets, infer hidden correlations and also reduce computational time during model prediction.

In line with the particular demands for efficiency of the *All-vs-All* mode, the task of automated conjunction screening was framed as a tabular ML classification task. This implies that, given a set of object pairs and their corresponding initial states, the resulting model will predict whether or not these pairs will be involved in a conjunction over the given screening period (binary label).

In this work, a feed-forward neural network for this task is employed, which was trained using a realistic catalogue-wide conjunction database generated by the Centre National d'Etudes Spatiales (CNES) BAS3E space surveillance simulation framework [Morand et al., 2019] and input Teo Line Elements (TLE) catalogue. Based on the initial state vectors of the object pairs, the model is trained to predict which of the pairs will undergo a close encounter (as defined by a 20 km spherical safety volume) over the next 7 days. These predictions are designed to serve as an initial first filter for the catalogue. Various methods were employed for forcing the importance of these cases including class rebalancing, weighted loss functions, and the tuning of the class probability threshold to ensure that only cases for which the model has high confidence are rejected. This threshold can be translated into a constraint on the number of

acceptable missed conjunctions by the model, and therefore to an operator decision. More details on the model, underlying database and training procedure can be found in [Stevenson et al., 2021].

The primary output of the *All-vs-All* mode is thus a list of risky object pairs requiring further consideration. Following this, the Time of Closest Approach (TCA) can be found, and the list of objects can be further refined through the inclusion of uncertainty data and evaluation of the collision risk in subsequent modules. At this stage, information on the properties of the objects involved in the conjunctions, for example, whether they are operational, can also be retrieved from catalogues such as ESA's DISCOS [European Space Agency, 2022], which can be used alongside the TCA to prioritise the analysis of certain object pairs. This information can also be used to ultimately determine an appropriate course of mitigation action, such as a CAM (as considered in this work), or even techniques such as *just-in-time* collision avoidance for non-maneuvrable debris-debris conjunctions [Bonnal et al., 2020].

One-vs-All

A second *One-vs-All* mode for the ACS is available. This mode was designed to provide more detailed information on possible conjunctions, including the TCA and miss distance of individual events. As such, this mode could be employed as a second higher-fidelity filter following the *All-vs-All* mode or for manoeuvre screening. In this latter scenario, the new orbit of an object undertaking a CAM to avoid a specific conjunction (the *one*), should be screened against the space object catalogue (the *all*) to ensure that no additional conjunctions will be incurred. This screening should be used to decide whether the proposed CAM, which may be optimal under given constraints to avoid the original conjunction, should go ahead, or whether a different solution should be found. This scenario is explored in Section 10.3.

The impact parameter is the norm of the relative distance vector between two objects in the so-called impact plane. Under the assumptions of a short-term encounter, the impact plane can be defined as the plane perpendicular to the relative velocity of the primary object at the encounter time, such that it contains both objects Eq. (5.9). This

definition of the impact parameter is therefore equivalent to the miss distance used in the calculation of thePoC [Alfano, 2007], and thus this quantity gives direct information on the proximity of two objects, with low values indicating a close encounter (assuming positional uncertainties are not considered).

As the impact parameter for a given object pair is dependent on the relative position and velocity vectors of both bodies and, therefore, varies in time, the prediction of this quantity is phrased as a time series ML regression task. Regression tasks in ML consist of predicting a continuous outcome y based on the value of one or more predictor variables \mathbf{x} . In this case, both \mathbf{x} and y are time series structured data, with \mathbf{x} consisting of the 6-channel ephemeris data of each object (12 variables in total), and y the future evolution of the impact parameter. In ML terms, this could be viewed as a univariate forecasting task with auxiliary variables, but this case is unusual in that the history of the forecast variable does not feature as an input to the predictive model. Nevertheless, to describe this problem, the forecasting terms *horizon* and *lookback* are used for the number of time steps to predict in y and the number of time steps used to create the prediction from \mathbf{x} , respectively.

In this work, the predictive model was trained using a synthetic database which comprised the ephemeris data of 200 objects over 7 days, with a timestep of 180 seconds, and the corresponding impact parameters for each pair (19,900 in total), calculated at each timestep. The initial parameters of these objects were restricted to the orbit regime given in Table 10.1. This range of orbits was restricted due to computational considerations but enables presenting a proof of concept of this mode and demonstrating the pipeline of the integrated system described in Section 10.3.

Table 10.1: Bounds on the initial orbital parameters of the orbits used to train the *One-vs-All* mode of the ACS.

Variable	Units	Lower bound	Upper bound
Semimajor axis	[km]	6900	7200
Eccentricity	-	10^{-5}	$5 \cdot 10^{-3}$
Inclination	[rad]	1.22173	1.91986
Right ascension of the ascending	[rad]	0	2π
Argument of perigee	[rad]	0	2π
True anomaly	[rad]	0	2π

The choice of the length and configuration of the lookback and horizon windows is application-dependent. For the case of manoeuvre screening, it is the new (future) orbit of an object following a CAM that needs to be considered, and not the past history of the object which is typically associated with the forecast lookback. As such, the lookback needs to be based on the post-manoeuve propagated state. The model input is chosen to be the 12 ephemeris variables of each object pair over a 1-day period post-CAM. The evolution of the impact parameter for each pair over a 3-day period post-CAM is intended to be predicted. This allows increasing the quantity of training data by using a sliding window over the 7 available days in the database, generating 20 training examples for each object pair. An example is illustrated in Fig. 10.2a, with truncated sections of the lookback and horizon windows for readability.

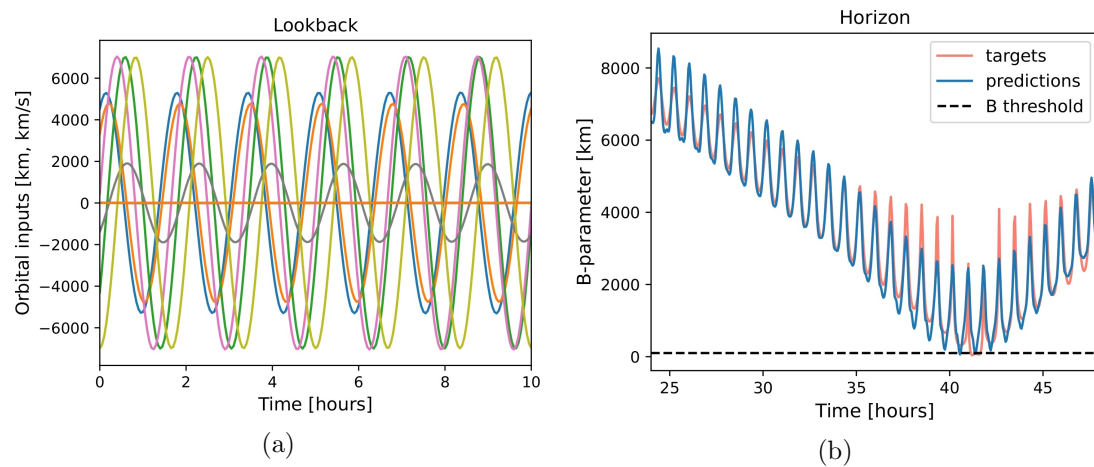


Figure 10.2: ACS *One-vs-All* mode for truncated sections of the 1-day lookback and 3-day horizon: (a) example of the input, (b) example of the output.

This dataset was then divided following an 80% to 20% splitting strategy into training and validation sets, ensuring that overlapping windows were not present in both to prevent data leakage. While the training set is used to train the model directly, the validation set is used to evaluate the performance of the model during training to ensure that the model is generalising well to unseen data, and not merely memorising the training data, as well as to tune higher level hyperparameters that are pre-set by the user and not learnt by the model.

In this work, the InceptionTime architecture [Fawaz et al., 2020] is employed for training the predictive model, a state-of-the-art deep neural architecture for time series tasks among the family of 1-dimensional Convolutional Neural Networks (CNNs). This family of networks is chosen as they are most suitable for capturing short-term patterns in the data, such as orbit oscillations, since they compute features using sliding convolutional filters. Deep Learning (DL) architectures such as this have a higher complexity and representation capacity compared to simpler tabular architectures, but come at the cost of increased computational expense as a result, motivating the two-mode nature of the ACS.

The training configuration used was as follows, for which the `tsai` [Oguiza, 2022] library was employed, which implements DL techniques and architectures for time series data. First, the neural network is built using six sequential inception modules to accept 12-channel inputs and a 1-channel output. The input data is standardised, transforming each variable to have zero mean and unit variance to account for differences in units and scales. For the loss function (the objective to be minimised while training), the nominal regression metric, the Root Mean Squared Error (RMSE), is used. For the optimiser (the component that updates the parameters of the neural network), Ranger was employed, an extension of the popular Adam optimiser that combines both RAdam [Liu et al., 2020] and Lookahead [Zhang et al., 2019a] optimisation algorithms. A dynamic learning rate (which determines the factor by which the weights of the neural network are updated in each training iteration) was chosen following a one-cycle schedule with cosine annealing. The model was then trained subject to early stopping criteria, whereby training is terminated once over-fitting becomes evident on the validation set, and the best-performing model (based on the validation loss) is taken.

This model can then be applied to new data to obtain the predicted evolution of the impact parameter for different possible conjunction pairs. Once this was obtained for a given pair, the TCA associated with possible conjunction events can then be identified by considering crossing points of the impact parameter with an operator-defined threshold (e.g. 20 km), as illustrated in Fig. 10.2b. The output of the *One-vs-All* mode is thus a list of conjunction events, the objects involved, their TCA and miss

distance.

10.2 Robust decision-making based on Bayesian state estimation framework

This section addresses the problem of automatically allocating CAMs under uncertainty by a robust Bayesian framework. This framework allows propagating the objects' state and uncertainty, predicting collisions, allocating manoeuvres, updating the state estimation with Bayesian inference, and redefining the manoeuvres, accounting at all steps for aleatory and epistemic uncertainty. The Bayesian framework combines a robust particle filter for state estimation and uncertainty propagation (RSE module), an intelligent agent for automatically classifying risk events and allocating avoidance manoeuvres (IDSS module) and a robust avoidance manoeuvres optimiser (CAM module). With this system, the intention is to close the loop between state estimation, uncertainty propagation, risk assessment under potential collisions, decision-making, CAM performance and observations acquisition.

Fig. 10.3 shows the overall architecture of the Bayesian framework. The *Noisy observations* and *Uncertain state estimation* boxes represent the RSE module. Note that, for this work, the observations were simulated. The RPF explained above works by relating these two blocks, estimating the uncertain state and updating it when new observations are available. The IDSS is represented by the *Intelligent Decision Support System* box, which receives the estimated state at the TCA from the RSE. The theory to handle epistemic uncertainty by the IDSS was provided in Chapter 3, and the intelligent component was introduced in Chapter 8, as explained before. The outcome of the IDSS is a classification presented in previous chapters, that can be summarised in the *High risk*, *Low risk* and *Uncertain* light-shade boxes. Each outcome has its respective suggested actions represented by the darker boxes: *Perform CAM*, *No action* and *Collect new measurements*, respectively. Finally, the system closes the loop by acquiring more observations (in this example, simulated by the RSE) and updating the state in the case of uncertain encounters or, in the case of high-risk events, by

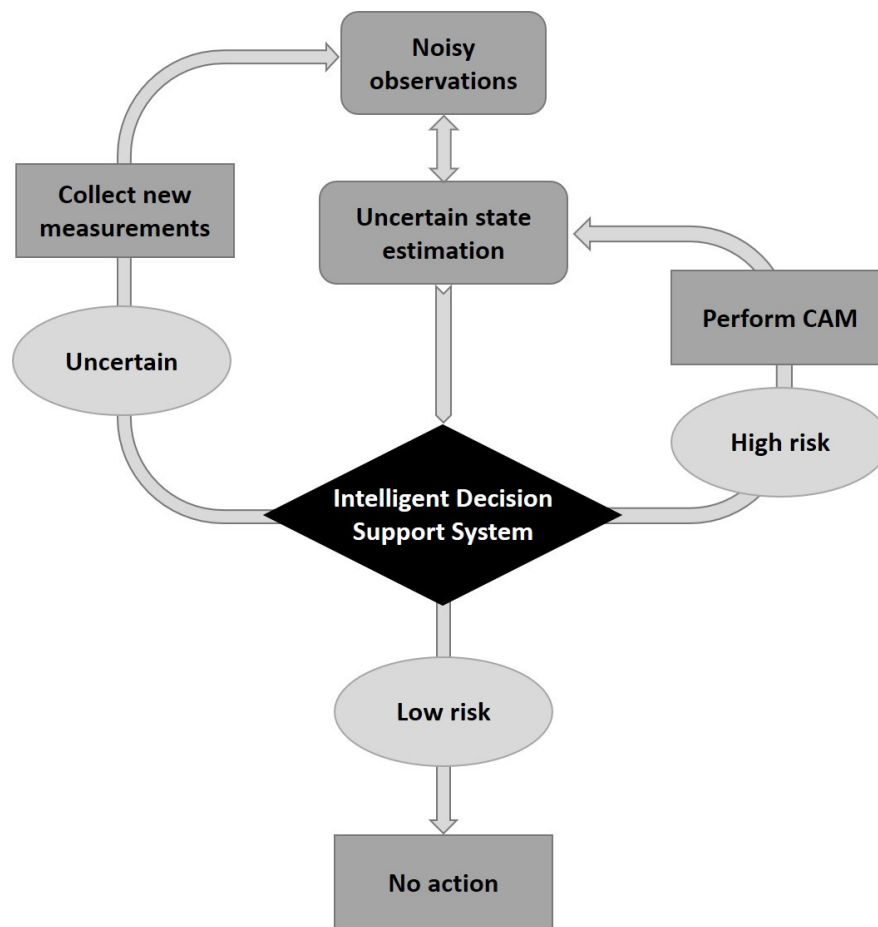


Figure 10.3: Diagram of robust Bayesian pipeline for optimal collision avoidance manoeuvre planning.

estimating the new state after executing a CAM, computed by the CAM module based on the methodology introduced in Chapter 5 as explained above.

10.2.1 Study case

This section discusses the operational scenarios on which the robust Bayesian agent is tested using a numerical example.

Satellite Conjunction Setup

The conjunction under consideration is between the operation satellite SENTINEL 2B (NORAD ID 42063) and a piece of debris from FENGYUN 1C (NORAD ID 30141). On

the 7th of January 2021, SOCRATES (Satellite Orbital Conjunction Reports Assessing Threatening Encounters in Space) [Celestrak, 2019] reported a potential collision between these objects at TCA 13th of January 2021 at 13:24:25 UTC. The nominal orbital elements for SENTINEL 2B and FENGYUN 1C DEB are reported in Table 10.2.

Table 10.2: Objects orbital elements from NORAD TLEs.

Variable	Units	Object 1	Object 2
NORAD ID	[-]	42063	30141
EPOCH	[UTC]	08/01/21 01:17:15	07/01/21 16:24:07
Semi-major axis (a)	[km]	7167.14	7180.78
Eccentricity (e)	[-]	1.1e-4	2.5e-3
Inclination (i)	[deg]	98.57	99.08
Right ascension of ascending node (Ω)	[deg]	85.33	183.01
Argument of perigee (ω)	[deg]	81.09	252.25
Mean anomaly (M)	[deg]	279.04	107.59

The dynamical system is described in Cartesian coordinates within an Earth-Centred Inertial (ECI) reference frame. The dynamical forces included are Earth’s gravity with harmonics up to degree and order 4, atmospheric drag using the Jacchia-Gill model, soli-lunar third-body gravitational attraction, and the solar radiation pressure with a conical shadow model for Earth’s eclipses.

In the two scenarios presented below, an operational satellite that is tracked with very low uncertainty is considered, e.g. due to GPS receivers, and, therefore, the approximation $\mathbf{x} = \mathbf{x}^{(2)}$ can be used. The debris object is affected by uncertainty on its state vector. Observations are simulated to improve the knowledge of the debris state. The measured quantities are the debris azimuth and elevation with respect to the equatorial plane [Schutz et al., 2004] obtained by means of optical measurements.

Robust decision-making

A multivariate Gaussian distribution is considered to model the aleatory uncertainty of the initial condition

$$\mathbf{X}_0 \sim \mathcal{N}(\mathbf{x}_0; \boldsymbol{\mu}_0, \boldsymbol{\Sigma}_0) . \quad (10.13)$$

The mean $\boldsymbol{\mu}_0$ is set to the Cartesian state resulting from the orbital elements in Table 10.2. The covariance $\boldsymbol{\Sigma}_0$ is constructed by taking typical errors associated to TLE from the European Space Agency (ESA) guidelines [Klinkrad et al., 2008]. The 1σ uncertainty on TLE for objects characterised by inclinations larger than 60 deg is summarised in Table 10.3 in radial, transversal and normal components. The covariance

Table 10.3: 1σ position (r) and velocity (v) uncertainty of TLEs for orbits with $e < 0.1$, $i > 60$ deg, perigee altitude ≤ 800 km, in radial (U), transversal (V), and normal components (W).

Component	Units	Value
$1\sigma_{r_U}$	[m]	104
$1\sigma_{r_V}$	[m]	556
$1\sigma_{r_W}$	[m]	139
$1\sigma_{v_U}$	[mm/s]	559
$1\sigma_{v_V}$	[mm/s]	110
$1\sigma_{v_W}$	[mm/s]	148

$\overline{\boldsymbol{\Sigma}}_0$ resulting from these standard deviations is then rotated in the standard Cartesian inertial frame by using the Jacobian of the radial-transversal-normal transformation.

However, the uncertainties in Table 10.3 are just presumed [Klinkrad et al., 2008] and therefore far from being well-characterised. Furthermore, because different sets of TLEs are usually estimated from different measurement stations, it may be impossible to define a single covariance which properly characterises the TLE uncertainty. Hence, epistemic uncertainty is introduced on the covariance by parameterising $\boldsymbol{\Sigma}_0$ using two epistemic parameters $\boldsymbol{\lambda}_0 = [\lambda_{0-1}, \lambda_{0-2}]$. The covariance parameterisation reads as follows

$$\boldsymbol{\Sigma}_0(\boldsymbol{\lambda}_0) = \begin{bmatrix} \lambda_{0-1} \overline{\boldsymbol{\Sigma}}_0(1:3, 1:3) & \mathbf{0}_{3 \times 3} \\ \mathbf{0}_{3 \times 3} & \lambda_{0-2} \overline{\boldsymbol{\Sigma}}_0(4:6, 4:6) \end{bmatrix}, \quad (10.14)$$

that is the epistemic parameters scale respectively the position and velocity blocks of the reference covariance $\overline{\boldsymbol{\Sigma}}_0$ computed as above.

The bounds considered for these multipliers are $\lambda_{0-1}, \lambda_{0-2} \in [1/5^2, 5^2]$, that is they can change the reference 1σ uncertainties by roughly shrinking them up to $1/5$, or expand them by a factor of 5. The measurements are simulated using the debris ref-

erence trajectory and then adding the sensor errors, drawn from a zero-mean normal distribution with diagonal covariance Σ_y . The reference uncertainty on the measurement is set to $1\sigma_{y_{az}} = 1$ and $\sigma_{y_{el}} = 10$ arcsec. Given that the optical measurements are acquired from non-professional stations, these 1σ values were again obtained from the literature and are not coming from a rigorous sensor characterisation. Thus, epistemic uncertainty is considered on the noise covariance by means of two parameters $\lambda_y = [\lambda_{y-az}, \lambda_{y-el}]$, similarly to what was done for the initial conditions in Eq. (10.14). The epistemic parameters range is set to $\lambda_{y-az}, \lambda_{y-el} \in [1/5^2, 5^2]$, in line with diverse 1σ values found in literature [Bennett et al., 2015, Li et al., 2016].

The values of the thresholds used by the IDSS for risk assessment (Section 10.1.3) are shown on Table 10.4. They include the two time thresholds (T_1, T_2) to discern among short-term, mid-term and long-term encounters; the threshold on the probability of collision (PoC_0) indicating the risk level; the value of the upper expectation at which the trust on the value is lost (Pl_0), and the value of the area between the curves above which the event is considered to be highly affected by uncertainty (A_0). In this work, the safe PoC threshold is set to $PoC_{CAM} = 10^{-6}$ according to ESA's guidelines [Braun et al., 2016].

Table 10.4: IDSS thresholds values for the RSE-IDSS-CAM implementation.

Threshold	Units	Value
T_1	[days]	2.0
T_2	[days]	4.0
PoC_0	-	10^{-6}
Pl_0	-	0.5
A_0^*	-	0.1

Results

Two operational scenarios are considered, one resulting in a collision and another in a near-miss conjunction.

Collision scenario In this case, the true unknown trajectory of the FENGYUN 1C DEB debris eventually results in a collision with SENTINEL 2B. It is assumed that observations are available up to 48 hours before TCA. The result of the robust Bayesian estimation at this point is displayed in Fig. 10.4.

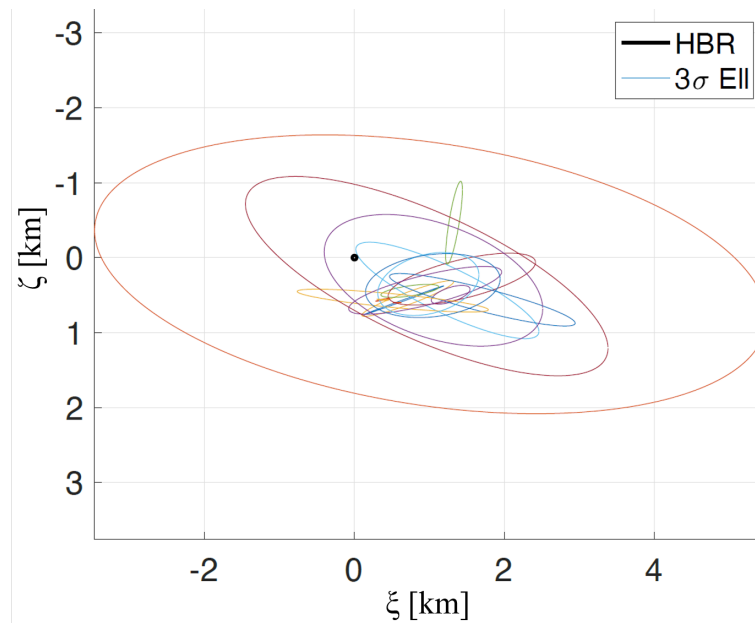


Figure 10.4: Impact plane 3σ ellipses for collision scenario with observations up to 48h before TCA.

In the plot, several 3σ ellipses, which correspond to different values of the epistemic parameters, are displayed on the impact plane. Those ellipses are bounded by the estimated bounds from Eq. (10.12) for the uncertain variables of the problem. Note that with the current approach, without losing generality, only one interval per source is obtained, thus the Joint Body of Evidence is compounded by a single Focal Element (FE). Thus, the resulting curves of the Pl and Bel for the PoC are a single-step function, jumping from one to zero at the maximum and minimum value of the PoC in the FE, respectively. The step for the Bel curve corresponds to the minimum value of the PoC among all the possible ellipses defined by the intervals, while the step for the Pl correspond to the *Worst Case* scenario, that is, the ellipse with the highest PoC. At this stage of the analysis, the value of the risk ranges between $PoC \in [10^{-30}, 2.5 \cdot 10^{-2}]$.

Hence, the IDSS is run to analyse the conjunction. The classification returns a

Class 3 scenario, which corresponds to a highly uncertain conjunction, as can be seen in the previous figure. This requires the acquisition of further measurements to make an informed action. Therefore, the agent decides to wait for them until the next checkpoint, 24 hours before TCA. At this point, after new observations are available, the robust Bayesian estimation is rerun and the results are displayed in Fig. 10.5.

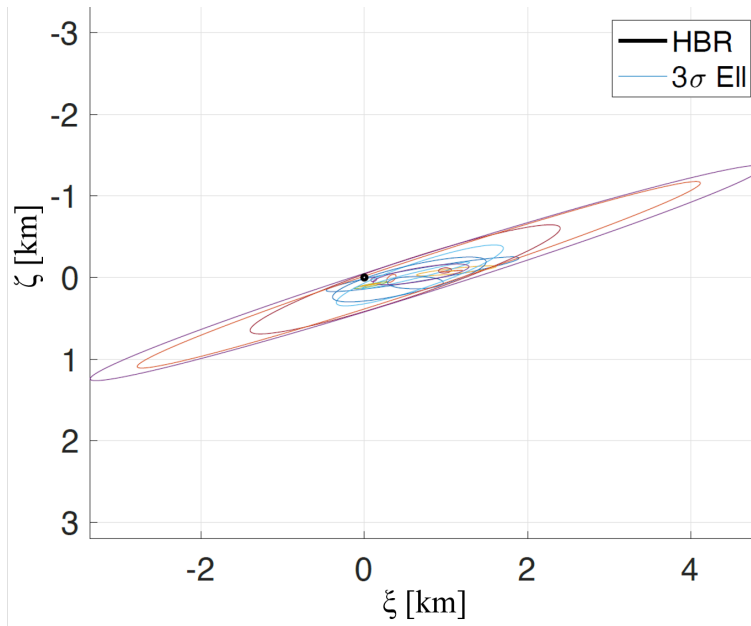


Figure 10.5: Impact plane 3σ ellipses for collision scenario with observations up to 24h before TCA.

The collision probability is now $\text{PoC} \in [0, 5.5 \cdot 10^{-2}]$. Still, Pl and Bel are single-step curves at the minimum and maximum values of the PoC, and the IDSS indicates a CAM is required. Thus, the CAM module is run to design a robust and optimal manoeuvre which provides a $\overline{\text{PoC}} < 10^{-6}$ while taking into account the state uncertainty. The CAM on SENTINEL 2B is designed 10 revolutions before the TCA. After the manoeuvre execution, the robust estimation is run again to check that the upper collision probability indeed satisfies the safety threshold. The resulting geometry is shown in Fig. 10.6, where it can be seen that there is no intersection between the 3σ ellipses and the Hard Body Raiud (HBR). In fact, the highest value of the PoC (the worst-case scenario) is $\overline{\text{PoC}} < 10^{-6}$, below the safety threshold. The evolution of the PoC bounds at the several checkpoints considered is shown in Figure 10.7.

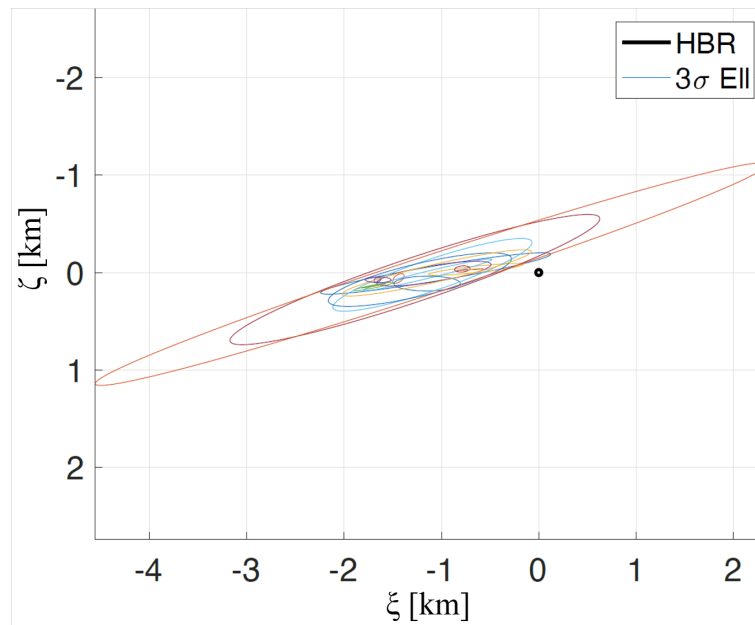


Figure 10.6: Impact plane 3σ ellipses for collision scenario after CAM.

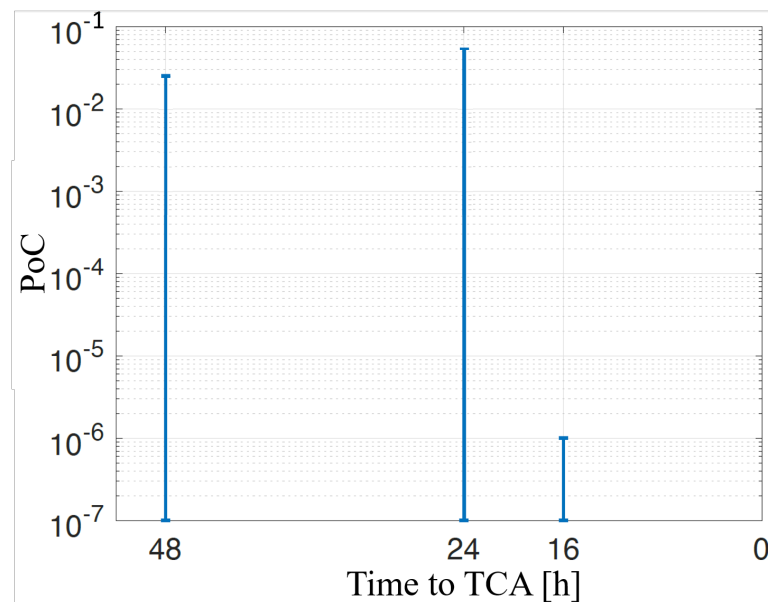


Figure 10.7: Evolution of PoC bounds for collision scenario.

The Bayesian agent performance for this scenario is reported in Table 10.5. The estimation box running the RPF requires the longest computational time, whereas the ML-based IDSS is inexpensive to evaluate. The CAM design module requires less than

two minutes to optimise the manoeuvre.

No-collision scenario In this scenario, the true unknown trajectory of the FENGYUN 1C DEB debris misses SENTINEL 2B by ~ 2 km. Again, it is assumed that observations are available up to 48 hours before the TCA. The result of the robust Bayesian estimation 48 hours before the TCA is depicted in Fig. 10.8. The probability interval (and thus, the steps of Pl and Bel in the curves) are $PoC \in [0, 7.5 \cdot 10^{-3}]$.

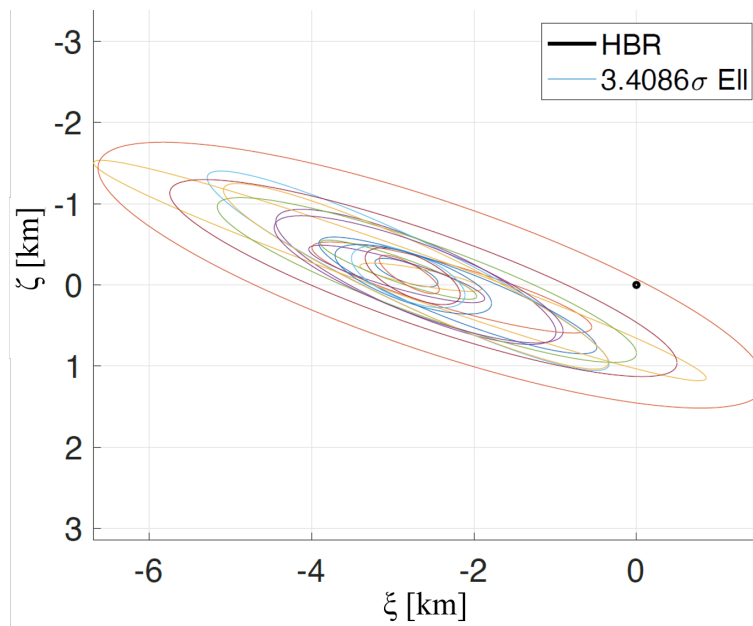


Figure 10.8: Impact plane 3σ ellipses for no-collision scenario with observations up to 48 h before TCA.

In both cases, the conjunction analysis is similar to the collision one at 48 hours before TCA. The IDSS is run and it returns a *Class 3* conjunction, labelling the encounter as a highly uncertain scenario with the need for further measurements to implement an informed action. Those further measurements are acquired until the 24-hour checkpoint, where the Bayesian estimation is updated. The resulting conjunction geometry is displayed in Fig. 10.9.

Here, it can be seen how the debris 3σ ellipses are rather distant from the HBR of the operational satellite and indeed centred on the true (unknown) trajectory. The IDSS now returns a *Class 5* conjunction labelling a safe conjunction. Indeed, the

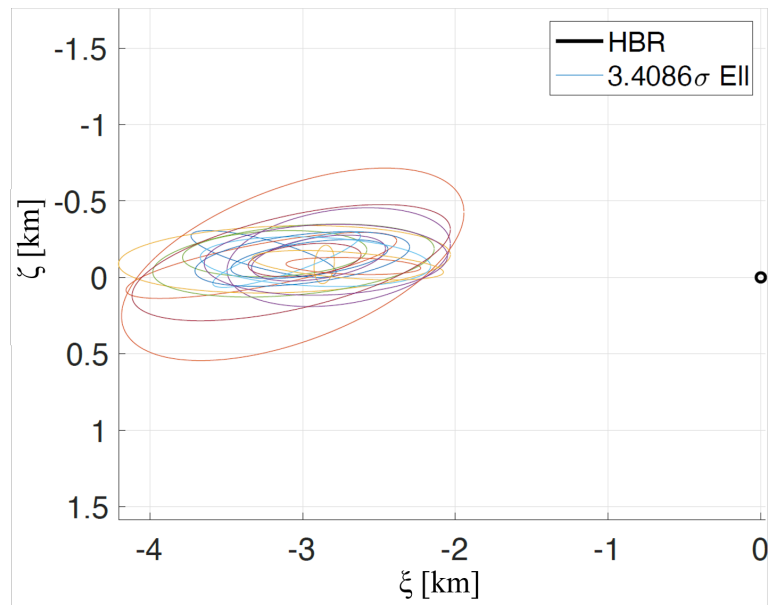


Figure 10.9: Impact plane 3σ ellipses for no-collision scenario with observations up to 24 h before TCA.

corresponding upper probability is estimated to be $\overline{\text{PoC}} < 10^{-10}$. The intelligent agent, therefore, suggests no further action to be taken. For the no-collision scenario, the PoC bounds estimated at the two different checkpoints are displayed in Figure 10.10.

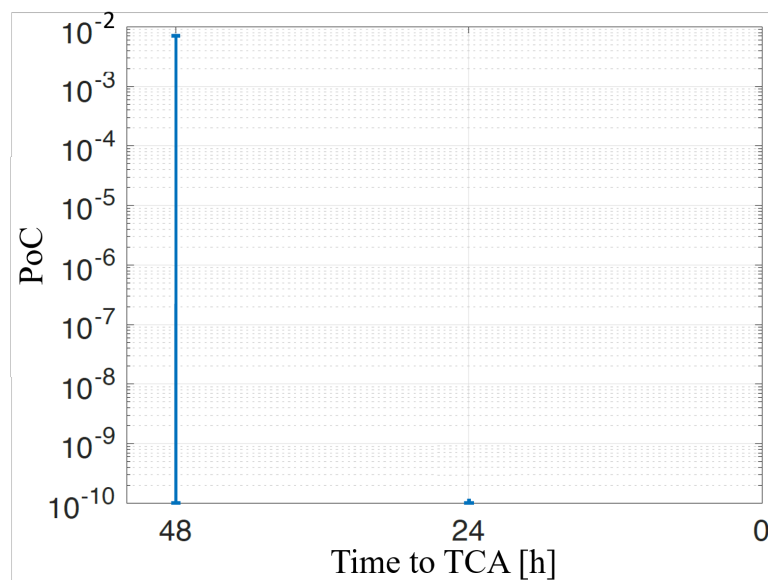


Figure 10.10: Evolution of PoC bounds for no-collision scenario.

The agent performance for the no-collision scenario is reported in Table 10.5 as well. The estimation box takes longer when compared to the collision scenario as the global minimum is isolated and, therefore, the optimisation results are more challenging. The IDSS is again inexpensive to evaluate and requires the same amount of computational time, while no CAM is designed in this scenario. The simulations were performed on Matlab R2020b on a macOS Big Sur 3.5GHz Dual-Core i7.

Table 10.5: Bayesian agent performance for different conjunction scenarios.

Instance	Time		
	Estimation [s]	ICS [s]	CAM [s]
Collision	295.8	0.015	108.2
No-collision	462.6	0.015	-

10.3 Robust catalogue screening

In this section, further integration of CASSANDRA’s modules is presented. Starting from the previous integration of the RSE, IDSS and CAM modules presented above, a new module is added to the pipeline: the ACS presented in Section 10.1.5. This scenario allows for closing the loop between catalogue screening, conjunction risk assessment, manoeuvre allocation and catalogue update.

An important element of such a system is its ability to cope efficiently with the scales associated with current and future space object populations. This is especially relevant in the *All-vs-All* problem (although also in the *One-vs-All* one), which considers all possible pairs of catalogued objects, both active and debris, and is therefore crucial to SEM, but a computational challenge owing to the vast and growing number of possible conjunction pairs. Another key element when dealing with the automation of high-risk scenarios is the treatment of uncertainty. In the case of STM, uncertainties in the state estimation and orbit propagation translate into uncertainty on the probability of collision between two objects, which is critical for effective decision-making. The integration presented below tackles both problems by implementing the AI techniques embedded in the ACS and the IDSS modules, and the modelling of the uncertainty

(both aleatory and epistemic) underlying the RSE, IDSS and CAM modules.

10.3.1 Pipeline

In this section, the integrated pipeline of the ACS, RSE, IDSS and CAM modules is presented. It describes the generic workflow and the different paths the decision-making process can follow.

Catalogue screening

The pipeline is illustrated in Fig. 10.11. The workflow starts in the left bottom corner of the figure with the automatic screening of the catalogue (*Catalogue* box in the figure) by the ACS (*ACS: All-vs-All* block). The catalogue includes information on the states of several objects at a certain epoch and information on the type of object (debris, operational satellite, manoeuvrable, etc.). Using the *All-vs-All* mode, the system can detect *NE* potential close encounters. After the analysis, the ACS provides an output file with a reduced set of potential conjunction pairs, indicating the objects requiring further screening. For this work, the time to TCA with respect to the epoch of the catalogue for individual encounters is computed by propagation, although this could be replaced using the *One-vs-All* mode as a second filter in future work.

State estimation and conjunction risk analysis

For each of the *NE* conjunction pairs identified by the ACS, a more detailed conjunction analysis is automatically activated, where information about the uncertainty on the state, both epistemic and aleatory, is included in the analysis. Thus, the RSE propagates the state and uncertainty of the objects to the TCA (*RSE: Orbit & Uncertainty Propagation* box in the figure). In case there are observations available for any of the objects involved, they can be included in the uncertainty propagation process (*RSE: State Estimation* box).

Once the uncertainty states of both objects are propagated to the TCA and the uncertain geometry of the encounter is defined, the IDSS will autonomously propose the most suitable action to be made to address the event, according to the risk, the

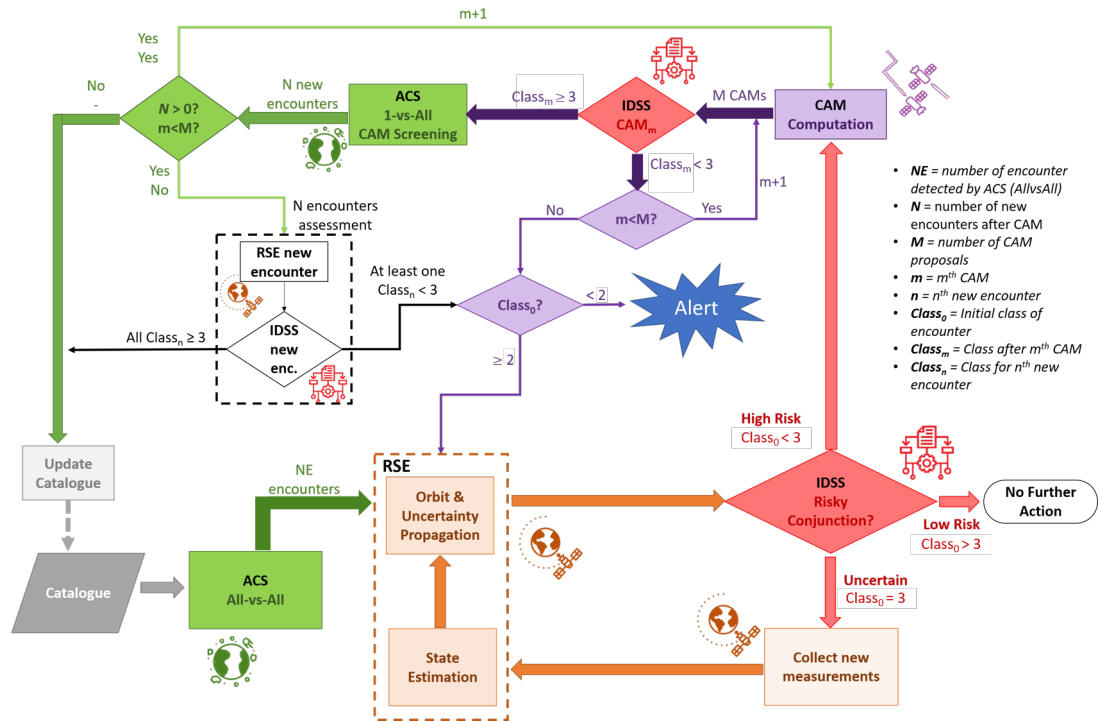


Figure 10.11: Pipeline of the modules to be integrated into this work.

available information and the confidence on this information (*IDSS. Risky Conjunction?* decision box). Three possible actions can be suggested:

- i) *Low Risk*, related with $Class_0 > 3$: no further action.
- ii) *High Risk*, associated with $Class_0 < 3$: compute CAMs.
- iii) *Uncertain*, corresponding to $Class_0 = 3$: allocate new observations.

If the event returns a low-risk situation, the event is safe enough not to require mitigation actions (*No further action* box on the right side of Fig. 10.11). In case the event is classified as *Uncertain*, new simulations will be allocated (*Collect new observations* box). In this work, the new observations are simulated with the RSE (see Section 10.3.2). These observations may introduce new uncertainty in the system (e.g. noise). The new state and uncertainty are fed again to the RSE (represented by the *RSE* dashed box in the figure). If the event is classified as *High Risk*, it is necessary to compute at least one CAM to avoid the encounter or reduce its risk (*CAM Computation* block on the right-top corner of Fig. 10.11). A more detailed explanation

of the interaction of RSE, IDSS and CAM modules to deal with encounter events was presented in the previous example (Section 10.2).

Collision avoidance manoeuvre and reassessment

In the event is classified as $Class_0 \leq 2$, a new iterative process starts. The CAM module will provide M robust optimal CAM candidates, sorted according to certain criteria and constraints, which can be selected by the operator [Sánchez and Vasile, 2021b], as shown in Chapter 6: time to the encounter, cost of the manoeuvres, reduction of the risk, disruption of the operational orbit, etc.

The first step after obtaining the list of candidates is to evaluate the safety of the new orbit, and whether it reduces the risk satisfactorily for the considered conjunction: the IDSS should output after the CAM a $Class_m \geq 3$ for the encounter to be safely avoided (*IDSS*, *CAM_m* and “ $m < M$?” decision boxes). In case this is not achieved by any of the proposed options (“*Class₀*?” decision box):

- If the original class before CAM was $Class_0 \geq 2$ (meaning a long/mid-term event), new observations are allocated, and the process returns to the RSE state estimation and uncertainty propagation.
- If the original class was $Class_0 < 2$ (short-term high-risk event), there is no time to allocate new measurements and an alert is raised to the operator (*Alert* box) to perform a manual detailed analysis: relax constraints on the computation of the CAM, widen the search of alternatives, etc.

For the CAM options that do reduce the risk of the event, the ephemerides associated with the new post-CAM orbit are subsequently computed, starting with the top-ranked alternative (as ranked by $Class_m$). These ephemerides are then used to screen the new orbit against all the objects in the catalogue to identify any new possible conjunctions. This operation is performed by the ACS under the *One-vs-All* mode (*ACS: 1-vs-All CAM Screening* module). If new encounters are predicted, the ACS generates a file containing the objects involved, predicted TCAs and the predicted impact parameters for the N new encounters. This can result in three different situations

(“ $N > 0?$, $m < M?$ ” decision box):

- a) No new encounters are found, in which case the execution of the manoeuvre is encouraged and the catalogue is updated accordingly (*Update Catalogue* box).
- b) New encounters are detected, but the analysed CAM is not the last of the proposed options. In this case, the system loops back to the CAM module and the next manoeuvre on the sorted list is selected. If the number of future encounters is lower than for previous CAMs, this alternative is saved as the most promising solution thus far.
- c) Future encounters are anticipated and there are no more alternative manoeuvres remaining, the CAM resulting in the minimum number of new encounters is selected for further analysis, which is further explained below.

These N new encounters are fed back to the RSE-IDSS loop (*N encounters assessment* dashed box): the new post-CAM orbit and that of the object in the catalogue are propagated, along with their uncertainties, to the new TCA using the RSE (*RSE new encounters* box). Then, the event is assessed with the IDSS (*IDSS new encounters* decision box). Depending on the $Class_n$ output by the IDSS for these N events, the following actions can be made:

- I) All events present $Class_n \geq 3$. This means there is no evidence that the new predicted events present a high risk. The best action is to perform the CAM to avoid the initial encounter and update the catalogue, dealing with the potential new encounters later.
- II) At least one event presents $Class_n < 3$ (high-risk event) and the original event without CAM was classified as $Class_0 \geq 2$. Since there is enough time, new measurements are allocated, returning to the RSE state estimation and uncertainty propagation stage.
- III) At least one event presents $Class_n < 3$ (high-risk event) and the original event was classified as $Class_0 < 2$ (e.g. short-term high-risk event): since there is no more time to acquire measurements and all the CAM alternatives involve new encounters, an alert is raised to the operator (*Alert* box). Possible alternatives the

operator can analyse are: to relax the constraints employed to obtain the list of CAM alternatives, or to consider the possibility of performing a multi-encounter CAM [Sánchez and Vasile, 2021b].

Pipeline exit points

In summary, there are 5 possible exit points of the process for each of the *NE* potential encounters detected by the ACS module in the *All-vs-All* mode. Once any of these are reached, the system will start the analysis for the next encounter identified from the catalogue.

1. The encounter does not present an actual risk ($Class_0 \geq 3$), and no further actions are required.
2. The encounter requires a CAM ($Class_0 < 3$), and the proposed CAMs do not create new encounters ($N = 0$). This implies the execution of the manoeuvre and updating of the catalogue.
3. The encounter requires a new CAM ($Class_0 < 3$), which generates new encounters ($N \neq 0$), but none of them present, at the moment of the decision, evidence of being high risk ($Class_n \geq 3 \forall n = 1, \dots, N$). This also implies the execution of the manoeuvre and updating of the catalogue.
4. The encounter presents a high risk, occurring in the short term ($Class_0 < 2$), and none of the proposed CAMs sufficiently reduce the risk ($Class_m \geq 3 \forall m = 1, \dots, M$). This scenario will raise an alert to the operators, who should decide what further actions to follow (e.g. obtain new CAMs alternatives, relax constraints, change criteria to compute alternatives).
5. The encounter presents a high risk, occurs in the short term ($Class_0 < 2$), and some of the new encounters generated by the new post-CAM orbit are also a high risk ($\exists n \mid Class_n \leq 2$ for $n = 1, \dots, N$). In this situation, another alert will be raised, indicating that the operator should start a multi-encounter CAM analysis.

10.3.2 Study case

In the rest of this section, an example of the workflow with a synthetic catalogue containing a potential encounter is presented.

Catalogue conjunctions

For this study case, a reduced synthetic catalogue containing 20 objects is used, including their state vector and associated uncertainty in EME2000 reference frame at CNESJD 25718.999594907 (31-05-2020, 23:59:25.00), including two synthetic objects (Object IDs 11111 and 22222) used to illustrate the rest of the pipeline. The catalogue also includes information on the type of object: operational with manoeuvre capabilities, non-maneuvrable, debris or unknown. For the scope of this work, and due to the characteristics of the database used to train the *One-vs-All* models of the ACS (Section 10.1.5), a reduced catalogue including only orbits falling within the bounds indicated in Table 10.1 is used.

The catalogue is automatically screened by the ACS in the *All-vs-All* mode. This mode takes the initial state vectors of each of the object pairs from the catalogue and returns a binary label as to whether the pairs will undergo a close encounter (as defined by a 20 km screening volume) over a screening period of 7 days. Further details of this mode are given in Section 10.1.5.

From the screening process, five pairs of potential encounters are detected (Table 10.6). Two output files are provided by the ACS. One includes the potential conjunction pairs found by the system, as well as the time to the encounter and the type of object involved. The other file contains the state vector at the initial epoch used for the screening, and the associated uncertainty (if any).

Conjunction risk assessment and decision-making

For the rest of this example, the study focuses on the first encounters (involving objects *ID 11111* and *ID 22222*), whose initial conditions are included in Table 10.7. Note that in this work, only the secondary object of the encounter is assumed to be affected by

Table 10.6: The 5 the potential encounters detected by the ACS: All-vs-All.

Obj. ID 1	Obj. ID 2	Time to TCA [days]	Manoeuvre capabilities	Number of encounters
11111	22222	6.956327887	OP-DEB	1
36345	41138	5.451224743	DEB-DEB	1
42127	36337	1.929933804	DEB-DEB	1
7959	10520	1.210088713	DEB-OP	1
6843	44547	4.574278349	DEB-OP	1

uncertainty, and the uncertainty is given in the object's $\langle T, N, H \rangle$ reference frame.

The primary object is assumed to be perfectly known.

Table 10.7: Initial state vector and uncertainty of objects involved in the first encounter detected by the ACS. Epoch CNESJD 25718.999594907 (31-05-2020, 23:59:25.00).

Obj. ID	\mathbf{X} [km]	\mathbf{Y} [km]	\mathbf{Z} [km]	\mathbf{V}_x [km/s]	\mathbf{V}_y [km/s]	\mathbf{V}_z [km/s]
11111	618.143	7143.340	7.183	1.119	-0.112	7.372
22222	-7183.237	-331.032	96.552	0.035	1.176	7.348

Obj. ID	σ_t [km]	σ_n [km]	σ_h [km]	σ_{vt} [km/s]	σ_{vn} [km/s]	σ_{vh} [km/s]
22222	0.104	0.556	0.139	$5.59 \cdot 10^{-6}$	$1.10 \cdot 10^{-6}$	$1.48 \cdot 10^{-6}$

Each of the encounters detected during the screening stage should undergo a detailed conjunction analysis through the RSE and IDSS modules. For this analysis, the first step is the propagation of the orbit and the uncertainty to the TCA using the RSE. However, the uncertainties in Table 10.7 are merely presumed [Klinkrad et al., 2008], and therefore far from being well-characterised. More in general, the values of uncertainty associated with the other objects in the catalogue lack details on how they were obtained. Hence, epistemic uncertainty is introduced on the covariance to account for this lack of information by parameterising Σ_0 using two epistemic parameters

$\lambda_0 = [\lambda_{0-1}, \lambda_{0-2}]$. The covariance parameterisation reads as follows

$$\Sigma_0(\lambda_0) = \begin{bmatrix} \lambda_{0-1} \bar{\Sigma}_0(1 : 3, 1 : 3) & \mathbf{0}_{3 \times 3} \\ \mathbf{0}_{3 \times 3} & \lambda_{0-2} \bar{\Sigma}_0(4 : 6, 4 : 6) \end{bmatrix}. \quad (10.15)$$

The epistemic parameters scale respectively the position and velocity blocks of the reference covariance $\bar{\Sigma}_0$ computed as above. The bounds considered for these multipliers are $\lambda_{0-1}, \lambda_{0-2} \in [1/5^2, 5^2]$, that is, they can change the reference 1σ uncertainties by roughly shrinking them up to $1/5$, or expanding them by a factor of 5.

In general, immediately after the ACS catalogue screening, no more observations are available for the objects involved in the encounter. Thus, a single prediction step is performed by the RSE. The outputs of this module are the bounds on the mean and covariance elements of the miss distance in the impact plane. This information, along with the time to the TCA, represents the inputs the IDSS uses to make the decision. The threshold values used by the IDSS are included in Table 10.8.

Table 10.8: IDSS thresholds values for the robust screening scenario.

Variable	Units	Value
T_1	[days]	2
T_2	[days]	4
PoC_0	[-]	10^{-6}
Pl_0	[-]	0.5
A_0^*	[-]	0.1
HBR	[m]	0.3

Due to the large propagation time interval (more than 6 days) and the initial uncertainty (both, aleatory and epistemic), the miss distance and relative position covariance intervals in the impact plane are very large (Table 10.9) and, as expected, the IDSS outputs a *Class 3*: the event is affected by such a degree of uncertainty at this step that no confident decision can be made. Thus, new measurements are allocated.

In this work, the observations are simulated within the RSE. The measurements are simulated using the debris reference trajectory and then adding the sensor errors, drawn from a zero-mean normal distribution with diagonal covariance Σ_y , whose non-

Table 10.9: Bounds output by the RSE if no observations available.

Variable	Units	Lower bound	Upper bound
μ_ξ	[km]	-1.830	-0.7759
μ_ξ	[km]	-23.939	36.722
σ_ξ^2	[km ²]	3.203	5.698
σ_ζ^2	[km ²]	$1.915 \cdot 10^3$	$5.9448 \cdot 10^4$
$\sigma_{\xi\zeta}$	[km ²]	-289.981	15.682

zero elements are: $1\sigma_{y_{az}} = 10$ arcsec and $\sigma_{y_{el}} = 10$ arcsec. Similarly to the uncertainty in the initial position, epistemic uncertainty on the observations is added to quantify the lack of detail on the observation sensors. The epistemic uncertainty is considered on the noise covariance by means of two parameters $\lambda_y = [\lambda_{y-az}, \lambda_{y-el}]$, which range in the interval $\lambda_{y-az}, \lambda_{y-el} \in [1/5^2, 5^2]$, in line with diverse 1σ values found in literature [Bennett et al., 2015, Li et al., 2016].

As mentioned above, the primary satellite is assumed to be perfectly known, so the observations refer only to the secondary object. Ten observations are simulated, evenly distributed between the initial epoch and one day before the TCA. Again, the initial state and uncertainty of the objects are propagated to the TCA, although in this case, the position is updated sequentially with the information provided by the measurements. The robust bounds of the new impact plane variables are included in Table 10.10. These bounds along with the new time to the encounter (1 day) are inserted in the IDSS, which classify the event as potential high-risk, proposing a CAM design and execution as the best action.

Table 10.10: Bounds output by the RSE when 10 measurements are received. The time to TCA after the last observation is 1 day.

Variable	Units	Lower bound	Upper bound
μ_ξ	[km]	$-2.0408 \cdot 10^{-2}$	$-1.1596 \cdot 10^{-2}$
μ_ξ	[km]	0.6783	1.20140
σ_ξ^2	[km ²]	$2.0571 \cdot 10^{-11}$	$2.1102 \cdot 10^{-4}$
σ_ζ^2	[km ²]	$9.7038 \cdot 10^{-4}$	$5.81921 \cdot 10^{-2}$
$\sigma_{\xi\zeta}$	[km ²]	$-2.0504 \cdot 10^{-4}$	$1.2473 \cdot 10^{-3}$

Avoidance collision strategy

This decision activates the CAM module, which computes a list of optimal manoeuvres. Seven possible CAMs are computed, executed half an orbit before the encounter position, for the 9 revolutions before the encounter, but the last two revolutions, $\theta_m \in \Theta_m = \{k\pi\}$ with $k = 5, 7, 9, \dots, 17$. The maximum capacity of the thruster is 10 cm/s. The only criterion considered to sort the proposed CAM options is the disruption of the orbit (i.e. time away of the nominal orbit before the encounter), thus the later manoeuvres are ranked first. For more information on other criteria, see Chapter 6. Table 10.11 includes the list of manoeuvres, expressed in the manoeuvrable satellite's $\langle T, N, H \rangle$ reference frame.

Table 10.11: List of ranked possible manoeuvres, expressed in the satellite's $\langle T, N, H \rangle$ reference frame. The last column includes the $Class_m$ of the event after the manoeuvre.

Alternative	Position (θ_m) [rad]	Impulsive CAM ($\delta\mathbf{v}$) [m/s]			Class _m
		δv_t	δv_n	δv_h	
CAM 1	5π	$9.9994 \cdot 10^{-2}$	$-1.0527 \cdot 10^{-4}$	0	5
CAM 2	7π	$9.9997 \cdot 10^{-2}$	$-7.4706 \cdot 10^{-5}$	0	5
CAM 3	9π	$9.9998 \cdot 10^{-2}$	$-5.7745 \cdot 10^{-5}$	0	5
CAM 4	11π	$9.9998 \cdot 10^{-2}$	$-4.6958 \cdot 10^{-5}$	0	5
CAM 5	13π	$9.9999 \cdot 10^{-2}$	$-3.9492 \cdot 10^{-5}$	0	5
CAM 6	15π	$9.9999 \cdot 10^{-2}$	$-3.4018 \cdot 10^{-5}$	0	5
CAM 7	17π	$9.9999 \cdot 10^{-2}$	$-2.9830 \cdot 10^{-5}$	0	5

The different CAM alternatives are evaluated in order of priority. First, the risk associated with the encounter after implementing the manoeuvre is computed. The encounter after the first manoeuvre is re-classified as *Class 5* (Table 10.11), meaning the new orbit is safe. Then, the new ephemerides are computed and further analysis is performed using the *One-vs-All* mode of the ACS to detect possible future conjunctions with other catalogued objects. Note, that in case the first alternative would not have reduced the risk of the event to *Class 4* or *5*, the next alternative would have been chosen.

The model used to predict future encounters in the *One-vs-All* ACS mode is de-

scribed in more detail in Section 10.1.5. This mode takes the newly computed ephemeris of the manoeuvred object and the ephemeris of the other catalogued objects over a 1-day period after the CAM as input, and predicts the evolution of the impact parameter for each possible conjunction pair over a 3-day screening period. The threshold on the impact parameter chosen to identify encounter events was set to 20 km.

The first CAM implemented already reduces the risk of the current encounter and, according to the *One-vs-All*, does not generate further encounters. This means that the system proposes the manoeuvre to the operators. In case the operators decide to execute it, the catalogue has to be updated accordingly. Once this first encounter is addressed, the system automatically starts the analysis of the next pair found by the *All-vs-All* module.

10.4 Chapter summary

This chapter introduced CASSANDRA, an intelligent agent to support operators with SEM/STM problems. It reflects the application of the methodologies and applications presented in this work, bringing them together to solve a common problem. Within the context of this work, CASSANDRA should be understood as the middle step from the theoretical developments introduced here and their applicability to the real world.

CASSANDRA has a modular architecture, with tools dedicated to specific problems. This chapter detailed those modules used during this chapter. More specifically, the ACS, RSE, IDSS and CAM modules were presented, with the latest two synthesizing the development introduced along this work: the DSt framework for conjunction analysis and CAM computation, the application of AI for Conjunction Assessment Risk Analysis and the multi-criteria decision making applied to avoidance strategies.

Two integration examples of those modules showing the functionality of CASSANDRA were presented. The first aims to close the loops of state estimation and observation update in the context of close encounter, conjunction decision-making and CAM allocation, including the robust reevaluation of corrected orbits accounting for uncertainty. An example was proposed with both a Collision and a No Collision encounter, detailing the steps required to be executed by each module. These examples

highlight the importance of receiving new measurements to update the uncertainty of the event and the availability of the system to provide robust solutions to handle that uncertainty.

The second integration example extends the previous case by adding the screening of the catalogue. Thus, the system can predict conjunctions among the different objects in the catalogue and individually assess all of them following the previous process. Moreover, it is also able to evaluate the impact of an avoidance manoeuvre on the background population and analyse if a better alternative is available, bearing in mind the overall catalogue safety.

Chapter 11

Conclusion

The main objective of the thesis was to improve the automation and robustness of Space Traffic Management (STM) tasks by implementing Artificial Intelligence (AI) techniques and modelling and quantifying the epistemic uncertainty involved in Conjunction Assessment Risk Analysis (CARA) and Conjunction Avoidance Manoeuvre (CAM) design. The aim is to enhance space safety by improving the STM in the context of the New Space, using new available theories and techniques, to ensure a safe and sustainable use of space. The aim of the thesis was met and the list of objectives listed in the introduction of this work were addressed in the different chapters compounding this thesis.

Part I included all theoretical contributions and the methodology proposed to address most of the objectives listed above. Each chapter was dedicated to one objective or one sub-objective: evidence-based conjunction risk assessment framework, Conjunction Data Messages (CDMs) epistemic uncertainty modelling, robust CAM design, and robust CAM decision-making support.

Chapter 3 introduced an evidence-based framework to account for mixed uncertainty on the objects' state vector for CARA. This framework allows quantifying both aleatory and more importantly, epistemic uncertainty, which has been usually left aside on conjunction assessment approaches. The proposed framework uses Dempster-Shafer theory of Evidence (DSt) to quantify uncertainty by quantifying the uncertain variables defining the geometry as intervals instead of well-defined variables, which quantify the

epistemic uncertainty affecting them based on the available information or the reliability of the sources (e.g. sensors, dynamic models, aleatory uncertainty quantification). The proposed approach models the aleatory uncertainty using a probabilistic approach (e.g. Gaussian distribution), and the epistemic uncertainty by quantifying the uncertainty on the distribution parameters (i.e. expected value and covariance matrix) with the width, number and overlapping of intervals for each variable. This approach is agnostic of the distribution function and can be applied to any generic distribution. In this work, the focus was on Gaussian distributions to facilitate the comparison with probabilistic-based CARA approaches using the Probability of Collision (PoC) definition derived from the fast encounter hypothesis. However, a more complex distribution can be used to define the aleatory uncertainty, and DSt will be applied similarly to the new parameters defining the distribution. The proposed approach uses DSt's combination rules to combine information provided by different sources of information. The combination rules give a means to address uncertain information coming from differently reliable sources of information (e.g. due to different sensors' quality or different uncertainty propagation models) within the context of DSt. More specifically, the mixing rule is employed, which allows for handling the conflict information that is expected in conjunction risk assessment. Finally, the evidence-based framework provided metrics to evaluate the confidence in the correctness of the value of a desired variable (e.g. PoC): the Plausibility and Belief functions. Based on the information extracted from these two metrics regarding the confidence in a given value provided the available information and the uncertainty affecting that information, some evidence-based classification criteria were proposed. The main contribution of those approaches, despite their differences, is the inclusion of a new category overlooked by pure probabilistic approaches: an "unknown" or "uncertain" class indicating the lack of evidence to make a confident decision. These classification criteria were compared with a probabilistic approach using exclusively the value of the PoC, highlighting the importance of accounting for epistemic uncertainty and considering a new class indicating the need for new observations.

Chapter 4 presented a methodology that extends the framework introduced in the

previous chapter to address the epistemic uncertainty in the CDMs. The CDMs are the current standard to communicate conjunction information among operators. However, they contain some sources of information not explicitly quantified in the message itself, which complicates the proper representation of the uncertainty distributions: observation errors of the sensors used (or even the quality and number of sensors), dynamic models employed for propagation or the parameters uncertainty, and the uncertainty approximation, assuming a multi-variate Gaussian distribution for the state vector uncertainty at the encounter, even though it is well known it is not an accurate model. The proposed methodology assumes the CDMs are samples drawn from an unknown distribution but no assumptions are made on the distribution itself. Instead, a bounding region among the provided samples is built using Dvoretzky-Kiefer-Wolfowitz (DKW) inequalities which includes all compatible distributions with the available information given a certain confidence interval. The bounded region can be interpreted as a p-box, quantifying the epistemic uncertainty affecting the sequence of CDMs of the specific encounter. Using the equivalence between p-boxes and DSt structures, the methodology presented in that chapter derived the set of intervals associated with the sequence of CDMs employed for the evidence-based classification criteria presented before. The methodology was subjected to a sensitivity analysis to understand the main parameters driving the interval quantification. The confidence interval that determines the width of the DKW band and the number of intervals to discretise the p-boxes are the main parameters affecting the degree of confidence on the value of the PoC when computing the Plausibility (Pl) and Belief (Bel). The other parameters have a smaller impact. In any case, the main structure of the curves indicating the degree of uncertainty is mainly unchanged regardless of the values of the parameters. Finally, the improvement in the robustness of the CARA analysis was shown by studying the effect of wrongly computed CDMs within a sequence. Due to the analysis of the whole sequence, the method is resilient to poor-quality information by automatically assigning greater weight to information coherent with the rest of the available information.

Chapter 5 proposed a method to compute robust CAM under the evidence-based framework accounting for aleatory and epistemic uncertainty. The CAM design is based

on a linear approximation of the effect of a manoeuvre on the relative position at the impact plane. From this approximation to compute the effect of impulsive manoeuvres, the robust manoeuvres are proposed by solving a min-max optimisation problem. The minimisation part of the problem computes the optimal manoeuvre that minimises the PoC of a given encounter geometry (relative position and uncertain ellipsoid). The properties of the linear approximation are exploited, so the optimisation problem can be solved by finding the eigenvalues of a matrix accounting for the covariance matrix and the state transition matrix of the linear problem. This solution was proven to provide accurate results when compared to the optimal manoeuvre obtained by a Monte Carlo run. The maximisation problem aims to address the epistemic component of the problem. When defining the uncertain geometries with intervals, the uncertain ellipsoids become a set of ellipsoids. Thus, a robust optimal CAM should minimise the PoC of the worst-case ellipse, that is, the ellipse in the set with the maximum PoC. The proposed methodology can cope with fixed thrust manoeuvres or optimise the manoeuvre magnitude subject to reduce the risk below a given threshold. The method was extended to handle the low-thrust scenario as well. The proposed approach for Low-Thrust (LT) manoeuvres assumes the direction of an equivalent optimal impulse manoeuvre executing at the midpoint of the thrust arc and then optimises the arc length, the thrust magnitude, or both simultaneously.

The last chapter of Part I, **Chapter 6** proposed a decision support system to assist operators in the planning and designing of avoidance strategies. From the method introduced in the previous chapter, given a high-risk encounter, several robust optimal CAMs could be obtained based on the manoeuvre position, the returning strategy to the original orbit or the risk and thrust thresholds. The proposed approach evaluates the possible alternatives against certain criteria, which usually are contradictory, to provide the operator with the best alternatives to maximise the reward on the most relevant criteria. This approach is based on Multi-Criteria Decision-Making (MCDM), which allows to weight of the criteria according to the operator necessities and provides a ranking of the preferred solutions. If the encounter involves other satellite operators by a different agent, its avoidance strategy may influence the preferred option. Thus,

the proposed decision support system for manoeuvre planning was enhanced with a non-cooperative capability to address this problem. This scenario represents a classical game theoretic scenario, where the best overall outcome is an alternative where no agent loses, even if it does not represent the preferred alternative if not considering the other agent's decision. Using Game Theory, these stability points are searched on the space of possible alternatives, thus an earlier manoeuvre may be the desired action finally selected by both agents to avoid a potential collision, although individually, they would prefer to be the other spacecraft which manoeuvres. The influence of the agent risk and cost perception was analysed to see the variation in the preferred output in different scenarios. These two approaches extended the whole evidence-based framework from the conjunction assessment in Chapter 3 and Chapter 4 to the optimal CAM design in Chapter 5 and the avoidance strategy planning. The whole framework improves the robustness of the system by accounting at all stages for both aleatory and epistemic uncertainty and facilitates automation with the proposal of the decision support system.

Part II proposed some application of the evidence-based framework on some STM problems, including the verification of the methodologies on real data, the application of AI, and addressing the multiple encounters scenario. Thus, the rest of the objectives listed in the introduction were addressed in these chapters, and the increase in automation and robustness on STM was also tackled in this part of the thesis.

Chapter 7 applied the methods proposed in Part I on real operational scenarios to provide robust conjunction risk assessment. Real sequences of CDMs were provided by two Space Agencies, ESA and CNES, along with their course of action under those events. First, the chapter introduced an update on the evidence-classification criterion to account for the uncertainty of the events based on the total gap between the *Pl* and *Bel* curves instead of the vertical gap at the PoC threshold, allowing for better capture of the total uncertainty and avoiding being affected for narrow jumps (small horizontal gap) in low-conflict events. From this modification, a methodology to establish the values of the epistemic threshold was proposed, aiming to select the value of Pl_0 that reduces the number of missing encounters or False Negatives, and the value of A_0 that minimises the number of false alerts or False Positives. The robust conjunction risk

assessment method was then applied to some real events provided by ESA and to an additional event provided by CNES. The three cases from ESA represent the three main possible outcomes of the analysis: low-risk, high-risk and uncertain scenario. When information on the sequence is coherent and not affected by further uncertainty, the outcome of the system matches the ESA's decision: a manoeuvre in the high-risk case, and not take further actions in the low-risk case. However, the proposed approach provides further insight when the sequence shows uncertainty or variability, indicating to the operator that any possible decision lacks complete support from the available information. When using CNES example, two further conclusions were obtained. On the one hand, the proposed approach was compared with the Scaled PoC (sPoC)-based methodology employed in the decision-making of this event, showing consistent decisions were provided by both methods. On the other, when comparing this case and the last example of ESA's events, it can be concluded that a further visual inspection of the *Pl* and *Bel* shape on cases affected by epistemic uncertainty can give more insights on the further evolution of the risk associated with the event. To finalise the validation process, the evidence-based framework was tested on a database of real events along several years of operations of an ESA mission to provide a statistical analysis of the system response. The number of CAM proposed from both approaches are in the same range, but the cases classified as uncertain requiring potential actions obtained from the evidence-based framework clearly exceed those identified by ESA as escalating events. On the one hand, no operational constraints were considered in the robust approach that may decrease this number and so may do the further visual analysis of the uncertain cases suggested from the previous analysis, but on the other hand, this may suggest that relying only on the last CDM without any confidence analysis may be too optimistic.

Chapter 8 presented some implementations of Machine Learning (ML) techniques aiming to automatise the methods proposed in the methodology section of the thesis by the construction of surrogate models that allow speeding up the steps involved. Three different AI approaches were proposed to address the methods introduced in the three first chapters of Part I: automatically classify events based on the evidence-based

framework, improving the decision-making accounting for the robust CAM, and predicting the best action given a sequence of CDMs. Overall, it can be said that ML techniques, and more specifically, Artificial Neural Networks (ANN), Deep Learning (DL) and bagging methods (Random Forests, RF, and Light Gradient Boosting Machine, LGBM), provide very good accuracy on the task of robustly classify risky events given the uncertain geometry. However, it is important to note the difference in performance if the system is tested on synthetic or real data. Synthetic datasets are useful for the training process since they allow complementing real datasets, especially in the case of unbalanced scenarios, to improve the model performance both in the synthetic and real databases. Moreover, being able to train on a virtual database allows for being independent of the availability of real observations. Real data, on the other hand, are more scarce and present a strong unbalanced distribution favouring less interesting low-risk conjunctions. Although balancing techniques helped to compensate for this situation, the difference in the structure of the database makes it hard, in general, to extrapolate the prediction capabilities of models trained on synthetic databases. Additionally, generating a representative virtual database may be hard, considering the number of sources of error and unknown parameters required to mimic real observations or real sequences of CDMs. Thus, as a conclusion of the application of AI for robust conjunction risk assessment, it can be said that ML techniques can provide very good results on the classification of risky events, but there is plenty of room for improvement both, from the available data (considering better synthetic databases or training on mixed datasets) and from the ML architectures, with this work just indicating the most promising techniques, without entering on the details of the models selection or their hyperparameter tuning.

Chapter 9 addressed the problem of multi-encounter events by extending the Decision Support System (DSS) methodology implemented in Chapter 6. The chapter addressed the problem from two different perspectives: a single satellite facing subsequent encounters, or several satellites belonging to the same constellation facing an encounter with the same object. In both cases, the multiple events can be considered as a collaborative scenario, so the MCDM approach was employed. In this chapter,

the flexibility of the method was shown by adding more alternatives and more criteria to the analysis without requiring any modification of the approach. The subsequent encounter scenario was addressed by adding to the avoidance manoeuvre of the individual encounter, alternatives with the possibility of avoiding every encounter either with a single manoeuvre or with multiple manoeuvres. The effectiveness of the MCDM methodology was shown with two opposite scenarios, differing on the location in the orbit of the encounters compounding the multiple events. Each case required a different avoidance strategy, which was well detected by the DSS. The second case proposed a problem likely occurring in the New Space context, involving a constellation in Low Earth Orbit (LEO) that had to keep the configuration that provides the best service without affecting space safety. Thus, the returning strategy to the original configuration was included in the alternatives and additional criteria referring to the total cost of the combined manoeuvres and the constellation figure of merit subject to the returning strategy were also considered. Different scenarios were addressed modifying the importance of the criteria. The proposed applications showed the improvement on STM that the proposed DSS extended capabilities can bring, being able to address the more complex scenarios of multiple encounters.

Finally, **Chapter 10** presented an intelligent agent, CASSANDRA, to address complex Space Environment Management (SEM) and STM problems combining the different methods proposed along this work, and other related works, including AI and ML techniques for providing an automated and robust solution to complex space safety tasks and involving different knowledge areas. The proposed agent has a modular structure, where each module addresses specific tasks (observations, uncertainty propagation, catalogue screening, CAM design, decision-making...). The modular architecture adds flexibility to the agent so that only the required modules are activated when necessary. It also reduces the amount of interaction among them, only requiring the definition of the inputs and output. A modular architecture allows the inclusion of new modules as well in case new problems are wanted to be solved. This agent illustrated how the work introduced in this thesis can be integrated into broader space safety projects. The chapter showed the integration into a single framework of algo-

rithms developed in this work with other methods to address uncertainty propagation and intelligent screening propagation to address a more complex problem than those tackled by the individual algorithms. Two specific applications of CASSANDRA were shown in the chapter. The first one addressed the problem of robust conjunction risk assessment and CAM design providing observations affected by uncertainty (aleatory and epistemic). Three modules are involved: the Robust State Estimator (RSE) that provides an estimate of the propagated state and the associated uncertainty, propagated with a Robust Particle Filter; the Intelligent Decision Support System (IDSS) that includes the evidence-based framework to provide robust decisions, and the CAM module to provide robust optimal manoeuvres if required. This example showed the capacity of the system to close the loop from observations to uncertainty propagation, conjunction assessment and collision avoidance. Different scenarios were proposed, including a near-missed encounter and a conjunction event. In both cases, due to the uncertainty affecting the observations, new measurements were required by the IDSS. In the collision scenario, a robust CAM was proposed and its effect was evaluated ensuring the effective reduction of risk. The second integration example proposed in the chapter presented a more complex pipeline and it is an extension of the previous scenario. The aim was to provide robust conjunction assessment to a whole catalogue. The pipeline of the previous scenario, including the RSE, IDSS and CAM modules was extended by including the ML-based Automated Conjunction Screening (ACS) module, with its two modes: *All-vs-All* and *One-vs-All*. Additionally, the examples showed also the integration of the MCDM-based DSS to propose the best manoeuvre accounting for the effect on the background population, that is, finding new potential encounters with the rest of the objects on the catalogue. Thus, this scenario shows the capacity of CASSANDRA to analyse a whole catalogue to detect potential conjunction given the set of Two Line Elements (TLEs) (although raw observations or CDMs would follow a similar approach) and to propagate the uncertainty, propose avoidance measurement and evaluate their impact on the background population

11.1 Recommendations

Next, some future developments are indicated that would help improve the maturity, applicability, and efficiency of the methods presented, as well as overcome some limitations currently affecting them.

The evidence-based framework was presented assuming the fast encounter hypothesis. The method is not limited to these assumptions, thus it would be desirable to implement a robust analysis to situations when one or more of these assumptions do not apply. First, Gaussian assumptions should be dropped. It is well known that the object's uncertain distribution does not remain the Gaussian after orbit propagation under non-linear dynamics, which affects the actual risk of the event. Gaussian Mixture Models could be used for modelling the uncertainty. This approach allows a more complex representation of the uncertainty, closer to the actual situation, and still provides the same kind of inputs to the evidence-based system, that is, the expected values and the covariance matrices of the Gaussian distributions. If dropping the fast encounter hypothesis, a new computation of the PoC or new metric risk should also be adopted. Different efforts are addressing the relaxation of some of the assumptions, like assuming uncertainty on the velocity, assuming more complex shapes of the objects or assuming encounters expanding through longer periods. In any case, it should be advisable to implement a dilution-free metric even if no epistemic uncertainty is modelled. This dilution-free metric should not decrease if poorer quality information is provided (no reduction of the risk metric when increasing the covariance). The proposed method should be able to cope with this approach with no great modifications. The inputs can be modelled interval-wise similarly, and the *Pl* and *Bel* curves would refer to the new risk metric. From a more practical point of view, improving the optimisation step on the computation of the *Pl* and *Bel*, which currently represent the slower step of the process, should enhance efficiency and allow increasing the number of intervals per variable for better quantification of the epistemic uncertainty.

Related to this aspect, the robust classification system can be improved by replacing the risk metric with a dilution-free metric. The current approach is robust in the

sense that it accounts for epistemic uncertainty, a necessary step to avoid dilution of probability. However, if all CDMs in the sequence, for example, falls within the dilution region, the proposed approach will not be able to provide information about this circumstance. A possible and relatively straightforward improvement of the model would be to use any of the metrics included in Appendix A or other similar ones so that confidence is obtained on a dilution-free variable, adding an extra layer of robustness to the methodology.

There is room for improvement in the design of robust collision manoeuvres. The current approach is based on a linear model assuming Keplerian motion. Thus, accounting for perturbations on the effect of the manoeuvre should be a desirable development. Regarding the automation capabilities and considering future on-board uses, the min-max optimisation problem can benefit from a more efficient implementation that speeds up the computation process and, more specifically, the maximisation step (the computation of the worst case on the uncertain variables space) and the optimisation of the magnitude, which currently are the more expensive steps. Further developments on the CAM design involved the automation of the design stage, implementing AI techniques as reinforcement learning to automatically provide safe avoidance strategies from the encounter geometry or the objects' state vector and uncertainty.

The framework was proven to be able to ingest CDMs, yet, it is possible to improve the model further. One improvement would be implementing methods to ingest other protocols or, even better, raw observations, which are expected to be more available in the future with the appearance of new commercial observation product providers. Also, computational efficiency can be gained with faster optimisation implementation on the p-box computation. Alternatively, the proposed ML approach may be a fast option to skip the explicit computations required in this step. The current implementation assumes independence on the input variables. Thus, addressing the dependency among variables (i.e. covariance matrix elements) when building the Focal Element (FE) and computing the PoC will probably be a more precise and formal approach.

After validating the methodology on real data and proposing a classification criterion and a threshold tuning method, further analysis of the preferred values for these

quantities should be performed. This may include a statistical approach similar to the one carried out by operators to determine the value of the PoC on their missions, based on the number of estimated encounters and a trade-off between the avoided and accepted risk. However, this should require access to statistical models or real databases. Regarding databases, the validation on real scenarios showed the method effectiveness in providing conjunction assessment in high-risk, low-risk and uncertain events. However, events in this last category require further analysis to develop an automated method to discern the event typology regarding the uncertainty (that is, the shape of the *Pl* and *Bel* curves), to be able to differentiate cases possessing actual high-risk, low-risk or trends on the risk evolution. Very related to this are the results concerning the statistical analysis of the database of CDMs. The results indicated that the number of proposed CAMs were in line with the actual manoeuvres implemented. However, there is a considerably higher number of cases catalogued as uncertain (which potentially requires a CAM) than escalated events in the real operational situation. Further analysis is advised accounting for the operational restrictions taken into consideration in the real scenarios to discern whether the proposed method is too cautious or the current operational implementations based on the last CDM computes risk are too permissive.

The application of ML techniques for robust conjunction assessment was proven successful. Different techniques were applied to predict the best action to be taken by the operators under conjunction scenarios. These implementations were proposed as proof of concepts more than final proposals, including a search of hyperparameters and a comparison of techniques. In any case, a more formal and systematic approach should be taken to decide which is the best approach. Moreover, the best approach may be application-dependent, for example, an on-board system may require faster execution or even faster training times, while critical applications may be preferred to have higher reliability despite longer training and prediction times. An interesting aspect provided by ML models not exploited in this work is the probability of the prediction, that is, the relative probability distribution the system assigns to the possible outcome labels. While the final decision will require a single class to be provided, a better insight into the probability distribution of the prediction may anticipate complex scenarios,

like the different typologies of Uncertain events mentioned before. Bayesian Networks can contribute to the exploitation of this information. A fundamental aspect affecting the AI systems in this work is the lack of data. Conjunction databases are strongly imbalanced, making it harder to predict the minority class, which also represents the event of interest (collision or high-risk). The alternative of using synthetic or mixed databases has a lot of potential, as shown in this work, however, these data must be realistic to allow the system to extrapolate to real information, which is not always an easy task. Greater gains in performance may be obtained with a populated, balanced and quality database than with model complexity. Thus, more effort into building such datasets, both synthetic and from real missions, should be made. The results of this work can be taken as the first stage through an AI-based STM system. Thus, more techniques can be implemented to replace current tasks, like automated CAM design, or to reduce workload, like predicting new CDMs anticipating the risk assessment. Another aspect treated in this work involving AI is CASSANDRA. The complexity and variability of problems related to STM tasks require that its automation has to be carried out by a complex system. CASSANDRA represents the beginning of such an intelligent agent, but further developments are required. Currently, AI techniques have been applied to different modules. The aim is that in the future, the whole system will work autonomously, powered by an AI assistant that autonomously assigns tasks to the different modules according to the proposed problem and interacts with the operator to translate commands into instructions understood by the modules or interpret the outcomes provided by the system.

Finally, the framework proposed in the thesis, which is applied to operational STM, may be extended to address other space safety scenarios. The CASSANDRA agent presented in this thesis showed how the algorithms introduced in the thesis can be integrated with other methodologies to address more complex space safety problems. Similarly, this can be extended to other scenarios. On the one hand, the longer sustainability of the Earth's environment could be addressed by modifying the current pipeline to handle longer time intervals. The current implementation uses operational information (PoC, CDMs...) which refers to short periods. Thus, it would be required

to redefine the risk metrics, uncertainty quantification or inputs provided. On the other hand, the parallelism between STM and Earth protection could be exploited to provide an equivalent system to address the deflection of Near Earth Objects (e.g. CASSANDRA-4NEO). An AI-based decision support system inspired by the IDSS presented in this work could be used to provide the best decision to address an asteroid approximating the Earth, an equivalent CAM module would compute the optimal deflection strategies, MCDM techniques could be used to rank them according to the specific restrictions, and DSt can be used to model the expected lack of knowledge affecting most of the object or the deflector parameters, especially in the earlier stages. Finally, the proposed methodologies and applications were developed having in mind the ground segment part of the STM, but future satellites are likely to have a greater level of autonomy in their operation, especially those included in constellations with thousands of satellites. Improving the computational efficiency and guaranteeing the reliability of the AI models would allow the creation of a lighter version of CASSANDRA to be implemented onboard satellites for real-time conjunction analysis and avoidance.

Part III

Appendices

Appendix A

Dilution-free metrics

Currently, the most common metric used to evaluate the risk possessed by an encounter is the Probability of Collision (PoC). It is very popular among operators, especially under the fast encounters hypothesis, is easy to compute and only requires information on the relative position of the objects involved in the encounters and their covariance matrices. However, it suffers from the dilution of probability, a counterintuitive phenomenon that suggests a safer encounter when evaluating the conjunction with poorer data (bigger covariance matrix), as explained in Chapter 3. The root of this problem is the lack of a model for the epistemic uncertainty when computing the PoC [Balch et al., 2019]. However, note that if all the Conjunction Data Messages (CDMs) of a sequence falls in the dilution region, the evidence-based classification system proposed in the main body of the thesis would not be error-free.

Thus, a dilution-free metric should be used whose main characteristic is the non-decreasing phenomenon when increasing the size of the uncertain ellipsoid. [Balch, 2016] proposed two dilution-free metrics: the red and blue-Plausibility of Collision (rPloC, bPloC), explained below. This appendix shows a preliminary implementation of this kind of metrics on the robust evidence-based framework presented in the main body of the thesis. The further development of that approach, left for future work, would provide a robust dilution-free conjunction assessment modelling both aleatory and epistemic uncertainty.

A.1 Dilution of probability and epistemic uncertainty

The lack of a model for epistemic uncertainty in collision risk assessment lies behind the probability of dilution problem. In this thesis, the Dempster-Shafer theory of evidence was used to model this type of uncertainty, while other authors proposed different, yet equivalent approaches. For example, [Balch, 2016] proposed using Possibility theory and random-to-fuzzy transformations to avoid this problem.

According to this approach, Possibility theory's concepts of *Necessity* and *Possibility*, which he renamed *Plausibility* and *Confidence*, are employed to bound the possible values of PoC. In this sense, those concepts are equivalent to the Dempster-Shafer theory of Evidence (DSt)'s terms of *Plausibility* and *Belief* employed in the main body of this thesis. Similarly, the author in [Balch, 2016] uses the concept of possibility function, $r : \mathbb{R} \rightarrow [0, 1]$, from which to obtain the *Plausibility* and *Confidence* of a desired variable or set similarly as basic probability assignments (*bpas*) and Focal Element (FEs) are employed in DSt:

$$\begin{aligned} \text{Plaus}_X(A) &= \max \{r(x) : x \in A\} \\ \text{Conf}_X(A) &= 1 - \max \{r(x) : x \in A^C\} \end{aligned} \tag{A.1}$$

with $A \subset \Omega$ an event or set of values, Ω the set of all possible values, and A^C the complement of A .

Finally, the dilution-free metrics introduced in [Balch, 2016] employed the same concept of impact plane defined in Eq. (5.9), introducing additional rotations and transformations. Thus, the impact plane reference frame $\langle \xi, \eta, \zeta \rangle$ centred at the Hard Body Radius (HBR) is rotated to be aligned with the axes of the combined uncertainty ellipse, $\langle X', Y', Z' \rangle$ (Fig. A.1):

$$\begin{bmatrix} x' \\ y' \end{bmatrix} = \mathbf{R}^T \begin{bmatrix} \xi \\ \zeta \end{bmatrix} \tag{A.2}$$

with \mathbf{R}^T the rotation matrix with the normalised eigenvalues of combined covariance matrix projected in the impact plane, Σ . The resulting reference frame is then displaced

to be centred at the ellipse instead of the HBR, $\langle X'', Y'', Z'' \rangle$:

$$\begin{aligned} x'' &= x' - x'_0 \\ y'' &= y' - y'_0 \end{aligned} \quad (\text{A.3})$$

where (x'_0, y'_0) are the coordinates of the ellipse centre in the rotated reference frame.

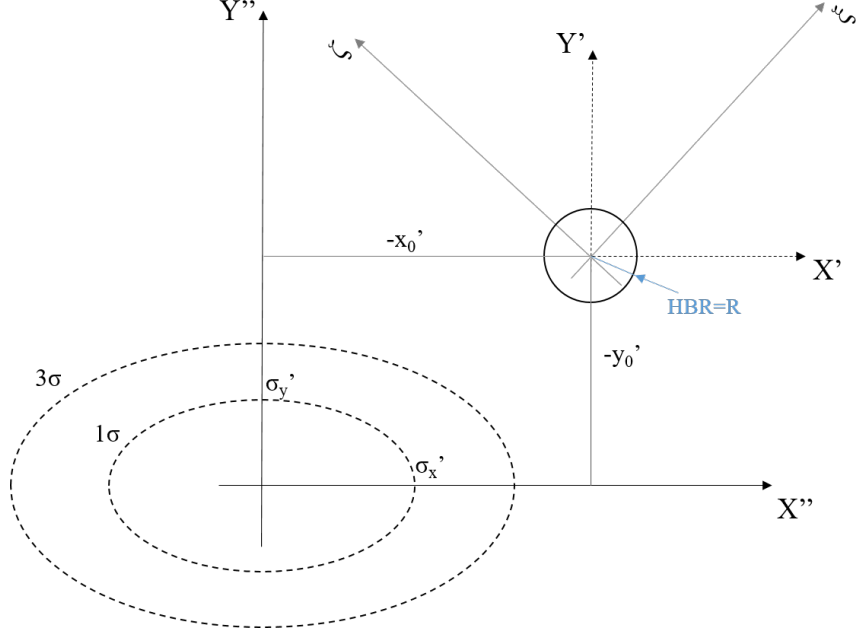


Figure A.1: Encounter geometry and different reference frames in the impact plane used to compute the PoC and the dilution-free metrics.

A.2 Red Plausibility of Collision

This metric is introduced in [Balch, 2016] as a non-decreasing metric to substitute the PoC in conjunction risk assessment. It is a likelihood-based approach applied in a normalised impact plane centred in the combined uncertain ellipse. In the normalised impact plane the reference frame axes, $\langle \Xi_1, \Xi_2 \rangle$, are aligned with the ellipse's axes and the ellipse becomes a circumference (Fig. A.2).

In this space, the HBR becomes an ellipse centred at $(x'_0/\sigma'_x, y'_0/\sigma'_y)$, whose semi-major axis is R/σ'_x and the semiminor axis $R\sigma'_y$, being parallel to $\langle \xi_1, \xi_2 \rangle$. R is

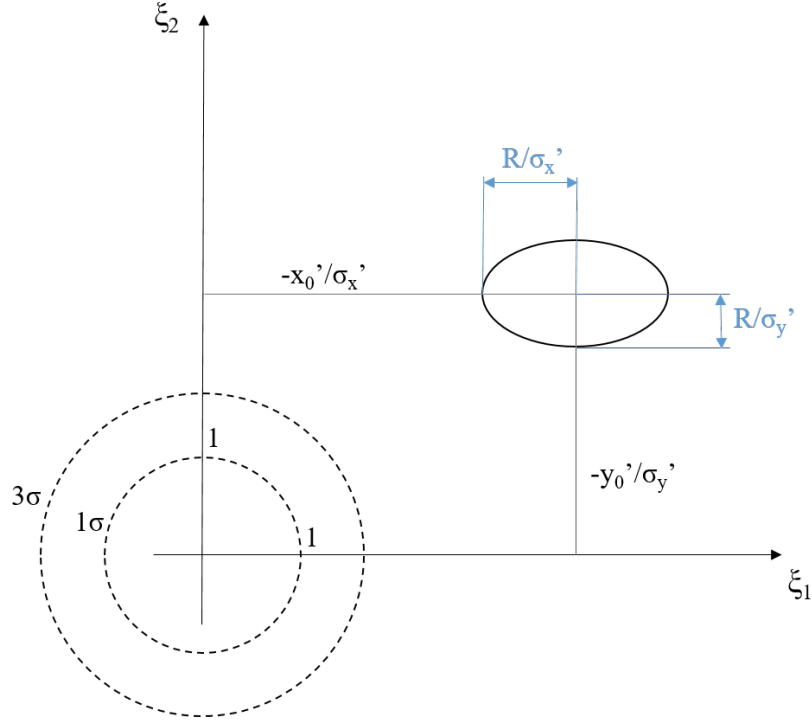


Figure A.2: Normalised reference frame in the impact plane used to compute the rPloC.

the size of the HBR, σ'_x and σ'_y are diagonal terms of covariance matrix expressed in $\langle X', Y' \rangle$.

The resulting metric results in:

$$rPloC = \max \left(r_{\Xi_1, \Xi_2}(\xi_1, \xi_2) : \left(\frac{\xi_1 + x'_0/\sigma'_x}{R/\sigma'_x} \right)^2 + \left(\frac{\xi_2 + y'_0/\sigma'_y}{R/\sigma'_y} \right)^2 \leq 1 \right) = e^{(-\frac{1}{2}\hat{\rho}^2)} \quad (\text{A.4})$$

where $\hat{\rho}$ is the smallest distance from the centre of the normalised ellipse to the ellipse-shaped HBR, and $r_{\Xi_1, \Xi_2}(\xi_1, \xi_2) = e^{\frac{1}{2}(\xi_1^2 + \xi_2^2)}$ is the possibility function that indicates the probability of randomly drawn a less likely point in the plane than the pair under inspection (ξ_1, ξ_2) .

This metric grows asymptotically to one when uncertainty increases ($\hat{\rho}$ tends to zero) and it values one ($rPloC = 1$) if the ellipse covers the centre of the HBR. This approach would be the expected behaviour of a metric indicating the risk of a collision when the event is driven by a lack of knowledge of the provided information: the poorer

the quality of the information, the greater the plausibility of a collision happening due to accurate knowledge of the event. However, from the point of view of the classification system and confidence quantification proposed in the main body of the thesis, this approach leads to over-conservative results (with respect to PoC [Balch, 2016]) as soon as some pieces of information fall in the dilution region or all the pieces of information are not coherent among each other (creating FEs with elements falling in the dilution region), making it difficult to extract useful outcome for the operators.

A.3 Blue Plausibility of Collision

This Blue Plausibility of Collision also presents a dilution-free asymptotic value, tending to the maximum value of the PoC (for a given miss distance and HBR), instead of the more conservative value of one of the red Plausibility of Collision. This metric presents closer values to the PoC when not in the dilution region, making it easier to relate with approaches based on this more common metric.

The Blue Plausibility of Collision uses the Cumulative Distribution Function (CDF) of the distance, $F_{\Delta}(d)$ with $d = \sqrt{x'^2 + y'^2}$, to build the possibility function (Fig. A.3):

$$r_{\Delta}(d) = \begin{cases} F_{\Delta}(d)/F_{\Delta}(D), & \text{if } d \leq D \\ (1 - F_{\Delta}(d))/(1 - F_{\Delta}(D)), & \text{if } d > D \end{cases} \quad (\text{A.5})$$

where D is the distance between the centre of the HBR and the centre of the ellipse and R is the size of the HBR. From here, the bPloC is defined as:

$$bPloC = \max(r_{\Delta}(d) : d \leq R) = \begin{cases} \frac{F_{\Delta}(R)}{F_{\Delta}(D)}, & \text{if } R \leq D \\ 1, & \text{if } R > D \end{cases} \quad (\text{A.6})$$

A.4 Comparison of metrics

In the next figures, the behaviour of the dilution-free metrics presented in the appendix is compared with the PoC.

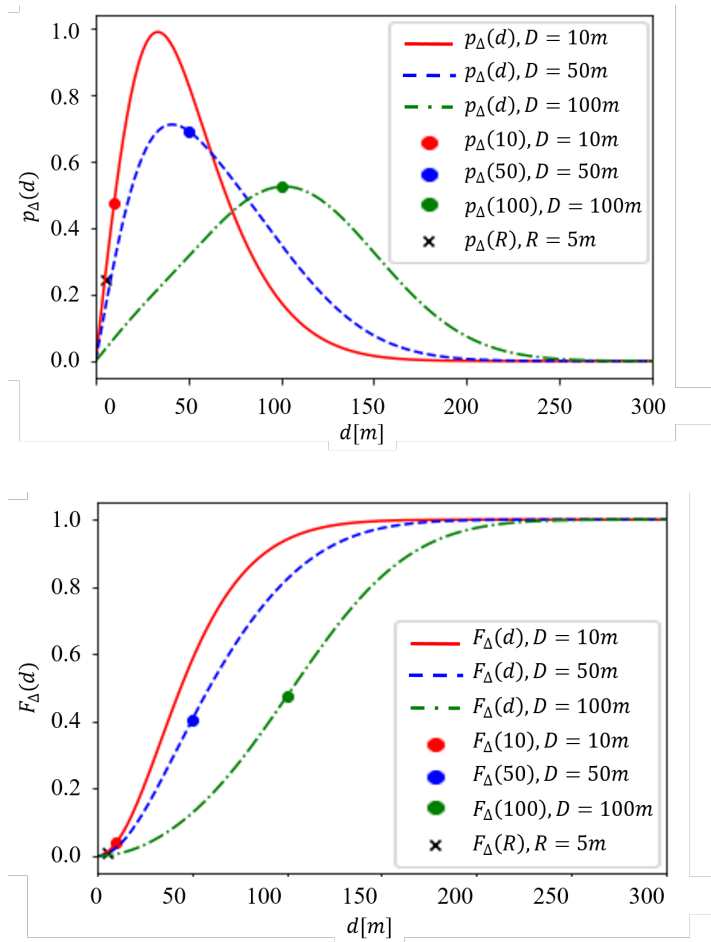


Figure A.3: Distance distribution for different values of the miss distance. (a) pdf, (b) CDF.

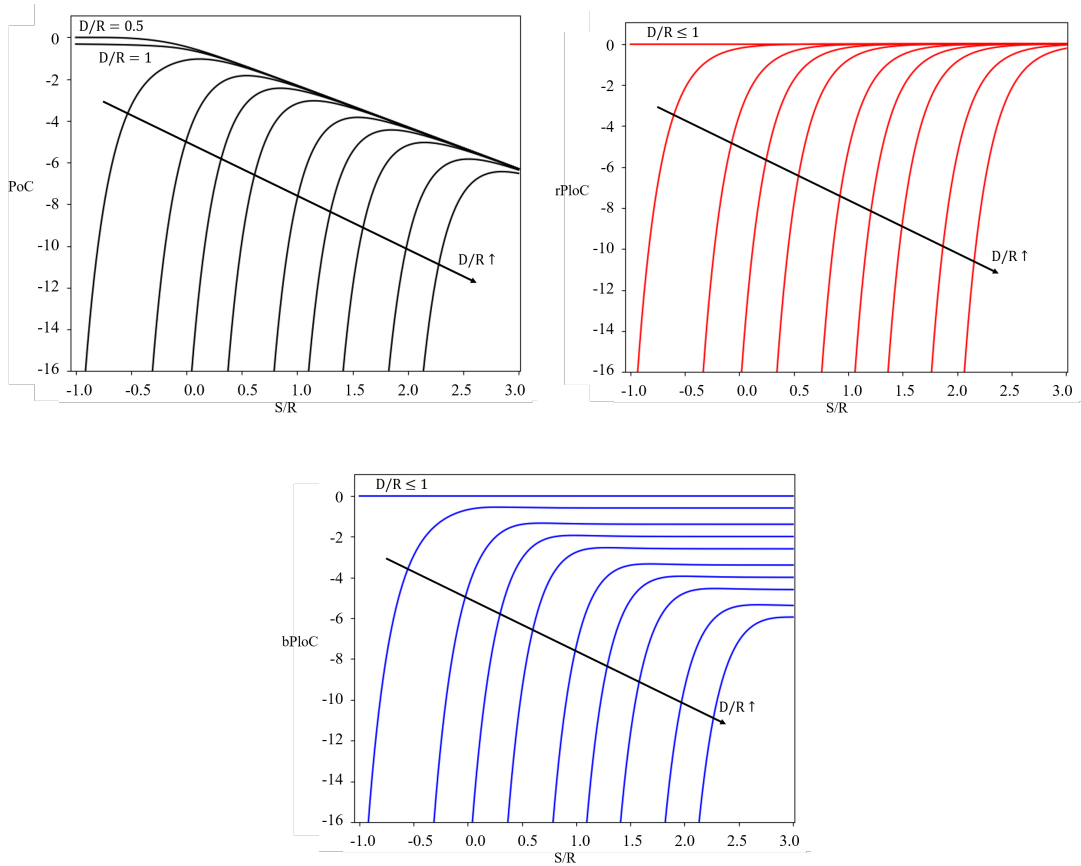


Figure A.4: Evolution of the conjunction assessment metrics with the covariance matrix for different values of the covariance matrix (with $\sigma'_x = \sigma'_y$). (a) Probability of collision, with dilution region, (b) Dilution-free Red Plausibility of Collision, (c) Dilution-free Blue Plausibility of Collision.

Fig. A.4 show the evolution of the rPloC and the bPloC as a function of S/R (the ratio between the ellipse size and the HBR), which measures the quality of the information, for different values of D/R (the ratio of the miss distance over the HBR), which indicates the proximity of the objects ($D/R < 1$ indicates the relative position is smaller than the combined size of the objects). It can be seen that for $D/R < 1$, both metrics equal one, no matter the covariance matrix. For $D > R$, both functions present an increasing behaviour, asymptotically increasing with the covariance matrix to one for the rPloC, and to the maximum PoC for the bPloC. Both metrics are free of dilution, with the red metric showing a more conservative approach.

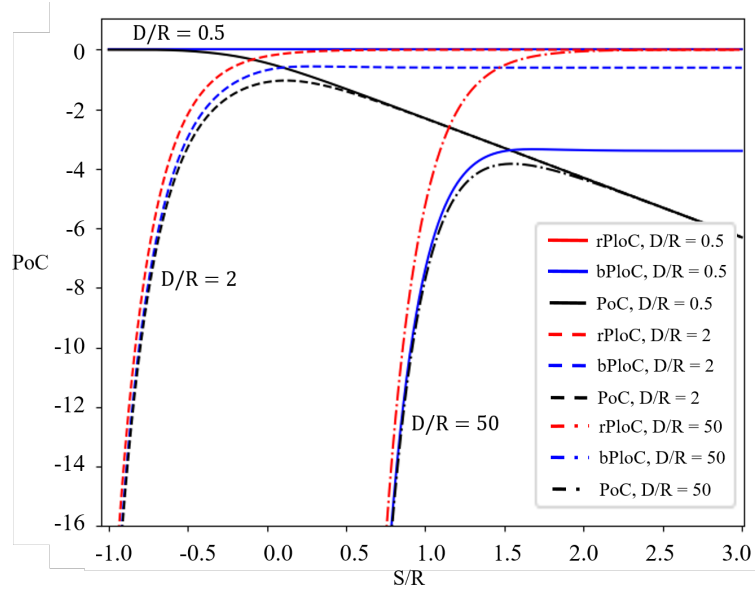


Figure A.5: Comparison of the evolution with the covariance matrix for different values of the covariance matrix (with $\sigma'_x = \sigma'_y$) of the PoC (black) with the free-dilution metrics (rPloC in red and bPloC in blue).

Fig. A.5 shows the behaviour of those metrics with the size of the covariance compared with the evolution of the PoC for different values of the miss distance. It can be seen how the bPloC shows a closer behaviour to the PoC than the rPloC, which increases more quickly towards one when entering the dilution region.

A.5 Introduction to dilution-free robust conjunction assessment

Finally, these metrics can be applied to the robust evidence-based framework proposed in the main text of the thesis. When accounting for both aleatory and epistemic uncertainty in the state of the objects involved in space conjunction, the uncertain encounter geometry would provide sets of ellipses from where a set of FEs can be obtained. In the same way, the minimum and maximum value of the PoC on each FE allowed to build the Plausibility (*Pl*) and Belief (*Bel*) curves in Chapter 3, the minimum and maximum rPloC and bPloC on each FE can be obtained to obtain dilution-free *Pl* and *Bel* curves.

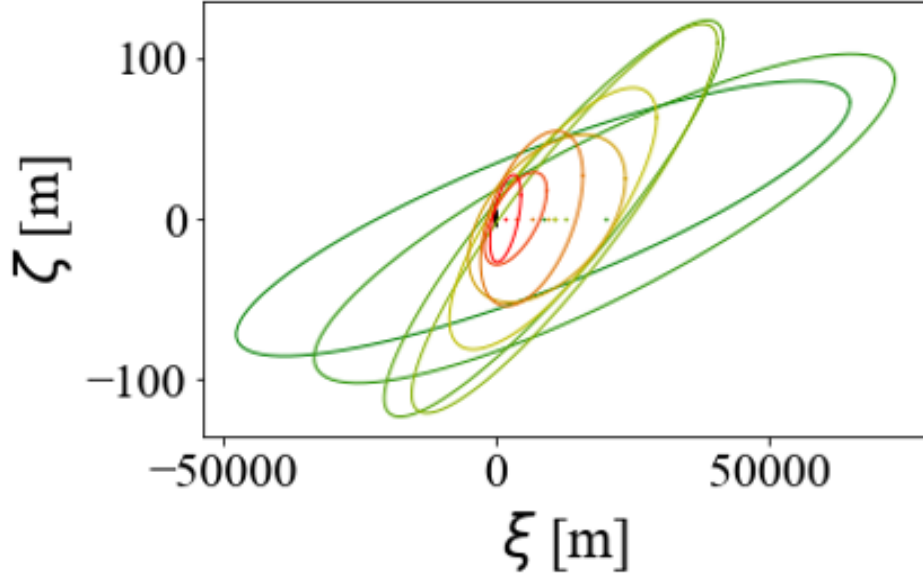


Figure A.6: Uncertain geometry of the encounter use to compute the Pl and Bel of the dilution-free metrics.

Fig. A.6 shows the uncertain geometry used to compute the Pl and Bel curves in Fig. A.6. In this last figure, the confidence curves are obtained for the three metrics considered in the appendix: the PoC, as in the rest of the thesis, and the rPloC and bPloC. The three cases show a high degree of uncertainty due to the disparity in the uncertain ellipses from the sequence of CDMs. But more interesting are the differences in the shape and values of the curves. The PoC present a low value of Bel and a higher value of Pl up to 10^{-4} , when it experiences a sharp drop. The Pl of the rPloC, however, remains high up to values $rPloC \sim 1$ to one and the Bel is greater than zero for $rPloC < 0.1$, indicating some of the ellipses, or some of the possible ellipses from the FEs, fall in the dilution region. Being an interesting piece of information, due to its great sensitivity to dilution, it does not allow extracting more detailed information to indicate the operator how to react. Finally, the curves for the bPloC are more similar to those of the PoC, which shows the less conservative approach towards dilution of this metric. There are two important differences concerning the PoC behaviour. First, the values at which the Pl falls are slightly bigger, especially after the small step at $Pl \sim 0.65$, which indicates some of the ellipses are close but to the right of the dilution

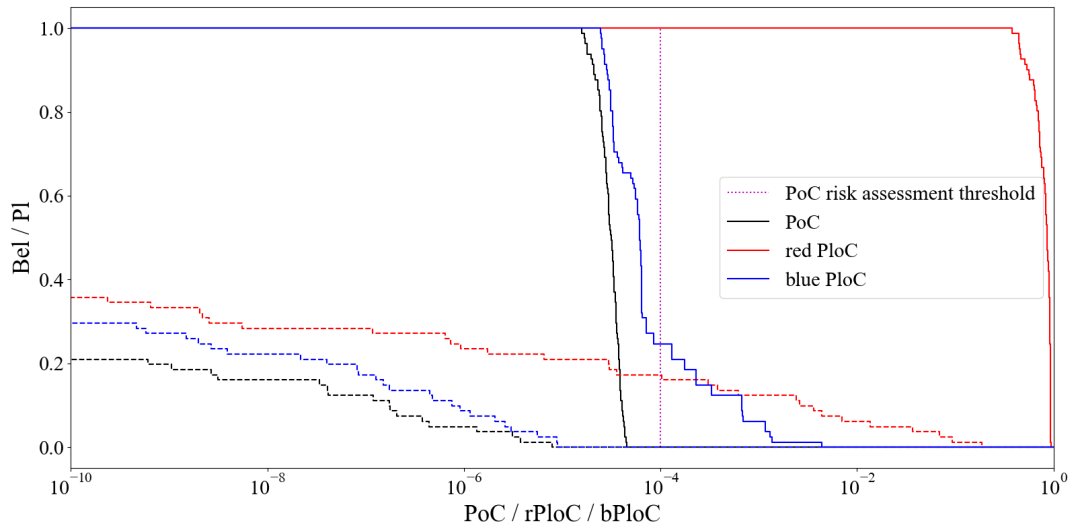


Figure A.7: Plausibility and Belief curves for PoC (black), red PloC (red) and blue PloC (blue).

region (see Fig. A.5 to see the comparative behaviour of PoC and bPloC). Second, the Pl curves present a tail that grows to values of $bPloC \sim 10^{-2}$, which suggests that part of the ellipses fall in the dilution region.

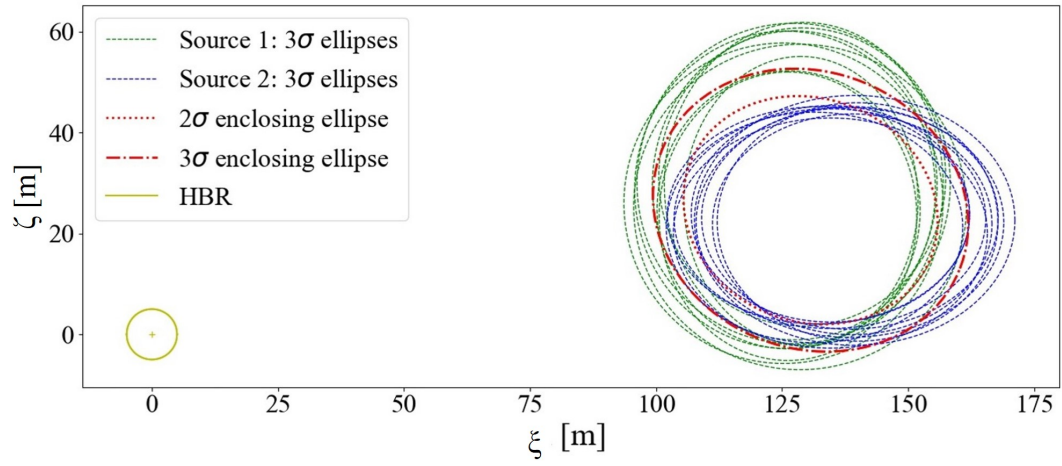
Further analyses are encouraged to implement the bPloC as a dilution-free metric within the robust evidence-based classification criteria introduced in the main body of the thesis.

Appendix B

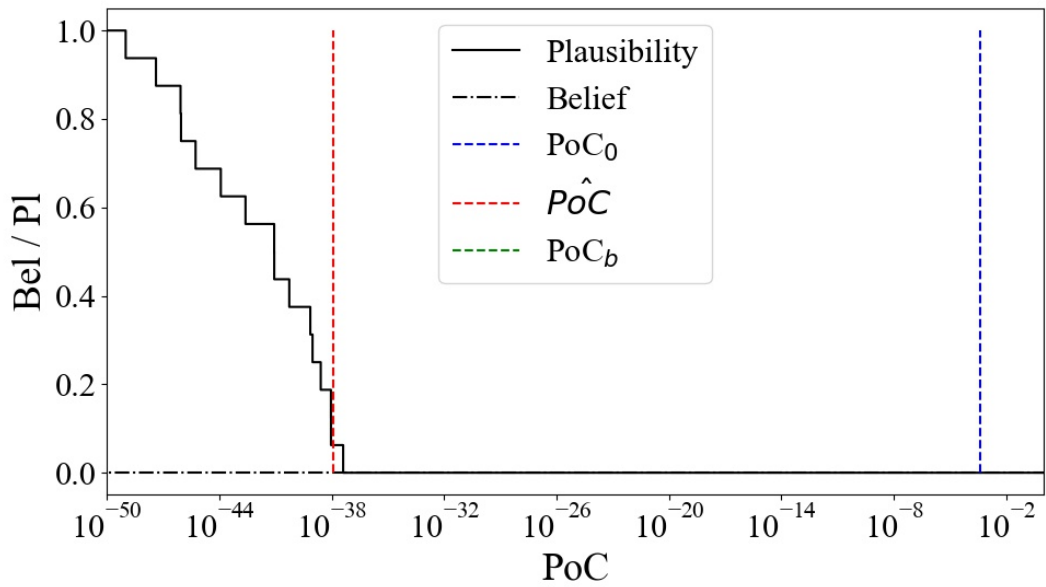
Geometries for conjunction classes

Figs. B.1 to B.4 shows representative examples of conjunction events for each of the families of geometries described in Table 3.4, but the set *Geo. 1*, which is shown in Fig. 3.8.

Tables B.1 to B.3 detail the outcome shown in Figs. 3.9 to 3.11, respectively, where the Evidence-based criteria presented in Tables 3.3, 3.6 and 3.7 (Criterion 1, Criterion 2 and Criterion 3, respectively) are compared with a purely Probabilistic classification criterion. The results are broken down by geometry families.

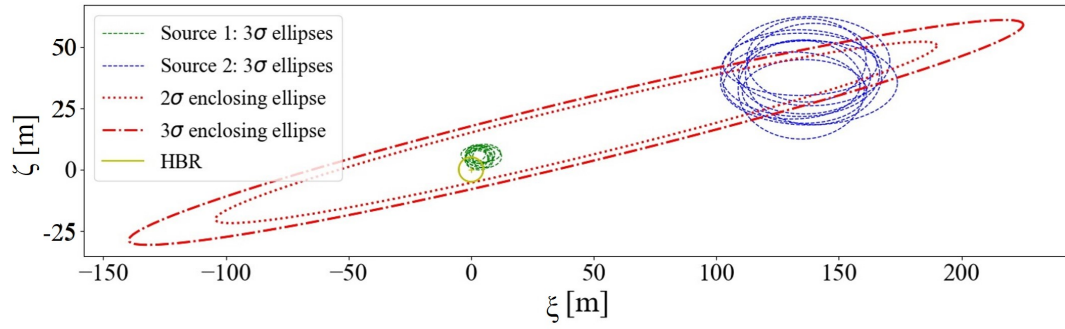


(a)

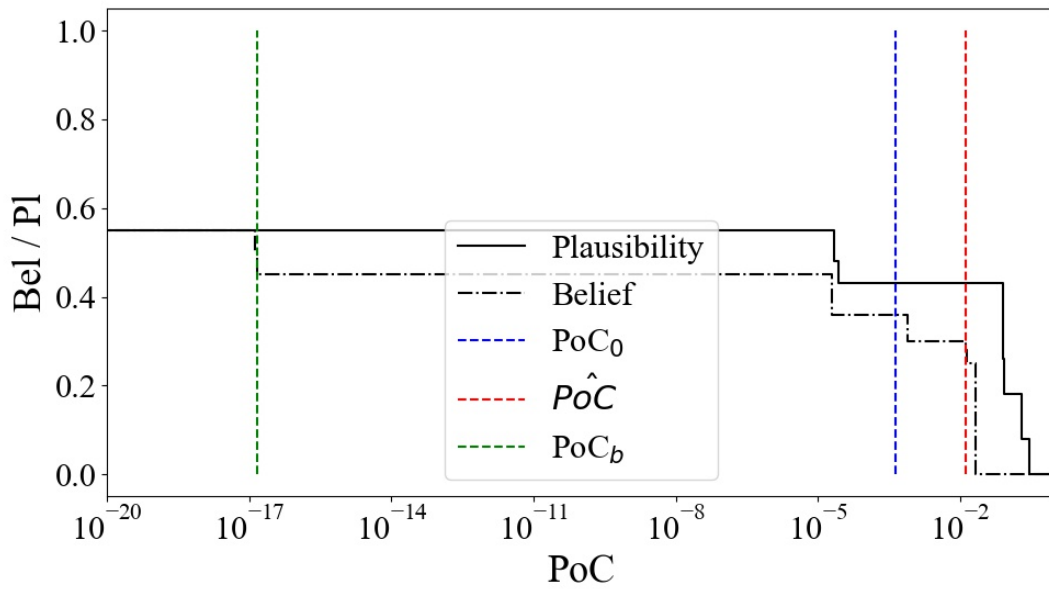


(b)

Figure B.1: Representative scenario of a single case of *Geo. 2*: (a) encounter geometry, (b) the associated *Bel* and *Pl* curves.

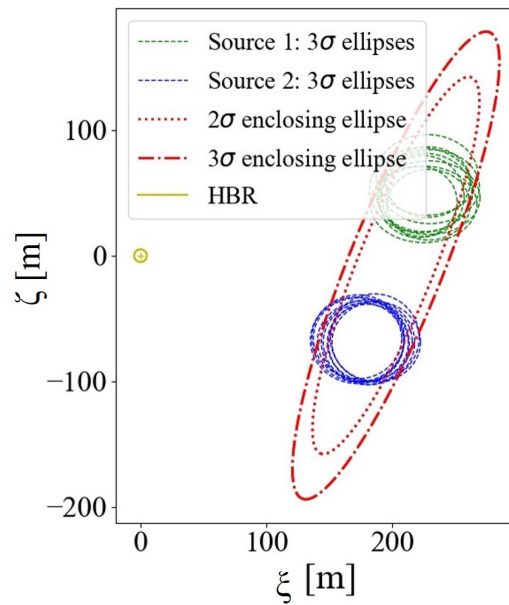


(a)

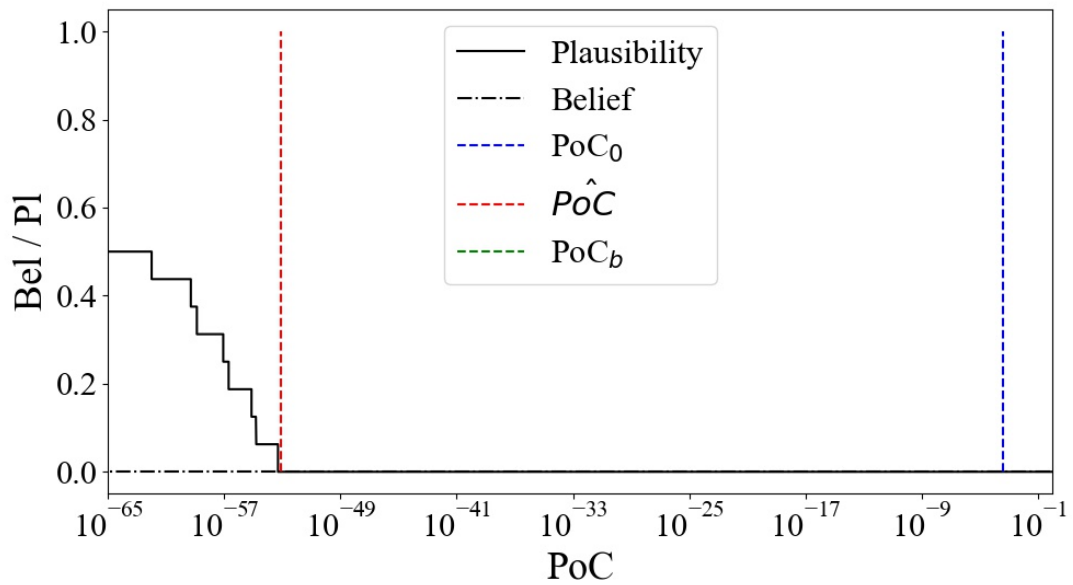


(b)

Figure B.2: Representative scenario of a single case of *Geo. 3*: (a) encounter geometry, (b) the associated *Bel* and *Pl* curves.

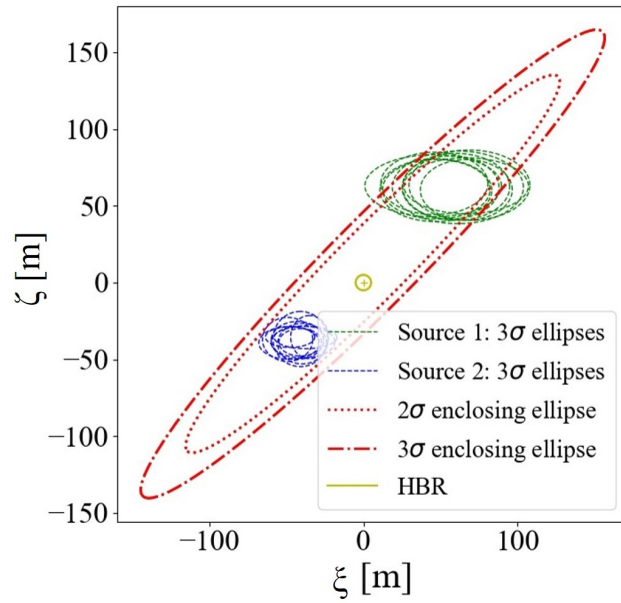


(a)

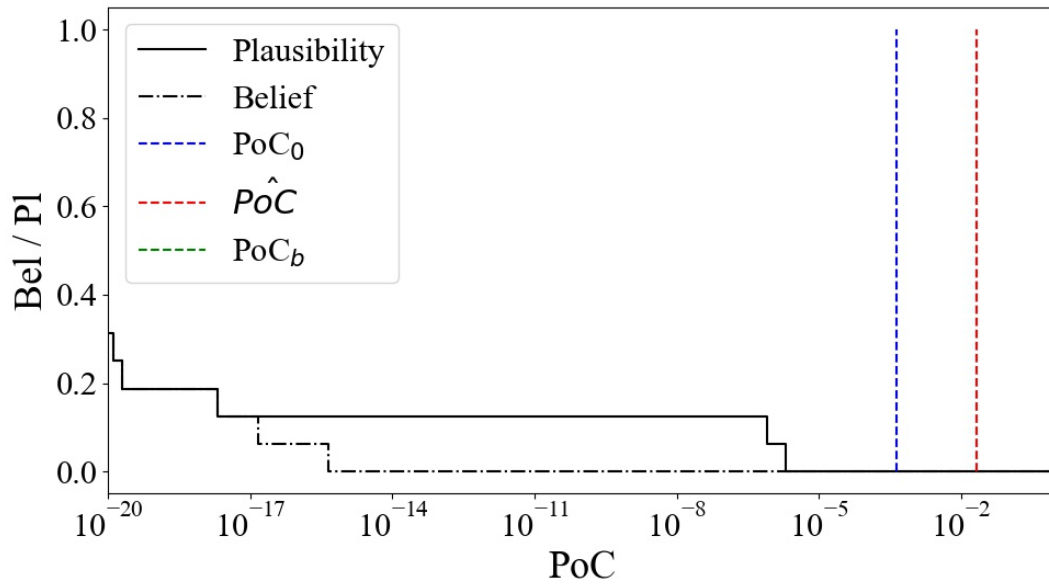


(b)

Figure B.3: Representative scenario of a single case of *Geo. 4*: (a) encounter geometry, (b) the associated *Bel* and *Pl* curves.



(a)



(b)

Figure B.4: Representative scenario of a single case of *Geo. 5*: (a) encounter geometry, (b) the associated *Bel* and *Pl* curves.

Table B.1: Classification distribution (in percentage) by sets using a criterion based only on PoC value and using E-b Criterion 1.

Set	Number samples	$P\hat{o}C$ based		Evidence based		
		Col. %	NoCol. %	HR %	LR %	NtKn. %
Total	3000	47.2	52.8	2.8	5.8	91.4
Geo. 1	600	96.3	3.7	0.0	0.0	100
Geo. 2	600	0.0	100	0.0	21.8	78.2
Geo. 3	600	66.7	33.3	14.0	0.0	86.0
Geo. 4	600	0.0	100	0.0	7.3	92.7
Geo. 5	600	72.8	27.2	0.0	0.0	100

Table B.2: Classification distribution (in percentage) by sets using a criterion based only on PoC value and using E-b Criterion 2.

Set	Number samples	$P\hat{o}C$ based		Evidence based		
		Col. %	NoCol. %	HR %	LR %	NtKn. %
Total	3000	47.2	52.8	11.1	75.7	13.1
Geo. 1	600	96.3	3.7	39.5	10.3	50.2
Geo. 2	600	0.0	100	0.0	100	0.0
Geo. 3	600	66.7	33.3	16.2	68.3	15.5
Geo. 4	600	0.0	100	0.0	100	0.0
Geo. 5	600	72.8	27.2	0.0	100	0.0

Table B.3: Classification distribution (in percentage) by sets using a criterion based only on PoC value and using E-b Criterion 3.

Set	Number samples	$P\hat{o}C$ based		Evidence based				
		Col. %	NoCol. %	C1 %	C2 %	C3 %	C4 %	C5 %
Total	9000	47.2	52.8	8.1	7.4	8.8	25.2	50.5
Geo. 1	1800	96.3	3.7	29.9	23.6	34.4	3.4	6.9
Geo. 2	1800	0.0	100	0.0	0.0	0.0	33.3	66.7
Geo. 3	1800	66.7	33.3	10.6	10.8	10.3	22.7	45.6
Geo. 4	1800	0.0	100	0.0	0.0	0.0	33.3	66.7
Geo. 5	1800	72.8	27.2	0.0	0.0	0.0	33.3	66.7

Appendix C

Algorithms for robust optimal collision avoidance manoeuvres

This appendix includes the algorithms required to compute the robust optimal Conjunction Avoidance Manoeuvre (CAM), both in the impulsive and in the Low-Thrust (LT) scenarios.

C.1 Min-max impulsive optimisation algorithm

This section includes the algorithm to compute the impulsive robust optimal manoeuvre under aleatory and epistemic uncertainty under a constant magnitude of the impulse, δv_0 .

Algorithm C.1: Impulsive for robust optimal CAM with constant magnitude.

```

1 Initialise  $\epsilon_{PoC}, \Delta PoC, \delta v_{max}$ 
2  $\mathbf{S} = \mathbf{I}$ 
3 for  $fe \in FE$  do
4      $\mathbf{u}_{fe} = \arg \max_{\mathbf{u} \in \Upsilon_{fe}} (PoC)$ 
5      $\mathbf{S} = \mathbf{S} + \Sigma_{fe}^{-1}$ 
6 end
7 Compute  $PoC_1$  with Eq. (3.1)
8 while  $\Delta PoC > \epsilon_{PoC}$  do
9      $\mathcal{T} = \mathbf{Q}\mathbf{T}^T\mathbf{S}\mathbf{T}\mathbf{Q}$ 
10    Compute  $\delta \mathbf{v}_{opt}$  with Eq. (5.17)
11    Compute deflection  $\delta \mathbf{x}_b$  with Eq. (5.1)
12     $\mathbf{S} = \mathbf{I}$ 
13    for  $fe \in FE$  do
14        Add  $\delta \mathbf{x}_b$  to the Focal Element (FE) limits on b parameter components:
15         $\underline{\mathbf{u}}_{fe} = \underline{\mathbf{u}}_{fe} + [\delta x_b(1), \delta x_b(3), 0, 0, 0]$ 
16         $\overline{\mathbf{u}}_{fe} = \overline{\mathbf{u}}_{fe} + [\delta x_b(1), \delta x_b(3), 0, 0, 0]$ 
17         $\mathbf{u}_{fe} = \arg \max_{\mathbf{u} \in \Upsilon_{fe}} (PoC; \delta \mathbf{x}_b)$ 
18         $\mathbf{S} = \mathbf{S} + \Sigma_{fe}^{-1}$ 
19    end
20    Compute  $PoC$  with Eq. (3.1)
21     $\Delta PoC = abs(PoC - PoC_1)$ 
22     $PoC_1 = PoC$ 
23 end
    
```

C.2 Min-max impulsive magnitude optimisation algorithm

This section includes the algorithm to compute the impulsive robust optimal manoeuvre with optimal impulse magnitude to reduce the Probability of Collision (PoC) under a desired threshold, PoC_0 .

Algorithm C.2: Impulsive robust optimal CAM with optimised magnitude.

```

1 Initialise  $\epsilon_{PoC}, \Delta PoC, \delta v_{step}$ 
2  $\mathbf{S} = \mathbf{I}$ 
3 for  $fe \in FE$  do
4      $\mathbf{u}_{fe} = \arg \max_{\mathbf{u} \in \Upsilon_{fe}} (PoC)$ 
5      $\mathbf{S} = \mathbf{S} + \mathbf{\Sigma}_{fe}^{-1}$ 
6 end
7 Compute  $PoC_1$  with Eq. (3.1)
8 while  $\Delta PoC > \epsilon_{PoC}$  do
9      $\mathcal{T} = \mathbf{Q}\mathbf{T}^T\mathbf{S}\mathbf{T}\mathbf{Q}$ 
10    Compute  $\mathbf{d}_{opt}$  with Eq. (5.17)
11     $\delta v_{opt} = \delta v_{max}$ 
12    Compute  $PoC$  with Eq. (3.1)
13    while  $PoC < PoC_0$  do
14         $\delta \mathbf{v}_{opt} = \delta v_{opt} \mathbf{d}_{opt}$ 
15        Compute deflection  $\delta \mathbf{x}_b$  with Eq. (5.1)
16         $\mathbf{S} = \mathbf{I}$ 
17        for  $fe \in FE$  do
18            Add  $\delta \mathbf{x}_b$  to the FE limits on b parameter components:
19             $\underline{\mathbf{u}}_{fe} = \underline{\mathbf{u}}_{fe} + [\delta x_b(1), \delta x_b(3), 0, 0, 0]$ 
20             $\bar{\mathbf{u}}_{fe} = \bar{\mathbf{u}}_{fe} + [\delta x_b(1), \delta x_b(3), 0, 0, 0]$ 
21             $\mathbf{u}_{fe} = \arg \max_{\mathbf{u} \in \Upsilon_{fe}} (PoC; \delta \mathbf{x}_b)$ 
22             $\mathbf{S} = \mathbf{S} + \mathbf{\Sigma}_{fe}^{-1}$ 
23        end
24        Compute  $PoC$  with Eq. (3.1)
25         $\delta v_{opt} = \delta v_{opt} - \delta v_{step}$ 
26    end
27     $\Delta PoC = \text{abs}(PoC - PoC_1)$ 
28     $PoC_1 = PoC$ 
29 end

```

C.3 Low-thrust collision avoidance manoeuvre optimisation

In this section, the algorithm to compute the robust optimal avoidance manoeuvre in the LT scenario is presented.

Algorithm C.3: LT robust optimal CAM.

```

1  Initialise  $\delta v_{max}, \varepsilon_{max}, \theta_m$ 
2  Stage 1: Optimal direction, acceleration magnitude and arc-length:
3       $\delta v_{opt} = \delta v_{max}$ 
4       $\mathbf{d}_{opt} |_{\theta_m}$ , using Algorithm C.1
5       $\Delta\theta_m = 2(\theta_c - \theta_m)$ 
6       $\theta_{mf} = \theta_c$ 
7       $\theta_{m0} = \theta_{mf} - \Delta\theta_m$ 
8       $\Delta t_b = f_1(\Delta\theta_m, \theta_m, \theta_c)$ 
9       $\varepsilon_{opt} = \varepsilon_{max}$ 
10 Stage 2: Deflection at b-plane,  $\delta\mathbf{x}_b$ :
11     Propagate modified orbit to Time of Closest Approach (TCA):
12     if  $\theta_{mf} = \theta_c$  then
13     |     Use Fable with  $\varepsilon_{opt}$  and  $\mathbf{d}_{opt}$  from  $\theta_{m0}$  to  $\theta_c$ 
14     | else
15     |     Use Fable with  $\varepsilon_{opt}$  and  $\mathbf{d}_{opt}$  from  $\theta_{m0}$  to  $\theta_{mf}$ 
16     |     Propagate coast-arc ( $\varepsilon = 0$ ) from  $\theta_{mf}$  to  $\theta_c$ 
17     | end
18     Compute deflection:
19     Project state on b-plane
20     Nominal miss distance after CAM:  $\mathbf{r}_{e_{LT}}$ 
21      $\delta\mathbf{x}_b = \mathbf{r}_{e_{LT}} - \mathbf{r}_{e_0}$ 
22 Stage 3: Worst-case scenario after CAM:
23      $\mathbf{u}_{WC_{LT}} = \mathbf{u}_{WC} + [\delta x_b(1), \delta x_b(3), 0, 0, 0]$ 

```

C.3.1 propellant saving optimisation: acceleration reduction

The following algorithm includes the variant to compute the robust optimal LT CAM, optimising the propellant consumption by minimising the magnitude of the acceleration.

Algorithm C.4: LT robust optimal CAM. propellant saving via min. acceleration.

```

1 Initialise  $\delta v_{max}, \varepsilon_{max}, \delta\varepsilon, \theta_m, PoC_0$ 
2 Call Algorithm C.3
3 if  $PoC < PoC_0$  then
4     while  $PoC < PoC_0$  and  $\varepsilon_{opt} > 0$  do
5          $\varepsilon_{opt} = \varepsilon_{opt} - \delta\varepsilon$ 
6         Call Stage 2 and Stage 3 of Algorithm C.3
7         Compute  $PoC = f(\varepsilon_{opt}, \mathbf{u}_{WC_{LT}}, \mathbf{d}_{opt}, \Delta\theta_m)$ 
8     end
9 end
    
```

C.3.2 propellant saving optimisation: burning-time reduction

The following algorithm includes the variant to compute the robust optimal LT CAM, minimising the burning-time to optimise the propellant consumption.

Algorithm C.5: LT robust optimal CAM. propellant saving via min. burning-time.

```

1 Initialise  $\delta v_{max}, \varepsilon_{max}, \delta\theta, \theta_m, PoC_0$ 
2 Call Algorithm C.3
3 if  $PoC < PoC_0$  then
4     while  $PoC < PoC_0$  and  $\varepsilon_{opt} > 0$  do
5          $\theta_{m0} = \theta_{m0} + \delta\theta$ 
6          $\theta_{mf} = \theta_{mf} - \delta\theta$ 
7          $\Delta\theta_m = \theta_{mf} - \theta_{m0}$ 
8         Call Stage 2 and Stage 3 of Algorithm C.3
9         Compute  $PoC = f(\varepsilon_{opt}, \mathbf{u}_{WC_{LT}}, \mathbf{d}_{opt}, \Delta\theta_m)$ 
10    end
11 end
    
```

Appendix D

Machine learning hyperparameters

Table D.1 shows the hyperparameters chosen for the best model of each technique on each of the four training scenarios detailed in Section 8.1.

Table D.2 includes the hyperparameters for the Artificial Neural Network (ANN) and the Random Forest (RF) best models for the case in Section 8.2.

Finally, Table D.3 shows the hyperparameters of the best models for the different techniques used in Section 8.3, both training in the synthetic and in one of the real databases.

Table D.1: Hyperparameters of the best model of each technique on each of the four training scenarios in Section 8.1.

ANN				
	System 1		System 2	
	DB₁₁	DB₂₁	DB₁₁	DB₂₁
Number of neurons in hidden layer	100	100	50	100
RF				
	System 1		System 2	
	DB₁₁	DB₂₁	DB₁₁	DB₂₁
Number of trees	50	100	200	400
Maximum depth of tress	'None'	'None'	'None'	'None'
Min. number samples at leaf node	1	1	1	1
Min. number samples to split node	20	2	2	2
Number features when looking for best split	'auto'	'auto'	'auto'	'auto'
KNN				
	System 1		System 2	
	DB₁₁	DB₂₁	DB₁₁	DB₂₁
Number of neighbors	1	1	20	20
Weight function	'uniform'	'uniform'	'uniform'	'uniform'
Leaf size	30	30	30	30
SVM				
	System 1		System 2	
	DB₁₁	DB₂₁	DB₁₁	DB₂₁
Decision function of shape	'ovo'	'ovo'	'ovo'	'ovo'

Table D.2: Hyperparameters of the best model of each technique on the example in Section 8.2.

ANN	
Number of neurons in hidden layer	100
RF	
Number of trees	100
Maximum depth of tress	'None'
Min. number samples at leaf node	1
Min. number samples to split node	2
Number features when looking for best split	'auto'

Table D.3: Hyperparameters of the best model of each technique trained on the synthetic and in the real databases in Section 8.3.

RF with intervals		
	Trained in Synthetics DB	Trained in Real DB
n_estimators	200	50
max_depth	'None'	'None'
min_samples_split	2	2
min_samples_leaf	1	1
max_features	0.5	0.5
RF with CDMs		
	Trained in Synthetics DB	Trained in Real DB
n_estimators	200	50
max_depth	'None'	50
min_samples_split	2	2
min_samples_leaf	10^{-7}	10^{-7}
max_features	0.5	0.5
Lag step	3	0
LGBm with CDMs		
	Trained in Synthetics DB	Trained in Real DB
n_estimators	10	5
max_depth	7	2
subsample	0.7	0.1
colsample_bytree	0.8	0.8
boosting_type	'rf'	'gbdt'
Lag step	4	1
Autoregressive LGBm		
	Trained in Synthetics DB	Trained in Real DB
n_estimators	10	10
max_depth	7	2
subsample	0.7	0.7
colsample_bytree	0.8	0.8
boosting_type	'gbdt'	'gbdt'
Lag step	1	2
Transformers		
	Trained in Synthetics DB	Trained in Real DB
depth	2	1
attn_dropout	0.1	0.2
res_dropout	0.3	0.2
wd	0.1	0.1
n_epochs	25	25

Bibliography

- [Abay et al., 2017] Abay, R., Brown, M., Boyce, R., and Karacor, A. (2017). Open Source Collision Avoidance Maneuver Planning Tool. In *68th International Astronautical Conference (IAC)*. Adelaide, Australia. Paper number: IAC-17,A6,7,3,x38098.
- [Acciarini et al., 2021] Acciarini, G., Pinto, F., Letizia, F., Martínez-Heras, J. A., Merz, K., Bridges, C. P., and Güneş Baydin, A. (2021). Kessler: a machine learning library for spacecraft collision avoidance. In *8th European Conference on Space Debris*. ESA/ESOC, Darmstadt, Germany.
- [Acciarini et al., 2020] Acciarini, G., Pinto, F., Metz, S., Boufelja, S., Kaczmarek, S., Merz, K., Martinez-Heras, J. A., Letizia, F., Brdiges, C., and Baydin, A. G. (2020). Spacecraft collision risk assessment with probabilistic Programming.
- [Aglietti et al., 2019] Aglietti, G. S., Taylor, B., Fellowes, S., Tye, D., Cox, C., Zarkesh, A., Mafficini, A., Vinkoff, N., Bashford, K., Salmon, T., Retat, I., Burgess, C., Hall, A., Chabot, T., Kanani, K., Pisseloup, A., Bernal, C., Chaumette, F., Pollini, A., and Steyn, W. H. (2019). RemoveDEBRIS: An in-orbit demonstration of technologies for the removal of space debris. *The Aeronautical Journal*, 124(1271):1–23. DOI: <https://doi.org/10.1017/aer.2019.136>.
- [Águeda Maté et al., 2021] Águeda Maté, A., Filotico, C., Alves, J., Zamora, D., Hrozensky, T., Pradal, R., Molina Valencia, M. J., Schildknecht, T., Piguet, L., Berend, N., Picard, Y., Reina, A., Smith, L. J., Siemssen, E., O’Donnel, S., Torres, R., Pate, S., Elson, A., Achilleas, P., and Molina Cobos, M. A. (2021). Eustm: European steps towards space traffic management. In *72nd International Astronautical Congress (IAC)*. Dubai, EAU.

- [Ailor et al., 2017] Ailor, W., Peterson, G., Womack, J., and Youngs, M. (2017). Effect of large constellations on lifetime of satellites in low earth orbits. *Journal of Space Safety Engineering*, 4(3-4):117–123. DOI: <https://doi.org/10.1016/j.jsse.2017.11.003>.
- [Airbus, 2021] Airbus (2021). CIMON-2 makes its successful debut on the ISS. <https://www.airbus.com/en/newsroom/press-releases/2020-04-cimon-2-makes-its-successful-debut-on-the-iss>.
- [Alfano, 2005a] Alfano, S. (2005a). A numerical implementation of spherical object collision probability. *Journal of the Astronautical Sciences*, 53:103–109. DOI: <https://doi.org/10.1007/BF03546397>.
- [Alfano, 2005b] Alfano, S. (2005b). Relating position uncertainty to maximum conjunction probability. *Journal of the Astronautical Sciences*, 53:193–205. DOI: <https://doi.org/10.1007/BF03546350>.
- [Alfano, 2007] Alfano, S. (2007). Review of conjunction probability methods for short-term encounters. *Advances in the Astronautical Sciences*, 127:719–746.
- [Alfano and Oltrogge, 2018] Alfano, S. and Oltrogge, D. (2018). Probability of collision: valuation, variability, visualization, and validity. *Acta Astronautica*, 148:301–316. DOI: <https://doi.org/10.1016/j.actaastro.2018.04.023>.
- [Alfriend et al., 1999] Alfriend, K. T., Akella, M. R., Frisbee, J., Foster, J. L., Lee, D. K., and Wilkins, M. (1999). Probability of collision error analysis. *Space Debris*, 1:21–35. DOI: <https://doi.org/10.1023/A:1010056509803>.
- [Arias et al., 2023] Arias, E., Sáez, D., Rubio, J., Escobar, D., González, O., and Pérez, C. (2023). Collision risk estimation in multi-event scenarios. In *74th International Astronautical Congress (IAC)*. Baku, Azerbaijan.
- [Aristoff et al., 2014] Aristoff, J. M., Horwood, J. T., Singh, N., and Poore, A. B. (2014). Nonlinear uncertainty propagation in orbital elements and transformation

- to Cartesian space without loss of realism. In *AAS/AIAA Astrodynamics Specialist Conference. San Diego, CA, US. 4-7 August*. San Diego, CA, US.
- [Augustin, 2005] Augustin, T. (2005). Generalized basic probability assignments. *International Journal of General Systems*, 34(4):451–463. DOI: <https://doi.org/10.1080/03081070500190839>.
- [Ayala Fernández et al., 2021] Ayala Fernández, L., Radtke, J., and Stoll, E. (2021). Impact of collision avoidance manoeuvres on large satellite constellations. In *8th European Conference on Space Debris*. ESA/ESOC, Darmstadt, Germany.
- [Aytekin, 2021] Aytekin, A. (2021). Comparative analysis of normalization techniques in the context of MCDM problems. *Decision Making: Applications in Management and Engineering*, 4(2):1–27. DOI: <https://doi.org/10.31181/dmame210402001a>.
- [Balch, 2016] Balch, M. (2016). A Corrector for probability dilution in satellite conjunction analysis. In *18th AIAA Non-Deterministic Approaches Conference*. San Diego, California, US.
- [Balch et al., 2019] Balch, M., Martin, R., and Ferson, S. (2019). Satellite conjunction analysis and the false confidence theorem. *Proceedings of the Royal Society A: Mathematical, Physical and Engineering Sciences*, 475(20180565). DOI: <https://doi.org/10.1098/rspa.2018.0565>.
- [Barhydt and Krishnamurthy, 2004] Barhydt, R. and Krishnamurthy, K. (2004). Design of a multi-mode flight deck decision support system for airborne conflict management. In *International Conference on Human Computer Interaction in Aeronautics*. Toulouse, France.
- [Bast and Krag, 2019] Bast, D. and Krag, H. (2019). Emergency command path for space traffic management. *Journal of Space Safety Engineering*, 6(2):138–144. DOI: <https://doi.org/10.1016/j.jsse.2019.05.005>.
- [Bastida Virgili et al., 2016a] Bastida Virgili, B., Dolado, J. C., Lewis, H., Radtke, H., Krag, H., Revelin, B., Cazaux, C., Colombo, C., Crowther, R., and Metz, K. (2016a).

- Risk to space sustainability from large constellations of satellites. *Acta Astronautica*, 126:154–162.
- [Bastida Virgili et al., 2019] Bastida Virgili, B., Flohrer, T., Krag, H., Merz, K., and Lemmens, S. (2019). CREAM — ESA’s proposal for Collision Risk Estimation and Automated Mitigation. In *1st International Orbital Debris Conference*. Sugar Land, Texas, US. Paper number: 6031.
- [Bastida Virgili and Krag, 2015] Bastida Virgili, B. and Krag, H. (2015). Small satellites and the future space debris environment. In *30th International Symposium on Space Technology and Science (ISTS)*. Kobe, Japan.
- [Bastida Virgili et al., 2016b] Bastida Virgili, B., Krag, H., Lewis, H., Radtke, J., and Rossi, A. (2016b). Mega-constellations, small satellites and their impact on the space debris environment. In *67th International Astronautical Congress (IAC)*. Guadalajara, Mexico.
- [Bennett et al., 2015] Bennett, J. C., Sang, J., Smith, C., and Zhang, K. (2015). An analysis of very short-arc orbit determination for low-Earth objects using sparse optical and laser tracking data. *Advances in Space Research*, 55(2):617–629. DOI: <https://doi.org/10.1016/j.asr.2014.10.020>.
- [Berleant, 1998] Berleant, D. (1998). A software tool for automatically verified operations on intervals and probability distributions. *Reliable Computing*, 4:71–82. DOI: <https://doi.org/10.1023/A:1009954817673>.
- [Bernelli-Zazzera et al., 2012] Bernelli-Zazzera, F., Lavagna, M., Armellin, R., Di Lizia, P., and Morselli, A. (2012). Trajectory Optimisation under Uncertainties. Technical report, European Space Agency.
- [Berquand et al., 2021] Berquand, A., Darm, P., and Riccardi, A. (2021). SpaceTransformers: language modeling for space systems. *EEE Access*, 9:133111–133122. DOI: <https://doi.org/10.1109/ACCESS.2021.3115659>.

- [Berquand and Ladeira, 2022] Berquand, A. and Ladeira, A. V. (2022). From mission description to knowledge graph: applying transformer-based models to map knowledge from publicly available satellite datasets. In *10th International Systems & Concurrent Engineering for Space Applications (SECESA)*. Noordwijk. The Netherlands.
- [Berquand and Riccardi, 2020] Berquand, A. and Riccardi, A. (2020). From engineering models to knowledge graph: delivering new insights into models. In *9th International Systems & Concurrent Engineering for Space Applications (SECESA)*. Digital Event.
- [Bishop, 2006] Bishop, C. M. (2006). *Pattern Recognition and Machine Learning*. Springer, New York, NY, 1 edition. ISBN: 978-0-387-31073-2.
- [Bombardelli and Hernando-Ayuso, 2015] Bombardelli, C. and Hernando-Ayuso, J. (2015). Optimal impulsive collision avoidance in Low Earth Orbit. *Journal of Guidance, Control and Dynamics*, 38(2):217–225. DOI: <https://doi.org/10.2514/1.G000742>.
- [Bonnal et al., 2020] Bonnal, C., McKnight, D., Phipps, C., Dupont, C., Missonnier, S., Lequette, L., Merle, M., and Rommelaere, S. (2020). Just in time collision avoidance – A review. *Acta Astronautica*, 170:637–651. DOI: <https://doi.org/10.1016/j.actaastro.2020.02.016>.
- [Botta et al., 2020] Botta, E., Miles, C., and Sharf, I. (2020). Simulation and tension control of a tether-actuated closing mechanism for net-based capture of space debris. *Acta Astronautica*, 174:247–358. DOI: <https://doi.org/10.1016/j.actaastro.2020.04.052>.
- [Braun et al., 2016] Braun, V., Flohrer, T., Krag, H., Merz, K., Lemmens, S., Bastida Virgili, B., and Funke, Q. (2016). Operational support to collision avoidance activities by ESA’s space debris office. *CEAS Space Journal*, 8(3):177–189. DOI: <https://doi.org/10.1007/s12567-016-0119-3>.
- [Breiman, 2001] Breiman, L. (2001). Random forest. *Machine Learning*, 45:5–32. DOI: <https://doi.org/10.1023/A:1010933404324>.

- [Briesboek et al., 2021] Briesboek, R., Aziz, S., Wolahan, A., Cipolla, S., Richard-Noca, M., and Piguet, L. (2021). The Clearspace-1 mission: ESA and Clearspace team up to remove debris. In *8th European Conference on Space Debris*. ESA/ESOC, Darmstadt, Germany.
- [Brown et al., 2020] Brown, T., Mann, B., Ryder, N., Subbiah, M., Kaplan, J., Dhariwal, P., Neelakantan, A., Shyam, P., Sastry, G., Askell, A., Agarwal, S., Herbert-Voss, A., Kruege, G., Henighan, T., Child, R., Ramesh, A., Ziegler, D., Wu, J., Winter, C., C. H., Chen, M., Sigler, E., Litwin, M., Gray, S., Chess, B., Clark, J., Berner, C., McCandlish, S., Radford, A., Sutskever, I., and Amodei, D. (2020). Language models are few-shot learners. DOI: <https://doi.org/10.48550/arXiv.2005.14165>.
- [Caldas et al., 2023] Caldas, F., Soares, C., Nunes, C., and Guimarães, M. (2023). Conjunction Data Messages for space collision behave as a Poisson process. In *31st European Signal Processing Conference (EUSIPCO)*. Helsinki, Finland.
- [Cano et al., 2023] Cano, A., Pastor, A., Escobar, D., Míguez, J., and Sanjurjo-Rivo, M. (2023). Covariance determination for improving uncertainty realism in orbit determination and propagation. *Advances in Space Research. Space Environment Management and Space Sustainability*, 72(7):2759–2777. DOI: <https://doi.org/10.1016/j.asr.2022.08.001>.
- [Carpenter, 2019] Carpenter, J. R. (2019). Covariance realism is not enough. In *AAS/AIAA Astrodynamics Specialist Conference*. Portland, Maine, US.
- [Carpenter et al., 2017] Carpenter, J. R., Salvatore, A., Hall, D. T., Hejduk, M. D., Gaebler, J. A., Jah, M. K., Hassan, S. O., Besser, R. L., DeHart, R. R., Duncan, M. G., Herron, M. S., and Guit, W. J. (2017). Relevance of the American Statistical Society’s Warning on P-Values for Conjunction Assessment. In *AAS/AIAA Astrodynamics Specialist Conference*. Stevenson, Wyoming, US.
- [CCSDS, 2013] CCSDS (2013). Recommendation for Space Data System Standards. Conjunction Data Message. Recommended Standard, Consultative Committee for

- Space Data Systems, Washington, DC, USA. <https://public.ccsds.org/Pubs/508x0b1e2s.pdf>.
- [Celestrack, 2022] Celestrack (2022). NORAD Two-Line Element Set Format. <https://celestrak.org/NORAD/documentation/tle-fmt.php>.
- [Celestrak, 2019] Celestrak (2019). Socrates - satellite orbital conjunction reports assessing threatening encounters in space. <http://celestrak.com/SOCRATES>.
- [Celletti et al., 2021] Celletti, A., Pucacco, G., and Vartolomei, T. (2021). Reconnecting groups of space debris to their parent body through proper elements. *Scientific Reports*, 11(22676). DOI: <https://doi.org/10.1038/s41598-021-02010-x>.
- [Chakraborty and Yeh, 2007] Chakraborty, S. and Yeh, C. H. (2007). A simulation based comparative study of normalization procedures in multiattribute decision making. In *6th WSEAS International Conference on Artificial Intelligence, Knowledge Engineering and Data Bases*. Corfu, Greece. DOI: <https://dl.acm.org/doi/10.5555/1348485.1348504>.
- [Chakraborty and Yeh, 2009] Chakraborty, S. and Yeh, C. H. (2009). A simulation comparison of normalization procedures for TOPSIS. In *2009 International Conference on Computers & Industrial Engineering*, pages 1815–1820. DOI: <https://doi.org/10.1109/ICCIE.2009.5223811>.
- [Chan, 1997] Chan, F. K. (1997). Collision probability analyses for Earth—orbiting satellite. *Advances in the Astronautical Sciences*, 96:1033–1048.
- [Chan, 2003a] Chan, F. K. (2003a). Improved analytical expressions for computing spacecraft collision probabilities. In *13th AAS/AIAA Space Flight Mechanics Meeting*. Ponce, Puerto Rico.
- [Chan, 2003b] Chan, F. K. (2003b). Spacecraft collision probability for long-term encounters. In *AAS/AIAA Astrodynamics Specialist Conference*. Big Sky, Montana, US.

- [Chan, 2008] Chan, F. K. (2008). *Spacecraft collision probability*. The Aerospace Press, El Segundo. ISBN: 978-1-884989-18-6.
- [Chojnacki et al., 2007] Chojnacki, E., Baccou, J., and Destercke, D. (2007). Numerical sensitivity and efficiency in the treatment of epistemic and aleatory uncertainty. In *5th International Conference on Sensitivity Analysis of Model Output*. Budapest, Hungary. DOI: <https://doi.org/10.48550/arXiv.0712.2141>.
- [Contant-Jorgenson et al., 2006] Contant-Jorgenson, C., Lála, P., and Schrogl, K. U. (2006). *Cosmic study on Space Traffic Management*. International Academy of Astronautics, BP 1268-16. F-75766 Paris Cedex 16, France. ISBN: 2-9516787-5-4.
- [Coppola, 2017] Coppola, V. T. (2017). Including velocity uncertainty in the probability of collision between space objects. *American Astronautical Society*, 247.
- [Cortes and Vladimir, 1995] Cortes, C. and Vladimir, N. (1995). Support-vector networks. *Machine Learning*, 20(3):273–297. DOI: <https://doi.org/10.1007/BF00994018>.
- [Cover and Hart, 1967] Cover, T. M. and Hart, P. E. (1967). Nearest neighbor pattern classification. *IEEE Transactions on Information Theory*, 13(1):21–27. DOI: <https://doi.org/10.1109/TIT.1967.1053964>.
- [Cybenko, 1989] Cybenko, G. (1989). Approximation by superpositions of a sigmoidal function. *Mathematics of Control, Signals and Systems*, 2:303–314. DOI: <https://doi.org/10.1007/BF02551274>.
- [da Graça Marto et al., 2023] da Graça Marto, S., Díaz Riofrío, S., Ilioudis, C., Clemente, C., and Vasile, M. (2023). Satellite manoeuvre detection with multi-static radar. *Journal of the Astronautical Sciences*, 70(36). DOI: <https://doi.org/10.1007/s40295-023-00399-3>.
- [Darm et al., 2022] Darm, P., Berquand, A., Mansilla, L., and Riccardi, A. (2022). A system engineering recommendation system based on language similarity analysis: an application to space systems conceptual design. In *10th International Systems &*

- Concurrent Engineering for Space Applications (SECESA)*. Noordwijk. The Netherlands.
- [Darm et al., 2023] Darm, P., Miceli-Barone, A. V., Cohen, S. B., and Riccardi, A. (2023). Knowledge base question answering for space debris queries. *arXiv*. DOI: <https://doi.org/10.48550/arXiv.2305.19734>.
- [De Vittori et al., 2022] De Vittori, A., Palermo, M. F., Di Lizia, P., and Armellin, R. (2022). Low-Thrust collision avoidance maneuver optimization. *Journal of Guidance, Control, and Dynamics*, 45(10):1815–1829. DOI: <https://doi.org/10.2514/1.G006630>.
- [Delande et al., 2018] Delande, E., Houssineau, J., and Jah, M. (2018). A New Representation of uncertainty for data fusion in SSA Detection and Tracking Problems. In *2018 21st International Conference on Information Fusion (FUSION)*. Cambridge, United Kingdom. DOI: <https://doi.org/10.23919/ICIF.2018.8455540>.
- [Delmas et al., 2023] Delmas, F., Perez, C., and Nunes, P. (2023). Future evolutions of eusst collision avoidance service. *Journal of Space Safety Engineering*, In press. DOI: <https://doi.org/10.1016/j.jsse.2023.11.002>.
- [DeMars et al., 2011] DeMars, K. J., Bishop, R. H., and Jah, M. K. (2011). A splitting Gaussian mixture method for the propagation of uncertainty in orbital mechanics. In *21st AAS/AIAA Space Flight Mechanics Meeting*. New Orleans, Louisiana, US.
- [Dempster, 1967] Dempster, A. P. (1967). Upper and lower probabilities induced by a multivalued mapping. *Journal of Mathematics and Statistics*, 38(2):325–339. DOI: <https://doi.org/10.1214/aoms/1177698950>.
- [Destercke et al., 2008] Destercke, S., Dubois, D., and Chojnacki, E. (2008). Unifying practical uncertainty representations – I: Generalized p-boxes. *International Journal of Approximate Reasoning*, 49(3):649–663. DOI: <https://doi.org/10.1016/j.ijar.2008.07.003>.

- [Di Carlo et al., 2018] Di Carlo, M., Romero Martin, J. M., and Vasile, M. (2018). CAMELOT - Computational-Analytical Multi-fidelity Low-thrust Optimisation Toolbox. *CEAS Space Journal*, 10:25–36. DOI: <https://doi.org/10.1007/s12567-017-0172-6>.
- [di Carlo et al., 2019] di Carlo, M., Vasile, M., Greco, C., and Epenoy, R. (2019). Robust optimisation of low-thrust interplanetary transfers using evidence theory. In *29th AAS/AIAA Space Flight Mechanics Meeting*. Ka’anapali, HI, US.
- [Dorelli et al., 2022] Dorelli, J. C., Bard, C., Chen, T. Y., Da Silva, D., Guides dos Santos, L. F., Ireland, J., Kirk, M., McGranaghan, R., Narock, A., Nieves-Chinchilla, T., Samara, M., Sarantos, M., Shuck, P., and Thompson, B. (2022). Deep learning for space weather prediction: bridging the gap between heliophysics data and theory. *arXiv*. DOI: <https://doi.org/10.48550/ARXIV.2212.13328>.
- [Dosovitskiy et al., 2020] Dosovitskiy, A., Beyer, L., Kolesnikov, A., Weissenborn, D., Zhai, X., Unterthiner, T., Dehghani, M., Minderer, M., Heigold, G., Gelly, S., Uszkoreit, J., and Houlsby, N. (2020). An image is worth 16x16 words: Transformers for image recognition at scale. *arXiv*. DOI: <https://doi.org/10.48550/arXiv.2010.11929>.
- [Downes et al., 2020] Downes, L. M., Steiner, T. J., and How, J. P. (2020). Lunar terrain relative navigation using a convolutional neural network for visual crater detection. In *2020 American Control Conference (ACC)*. Denver, Colorado, US. DOI: <https://doi.org/10.23919/ACC45564.2020.9147595>.
- [Drummond et al., 2007] Drummond, O., Ogle, T., and Waugh, S. (Sep 2007). Metrics for evaluating track covariance consistency. *Proceeding of Signal and Data Processing of Small Targets 2007*. 669916. DOI: <https://doi.org/10.1117/12.740303>.
- [Dubois, 2006] Dubois, D. (2006). Possibility theory and statistical reasoning. *Computational Statistics & Data Analysis*, 51(1):47–69. DOI: <https://doi.org/10.1016/j.csda.2006.04.015>.

- [Dubois and Prade, 1986] Dubois, D. and Prade, H. (1986). A set-theoretic view on belief functions: logical operations and approximations by fuzzy sets. *International Journal of General Systems*, 12:193–226. DOI: <https://doi.org/10.1080/03081078608934937>.
- [Dubois and Prade, 1988] Dubois, D. and Prade, H. (1988). *Possibility theory*. Plenum Press, New York, US. DOI: https://doi.org/10.1007/978-1-4614-1800-9_139.
- [Dubois and Prade, 1992] Dubois, D. and Prade, H. (1992). *Reliability Data Collection and Analysis*, chapter On the combination of evidence in various mathematical frameworks, pages 213–241. Springer, Brussels.
- [Duncan et al., 2011] Duncan, M., Wysack, J., and Wainwright, B. (2011). Optimal collision avoidance for multiple conjunction events. In *AAS-AIAA Conference*. Greenwood, Alaska, US.
- [Dvoretzky et al., 1956] Dvoretzky, A., Kiefer, J., and Wolfowitz, J. (1956). Asymptotic minimax character of the sample distribution function and of the classical multinomial estimator. *Annals of Mathematical Statistics*, 27(3):642–669. DOI: <https://doi.org/10.1214/aoms/1177728174>.
- [Díaz Riofrío et al., 2021] Díaz Riofrío, S., Ilioudis, C., Clemente, C., and Vasile, M. (2021). Multiple observation integration approach for sisar imaging radar systems with the purpose of space surveillance. In *21st International Radar Symposium (IRS)*. Berlin, Germany.
- [ESA, 2020] ESA (2020). Swarm - earth online. <https://earth.esa.int/eogateway/missions/swarm>.
- [ESA, 2023a] ESA (2023a). ESA Space Debris Mitigation Compliance Verification Guidelines. Technical report, ESA Space Debris Mitigation WG. DOI: <https://sdup.esoc.esa.int/documents/download/ESSB-HB-U-002-Issue214February2023.pdf>.

- [ESA, 2023b] ESA (2023b). ESA's Annual Space Environment Report. Technical report, European Space Agency - Space Debris Office, ESA/ESOC. Reference: GEN-DB-LOG-00288-OPS-SD. https://www.sdo.esoc.esa.int/environment_report/Space_Environment_Report_latest.pdf.
- [ESA's Advanced Concepts Team, 2023] ESA's Advanced Concepts Team (2023). Kelvins - ESA's Advanced Concepts Competition Webpage. <https://kelvins.esa.int>.
- [Esquilo, 1986] Esquilo (1986). Agamenón. In Galiano, M. F. and Morales, B. P., editors, *Tragedias. Biblioteca Clásica Gredos (97)*, pages 421–422. Editorial Gredos, Madrid. ISBN: 84-249-1046-X.
- [European Space Agency, 2019] European Space Agency (2019). Kelvins 'Collision Avoidance' Challenge. <https://kelvins.esa.int/collision-avoidance-challenge/home>.
- [European Space Agency, 2020] European Space Agency (2020). Kelvins 'Spot the GEO satellites' Challenge. <https://kelvins.esa.int/spot-the-geo-satellites>.
- [European Space Agency, 2021a] European Space Agency (2021a). Kelvins 'Pose estimation' Challenge. <https://kelvins.esa.int/pose-estimation-2021>.
- [European Space Agency, 2021b] European Space Agency (2021b). Kelvins 'Space debris: the origin' Challenge. <https://kelvins.esa.int/space-debris-the-origin>.
- [European Space Agency, 2021c] European Space Agency (2021c). Space Debris: Frequently asked questions. https://www.esa.int/Space_Safety/Space_Debris/FAQ_Frequently_asked_questions.
- [European Space Agency, 2022] European Space Agency (2022). Database and information system characterising objects in space. <https://discosweb.esoc.esa.int>.

- [EvalAI and ARCLab - Massachusetts Institute of Technology, 2023] EvalAI and ARCLab - Massachusetts Institute of Technology (2023). MIT ARCLab Prize for AI Innovation in Space 2024. <https://eval.ai/web/challenges/challenge-page/2164/overview>.
- [Falchi et al., 2017] Falchi, A., Renato, V., Minisci, M., and Vasile, M. (2017). FOSTRAD: an advanced open source tool for re-entry analysis. In *15th Reinventing Space Conference*. Glasgow, United Kingdom.
- [Faucher et al., 2020] Faucher, P., Peldszuz, R., and Gravier, A. (2020). Operational space surveillance and tracking in europe. *Journal of Space Safety Engineering*, 7(3):420–425. DOI: <https://doi.org/10.1016/j.jsse.2020.07.005>.
- [Fawaz et al., 2020] Fawaz, H. I., Lucas, B., Forestier, G., Pelletier, C., Schmidt, D. F., Weber, J., Webb, G. I., Idoumghar, L., Muller, P., and Petitjean, F. (2020). InceptionTime: finding AlexNet for time series classification. *Data Mining and Knowledge Discovery*, 34(6):1936–1962. DOI: <https://doi.org/10.1007/s10618-020-00710-y>.
- [Federal Communications licensing website, 2023] Federal Communications licensing website (2023). https://licensing.fcc.gov/cgi-bin/ws.exe/prod/ib/forms/reports/swr031b.hts?q_set=V_SITE_ANTENNA_FREQ.file_numberC/File+Number/%3D/SESSTAINTR201601453&prepare=&column=V_SITE_ANTENNA_FREQ.file_numberC/File+Number.
- [Ferson et al., 2003] Ferson, S., Kreinovich, V., Ginzburg, L., Sentz, K., and Myers, D. S. (2003). Constructing probability boxes and Dempster-Shafer structures. Technical report, Sandia National Lab., Albuquerque, NM, United States. DOI: <https://doi.org/10.2172/809606>.
- [Ferson et al., 2007] Ferson, S., Kreinovich, V., Hajagos, J., Oberkampf, W., and Ginzburg, L. (2007). *Experimental uncertainty estimation and statistics for data having interval uncertainty*, chapter Chapter 4. Descriptive statistics for interval data.

- Princeton University Press, Sandia National Laboratories (SNL), Albuquerque, NM, and Livermore, CA (United States). DOI: <https://doi.org/10.2172/910198>.
- [Ferson et al., 2004] Ferson, S., Nelsen, R. B., Hajagos, J., Berleant, D. J., Zhang, J., Troy Tucker, W., Ginzburg, L. R., and Oberkampf, W. L. (2004). Dependence in probabilistic modeling, Dempster-Shafer theory, and probability bounds analysis. Technical report, Sandia National Lab., United States. DOI: <https://doi.org/10.2172/919189>.
- [Filippi and Vasile, 2019] Filippi, G. and Vasile, M. (2019). A memetic approach to the solution of constrained min-max problems. In *IEEE Congress on Evolutionary Computation*. Wellington, New Zealand. DOI: <https://doi.org/10.1109/CEC.2019.8790124>.
- [Flohrer et al., 2019] Flohrer, T., Krag, H., Merz, K., and Lemmens, S. (2019). CREAM - ESA's Proposal for Collision Risk Estimation and Automated Mitigation. In *Proceedings of the Advanced Maui Optical and Space Surveillance Technologies Conference (AMOS)*. Maui, Hawaii, US. <http://adsabs.harvard.edu/abs/2019amos.confE..57F>.
- [Flohrer et al., 2020] Flohrer, T., Merz, K., and Siminski, J. (2020). Update on ESA's Space Safety Programme and its Cornerstone on Collision Avoidance. In *Proceedings of the Advanced Maui Optical and Space Surveillance Technologies Conference (AMOS)*. Maui, Hawaii, US.
- [Fonder et al., 2017] Fonder, G. P., Hack, P. J., and Hughes, M. R. (2017). AN/FSY-3 Space Fence system - sensor site one/operations centre integration status and sensor site two planned capability. In *Proceedings of the Advanced Maui Optical and Space Surveillance Technologies Conference (AMOS)*. Maui, Hawaii, US.
- [Forshaw et al., 2018] Forshaw, J. L., Lopez, R., Okamoto, A., Blackerby, C., and Okada, N. (2018). The ELSA-d end-of-life debris removal mission: mission design, in flight safety and preparations for launch. In *Proceedings of the Advanced Maui Optical and Space Surveillance Technologies Conference (AMOS)*. Maui, Hawaii, US.

- [Foster and Estes, 1992] Foster, J. L. and Estes, H. S. (1992). A parametric analysis of orbital debris collision probability and maneuver rate for space vehicles. Technical report, NASA/JSC.
- [Foster and Frisbee Jr, 1998] Foster, J. L. and Frisbee Jr, J. H. (1998). Position error covariance matrix scaling factors for early operational ISS debris avoidance. Technical report DM33, Johnson Space Center, Houston, Texas, USA.
- [Fraser and Hipel, 1979] Fraser, N. M. and Hipel, K. W. (1979). Solving complex conflicts. *IEEE Transactions on Systems, Man and Cybernetics*, 9(12):805–816. DOI: <https://doi.org/10.1109/TSMC.1979.4310131>.
- [Frey and Lemmens, 2017] Frey, S. and Lemmens, S. (2017). Status of the space environment: current level of adherence to the space debris mitigation policy. In *7th European Conference on Space Debris*. ESA/ESOC, Darmstadt, Germany.
- [Frontier Development Lab Europe, 2020] Frontier Development Lab Europe (2020). FDL Europe 2020. Research. <https://fdleurope.org/fdl-europe-2020>.
- [Furfaro et al., 2018] Furfaro, R., Linares, R., and Reddy, V. (2018). Space objects classification via light-curve measurements: deep convolutional neural networks and model-based transfer learning. In *Proceedings of the Advanced Maui Optical and Space Surveillance Technologies Conference (AMOS)*. Maui, Hawaii, US.
- [Furfaro et al., 2019] Furfaro, R., Linares, R., and Reddy, V. (2019). Shape identification of space objects via light curve inversion using deep learning models. In *Proceedings of the Advanced Maui Optical and Space Surveillance Technologies Conference (AMOS)*. Maui, Hawaii, US.
- [Furfaro et al., 2020] Furfaro, R., Scorsoglio, A., Linares, R., and Massari, M. (2020). Adaptive generalized ZEM-ZEV feedback guidance for planetary landing via a deep reinforcement learning approach. *Acta Astronautica*, 171:156–171. DOI: <https://doi.org/10.1016/j.actaastro.2020.02.051>.

- [Fülöp, 2005] Fülöp, J. (2005). Introduction to decision making methods. In *BDEI-3 workshop*. Washington DC, USA. DOI: <https://doi.org/10.1.1.86.6292>.
- [García-Cascales and Lamata, 2012] García-Cascales, S. and Lamata, T. (2012). On rank reversal and TOPSIS method. *Mathematical and Computer Modelling*, 56(5):123–132. DOI: <https://doi.org/10.1016/j.mcm.2011.12.022>.
- [Gaudet and Furfaro, 2014] Gaudet, B. and Furfaro, R. (2014). Adaptive pinpoint and fuel efficient mars landing using reinforcement learning. *IEEE/CAA Journal of Automatica Sinica*, 1(4):397–411. DOI: <https://doi.org/10.1109/JAS.2014.7004667>.
- [Gaudet et al., 2020] Gaudet, B., Linares, R., and Furfaro, R. (2020). Adaptive guidance and integrated navigation with reinforcement meta-learning. *Acta Astronautica*, 169:180–190. DOI: <https://doi.org/10.1016/j.actaastro.2020.01.007>.
- [Ghrist and Plakalovic, 2012] Ghrist, R. W. and Plakalovic, D. (2012). Impact of non-Gaussian error volumes on conjunction assessment risk analysis. In *AAS/AIAA Astrodynamics Specialist Conference*. Minneapolis, Minnesota, US.
- [Gonzalo et al., 2020] Gonzalo, J. L., Colombo, C., and di Lizia, P. (2020). Introducing MISS, a new tool for collision avoidance analysis and design. *Journal of Space Safety Engineering*, 7(3):282–289. DOI: <https://doi.org/10.1016/j.jsse.2020.07.010>.
- [Greco et al., 2022] Greco, C., Campagnola, S., and Vasile, M. (2022). Robust space trajectory design using belief stochastic optimal control. *Journal of Guidance, Control, and Dynamics*, 45(6):1060–1077. DOI: <https://doi.org/10.2514/1.G005704>.
- [Greco et al., 2021] Greco, C., Sánchez, L., and Vasile, M. (2021). A robust Bayesian agent for optimal collision avoidance manoeuvre planning. In *8th European Conference on Space Debris*. ESA/ESOC, Darmstadt, Germany.
- [Greco and Vasile, 2021] Greco, C. and Vasile, M. (2021). Robust Bayesian particle filter for space object tracking under severe uncertainty. *Journal of Guidance, Control, and Dynamics*, 45(3):481–498. DOI: <https://doi.org/10.2514/1.G006157>.

- [Hagan and Menhaj, 1994] Hagan, M. T. and Menhaj, M. B. (1994). Training feed-forward networks with the Marquardt algorithm. *IEEE Transactions on Neural Networks*, 5(6):989–993. DOI: <https://doi.org/10.1109/72.329697>.
- [Haimerl and Fonder, 2015] Haimerl, J. A. and Fonder, G. P. (2015). Space fence system overview. In *Proceedings of the Advanced Maui Optical and Space Surveillance Technologies Conference (AMOS)*. Maui, Hawaii, US.
- [Hall et al., 2017] Hall, D. T., Hejduk, M. D., and Johnson, L. C. (2017). Time dependence of collision probabilities during satellite conjunctions. In *AAS/AIAA Space Flight Mechanics Meeting*. San Antonio, Texas, US.
- [Hallgarten la Casta et al., 2022] Hallgarten la Casta, M., Sánchez, L., Amato, D., and Vasile, M. (2022). Non-linear set propagation with generalised equinoctial orbital elements. In *5th International Workshop on Key Topics in Orbit Propagation Applied to SSA (KePASSA)*. Logroño, Spain.
- [Hastie et al., 2009] Hastie, T., Tibshirani, R., and Friedman, J. (2009). *The elements of statistical learning. Data mining, inference, and prediction*, chapter Chapter7: Model assessment and selection, page 242. Springer, New York, NY, 2 edition. ISBN: 978-0-387-84857-0. DOI: <https://doi.org/10.1007/978-0-387-84857-0>.
- [He et al., 2015] He, Y., Mirzargar, M., and Kirby, R. M. (2015). Mixed aleatory and epistemic uncertainty quantification using fuzzy set theory. *International Journal of Approximate Reasoning*, 66:1–15. DOI: <https://doi.org/10.1016/j.ijar.2015.07.002>.
- [Hejduk, 2016] Hejduk, M. D. (2016). Covariance manipulation for conjunction assessment. In *AAS/AIAA Space Flight Mechanics Meeting*. Napa, California, US.
- [Hejduk and Johnson, 2016] Hejduk, M. D. and Johnson, L. C. (2016). Approaches to evaluating probability of collision uncertainty. In *AAS/AIAA Space Flight Mechanics Meeting*. Napa, California, US.

- [Hejduk and Snow, 2019] Hejduk, M. D. and Snow, D. E. (2019). Satellite conjunction “Probability,” “Plausibility,” and “Possibility”: a categorization of competing satellite conjunction assessment risk analysis paradigms. In *AAS/AIAA Astrodynamics Specialist Conference*. Portland, Maine, US.
- [Helton, 1997] Helton, J. C. (1997). Uncertainty and sensitivity analysis in the presence of stochastic and subjective uncertainty. *Journal of Statistical Computation and Simulation*, 57:3–76. DOI: <https://doi.org/10.1080/00949659708811803>.
- [Helton et al., 2005] Helton, J. C., Oberkampf, W. L., and Johnson, J. D. (2005). Competing failure risk analysis using evidence theory. *Risk Analysis*, 25(4):973–995. DOI: <https://doi.org/10.1111/j.1539-6924.2005.00644.x>.
- [Hernando-Ayuso and Bombardelli, 2020] Hernando-Ayuso, J. and Bombardelli, C. (2020). Low-thrust collision avoidance in circular orbits. *Journal of Guidance, Control, and Dynamics*, 44(5):983–995. DOI: <https://doi.org/10.2514/1.G005547>.
- [Hipel et al., 1993] Hipel, K. W., Radford, K. J., and Fang, L. (1993). Multiple participant-multiple criteria decision making. *IEEE Transactions on Systems, Man and Cybernetics*, 23(4):1184–1189. DOI: <https://doi.org/10.1109/21.247900>.
- [Hoffman and Hammonds, 1994] Hoffman, F. O. and Hammonds, J. S. (1994). Propagation of uncertainty in risk assessments: the need to distinguish between uncertainty due to lack of knowledge and uncertainty due to variability. *Risk Analysis*, 14(3):707–712. DOI: <https://doi.org/10.1111/j.1539-6924.1994.tb00281.x>.
- [Horwood et al., 2011] Horwood, J. T., Aragon, N. D., and Poore, A. B. (2011). Gaussian sum filters for space surveillance: theory and simulations. *Journal of Guidance, Control and Dynamics*, 34(6):1839–1851. DOI: <https://doi.org/10.2514/1.53793>.
- [Howard, 1971] Howard, N. (1971). *Paradoxes of rationality: theory of metagames and political behavior*. MIT press, Cambridge. DOI: <https://doi.org/10.2307/1958795>.

- [IADC, 2022] IADC (2022). IADC Space Debris Mitigation Guidelines. Technical report, Inter-Agency Space Debris Coordination Committee. DOI: <https://orbitaldebris.jsc.nasa.gov/library/iadc-space-debris-guidelines-revision-2.pdf>.
- [Inagaki, 1991] Inagaki, T. (1991). Independence between safet-control policy and multiple-sensor schemes via Dempster-Shafer theory. *IEEE Transactions on Reliability*, 40(2):182–188. DOI: <https://doi.org/10.1109/24.87125>.
- [Innocenti et al., 2013] Innocenti, L., Soares, T., Delaval, J., and Rinalducci, A. (2013). ESA Clean Space Initiative. In *6th IAASS Conference, Safety is Not an Option*. Montreal, Canada.
- [Izzo et al., 2019] Izzo, D., Märten, M., and Pan, B. (2019). A survey on artificial intelligence trends in spacecraft guidance dynamics and control. *Astrodynamics*, 3(4):287–299. DOI: <https://doi.org/10.1007/s42064-018-0053-6>.
- [Izzo and Pettazzi, 2007] Izzo, D. and Pettazzi, L. (2007). Autonomous and distributed motion planning for satellite swarm. *Journal of Guidance, Control and Dynamics*, 30(2):449–459. DOI: <https://doi.org/10.2514/1.22736>.
- [Jahan and Edwards, 2015] Jahan, A. and Edwards, K. (2015). A state-of-the-art survey on the influence of normalization techniques in ranking: Improving the materials selection process in engineering design. *Materials & Design (1980-2015)*, 65:335–342. DOI: <https://doi.org/10.1016/j.matdes.2014.09.022>.
- [Jian and Deng, 2014] Jian, W. and Deng, Y. (2014). A new method to determine BPA in Evidence Theory. *Journal of Computers*, 6(6):1162–1167.
- [Jones and Doostan, 2016] Jones, B. A. and Doostan, A. (2016). Satellite collision probability estimation using polynomial chaos expansions. *Advances in Space Research*, 52:1860–1875. DOI: <https://doi.org/10.1016/j.asr.2013.08.027>.
- [Jones et al., 2013] Jones, B. A., Doostan, A., and Born, G. H. (2013). Nonlinear propagation of orbit uncertainty using nonintrusive polynomial chaos. *Journal of*

- Guidance, Control and Dynamics*, 36(2):430–444. DOI: <https://doi.org/10.2514/1.57599>.
- [Julian et al., 2016] Julian, K. D., Lopez, J., Brush, J. S., Owen, M. P., and Kochenderfer, M. J. (2016). Policy compression for aircraft collision avoidance systems. In *IEEE/AIAA 35th Digital Avionics Systems Conference (DASC)*. Sacramento, CA, US. DOI: <https://doi.org/10.1109/DASC.2016.7778091>.
- [Kaluthantrige et al., 2023] Kaluthantrige, A., Feng, J., and Gil-Fernández, J. (2023). CNN-based image processing algorithm for autonomous optical navigation of Hera mission to the binary asteroid Didymos. *Acta Astronautica*, 211:60–75. DOI: <https://doi.org/10.1016/j.actaastro.2023.05.029>.
- [Ke et al., 2017] Ke, G., Meng, Q., Finley, T., Wang, T., Chen, W., Ma, W., Ye, Q., and Liu, T. Y. (2017). LightGBM: a highly efficient gradient boosting decision tree. In *31st Conference in Neural Information Processing Systems (NIPS)*, volume 30, page 3149–3157.
- [Khoei et al., 2023] Khoei, T., Ould Slimane, H., and Kaabouch, N. (2023). Deep learning: systematic review, models, challenges, and research directions. *Neural Computing and Applications*, 35:23103–23124. DOI: <https://doi.org/10.1007/s00521-023-08957-4>.
- [Kim et al., 2012] Kim, E. H., Kim, H. D., and Kim, H. J. (2012). A study on the collision avoidance maneuver optimization with multiple space debris. *Journal of Astronautical Sciences*, 29(1):11–21. DOI: <https://doi.org/10.5140/jass.2012.29.1.011>.
- [Kingma and Ba, 2014] Kingma, D. P. and Ba, J. (2014). Adam: A method for stochastic optimization. *arXiv preprint arXiv:1412.6980*. DOI: <https://doi.org/10.48550/arXiv.1412.6980>.
- [Klinkrad et al., 2008] Klinkrad, H., Alarcon, J. R., and Sanchez, N. (2008). Collision avoidance for operational ESA satellites. In *4th European Conference on Space Debris*. ESA/ESOC, Darmstadt, Germany.

- [Kochenderfer and P., 2011] Kochenderfer, M. J. and P., C. J. (2011). Robust airborne collision avoidance through dynamic programming. Technical report, Lincoln Laboratory, Massachusetts Institute of Technology.
- [Koks and Challa, 2003] Koks, D. and Challa, S. (2003). An introduction to Bayesian and Dempster-Shafer data fusion. Technical report, Electronic Warfare and Radar Division. Systems Sciences Laboratory, DSTO, Australia.
- [Kolios et al., 2016] Kolios, A., Mytilinou, V., Lozano-Minguez, E., and Salonitis, K. (2016). A comparative study of multiple-criteria decision-making methods under stochastic inputs. *Energies*, 9(7):566. DOI: <https://doi.org/10.3390/en9070566>.
- [Kubat, 2017] Kubat, M. (2017). *An Introduction to Machine Learning*. Springer Publishing Company, Incorporated, Cham, Switzerland, 2 edition. ISBN: 978-3-319-63912-3. DOI: <https://doi.org/10.1007/978-3-319-63913-0>.
- [Laporte, 2014a] Laporte, F. (2014a). JAC Software, dedicated to the analysis of Conjunction Messages. In *SpaceOps 2014 Conference*. Pasadena, CA, US. DOI: <https://doi.org/10.2514/6.2014-1774>.
- [Laporte, 2014b] Laporte, F. (2014b). JAC Software, solving conjunction assessment issues. In *Proceedings of the Advanced Maui Optical and Space Surveillance Technologies Conference (AMOS)*. Maui, Hawaii, US.
- [Laporte and Moury, 2013] Laporte, F. and Moury, M. (2013). CAESAR, French proactive public service for in-orbit collision avoidance. In *6th European Conference on Space Debris*. ESA/ESOC, Darmstadt, Germany.
- [Lederer, 2021] Lederer, J. (2021). Activation Functions in Artificial Neural Networks: A Systematic Overview. *arXiv*. DOI: <https://doi.org/10.48550/arXiv.2101.09957>.
- [Letizia et al., 2019] Letizia, F., Lemmens, S., Bastida Virgili, B., and Krag, H. (2019). Application of a debris index for global evaluation of mitigation strategies. *Acta*

- Astronautica*, 161:348–361. DOI: <https://doi.org/10.1016/j.actaastro.2019.05.003>.
- [Lewis et al., 2017a] Lewis, H., Radtke, J., Beck, J., Bastida Virgili, B., and Krag, H. (2017a). Self-induced collision risk analysis for large constellations. In *7th European Conference on Space Debris*. ESA/ESOC, Darmstadt, Germany.
- [Lewis et al., 2017b] Lewis, H., Radtke, J., Rossi, A., Beck, J., Oswald, M., Anderson, P., Bastida Virgili, B., and Krag, H. (2017b). Sensitivity of the space debris environment to large constellations and small satellites. In *8th European Conference on Space Debris*. ESA/ESOC, Darmstadt, Germany.
- [Lewis et al., 2014] Lewis, H., Schwarz, S., George, S., and Stokes, H. (2014). An assessment of cubesat collision risk. In *65th International Astronautical Congress (IAC)*. Toronto, Canada.
- [Li et al., 2016] Li, B., Sang, J., and Zhang, Z. (2016). A real-time orbit determination method for smooth transition from optical tracking to laser ranging of debris. *Sensors*, 16(7):962. DOI: <https://doi.org/10.3390/s16070962>.
- [Linares and Furfaro, 2016a] Linares, R. and Furfaro, R. (2016a). Dynamic sensor tasking for space situational awareness via reinforcement learning. In *Proceedings of the Advanced Maui Optical and Space Surveillance Technologies Conference (AMOS)*. Maui, Hawaii, US.
- [Linares and Furfaro, 2016b] Linares, R. and Furfaro, R. (2016b). Space object classification using deep convolutional neural networks. In *19th IEEE International Conference on Information Fusion (FUSION)*. Heidelberg, Germany.
- [Linares and Furfaro, 2017] Linares, R. and Furfaro, R. (2017). Space objects maneuvering detection and prediction via inverse reinforcement learning. In *Proceedings of the Advanced Maui Optical and Space Surveillance Technologies Conference (AMOS)*. Maui, Hawaii, US.

- [Linares et al., 2020] Linares, R., Furfaro, R., and Reddy, V. (2020). Space objects classification via light-curve measurements using deep convolutional neural networks. *The Journal of the Astronautical Sciences*, 67:1063–1091. DOI: <https://doi.org/10.1007/s40295-019-00208-w>.
- [Liu et al., 2020] Liu, L., Jiang, H., He, P. and Chen, W., Liu, X., Gao, J., and Han, J. (2020). On the variance of the adaptive learning rate and beyond. In *8th International Conference on Learning Representations (ICLR)*. Addis Ababa, Ethiopia.
- [Liu et al., 2017a] Liu, X., Yin, L., Hu, L., and Zhang, Z. (2017a). An efficient reliability analysis approach for structure based on probability and probability box models. *Structural and Multidisciplinary Optimization*, 56:167–181. DOI: <https://doi.org/10.1007/s00158-017-1659-7>.
- [Liu et al., 2017b] Liu, X., Yin, L., and Zhang, Z. (2017b). An efficient reliability analysis approach for structure based on probability and probability box models. *Structural and Multidisciplinary Optimization*, 56:167–181. DOI: <https://doi.org/10.1007/s00158-017-1659-7>.
- [Ludwig et al., 2019] Ludwig, J., Cline, D., Spradley, T., Militello, L., and Dilulio, J. (2019). A virtual assistant for space situational awareness. In *Proceedings of the Advanced Maui Optical and Space Surveillance Technologies Conference (AMOS)*. Maui, Hawaii, US.
- [Ludwig et al., 2021] Ludwig, J., Presnell, B., and Richard, S. (2021). Developing a Virtual Assistant for Space Operations. In *Proceedings of the Advanced Maui Optical and Space Surveillance Technologies Conference (AMOS)*. Maui, Hawaii, US.
- [Madani, 2010] Madani, K. (2010). Game theory and water resources. *Journal of Hydrology*, 381(3):225–238. DOI: <https://doi.org/10.1016/j.jhydro.2009.11.045>.
- [Madani and Hipel, 2011] Madani, K. and Hipel, K. W. (2011). Non-cooperative stability definitions for strategic analysis of generic water resources conflicts. *Water Resour*

- Management*, 25:1949–1977. DOI: <https://doi.org/https://doi.org/10.1007/s11269-011-9783-4>.
- [Madani and R., 2011] Madani, K. and R., L. J. (2011). A Monte-Carlo game theoretic approach for multi-criteria decision making under uncertainty. *Advances in Water Resources*, 34:607–616. DOI: <https://doi.org/10.1016/j.advwatres.2011.02.009>.
- [Mancini et al., 2023] Mancini, P., Cannici, M., and Matteucci, M. (2023). Deep learning for asteroids autonomous terrain relative navigation. *Advances in Space Research*, 71(9):3748–3760. DOI: <https://doi.org/10.1016/j.asr.2022.04.020>.
- [Manfletti et al., 2023] Manfletti, C., Guimarães, M., and Soares, C. (2023). AI for space traffic management. *Journal of Space Safety Engineering*, 10(4):495–504. DOI: <https://doi.org/10.1016/j.jsse.2023.08.007>.
- [Manzi and Vasile, 2020a] Manzi, M. and Vasile, M. (2020a). Discovering unmodeled components in astrodynamics with symbolic regression. In *IEEE Congress on Evolutionary Computation (CEC)*. Glasgow, United Kingdom.
- [Manzi and Vasile, 2020b] Manzi, M. and Vasile, M. (2020b). Orbital anomaly reconstruction using deep symbolic regression. In *71st International Astronautical Congress (IAC)*. The Cyber Space Edition.
- [Manzi and Vasile, 2021] Manzi, M. and Vasile, M. (2021). Autoencoder-based thermospheric density model for uncertainty quantification and real-time calibration. In *8th European Conference on Space Debris*. ESA/ESOC, Darmstadt, Germany.
- [Maric et al., 2023] Maric, N., Arias, E., Gago, P., Porcelli, L., Saez, D., Escobar, D., Stanculescu, A., Solomon, A., Muntean, G., Ma, H., Letizia, F., Bastida Virgili, B., and Merz, K. (2023). Automated collision risk assessment and mitigation. In *2nd NEO and Debris Detection Conference*. ESA/ESOC, Darmstadt, Germany.
- [Mashiku et al., 2018] Mashiku, A., Frueh, C., and Memarsadeghi, N. (2018). Supervised-machine Learning for intelligent collision avoidance decision-making

- and sensor tasking. Available at <https://asd.gsfc.nasa.gov/conferences/ai/program/017-AMashikuAIWorkshopPresentation.pdf> (27/11/2018). NASA Goddard Workshop on Artificial Intelligence.
- [Mashiku et al., 2019] Mashiku, A., Frueh, C., Memarsadeghi, N., Gizzi, E., Zielinki, M., and Burton, A. (2019). Predicting satellite close approaches in the context of artificial intelligence. In *AAS/AIAA Astrodynamics Specialist Conference*. Portland, Maine, US.
- [Masson et al., 2022] Masson, M., Arzelier, D., Joldes, M., Revelin, B., and Thomassin, J. (2022). Multi-maneuvers algorithms for multi-risk collision avoidance via nonconvex quadratic optimization. *Hal Open Science*. <https://hal.laas.fr/hal-03847541>.
- [Mateo, 2012] Mateo, J. R. S. C. (2012). *Multi Criteria Analysis in the Renewable Energy Industry. Green Energy and Technology*, chapter Weighted sum method and weighted product method. Springer, London. DOI: https://doi.org/10.1007/978-1-4471-2346-0_4.
- [Matlab, 2021] Matlab (2021). MATLAB *Deep Learning* Toolbox. <https://uk.mathworks.com/help/deeplearning/index.html>.
- [McKnight et al., 2021] McKnight, D., Witner, R., Letizia, F., Lemmens, S., Anselmo, L., Pardini, C., Rossi, A., Kunstadter, C., Kawamoto, S., Aslanov, V., Dolado Perez, J. C., Ruch, V., Lewis, H., Nicolls, M., Jing, L., Dan, S., Dongfang, W., Baranov, A., and Gishko, D. (2021). Identifying the 50 statistically-most-concerning derelict objects in LEO. *Acta Astronautica*, 181:282–291. DOI: <https://doi.org/10.1016/j.actaastro.2021.01.021>.
- [McNally et al., 2021] McNally, K., Ramírez, D., Antón, A. M., Smith, D., and Dick, J. (2021). Artificial intelligence for space resident objects characterisation with lightcurves. In *8th European Conference on Space Debris*. ESA/ESOC, Darmstadt, Germany.

- [Merz et al., 2017] Merz, K., Braun, V., Bastida Virgili, B., Flohrer, T., Funke, Q., Krag, H., and Lemmens, S. (2017). Current collision avoidance service by ESA’s Space Debris Office. In *7th European Conference on Space Debris*. ESA/ESOC, Darmstadt, Germany.
- [Moore et al., 2009] Moore, R. E., Kearfott, R. B., and Cloud, M. J. (2009). *Introduction to Interval Analysis*. Society for Industrial and Applied Mathematics (SIAM). DOI: <https://doi.org/10.1137/1.9780898717716>.
- [Morand et al., 2019] Morand, V., Yanez, C., Dolado Pérez, J. C., Fernández, C., Rousel, S., Pucel, X., and Vidal, V. (2019). BAS3E: A framework to conceive, design, and validate present and future SST architectures. In *1st NASA International Orbital Debris Conference*. Sugar Land, Texas, US.
- [Muelhaupt et al., 2019] Muelhaupt, T., Sorge, M., Morin, J., and Wilson, R. (2019). Space Traffic Management in the New Space era. *Journal of Spacecraft Safety Engineering*, 6:80–87. DOI: <https://doi.org/10.1016/j.jsse.2019.05.007>.
- [Myerson, 1984] Myerson, R. B. (1984). An introduction to game theory. Technical report, Northwestern University, Center for Mathematical Studies in Economics and Management Science. Discussion Papers: 623.
- [Nag et al., 2018] Nag, S., Murakami, D., Lifson, M., and Kopardekar, P. (2018). System autonomy for Space Traffic Management. In *2018 IEEE/AIAA 37th Digital Avionics Systems Conference (DASC)*. London, United Kingdom. DOI: <https://doi.org/10.1109/DASC.2018.8569343>.
- [Nag et al., 2021] Nag, S., Murakami, D., Marker, N., Lifson, M., and Kopardekar, P. (2021). Prototyping operational autonomy for Space Traffic Management. *Acta Astronautica*, 180:489–506. DOI: <https://doi.org/10.1016/j.actaastro.2020.11.056>.
- [NASA, 2023] NASA (2023). NASA Orbital Debris Quarterly. Technical Report 4, National Aeronautics and Space Administration - Orbital Debris Program Office,

- NASA/ODPO. <https://orbitaldebris.jsc.nasa.gov/quarterly-news/pdfs/ODQNv27i4.pdf>.
- [Nash, 1950] Nash, J. F. (1950). Equilibrium points in n-person games. *Proceedings of the National Academy of Sciences*, 36(1):48–49. DOI: <https://doi.org/10.1073/pnas.36.1.48>.
- [Newman et al., 2014] Newman, L., Hejduk, M., Frigm, R., and Duncan, M. (2014). Evolution and implementation of the NASA robotic conjunction assessment risk analysis concept of operations. In *Proceedings of the Advanced Maui Optical and Space Surveillance Technologies Conference (AMOS)*. Maui, Hawaii, US.
- [Newman et al., 2019] Newman, L. K., Mashiku, A. K., Hejduk, M. D., Johnson, M. D., and Rosa, J. D. (2019). NASA Conjunction Assessment Risk Analysis (CARA) updated requirements architecture. In *AAS/AIAA Astrodynamics Specialist Conference*. Portland, Maine, US.
- [Nicholas, 2009] Nicholas, J. (2009). The collision of Iridium 33 and Cosmos 2251: the shape of things to come. In *60th International Astronautical Congress (IAC)*. Daejeon, Republic of Korea.
- [Oberkampf and Helton, 2002] Oberkampf, W. L. and Helton, J. C. (2002). Investigation of evidence theory for engineering applications. In *43rd AIAA/ASME/ASCE/AHS/ASC Structures, Structural Dynamics, and Materials Conference*. Denver, Colorado, US. DOI: <https://doi.org/10.2514/6.2002-1569>.
- [Oestreich et al., 2021] Oestreich, C. E., Linares, R., and Gondhalekar, R. (2021). Autonomous six-degree-of-freedom spacecraft docking with rotating targets via reinforcement learning. *Journal of Aerospace Information Systems*, 18(7):417–428. DOI: <https://doi.org/https://doi.org/10.2514/1.I010914>.
- [Oguiza, 2022] Oguiza, I. (2022). tsai - A state-of-the-art deep learning library for time series and sequential data. Github: <https://github.com/timeseriesAI/tsai>.

- [Palermo et al., 2021] Palermo, M. F., Di Lizia, P., and Armellin, R. (2021). Numerically efficient methods for low-thrust collision avoidance maneuver design. In *8th European Conference on Space Debris*. ESA/ESOC, Darmstadt, Germany.
- [Pardini and Anselmo, 2009] Pardini, C. and Anselmo, L. (2009). Assessment of the consequences of the Fengyun-1C breakup in low Earth orbit. *Advances in Space Research*, 44(5):545–557. DOI: <https://doi.org/10.1016/j.asr.2009.04.014>.
- [Pardini and Anselmo, 2011] Pardini, C. and Anselmo, L. (2011). Physical properties and long-term evolution of the debris clouds produced by two catastrophic collisions in Earth orbit. *Advances in Space Research*, 48(3):557–569. DOI: <https://doi.org/10.1016/j.asr.2011.04.006>.
- [Patera, 2001] Patera, R. (2001). General method for calculating satellite collision probability. *Journal of Guidance, Control and Dynamics*, 24:716–722. DOI: <https://doi.org/10.2514/2.4771>.
- [Patera, 2003] Patera, R. P. (2003). Satellite collision probability for non-linear relative motion. *Journal of Guidance, Control and Dynamics*, 26(5):728–733. DOI: <https://doi.org/10.2514/2.5127>.
- [Patera, 2006] Patera, R. P. (2006). Collision probability for larger bodies having non-linear relative motion. *Journal of Guidance, Control and Dynamics*, 29(6):1468–1471. DOI: <https://doi.org/10.2514/1.23509>.
- [Paulete et al., 2021] Paulete, C., Cano, D., Siminski, J., Pérez, C., Escobar, D., and Tirado, J. (2021). AIMLRCS: a machine learning approach to spacecraft attitude and object identification based on RCS from the S3TSR. In *8th European Conference on Space Debris*. ESA/ESOC, Darmstadt, Germany.
- [Peddakotla et al., 2022] Peddakotla, S. A., Morgado, F., Thillaithevan, D., O’Driscoll, D., Santer, M., Maddock, C., Vasile, M., and Fossati, M. (2022). Multi-fidelity and multi-disciplinary approach for the accurate simulation of atmospheric re-entry. In *73rd International Astronautical Congress (IAC)*. Paris, France. Paper number: IAC–22–A6.IPB.2x73592.

- [Peng and Bai, 2017] Peng, H. and Bai, X. (2017). Limits of machine learning approach on improving orbit prediction accuracy using support vector machine. In *Proceedings of the Advanced Maui Optical and Space Surveillance Technologies Conference (AMOS)*. Maui, Hawaii, US.
- [Peng and Bai, 2018a] Peng, H. and Bai, X. (2018a). Artificial neural network-based machine learning approach to improve orbit prediction accuracy. *Journal of Spacecraft and Rockets*, 55:1248–1260. DOI: <https://doi.org/10.2514/1.A34171>.
- [Peng and Bai, 2018b] Peng, H. and Bai, X. (2018b). Exploring capability of support vector machine for improving satellite orbit prediction accuracy. *Aerospace Information Systems*, 15(6):366–381. DOI: <https://doi.org/10.2514/1.I010616>.
- [Peng and Bai, 2018c] Peng, H. and Bai, X. (2018c). Improving orbit prediction accuracy through supervised machine learning. *Advances in Space Research*, 61(10):2628–2646. DOI: <https://doi.org/10.1016/j.asr.2018.03.001>.
- [Peterson et al., 2016] Peterson, G., Jenkin, A., Sorge, M., and McVey, J. (2016). Implications of proposed small satellite constellations on space traffic management and long-term growth in near-earth environment. In *67th International Astronautical Congress (IAC)*. Guadalajara, Mexico.
- [Peterson et al., 2018] Peterson, G., Sorge, M., and Ailor, W. (2018). Space Traffic Management in the age of New Space. *Center for Space Policy and Strategy*, 18-21 April. The Aerospace Corporation.
- [Petit et al., 2021] Petit, A., Rossi, A., and Alessi, E. M. (2021). Assessment of the close approach frequency and collision probability for satellites in different configurations of large constellations. *Advances in Space Research*, 67(12):4177–4192. DOI: <https://doi.org/10.1016/j.asr.2021.02.022>.
- [Pinto et al., 2020] Pinto, F., Acciarini, G., Metz, S., Boufelja, S., Kaczmarek, S., Merz, K., Martínez-Heras, J., Letizia, F., Bridges, C., and Baydin, A. (2020). Towards automated satellite conjunction management with bayesian deep learning. In

- AI for Earth Sciences Workshop at NeurIPS*. https://nips.cc/virtual/2020/public/workshop_16105.html.
- [Pontijas Fuentes et al., 2019] Pontijas Fuentes, I., Bonetti, D., Letterio, F., Vicario de Miguel, G., Blanco Arnao, G., Palomo, P., Parigini, C., Lemmens, S., Lips, T., and Kanzler, R. (2019). Upgrade of ESA’s Debris Risk Assessment and Mitigation Analysis (DRAMA) tool: Spacecraft Entry Survival Analysis Module. *Acta Astronautica*, 158:148–160. DOI: <https://doi.org/10.1016/j.actaastro.2017.12.001>.
- [Poore et al., 2016] Poore, A. B., Aristoff, J. M., Horwood, J. T., Armellin, R., Cerven, W. T., Cheng, Y., Cox, C. M., Erwin, R. S., and Frisbee, J. H. (2016). Covariance and uncertainty realism in space surveillance and tracking. Technical report, Numerica Corporation Fort Collins United States, Washington, DC, USA.
- [Priyant Mark and Kamath, 2019] Priyant Mark, C. and Kamath, S. (2019). Review of active space debris removal methods. *Space Policy*, 47:194–206. DOI: <https://doi.org/10.1016/j.spacepol.2018.12.005>.
- [Pugliatti et al., 2023] Pugliatti, M., Scorsoglio, A., Furfaro, R., and Topputo, F. (2023). Onboard state estimation around Didymos with recurrent neural networks and segmentation maps. *IEEE Transactions on Aerospace and Electronic Systems*. DOI: <https://doi.org/10.1109/TAES.2023.3288506>.
- [Python, 2023] Python (2023). LightGBM’s documentation. <https://lightgbm.readthedocs.io/en/latest/index.html>.
- [Quinlan, 1986] Quinlan, J. R. (1986). Induction of decision trees. *Machine Learning*, 1(1):81–106.
- [Radtke et al., 2017a] Radtke, H., Kebschull, C., and Stoll, E. (2017a). Interactions of the space debris environment with mega constellations—Using the example of the OneWeb constellation. *Acta Astronautica*, 131:55–68.
- [Radtke et al., 2017b] Radtke, J., Stoll, E., Lewis, H., and Bastida Virgili, B. (2017b). The impact of the increase in small satellite launch traffic on the long-term evolu-

- tion of the space debris environment. In *7th European Conference on Space Debris*. ESA/ESOC, Darmstadt, Germany.
- [Ramírez-Atencia et al., 2017] Ramírez-Atencia, C., Bello-Orgaz, G., R-Moreno, M. D., and D., C. (2017). Solving complex multi-UAV mission planning problems using multi-objective genetic algorithms. *Soft Computing*, 21(17):4883–4900. DOI: <https://doi.org/10.1007/s00500-016-2376-7>.
- [Ramírez-Atencia et al., 2020] Ramírez-Atencia, C., Rodríguez-Fernández, V., and Camacho, D. (2020). A revision on multi-criteria decision making methods for Multi-UAV mission planning support. *Expert Systems with Applications*, 160:113708. DOI: <https://doi.org/10.1016/j.eswa.2020.113708>.
- [Ramírez-Atencia et al., 2017] Ramírez-Atencia, C., Rodríguez Fernández, V., González Pardo, A., and Camacho, D. (2017). New artificial intelligence approaches for future UAV ground control stations. In *2017 IEEE Congress on Evolutionary Computation (CEC)*. Donostia-San Sebastián, Spain.
- [Raschka, 2018] Raschka, S. (2018). Lecture notes on k-nearest neighbors. Stat 479: Machine Learning (FS18). https://sebastianraschka.com/pdf/lecture-notes/stat479fs18/02_knn_notes.pdf.
- [Reihs et al., 2017] Reihs, B., McLean, F., Lemmens, S., Merz, K., and Krag, H. (2017). Analysis of CDM covariance consistency in operational collision avoidance. In *7th European Conference on Space Debris*. ESA/ESOC, Darmstadt, Germany.
- [Robbins and Monro, 1951] Robbins, H. and Monro, S. (1951). A stochastic approximation method. *The Annals of Mathematical Statistics*, 22(3):400. DOI: <https://doi.org/10.1214/aoms/1177729586>.
- [Roberts and Linares, 2021] Roberts, T. G. and Linares, R. (2021). Geosynchronous satellite maneuver classification via supervised machine learning. In *Proceedings of the Advanced Maui Optical and Space Surveillance Technologies Conference (AMOS)*. Maui, Hawaii, US.

- [Rojers and Whiteson, 2017] Roijers, D. M. and Whiteson, S. (2017). *Multi-Objective Decision Making*. Springer Cham, Switzerland. DOI: <https://doi.org/10.1007/978-3-031-01576-2>.
- [Rosin and Fierens, 1995] Rosin, P. L. and Fierens, F. (1995). Improving neural network generalisation. *In proceeding of 1995 International Geoscience and Remote Sensing Symposium (IGARSS). Quantitative Remote Sensing for Science and Applications. Firenze, Italy*, 2:1255–1257. DOI: <https://doi.org/10.1109/IGARSS.1995.521718>.
- [Rossi et al., 2017] Rossi, A., Alessi, E., Valsecchi, G. B., Lewis, H., Radtke, J., Bombardelli, C., and Bastida Virgili, B. (2017). A quantitative evaluation of the environmental impact of the mega constellations. In *7th European Conference on Space Debris*. ESA/ESOC, Darmstadt, Germany.
- [Russell and Norvig, 2009] Russell, S. and Norvig, P. (2009). *Artificial Intelligence. A Modern Approach*. Prentice Hall Press, Upper Saddle River, 07458, New Jersey, US, 3rd edition. ISBN: 978-0-13-604259-4.
- [Rüdissler et al., 2022] Rüdissler, H. T., Windisch, A., Amerstorfer, U. V., Möstl, C., Amerstorfer, T., Bailey, R. L., and Reiss, M. A. (2022). Automatic detection of interplanetary coronal mass ejections in solar wind in situ data. *Space Weather*, 2022(10). DOI: <https://doi.org/10.1029/2022sw003149>.
- [Salvatelli et al., 2022] Salvatelli, V., Guides dos Santos, L. F., Bose, S., Neuberg, B., Cheung, M. C. M., Janvier, M., Jin, M., Gal, Y., and Baydin, A. G. (2022). Exploring the limits of synthetic creation of solar EUV images via image-to-image translation. *The Astrophysical Journal*, 937(100). DOI: <https://doi.org/10.3847/1538-4357/ac867b>.
- [Sánchez et al., 2023] Sánchez, L., Rodríguez-Fernández, V., and Vasile, M. (2023). Robust classification with belief functions and deep learning applied to space traffic management. In *2024 IEEE World Congress on Computational Intelligence (WCCI)*. Yokohama, Japan. Accepted.

- [Sánchez et al., 2022a] Sánchez, L., Stevenson, E., Vasile, M., Rodríguez-Fernández, V., and Camacho, D. (2022a). An intelligent system for robust decision-making in the all-vs-all conjunction screening problem. In *3rd IAA Conference on Space Situational Awareness (ICSSA)*. Tres Cantos, Madrid, Spain.
- [Sánchez and Vasile, 2020a] Sánchez, L. and Vasile, M. (2020a). AI for autonomous CAM execution. In *71st International Astronautical Congress (IAC)*. The Cyber Space Edition. Paper number: IAC-20-A6,2,12,x58045.
- [Sánchez and Vasile, 2020b] Sánchez, L. and Vasile, M. (2020b). On the use of machine learning and evidence theory to improve collision risk assessment. In *2nd IAA Conference on Space Situational Awareness (ICSSA)*. Washington DC, US.
- [Sánchez and Vasile, 2021a] Sánchez, L. and Vasile, M. (2021a). CASSANDRA: Computational Agent for Space Situational Awareness aNd Debris Remediation Automation. In *Stardust-R – Second Global Virtual Workshop (GVW-II)*. Darmstadt, Germany.
- [Sánchez and Vasile, 2021b] Sánchez, L. and Vasile, M. (2021b). Constrained optimal collision avoidance manoeuvre allocation under uncertainty for subsequent conjunction events. In *72nd International Astronautical Congress (IAC)*. Dubai, EAU.
- [Sánchez and Vasile, 2021c] Sánchez, L. and Vasile, M. (2021c). On the use of machine learning and evidence theory to improve collision risk management. *Acta Astronautica*, 181:694–706. DOI: <https://doi.org/10.1016/j.actaastro.2020.08.004>.
- [Sánchez and Vasile, 2023] Sánchez, L. and Vasile, M. (2023). Intelligent agent for decision-making support and collision avoidance manoeuvre design on Space Traffic Management. *Advances in Space Research*, 72(7):2627–2648. DOI: <https://doi.org/10.1016/j.asr.2022.09.023>.
- [Sánchez et al., 2019] Sánchez, L., Vasile, M., and Minisci, E. (2019). AI to support decision making in collision risk assessment. In *70th International Astronautical Congress (IAC)*. Washington DC, US. Paper number: IAC-19-A6,IP,20,x53728.

- [Sánchez et al., 2020] Sánchez, L., Vasile, M., and Minisci, E. (2020). AI and space safety: collision risk assessment. In Schrogl, K.-U., editor, *Handbook of Space Security*, pages 941–959. Springer, Cham.
- [Sánchez et al., 2024] Sánchez, L., Vasile, M., Sanvido, S., Merz, K., and Taillan, C. (2024). Treatment of epistemic uncertainty in conjunction analysis with Dempster-Shafer theory. In press. DOI: <https://doi.org/10.1016/j.asr.2024.09.014>.
- [Sánchez et al., 2022b] Sánchez, L., Vasile, M., and Taillan, C. (2022b). Close encounter decision-making: comparing CASSANDRA and CNES operational processes. In *2nd Stardust Final Conference (STARCON-2)*. ESA/ESTEC, Noordwijk, The Netherlands.
- [Sanvido, 2023] Sanvido, S. (2023). Private communication. ESA Space Debris Office. 23 February 2023.
- [Schutz et al., 2004] Schutz, B., Tapley, B., and Born, G. H. (2004). *Statistical Orbit Determination*. Elsevier. ISBN: 978-0-12-683630-1. DOI: <https://doi.org/10.1016/B978-0-12-683630-1.X5019-X>.
- [Scikit-learn, 2021a] Scikit-learn (2021a). Python Scikit learn library. KNN Classifier. <https://scikit-learn.org/stable/modules/generated/sklearn.neighbors.KNeighborsClassifier.html>.
- [Scikit-learn, 2021b] Scikit-learn (2021b). Python Scikit learn library. RFF Ensemble Classifier. <https://scikit-learn.org/stable/modules/generated/sklearn.ensemble.RandomForestClassifier.html>.
- [Scikit-learn, 2021c] Scikit-learn (2021c). Python Scikit learn library. SVM Classifier (SVC). <https://scikit-learn.org/stable/modules/generated/sklearn.svm.SVC.html#sklearn.svm.SVC>.

- [Sentz and Ferson, 2022] Sentz, K. and Ferson, S. (2022). Combination of evidence in Dempster-Shafer Theory. Technical report, Sandia National Lab., United States. DOI: <https://www.osti.gov/biblio/800792>.
- [Serra et al., 2016] Serra, R., Arzelier, D., Joldes, M., Lasserre, J. B., Rondepierre, A., and Salvy, B. (2016). Fast and accurate computation of orbital collision probability for short-term encounters. *Journal of Guidance, Control, and Dynamics*, 39:1–13. DOI: <https://doi.org/10.2514/1.G001353>.
- [Shafer, 1976] Shafer, G. (1976). *A mathematical theory of evidence*. Princeton University Press, Princeton, NJ, 1 edition. ISBN: 9780691100425.
- [Shen, 2020] Shen, D. (2020). *Satellite Systems-Design, Modeling, Simulation and Analysis*, chapter Game theoretic training enabled deep learning solutions for rapid discovery of satellite behaviors. IntechOpen, Rijeka. DOI: <https://doi.org/10.5772/intechopen.92636>.
- [Shen et al., 2019] Shen, D., Lu, J., Chen, G., Blasch, E., Sheaff, C., Pugh, M., and Pham, K. (2019). Methods of machine learning for space object pattern classification. In *2019 IEEE National Aerospace and Electronics Conference (NAECON)*. Piscataway, New Jersey, US. DOI: <https://doi.org/10.1109/NAECON46414.2019.9058182>.
- [Shim et al., 2002] Shim, J. P., Warkentin, M., Courtney, J. F., Power, D. J., Sharda, R., and Carlsson, C. (2002). Past, present, and future of decision support technology. *Decision Support Systems*, 33(2):111–126. DOI: [https://doi.org/10.1016/S0167-9236\(01\)00139-7](https://doi.org/10.1016/S0167-9236(01)00139-7).
- [Siew et al., 2023a] Siew, P. M., Smith, T., Ponmalai, R., and Linares, R. (2023a). Scalable Multi-Agent Sensor Tasking Using Deep Reinforcement Learning. In *Proceedings of the Advanced Maui Optical and Space Surveillance Technologies Conference (AMOS)*. Maui, Hawaii, US.
- [Siew et al., 2023b] Siew, P. M., Solera, H. S., Roberts, T. G., Jang, D., Rodríguez-Fernández, V., and Linares, R. (2023b). AI SSA Challenge Problem: Satellite

- Pattern-of-Life Characterization Dataset and Benchmark Suite. In *Proceedings of the Advanced Maui Optical and Space Surveillance Technologies Conference (AMOS)*. Maui, Hawaii, US.
- [Simarro Mecinas et al., 2022] Simarro Mecinas, F. J., Serrano Sánchez, J., and Pérez Hernández, C. (2022). Conan: Conjunction analysis tool for eu sst ca service users. In *3rd IAA Conference on Space Situational Awareness (ICSSA)*. Tres Cantos, Madrid, Spain.
- [Slater et al., 2006] Slater, G. L., Byram, S. M., and Williams, T. W. (2006). Collision avoidance for satellites in formation flight. *Journal of Guidance, Control and Dynamics*, 29(5):1139–1146. DOI: <https://doi.org/10.2514/1.16812>.
- [Song et al., 2022] Song, J., Rondao, D., and Aouf, N. (2022). Deep learning-based spacecraft relative navigation methods: A survey. *Acta Astronautica*, 191:22–40. DOI: <https://doi.org/10.1016/j.actaastro.2021.10.025>.
- [Soundappan et al., 2004] Soundappan, P., Nikolaidis, E., Haftka, R. T., Grandhi, R., and Canfield, R. (2004). Comparison of evidence theory and Bayesian theory for uncertainty modeling. *Reliability Engineering & System Safety*, 85(1-3):295–311. DOI: <https://doi.org/10.1016/j.ress.2004.03.018>.
- [Statheros et al., 2008] Statheros, T., Howells, G., and McDonald-Maier, K. (2008). Autonomous ship collision avoidance navigation concepts. *Journal of navigation*, 61(1):129–142. DOI: <https://doi.org/10.1017/S037346330700447X>.
- [Stevenson et al., 2022a] Stevenson, E., Martínez, R., Rodríguez-Fernández, V., and Camacho, D. (2022a). Predicting the effects of kinetic impactors on asteroid deflection using end-to-end deep learning. In *2022 IEEE Congress on Evolutionary Computation (CEC)*. Padova, Italy. DOI: <https://doi.org/10.1109/CEC55065.2022.9870215>.
- [Stevenson et al., 2022b] Stevenson, E., Rodríguez-Fernández, V., Minisci, E., and Camacho, D. (2022b). A deep learning approach to solar radio flux forecasting. *Acta*

- Astronautica*, 193:595–606. DOI: <https://doi.org/10.1016/j.actaastro.2021.08.004>.
- [Stevenson et al., 2021] Stevenson, E., Rodríguez-Fernández, V., Urrutxua, H., Morand, V., and Camacho, D. (2021). Artificial intelligence for all vs. all conjunction screening. In *8th European Conference on Space Debris*. ESA/ESOC, Darmstadt, Germany.
- [Stoll et al., 2011] Stoll, E., Shulze, R., Souza, B., and Oxfort, M. (2011). The impact of collision avoidance maneuvers on satellite constellation management. In *European Space Surveillance Conference*. Madrid, Spain.
- [Stroe et al., 2021] Stroe, I. F., Stanculescu, A. D., Iliaica, P. B., Blaj, C. F., Nita, M. A., Butu, A. F., Escobar, D., Tirado, J., Bija, B., and Saez, D. (2021). AUTOCA Autonomous Collision Avoidance System. In *8th European Conference on Space Debris*. ESA/ESOC, Darmstadt, Germany.
- [Tail et al., 2020] Tail, T., Bateman, S., and Schaub, H. (2020). Autonomous on-orbit optical navigation techniques for robust pose-estimation. *Advances in the Astronautical Sciences AAS Guidance, Navigation, and Control*, 172.
- [Taillan and Laporte, 2022] Taillan, C. and Laporte, F. (2022). Private communication. CNES. Toulouse, 28 May 2022.
- [Tardioli et al., 2020] Tardioli, C., Farnocchia, D., Vasile, M., and Chesley, S. R. (2020). Impact probability under aleatory and epistemic uncertainties. *Celestial Mechanics and Dynamical Astronomy*, 132(54). DOI: <https://doi.org/10.1007/s10569-020-09991-3>.
- [Tardioli and Vasile, 2015] Tardioli, C. and Vasile, M. (2015). Collision and re-entry analysis under aleatory and epistemic uncertainty. *Advances in Astronautical Sciences*, 156:4205 – 4220.

- [Tofallis, 2014] Tofallis, C. (2014). Add or multiply? A tutorial on ranking and choosing with multiple criteria. *INFORMS Transactions on Education*, 14(3):109–119. DOI: <https://doi.org/10.1287/ited.2013.0124>.
- [Triantaphyllou, 2000] Triantaphyllou, E. (2000). *Multi-Criteria Decision Making Methods: A Comparative Study. Applied Optimization*. Springer US, Boston, MA. DOI: <https://doi.org/10.1007/978-1-4757-3157-6>.
- [Triantaphyllou and Shu, 2001] Triantaphyllou, E. and Shu, B. (2001). On the maximum number of feasible ranking sequences in multi-criteria decision making problems. *European Journal of Operational Research*, 130(3):665–678.
- [Triantaphyllou et al., 1998] Triantaphyllou, E., Shu, B., Nieto Sánchez, S., and Ray, T. G. (1998). Multi-criteria decision making: an operations research approach. *Encyclopedia of Electrical and Electronics Engineering*, 15:175–186.
- [tsai, 2023] tsai (2023). State-of-the-art Deep Learning library for Time Series and Sequences. <https://timeseriesai.github.io/tsai>.
- [Tulczyjew et al., 2020] Tulczyjew, L., Myller, M., Kawulok, M., Kostrzewa, D., and Nalepa, J. (2020). Toward automated collision avoidance: predicting the risk of satellite collisions using machine learning-powered technique. In *71st International Astronautical Congress (IAC)*. The Cyber Space Edition. Paper number: IAC-20,A6,VP,13,x57288.
- [Tulczyjew et al., 2021] Tulczyjew, L., Myller, M., Kawulok, M., Kostrzewa, D., and Nalepa, J. (2021). Predicting risk of satellite collisions using machine learning. *Journal of Space Safety Engineering*, 8(4):339–344. DOI: <https://doi.org/10.1016/j.jsse.2021.09.001>.
- [UNOOSA, 2010] UNOOSA (2010). Space Debris Mitigation Guidelines of the Committee on the Peaceful Uses of Outer Space. Technical report, U.N. Office for outer space affairs, Vienna. DOI: https://www.unoosa.org/pdf/publications/st_space_49E.pdf.

- [Uriot et al., 2022] Uriot, T., Izzo, D., Simões, L. F., Abay, R., Einecke, N., Rebhan, S., Martinez-Heras, J. A., Letizia, F., Siminski, J., and Merz, K. (2022). Spacecraft collision avoidance challenge: design and results of a machine learning competition. *Astrodynamics*, 6(2):121–140. DOI: <https://doi.org/10.1007/s42064-021-0101-5>.
- [Vafaei et al., 2016] Vafaei, N., Ribeiro, R., and Camarinha-Matos, L. (2016). Normalization techniques for multi-criteria decision making: Analytical Hierarchy Process case study. In Camarinha-Matos, L.M. and Falcão, A.J. and Vafaei, N. and Najdi, S., editor, *Technological Innovation for Cyber-Physical Systems. DoCEIS 2016. IFIP Advances in Information and Communication Technology*, volume 470. Springer, Cham. DOI: https://doi.org/10.1007/978-3-319-31165-4_26.
- [Vafaei et al., 2018] Vafaei, N., Ribeiro, R., and Camarinha-Matos, L. (2018). Data normalisation techniques in decision making: case study with TOPSIS method. *International Journal of Information and Decision Sciences*, 10(1):19–38. DOI: <https://doi.org/10.1504/IJIDS.2018.090667>.
- [Vafaei et al., 2022] Vafaei, N., Ribeiro, R., and Camarinha-Matos, L. (2022). Assessing normalization techniques for simple additive weighting method. *Procedia Computer Science*, 199:1229–1236. DOI: <https://doi.org/10.1016/j.procs.2022.01.156>.
- [Vasile and Colombo, 2008] Vasile, M. and Colombo, C. (2008). Optimal impact strategies for asteroid deflection. *Journal of Guidance, Control and Dynamics*, 31(4):858–872. DOI: <https://doi.org/10.2514/1.33432>.
- [Vasile et al., 2017a] Vasile, M., Filippi, G., Ortega Absil, C., and Riccardi, A. (2017a). Fast belief estimation in evidence network model. In *12th International Conference on Evolutionary and Deterministic Methods for Design, Optimization and Control (EUROGEN)*. Madrid, Spain.
- [Vasile et al., 2017b] Vasile, M., Rodríguez-Fernández, V., Serra, R., Camacho, D., and Riccardi, A. (2017b). Artificial intelligence in support to space traffic management. In

- 68th *International Astronautical Congress (IAC)*. Adelaide, Australia. Paper number: IAC-17-A6,7,1,x41479.
- [Vasile and Sánchez, 2022] Vasile, M. and Sánchez, L. (2022). Robust optimisation of coordinated collision avoidance manoeuvres in large constellations. In *11th International Workshop on Satellites Constellations and Formation Flying (IWSCFF)*. Milan, Italy.
- [Vasile et al., 2023] Vasile, M., Walker, L., Dunphy, D., Zabalza, J., Murray, P., Marshall, S., and Savitski, V. (2023). Intelligent characterisation of space objects with hyperspectral imaging. *Acta Astronautica*, 203:510–534. DOI: <https://doi.org/10.1016/j.actaastro.2022.11.039>.
- [Vaswani et al., 2017] Vaswani, A., Shazeer, N., Parmar, N., Uszkoreit, J., Jones, L., and Gomez, A. N. (2017). Attention is all you need. In *31st Conference in Neural Information Processing Systems (NIPS)*, volume 30, page 5998–6008. DOI: <https://doi.org/10.48550/arXiv.1706.03762>.
- [Vittaldev and Russell, 2016] Vittaldev, V. and Russell, R. P. (2016). Space object collision probability using multidirectional Gaussian mixture models. *Journal of Guidance, Control and Dynamics*, 39(9):2161–2167. DOI: <https://doi.org/10.2514/1.G001610>.
- [Walker, 1977] Walker, J. G. (1977). *Continuous whole-earth coverage by circular-orbit satellite patterns*. Procurement Executive, Ministry of Defence.
- [Walley and Cooman, 2001] Walley, P. and Cooman, G. D. (2001). A behavioral model for linguistic uncertainty. *Information Sciences*, 134(1-4):1–37. DOI: [https://doi.org/10.1016/S0020-0255\(01\)00090-1](https://doi.org/10.1016/S0020-0255(01)00090-1).
- [Walley and Fine, 1982] Walley, P. and Fine, T. L. (1982). Towards a frequentist theory of upper and lower probability. *Annals of Statistics*, 10(3):741–761. DOI: <https://doi.org/10.1214/aos/1176345868>.

- [Wasserstein and Lazar, 2016] Wasserstein, R. L. and Lazar, N. A. (2016). The ASA’s statement on p-Values: context, process, and purpose. *The American Statistician*, 70(2):129–133. DOI: <https://doi.org/10.1080/00031305.2016.1154108>.
- [Weeden et al., 2019] Weeden, C., Blackberry, C., Forshaw, J., Martin, C., Lopez, R., Yamamoto, E., and Okada, N. (2019). Development of global policy for active debris removal services. In *1st International Orbital Space Debris Conference*. Sugar Land, Texas, US.
- [WEF, 2023] WEF (2023). Space Industry Debris Mitigation Recommendations. Technical report, World Economic Forum. DOI: https://www3.weforum.org/docs/WEF_Space_Industry_Debris_Mitigation_Recommendations_2023.pdf.
- [Wijayatunga et al., 2023] Wijayatunga, M. C., Aremlin, R., Holt, H., Pirovano, L., and Lidtke, A. A. (2023). Design and guidance of a multi-active debris removal mission. *Astrodynamics*, 7:383–399. DOI: <https://doi.org/10.1007/s42064-023-0159-3>.
- [Williamson and Downs, 1990] Williamson, R. C. and Downs, T. (1990). Probabilistic arithmetic. I. Numerical methods for calculating convolutions and dependency bounds arithmetic. *International Journal of Approximate Reasoning*, 4(2). DOI: [https://doi.org/10.1016/0888-613X\(90\)90022-T](https://doi.org/10.1016/0888-613X(90)90022-T).
- [Wilson and Riccardi, 2023] Wilson, C. and Riccardi, A. (2023). Improving the efficiency of reinforcement learning for a spacecraft powered descent with Q-learning. *Optimization and Engineering*, 24(1):223–255. DOI: <https://doi.org/10.1007/s11081-021-09687-z>.
- [Wormnes et al., 2013] Wormnes, K., Le Letty, R., Summerer, L., Schonenborg, R., Dubois-Matra, O., Luracshi, E., Cropp, A., Krag, H., and Delaval, J. (2013). ESA technologies for space debris remediation. In *6th European Conference on Space Debris*. ESA/ESOC, Darmstadt, Germany.
- [Wu and Rosengren, 2023] Wu, D. and Rosengren, A. J. (2023). An investigation on space debris of unknown origin using proper elements and neural networks. *Celestial*

- Mechanics and Dynamical Astronomy*, 135(44). DOI: <https://doi.org/10.1007/s10569-023-10157-0>.
- [Yager, 1987] Yager, R. R. (1987). On the Dempster-Shafer framework and new combination rules. *Information Sciences*, 41(2):93–137.
- [Zadeh, 1965] Zadeh, L. A. (1965). Fuzzy sets. *Information and Control*, 8(3):338–353. DOI: [https://doi.org/10.1016/S0019-9958\(65\)90241-X](https://doi.org/10.1016/S0019-9958(65)90241-X).
- [Zadeh, 1984a] Zadeh, L. A. (1984a). Fuzzy probabilities. *Information Processing & Management*, 20(3):363–372. DOI: [https://doi.org/10.1016/0306-4573\(84\)90067-0](https://doi.org/10.1016/0306-4573(84)90067-0).
- [Zadeh, 1984b] Zadeh, L. A. (1984b). Review of A Mathematical Theory of Evidence. *AI Magazine*, 5(3):81. DOI: <https://doi.org/10.1609/aimag.v5i3.452>.
- [Zervas et al., 2011] Zervas, E., Mpimpoudis, A., Anagnostopoulos, C., Sekkas, O., and Hadjiefthymiades, S. (2011). Multisensor data fusion for fire detection. *Information Fusion*, 12:150–159. DOI: <https://doi.org/10.1016/j.inffus.2009.12.006>.
- [Zhang, 1994] Zhang, L. (1994). *Advances in the Dempster-Shafer Theory of Evidence*, chapter Representation, independence, and combination of evidence in the Dempster-Shafer theory, pages 51–69. John Wiley & Sons, Inc., New York.
- [Zhang et al., 2019a] Zhang, M. R., Lucas, J., Ba, J., and Hinton, G. (2019a). Lookahead optimizer: k steps forward, 1 step back. In *Advances in Neural Information Processing Systems. Annual Conference on Neural Information Processing Systems (NeurIPS)*. Vancouver, BC, Canada.
- [Zhang et al., 2019b] Zhang, Q., Jiang, K. X., Yan, M., and Ma, J. Y. (2019b). A competitive multiattribute group decision-making approach for the game between manufacturers. *Computational Intelligence and Neuroscience*, 2019. DOI: <https://doi.org/10.1155/2019/8389035>.
- [Zhu et al., 2023] Zhu, T., Qiao, D., and Han, H. (2023). Artificial intelligence-assisted spacecraft swarm reconfiguration planning. In *5th Chinese Conference on Swarm*

Intelligence and Cooperative Control. Lecture in Electrical Engineering, volume 934, pages 583–592. DOI: https://doi.org/10.1007/978-981-19-3998-3_56.

[Zuiani and Vasile, 2014] Zuiani, F. and Vasile, M. (2014). Extended analytical formulas for the perturbed Keplerian motion under a constant control acceleration. *Celestial Mechanics and Dynamical Astronomy*, 121:275–300. DOI: <https://doi.org/10.1007/s10569-014-9600-5>.